

Ultimate bodybuilding: The
quest for exoskeletons p. 270

Giving a boost to quantum
electronics pp. 280 & 307

Engineering remote-
controlled T cells p. 293

Science

\$10
16 OCTOBER 2015
sciencemag.org

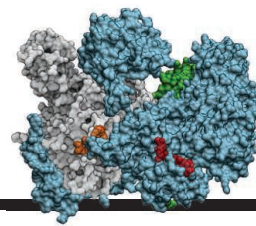
AAAS



Flying past Pluto

New Horizons finds surprises
at Pluto and Charon pp. 260 & 292

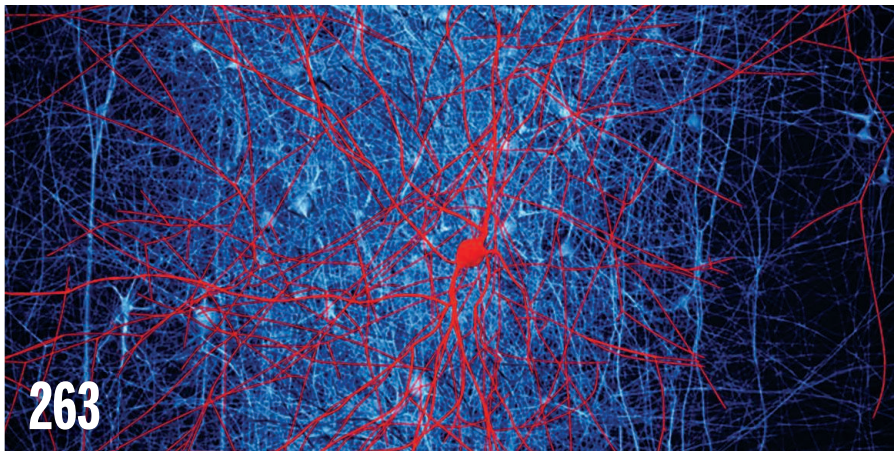
CONTENTS



278 & 291

Structural insight into gene silencing

16 OCTOBER 2015 • VOLUME 350 • ISSUE 6258



263

NEWS

IN BRIEF

258 Roundup of the week's news

IN DEPTH

260 LATE HARVEST FROM PLUTO REVEALS A COMPLEX WORLD

Months after its famed flyby, New Horizons is still giving scientists plenty to ponder *By E. Hand*

► RESEARCH ARTICLE P. 292

261 NIH DEBATES HUMAN-ANIMAL CHIMERAS

Grant to add human cells to animal embryos is delayed *By G. Vogel*

263 VIRTUAL RAT BRAIN FAILS TO IMPRESS ITS CRITICS

The Blue Brain Project publishes its simulation of 30,000 neurons *By K. Kupferschmidt*

264 FIRST MODERN HUMANS IN CHINA

Contemporary-looking teeth found in cave suggest that *Homo sapiens* left Africa much earlier than expected *By A. Gibbons*

265 NOBEL FOR ANTIMALARIAL DRUG HIGHLIGHTS EAST-WEST DIVIDE

Traditional Chinese medicine's vast cornucopia has produced many claims, few bona fide drugs *By D. Normile*

266 DNA'S REPAIR TRICKS WIN CHEMISTRY'S TOP PRIZE

Experiments showed how enzymes keep mutations from wrecking the molecule of life *By E. Stokstad*

FEATURES

267 BUZZ FOOD

Feeding insect meal to livestock could help the planet, but will it be good for people? *By K. Kupferschmidt*

270 IN PURSUIT OF THE PERFECT POWER SUIT

A longstanding quest to augment human performance with robotic exoskeletons takes a softer approach *By W. Cornwall*



259

INSIGHTS

PERSPECTIVES

274 RESTORING THE SENSE OF TOUCH

Flexible circuitry mimics the way skin transduces pressure signals *By P. Anikeeva and R. A. Koppes*

► REPORT P. 313

275 WHEN SUGAR IS NOT SO SWEET

Chemical synthesis of glucosepane promises insights into the role of this molecule in diseases of aging

By D. L. Boger

► REPORT P. 294

277 COMET SIDING SPRING, UP CLOSE AND PERSONAL

Observations during a close flyby of Mars shed light on a little-understood group of comets

By C. Lisse

278 CHROMATIN COMPLEX, CRYSTAL CLEAR

The long-sought structure of an active polycomb repressive complex is solved *By M. Schapira*

► RESEARCH ARTICLE P. 291

280 PUMPING UP THE QUANTUM

A superconducting amplifier is used to boost quantum signals

By A. N. Cleland

► REPORT P. 307

281 CHALLENGE FACULTY TO TRANSFORM STEM LEARNING

Focus on core ideas, crosscutting concepts, and scientific practices

By M. M. Cooper et al.

282 PERSONALIZATION IN PRACTICE

Dynamic computational modeling integrated with experimentation can enable precision medicine

By R. Iyengar et al.

BOOKS ET AL.

284 WHY TORTURE DOESN'T WORK

By S. O'Mara, reviewed by R. J. McNally

285 57 WAYS TO SCREW UP IN GRAD SCHOOL

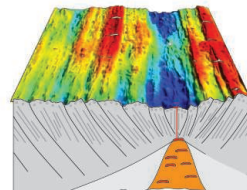
By K. D. Haggerty and A. Doyle, reviewed by O. Parsons

285 SODA POLITICS

By M. Nestle

Science Staff	256
New Products	343
Science Careers	344

CONTENTS



310

Origins of Earth's
seafloor hills

16 OCTOBER 2015 • VOLUME 350 • ISSUE 6258

LETTERS

286 MANY PATHS TO PARITY FOR WOMEN IN SCIENCE

By D. Burstein et al.

286 RELOCATION RISKY FOR BUMBLEBEE COLONIES

By J. D. Lozier et al.

287 RESPONSE

By J. T. Kerr et al.

RESEARCH

IN BRIEF

288 From *Science* and other journals

RESEARCH ARTICLES

291 TRANSCRIPTION

Structural basis of histone H3K27 trimethylation by an active polycomb repressive complex 2 L. Jiao and X. Liu

RESEARCH ARTICLE SUMMARY; FOR FULL TEXT:

dx.doi.org/10.1126/science.aac4383

► PERSPECTIVE P. 278

292 PLANETARY SCIENCE

The Pluto system: Initial results from its exploration by New Horizons S. A. Stern et al.

RESEARCH ARTICLE SUMMARY; FOR FULL TEXT:

dx.doi.org/10.1126/science.aad1815

► NEWS STORY P. 260; PODCAST

293 SYNTHETIC BIOLOGY

Remote control of therapeutic T cells through a small molecule-gated chimeric receptor C.-Y. Wu et al.

RESEARCH ARTICLE SUMMARY; FOR FULL TEXT:

dx.doi.org/10.1126/science.aab4077



REPORTS

294 ORGANIC SYNTHESIS

Concise total synthesis of glucosepane C. Draghici et al.

► PERSPECTIVE P. 275

298 CATALYSIS

Hydrogenation of carboxylic acids with a homogeneous cobalt catalyst

T. J. Korstanje et al.

302 SEPARATION MEMBRANES

CO₂ capture from humid flue gases and humid atmosphere using a microporous coppersilicate S. J. Datta et al.

307 QUANTUM INFORMATION

A near-quantum-limited Josephson traveling-wave parametric amplifier

C. Macklin et al.

► PERSPECTIVE P. 280

310 OCEANOGRAPHY

Sensitivity of seafloor bathymetry to climate-driven fluctuations in mid-ocean ridge magma supply

J.-A. Olive et al.

313 BIOMATERIALS

A skin-inspired organic digital mechanoreceptor B. C.-K. Tee et al.

► PERSPECTIVE P. 274

317 NEURAL PROGENITORS

Opposing intrinsic temporal gradients guide neural stem cell production of varied neuronal fates Z. Liu et al.

320 OCEAN VARIABILITY

The Atlantic Multidecadal Oscillation without a role for ocean circulation

A. Clement et al.

325 GENE EXPRESSION

Suboptimization of developmental enhancers E. K. Farley et al.

328 T CELL IMMUNITY

RIPK1 and NF- κ B signaling in dying cells determines cross-priming of CD8⁺ T cells N. Yatim et al.

334 T CELL IMMUNITY

Stable inhibitory activity of regulatory T cells requires the transcription factor Helios H.-J. Kim et al.

339 SMALL NONCODING RNA

Panoramix enforces piRNA-dependent cotranscriptional silencing Y. Yu et al.

DEPARTMENTS

257 EDITORIAL

Violence and women's health

By Nancy E. Adler and Paula A. Johnson

350 WORKING LIFE

The rewards of roughing it

By Xin Lu



ON THE COVER



The New Horizons probe captured this backlit image of Pluto as it flew past the dwarf planet on 14 July 2015. Scattered sunlight reveals numerous haze layers within Pluto's thin atmosphere, while

the surprisingly diverse surface landscape indicates ongoing geological activity. Studying Pluto and its moon Charon will help us understand how the solar system formed and our place within it. See pages 260 and 292 and dx.doi.org/10.1126/science.aad1815. Photo: NASA/Johns Hopkins University Applied Physics Laboratory/Southwest Research Institute

SCIENCE (ISSN 0036-8075) is published weekly on Friday, except the last week in December, by the American Association for the Advancement of Science, 1200 New York Avenue, NW, Washington, DC 20005. Periodicals mail postage (publication No. 484460) paid at Washington, DC, and additional mailing offices. Copyright © 2015 by the American Association for the Advancement of Science. The title SCIENCE is a registered trademark of the AAAS. Domestic individual membership and subscription (51 issues): \$153 (\$74 allocated to subscription). Domestic institutional subscription (51 issues): \$1282. Foreign postage extra: Mexico, Caribbean (surface mail) \$55; other countries (air assist delivery) \$85. First class, airmail, student, and emeritus rates on request. Canadian rates with GST available upon request. GST #1254 88122. Publications Mail Agreement Number 1069624. Printed in the U.S.A. Change of address: Allow 4 weeks, giving old and new addresses and 8-digit account number. Postmaster: Send change of address to AAAS, P.O. Box 96178, Washington, DC 20090-6178. Single-copy sales: \$10.00 current issue, \$15.00 back issue prepaid includes surface postage; bulk rates on request. Authorization to photocopy material for internal or personal use under circumstances not falling within the fair use provisions of the Copyright Act is granted by AAAS to libraries and other users registered with the Copyright Clearance Center (CCC) Transactional Reporting Service, provided that \$30.00 per article is paid directly to CCC, 222 Rosewood Drive, Danvers, MA 01923. The identification code for Science is 0036-8075. Science is indexed in the Reader's Guide to Periodical Literature and in several specialized indexes.

Violence and women's health

Last month, the Association of American Universities' Campus Climate Survey provided a disturbing picture of the extent of sexual assault on campuses in the United States. Almost a quarter of female graduates surveyed from 27 institutions indicated having experienced sexual assault during their undergraduate period. Distressingly, violence on campuses is part of a larger epidemic of sexual violence in the United States, making it a major women's issue. The widespread prevalence of exposure to violence and its immediate harm and long-term health consequences argue for greater efforts in both research and treatment.

It is estimated that a third of U.S. women will be assaulted at some point in their lives, and one in four will experience intimate partner violence. Women appear to suffer disproportionate long-term effects, showing increases of 80% in stroke and 70% in heart disease, asthma, and alcohol abuse.* Males and females differ both in the types of violence they are likely to encounter and in their responses, including the capacity to extinguish fear responses. As a result, women are more likely to develop post-traumatic stress disorder.†

Given gender differences in exposure, vulnerability, and response, strategies for gender-specific research and intervention spanning science, public health, and health care delivery are needed. Fortunately, efforts to identify and treat women's exposure to violence are increasing. Under the Affordable Care Act, screening and counseling for exposure to intimate partner violence and domestic violence is reimbursable for women from adolescence to age 65. In 2014, an Institute of Medicine committee on core social and behavioral information for electronic health records recommended a four-item screen assessing physical, sexual, and emotional abuse for reproductive-age women. The health care provider Kaiser-Permanente has been screening for intimate partner violence for over a decade. During this time, detection rates for women in-

creased 10-fold, awareness of this type of violence grew among health plan members and clinicians, and patients identified through screening were connected to mental health, crisis, and advocacy services. A "Trauma-Informed Care" approach to treatment that acknowledges gender-specific health effects of violence and promotes interprofessional collaboration is being implemented in several U.S. health care institutions. It is promising, but not yet standardized or broadly evaluated.



"...a third of U.S. women will be assaulted at some point in their lives..."

Silos within and across science, public health, and health care systems hamper our understanding of the determinants and consequences of violence. Research that informs primary prevention of the occurrence of violence, and secondary prevention of chronic diseases after exposure, must encompass biological, behavioral, and social determinants. Effective interventions need to integrate public health's expertise in surveillance and community triggers of violence with screening and treatment of individuals in the context of health care. The studies, ranging from basic research to clinical and community

intervention trials, will need to be adequately powered and include enough males and females to enable stratified analysis that can determine common and unique dynamics and needs of males and females.

The health of women is a major determinant of the health of communities. Women constitute over 50% percent of the population, and their health differentially affects the health and well-being of the next generation. An integrated research agenda is justified by the number and range of people affected by violence and its costs to individuals and to society. If a gene were identified that had the equivalent population penetrance and impact, few would question the need for substantial investment in understanding its mechanism of action and developing ways to avert the resulting health problems. We should do the same for violence.

– Nancy E. Adler and Paula A. Johnson



Nancy E. Adler is the Lisa and John Pritzker Professor of Medical Psychology, vice-chair of the Department of Psychiatry, and director of the Center for Health and Community at the University of California at San Francisco, San Francisco, CA. E-mail: nancy.adler@ucsf.edu



Paula A. Johnson is professor of Medicine at Harvard Medical School and executive director of the Connors Center for Women's Health and Gender Biology at Brigham and Women's Hospital, Boston, MA. E-mail: pajohnson@partners.org

*M. C. Black, M. J. Breiding, *Morb. Mortal. Wkly. Rep.* **57**, 113 (2008).

†National Comorbidity Survey, NCS-R Appendix Tables 1 and 2; available at www.hcp.med.harvard.edu/ncs.

“Last week we were reminded that U.S. weather forecasting is not what it should be.”

Representative Bill Foster (D-IL), a physicist, arguing for more research spending after a European model correctly predicted Hurricane Joaquin's path out to sea, whereas U.S. models forecast a direct hit.

IN BRIEF



A marine biologist assesses bleaching at Airport Reef in American Samoa in February 2015.

Third global coral bleaching event on record is underway

A trifecta of coupled climate-ocean events—ongoing global warming, a strong El Niño, and the warm “blob” in the Pacific Ocean—have led to the third worldwide coral bleaching event on record, scientists with the National Oceanic and Atmospheric Administration (NOAA) announced 8 October. The bleaching could ultimately destroy more than 12,000 square kilometers of coral this year. The

event began last year in the north Pacific and expanded this year into the south Pacific and the Indian Ocean. NOAA's models suggest that a strong El Niño will extend the global bleaching well into 2016. U.S. coral reefs in Hawaii and the Caribbean have already been acutely affected, NOAA says, and 95% of U.S. reefs will have been exposed to warm ocean temperatures that can cause bleaching by the end of the year.

AROUND THE WORLD

U.K. launches cancer challenge

LONDON | Cancer Research UK, the giant U.K. research charity, announced a £100 million (\$150 million), 5-year “grand challenge” competition that invites scientists to tackle seven tough questions in cancer. Teams including industry and academic researchers from around the world can submit ideas for solving the challenges, which range from distinguishing between lethal and nonlethal tumors to devising drugs that target *MYC*, a gene involved in many cancers. Preproposals are due in February and the first winning team, which will receive a grant of up to £20 million, will be announced in fall 2016. Cancer Research UK

plans to fund a new challenge each year for 5 years. <http://scim.ag/UKgrandchall>

Finding refugees science jobs

BRUSSELS | More than 500,000 refugees fled civil war and unrest in 2015 and sought safety in the European Union. Last week, the European Commission launched Science4Refugees, a program it says will help match refugees who are scientists with universities willing to hire them. Refugees and asylum-seekers with a science background can upload their resume on Euraxess, the E.U. research careers website; universities willing to help can advertise jobs, internships, or training programs as refugee-friendly. The program follows other

efforts to support refugees at the local or national level, including a planned pilot project by the Fraunhofer and Max Planck societies in Germany to ease integration of refugee scientists, and the United Kingdom's Council for At-Risk Academics, which in the 1930s helped scientists escape



Syrian refugees arrive in Greece in October.

the Nazi threat and is now helping scientists from Syria. <http://scim.ag/ECsciref>

Consumer spending nabs Nobel

STOCKHOLM | This year's Nobel Prize in Economics went to Angus Deaton, 69, a British-American economist at Princeton University whose work pioneered the study of consumption among poor families and individuals and how it differs from that of more affluent people. Deaton's research has injected data into the realm of conjecture and enabled economists to better model overall consumption and the effects of economic policies, playing an important role in the dramatic reduction in abject poverty seen globally in the past 3 decades. "It's long overdue," says Oriana Bandiera, a labor and development economist at the London School of Economics and Political Science, of Deaton's prize. "Professor Deaton's contributions to the field have been profound and transformative." <http://scim.ag/DeatonNobel>

Patients win gene patent victory

MELBOURNE, AUSTRALIA | On 6 October, Australia's highest court ended a legal saga over whether two genes related to breast and ovarian cancer—called *BRCA1* and *BRCA2*—can be patented. The court ruled that an isolated gene sequence is not a "patentable invention." In 2010, cancer survivor Yvonne D'Arcy challenged the patents, held by U.S. firm Myriad Genetics and its Melbourne-based licensee Genetic Technologies. Myriad had used the genetic information to develop diagnostic tests over which it held a potentially lucrative monopoly. The ruling aligns Australian legislation with that of the United States, South America, and most of Asia. Canada allows human gene patenting, as does the European Union if the biological material has been isolated by a technical process. <http://scim.ag/Ausgenepat>

FINDINGS

Gene editing for safer organs

Researchers have made a stride toward engineering safer pig organs for human transplants, thanks to the powerful gene-editing technique CRISPR. As reported this week in *Science*, the technology can slice up and inactivate potentially harmful viral sequences, known as porcine endogenous retroviruses, from 62 locations in the DNA of pig kidney cells. When tested in a lab dish, the edited cells showed as much as a 1000-fold reduction in their ability to infect human kidney cells with the retrovirus. The



NASA last week put thousands of images from the Apollo missions on Flickr, including this Apollo 11 astronaut's boot and footprint.

Russian project proposes to 'verify' Apollo moon landing

Even as NASA released a treasure trove of archived photos of the Apollo missions to the moon last week (<https://www.flickr.com/photos/projectpolloarchive/albums/>), a Russian team of space enthusiasts has announced a plan to convince stubborn skeptics that the landing actually happened. Led by Vitaly Yegorov, a public relations specialist with Moscow-based Dauria Aerospace, the group is proposing to build a private satellite that would head to the moon and snap high-resolution pictures of the U.S. landing sites there—along with any lingering traces of the astronauts' presence, if they can be seen. The group hoped to crowdfund the mission by raising at least 1 million rubles on Boomstarter.ru for the research stage of the project and to attract investors; at press time they had raised about 1,200,000 rubles (about \$20,000).

results are the most extreme example yet of the scope of genetic alterations possible with gene editing—previous work has altered only six sites at a time. The group must next demonstrate the same feat in pig embryos, which could be implanted into surrogate mothers. <http://scim.ag/geneedittrans>

NEWSMAKERS

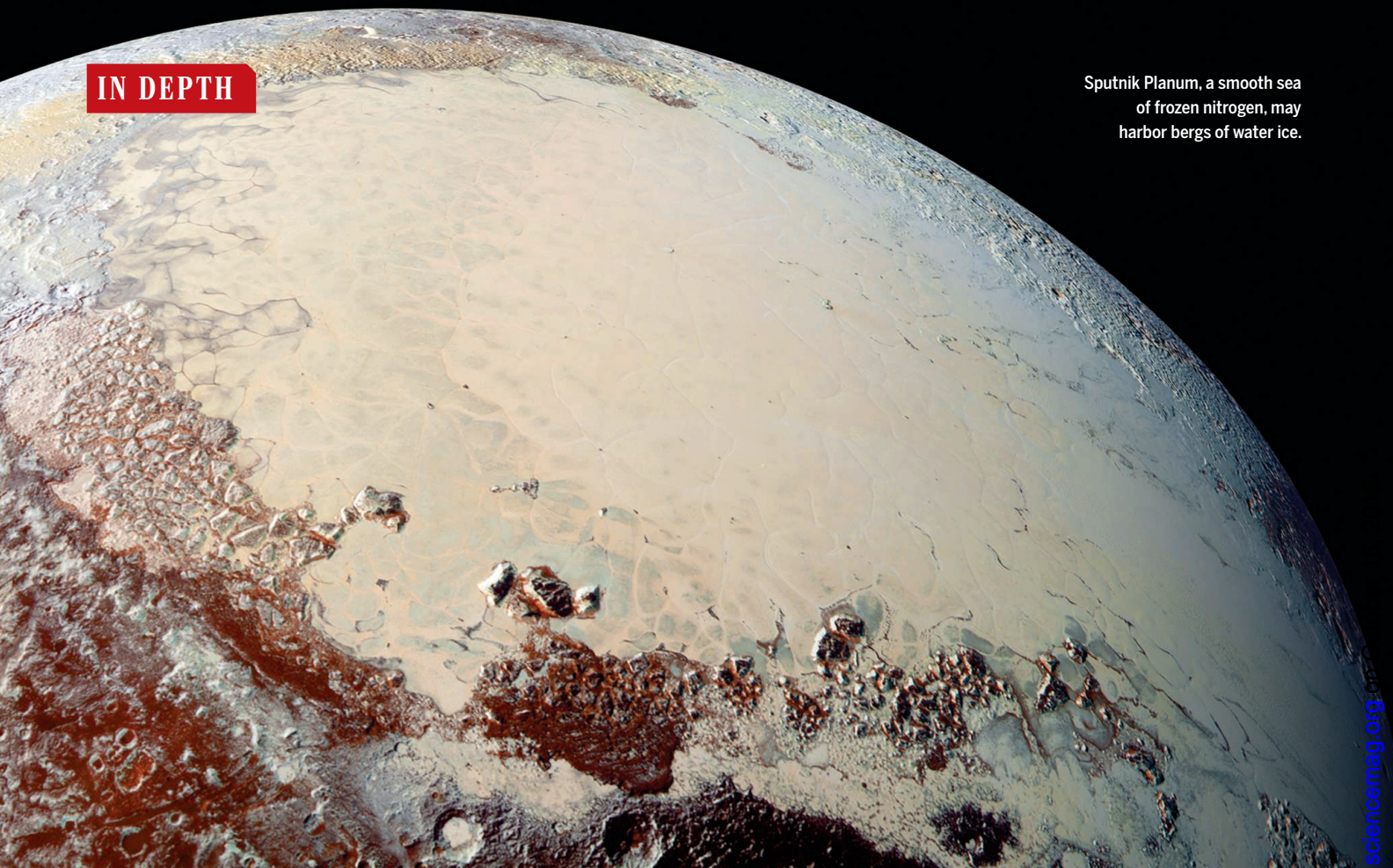
AIDS pioneer starts vaccine trial

Robert Gallo's U.S. National Cancer Institute laboratory published the four landmark papers in *Science* in 1984 that convinced the world that HIV causes AIDS. Although he has closely monitored the AIDS vaccine search, which has seen more than 100 products tested in humans, he has remained a spectator—until now. Gallo, 78, now runs the Institute of Human Virology (IHV) in Baltimore, Maryland. In collaboration with Profectus BioSciences, a biotech that spun off from IHV, Gallo and his team are launching their first clinical trial of an AIDS vaccine. The vaccine has an unusual method of protection: It attempts to trigger an antibody that can attach to HIV at a point in the infection process when the

virus temporarily shows a vulnerable side. The trial is expected to enroll 60 people and will assess safety and immune responses to the "full-length single chain" vaccine. <http://scim.ag/Gallovacctrtrial>

Astronomer guilty of harassment

A prominent astronomer at the University of California, Berkeley, has been found to have violated the university's policies on sexual harassment and told to shape up. But neither **Geoffrey Marcy** nor the university, which earlier this year completed its investigation into complaints against him going back more than a decade, is providing any details of the case, first reported last week by the website BuzzFeed. And the American Astronomical Society has rejected his request to publish an intended letter of apology that he posted on his website. Berkeley said Marcy has agreed to follow "clear expectations" regarding his conduct with students or face the possibility of immediate "sanctions." Marcy says in his letter, "While I do not agree with each complaint that was made, it is clear that my behavior was unwelcomed by some women." http://scim.ag/_Marcy



PLANETARY SCIENCE

Late harvest from Pluto reveals a complex world

Months after its famed flyby, New Horizons is still giving scientists plenty to ponder

By Eric Hand

In the buildup to the New Horizons encounter with Pluto in July, principal investigator Alan Stern said repeatedly that he was ready to be surprised. But now, as he examines the icy oddities in images beamed down from the spacecraft, he admits that New Horizons has outstripped his imagination. “The level of complexity is beyond what I expected,” says Stern, a planetary scientist at Southwest Research Institute (SwRI) in Boulder, Colorado. “There’s so much going on.”

Stern and his New Horizons colleagues this week publish their first results in a paper on page 292. They describe features of Pluto’s surface and atmosphere including a crust of water ice veneered with other frozen chemicals; a region of smooth, strangely youthful terrain; and a hazy atmosphere that has so far withstood the intensifying cold but is expected to freeze solid in the coming years.

But the surprises have not stopped coming. As New Horizons streaks outward into the region of icy worlds known as the Kuiper belt, it is sending back the data stored during its encounter in a stream limited by distance and the power of its transmitter. Bit by bit the data are building up into ever-better images and measurements of Pluto and its moons, and the researchers are scrambling to keep up. “Every week, a lot of new data land, and our jaws are on the ground,” Stern says.

Among the highlights so far:

“Snakeskin” terrain. Bladelike ridges, standing hundreds of meters tall, form rippled, scaly patterns in an area to the east of Sputnik Planum, a smooth, bright plain that dominates the planet. “It’s so bizarre,” Stern says. He says the ridges could have formed when ices of nitrogen, carbon monoxide, and methane sublimed into the atmosphere at different rates. Or they could have been scoured by wind. The thinness

of Pluto’s atmosphere suggests that only relatively weak winds blow there today. But millions of years ago, Stern says, idiosyncrasies of Pluto’s orbit could have made the dwarf planet warmer, with a thicker, Mars-like atmosphere. Under those conditions, Pluto could have spawned winds powerful enough to sculpt the ridges.

Ice mountains. Water ice is the only material on Pluto strong enough to jut several kilometers above the surface, Stern and his colleagues think. But a jumbled-up cluster of mountains on the edge of a region called Sputnik Planum may in fact be icebergs: chunks of water ice crust floating in a deep pool of frozen nitrogen. “Pretty trippy, huh?” says Jeff Moore, a New Horizons scientist at NASA’s Ames Research Center in Mountain View, California.

What could have severed the icebergs from the bedrock? William McKinnon, a New Horizons scientist at Washington University

in St. Louis in Missouri, says that, at depth, pressures and temperatures would allow nitrogen ice to melt. “Liquid nitrogen could be a sort of groundwater on Pluto,” he says. “It could be coursing through the ice crust, and it could perhaps undermine terrain and lead to the dislocation of crustal blocks.”

Sputnik Planum itself. The smoothest part of Pluto’s bright heart raises a broader riddle: how this lake of frozen nitrogen, hundreds of kilometers across, got there, and when. The lack of impact craters suggests the surface is at most 100 million years old, but what goes on beneath it is a mystery. “What we can’t see is the plumbing,” McKinnon says. Moore says that as higher resolution topography becomes available, the team will scan it for any subtle warping that could indicate warmer plumes of nitrogen ice pushing up from below.

High haze. When New Horizons turned back to look as Pluto blotted out the sun, the spacecraft saw layers of haze ringing the planet: particles made of frozen acetylene, ethylene, and other molecules, floating as much as 150 kilometers up. Deputy project scientist Cathy Olkin of SwRI is trying to trace where it comes from. “Are you forming it that high up, or are you lofting it upward?” she asks. One possibility, she says, is that molecules high in the atmosphere absorb cosmic rays or UV light from the sun, triggering chemical changes that allow haze particles to form. She is analyzing spectral data to determine the chemistry of the haze, which could show whether that origin story is true.

A doomed atmosphere? In 1989, Pluto passed its closest point to the sun in its elliptical orbit and started getting colder. Some models predict that sometime in the next decade, its atmosphere will collapse when the nitrogen freezes out. Yet Earth-based observations of starlight passing through Pluto’s atmosphere, made over the past 25 years, suggest that, far from freezing out, the atmosphere is actually expanding a bit.

Now, a radio instrument on board New Horizons has detected a low surface pressure, which at first blush might signal that the freeze-out is underway. But Michael Person, a planetary scientist at the Mas-

sachusetts Institute of Technology in Cambridge, says the low pressure can be reconciled with the Earth-based observations, which are sensitive only to the upper part of Pluto’s atmosphere. “If there is a freeze-out coming, it hasn’t started yet,” Person says. “But that doesn’t mean it won’t start soon.”

Density and deep history. In a simple but potentially far-reaching discovery, New Horizons has measured Pluto’s diameter far more precisely than ever before. The new number, 2374 kilometers, is smaller than previous measurements—which makes Pluto’s density higher and closer to that of its largest moon, Charon. That’s important, because Pluto and Charon—like Earth and its moon—are thought to have formed billions of years ago in a giant collision between two progenitor bodies. The similar densities suggest that those predecessors were also similar, Stern says. That could mean that the tremendous diversity astronomers see in Kuiper belt objects (KBOs) today all evolved after the objects formed, in the past 4.5 billion years. “You can’t judge a book by its cover—the



Backlit images of Pluto’s atmosphere revealed a puzzling high-altitude haze.

same is true of [KBOs],” he says. “This could argue in a profound way for a more homogeneous population” of progenitors.

New Horizons’ best images are yet to come. Project scientist Hal Weaver, of the Johns Hopkins University Applied Physics Laboratory in Laurel, Maryland, says the highest resolution images, about 70 meters per pixel, are scheduled to be downloaded in November. Meanwhile, the New Horizons team is looking ahead to other KBOs. Over 2 weeks beginning on 22 October, New Horizons will change course toward a New Year’s Day 2019 rendezvous with 2014 MU69, an object less than 50 kilometers across. Weaver says the team plans to send the spacecraft within 20,000 kilometers of the object. (It flew within 12,500 kilometers of Pluto.)

In the meantime, New Horizons will be keeping its eyes open. En route to 2014 MU69, it ought to see about a dozen KBOs at least as well as the Hubble Space Telescope can. Although the images will be little more than points of light, they should reveal information about the objects’ surface textures, as well as whether they are binaries, as most KBOs are suspected to be.

Stern is ready for the next surprise. ■

STEM CELLS

NIH debates human-animal chimeras

Grant to add human cells to animal embryos is delayed

By Gretchen Vogel

Few grants are more coveted than a Pioneer Award from the U.S. National Institutes of Health (NIH), which provides up to \$500,000 annually for 5 years to a researcher pursuing innovative, potentially groundbreaking research. So when Juan Carlos Izpisua Belmonte, a developmental biologist at the Salk Institute for Biological Studies in San Diego, California, heard from NIH earlier this year that his was among the top-ranked applications, he was thrilled—but there was a catch. The application is on hold, the agency has told him, as NIH reconsiders its rules for the kind of experiments he wants to do: mixing human stem cells into very early animal embryos and letting them develop, a strategy that could produce tissues or organs for transplantation.

On 23 September, NIH issued a notice saying that it will not fund such research “while the Agency considers a possible policy revision in this area.” And it has invited scientists and bioethicists to a meeting on 6 November to discuss the ethical questions raised by such experiments. Izpisua Belmonte took the news in stride. “I’m not upset. Quite the opposite. I think it is great that we openly discuss this and hope that a conclusion is reached,” he says.

The mixtures of cells under debate are called chimeras, named for a monster of Greek mythology that had the body and head of a lion, a fire-breathing goat’s head on its back, and a snakelike tail. In ancient Greece, the chimera was a bad omen, appearing before shipwrecks, volcanoes, and other disasters.

Scientists see the term in a more positive light, using animal chimeras in a range of developmental biology and stem cell experiments. Chimeras that combine animal and human cells, especially those that involve pluripotent human cells, raise ethical questions, however. Pluripotent cells are a powerful type of stem cell that can become any cell type in the body. Some worry that such human cells, when combined with animal em-

bryos, could develop into brain cells, sperm, or egg cells in the chimeric offspring.

The U.S. National Research Council and the Institute of Medicine recommended limits on such research in 2005, among them that no human stem cells be added to primate embryos and that animal-human chimeras not be allowed to breed (*Science*, 29 April 2005, p. 611). Current NIH funding guidelines, finalized in 2009, reflect those recommendations. They prohibit breeding animals in which human stem cells might have become sperm or eggs, and they rule out primate-human experiments. They do not, however, prohibit injecting human pluripotent cells into the embryos of other animals and letting the chimeras develop.

That is what several groups of researchers are now trying to do. Their goal is to learn how to coax stem cells to become specific tissues or organs. Doing that in the lab, by recreating the 3D environment of a developing organ and reproducing all the signals it receives, is very difficult. “We don’t know how to guide the cells to become the cells we want,” Izpissúa Belmonte says. Instead, he and his colleagues want “to use the animals as an incubator. We don’t know how they do it, but every day [developing animals] produce perfect organs.”

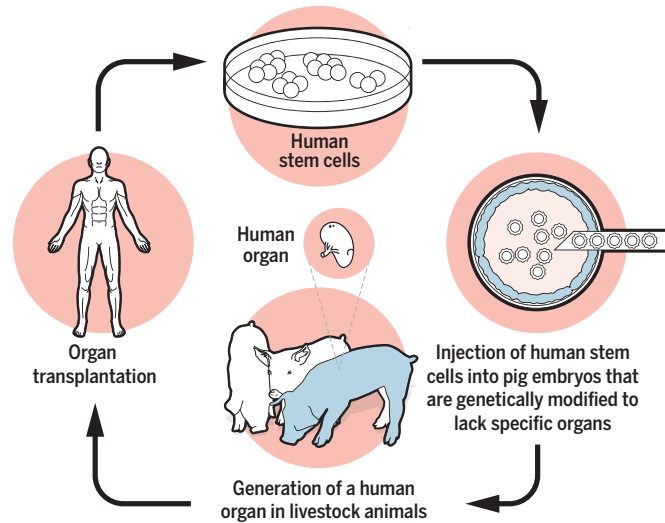
So, Izpissúa Belmonte and others have set out to knock out the genes that drive the creation of specific organs or tissues, such as the pancreas, in an animal embryo and then inject human pluripotent stem cells into it. They hope that the human cells will preferentially fill the void left by the animal’s missing pancreatic cells, forming a human pancreas in the developing animal.

Earlier this year he and his colleagues identified a new type of human pluripotent stem cell that seems to be especially good at contributing to animal embryos. By injecting these cells into pig embryos, they have now made chimeras that have developed for 2 to 3 weeks. (He uses non-NIH funds for the work.) So far, Izpissúa Belmonte says, no human cells have been seen in the nervous system. The cells do, however, contribute to the developing pancreas and heart.

The Pioneer Award would have enabled him to take the effort further, but last month Izpissúa

Using chimeric animals as organ incubators

Some researchers hope to grow human organs from stem cells by adding them to developing animals.



Belmonte received a letter from NIH saying that the application had been put on hold and inviting him to the upcoming meeting on chimeras. Izpissúa Belmonte will be there. “I applaud this workshop. It’s important to have guidelines so that researchers have a clear path in this promising and fast-moving area.”

An NIH spokesperson tells *Science* that the agency wants to “evaluate the state of the science in this area, the ethical issues that should be considered, and the relevant animal welfare concerns.” NIH says that no current grant has been halted by the funding pause, but other scientists fear that the workshop is a step toward broader restrictions, says Steve Goldman, a neuroscientist at the University of Rochester in New York whose work involves injecting human stem cells into mouse brains. That approach is not affected by the new rule, since he doesn’t work with early embryos, but NIH



A mouse, a mouse made with rat stem cells, a rat with mouse stem cells, and a rat.

has asked him to speak at the November meeting.

Sean Wu, who studies heart stem cells at Stanford University in Palo Alto, California, says the NIH notice prompted Stanford to urge scientists to be sure their experiments didn’t violate the new rules. “We were bombarded” with emailed warnings, says Wu, who received an NIH New Innovator Award in 2008 to study interspecies chimeras. The university announcement came “out of the blue”, he notes, and has spread confusion and concern. An NIH decision not to fund the work would be a big blow to the field, Wu says. “No one wants to do it if NIH won’t fund it.”

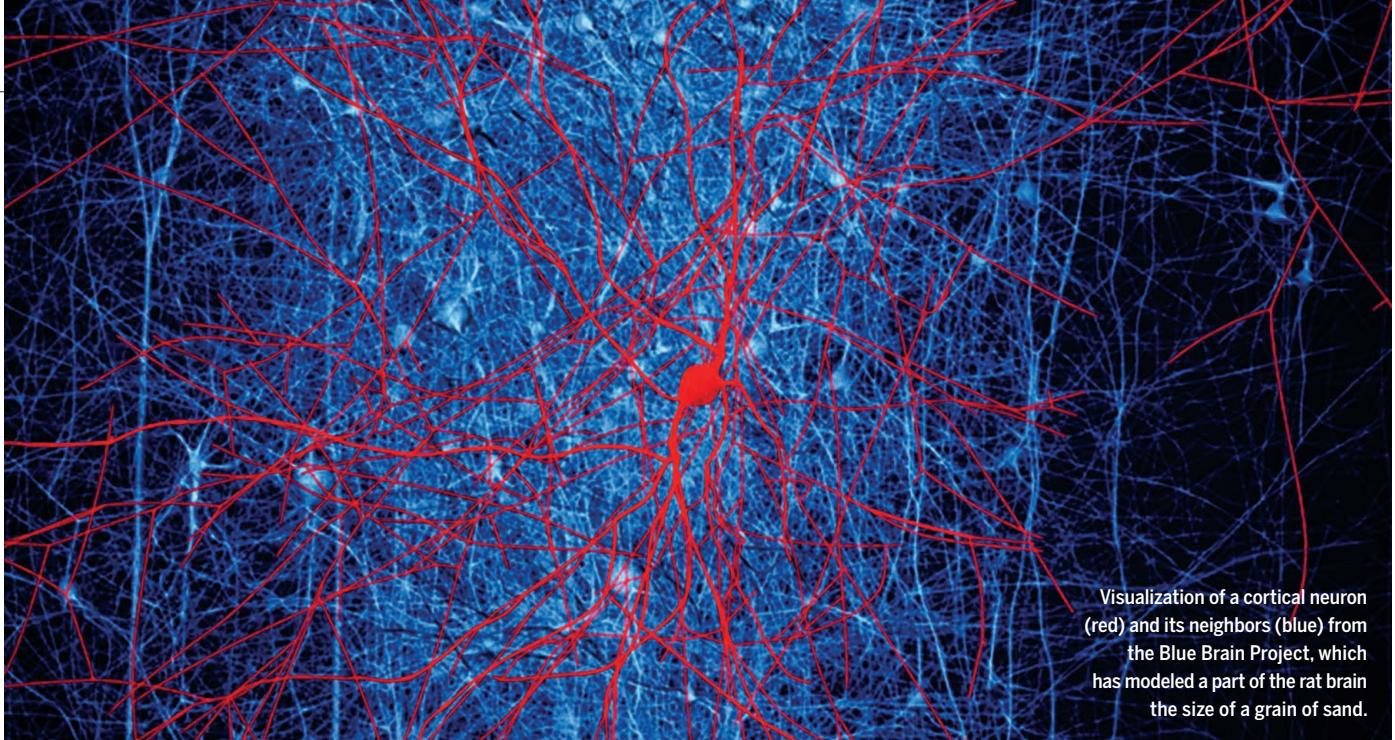
For Hiromitsu Nakauchi, a stem cell scientist at Stanford University, and the University of Tokyo, the debate is familiar. He showed in 2010 that

by adding rat stem cells to mice embryos lacking a pancreas gene, he could grow a rat pancreas in a mouse. The technique also enabled his team to grow a pancreas from one pig species in the body of another. But the follow-up experiments he wanted to do with human stem cells in goat or pig embryos were forbidden in Japan (*Science*, 28 June 2013, p. 1509). An ethics commission decided that the experiments should be allowed, but official regulations still aren’t in place, Nakauchi says. In part because of the restrictions in Japan, he accepted a position at Stanford University, where he received \$6.2 million for the work from the California Institute for Regenerative Medicine (CIRM).

Nakauchi’s project is proceeding with colleagues at the University of California, Davis, and at Stanford, where they have injected human induced pluripotent stem cells into sheep embryos. He was planning to apply for NIH funding to continue the work, and the agency’s announcement surprised him.

Using chimeras to grow human tissues is a long way from the clinic, Izpissúa Belmonte stresses, but his initial results have him optimistic that the approach is a viable one. “I am very excited about this project,” he says. “We need to do the experiments and see.” Whether NIH will support that work may be determined next month. ■

With reporting by Jocelyn Kaiser.



Visualization of a cortical neuron (red) and its neighbors (blue) from the Blue Brain Project, which has modeled a part of the rat brain the size of a grain of sand.

NEUROSCIENCE

Virtual rat brain fails to impress its critics

The Blue Brain Project publishes its simulation of 30,000 neurons

By Kai Kupferschmidt

Critics of Henry Markram—and there are many—complain that he promises far more than he can deliver. A charismatic and mediagenic neuroscientist working at the Swiss Federal Institute of Technology (EPFL) in Lausanne, Markram persuaded the European Commission to fund the Human Brain Project (HBP), a €1 billion plan to simulate the entire human brain in a computer—an effort doomed to fail, many scientists say. As proof, they have cited the Blue Brain Project, another Markram endeavor that was lavishly funded by the Swiss government. It set out in 2005 with the more modest target of modeling the rat brain but produced few tangible results.

But now, the Blue Brain Project finally has something to show for the investment. In a *Cell* paper published last week, researchers unveiled the most detailed digital reconstruction of brain tissue ever built: A simulation of 30,000 neurons, connected by almost 40 million synapses, in a piece of rat brain about the size of a grain of sand. The sprawling 37-page paper, co-authored by 82 scientists in eight countries, shows that building an in silico model of the human brain is feasible as well, Markram says—and that he's not selling pipe dreams. "When I started at EPFL, this is what I promised to deliver," he says, "and I have

delivered it."

Some scientists are impressed, including Christof Koch, the head of the Allen Institute for Brain Science in Seattle, Washington. "Following Richard Feynman's dictum 'What I cannot create, I do not understand,' this amounts to a hard-nosed, engineering demonstration of how much progress the field has made over the last few decades in synthesizing the behavior of neuronal networks," he says.

But the paper has done little to convince skeptics. "This is an enormous amount of neuroanatomy work and there is no doubt that that is important," says Alexandre Pouget, a computational neuroscientist at the University of Geneva in Switzerland and a longtime critic of the HBP. "But the model teaches us nothing. It computes nothing, it represents nothing." Nor does it prove that the attempt to model the human brain—which is 2 million times the size of the speck covered in the new paper—can achieve anything worthwhile, he adds. But Pouget suspects it's good PR nonetheless. "If we're talking politics and perception, I think this is good news for the [HBP]."

Peter Latham, a neuroscientist at University College London, agrees. "I think the [HBP] is a waste of money, but after reading this paper I am slightly more in favor of it," he says. "This paper may actually save the [HBP]."

The HBP was foundering last year after

hundreds of scientists signed an open letter charging that it was badly managed and too narrowly focused scientifically. The signatories threatened to boycott the project unless the program was broadened and its governance improved. An independent review ordered by the European Commission and a mediation panel largely agreed with the critics, which led to a series of structural reforms at the HBP and a diminished role for Markram (*Science*, 27 March, p. 1406). "As you can imagine, publishing this paper was very tough in a climate of extreme prejudice based on second-hand information," Markram says. "Now, at least everyone can judge the science directly for themselves."

The Blue Brain team set out to model a piece of rat sensory cortex that processes information from a hindlimb. In a first step, the scientists had to recreate the anatomy of this area. The team took measurements of thousands of neurons in rat brains, from their form and size to the electrical signals they produced. Based on those data and the scientific literature, the scientists came up with 55 distinctive types of neurons. Guided by measurements of cell type density, the researchers distributed thousands of neurons in the simulated brain tissue.

The model predicted that the virtual neurons would connect and exchange information at 200 million synapses, which was much more than expected in such a

tiny piece of tissue. The scientists used an algorithm to limit the number to a more realistic 37 million. In a second step, each neuron was matched with a certain pattern of electrical activity, based on years of recording neurons, and each synapse assigned to either activate a neighboring neuron or inhibit it. Simulations of electrical activity run on the model match measurements in living cells and animals, the team writes in *Cell*.

The model leaves out many features of brain tissue, such as blood vessels and glial cells, which account for 90% of the cells in the brain but are generally not involved in relaying signals. That's because it's only a first draft, Markram emphasizes: "We will include more data in the future."

Chris Eliasmith, a theoretical neuroscientist at the University of Waterloo in Canada, argues that the model may already have too much information. The researchers were successful in replicating certain of the brain's behaviors, he says. "But you can get all those results with a way less complicated model." In 2012, Eliasmith published a model that includes 2.5 million neurons with about a billion connections, although at a much lower resolution than the Blue Brain version (*Science*, 30 November 2012, p. 1202). "If we build highly detailed neural models, we should ask questions that show how and why those details matter," he wrote in an email. "That was not done here. Complexity for complexity's sake is a mug's game."

The Blue Brain team has made their model available online; anyone can examine it on their PC, but to run a simulation you need the power of a supercomputer, Markram says. He says the model has already proven useful for generating hypotheses. For instance, the researchers found that reducing the amount of calcium ions in the model led to a change in the activity patterns, from synchronized bursts of firing to an asynchronous pattern. "There is a transition there. That is an interesting finding," Markram says—and neuroscientists will be able to uncover other phenomena using the model, he argues.

In the end, the question is whether such new insights are worth the massive investment, Latham says. "Do you want to spend a billion euros on this? That's the question." Markram has no doubt that the answer is yes. A hundred years ago, Spanish biologist Santiago Ramón y Cajal made invaluable contributions to neuroscience by peering through a microscope and drawing the cells he saw in brain tissue, he says. "What do you think Ramón y Cajal would be doing today? He would do what we are doing." ■

HUMAN EVOLUTION

First modern humans in China

Contemporary-looking teeth found in cave suggest that *Homo sapiens* left Africa much earlier than expected

By Ann Gibbons

For decades, anthropologists have tried to trace the patchy trail left by the earliest modern humans out of Africa. But they have been stymied by gaps in the fossil record or unreliable dates, especially in East Asia. Now, Chinese anthropologists report 47 teeth of *Homo sapiens* from a cave in southern China, dated to 80,000 to 120,000 years ago. If the dating is accurate, the discovery pushes back the appearance of our species in Asia by at least 30,000 years, wiping out a long-standing picture in which modern humans swept out of Africa in a single wave 50,000 to 70,000 years ago.

"This changes everything. It's the best evidence we have for modern humans in East Asia this early," says archaeologist Michael Petraglia of the University of Oxford in the United Kingdom, who was not part of the work but has long advocated an early migration out of Africa. Others question the dates. "This case is better than the previous similar claims, but it is not fully convincing," says paleoanthropologist Yousuke Kaifu of the National Museum of Nature and Science in Tokyo.

Most researchers agree that modern humans arose in Africa and first ventured out of that continent into the Middle East about 120,000 to 90,000 years ago, as shown by skulls from Israel. But *H. sapiens* remains don't appear in Europe, East Asia, and Australia until 40,000 to 50,000 years ago. Older fossils in Asia proposed as *H. sapiens* are controversial. Genetic studies, too, suggest that humanity's great global expansion began just 50,000 to 70,000 years ago.

But Petraglia and others have unearthed sophisticated stone tools from the Arabian Peninsula and India, persuading him that modern humans left Africa as long ago as

125,000 years, settled in a then-wet Arabia, then pushed into India and eastward (*Science*, 29 August 2014, p. 994). Skeptics counter that other archaic humans could have made the tools, and that fossils are needed as proof.

Hence the excitement about the teeth reported this week in *Nature*, from Fuyan Cave in Daoxian in southern China, about 600 kilometers northwest of Hong Kong. A team led by Wu Liu and Xiu-Jie Wu of the Chinese Academy of Sciences' Institute of Vertebrate Paleontology and Paleoanthropology in Beijing found small teeth

with slender roots that barely differed from modern Chinese teeth. Indeed, the wear pattern and shape of the teeth are so modern that some wonder how they could be so old.

The dates come from a small stalagmite, part of a flowstone that capped the layer holding the teeth. The team used the radioactive decay of uranium to thorium to date this stalagmite to 80,000 years ago—a minimum age for the teeth. Fossils of extinct elephants, and



These fossil teeth may have belonged to the first *Homo sapiens* in China.

pandas in the hominin layer are 120,000 years old at most, so the team concluded that the teeth are 80,000 to 120,000 years old, says co-author Maria Martín-Torres of University College London.

But the dated stalagmite came from a different trench than the teeth, and may be of a different age, says paleoanthropologist Russell Ciochon of the University of Iowa in Iowa City: "The actual dates reported for Fuyan Cave are probably good but I doubt that the teeth are that old."

The authors insist that the stratigraphy in the cave is clear. Liu even argues that the find supports the radical—and minority—view that our species was born in China, not Africa. The discovery is likely to spur "a lot of debate," Martín-Torres says, "and force a new look at other alleged [*H. sapiens*] sites in China." ■



Some claim this year's medicine Nobel endorses TCM, seen here for sale in Suzhou, China.

and prescription medications for asthma, was isolated from the Chinese medicinal herb ma huang (*Ephedra sinica*) in the 1880s. In recent decades, TCM has yielded both artemisinin and arsenic trioxide, a treatment for acute promyelocytic leukemia.

Many groups are trying to extend the list of TCM-derived drugs. A screening effort at the Hong Kong University of Science and Technology (HKUST) launched in 1999 has produced "a portfolio of promising drug leads for the treatment of brain diseases and disorders," says Sejal Mody, a researcher at HKUST's Biotechnology Research Institute. A similar screening effort called the Herbalome Project, started in 2008 at the Dalian Institute of Chemical Physics, has found a promising painkiller in *Corydalis yanhusuo*, a flowering plant. Described in *Current Biology* in 2014, the compound, dehydrocorybulbine, is undergoing further study. Project director Xinniao Liang says several other active compounds are being tested in animals.

TCM's practitioners say, however, that no single compounds can explain the effectiveness of their remedies. Instead TCM relies on mixtures of ingredients, tailored to a patient, working synergistically. But rigorously testing such customized mixtures isn't easy. One much-touted example is the individualized TCM concoctions used throughout the world to ameliorate the toxicity of cancer chemotherapy. To test their effectiveness, Tony Mok, a clinical oncologist at the Chinese University of Hong Kong, ran a trial in which cancer patients received either a customized prescription of TCM herbs or similarly prepared placebo. His team found that the TCM preparations had no effect on toxicity.

Alternative medicine skeptic Edzard Ernst, formerly of the University of Exeter in the United Kingdom, has scoured the literature for similar rigorous trials of individualized TCM treatments; the few he has found were all negative. There is "no convincing evidence to support the use of individualized herbal medicine in any indication," he says.

TCM proponents say it's a matter of getting the recipes right. The key is "the application of a holistic approach, namely, the use of standardized TCM formulas," says Tianhan Xue, a natural products chemist in California who has worked on TCM-based drug discovery. He claims there is lab evidence of a synergistic effect when using combinations of herbal materials. "Though I do agree that we need more quality studies," he says.

"Quality science is the only solution," Mok says. "But once science is in, is it still TCM?" ■

With reporting by Hao Xin.

DRUG DISCOVERY

Nobel for antimalarial drug highlights East-West divide

Traditional Chinese medicine's vast cornucopia has produced many claims, few bona fide drugs

By Dennis Normile, in Shanghai, China

The question at last week's press conference announcing the Nobel Prize in Physiology or Medicine sparked a frisson of tension in the staid Stockholm hall. Referring to the award of half of the prize to pharmacologist Youyou Tu for deriving the antimalarial drug artemisinin from a plant used in traditional Chinese medicine (TCM), a Chinese reporter asked: "Can we say this is the first time you award [recognition to] TCM?" "We are not giving a prize to traditional medicine," shot back Hans Forsberg, a member of the selection committee. TCM was a source of inspiration, he explained, but the prize was for discovering a new drug.

That message was widely missed, especially in China. The laureate—at the China Academy of Traditional Chinese Medicine in Beijing—proclaimed artemisinin "a gift from TCM to the world," in an interview with Xinhua News Agency. Xinhua also quoted a congratulatory letter from Premier Li Keqiang saying the Nobel "marks a great contribution of traditional Chinese medicine (TCM) to the cause of human health." Encompassing herbal medicine, acupuncture, and other practices based on principles dating back 2000 years, TCM is big business in China, generating \$95 bil-

lion in revenue in 2014.

Commentators outside China also saw a victory for alternative medicine in the award, which Tu split with two other scientists, who derived an antiparasitic drug from a soil bacterium. "Nobel Goes to Pioneers of Natural-Based Medicines," read a headline on the NBC News website. The Association of Accredited Naturopathic Medical Colleges, based in Washington, D.C., portrayed the award as an endorsement for its practitioners' embrace of acupuncture, herbalism, and other natural remedies. "Naturopathic Medicine is front and center for this year's Nobel Prize in Medicine," the group boasted on Facebook.

In fact the award exposes a widening rift between the biomedical mainstream and proponents of alternative therapies. Yi Rao, a neuroscientist at Peking University in Beijing, calls Tu's recognition well-deserved: artemisinin has saved millions of lives, and Rao believes more gems will be found among TCM's formidable formulary. But it will take scientific methods to discover those gems, he says. Claims of benefits for TCM herbal recipes themselves "have never been proven."

Drugs derived from natural products make up a significant part of the modern pharmacopeia, but so far few of them came from TCM. Ephedrine, an amphetaminelike stimulant used in over-the-counter decongestants

NOBEL PRIZES

DNA's repair tricks win chemistry's top prize

Experiments showed how enzymes keep mutations from wrecking the molecule of life

By Erik Stokstad

Considering how much depends on the messages it bears, DNA is an alarmingly fragile molecule. It's vulnerable to UV light and mutagenic chemicals, as well as spontaneous decay. Life has survived through the ages because enzymes inside every cell ensure that DNA remains in proper working order. This year's Nobel Prize in chemistry, announced 7 October, recognizes three scientists who discovered key mechanisms for fixing the damage. "These are classic studies and a great prize for DNA repair," says Jacqueline Barton, a chemist at California Institute of Technology in Pasadena.

The discoveries were made in the 1970s and 1980s by Paul Modrich of Duke University School of Medicine in Durham, North Carolina; Aziz Sancar of the University of North Carolina, Chapel Hill—the first Turkish scientist to receive a Nobel—and Tomas Lindahl of the Francis Crick Institute at Clare Hall Laboratory in Hertfordshire, U.K. "I feel very lucky and proud to be selected," Lindahl said by phone during the press conference in Stockholm at which the prize was announced.

Biologists have long known that DNA wasn't rock solid. Blasts of x-rays, for example, could cause mutations in cells. Yet most researchers believed that the molecule was inherently stable. After all, cancer and other genetic malfunctions are the exception, not the rule.

As a postdoc in the late 1960s, however, Lindahl began to have doubts. Samples of RNA in his experiments rapidly degraded when heated. Further experiments showed that even under normal conditions, DNA quickly suffered enough damage to make life impossible. A light bulb went on. "Lindahl had the critical insight," says biochemist Bruce Alberts of the University of California, San Francisco.

Lindahl began to search for enzymes that might repair this unseen damage. Among other things, he studied a malfunction in which a part of the

nucleotide cytosine—one of the four bases that make up DNA—degrades at everyday temperatures. When the DNA molecule replicates, this damaged base matches up with the wrong kind of nucleotide, thus introducing errors into the genetic code. Lindahl discovered a process, now called base excision repair, in which enzymes continually spot and replace such interloper bases. He and colleagues described the mechanism in 1974.

At about this time, Sancar, who was working as a doctor in the Turkish countryside, decided he would rather study biochemistry. During his doctoral research at the University of Texas, Dallas, he cloned the gene for photolyase, an enzyme that helps bacteria fix damage from otherwise lethal doses of UV light. Later, while working as a lab technician at Yale University School of Medicine, Sancar uncovered another repair mechanism, nucleotide excision repair, which allows cells to fix a different kind of damage from the one Lindahl studied, using different enzymes.

Modrich tackled a third source of error: mistakes that happen during replication, when the two strands of DNA unzip and are copied. A common problem is that a wrong

nucleotide is added to the new strand, resulting in an error called a mismatch of base pairs. Enzymes efficiently fix these errors—and Modrich helped figure out how it happens. In the late 1970s, he was studying an enzyme called Dam methylase, which dots DNA with side chains made of carbon and hydrogen atoms, called methyl groups. Modrich's experiments proved that so-called restriction enzymes use these methyl groups as guidemarks for cutting DNA. Subsequent discoveries resulted in a step-by-step description (*Science*, 14 July 1989, p. 160) of how bacterial enzymes spot, mark, and repair mismatched base pairs in a freshly copied double helix (see diagram, below).

Many other mechanisms also fix faulty DNA, and many other researchers have made key contributions to their study. That fact has raised the inevitable question of who should have won the Nobel for DNA repair. "Lindahl was a clear choice. That was to be expected," says Björn Schumacher, who studies DNA repair in aging at the University of Cologne in Germany. But Modrich and Sancar were less familiar to him: "It would be easy to come up with the names of other scientists who are of similar importance," he says.

Indeed, last month another prestigious prize—the Albert Lasker Basic Medical Research Award, often a predictor of the Nobel—went to two other DNA repair researchers (<http://scim.ag/Laskerprizes>): Evelyn Witkin of Rutgers University, New Brunswick, in New Jersey (who showed how changes in gene expression help bacteria cope with DNA damaged by UV light), and Stephen Elledge of Brigham and Women's Hospital in Boston (for further discoveries of DNA repair in yeast and humans). But Thomas Carell, who studies nucleic acid chemistry at Ludwig Maximilian University of Munich in Germany, says the Nobel Committee got it right. "This is perfect," he says. "DNA repair is a hugely important topic, and these three were the first to describe the repair mechanisms." ■

CHEMISTRY NOBEL

"... for mechanistic studies of DNA repair"

Tomas Lindahl

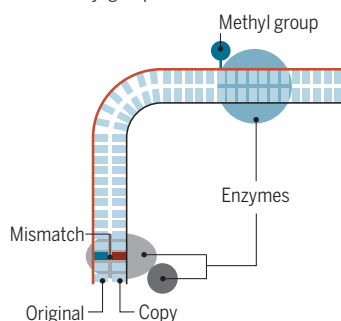
Paul Modrich

Aziz Sancar

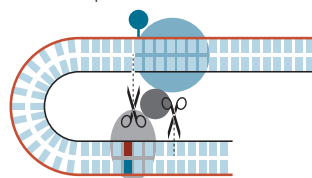
Repair crew

When DNA is copied, the new strand often gets the wrong nucleotide and is mismatched with its peer on the original strand. Here's how diligent teams of enzymes check for mismatches and fix them.

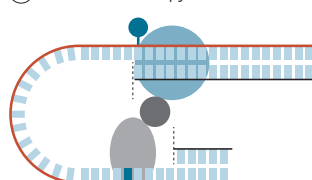
- 1 Two enzymes spot a mismatch. Another identifies the strand with the correct nucleotide by its methyl group.



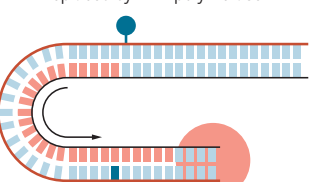
- 2 The enzymes cut the other strand in two places.



- 3 The defective copy is discarded.



- 4 The missing nucleotides are replaced by DNA polymerase.





Dried and crushed mealworms could be fed to cattle, pigs, poultry, and fish.

BUZZ FOOD

Feeding insect meal to livestock could help the planet, but will it be good for people? *By Kai Kupferschmidt*

Mick Grant is a farmer in Roos, U.K., a burly fellow with strong hands and a quick smile. His great-grandfather started out with a shop and two cows. Out of that grew Elm Farm, a 450-hectare estate on which Grant is raising pigs and growing wheat, peas, and oil seed rape. Recently, Grant has added a new species of livestock: housefly larvae, also known as maggots.

In two blue shipping containers a short drive from the farmhouse, Grant is raising them by the tens of thousands. They grow on manure from a nearby chicken farm—the fresher the better, Grant says: “As it gets older it crusts and gets fungus in it.” Maggots from old manure, he says, “are not as good a maggot as they are at the beginning.”

Grant has produced hundreds of kilos of dried maggots in the last few months as part of an E.U.-funded research project called PROteINSECT. They are now being fed to fish, pigs, and chickens in large

trials designed to answer an increasingly urgent question: Are insects the animal feed of the future?

Some scientists are convinced the answer is yes. The world’s appetite for meat is growing, and the production of animal feed is an increasing strain on land and water. Insects could provide much of the protein animals need at a much lower environmental cost; many insect species can feed on manure, like Grant’s maggots, or other types of organic waste, such as leftover food, offal, and grains discarded by breweries.

Regulatory agencies are beginning to weigh the benefits against potential safety risks, including the possibility that insects might accumulate environmental toxins or even transmit diseases to the farm animals that eat them. On 8 October, the European Food Safety Authority (EFSA) in Parma, Italy, released its first report on the risks of using insects as food and animal feed. It concluded that the risks depend on the insect species used—and that more studies like PROteINSECT are needed before live-

stock or fish are switched to this new diet. But in other countries the brave new world of industrial-scale insect farming is already on view.

THE BEST WAY TO TURN INSECTS into food is simply to eat them—and in many countries people already do. More than 2 billion people occasionally cook caterpillars, boil beetles, or marinate maggots as part of their traditional diet. In Southern Africa, 9.5 billion mopane caterpillars—named for their favorite tree—are harvested every year for human consumption, and in Uganda, a kilogram of grasshoppers is more expensive than a kilogram of beef.

Environmentally speaking, it’s a great choice, says Arnold van Huis, an entomologist at Wageningen University in the Netherlands who co-authored an insect cookbook. Insects produce body mass at an astonishing rate, in part because as cold-blooded animals they don’t need to expend energy on regulating their body temperature. Crickets need only 1.7 kilograms of feed

to gain a kilogram of body weight; a typical U.S. chicken consumes 2.5 kilograms, pigs 5 kilograms, and cattle 10 kilograms. Another advantage: Most insects can be eaten whole. Only about half of a chicken or a pig is edible; for a cow the fraction is even less. As a result, raising a kilogram of insect protein produces less CO₂ than rearing pigs or cattle, Van Huis says, and takes up only one-tenth the land.

Edible species, of which there are some 2000, are high in protein and rich in micronutrients such as iron and vitamins, several studies have found. A 2012 report by the Food and Agriculture Organization of the United Nations (FAO), co-authored by Van Huis, noted “the huge potential that insects offer for enhancing food security.”

But beyond the safety unknowns, putting insects on the menu faces a bigger obstacle, Van Huis says: “Most people are simply disgusted by the idea of eating insects.” Feeding insects to livestock may have a lower environmental payoff but could be easier to sell to the public, and it makes the safety concerns less acute. (And, who knows, insect enthusiasts say, once farm animals start eating insects, humans might begin to find the idea less repulsive.)

Studies suggest that many animals do just fine on insects—which after all are a natural staple for creatures from chicken to trout. A 2014 review by FAO scientists of feeding trials conducted on catfish, tilapia, rainbow trout, and several other fish species, as well as crustaceans, chickens, and pigs, concluded that insect meal could replace between 25% and 100% of soy meal or fish meal in the animals’ diets with no adverse effects. Most insect meals were deficient in calcium and the amino acids methionine and lysine, but those can be added cheaply. The authors noted that the aroma and texture of fish did not change when they were fed on black soldier fly larvae.

EUROPEAN FARMERS have little experience raising insects, but Grant didn’t have to start from scratch. Elm Farm has produced bluebottle larvae for decades, as bait for recreational fishers. They grow on abattoir waste—kidneys, livers, and hearts, glisten-

ing in nauseating reds, greens, and browns. Within a few days they’re covered by thousands of maggots, as if they had come back to writhing, pulsing life.

These larvae are an important moneymaker for Grant in the summer. But with the houseflies he is raising next door, he hopes to break into an even bigger market. In one of the shipping containers, thou-

which is kept moist, and slowly burrow into it. After a few days they move toward the sides of the tray; that means they are ready to harvest. Some of the maggots get a little extra nutrition: fish scraps. Grant uses those maggots to replenish the stock of flies next door. “The fish just gives the flies a certain va-va-voom,” he says. “They are just fitter and lay more eggs.” But most of the maggots are destined to be animal feed. They are sieved from the manure, then dumped into a cement mixer, where they are dried and left to fall apart, resulting in a fine insect powder.

For now, it’s all for research purposes. But Grant likes to imagine a building where all of this is automated so that he can churn out tons of animal feed. “The potential is huge,” Van Huis says. In 2014, the world produced about 980 million tons of feed, worth about \$460 billion. With meat consumption growing, those numbers will only rise. Already, more than 80% of the world’s soybeans are used as feed; their cultivation takes up huge amounts of land and water. Insect meal could never replace soy feed entirely, but it could take some pressure off, says PROTEINSECT coordinator Elaine Fitches, a researcher at the Food and Environment Research Agency (FERA), a partly privatized U.K. government institute in York. It takes about a hectare of land to produce a ton of soy per year; the same area could produce up to 150 tons of insect protein, she estimates.

Insect protein could make an even bigger impact in aquaculture, which consumes 10% of the world’s fish production as feed for other fish. The availability of fishmeal has been erratic and its prices are rising rapidly, says Jason Drew, a U.K. entrepreneur—from about \$500 per ton in the 1990s to \$1500 to \$2500 in recent years. “Companies are looking for solutions to the looming protein crisis, Drew says. “I think insect protein will replace fishmeal. We can then leave this food source at the bottom of the food chain, where it should be—in our seas.”

Drew is one of the founders of AgriProtein Technologies, a company in Cape Town, South Africa, that many observers agree is furthest along in rearing insects at an indus-

From spare food to spare ribs

Researchers are studying how to use insects raised on waste to feed farm animals and fish.

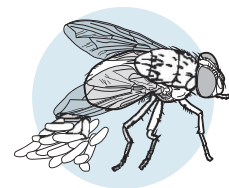
Waste

Insects can feed on leftover food, grains discarded by distilleries, or even manure.



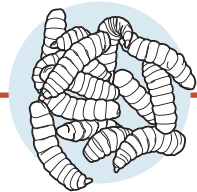
Flies

Adult flies are kept in a room; their eggs are collected.



Larvae

The eggs develop into larvae. Some of them are allowed to grow into flies to lay more eggs.

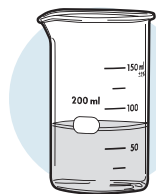


Pressing

Drying

Oil

Insect oil could replace fish oil or soy oil in animal feed.



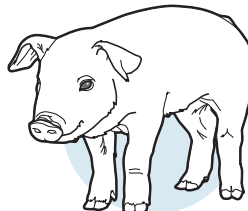
Meal

Insect meal could replace fish meal or soy meal.



Livestock and fish

Feeding trials are ongoing; regulators are studying the risks of allowing insect-fed animals into the human food chain.



sands of flies buzz in a huge wooden compartment. Early in the morning, a farmhand places trays of fresh chicken manure on the floor of the container. For 2 hours, the flies are allowed to lay their eggs on the manure. Then, the trays are put inside the other container to hatch.

Larvae start hatching from the eggs within hours. They feed on the manure,



Many people find the idea of eating mealworms repulsive. Feeding them to animals avoids that problem.

trial scale. With \$11 million from the Bill & Melinda Gates Foundation and private investors, the company has built a huge factory next to Cape Town International Airport that is now ramping up production. Once it reaches capacity, soldier fly larvae will consume 110 tons of organic waste daily to produce 24 tons of maggots. Dried and ground to a powder, they will be sold to South African farmers as feed at a lower price than fish meal, Drew says. Nothing prevents him from taking his product to the market, and he already has plans for a second factory. Drew thinks maggots will make him a millionaire.

REGULATORS IN EUROPE and the United States, however, still have concerns. In the United States, using insects as feed is allowed in some states but not others. EnviroFlight, a company based in Yellow Springs, Ohio, is rearing black soldier fly maggots and selling them as food for pets and zoo animals. The company is working with the Food and Drug Administration to prove it's also safe to feed its larvae to animals eaten by humans. Feeding trials, mainly of fish, are underway, and nationwide approval could come as early as September 2016, predicts EnviroFlight's founder and director Glen Courtright. "That would open the flood gates."

Europe is warier, in part because of the outbreak of bovine spongiform encephalopathy (BSE), better known as mad cow disease, in the 1980s and 1990s. BSE is caused by misfolded brain proteins. It spread among cows because they were fed proteins extracted from the remains of other cows, and a few hundred people who ate infected beef caught a fatal human form of the disease, variant Creutzfeldt-Jakob disease. In response, the European Union banned the feeding of almost any type of animal protein to farmed animals.

No one thought of insects at the time, but today, the regulation is holding back development, complains Antoine Hubert, a French scientist who co-founded Ynsect, a company that aims to rear insects for feed and other applications. Because insects and mammals are so distantly related, the risk of prions or other pathogens making the jump is much smaller than it is between mammals, Hubert argues.

In 2013, the European Union relaxed the rules a bit to allow the use of animal proteins in aquaculture. But there is one problem: Animals used as fish feed have to be killed in a certified slaughterhouse with a welfare officer present, a rule clearly not written with maggots in mind. As a result, fish farms can now feed their animals chicken offal but not insects—even though many fish species eat insects in nature but not chicken. "That's just absurd," Hubert says.

Hubert is now lobbying for changes in the regulations through the International Platform of Insects for Food and Feed, which he founded in April together with representatives of AgriProtein and companies from France, Germany, and the Netherlands. The European Commission is paying attention: Also in April, it asked EFSA, its food watchdog, to look into the risks posed by the use of insects in food and feed. The resulting report, issued last week, mentions the buildup of

chemicals such as heavy metals or arsenic as one possible risk. It also discusses infectious diseases, but finds that the risks aren't higher than with other sources of animal protein.

Insects aren't even known to develop prion diseases, the report notes, and it agrees with Hubert that any bacteria or viruses that harm insects are most likely harmless to humans. Insects could conceivably pick up pathogens of fish, birds, or mammals through their diet and passively spread them, but there are ways to mitigate those risks, the report says, such as carefully choosing the insects' food source.

On many issues, however, there's simply not enough information. There are reports of allergic reactions in humans after eating insects, for instance, and even a case of anaphylactic shock. But such allergic reactions have never been reported in farm animals, although they should be monitored for that, the authors write.

MICK GRANT'S MAGGOTS could help provide more answers. At FERA, scientists have pureed the maggots and investigated them for pesticides, heavy metals, and traces of antibiotics and growth hormones. "Anything that we find on a farm could find its way into the maggots and in our food chain," says Michael Dickinson, a scientist at the institute. "But we have not found any

red flags so far." The maggots are now being fed to pigs and chickens in Belgium. The growth of the animals as well as their health and the meat quality is compared with animals on a standard diet. By the end of the year, results from these trials should be available for EFSA to take into account.

Whether maggot-fed meat eventually makes its way to the table will depend in part on public acceptance—and Hubert worries that PROteINSECT's use of manure as a food source will not help. "The public won't accept feeding insects on manure," Hubert says. (Ynsect, his own company, only uses food industry byproducts that are allowed as feed.)

Mick Grant, for his part, sees no problem. For him, insects are all about efficiency. "If you can use waste to make something, it makes more sense than anything, doesn't it?" ■



Mick Grant, a farmer in the United Kingdom, has long raised bluebottle larvae for anglers.

IN PURSUIT OF THE PERFECT POWER SUIT

A longstanding quest to augment human performance with robotic exoskeletons takes a softer approach

By Warren Cornwall

A lone soldier stands in a dark alley, eyeing a door. Even though he's covered in bulky armor, he charges forward and bursts through, and is engulfed in a barrage of gunfire. Rather than retreat, the soldier stands tall as bullets ping off him harmlessly.

This isn't a trailer for the latest superhero movie. It's an animation produced by the U.S. military, designed to show off its vision for a brawny robotic exoskeleton that it hopes to deploy with elite commandos. Dubbed the Tactical Assault Light Operator Suit, or TALOS, it's the focus of a multimillion dollar research project catalyzed by a commando's death during a hostage rescue in Afghanistan. The TALOS's name pays homage to a metal giant of Greek mythology who guarded the island of Crete, effortlessly circling it three times a day. More casually, it is called the Iron Man suit.

The TALOS is just one part of a much larger, global research push to develop exoskeletons that would endow people with superhuman strength and endurance. But imagining Iron Man in comic books and movies has proven easier than building him. The effort is littered with failures. A predecessor to the TALOS, called the Human Universal Load Carrier (HULC), was shelved after it proved impractical, exhausting users instead

A soldier tries out a so-called soft exosuit at the Army's Aberdeen Proving Ground in Maryland. Tests have found it can help a person walk more efficiently.



of supercharging them. And some scientists are skeptical that the TALOS and similar heavy, hard-bodied exoskeleton designs will work anytime soon, saying they often fail to address fundamental physiological issues.

Improving on the effortlessness of the human stride—little more than a forward lean and a flick of the calf—turns out to be a daunting engineering challenge. Building a machine to help someone with a disability is one thing, but “it’s very difficult from a design perspective to augment human walking and running, because we’re so good at it,” says Hugh Herr, an engineer at the Massachusetts Institute of Technology (MIT) in Cambridge. The exoskeletons developed so far, he says, are too bulky and tend to fight the natural rhythms of the body, which turns them into “fancy exercise machines.”

As a result, some researchers are lowering their sights. They are taking a softer, smaller approach, building suits that resemble running tights hooked to motorized wires, or a modest ankle brace. In just the last few years, they have finally achieved a long-sought goal: creating an exoskeleton that actually saves the user energy while walking on a level treadmill.

That achievement is a long way from a supersoldier smashing through a door, but it is raising hopes that machinery and microprocessors can truly augment a healthy human. “I think we’re in the stage where the Wright brothers can get the plane up for a bit, but it doesn’t stay up for long,” says Dan Ferris, a leading exoskeleton scientist at the University of Michigan (UM), Ann Arbor.

MILITARY LEADERS seeking to give soldiers more strength, stamina, and protection have long dreamed of something similar to Marvel Comics’s Iron Man, whose powers came from a robotic suit. In the late 1960s, the U.S. Office of Naval Research funded development of Hardiman, a massive, 680-kilogram exoskeleton built by General Electric Global Research. Hardiman was ultimately abandoned, but the idea didn’t die.

In 2000, the Defense Advanced Research Projects Agency (DARPA), a Pentagon agency best known for helping invent the Internet, radar-evading stealth aircraft, and pilotless drones, began funding research into exoskeletons that could improve combat performance. The results included a variety of high-tech hinged metal leg braces. One design from a lab at the University of California (UC), Berkeley, evolved into the HULC.

By 2011, defense contractor Lockheed Martin, which had licensed the rights to use the UC Berkeley system, was ready to test an updated HULC, which featured slimmed-down braces and motor-driven joints, at the U.S. Army’s Natick Soldier Re-

search, Development and Engineering Center in Massachusetts.

The hype was substantial. The HULC “will enable soldiers to do things they cannot do today, while helping to protect them from musculoskeletal injuries,” declared Lockheed project manager Jim Ni in a press release. The HULC would enable soldiers to carry 90 kilograms up to 20 kilometers on a single battery charge, the company claimed.

The celebration was short-lived. When soldiers strapped into the 40-kilogram suit and walked on a treadmill, tests showed they burned more energy than they did walking unaided. In one trial involving eight HULC wearers, their heart rates jumped by 26% on average, while their oxygen consumption rose 39%, compared with when they didn’t use the machine.

One big problem was that the HULC

who until last year led the Pentagon’s Special Operations Command (SOCOM). After a SEAL commando died, shot while entering a room during a hostage rescue, McRaven says someone asked him why the military still didn’t have a good way to protect soldiers in those situations. “He said, ‘Where is our Iron Man suit?’” recalls McRaven, now chancellor of the University of Texas system. “I didn’t have a good answer for him.” In early 2013, McRaven’s command launched a 5-year research program.

From the start, the TALOS had a touch of Hollywood, and not just in the promotional video. Among the project’s contractors was Legacy Effects, a California company that built the suits for the *Iron Man* movies. “Science fiction can drive the science,” McRaven says. “We may never get something that looks just like Iron Man, but that’s what we’re looking for.”

VIDEO

To watch a video, go to http://scim.ag/6256_vid



A team of technicians trails a military exosuit tester, gathering data that will reveal whether the device is aiding—or hurting—the soldier’s performance.

forced wearers to walk in an unfamiliar way, says Karen Gregorczyk, a biomechanical engineer at the Army’s Natick center who led the tests. That difficulty was compounded by a lack of coordination between human and machine. “It’s trying to kick your leg forward and you’re not ready to kick your leg forward,” says Gregorczyk, who spent a half hour trying the suit. “It was a workout.”

Today, the last of the HULC prototypes are parked at a company lab in Orlando, Florida. Work is also on hold on XOS 2, a similar DARPA-born exoskeleton that Raytheon acquired.

THE HULC’S DOWNFALL hasn’t stopped the military from trying again to go big. Now, the focus is on the TALOS, a brain-child of former Navy Admiral Bill McRaven,

So far, there are few public details about the TALOS’s design. In written responses to questions from *Science*, Lieutenant Commander Matt Allen, a SOCOM spokesman, painted a picture of a full-body exoskeleton capable of carrying heavy body armor, as well as antennae and computers to provide battlefield information, and sensors to track the soldier’s physical condition. Photos and promotional video of prototypes show devices that bear a strong resemblance to the HULC, with rigid, hinged frames running down the legs.

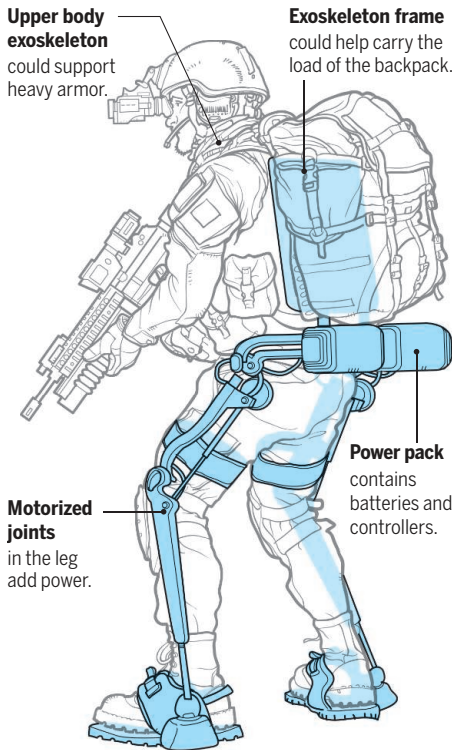
But Russ Angold, an engineer and co-founder of the Richmond, California, company Ekso Bionics, says the TALOS designers have learned from the shortcomings of past designs. The company was created to commercialize the UC Berkeley exoskeleton, and

Giving soldiers a robotic boost

The U.S. military, and others around the world, are trying to build exoskeletons to enhance soldiers' strength and stamina. Several designs are in development.

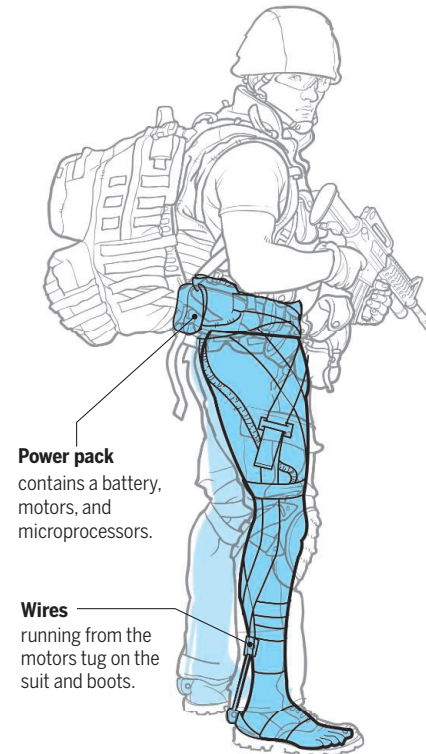
Rigid exoskeleton

A rigid frame with motorized joints could greatly boost strength and load capacity.



Soft exoskeleton

Fabric, often stretchy, is mated with cables and small motors to deliver a modest assist.



Advantages and disadvantages



- Can take **weight off the soldier**, enabling the user to carry heavy equipment.



- **Heavy, and locks users into particular joint movements.** Current designs suffer from slow response.
- **Uses a lot of power.**
- **Exhausting to wear** and has not been shown to boost performance.



- **Lightweight, energy efficient,** and easy to wear. May boost performance.



- **Doesn't take weight off the soldier,** limiting extra load.
- **Current design isn't tuned to handle running or walking** over uneven ground.

invented the first HULC. Now, it has contracts to build prototypes for the TALOS. "I think every problem can be solved," he says. "It's just a matter of time."

Researchers are "extensively" investigating tradeoffs between weight, mobility, and endurance, Allen wrote. Although media reports have put the project's budget at \$80 million, Allen wrote "we do not know how much TALOS will cost."

When the exoskeleton might appear is also unclear. A timetable that calls for producing a fully functional prototype by 2018 "is on

track right now," said Army General Joseph Votel, SOCOM's current leader, at a conference this past January. But he noted that "many significant challenges remain."

UM's Ferris believes the needed technical advances—to shave weight, boost battery performance, and get the machine to move in perfect synchrony with a person—are still far off. "The reality is, they don't understand the engineering and the science," he says of SOCOM. "They don't understand the leap we need to make." And he estimates that TALOS backers will "need a budget of \$500 million

to make this happen." Such concerns got now-retired Senator Tom Coburn (R-OK) to include the TALOS in the 2014 edition of his annual *Wastebook* of projects he considered government boondoggles.

Scientists at the Natick Army research lab also have expressed concerns. The military still lacks a grasp of the basic biomechanics needed for a successful leg exoskeleton, Gregorczyk and several others concluded in a recent research proposal. The result has been a "best guess" approach that has produced several "poorly functioning devices," including the HULC. They're calling for more fundamental studies to understand how an exoskeleton and human leg interact. "I think Iron Man's too big," Gregorczyk says. "I think we have to start small and see how that works first."

Herr, whose MIT lab has built a small, motorized ankle exoskeleton that broke new ground by showing that it could actually improve walking performance, laments the military's preoccupation with big, bulky designs. "I've been passionately trying to convince the [Department of Defense] to just stop obsessing with that type of architecture," he says.

A MORE PROMISING ALTERNATIVE, some exoskeleton advocates say, can be found in a Cambridge, Massachusetts, lab that looks like a cross between a robotics shop and a fashion design studio. In addition to a treadmill and the usual motors and wiring, engineer Conor Walsh's space at Harvard University features four sewing machines, bins filled with fabric, and a wheeled rack hung with black clothes.

The clothes are emblematic of a different approach to exoskeleton design. Born of a new DARPA program called Warrior Web, it's the antithesis of the TALOS. Rather than building a hefty metal machine that bears the weight of a load—and that can get in the way of normal movement—Walsh and his team are using fabric, flexible cables, and small motors to inject an extra shot of energy into each stride while letting a person move freely. These "soft exosuits" weigh just 9 kilograms, and use just 140 watts of electricity—slightly more than a desktop computer. In theory, the suits could mean soldiers arrive at the end of a long patrol less tired and injury-prone.

To demonstrate how it actually works, Walsh's team let a reporter try out the system. Getting outfitted is a bit like being a model preparing to hit the runway. I pull on a pair of black tights; then Diana Wagner, who's in charge of the fabric side of the project, laces me into the rest of the outfit. Straps wrap corset-tight around my waist, hips, thighs, and calves. Everything has to be snug and form-fitting so that when the motors start

pulling, nothing jerks out of place. Sensors tucked into the bootlaces and thigh straps will monitor my legs' movements, telling the machine when to kick in.

After 45 minutes of adjusting, I'm ready to climb on the treadmill. Two engineers lower a backpack adorned with boxes and dangling cables onto my shoulders. They latch the cables into connectors on my waist and legs, and on carbon-fiber spurs that jut from the heels of my Army boots. I pose midstride so that the machine can correctly adjust the cables. Then, Ignacio Galiana, one of the engineers, starts the treadmill. I'm walking at a pace of about 5 kilometers an hour.

My first step is met with a surprisingly abrupt yank on my heel. It lets go and almost immediately my other leg is tugged up and back. I keep my balance and settle into a brisk walk, the tiny electric motors and gears keeping time with a frenetic whirring. They retrieve and release the wires with every step, synced to my pace by microprocessors and the motion sensors. Even after a few minutes, each pull is slightly jarring, a bit like being a marionette with four wires controlling my legs. Am I walking in the suit, or is it walking me?

"We're doing a significant percentage of what your body needs," Galiana explains. "It takes a little bit to get used to these additional forces and be fully relaxed."

After 12 minutes on the treadmill, he turns off the exoskeleton as I keep walking. Something unexpected happens. My legs suddenly feel slower, the boots heavier. There is less pep in my stride.

"That's what we hear often," Galiana says with a grin. "People feel like they are walking in mud."

The suit's benefit, Walsh says, is borne out by the numbers. In a recent test, seven people walking in the suits, and carrying loads equal to 30% of their bodyweight, were on average 7% more efficient than without the suits.

PERFORMING ON A LAB TREADMILL is one thing. But does the soft suit work in the real world?

To answer that question, Walsh and DARPA go to the backwoods of the U.S. Army's Aberdeen Proving Ground, a sprawling 30,000-hectare base north of Baltimore, Maryland. This past summer,

on a humid 28°C morning, 21-year-old U.S. Army Specialist Cacciatore (he wouldn't give his first name) goes out for a hike. But this is no normal workout. The only thing standard issue is his close-cropped haircut. And he is trailed by a 12-person entourage of Harvard engineers, Army scientists, and DARPA officials, slipping in the mud and swatting mosquitos.

Before setting out in a soft exosuit and gear totaling 40 kilograms, Cacciatore spends 5 minutes in a lab walking and jumping on a treadmill that measures the force of each step. A facemask helps researchers gauge how much oxygen he is using. On another day, he'll do the same thing, minus the exosuit, to compare the results.



The HULC, a rigid, battery-powered exoskeleton developed by the U.S. military in the late 2000s, failed to deliver predicted performance boosts. Wearing the suit "was a workout," one tester said.

Then, Cacciatore marches at breakneck speed down a muddy path in a tan T-shirt and the black tights, the exosuit's noisy gears giving him a distinctly robotic air. As he tromps along, two following engineers, laptops suspended from their necks, peer at a collage of graphs tracing the machinery's performance.

When Cacciatore reaches a downed tree, he easily steps up and over it. The wires go slack because motion sensors detect something other than regular walking.

Observers are impressed. "I've gotta tell you, it's cool," says Michael LaFiandra, a biomechanics expert and chief of the Dismounted Warrior Branch at the Army Research Laboratory at Aberdeen. "Physical augmentation was kind of a pipe dream. And now it seems like it could be a reality?"

Still, there are problems. It's a prototype, after all, not built to withstand battlefield rigors. Twice during the hike, something malfunctions or breaks. Like a pit crew at the Indianapolis 500, the engineers swarm over the soldier, swiftly making repairs.

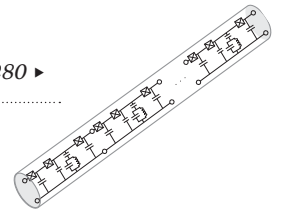
Later, Walsh won't detail the overall result of the tests. "I can say that it was positive," he allows. The mechanical problems that morning were the only ones in 2 weeks of testing, he says.

Still, Walsh cautions against unrealistic expectations, ticking off a host of challenges. The soft exosuit is programmed for walking, for instance, but not running. It has proven difficult to design a system that kicks in at the right time when someone is traveling

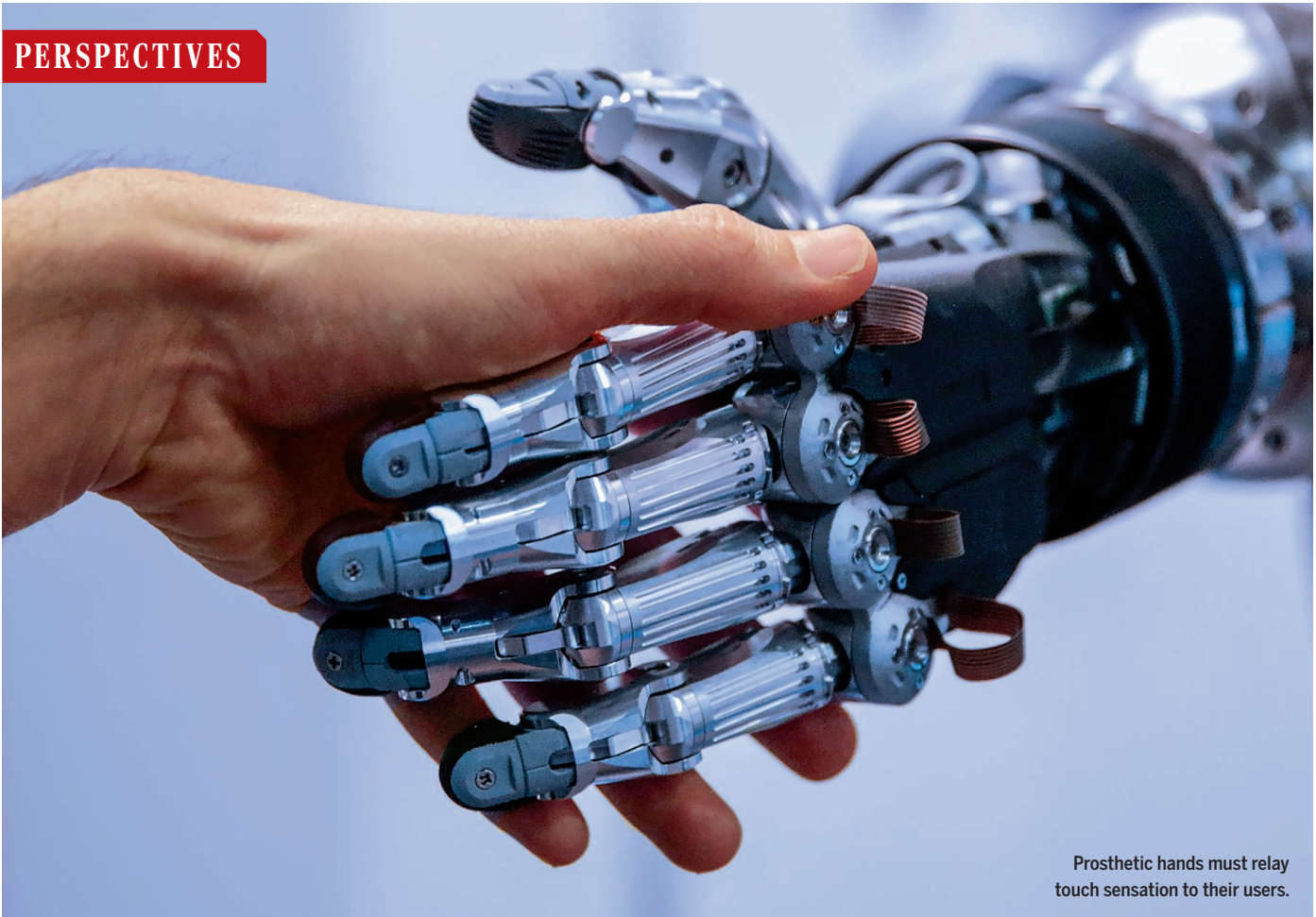
over uneven terrain. Some people have an easier time adapting to the suit than others, suggesting any benefit could vary from user to user. And any final version would have to integrate with the many other parts of a military outfit.

The Army's Gregorczyk offers another sobering list of questions that any real-world Iron Man suit—soft or hard—will have to confront. Could using an exoskeleton cause its own set of injuries? Would the performance benefit outweigh the cost? "Say a device reduces the metabolic cost of a soldier carrying a load by 5%," she says. "Does that translate into an operational benefit? Does it mean anything?" ■

Warren Cornwall is a freelance writer in Bellingham, Washington.



PERSPECTIVES



Prosthetic hands must relay touch sensation to their users.

BIOENGINEERING

Restoring the sense of touch

Flexible circuitry mimics the way skin transduces pressure signals

By Polina Anikeeva^{1,2} and Ryan A. Koppes^{1,3}

Amputation of damaged tissue is one of the oldest surgical techniques, reaching prevalence in the 16th century (1). Improved emergency medicine has allowed more individuals to survive traumatic injuries as amputees, but prosthetic limbs remain the only means to restore any degree of function to these patients. Inadequate tactile feedback is a leading shortcoming of prosthetic limbs, but for

artificial hands, just a few sensors that relay grasp pressure back to the user can provide the functionality needed to enable delicate tasks (2). In addition to improved motor control, sensory stimulation could alleviate phantom limb pain, which affects ~80% of amputees (2). On page 314 of this issue, Tee *et al.* (3) report a Digital Tactile System (“DiTact”) based on a low-power flexible organic transistor circuit that transduces pressure stimuli into oscillating signals like those generated by skin mechanoreceptors.

Mammalian skin is a multilayered viscoelastic material that can stretch up to ~125% from its resting dimensions without any apparent loss in sensitivity to external stimuli such as pressure or temperature. Replicating skin mechanical and functional properties remains an elusive engineering challenge. Meanwhile, the rapidly expanding field of flexible electronics has made substantial strides, and complex circuits can now be produced on soft substrates. Advances in microcontact printing, inkjet

deposition, and organic electronics have delivered stretchable and flexible, wearable, and even epidermal sensors (4–6).

These lightweight imperceptible devices, however, are often limited by the power requirements of direct-current (dc) circuits. Biological mechanosensing circuits are characterized by low power consumption and minimal noise and drift afforded, in part, by frequency encoding of pressure information: Higher pressures cause the mechanoreceptors in the skin to fire action potentials with higher frequencies. Inspired by this mechanism, Tee *et al.* developed a flexible organic ring-oscillator circuit that translates pressure input into a digital signal of variable frequency that scales with pressure. The DiTact prototype uses a piezoresistive voltage divider element based on a microstructured elastomer layer impregnated with carbon nanotubes. Pressure on the elastomer reduces the distance and hence decreases the tunneling impedance between the nanotubes and the electrode. The increased voltage output of the divider translates into a lower time delay of the gates of the inverters constituting the ring oscillator circuit, which increases its oscillation frequency. Being inherently digital, DiTact avoids the noise and drift that plague dc-modulated circuits. The pressure-controlled frequency modulation eliminates the need for computing elements, as the output signal can be directly used to drive neural activity. Output frequencies up to 200 Hz were achieved at 11 V in a device with low power consumption (<20 μ W), which will allow for future expansion of sensor density.

Prosthetic limbs remain largely limited by the technology connecting artificial driving and recording circuits to the biological sensory and motor pathways. In recent studies by Tyler, Micera, and co-workers, electrical stimulation of peripheral nerves improved the sensorimotor feedback in upper and lower limb prostheses (2, 7). A clinically relevant method, electrical stimulation, lacks the specificity needed to resolve efferent and afferent pathways (signals moving from brain to muscle and from skin to brain, respectively), let alone uniquely access specific fascicles (bundles of neuronal processes) within the peripheral nerves.

Optogenetics holds promise for improving signal transduction and cell specificity to the afferent nervous system. Through a multidimensional strategy of cell-specific

promoters, opsins with distinct activation spectra, and spatiotemporally encoded optical stimulation, highly specific neural pathways can, in principle, be targeted. By optogenetic decoupling of the sensory and motor pathways, future prostheses can be integrated with minimal invasiveness, avoiding the need for convoluted wiring and establishing direct feedback from an artificial limb to the brain.

Tee *et al.* outline a route to such optogenetic biointegration by combining the DiTact platform with blue light-emitting devices and a custom-engineered channel-rhodopsin 2 mutant, bC1C2(s/v), with improved kinetics to better match the output frequencies of their system. In combination with the DiTact platform, fast-spiking (parvalbumin-positive) mouse cortical neurons expressing this opsin demonstrated a high correlation of their firing rate to increasing pressure, highlighting the close integration of machine and biology.

Although the advantages of optical neuromodulation over electrical stimulation are becoming more convincing, the future of genetic modification necessary for this technology to work in human patients remains unclear. Improved methods for induced pluripotency and on-demand stem cell differentiation (8) may someday enable optogenetic nerve-machine interfaces without the need for viral delivery of transgenes to patients (9). Furthermore, by triggering the innate mechanisms of neural repair (10) and plasticity, optical stimulation may allow for more intimate integration of synthetic tactile platforms with the patients' nervous systems.

Even with improved technology, broad adoption of advanced artificial limbs will ultimately be determined by patients' comfort. The latter will depend on the ability of the tactile feedback systems to faithfully represent the sense of touch, which remains a scientific challenge because of our incomplete understanding of proprioception. Biomimetic platforms, such as DiTact artificial skin, are bound to aid the study of tactile perception; with further development of dynamic response, they may enable prostheses that deliver a sense of touch. ■

REFERENCES

1. M. Sachs, J. Bojunga, A. Encke, *World J. Surg.* **23**, 1088 (1999).
2. D. W. Tan *et al.*, *Sci. Transl. Med.* **6**, 257ra138 (2014).
3. B. C.-K. Tee *et al.*, *Science* **350**, 314 (2015).
4. M. Kaltenbrunner *et al.*, *Nature* **499**, 458 (2013).
5. Q. Li *et al.*, *Nature* **523**, 576 (2015).
6. D.-H. Kim *et al.*, *Science* **333**, 838 (2011).
7. S. Raspopovic *et al.*, *Sci. Transl. Med.* **6**, 222ra19 (2014).
8. Z. P. Pang *et al.*, *Nature* **476**, 220 (2011).
9. J. B. Bryson *et al.*, *Science* **344**, 94 (2014).
10. S. Park *et al.*, *Sci. Rep.* **5**, 9669 (2015).

¹Research Laboratory of Electronics, Massachusetts Institute of Technology, Cambridge, MA 02139, USA. ²Department of Materials Science and Engineering, Massachusetts Institute of Technology, Cambridge, MA 02139, USA. ³Department of Chemical Engineering, Northeastern University, Boston, MA 02115, USA. E-mail: anikeeva@mit.edu

ORGANIC SYNTHESIS

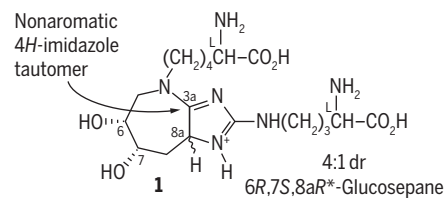
When sugar is not so sweet

Chemical synthesis of glucosepane promises insights into the role of this molecule in diseases of aging

By Dale L. Boger

Unadvent modifications of proteins by metabolites have been implicated in numerous disorders, including inflammation, diabetes, and human aging. Despite their importance, little is known about the formation and effect of such protein modifications. A major obstacle to the study of their role in disease is the limited access to pure samples of protein modifications of this kind. On page 294 of this issue, Draghici *et al.* (1) provide a much-needed advance by reporting the total synthesis of glucosepane (1, see the first figure), the core of a harmful

Unusual tautomer. Draghici *et al.*'s synthesis yields the nonaromatic 4*H*-imidazole tautomer 1.



protein modification that arises from reaction of the common metabolite glucose (4, see the second figure).

One way in which metabolites can modify proteins is through the Maillard reaction, also known as nonenzymatic browning or glycation. It involves the condensation of aldehydes derived from reducing carbohydrates, including glucose, usually with the side chains of lysine or arginine residues. The primary products are Amadori adducts (aminoketoses) (2). Cross-linking of the initial Amadori adducts then yields stable modifications of long-lived proteins (3). Such stable cross-links may decrease protein turnover, affect collagen flexibility, inhibit collagen integrin binding, and diminish lens clarity in cataracts. They may also break self-

Department of Chemistry, The Scripps Research Institute, La Jolla, CA 92037, USA. E-mail: boger@scripps.edu

tolerance, triggering chronic inflammation and inducing autoimmune processes (4–6).

Accumulated stable modifications on long-lived proteins (such as collagen and crystallin) may play a role in diseases of aging. Such modifications have therefore been called advanced glycation end products (AGEs) (7). The detection, isolation, identification, characterization, and establishment of the effect of AGEs is an important, yet underexplored, frontier for chemistry, with broad implications in human health (2).

Lederer and co-workers have shown that the lysyl-arginine cross-link glucosepane (2) is the main *in vivo* cross-link (8). It has been identified in diabetes and aging, and its relative amounts are predictive of microvascular complications in diabetes (4, 5). Without a reported synthesis of glucosepane, the individual diastereomers are not available, and glucosepane isolation from modified proteins is not practical even as a mixture of all diastereomers. Advances in the understanding of glucosepane AGEs, including verification of the structure, requires access to pure diastereomers.

As Lederer and co-workers have shown, glucosepane can be formed *in vitro* in a biomimetic reaction involving D-glucose, lysine, and arginine (9). In this reaction, glucosepane forms in vanishingly small yields (~2%) as a mixture of all eight diastereomers (9, 10). In the reaction, the carbonyl of an initial lysine Amadori adduct **2** moves down the entire carbohydrate chain by serial tautomerizations to provide **3**, with each intervening stereocenter undergoing epimerization before reaction with arginine (see the second figure) (10). However, low yields prevent isolation of the individual pure en-

“...the effect of AGEs [advanced glycation end products] is an important, yet underexplored, frontier for chemistry...”

antiomers. Even the preparation of partially purified diastereomeric mixtures required heroic chromatographic resolutions.

Draghici *et al.* now report a highly creative, concise (eight-step), and enantioselective total synthesis of the defined diastereomer **1** of glucosepane (in which one chiral center isomerizes easily and reversibly) (see the first figure). The remaining six diastereomers can be synthesized by adjusting the stereochemistry in three alternative starting materials. The synthesis includes two key steps to assemble the densely functionalized structure, one being a new method for the synthesis of the unusual nonaromatic 4*H*-imidazole.

The first steps of the synthesis introduce the lysine subunit, incorporate the C6 and C7 stereocenters, and generate the seven-membered ring core **5** by a series of reactions, including an Amadori rearrangement (see the second figure). The second key reaction represents a creative solution to imidazole synthesis, requiring only a ketone in the substrate to permit implementation. Treatment of ketone **5** with a protected N-amino-arginine provided the adduct **6**. This adduct undergoes tautomerization to **7**, followed by [3,3]-sigmatropic rearrangement to **8** and its ring closure to the imidazole

with isomerization to the thermodynamically most stable 4*H*-tautomer **9** (see the second figure). The [3,3]-sigmatropic rearrangement represents a new pericyclic reaction that, like the venerable Fischer indole cyclization, is sure to find widespread use.

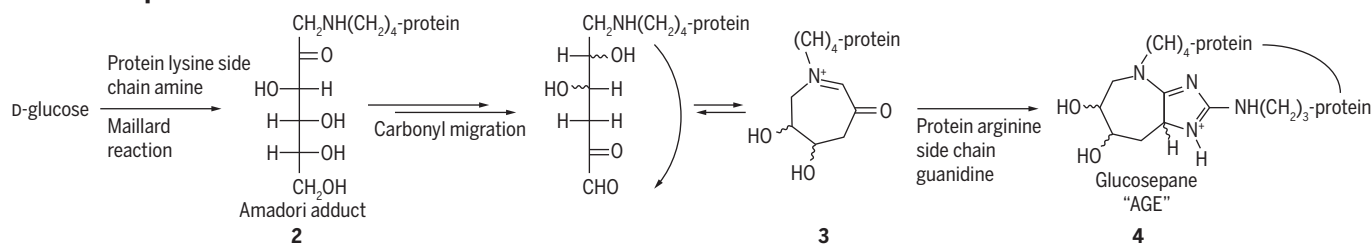
Draghici *et al.*'s study paves the way for site-specific incorporation of glucosepane in synthetic oligopeptides, the preparation of affinity reagents to identify molecular targets, and the generation of antibody detection reagents. By permitting the study of AGEs at a previously unobtainable level of resolution with enantiomerically and diastereomerically pure material, it will help to advance understanding of the role of AGEs in disease. The synthetic methodology introduced in the work—Spiegel imidazole synthesis—is important in its own right and will find applications well beyond that envisioned by the authors. ■

REFERENCES

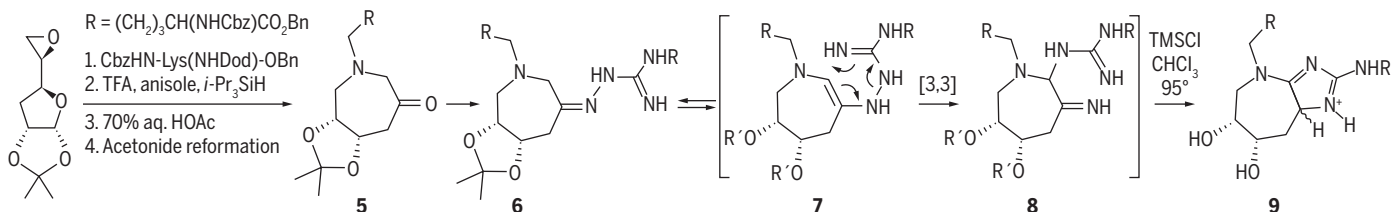
1. C. Draghici, T. Wang, D. A. Spiegel, *Science* **350**, 294 (2015).
2. M. Hellwig, T. Henle, *Angew. Chem. Int. Ed. Engl.* **53**, 10316 (2014).
3. V. M. Monnier *et al.* *Ann. N. Y. Acad. Sci.* **1043**, 533 (2005).
4. V. M. Monnier, W. Sun, D. R. Sell, X. Fan, I. Nemet, S. Genuth, *Clin. Chem. Lab. Med.* **52**, 21 (2014).
5. V. M. Monnier, D. R. Sell, C. Strauch, W. Sun, J. M. Lachin, P. A. Cleary, S. Genuth, DCCT Research Group, *J. Diabetes Complicat.* **27**, 141 (2013).
6. M. Chikazawa *et al.*, *J. Biol. Chem.* **288**, 13204 (2013).
7. R. Singh, A. Barden, T. Mori, L. Beilin, *Diabetologia* **44**, 129 (2001).
8. K. M. Biemel, D. A. Friedl, M. O. Lederer, *J. Biol. Chem.* **277**, 24907 (2002).
9. M. O. Lederer, H. P. Buhler, *Bioorg. Med. Chem.* **7**, 1081 (1999).
10. K. M. Biemel, J. Conrad, M. O. Lederer, *Angew. Chem. Int. Ed. Engl.* **41**, 801 (2002).

10.1126/science.aad3298

A Glucosepane cross-link formation



B Key steps in glucosepane total synthesis



Synthetic success. (A) Glucosepane protein cross-links (AGEs) are formed as a mixture of all possible diastereomers. Their formation arises from a remarkable reaction sequence that racemizes each chiral center in the entire carbohydrate chain by serial keto-enol tautomerizations. (B) Key steps in the enantioselective total synthesis of glucosepane reported by Draghici *et al.*, including the [3,3]-sigmatropic rearrangement used to introduce the 4*H*-imidazole.



Close encounter.
Photomontage of Hubble
Space Telescope images
showing Mars and
Comet Siding Spring on
19 October 2014.

PLANETARY SCIENCE

Comet Siding Spring, up close and personal

Observations during a close flyby of Mars shed light on a little-understood group of comets

By **Carey Lisse**

On 19 October 2014, a comet from the very edge of our solar system flew extremely closely by our sister planet Mars. Using an international fleet of modern spacecraft orbiting above and roving on the surface of the planet, scientists found that the comet consists of a kilometer-sized dirty iceball emitting gas and dust from numerous jets. The comet survived its extremely close passage by Mars without much change. It did, however, dump appreciable amounts of material into the martian atmosphere, and the effects from this material lingered for days. These observations of a comet from the surface and sky of another planet herald an era of solar system study based on multiple observations from stations throughout the solar system.

Comets are small, primordial, icy, planet-building bodies formed early in the protoplanetary disk that orbited our Sun in the first few million years of its existence. Older than Earth and no longer stable in the inner system, comets have orbited the Sun for the last 4.5 billion years in two populations: the Kuiper Belt at ~30 to 50 astronomical

units (AU) (1 AU is the distance from Earth to the Sun), at the edge of the Sun's original protoplanetary disk; and a large spherical cloud at the edge of the present solar system between 10,000 and 100,000 AU.

Kuiper Belt objects, scattered into the inner system over thousands of years by encounters with the giant planets, supply the population of low-inclination comets with short periods (less than 70 years) that repeatedly fly near Earth. Five of these, all well observed through multiple solar perihelion passages, have now been encountered by spacecraft. The best current knowledge of the solar system's primitive planet-forming icy planetesimals thus comes from spacecraft flybys of thermally processed nuclei originally formed near the outermost edges of the protoplanetary disk.

The Oort cloud comets formed in the middle of the protoplanetary disk between Jupiter and Neptune and scattered outward onto million-year orbits with high inclinations in near-miss attempts to aggregate into the nascent giant planets. They have likely never been in the inner solar system. Nor have they been closely visited by spacecraft, even though orbital perturbations caused by stars passing our solar system and galactic tides occasionally cause Oort cloud comets to come into the inner solar

system. Thus, we know little about the nuclei at the center of these comets.

On 19 October 2014 at ~1700 UT, this changed, when scientists were able to use the fleet of spacecraft now installed on and above the planet Mars to observe Oort Cloud Comet C/2013 A1 (Siding Spring). The comet passed within 135,000 km of Mars. This is only one-third the Earth-Moon distance—close enough for Mars to be within the comet's outer atmosphere, or coma, and for the comet's nucleus to be well within Mars' gravitational influence.

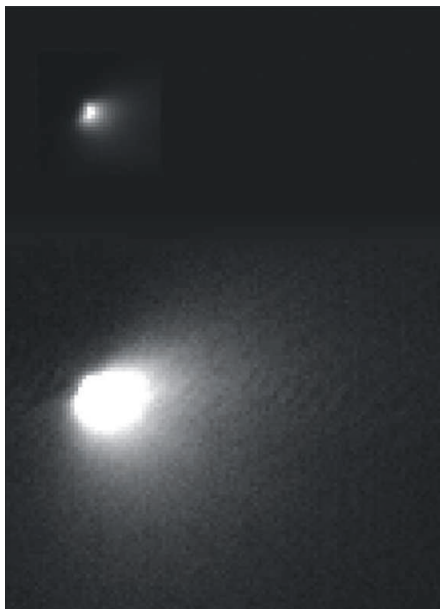
During its close flyby of Mars, the comet was the subject of an intense ground- and space-based observing campaign to determine its size, composition, behavior, and effect on the Red Planet. Over 19 spacecraft pointed at the comet, with at least 13 reporting detections ranging from x-ray through infrared wavelengths. Even though the comet was poorly situated for optimal observing from Earth, more than 20 ground-based observatories detected it at ultraviolet-to-radio wavelengths. Some problems were encountered in detecting the comet when its activity dipped inexplicably during the week before the Mars flyby; a week after its perihelion passage, the comet had increased in brightness and activity again by a factor of 2 to 3. Mars was also hit by a solar coronal mass ejection event on 19 October

PHOTO: NASA/ESA, HST/WFC3/UVIS, STSCL/PRC14-45

Applied Physics Lab John Hopkins University, Baltimore, MD
20723, USA. E-mail: carey.lisse@jhuapl.edu

2014, and there was a dust storm on the surface of Mars near the rovers.

Despite these impediments, good in situ detections of the comet were reported by six Mars spacecraft and rovers. The comet was also detected remotely by seven spacecraft spread throughout the inner solar system (1–3) (see the first figure). Important findings



Small nucleus. MRO/HiRISE detection of Comet Siding Spring's nucleus (top) and surrounding coma (bottom) and nucleus (top) 2 hours before the comet's close flyby of Mars (2). Pixel size, ~140 m by ~140 m.

concerning the comet's rotation rate, dust-to-gas ratio, composition, and coma and tail structure were made during the comet's close flyby (4) (see the second figure). Its nucleus was resolved by the Mars Reconnaissance Orbiter (MRO) HiRISE instrument and was found to be small compared to the Kuiper Belt comets, with a radius <0.7 km, but similarly elongated (shoe- or football-shaped). Coma imagery from MRO/HiRISE and CRISM (Compact Reconnaissance Imaging Spectrometer for Mars) found an elongated coma with at least three jets rotating with a roughly 8-hour period. No obvious auroral effects or meteor trails were found with remote observations by Chandra and Hubble Space Telescope (HST) during the flyby. However, in situ measurements of the martian exosphere and ionosphere by MRO, MAVEN (Mars Atmosphere and Volatile Evolution), and Mars Express did detect the input of cometary dust and electrons within a few hours from the time of closest approach of the comet. These data suggest some 1000 to 10,000 kg of dust input (and a similar amount of gas) into the martian skies (5–9). The effects lasted for 1 to 2 martian days and dissipated soon afterwards. The Mars surface rovers also pro-

duced the first images of a comet from the surface of another planet.

The comet, for its part, seems to have had little reaction to its close flyby of the planet (10–13). No sudden change in its brightness was found following its close planetary encounter, and post-encounter monitoring over the next few months showed a healthy comet heading back out to the Oort cloud. The coma structure and rotation rate found for the comet by MRO and HST at Mars were consistent with those found months before the encounter by HST (1) and NEO-WISE (Near-Earth Object Wide-field Survey Explorer) (14).

Comet Siding Spring represented another first: a close collaboration of the Mars, comet, and amateur astronomer communities, aided by a NASA volunteer group called the Comet Investigative Observing Campaign (CIOC) (3, 13) and NASA's Mars Program office. Given the diversity of professional interest in the comet, this neutral, and knowledgeable team of experts was useful for maximizing the scientific return (in fact without them, the Mars spacecraft would not have pointed at the proper part of the sky to observe the comet) while diffusing some of the more unusual cometary theories that were promulgated. The CIOC was also highly useful for the public and press to refer to and for disseminating up-to-date news and lessons learned.

This extremely rare close flyby not only highlighted humankind's growing ability to study and explore our solar system, but also showed that comets continue to add material to the inner planets. Given that cometary material is similar to the composition of Mars' polar caps, we may have witnessed another small addition to the martian surface. The NASA CSS observing campaign should also serve as a useful template for Earth's next close comet encounter in December 2018, when Kuiper Belt comet 45P/Wirtanen comes within 30 times the Earth-moon distance. ■

REFERENCES

1. J.-L. Li, et al., *Astrophys. J. Lett.* **797**, L8 (2014).
2. C. M. Lisse et al., *Bull. Am. Astron. Soc.* **46** (5), abstr.110.06 (2014).
3. C. M. Lisse et al., 46th Lunar and Planetary Science Conference, LPI contribution **1332**, 2377 (2015).
4. A. Delamere et al., *Bull. Am. Astron. Soc.* **46** (5), abstr. 110.04 (2014).
5. M. Benna et al., *Geophys. Res. Lett.* **42**, 4670 (2015).
6. D.A. Gurnett et al., *Geophys. Res. Lett.* **42**, 4745 (2015).
7. M. Restano et al., *Geophys. Res. Lett.* **42**, 4663 (2015).
8. N. M. Schneider et al., *Geophys. Res. Lett.* **42**, 4755 (2015).
9. P. Tricarico, *Geophys. Res. Lett.* **42**, 4752 (2015).
10. C. Kiss et al., IAU Meeting **29**, 2258216 (2015), see <http://adsabs.harvard.edu/abs/2015IAUGA..2258216K>.
11. D. Bodewits et al., *Astrophys. J. Lett.* **802**, L6 (2015).
12. www.cobs.si/analysis
13. www.cometcampaign.org
14. R. Stevenson, J. M. Bauer, R. M. Cutri, A. K. Mainzer, F. J. Masci, *Astrophys. J.* **798**, L31 (2015).

10.1126/science.aac7879

STRUCTURAL BIOLOGY

Chromatin complex, crystal clear

The long-sought structure of an active polycomb repressive complex is solved

By **Matthieu Schapira**

Epigenetic mechanisms control the combination of genes that are switched on and off in any given cell. In turn, this combination, called the transcriptional program, determines the identity and the fate of cells, which are deregulated in diseases such as cancer, inflammation, or neurological disorders. Chemical modifications (such as methylation or acetylation) of chromatin—an ensemble of nuclear factors, especially histone proteins around which DNA is wrapped—act as epigenetic signals. Enzymes that write or erase these chemical “marks,” and proteins that bind and interpret them, represent an important target class for drugs (1). On page 291 of this issue, Jiao and Liu (2) report the crystal structure of one prominent such enzyme called enhancer of zeste homolog 2 (Ezh2) in complex with obligatory protein binding partners. This structure, which has been largely elusive, provides clarity on the regulation of EZH2 catalytic activity and is an important step toward rational drug design.

EZH2 is part of a larger protein complex called polycomb repressive complex 2 (PRC2). The enzyme methylates lysine 27 of histone 3 (H3K27) to turn down gene expression (see the figure). Compounds that inhibit EZH2 are currently in clinical trials for cancer therapy. Hyperactivating mutations of EZH2 drive 22% of diffuse large B cell lymphoma, a form of blood cancer, which is sensitive to EZH2 inhibitors (3, 4); solid tumors carrying predefined genetic or epigenetic signatures are also vulnerable to EZH2 inhibition (5–7).

High-resolution crystal structures of many protein methyltransferases—enzymes that transfer a methyl group from the cofactor *S*-adenosylmethionine onto

Structural Genomics Consortium and Department of Pharmacology & Toxicology, University of Toronto, Toronto, Canada. E-mail: matthieu.schapira@utoronto.ca

side chains of substrate proteins—have been solved (including that of 39 out of 68 human enzymes). Given its prominence, considerable effort has been invested into solving the EZH2 structure. What makes this enterprise particularly challenging is that EZH2 is active only when it is part of PRC2. Other components of the PRC2 complex include the proteins embryonic ectoderm development (EED), suppressor of zeste 12 homolog (SUZ12), and retinoblastoma binding protein 4/7 (RBBP4/7). In particular, EED and a specific domain of SUZ12 [called Vrn2-Emf2-Fis2-Su(z)12 (VEFS)] are essential for the catalytic activity of EZH2. Crystal structures of human EZH2 isolated from the PRC2 complex were previously solved (8, 9), but both substrate and cofactor binding sites were impaired in these incomplete structures. A low-resolution structure of the human PRC2 complex was also solved by electron microscopy, and provided information on the relative arrangement of the different components of the complex (10). However, the resolution was too low for detailed mechanistic analysis of the PRC2 machinery, interpretation of structural mechanisms underlying disease-associated mutations, or the exploration of novel opportunities for drug discovery. Jiao and Liu report the high-resolution (2.3 Å) crystal structure of an active form of the yeast *Chaetomium thermophilum* Prc2 complex composed of full-length Ezh2, Eed, the VEFS domain of Suz12, a stimulatory trimethylated H3K27 (H3K27me3) peptide, and an inhibitory peptide from mutant his-

“This structure...is an important step toward rational drug design.”

tone H3 (a mutation that drives pediatric brain cancer). The authors also present a Prc2 structure in the basal state, in the absence of stimulatory peptide.

What are the lessons learned from the Prc2 structure? Foremost is a fundamental understanding at the atomic level of the mechanism behind the propagation of trimethylated H3K27 (H3K27me3). H3K27me3, the reaction product of EZH2, can bind to EED, which in turn stimulates EZH2 activity. This positive feedback loop is believed to play a central role in the efficient propagation of H3K27me3 along chromatin (11). At sites devoid of H3K27me3, PRC2 can recruit and trimethylate Jumonji, AT-rich interactive domain 2 (Jarid2), a chromatin-targeting protein that, once methylated, mimics H3K27me3 in stimulating PRC2, and initiates H3K27 methylation (12). The Prc2 structure of Jiao and Liu reveals that the amino-terminal half of Ezh2 wraps like a belt around Eed (clearly showing that Ezh2 requires Eed to fold properly). Of particular interest, a previously unknown stimulation-responsive motif (SRM) docks onto a surface composed of Eed and the stimulatory peptide H3K27me3, but is disordered in the absence of peptide. Proper folding of the SRM propagates to the catalytic site and facilitates

the methylation of a distinct H3K27 peptide, revealing how H3K27me3 stimulates methylation of neighboring H3K27 substrates.

Mutation of H3K27 into a methionine (H3K27M) is the genetic cause behind 80% of diffuse intrinsic pontine gliomas, and 22% of non-brain stem gliomas, two forms of brain cancer found in children (13). EZH2 binds the mutant histones and remains trapped at H3K27M sites, resulting in a global decrease in H3K27 methylation (14). Given that both lysine and methionine have long, linear side chains, the H3K27M residue would be expected to occupy the substrate H3K27 binding site in EZH2, while the binding pose of flanking residues would remain unchanged. Surprisingly, in the Prc2 structure of Jiao and Liu, it is the arginine immediately upstream of residue 27 (H3R26) that occupies the substrate-binding cavity, while H3K27M projects away from the catalytic site and is partially unfolded. Whether this unexpected arrangement holds in the human PRC2 complex has yet to be determined.

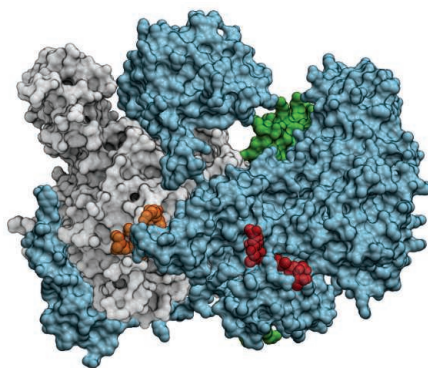
Although the structure solved by Jiao and Liu is that of a PRC2 ortholog from yeast, it is in agreement with the low-resolution human PRC2 structure and the high-resolution but incomplete human EZH2 structure. This tour-de-force in crystallizing a catalytically active Prc2 complex constitutes a major breakthrough on the road to a human PRC2 structure. This will undoubtedly help to understand the elusive binding mode of existing EZH2 inhibitors in clinical trials. The structural mechanism underlying EZH2 mutations that confer resistance to anticancer drugs should also gain clarity from a human PRC2 complex (15), and rational design strategies to overcome drug resistance may follow. In-depth analysis of this and future PRC2 structures may reveal novel binding sites—for instance, at the EZH2-EED interface—that could be targeted by next-generation drug candidates to allosterically inhibit both wild-type and mutant PRC2. ■

REFERENCES

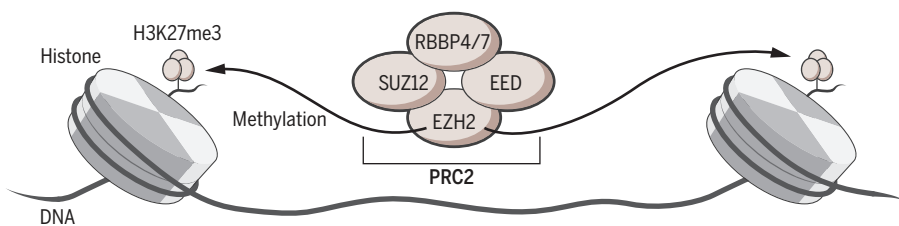
1. C. H. Arrowsmith *et al.*, *Nat. Rev. Drug Discov.* **11**, 384 (2012).
2. L. Jiao, X. Liu, *Science* **350**, aac4383 (2015).
3. S. K. Knutson *et al.*, *Nat. Chem. Biol.* **8**, 890 (2012).
4. M. T. McCabe *et al.*, *Nature* **492**, 108 (2012).
5. B. G. Bitler *et al.*, *Nat. Med.* **21**, 231 (2015).
6. S. C. Mack *et al.*, *Nature* **506**, 445 (2014).
7. S. K. Knutson *et al.*, *Proc. Natl. Acad. Sci. U.S.A.* **110**, 7922 (2013).
8. S. Antonyamy *et al.*, *PLOS One* **8**, e84147 (2013).
9. H. Wu *et al.*, *PLOS One* **8**, e83737 (2013).
10. C. Ciferri *et al.*, *Elife* **1**, e00005 (2012).
11. R. Margueron *et al.*, *Nature* **461**, 762 (2009).
12. S. Sanulli *et al.*, *Mol. Cell* **57**, 769 (2015).
13. G. Wu *et al.*, *Nat. Genet.* **44**, 251 (2012).
14. P. W. Lewis *et al.*, *Science* **340**, 857 (2013).
15. V. Gibaja *et al.*, *Oncogene* **10.1038/onc.2015.114** (2015).

Prc2 structure (active)

- Ezh2
- Eed
- Suz12
- H3K27me3 stimulatory peptide
- H3K27M inhibitory peptide



PRC2 represses gene expression



Long-sought structure. Structure of an active Prc2 complex (from yeast) provides insights into the propagation of the epigenetic mark H3K27me3 and the mechanism of disease-associated mutations. It should also lead to the structure of human PRC2 and thereby accelerate drug discovery efforts. Protein structure image was generated by M. Schapira with data from (2).

CREDIT: P. HUEY/SCIENCE

PHYSICS

Pumping up the quantum

A superconducting amplifier is used to boost quantum signals

By Andrew N. Cleland

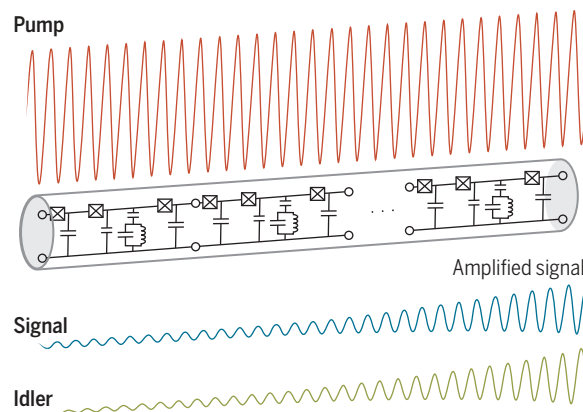
The detection of quantum signals from electronic devices requires exquisite instrumentation: The energy of a single photon from a cell phone, for example, is more than five orders of magnitude smaller than that of a visible-light photon. However, experiments on superconducting and semiconducting quantum bits require this level of sensitivity, as these quantum systems operate in the same band of frequencies as cell phones and microwave ovens. On page 307 of this issue, Macklin *et al.* (1) demonstrate a new kind of microwave amplifier that achieves the requisite sensitivity: a traveling-wave parametric amplifier, which uses a chain of superconducting amplifying elements, linked together in a nonlinear transmission line. This device can amplify microwave signals over a broad range of frequencies, while adding an extremely small amount of noise—close to the minimum amount of noise as set by quantum mechanics. This innovation represents an improvement over the previous amplifiers, which while achieving roughly equivalent performance in terms of quantum-limited noise (2), only work over a narrow range of frequencies and for very small microwave powers. The latter two limitations have now been substantially lifted.

The way a parametric amplifier works can be understood by using the example of a child on a swing. Sensing the motion of the swing, the child increases (amplifies) the motion by pumping with her legs, slightly increasing the motion of the swing on each pass. The swing is a type of resonator, storing the energy pumped into it by the child; this energy increases as long as the child's pumping action matches the motion of the swing. A peculiarity of the swing is its nonlinearity: As its amplitude of motion increases, its frequency falls, so the child must adjust the rate that she pumps her legs to stay in phase with the swing. If the child were replaced by a motor that pumped at regular intervals, matching the swing's fre-

quency for small motions, the swing's amplitude would increase, and its frequency fall, only until it was out of phase with the motor's pumping action, thereby limiting the maximum amplitude of motion of the swing.

A similar problem is encountered in electrical resonant amplifiers. Here, however, the nonlinearity usually appears as a result of the amplification process itself: It is difficult to get sufficient amplification with just one resonator driven by a single amplifier. In high-power electronic amplifiers, such as the klystron (3), one solution is to use a traveling-wave amplifier, distributing the amplification process among a series of amplifiers positioned along the length of

Crank it up some more. Schematic of a Josephson traveling-wave parametric amplifier, with a pump tone (red) amplifying a signal (blue) and idler (green) as all three signals travel through the nonlinear transmission line.



a transmission line. In a sense, the single motor on a swing is replaced by a series of motors on swings, where the motor-driven swings are linked together so that the motion of one swing is passed to its neighbor, and each motor slightly amplifies the motion as it is passed along the chain. This reduces the demand on each motor.

A challenge, then, is to make sure that the pumping action occurs at the proper phase of motion, so that each pump increases the motion. This can be achieved by careful design of the swings and the links between them. In addition to this design allowing much larger amplification, it also greatly increases the range of frequencies that can be amplified: The strongly linked resonant elements, such as the coupled swings, greatly increase the ef-

fective frequency range compared to that of a single swing. Macklin *et al.* take this concept, previously used for high-power electronics such as those in radio satellites or microwave transmitters, to demonstrate a quantum-limited microwave amplifier. Their amplifier relies on a linked chain of Josephson parametric amplifiers, placed at regular intervals along a superconducting transmission line, where each amplifier slightly increases the signal as it travels down the transmission line (see the figure).

The amplifier involves three transmitted microwave tones: a pump, provided by an external microwave source; the signal to be amplified; and, owing to the action of the parametric elements, a third signal, the “idler” (the signal and idler frequencies sum to twice the pump frequency). The pump tone acts with each nonlinear Josephson element to increase the energy in both the signal and idler as the three tones travel down the transmission line. A critical requirement was to work out how to achieve the requisite phase matching so that the three tones remain in the appropriate phase relation to achieve amplification—an especially difficult task because the wave speed of these tones changes with the amplitude of the waves. The prior theoretical development (4) showed that this could be done with an approach termed “resonant phase matching,” involving a careful design of the nonlinear transmission line, including the amplifiers.

The immediate application for this new amplifier is in quantum measurement of microwave frequency qubits used for quantum computation. Measurement of quantum systems (such as quantum bits or qubits) needs to be fast and accurate both for correcting errors and for evaluating a result, and is presently a resource-intensive process. This amplifier, providing a means to measure many qubits in a short time, would reduce those resource requirements. More broadly, however, a simple, plug-and-play quantum-limited microwave amplifier with broadband response will simplify quantum measurements in general, providing a straightforward means to develop quantum electronic devices, and possibly for exploring the quantum measurement process itself. ■

REFERENCES

1. C. Macklin *et al.*, *Science* **350**, 307 (2015).
2. M. Castellanos-Beltran, K. Lehnert, *Appl. Phys. Lett.* **91**, 083509 (2007).
3. R. H. Varian, F. Varian, *J. Appl. Phys.* **10**, 321 (1939).
4. K. O'Brien, C. Macklin, I. Siddiqi, Z. Zhang, *Phys. Rev. Lett.* **113**, 157001 (2014).

Institute for Molecular Engineering, University of Chicago, Chicago, IL 60637, USA. E-mail: anc@uchicago.edu

10.11263/science.aad0858

Challenge faculty to transform STEM learning

Focus on core ideas, crosscutting concepts, and scientific practices

By **Melanie M. Cooper***, **Marcos D. Caballero**, **Diane Ebert-May**, **Cori L. Fata-Hartley**, **Sarah E. Jardeleza**, **Joseph S. Krajcik**, **James T. Laverty**, **Rebecca L. Matz**, **Lynmarie A. Posey**, **Sonia M. Underwood**

Models for higher education in science, technology, engineering, and mathematics (STEM) are under pressure around the world. Although most STEM faculty and practicing scientists have learned successfully in a traditional format, they are the exception, not the norm, in their success. Education should support a diverse population of students in a world where

using knowledge, not merely memorizing it, is becoming ever more important. In the United States, which by many measures is a world leader in higher education, the President's Council of Advisors on Science and Technology (PCAST) recommended sweeping changes to the first 2 years of college, which are critical for recruitment and retention of STEM students (1). Although reform efforts call for evidence-based pedagogical approaches, supportive learning environments, and changes to faculty teaching culture and reward systems, one important aspect needs more attention: changing expectations about what students should learn, particularly in college-level introductory STEM courses. This demands that faculty seriously discuss, within and across disciplines, how they approach their curricula.

Compared with lecture-only courses, active-learning pedagogies (e.g., the use of personal response “clicker” systems or peer instruction) can improve retention and course grades, particularly for underprepared and underrepresented students (2). But conversation must extend beyond interactive classrooms to how to support students to develop and use deep, transferrable knowledge. Even after successful completion of several college-level science courses, there are huge challenges to understanding and using scientific knowledge (3). *A Framework for K-12 Science Education: Practices, Crosscutting Concepts, and Core Ideas* (4) provides the most up-to-date, research-based strategies for pro-

moting deep learning and is well aligned with other international initiatives. These strategies were developed for K-12 (primary and secondary education), but we believe the approach is valid for the first 2 years of college.

CORE IDEAS, CROSSCUTTING CONCEPTS.

Disciplinary experts have a great deal of knowledge—organized and contextualized around important concepts (5). Students should develop knowledge around these “disciplinary core ideas” rather than try to assemble understanding from many disparate ideas and activities. Core ideas should be advanced over time through carefully developed progressions of learning activities



and assessments that provide students and instructors with feedback about student understanding (6). This is at odds with most introductory science courses that attempt to provide an overview of the discipline. Ideas and concepts are often compartmentalized by chapter, which obscures connections within and across courses and makes it difficult for students to correlate facts, ideas, and exercises (1).

Several initiatives have developed around a model for organizing ideas in a discipline. *Vision and Change...* (7) identified core ideas in biological sciences. Reforms of Advanced Placement courses in the United States and Canada, which offer college-level courses to secondary students, were built around “big ideas” in biology, chemistry, and physics (8). Although efforts must be informed by

national-level initiatives and the research literature, we believe that core ideas must be negotiated locally by faculty in each discipline in order to build ownership and buy-in.

For example, core ideas that emerged from cross-disciplinary discussions at our institution, Michigan State University (MSU), include “evolution” for biology, “structure and properties” for chemistry, and “interactions cause changes in motion” for physics. Focusing on core ideas within each discipline allows reduction of the amount of material that many agree has become overwhelming (the “mile-wide, inch-deep” problem). Faculty agreement on what is centrally important moves the conversation from what to eliminate to what supports core ideas.

There are also ideas that span disciplines—“crosscutting concepts,” such as cause and effect, conservation of energy and matter, and systems thinking. Energy itself is a core idea in each discipline, yet we rarely note the different ways disciplines treat energy, leaving students often unable to apply what they have learned in one discipline to another. If each discipline were to agree on a coherent approach, it would allow students to construct understanding and to apply that knowledge across disciplines.

PRACTICES AND LEARNING.

Although many reform efforts have focused on “inquiry”—an idea with different connotations depending on context and audience (9)—the *Framework* describes eight “scientific and engineering practices” that can be thought of as disaggregated components of inquiry, e.g., developing and using models and engaging in arguments from evidence. Descriptions of these practices make it more likely that they will be incorporated into teaching and learning. Such descriptions will aid design of assessments that require students to use content knowledge (core ideas) in the same ways scientists do (by engaging in scientific practices). These practices can actively engage students in using their knowledge to predict, model, and explain phenomena—which one might argue is the primary goal of science.

Instead of developing or assessing core ideas, crosscutting concepts, and scientific practices separately, they should be integrated into “three-dimensional learning” (10). Emphasizing and integrating the

Michigan State University, East Lansing, MI 48824 USA.
*Correspondence to: mmc@msu.edu

three dimensions will necessarily change our approach to instruction. Providing students with opportunities to develop models, construct explanations, and engage in arguments using evidence requires that courses become more student-centered. Assessments must measure not only what students know but also how they use their knowledge. Although some transformation efforts have measured reforms' success by using multiple choice assessments [e.g. concept inventories (11)], these do not address how students use knowledge in the ways we have discussed here.

At MSU we are developing evidence-based approaches to assessment and instruction that incorporate the three dimensions (10, 12). Although constructing and scoring these items is more difficult and time-consuming than traditional questions, assessments must change, or students will not learn to use scientific practices and core ideas to make sense of phenomena.

The pace of change in higher education can be glacially slow. Increasing numbers of students will enter college whose learning has been informed by the *Framework*. Higher education should capitalize on their carefully scaffolded knowledge. It would be a disservice to throw these students back into typical introductory courses that focus on memorizing facts and algorithmic calculations. ■

REFERENCES AND NOTES

1. PCAST, "Engage to excel: Producing one million additional college graduates with degrees in science, technology, engineering, and mathematics" (White House, Washington, DC, 2012); <http://1.usa.gov/10wzsbh>.
2. S. Freeman et al., *Proc. Natl. Acad. Sci. U.S.A.* **111**, 8410 (2014).
3. National Research Council, *Discipline-Based Education Research: Understanding and Improving Learning in Undergraduate Science and Engineering* (National Academies Press, Washington, DC, 2012).
4. National Research Council, *A Framework for K-12 Science Education: Practices, Crosscutting Concepts, and Core Ideas* (National Academies Press, Washington, DC, 2012).
5. National Research Council, *How People Learn: Brain, Mind, Experience, and School* (National Academies Press, Washington, DC, 1999).
6. J. S. Krajcik, L. M. Sutherland, K. Drago, J. Merritt, in *Making It Tangible: Learning Outcomes in Science Education*, S. Bernholt, K. Neumann, P. Nentwig, Eds. (Waxmann, Münster, 2012), pp. 261–284.
7. AAAS, *Vision and Change in Undergraduate Biology Education: A Call to Action* (AAAS, Washington, DC, 2011).
8. W. B. Wood, *Science* **325**, 1627 (2009).
9. M. Windschitl, *J. Res. Sci. Teach.* **41**, 481 (2004).
10. National Research Council, *Developing Assessments for the Next Generation Science Standards* (National Academies Press, Washington, DC, 2014).
11. R. R. Hake, *Am. J. Phys.* **66**, 64 (1998).
12. National Research Council, *Knowing What Students Know: The Science and Design of Educational Assessment* (National Academies Press, Washington, DC, 2001).

ACKNOWLEDGMENTS

This project was supported by the Association of American Universities' Undergraduate STEM Education Initiative, funded by the Helmsley Charitable Trust, and by the Office of the Provost of Michigan State University.

10.1126/science.aab0933

MEDICINE

Personalization in practice

Dynamic computational modeling integrated with experimentation can enable precision medicine

By Ravi Iyengar,¹ Russ B. Altman,² Olga Troyanskaya,³ Garret A. FitzGerald⁴

Last month, an advisory committee released recommendations for recruiting at least 1 million individuals to participate in the U.S. National Institutes of Health's Precision Medicine Initiative. This bold approach to disease treatment and prevention seeks to account for an individual's genes, environment, and lifestyle to improve health outcomes. The ability to collect, integrate, analyze, and model relevant data streams is central to this effort. Moving beyond "just" massive data collection will require structured convergence among various disciplines. So, how should data be gathered? Here, computational modeling can be a useful guide. Modeling at the molecular, cellular, tissue, and organismal level will be essential to identify the molecular interactions that underlie progressive diseases and to generate a comprehensive and dynamic picture of the individual.

"If you want me to play only the notes without any specific dynamics, I will never make one mistake."

Vladimir Horowitz

In 2011, precision medicine was described by the U.S. National Research Council as resting on a "new taxonomy for human disease based on molecular biology" (1), but implicit in this notion is the assumption that defining noncommunicable diseases on the basis of an individual's genomic and epigenomic determinants alone will enable

the personalization of therapy. This has led to conflation of the terms "personalized" and "precision." The overlap is reasonable when the dominant driver of a disease is largely genomic, as in most cancers. However, for many other progressive conditions such as type 2 diabetes, psychiatric diseases, and heart failure, it is not clear whether genomic status is the major driver. All progressive diseases have genomic underpinnings, but it is the impact of diverse environmental influences—mostly unrecognized—on individual genomes that determines interindividual variation in disease progression and drug response (2). In short, we need to know the dynamics of an individual's physiology and pathophysiology.

Empowering the Precision Medicine Initiative requires a formalism to describe relationships between scales of organization and different time domains. This involves a convergence of measurements—from human cell culture experiments to studies in model organisms and clinical measurements in patients—and modeling to reflect unique and general aspects of each system and its relationship to human health and disease throughout the lifetime of an individual. There are several emerging powerful experimental and modeling technologies to do this. For example, induced pluripotent stem cells (iPSCs) enable cell type-specific measurements and provide the opportunity for in vitro experimentation with tissues at the level of an individual. Systems biology provides modeling formalisms to match key features of the molecular, cellular, tissue, and whole-organ physiologies for simulations. Here, Bayesian integration of heterogeneous data (3) can be a good starting point. Graph theory helps build networks that describe the local and regional geography of cells, organs, and organ systems. Dynamical modeling describes how this biological geography changes with environment, lifestyle, and age. Some of the dynamic modeling approaches are monomorphic (e.g., differential equation-based models), whereas some are more modular (linked simulations with different formalisms for different subsystems). Irrespective of the approaches used, modeling disease dynamics must start early, with incomplete data. Simulations can then drive the design of large-scale studies that are both clinical and laboratory-based.

¹Department of Pharmacology and Systems Therapeutics, Systems Biology Center New York, Icahn School of Medicine at Mount Sinai, New York, NY 10029, USA. ²Department of Bioengineering, Stanford University School of Medicine, Stanford, CA 94305, USA. ³Department of Computer Science and Lewis-Sigler Institute of Integrative Genomics, Princeton University, Princeton, NJ 08544, USA, and Simons Center for Data Analysis, Simons Foundation, New York, NY 10010, USA. ⁴Department of Systems Pharmacology and Translational Therapeutics, Perelman School of Medicine, University of Pennsylvania, Philadelphia, PA 19104, USA. E-mail: ravi.iyengar@mssm.edu; garret@exchange.upenn.edu

Why do we need to consider dynamics at multiple levels? Empirical observations indicate that genomic and molecular diversity often leads to phenotypic convergence, resulting in a limited number of phenotypes. Dynamic processes at multiple levels are likely to drive phenotypic convergence. Such convergence can offer opportunities for shared treatments for maladies that have different underlying molecular and cellular architectures. For instance, a single kind of arrhythmia such as long-QT syndrome can arise from mutations in multiple genes encoding ion channels (4). As there is little research relating mutations to drug targets and therapy, knowledge of which genes are mutated offers no particular advantage when deciding therapeutic strategies for arrhythmias. Another example is hypertension, which can be treated with drugs that are molecularly diverse (e.g., diuretics that act on renal tubules; ACE inhibitors that regulate vessel wall function; beta blockers that act predominantly on the heart). This reflects the molecular and tissue-based diversity underlying this phenotype. Currently, treatment for hypertension, although broadly effective, remains empirical, wherein both the type and timing of drug(s) used are arrived at by trial and error.

It may be possible to make therapy predictable by integrating several types of models—stochastic and statistical models that relate molecular and environmental determinants to disease origin and progression, and dynamical models of the pathophysiological process and effects of drug treatment. Clinical data such as brain imaging or circulating amounts of a peptide hormone or blood sugar would constrain such models. Modeling should then allow one to frame hypotheses for additional cell-based experiments and even clinical data gathering. These experiments include using human iPSC-derived cells that produce organs on engineered chips for high throughput analysis (5) or using humanized animal models wherein the cellular circuitries have been reengineered to reflect the human genomic and epigenomic determinants. Data from cell-level and humanized model system experiments could, in turn, enable better selection criteria for clinical data gathering. iPSC-derived cell types from patients are showing promise in modeling disease processes (6), and the combination of cell-level experiments with clinical data

could enumerate the canonical molecular mechanisms underlying disease and explain how variations in such mechanisms drive disease progression (or lack thereof) in individual patients. In addition, models need to be well coupled to individual pharmacokinetic-pharmacodynamic profiles. Pharmacodynamic analysis is largely conducted early in studies of tolerability after the first introduction of a drug into humans. Given the potential role of the mi-

figure). Such predictions could specify which clinical parameters to measure and at what intervals. The clinical measurements could include readouts of environmental influences, such as metabolomics and proteomics, and quantitative and integrative measures of whole-body physiology (e.g., blood pressure, heart rate) and noninvasive imaging of organ functions, such as with functional magnetic resonance imaging. The results of model-directed experiments and clinical readouts

would in turn be used to update the initial models, yielding better predictions of molecular, cellular, and organismal pathophysiology and providing directions for further experimental follow-up. This iterative approach to modeling should accelerate convergence to more accurate models by directing experiments to areas where additional information is most necessary.

It is likely that initial integrated models that drive further data gathering will only be partially correct, as our biochemical and cell physiological knowledge of health and disease is incomplete. However, initial poorly performing models can indeed converge to high-performance models through multiple rounds of experimentation and model refinement. A recent example of this comes from animal model studies of kidney disease progression, where better model predictions “treated” a kidney disease by directing drug therapy that reversed one cellular basis for the disease phenotype (7).

The million-person cohort envisaged by the Precision Medicine Initiative should provide an unprecedented wealth and breadth of data. Gathering these data should be driven by modeling analyses



Data and dynamics. Empowering precision medicine requires an iterative process of gathering data in a manner that is driven by integrative computational models. New data can then lead to model refinement, experimental follow-up, and further data, thereby capturing the dynamics of a biological process.

robiome in controlling disease origination and progression as well as drug disposition and efficacy (and its dependence on diet and time of day), integration of such data may be necessary for pharmacological modeling of precision therapy.

Currently, data gathering, even for big data sets, is largely empirical and is not driven by computational models that can enable predictive simulations of dynamics. Modelers generally only provide input about experimental design relating to considerations of sample size to enable sound statistical correlations. However, what is needed is to build initial integrative models based on current knowledge of genomics and epigenomics and the relevant biochemistry and cellular-tissue physiology, to predict how the to obtain data from these very large cohorts (see the

that capture the dynamics of disease evolution at multiple scales of organization. These data and models should enable predictions of efficacious therapies over time for an individual, making the aspiration of precision medicine a reality. ■

REFERENCES

1. National Research Council, *Toward Precision Medicine: Building a Knowledge Network for Biomedical Research and a New Taxonomy of Disease* (National Academies Press, Washington, DC, 2011).
2. S. Fries *et al.*, *Gastroenterology* **130**, 55 (2006).
3. C. S. Greene *et al.*, *Nat. Genet.* **47**, 569 (2015).
4. L. Crotti, G. Celano, F. Dagradi, P. J. Schwartz, *Orphanet J. Rare Dis.* **3**, 18 (2008).
5. S. N. Bhatia, D. E. Ingber, *Nat. Biotechnol.* **32**, 760 (2014).
6. G. Tiscornia, E. L. Vivas, J. C. Izpisua Belmonte, *Nat. Med.* **17**, 1570 (2011).
7. E. U. Azeloglu *et al.*, *Sci. Signal.* **7**, ra12 (2014).

BOOKS *et al.*

NEUROSCIENCE

Cruel and unuseful punishment

Psychological studies call into question the efficacy of enhanced interrogation techniques

By **Richard J. McNally**

Following the 9/11 attacks, the Bush Administration secretly authorized the use of “enhanced interrogation techniques” to compel suspected terrorists to divulge threats to America’s national security. Widely regarded as a euphemism for torture, these techniques included depriving detainees of sleep, food, clothing, and toilets for prolonged periods while forcing them to assume painful positions in frigid isolation cells. Some suspects were subjected to “waterboarding”—terrifying episodes of interrupted drowning in which water is poured over a cloth covering the nose and mouth. Outrage occurred when these practices became public, and the moral reputation of the United States was damaged throughout the world.

While denying that these practices qualified as torture, the Administration and its allies also invoked the “ticking time bomb” defense to justify their efforts. In this thought experiment, law enforcement officers have seized a suspected terrorist who harbors information about an imminent attack on American soil. Should interrogators torture the detainee, forcing him to disclose details of the attack? Or should their moral aversion to inflicting temporary pain cost the lives of countless innocent civilians? Advocates of enhanced interrogation argue that, although torture is abhorrent, we must do whatever we can to prevent acts of terrorism.

Legal scholars have published persuasive moral rebuttals to the ticking time bomb defense for torture (1). Yet does torture actually work? To be sure, it can compel people

The reviewer is at the Department of Psychology, Harvard University, Cambridge, MA 02138, USA.
E-mail: rjm@wjh.harvard.edu



A protestor kneels on the ground outside the 9th U.S. Circuit Court of Appeals in Pasadena, California.

to confess to crimes and to repudiate their religious and political beliefs. But there is a world of difference between compelling someone to speak and compelling them to tell the truth. As Khalid Sheikh Mohammed said, “During the harshest period of my interrogation I gave a lot of false information in order to satisfy what I believed the interrogators wished to hear in order to make the ill-treatment stop.” Yet the assumption underlying the ticking time bomb defense is that abusive questioning reliably causes people to reveal truthful information that they would otherwise refuse to disclose. Few scholars have scrutinized this assumption—and none with the rigor, depth, and clarity of Shane O’Mara in his excellent book, *Why Torture Doesn’t Work: The Neuroscience of Interrogation*.

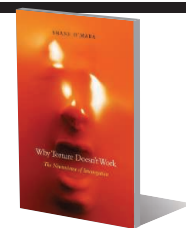
O’Mara is professor of experimental brain research at the University of Dublin’s Trinity College and director of its Institute of Neuroscience. Although he agrees “with the moral, ethical, and legal case against torture,” his argument against it occurs within an empirical, consequentialist framework, not an ethical one. Invoking the relevant science, he shows that torture undermines the very neurocognitive mechanisms requisite for recalling veridical information from memory.

The book’s subtitle underestimates its range. In addition to neuroscience, O’Mara draws on cognitive, social, and clinical psychology to document his case against the efficacy of torture. After providing an accessible survey of the brain circuits that mediate cognitive functions, O’Mara reviews studies in which volunteers were exposed to moderate levels of emotional stress, pain, sleep deprivation, and cold temperatures and then asked to recall the details of various hypothetical scenarios. Despite their motivation to recall and disclose this information, subjects exposed to such stressors performed far worse than control subjects. Other studies involving volunteers from elite

Why Torture Doesn't Work The Neuroscience of Interrogation

Shane O’Mara

Harvard University Press,
2015. 330 pp.



Special Forces units who were subjected to intense, abusive mock interrogations confirm the neurocognitive deficits that occur under these conditions.

For obvious reasons, there are no randomized controlled trials comparing the relative efficacy of enhanced interrogation techniques with traditional interrogation. However, it is reasonable to assume that if subjects exposed to relatively moderate stressors exhibit pronounced neurocognitive impairments, then torture will surely make matters much worse.

O’Mara debunks the hyperbolic promises of functional magnetic resonance imaging and other questionable methods of detecting deception and discusses the collateral emotional damage suffered by many perpetrators of torture, including posttraumatic stress disorder and unremitting guilt. In the book’s closing chapter, he shows that the most reliable method for obtaining factual information from detainees is to foster rapport and use nonabusive questioning.

O’Mara advises counterterrorism officials to heed the advice of Napoleon Bonaparte, who said, “The barbarous custom of having men beaten who are suspected of having important secrets to reveal must be abolished.... The poor wretches say anything that comes into their mind and what they think the interrogator wishes to know.”

REFERENCES

1. Y. Ginbar, *Why Not Torture Terrorists?* (Oxford University Press, Oxford, 2008).

10.1126/science.aad2340

How to fail out of your graduate program

A tongue-in-cheek guide aims to help students avoid common grad school mistakes

By Owen Parsons

Thinking of applying to work in a laboratory just because the supervisor is hip and happening? Or perhaps you're planning on getting a doctorate to please your overbearing parents? If so, you might want to consider picking up a copy of Kevin Haggerty and Aaron Doyle's handbook on these and other surefire ways to jeopardize your postgraduate studies.

57 Ways to Screw Up in Grad School is a lighthearted yet comprehensive guide to making it through postgraduate education in one piece. The book covers everything from deciding where to apply and putting together an application through submitting your thesis and taking the next steps

The reviewer is at the Autism Research Centre, University of Cambridge, Cambridge CB2 1TN, UK. E-mail: oep20@cam.ac.uk

in your career. Each of the book's 57 pieces of advice starts with a tongue-in-cheek title, offering up different ways in which you could potentially shoot yourself in the foot during your graduate studies, such as "Avoid your supervisor and committee" or "Expect people to hire you to teach your thesis." The authors then present sensible and sound advice on how to avoid such pitfalls. The guide also covers topics such as having an active social life, developing a range of transferable skills, and even avoiding a social media crisis.

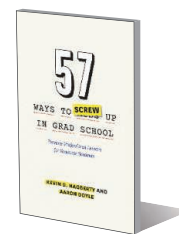
Haggerty and Doyle present their advice in the singular first person, combining their academic nous to provide a clear and identifiable narrative throughout the book. The two authors are well equipped to offer advice on the ins and outs of grad school, having both served as graduate chairs for their respective departments. They apply this experience well throughout the book, recalling a compendium of mistakes that

57 Ways to Screw Up in Grad School

Perverse Professional Lessons for Graduate Students

Kevin D. Haggerty and Aaron Doyle

University of Chicago Press, 2015. 199 pp.



they have either committed themselves or observed firsthand. Although the material covered predominantly focuses on the American graduate school structure, it is still relevant to international students if taken with a pinch of salt.

While the book is primarily geared toward prospective graduate students, it also offers a host of helpful tips for those in the midst of their doctorates. The chapters are well structured and coherently grouped into topics ranging from working with your advisor(s) to managing your research program to preparing for graduation, allowing readers to dip in and out as they please.

Literally following the "57-step program" would undoubtedly guarantee disaster. Luckily, this book offers readers practical and entertaining advice on how to get the most out of the graduate school experience.

10.1126/science.aad2071



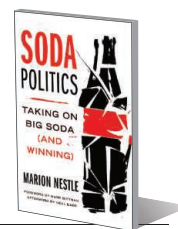
Little more than flavored sugar water, soft drinks have become a ubiquitous fixture in the modern world.

PUBLIC HEALTH

Soda Politics Taking on Big Soda (and Winning)

By Marion Nestle

Oxford University Press, 2015. 524 pp.



The standard operating practices of companies like Coca-Cola and PepsiCo demand the same level of scrutiny as cigarette companies, and for many of the same reasons, argues Marion Nestle in the introduction of her new book, *Soda Politics*. What follows is a thorough and unflinching look at the soft-drink industry's role in promoting the consumption of sugary drinks despite growing evidence that they are detrimental to our health. The book begins with a basic primer of the range of health problems that have been linked to soda consumption, from tooth decay to obesity and diabetes, hitting its stride with an eviscerating assessment of the industry's marketing and advocacy practices.

10.1126/science.aad5217

LETTERS

Edited by Jennifer Sills

Many paths to parity for women in science

IN HER LETTER “Sexism discussion misses the point” (24 July, p. 390), H. S. Young advocates for improved infrastructure to assist women in the child-bearing years, when “research productivity needs to be the highest.” She contends that the lack of support mechanisms that enable women to work at this level is the substantial barrier that impedes women from reaching full equality in science. We also advocate for improved infrastructure for women who desire to work within the framework of a standard career trajectory, but we are concerned by the underlying assumption that this is the only path to parity.

The prevailing notion that research productivity needs to be the highest during typical child-bearing years has the underlying message that women need to be working fully and aggressively during that period in order to be successful. Many women are not willing, or able, to take on that lifestyle. Faced with this choice, even in the presence of strong departmental support and outstanding childcare facilities, many opt out completely.

Alternative frameworks are needed to keep talented women (and increasingly men who share child-rearing) in science. Working at a limited scope full-time, or working part-time, can and does yield important work, and this must be respected and recognized by the community and by institutions. Additional mechanisms and practices need to be developed to engage women without the current level of time and travel commitment, and the standard criteria for institutional promotion need to be reexamined to reward a broader range of substantial contributions.

As senior women members of the International Society of Magnetic Resonance in Medicine (ISMRM), we are working with other members in the society and with ISMRM leadership and staff to develop such mechanisms in our organization, and we encourage other organizations and institutions to do the same.

Deborah Burstein,^{1*} Margaret Hall-Craggs,² Clare Tempany³

¹Beth Israel Deaconess Medical Center and Harvard Medical School, Boston, MA 02115, USA. ²University College Hospital London, London, NW1 6BU, UK. ³Brigham and Women’s Hospital, Boston, MA 02115, USA.

*Corresponding author. E-mail: dburstei@bidmc.harvard.edu

REFERENCE NOTE

1. The authors endorse this letter along with 37 additional senior international signatories, available online as supplementary material.

SUPPLEMENTARY MATERIAL

www.sciencemag.org/content/350/6258/286/suppl/DC1
Full author list

Relocation risky for bumblebee colonies

WE DO NOT dispute the results of the Report “Climate change impacts on bumblebees converge across continents” (10 July, p. 177),



in which J. T. Kerr *et al.* show that shrinking bumblebee ranges track temperature changes in unexpected and alarming ways at a continental scale, supporting previous suggestions (1) that climate change will affect *Bombus* distributions. We are concerned, however, by Kerr *et al.*’s suggestion that “[e]xperimental relocation of bumblebee colonies into new areas could mitigate these range losses.”

Such a simple solution may have great appeal to the public and policy-makers, but complex and unpredictable repercussions if put into practice. Movement of bumblebee species for pollination services has been implicated in threats to native bumblebee fauna worldwide (2). For example, the introduction of European species into South America has contributed to the catastrophic collapse of native bumblebees (3). At a time when researchers are arguing for greater

regulation of bumblebee movement [e.g., (4, 5)], Kerr *et al.*’s suggestion of colony relocation as a conservation strategy should be approached with caution.

Perhaps the greatest risk of interregional transportation lies with the spread of disease, a factor not considered by Kerr *et al.*, but suspected to be behind the decline of some species (6). Bumblebees may host a diversity of parasites and pathogens, and relocated colonies reared in captivity may negatively affect native pollinator communities through co-introduction and spread of disease (5). Competition with native fauna is also a concern (2), as are population genetic factors (e.g., incomplete knowledge of taxonomy and population structure resulting in unfavorable outbreeding) (7). Concerns are not limited to intercontinental transportation, but also apply to movement of native species within and between regions (5, 7).

In the absence of comprehensive mechanistic knowledge, it may be preferable to facilitate natural range changes through habitat management, rather than conducting interventions that may have short-term benefits to ecosystem services but long-term consequences for global pollinator communities. Ultimately, efforts to overcome perceived challenges to a species’ natural ability to match climatic shifts should be preceded by detailed ecological and evolutionary studies in both source and destination regions.

Jeffrey D. Lozier,^{1*} Sydney A. Cameron,² Michelle A. Duennes,² James P. Strange,³ Paul H. Williams,⁴ David Goulson,⁵ Mark J. F. Brown,⁶ Carolina Morales,⁷ Sarina Jepsen⁸

¹Department of Biological Sciences, University of Alabama, Tuscaloosa, AL 35487, USA. ²Department of Entomology, University of Illinois, Urbana, IL 61801, USA. ³USDA-ARS, Pollinating Insect Research Unit, Utah State University, Logan, UT 84322, USA. ⁴Department of Life Sciences, Natural History Museum, London, SW7 5BD, UK. ⁵Evolution, Behaviour, and Environment, School of Life Sciences, University of Sussex, Falmer, East Sussex, BN1 9QG, UK. ⁶School of Biological Sciences, Royal Holloway University of London, Egham, TW20 0EX, UK. ⁷Laboratorio Ecotono, INIBIOMA (Universidad Nacional del Comahue-CONICET), Bariloche, Rio Negro, Argentina. ⁸The Xerces Society for Invertebrate Conservation, Portland, OR 97232, USA.

*Corresponding author. E-mail: jlozier@ua.edu

REFERENCES

1. P. H. Williams, M. Araujo, P. Rasmont, *Biol. Conserv.* **138**, 493 (2007).
2. D. Goulson, *Appl. Entomol. Zool.* **45**, 7 (2010).
3. C. L. Morales, M. P. Arbetman, S. A. Cameron, M. A. Aizen, *Front. Ecol. Environ.* **11**, 529 (2013).
4. International Union for Conservation of Nature

Bumblebee Specialist Group, Commercial Bumblebee Policy Statement (www.iucn.org/about/work/programmes/species/who_we_are/ssc_specialist_groups_and_red_list_authorities_directory/invertebrates/bumblebee_specialist_group/commercial_bumblebee_policy_statement/).

5. D. Goulson, W. O. H. Hughes, *Biol. Conserv.* **191**, 10 (2015).
6. S. A. Cameron *et al.*, *Proc. Natl. Acad. Sci. U.S.A.* **108**, 662 (2011).
7. S. H. Woodard *et al.*, *Mol. Ecol.* **24**, 2916 (2015).

Response

LOZIER *ET AL.* accept our findings but take issue with a concluding sentence alluding to relocation to mitigate potential climate change impacts on bumblebee species. We welcome thoughtful discussion of this admittedly difficult area (1). However, Lozier *et al.* present an idiosyncratic view of managed relocation involving indiscriminate movement of colonies into new continents or islands. Such “maverick” (2) relocation approaches do not represent best practices to mitigate climate change impacts (3). Instead, we recommend well-known criteria for evaluating the appropriateness and safety of relocation (4–6). If implemented, managed relocation would experimentally nudge colonies beyond historical boundaries into areas

made newly available by changing climatic conditions. Species relocated to adjacent areas would encounter other bumblebee species with which they are already sympatric. Managed relocation frameworks require understanding of pathogen risks (4).

Lozier *et al.* propose managing habitats in areas near species’ range limits and hoping that bumblebee species will generally begin to shift north. The desired outcome, scale, and risks for this intervention match relocation. However, managing habitats on two continents for bees to enable range expansion will incur costs that are hard to calculate and could harm nontarget taxa. It may also fail, as range expansion in bumblebees over several decades has not compensated for rapid range losses from the south. Habitat management alone will not conserve even relatively thermophilic organisms if climate changes continue unabated (7).

**Jeremy T. Kerr,^{1*} Alana Pindar,¹
Paul Galpern,² Laurence Packer,³
Simon G. Potts,⁴ Stuart M. Roberts,⁴
Pierre Rasmont,⁵ Oliver Schweiger,⁶
Sheila R. Colla,⁷ Leif L. Richardson,⁸
David L. Wagner,⁹ Lawrence F. Gall,¹⁰
Derek S. Sikes,¹¹ Alberto Pantoja^{12†}**

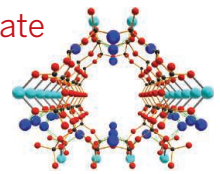
¹Department of Biology, University of Ottawa, Ottawa, ON, K1N6N5, Canada. ²Faculty of Environmental Design, University of Calgary, Calgary, AB, T2N 1N, Canada. ³Department of Biology, York University, Toronto, ON, M3J 1P3, Canada. ⁴School of Agriculture, Policy and Development, The University of Reading, Reading, RG6 6AR, UK. ⁵Department of Zoology, Université de Mons, Mons, 7000, Belgium. ⁶Department of Community Ecology, Helmholtz Centre for Environmental Research, Halle, 06120, Germany. ⁷Wildlife Preservation Canada, Guelph, ON, N1H 6J2, Canada. ⁸Gund Institute, University of Vermont, Burlington, VT 05405, USA. ⁹Department of Ecology and Evolutionary Biology, University of Connecticut, Storrs, CT 06269, USA. ¹⁰Peabody Museum of Natural History, Entomology Division, Yale University, New Haven, CT 06511, USA. ¹¹University of Alaska Museum, University of Alaska Fairbanks, Fairbanks, AK 99775, USA. ¹²U.S. Department of Agriculture, Agricultural Research Service, Subarctic Agricultural Research Unit, Fairbanks, AK 99775, USA.

*Corresponding author. E-mail: jkerr@uottawa.ca

†Present address: United Nations Food and Agriculture Organization, Santiago, 7630412, Chile.

REFERENCES

1. N. Hewitt *et al.*, *Biol. Conserv.* **144**, 2560 (2011).
2. J. S. McLachlan, J. J. Hellmann, M. W. Schwartz, *Conserv. Biol.* **21**, 297 (2007).
3. M. W. Schwartz *et al.*, *BioScience* **62**, 732 (2012).
4. O. Hoegh-Guldberg *et al.*, *Science* **321**, 345 (2008).
5. D. M. Richardson *et al.*, *Proc. Natl. Acad. Sci. U.S.A.* **106**, 9721 (2009).
6. P. Rasmont *et al.*, *BioRisk* **10**, 1 (2015).
7. T. H. Oliver *et al.*, *Nat. Clim. Change* **5**, 941 (2015).



IN SCIENCE JOURNALS

Edited by Stella Hurtley

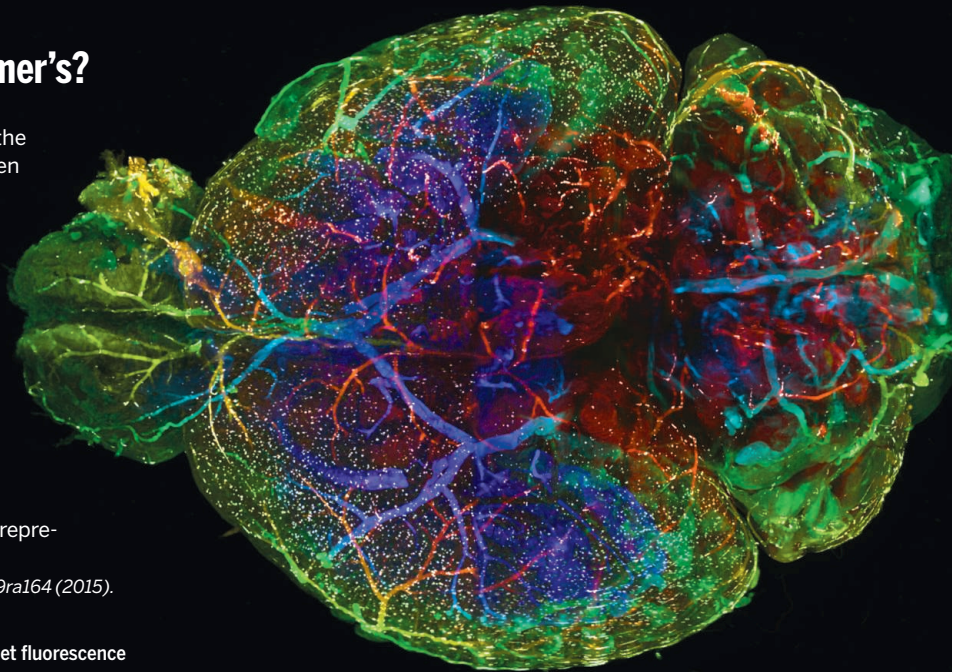
ALZHEIMER'S DISEASE

New drug target for Alzheimer's?

Mouse models do not fully capture the degeneration of brain networks seen in human Alzheimer's disease (AD). Thus, extensive validation of therapeutic targets in many animal models must precede human clinical research. Huang *et al.* now show that the absence of G protein-coupled receptor 3 (GPR3), a protein expressed in the brain, alleviated cognitive deficits and reduced amyloid pathology in four disease-relevant mouse models of AD. Furthermore, postmortem brain tissue from a subset of AD patients revealed elevated GPR3. Thus, GPR3 may represent a therapeutic target in AD. — OMS

Sci. Transl. Med. 7, 309ra164 (2015).

AD transgenic mouse brain imaged using lightsheet fluorescence microscopy. Blood vessels (blue); amyloid plaques (yellow)



OCEAN VARIABILITY

Ocean circulation changes not needed

What causes the pattern of sea surface temperature change that is seen in the North Atlantic Ocean? This naturally occurring quasi-cyclical variation, known as the Atlantic Multidecadal Oscillation (AMO), affects weather and climate. Some have suggested that the AMO is a consequence of variable large-scale ocean circulation. Clement *et al.* suggest otherwise. They find that the pattern of AMO variability can be produced in a model that does not include ocean circulation changes, but only the effects of changes in air temperatures and winds. — HJS

Science, this issue p. 320

QUANTUM INFORMATION

Stringing together a powerful amplifier

Amplifying microwave signals with high gain and across a broad range of frequencies is crucial in solid-state quantum information processing (QIP). Achieving broadband operation is especially tricky. Macklin *et al.* engineered an amplifier that contains a long chain of so-called Josephson junctions (see the Perspective by Cleland). The amplifier exhibited high gain over a gigahertz-sized bandwidth and was able to perform high-fidelity qubit readout. Because the amplifier will be capable of reading out as many as 20 qubits simultaneously, it may help to scale up

QIP protocols. — JS

Science, this issue p. 307; see also p. 280

NEURAL PROGENITORS

Changes over time build neuronal diversity

Although neural progenitors can keep generating new neurons, they can generate different neurons as the organism develops. Two different sections of the *Drosophila* brain, the mushroom bodies and the antennal lobes, show this characteristic, although the antennal lobes produce more different types of neurons over development than do the mushroom bodies. Liu *et al.* identified two RNA-binding proteins that manage

this change over development in both settings. — PJH

Science, this issue p. 317

GENE EXPRESSION

For gene enhancers, less is more

Weak enhancer sequences provide just the right amount of gene activity. Farley *et al.* systematically examined millions of synthetic variants of the Otx enhancer, a motif needed for gene expression in the nervous system of the sea squirt *Ciona*. Proper gene activity resulted when there were imperfect matches to the motif showing strongest enhancer binding and gene activation. When "optimal" motifs were incorporated,

ectopic expression ensued, with aberrant gene activation outside the nervous system. — BAP

Science, this issue p. 325

SMALL NONCODING RNA

A Gaulish partner in silencing transposons

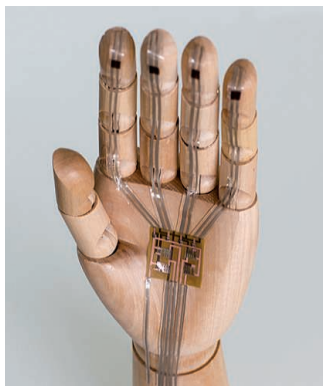
Small noncoding piRNAs protect animal germline genomes from devastating mutation and rearrangement caused by transposons. In fruit fly ovaries, piRNAs bind to Piwi proteins, and together they are required for the recognition and silencing of these parasitic DNA elements. Yu *et al.* show that the gene *Panoramix* acts downstream of the piRNA-driven recognition of transposons to silence their transcription. *Panoramix* does this by binding newly synthesized transposon RNAs. — GR

Science, this issue p. 339

BIOMATERIALS

Sensing the force digitally

Our skin provides us with a flexible waterproof barrier, but it also contains a sensor array that feels the world around us. This array provides feedback and helps us to avoid a hot object or increase the strength of our grip on an object that may be slipping away. Tee *et al.* describe an approach to simulate the mechanoreceptors of human skin, using pressure-sensitive foils and printed ring



Artificial sensors will measure grip strength

PHOTOS: (FROM TOP) CYRIL RUOSO/CORBIS; TEE ET AL.

oscillators (see the Perspective by Anikeeva and Koppes). The sensor successfully converted pressure into a digital response in a pressure range comparable to that found in a human grip. — MSL

Science, this issue p. 314; see also p. 274

T CELL IMMUNITY

Dying to impress the immune system

Besides reacting to microbes, T cells can also mount immune responses to fragments of dying cells, which they encounter displayed on dendritic cells. Not all dying cells activate T cells, however, so what differentiates the dying cells that do? Yatim *et al.* studied two forms of programmed cell death: apoptosis and necroptosis. Using mouse cells in culture and mouse models of inflammatory cell death and anti-tumor immunity, they found that programmed cell death initiated T cell immunity only when the dying cells signaled through the enzyme RIPK1 and the transcription factor NF- κ B. — KLM

Science, this issue p. 328

CALCIUM SIGNALING

Calcium signals down to the millisecond

Engagement of the T cell receptor (TCR) stimulates Ca^{2+} signaling, which is required for T cell activation. The earliest, short-lived Ca^{2+} signals appear near the sites of TCR stimulation. Wolf *et al.* performed high-resolution imaging of Ca^{2+} signals within milliseconds of stimulation of the TCR in live mouse and human T cells. Microinjection of cells with the second messenger NAADP, which is generated upon T cell activation, produced a similar spatiotemporal pattern of Ca^{2+} signals in the absence of TCR activation. Both TCR- and NAADP-dependent signals appeared to trigger the release of Ca^{2+} from the endoplasmic reticulum. — JFF

Sci. Signal. **8**, ra102 (2015).

IN OTHER JOURNALS

Edited by **Kristen Mueller** and **Jesse H. Smith**



Great apes can remember and anticipate surprising events

PRIMATE BEHAVIOR

Great apes can anticipate

Humans can process and store memories as events occur. For example, when we rewatch movies, we can recall and anticipate what will happen next. Kano and Hirata tested whether nonhuman primates also possess this skill by presenting bonobos and chimpanzees with short films and tracking their eye movements. In one film, the apes watched as a villain attacked an actor in a King-Kong suit with one of two objects. Twenty-four hours later, the scientists presented the apes with the same scene, but switching the objects' location. Most of the apes focused their attention on the previously weaponized object shortly before the attack, indicating that they had memorized the events during the previous viewing and could anticipate what happens next. — LNS

Curr. Biol. **25**, 2513 (2015).

RNA PROCESSING

Tipping your RNA cap to stressful times

RNAs transcribed by RNA polymerase II have a chemical "cap" added to their 5' ends. The cap binding complex (CBC), which consists of the nuclear cap binding protein (NCBP) 1 and NCBP2, binds to the cap and ensures proper RNA processing and localization within the cell. Gebhardt *et al.* discovered a second, alternative CBC, which consists of NCBP1 and a previously poorly characterized but highly conserved protein, christened NCBP3. The two

CBCs have both redundant and specific functions, with the alternative CBC seemingly being specifically critical for survival under stressful conditions, such as viral infection. — GR

Nat. Comm. **6**, 10.1038/ncomms9192 (2015).

CANCER

Disrupted signaling networks in cancer

For personalized cancer therapy to succeed in the clinic, scientists need to identify and understand how genetic mutations in tumor cells can drive



Bacteria that adhere to intestinal epithelial cells induce T helper 17 cells

MUCOSAL IMMUNOLOGY

For gut T cells, it's location, location, location

Specific members of the gut microbiota promote the development of different subsets of T lymphocytes in the gut, thereby modulating gut immunity. One example is segmented filamentous bacteria (SFB), which drive the differentiation of T helper 17 (T_H17) cells. The cellular and molecular mechanisms that support this process remain poorly understood. Atarashi *et al.* now demonstrate that several species of bacteria able to adhere to intestinal epithelial cells, including SFB, drive T_H17 cell differentiation in rodents. Sano *et al.* found that SFB primed T_H17 cells in mesenteric lymph nodes. However, these cells only produced interleukin-17, their signature cytokine, in regions of the gut where SFB makes contact with epithelial cells that secrete the inflammatory protein serum amyloid A. — KLM

Cell 10.1016/j.cell.2015.08.058; 10.1016/j.cell.2015.08.061 (2015).

uncontrolled cell growth. In two studies, Creixell *et al.* present theoretical, computational, and experimental analysis of the mechanisms by which mutations might alter a cancer cell's biochemical regulatory networks. A computational approach helped define the molecular basis of substrate specificity of protein kinases, enzymes well known to contribute to certain forms of cancer. Such understanding can help define mutations that would cause signaling to go awry in cancer cells. Their results support the idea that besides modifications that activate or suppress normal signaling events, cancer cells may also accumulate mutations

that actually rewire regulatory pathways. — LBR

Cell 163, 187; 202 (2015).

HYDROLOGY

Smart rocks teach river lessons

Rivers are conveyor belts of erosion, transporting material from continents to the oceans. Measuring how larger gravel and cobbles travel along a riverbed is challenging because of the stochastic nature of grain movement and the dependence on infrequent yet powerful flood events. Olinde and Johnson measured bed load transport in Reynolds Creek in the Owyhee

Mountains (Idaho, USA) using hundreds of natural and artificial rocks with radio-frequency identification (RFID) tags and accelerometers as passive and active tracers. After a series of flood and snowmelt events, these



"Smart rock" with an embedded accelerometer and radio frequency identification tag

"smart rocks" provided direct statistics on bed load displacement, in some cases over 7 km downstream, and rest times as a function of discharge. — NW

Water Resour. Res. 10.1002/2014WR016120 (2015).

QUANTUM ELECTRONICS

Quantum processing takes to the waves

The power of quantum computers is expected to be realized only once the individual components, the quantum bits (or qubits), can be linked up into a large-scale system. Success also requires that the quantum information be reliably transported from one part of the system to another for processing. With several different approaches being undertaken, Schuetz *et al.* propose that surface acoustic waves could propagate the quantum information across a diverse set of solid-state architectures. With piezoeactive materials forming a connected network between qubits, they show theoretically that the quanta should be able to "surf" the acoustic excitations for a variety of on-chip implementations of a quantum computer. — ISO

Phys. Rev. X 5, 31031 (2015).

GEOPHYSICS

Coupled constraints on core formation

The composition of Earth's core puts important constraints on the formation and evolution of the planet. Badro *et al.* apply a new approach that requires harmony between the geochemistry of the rocky mantle and the seismic wave speed velocities in the metal core. The approach requires a core with more oxygen and less silicon than in older models. Surprisingly, this in turn requires a more oxidized mantle for the early Earth, similar to that of the asteroid 4-Vesta. Core formation then dramatically alters mantle chemistry, producing the more reduced mantle observed today. — BG

Proc. Natl. Acad. Sci. U.S.A. 10.1073/pnas.1505672112 (2015).

ALSO IN SCIENCE JOURNALS

Edited by Stella Hurtley

TRANSCRIPTION

A tripartite gene silencing complex

The formation of specialized cell types during development involves the silencing of genes not required in those cell types. An important player in this silencing process is the polycomb repressive complex 2 (PRC2), which methylates histone H3 on lysine residue 27 (H3K27me). Jiao and Liu determined the x-ray crystal structure of a functional PRC2 complex from a thermophilic yeast species (see the Perspective by Schapira). The intimate association of the three subunits confers stability to PRC2. The structure also reveals how the reaction product, H3K27me, stimulates PRC2 allosterically and how a cancer-associated histone mutation blocks the PRC2 active site. — GR

Science, this issue p. 291;
see also p. 278

PLANETARY SCIENCE

New Horizons' views of Pluto

The flyby of Pluto and its moon Charon by the New Horizons spacecraft generated news coverage around the world. Now Stern *et al.* report the first scientific results from the high-speed encounter. The surface of Pluto is surprisingly diverse, with large regions of differing brightness and composition. There is ample evidence for ongoing rich geological processes that act to sculpt its surface. Charon's surface is similarly complex, with numerous relief structures and varied coloration. Pluto's atmosphere is extensive but less dense than expected, whereas Charon has no detectable atmosphere. — KTS

Science, this issue p. 292

SYNTHETIC BIOLOGY

Keeping a leash on cancer-killing cells

Redirecting the immune system to attack tumor cells is proving to be an effective therapy against cancer. However, when patients are exposed to T cells engineered to recognize and attack cancer cells, there is a risk of runaway or excessive activity or of off-target effects, both of which can themselves be deadly. Wu *et al.* designed T cells expressing chimeric antigen receptors that recognize and attack cancer cells with an additional control system. This mechanism would allow a doctor administering the therapy to turn the engineered T cell "on" or "off" by administering a small molecule that is required along with cancer cell antigen to stimulate the T cells and activate their tumor cell-killing properties. — LBR

Science, this issue p. 293

ORGANIC SYNTHESIS

Getting a handle on a cross-linking motif

Although protein backbones consist exclusively of amino acids, various other molecules in the cell often get latched on afterward in a process termed posttranslational modification. In one such motif, called glucosepane, the side chains of lysine and arginine form a condensed cross-link through a reaction sequence with glucose. Formation of this cross-link is of interest in diabetes research. Draghici *et al.* now report a chemical synthesis of glucosepane outside the broader environment of a surrounding protein (see the Perspective by Boger). This synthesis should facilitate more precise characterization of the structure and

function of the motif in vivo.

— JSY

Science, this issue p. 294;
see also p. 275

CATALYSIS

A direct route from acids to alcohols

Making alcohols via hydrogen addition to C=O bonds is among the most widely applied reactions in chemistry. The transformation has also garnered renewed interest for generating commodity chemicals from biomass. Korstanje *et al.* now show that a cobalt compound can catalyze hydrogenation of the C=O bonds in carboxylic acids. These constitute a particularly challenging substrate class, given the propensity of many other catalysts to degrade under acidic conditions. The cobalt catalyst tolerates a versatile substrate range, and the Earth abundance of the metal bodes well for long-term utility. — JSY

Science, this issue p. 298

OCEANOGRAPHY

Understanding abyssal hill spacing

The most prominent topographic features on Earth are abyssal hills found on the bottom of the ocean floor. Olive *et al.* wanted to understand the spacing and size of these hills. They used a model that combines magma supply and the mechanical response of the crust. The model explains observations of hill spacing around mid-ocean ridges. Crustal topography appears to be a poor recorder of changes in magma supply. However, magma supply changes may be faithfully recorded at the base of

the crust. — BG

Science, this issue p. 310

SEPARATION MEMBRANES

Grabbing CO₂ from wet gas streams

It is a challenge to extract CO₂ from typical gas streams, such as the flue gas from a power plant. This is because any water in the stream tends to prevent CO₂ absorption and may also degrade the absorbing material. Datte *et al.* developed a microporous copper silicate that avoids these problems. Most other materials have sites that absorb both water and CO₂ at the same sites, and in that fight, the water tends to win. Although their material still absorbs water, it has separate sites for the CO₂ absorption. It also shows good stability despite the absorbed water and can be reused. — MSL

Science, this issue p. 302

T CELL IMMUNITY

How T cells maintain their identity

Although best known for their pathogen-fighting prowess, T lymphocytes also ensure that the immune response does not run amok. A subset of T cells called regulatory T cells (T_{regs}) performs this function by, for example, making sure T cells only attack pathogens and not self. T cells can exhibit plasticity in their functions in the face of an inflammatory stimulus. Kim *et al.* sought to identify the molecules that ensure the stable maintenance of T_{regs}. Using genetically modified mice, they found that both CD4⁺ and CD8⁺ T_{regs} require the transcription factor Helios to stably maintain their identity. — KLM

Science, this issue p. 334

PLANETARY SCIENCE

**Close encounter with
Mars**

On 19 October 2014, comet Siding Spring passed Mars, close enough for numerous spacecraft and rovers on the red planet to study it. In a Perspective, Lisse explains that the comet came from the Oort Cloud in the far reaches of the solar system. Little is known about the Oort Cloud comets, few of which ever visit the inner solar system. The flyby yielded unprecedented data about the size, chemical composition, and other properties of Siding Spring. It also showed that comets can deposit substantial amounts of material in planetary atmospheres. — JFU
Science this issue p. 277

RESEARCH ARTICLE SUMMARY

TRANSCRIPTION

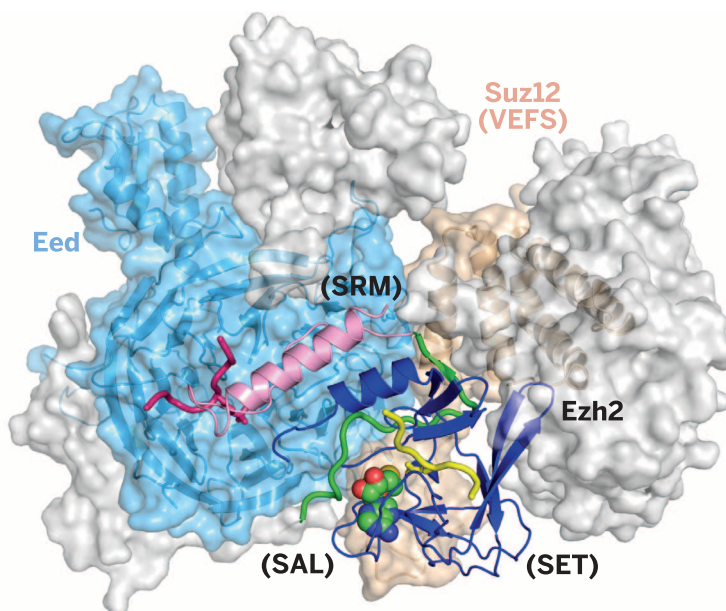
Structural basis of histone H3K27 trimethylation by an active polycomb repressive complex 2

Lianying Jiao and Xin Liu*

INTRODUCTION: Polycomb-group (PcG) proteins are key epigenetic regulators of cell identity determination and maintenance. As one of the main PcG protein complexes, polycomb repressive complex 2 (PRC2) mediates trimethylation of histone H3 at lysine 27 (H3K27me3), a hallmark of gene silencing and facultative heterochromatin formation. Dysregulation of PRC2 function is broadly linked to human diseases, including hematological malignancies, Weaver syndrome, and childhood glioblastoma. PRC2 consists of four core subunits—Ezh2, Eed, Suz12, and Rbbp4—among which Ezh2 is the catalytic subunit, which minimally requires Eed and Suz12 for catalysis. Although the histone methyltransferase activity of PRC2 was discovered more than a decade ago, the catalytic mechanism of PRC2 remains poorly understood. In addition, the end product of PRC2 catalysis, H3K27me3, is known to interact with Eed to stimulate the enzymatic activity of PRC2 allosterically. The details of this positive feedback loop, which is believed to account for spreading of the repressive H3K27me3

histone mark on silent chromatin, are also not fully understood. Additionally, a histone H3K27M missense mutation found in some pediatric brain cancers leads to a global decrease in the amount of H3K27me3 by inhibiting PRC2 through a so far uncharacterized mechanism. To begin to address these outstanding questions regarding PRC2 function and regulation, we report the crystal structures of an active PRC2 complex of 170 kD from the fungus *Chaetomium thermophilum* in both basal and stimulated states at 2.7 and 2.3 Å resolution, respectively.

RATIONALE: As an evolutionarily conserved complex, PRC2 proteins from different species share compositional and functional similarities. Indeed, some fundamental aspects of human PRC2 catalysis and regulation, in particular the H3K27me3-mediated enzyme stimulation and the H3K27M-mediated enzyme inhibition, were faithfully recapitulated in our assays with the reconstituted minimal fungal



Overall structure of an active PRC2 in the stimulated state. The Ezh2, Eed, and Suz12 (VEFS) subunits are shown as gray, light blue, and light brown surfaces, respectively, except for the SET activation loop (SAL), the stimulation-responsive motif (SRM), and the SET regions of Ezh2, which are highlighted as cartoons. The SAL is colored in green, SRM in pink, and SET in blue.

PRC2, containing Ezh2, Eed, and the VEFS domain of Suz12 [Suz12(VEFS)], which was also used for crystallization.

RESULTS: An *S*-adenosyl-*L*-homocysteine (SAH) cofactor and an inhibiting H3K27M cancer mutant peptide bound to the catalytic SET domain of Ezh2 were captured in the crystal structures of both basal and stimulated complexes. In addition, a stimulating H3K27me3 peptide bound to both Ezh2 and Eed was also resolved in the latter. Structural analysis and accompanying biochemical assays provided the

following mechanistic insights into PRC2 catalysis and regulation. First, Ezh2, Eed, and Suz12(VEFS) associate intimately. The Eed subunit is engulfed by a belt-like structural feature

ON OUR WEB SITE

Read the full article at <http://dx.doi.org/10.1126/science.aac4383>

of Ezh2, and Suz12(VEFS) contacts both of these two subunits to confer enzyme activity. Second, two separate regions of Ezh2, including the SET activation loop (SAL) and SET, are together required to form the active catalytic domain of PRC2. Eed and Suz12(VEFS) are structurally important in maintaining the positioning and local conformation of the SAL of Ezh2, which may explain, at least in part, the indispensable role of Eed and Suz12 in PRC2 catalysis. Third, the H3K27M cancer mutant inhibits PRC2 enzyme activity by a direct competition mechanism, with residue H3R26, in the context of the lysine-to-methionine mutation, occupying the lysine access channel of the active site and thus occluding substrate binding. Lastly, the flexible stimulation-responsive motif (SRM) of

Ezh2 responds to H3K27me3-mediated enzyme stimulation by forming a sandwich-like assembly with the H3K27me3 peptide and Eed. The SRM exhibits a dramatic disorder-to-order conformational transition upon binding of this stimulating peptide. This initiates an allosterically regulated pathway that communicates with the active site.

CONCLUSION: This work has resolved some long-standing questions regarding PRC2 structure and function and provides a structural framework for future functional studies. PRC2 is a representative of a distinct family of lysine methyltransferases. The unique structural arrangement of PRC2 revealed here underlies PRC2-mediated H3K27 trimethylation. The

enzymatic activity of PRC2 is subject to complex regulation by a plethora of protein factors and noncoding RNAs in cells. Regulatory signals transmitted from discrete, distant surfaces of PRC2, such as that transferred by the SRM of Ezh2, are interpreted and integrated at the enzyme active site to generate distinct cellular outputs. ■

The list of author affiliations is available in the full article online.
*Corresponding author. E-mail: xin.liu@utsouthwestern.edu
Cite this article as L. Jiao, X. Liu, *Science* 350, aac4383 (2015). DOI: 10.1126/science.aac4383

RESEARCH ARTICLE

TRANSCRIPTION

Structural basis of histone H3K27 trimethylation by an active polycomb repressive complex 2

Lianying Jiao and Xin Liu*

Polycomb repressive complex 2 (PRC2) catalyzes histone H3K27 trimethylation (H3K27me₃), a hallmark of gene silencing. Here we report the crystal structures of an active PRC2 complex of 170 kilodaltons from the yeast *Chaetomium thermophilum* in both basal and stimulated states, which contain Ezh2, Eed, and the VEFS domain of Suz12 and are bound to a cancer-associated inhibiting H3K27M peptide and a S-adenosyl-L-homocysteine cofactor. The stimulated complex also contains an additional stimulating H3K27me₃ peptide. Eed is engulfed by a belt-like structure of Ezh2, and Suz12(VEFS) contacts both of these two subunits to confer an unusual split active SET domain for catalysis. Comparison of PRC2 in the basal and stimulated states reveals a mobile Ezh2 motif that responds to stimulation to allosterically regulate the active site.

Polycomb-group proteins mediate gene silencing as multisubunit protein complexes by modifying histone tails and altering high-order chromatin structure. Polycomb repressive complex 2 (PRC2) catalyzes trimethylation of histone H3 at lysine 27 (H3K27me₃), an epigenetic hallmark of repressed chromatin (1–6). PRC2 consists of four core subunits—Ezh2, Eed, Suz12, and Rbbp4. In addition, auxiliary subunits—such as Aebp2, Jarid2, and mammalian orthologs of *Drosophila melanogaster* polycomb-like (Pcl) protein (Phf1, Phf19, and Mtf2)—associate with the core PRC2, modulate its enzyme activity, and facilitate its recruitment to target genomic loci (1–3, 5, 6).

A catalytic SET [su(var)3-9, enhancer-of-zeste and trithorax] domain is located at the C terminus of Ezh2, which minimally requires the Eed subunit and the VEFS [Vrn2-Emf2-Fis2-Su(z)12] domain from the C terminus of Suz12 to confer catalytic activity toward H3K27me₃ (7). PRC2 is likely also responsible for the deposition of mono- and dimethyl marks on H3K27 (8). Whereas H3K27me₁ is accumulated within actively transcribed genes, H3K27me₂ is pervasive throughout large chromatin domains (8).

The end product of PRC2 catalysis, H3K27me₃, interacts with Eed and stimulates the successive methyltransferase activity of PRC2, a mechanism believed to account for the propagation of the repressive H3K27me₃ histone mark and hence the spreading of the facultative heterochromatin

(9–11). Moreover, chromatin context-dependent regulation of the H3K27me₃ deposition by methylated Jarid2 is achieved, at least in part, with a similar Eed-bridged mechanism (12).

PRC2 and, in particular, some of its core components have been previously subjected to structural analyses. An earlier negative-stain electron microscopy study defined the overall structural architecture of a human holo-PRC2 (i.e., Ezh2-Eed-Suz12-Rbbp4-Aebp2) at low resolution (13). In addition, a series of crystal structures of Eed in complex with an Ezh2 peptide and a variety of trimethylated histone and nonhistone peptides highlighted the critical roles of Eed in mediating Ezh2 binding and allosteric regulation of PRC2 (10–12, 14). Moreover, the recent crystal structures of an isolated inactive catalytic domain of Ezh2 revealed an autoinhibited conformation, implying that structural rearrangement of this domain is likely required for an active PRC2 (15, 16). Finally, the crystal structures of NurF55, a *Drosophila* homolog of Rbbp4, bound to a Suz12 peptide and an N-terminal histone H3 peptide provided insights into PRC2 association with nucleosomal substrates (17).

Aberrant PRC2 activity, in particular that caused by Ezh2 mutations, is broadly linked to human diseases, including hematological malignancies and Weaver syndrome (18–21). In addition, a histone H3K27M missense mutation is present in some pediatric brain cancers and leads to a global decrease in the amount of H3K27me₃, possibly by targeting the catalytic domain of Ezh2 to mediate PRC2 enzyme inhibition (22). Mechanistic understanding of the complex PRC2 function and regulation has so far been limited. We report here the high-resolution crystal structures of an active PRC2 from a thermophilic yeast, *C. thermophilum* (hereafter referred to as “*ct*”), containing the Ezh2-

Eed-Suz12(VEFS) ternary complex of 170 kD in both basal and stimulated states.

Characterization and crystallization of the active *ct*PRC2 complex

On the basis of sequence alignment with the corresponding human copies, we identified sequences of Ezh2, Eed, and Suz12(VEFS) for *C. thermophilum* (fig. S1) (23). We overexpressed the Ezh2-Eed-Suz12(VEFS) ternary complex in *Saccharomyces cerevisiae*. The regions of Ezh2 (residues 191 to 950) and Suz12(VEFS) (residues 530 to 691) were chosen for complex formation on the basis of their sequence homology to the full-length human Ezh2 and the reported minimal *Drosophila* Suz12 construct required for PRC2 catalysis, respectively (7). To maintain the stoichiometry of the complex, these Ezh2 and Suz12(VEFS) regions were expressed as a single fusion protein, which was coexpressed with Eed (residues 1 to 565) to allow reconstitution and purification of the ternary complex. We established biochemical assays to show that the ternary complex, but not the binary Ezh2-Eed or Ezh2-Suz12(VEFS) complexes, displayed robust enzyme activity toward H3K27me₃ (fig. S2, A and B). In addition, we demonstrated that the basal enzyme activity of the complex is stimulated by an H3K27me₃ product peptide and inhibited by a substrate H3 peptide harboring a K27M cancer mutation (fig. S2C), indicating functional conservation of *ct*PRC2 with its human and *Drosophila* orthologs. Indeed, a stimulating H3K27me₃ product peptide, a cancer-associated inhibiting H3K27M peptide, and a S-adenosyl-L-homocysteine (SAH) cofactor were required for generating initial crystallization hits and for crystal refinement. Whereas the PRC2 complex lacking the H3K27me₃ peptide was less prone to crystallize, omitting the H3K27M peptide from the complex made it impossible for us to generate crystals of sufficient quality for structural determination.

The overall structure

The crystal structure of the Ezh2-Eed-Suz12(VEFS) ternary complex bound to a stimulating H3K27me₃ product peptide was determined at 2.3 Å resolution, and that of the same complex lacking the peptide and representing the basal state was determined at 2.7 Å resolution (Fig. 1, A and B, and table S1). An SAH cofactor and an inhibiting H3K27M peptide bound to the catalytic SET domain were also captured in both crystal structures (Fig. 1, A and B). Both complexes adopt a similar overall structure except for an exposed Ezh2 motif, which directly binds to the stimulating peptide and becomes disordered in its absence. Most of the structural analyses are for the stimulated complex at 2.3 Å resolution, except for when the structures of the two states are compared.

Nearly 17,000 Å² of solvent-accessible surface area is buried upon formation of the ternary complex. The complex adopts an overall compact structural arrangement, which is roughly divided into the regulatory moiety and the catalytic moiety (Fig. 1B). Sites of stimulation and catalysis are separated by more than 30 Å, suggesting an allosteric mechanism for product stimulation through long-range

Cecil H. and Ida Green Center for Reproductive Biology Sciences and Division of Basic Research, Department of Obstetrics and Gynecology and Department of Biophysics, University of Texas Southwestern Medical Center, Dallas, TX 75390, USA.

*Corresponding author. E-mail: xin.liu@utsouthwestern.edu

communication. The atomic structure of the complex fits well into corresponding regions of the reported negative-stain electron microscopy map of a human holo-PRC2 (13), suggesting conservation across species of the overall structural architecture (fig. S3).

Ten structurally and functionally discrete Ezh2 domains are dispersed across the entire active complex and compose an extended structural scaffold to accommodate juxtaposed Eed and Suz12(VEFS) (Fig. 1, B and C). The N terminus of Ezh2 forms an intramolecular interaction with the SANT1-like (SANT1L) domain of Ezh2 and is referred to as the SANT1L-binding domain (SBD). The Eed-binding domain (EBD) was previously characterized for mouse Ezh2 (14) and is found next to the SBD in the current structure, where the EBD similarly occupies a surface groove across the bottom face of the Eed WD40 domain (24) (fig. S4). Continuation of the EBD on the side face of Eed leads to the β -addition motif (BAM), consisting of three β strands that are added to the β -propeller fold of the WD40 repeats of Eed. Following the BAM, an Ezh2 loop region migrates away from the Eed surface, extends to the back of the SET domain of the catalytic moiety, and is

referred to as SET activation loop (SAL). The buried SAL emerges from between the SET domain and Suz12(VEFS) to directly connect to the stimulation-responsive motif (SRM), which sits on the stimulating peptide at the center of the top face of Eed and forms a sandwich-like assembly with Eed and the H3K27me3 peptide. Following the SRM, the SANT1L domain adopts a helix bundle structure, analogous to the predicted SANT1 domain of human Ezh2 (fig. S1), and binds to the SBD. Together, the SBD, EBD, BAM, SAL, SRM, and SANT1L regions complete the belt-like structure of Ezh2 that surrounds Eed (Fig. 1C and fig. S5).

Entering the catalytic moiety, the SANT2-like (SANT2L) domain is linked to the SANT1L domain through the motif connecting SANT1L and SANT2L (MCSS), which harbors two helices, a zinc-binding motif, and a β hairpin, and interacts with multiple surfaces. The SANT2L domain coordinates a zinc ion as well and is analogous to the SANT2 domain of human Ezh2 based on secondary-structure prediction (fig. S1). The CXC and SET domains resemble human counterparts (15, 16). The CXC domain contains a Zn_3Cys_8His and a Zn_3Cys_9 cluster. The SET domain is posi-

tioned above Eed and Suz12(VEFS) and adjacent to the SRM. The overall structure of the active ternary complex, and in particular the location of the catalytic domain, underlies allosteric modulation of the enzyme activity through various functional surfaces within the complex.

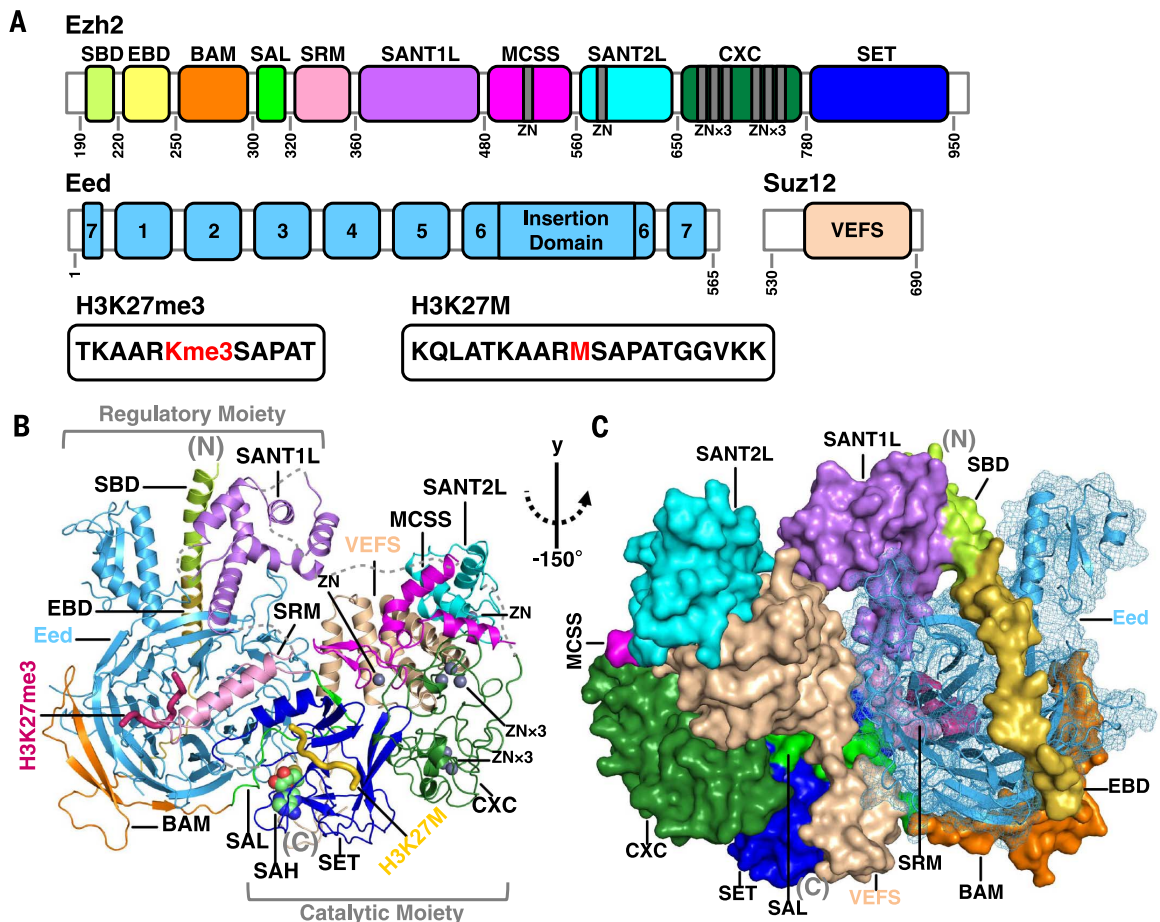
Association of the ternary complex

Comparison of the current structure to the structure of the mouse Eed-EBD binary complex reveals that the helix and loop regions of the EBD of Ezh2, which vary in lengths, govern Eed binding on its bottom face in both structures (Fig. 2A; the close-up views hereafter are mapped to the overall structure as in fig. S6) (14). The seven-bladed β -propeller WD40 domains of Eed from both species are well aligned with a root mean square deviation (RMSD) of 0.9 Å, except for a yeast-specific insertion domain, which protrudes away from the WD40-containing region (Fig. 2A). Following the EBD, the three β strands of the BAM are added to the first and seventh blade of the β propeller, further securing the Ezh2-Eed association (Fig. 2A).

Both SBD and SANT1L of Ezh2 abut Eed, and the SBD-SANT1L binary complex appears to tighten the Ezh2 belt-like structure around Eed like a

Fig. 1. Overall structure of the active Ezh2-Eed-Suz12 (VEFS) ternary complex. (A) Schematic domain structures of Ezh2, Eed, and Suz12 (VEFS) are shown.

Individual functional domains of Ezh2 are labeled, and locations of zinc-coordinating structures are indicated. Seven blades of the β -propeller structure of the Eed WD40 domain are numbered, and an insertion domain specific to *C. thermophilum* Eed is indicated. Peptides included for crystallization are also shown, with modified or mutated residues colored in red. (B) The overall structure of the active ternary complex bound to the stimulating H3K27me3 peptide, inhibiting H3K27M cancer mutant peptide, and cofactor SAH is shown in cartoon representation. Functional domains are colored as in (A). Zn^{2+} ions and SAH are shown as spheres, and the two peptide ligands are shown as thick ribbons. The regulatory and catalytic moieties of the complex are also indicated. (C) Ezh2 and Suz12(VEFS) subunits of the ternary complex are shown in surface representation, and Eed is in mesh. Eed is engulfed by the belt-like structure of Ezh2 within the regulatory moiety.



buckle (Fig. 2B and fig. S5). Compared to an SBD-like region of human Ezh2 that also immediately precedes the EBD, some hydrophobic residues of the SBD are aligned and involved in binding to a surface groove on the SANT1L domain (Fig. 2B and fig. S1). Although poorly conserved in sequence, the SANT1L shares a key feature of the canonical SANT domain, which is the enrichment of bulky aromatic and hydrophobic residues in the core of the α -helix bundle (Fig. 2B) (25). The SBD-SANT1L intramolecular interaction of Ezh2 may provide stability for Eed in the complex in addition to that offered by the EBD and BAM of Ezh2. Moreover, because the SANT1L is directly connected to the SRM of Ezh2 at the site of stimulation, the SBD-SANT1L assembly may play a role in enzyme regulation as well. Ezh2-S21, a previously mapped phosphorylation site of human Ezh2, is located in the middle of the SBD based on sequence and structural homology, raising a possibility that the reported diminution of en-

zyme activity for the Ezh2-S21-phosphorylated human PRC2 is caused allosterically by a disturbed SBD-SANT1L interaction (26).

Suz12(VEFS) is located in the space behind the MCSS, SANT2L, CXC, and SET of Ezh2 (Figs. 1C and 2, C and D). Similar to the canonical SANT domain, the SANT2L structurally aligns well with a Myb DNA binding domain, except that the SANT2L also contains a zinc-binding motif (fig. S7). While the helical contents of Suz12(VEFS) form the 10-helix bundle with the MCSS and SANT2L, the N-terminal loop region of Suz12(VEFS) cements together Eed and the SAL and SET regions of Ezh2 (Figs. 1C and 2D). Disease-causing mutations of several conserved residues of Suz12(VEFS)—including L593, F596, D598, E603, W610, and D611 (numbered by *ctSuz12*) (fig. S1)—result in impaired complex integrity and weakened methyltransferase activity (27–29). These residues are scattered around the vicinity of the MCSS of Ezh2, in particular its conserved zinc-binding motif, and make various interactions in

the catalytic moiety (Fig. 2C). The previously proposed noncoding RNA binding region of Ezh2 (30), though not conserved in the current structure, is projected to be situated in a conserved zinc-coordinating loop of the SANT2L domain, neighboring to Suz12(VEFS) and the MCSS (figs. S1, S6A, and S7).

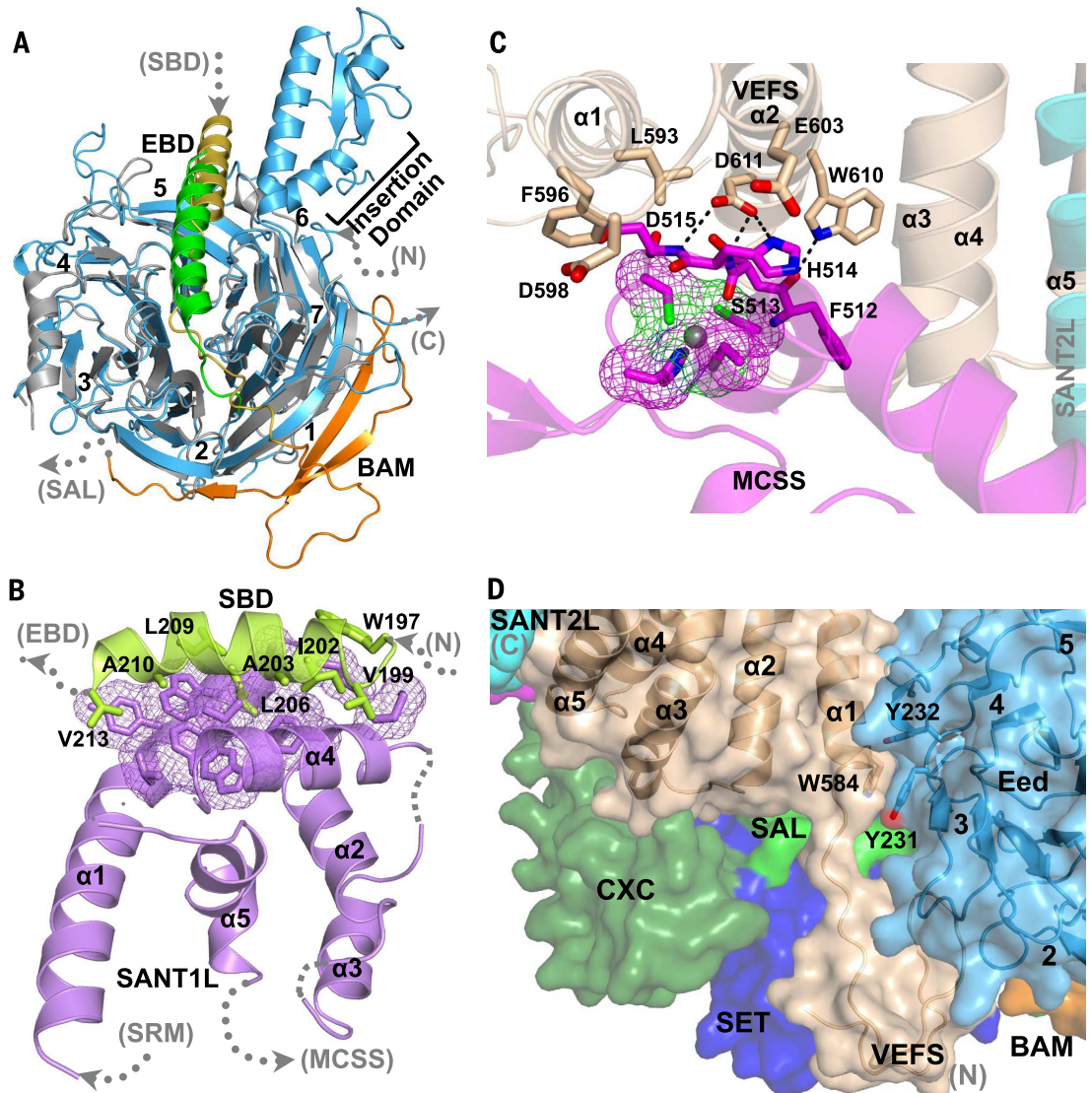
Although the Eed-Suz12(VEFS) interface is relatively small compared with that for the Ezh2-Eed and Ezh2-Suz12(VEFS) pairs, it nonetheless appears to be important for optimal enzyme activity of PRC2. Conserved W584 residue at the junction of the helical and loop contents of Suz12(VEFS) is involved in hydrophobic interaction with Y231 and Y232 of Eed (Fig. 2D), and mutation of this tryptophan residue leads to a reduced enzyme activity of *Drosophila* PRC2 (29).

Split catalytic domain

The catalytic SET domain of Ezh2 preserves most of the essential sequence and structural features

Fig. 2. Close-up views of the intra- and intermolecular interactions in the active ternary complex.

(A) The crystal structure of the stimulated ternary complex is superimposed with the mouse Eed-EBD binary complex (PDB: 2QXV). Mouse Eed and EBD are shown in gray and green, respectively. The BAM of Ezh2 in orange is also shown interacting with the WD40 domain of Eed. To indicate the close-up views in the context of the overall structure, Ezh2 domains preceding and following the shown ones are hereafter denoted by the dotted gray arrows. A map of the close-up views is also provided in fig. S6 for the same purpose. (B) Intramolecular hydrophobic interactions between the SBD and SANT1L regions of Ezh2 are shown, with involved residues highlighted as sticks. (C) Interactions between the MCSS region of Ezh2 and Suz12(VEFS) are shown, with the disease mutation residues of Suz12(VEFS) and their interacting residues in the MCSS highlighted as sticks. The zinc-coordinating motif of the MCSS is shown as mesh. (D) Suz12(VEFS) sits in the interface of the regulatory and catalytic moieties on the back of the SET domain. Conserved interacting residues of Suz12(VEFS) and Eed are highlighted as sticks.



observed for other SET-containing methyltransferases (fig. S8). An isolated CXC-SET domain of human Ezh2 displays an autoinhibited state of the SET domain (15, 16). The SET-I and post-SET regions adopt atypical conformations, with an inaccessible substrate-binding groove and an incomplete cofactor-binding pocket, which is in line with the requirement of Eed and Suz12(VEFS) for catalysis. Structural comparison of the inactive SET domain with the current structure captured in the active state provides a mechanism for SET activation. The overall structures of the SET domains in both states are aligned with an RMSD of 1.6 Å (Fig. 3, A and B). During activation, the SET-I region is rotated over 20° counterclockwise, such that it swings away from the otherwise blocked peptide substrate-binding groove on one side and close to the cofactor-binding pocket on the other side (Fig. 3B). The conformational change of SET-I exposes the peptide substrate binding site and results in the completion of the cofactor-binding pocket, with placement of the post-SET region in a typical conformation for cofactor SAH binding (Fig. 3B). Specifically, in the active state of PRC2, the cofactor SAH is stabilized by extensive hydrophobic and hydrogen-bonding interactions with residues from all subregions of the Ezh2-SET domain, including the SET-N, SET-I, SET-C, and post-SET (Fig. 3C and fig. S8). Many of these residues may also be involved in orienting the methyl donor S-adenosylmethionine (SAM) to allow catalysis.

The SET activation loop SAL from the N-terminal portion of Ezh2 sequence extends from the Eed surface toward the SET domain and exits the catalytic moiety along the side of the last β strand of SET-N (Fig. 3A). The SAL of Ezh2 is engaged in extensive interactions with the SET, the MCSS, Eed, and Suz12(VEFS), whereby it maintains the active conformation of the SET domain (fig. S9). Consistently, deletion or mutation of a number of six semi-conserved amino acids (residues 310 to 315) in the SAL abolishes enzyme activity completely, with little effect on complex assembly (Fig. 3D). Furthermore, alteration of only three amino acids in this region (residues 313 to 315) is sufficient to abrogate catalysis (fig. S10). Therefore, at least two split regions of the Ezh2 sequence, the SAL segment and the SET domain, are required to compose the active catalytic domain (Figs. 1A and 3, A and B). Further structural alignment with SET domains from other methyltransferase families reveals that the SAL mimics a similar loop structure found in the N-flanking regions of some SET domains, including G9a, Ash1l, and Atrx5 (fig. S11). These N-flanking regions diverge structurally and are thought to stabilize SET (31); however, whether the SAL-aligned regions in those SET domains are similarly required for catalysis remains to be tested. Lastly, whereas Eed seems to be critical for the overall positioning of the SAL onto the back of the SET domain, the MCSS and Suz12(VEFS) may guide formation of the unique local SAL

conformation for SET interaction (Fig. 3, A and B, and fig. S9).

Inhibition of PRC2 active site by the H3K27M cancer mutant

A histone H3 substrate peptide harboring a K27M cancer mutation is captured bound to the canonical substrate-binding cleft of the SET domain. This mutant peptide was shown to inhibit enzyme activity of human PRC2 by targeting Ezh2 directly (22). Residue H3R26 of the mutant peptide occupies the lysine-binding channel of the active site and occludes substrate binding (Fig. 3E), reminiscent of autoinhibition of human Setd2 mediated by an arginine residue from the post-SET loop (32). Whereas the aliphatic portion of H3R26 side chain is surrounded by a group of aromatic residues, the guanidinium part is trapped by the invariant Y645 and the carbonyl cage at the active site (Fig. 3E). The same set of residues may also direct H3K27 methylation when wild-type substrate is bound (15, 16, 31). In addition, residue H3A25 sits in a shallow pocket of SET-I, which would exclude a bulkier side chain at this position of H3, a feature also contributing to the binding specificity of the inhibitory H3K27M mutant peptide. Consistently, the H3K27M mutant peptide harboring an additional H3R26A mutation is incapable of mediating PRC2 enzyme inhibition, confirming the critical role of residue H3R26 in such a process in solution (Fig. 3F).

The side chain of the mutated methionine is not resolved in the current structure, leaving open the question of why a H3K27M mutation is more potent than other amino acid substitutions for PRC2 inhibition (fig. S12) (22).

Mobile stimulation-responsive motif

The PRC2 enzyme activity is stimulated by its own reaction product, generating a positive feedback loop. The H3K27me3 product peptide is directly recognized by the WD40 region of Eed and leads to allosteric stimulation of PRC2 activity, a mechanism believed to account for propagation of the H3K27me3 histone marks in the repressive chromatin domains (9–11). Moreover, K116 of Jarid2 is also trimethylated by PRC2 and is thought to facilitate H3K27me3 deposition at loci devoid of such a histone mark in a similar manner (12). However, the mechanism whereby Ezh2, the catalytic subunit of PRC2, receives and translates the stimulating signal remains unknown. The crystal structure of the H3K27me3-bound ternary complex, together with the basal state of the complex in the absence of the stimulating peptide determined at 2.7 Å resolution, provides a molecular mechanism for this allosteric regulation. In the stimulated state, the H3K27me3 peptide is sandwiched between Eed and an exposed Ezh2 motif, which immediately follows the SAL of Ezh2 and is referred to as the stimulation-responsive motif (SRM) (Fig. 1, A and B). The SRM is not visible in the electron density map of the ternary complex in the basal state, suggesting that it is highly flexible in the absence of the stimulating H3K27me3 peptide (fig. S13). Because both basal and stimulated PRC2 complexes were

crystallized in the same crystal lattice under the same crystallization conditions, it is unlikely that the observed dramatic conformational change of the SRM of Ezh2 is due to differences in crystal packing. A structural alignment indicates that the entire catalytic moiety—including the MCSS, SANT2L, CXC, SET, and Suz12(VEFS)—is rotated counterclockwise toward the SRM along the interface of the two moieties from the basal to stimulated state, which implies that a large domain-wise motion is likely associated with stimulation in solution (Fig. 4A).

Analysis of the sandwich structure at the site of stimulation reveals that the trimethylated H3K27 side chain is bound within an aromatic cage on the Eed surface, akin to that in the previous crystal structure of the Eed-H3K27me3 binary complex (fig. S14). Main-chain atoms of the A25, K27me3, and S28 residues of the H3K27me3 peptide provide a unique docking surface for the SRM of Ezh2, by making hydrogen-bonding interactions with the side chains of H326 and D329 of the SRM (Fig. 4B). Conserved residues from this region of the SRM, including P325 and L327, are hotspots for disease mutations in human Ezh2 (21, 33).

Most of the sequence contents, including the signature A-R-Kme3-S sequence of the H3K27me3 peptide, are discriminated by Eed through hydrogen bonding or steric exclusion, except that residue H3A24 is bound by a part of the SRM surface that excludes bulky side chains (Fig. 4B). This structural mechanism may account for the observed specificity of enzyme stimulation. A linker histone H1K26me3 peptide contains a bulkier lysine residue at the equivalent position of residue H3A24 relative to the trimethylated lysine (fig. S15). Although the H1K26me3 peptide binds to Eed with an affinity comparable to that of the stimulating H3K27me3 peptide, it is incompetent for PRC2 stimulation (11), probably owing to the steric exclusion that prevents binding of the SRM of Ezh2 to the H1K26me3 peptide.

On the back of the Eed-H3K27me3-SRM sandwich structure and at the border of the two moieties, the SRM makes extensive interactions, mostly hydrophobic ones, with the helix region of SET-I (Fig. 4C). A short loop region following the SET-I helix is also involved in binding of the SRM and becomes disordered together with the latter in the basal state (Fig. 4C).

The SRM of Ezh2 establishes a possible allosteric pathway to communicate with the catalytic site for stimulation, which involves the H3K27me3-SRM and SRM-SET-I interactions. At the H3K27me3 binding site, mutations of P325, H326, and D329 of the SRM largely abolish enzyme stimulation while resulting in moderately reduced basal activities, likely due to an impaired binding of the SRM to the docking surface on the stimulating peptide (Fig. 4, C and D, and fig. S16). Furthermore, we show that deletion of L350 in the SRM on the SRM-SET-I binding interface slightly decreases the H3K27me3-mediated stimulation as well (Fig. 4, C and D, and fig. S16). Along this pathway, R839 and D868 of SET-I form a strictly conserved salt bridge, connecting the endpoint of the pathway directly to the catalytic site

(Fig. 4C and fig. S8). Mutating R839 to an aspartate blocks stimulation completely (Fig. 4D and fig. S16). A subtle conformational change of the active site may have a large effect on catalysis. Indeed, an A677G cancer-related mutation of human Ezh2 results in an enhanced catalytic efficiency in converting H3K27me₂ to H3K27me₃ without compromising the mono- and dimethylation steps, probably owing to a slightly expanded substrate lysine channel that is otherwise spatially restrictive for lysine trimethylation (34). A677 of human Ezh2 is the equivalent of A869 in yeast Ezh2 in the current structure, and in this regard, allosteric effects exerted on D868 through the salt bridge may spread to the next residue A869 to allow enzyme stimulation with an analogous mechanism employed by the A677G human cancer-causing mutant.

Allosteric regulation may not be limited to the SRM-mediated pathways. A small acidic patch of Suz12(VEFS) is known to be important for the basal enzyme activity and for the enzymatic

stimulation of *Drosophila* PRC2 by a fragment of histone H3 (residues 31 to 42) in a dense chromatin environment (7). Though not conserved in the active ternary complex here, these acidic amino acids next to the W584 residue of Suz12(VEFS) are predicted to be located adjacent to the SAL of Eh22 on the back of the SET domain based on the current structure (Fig. 2D), through which allosteric stimulation also becomes possible.

Conclusions

Ezh2, Eed, and Suz12(VEFS) associate intimately, and the intramolecular and intermolecular binding interface of these subunits seems to underlie many aspects of enzyme regulation. The ternary complex undergoes structural interconversion between the autoinhibited, basal, and stimulated states of catalysis, during which local and global conformational changes are observed. In addition, the SAL and SET regions together compose a split catalytic domain of Ezh2, and this domain

is efficiently inhibited by the H3K27M cancer mutant, for which the H3R26 residue plays an important role. The SRM, a structural element of Ezh2, mediates the H3K27me₃ product stimulation through an allosteric mechanism. Both SRM and SAL bind to Eed and Suz12(VEFS), transmit regulatory signals from different distant surfaces, and are therefore at the center of PRC2 enzyme regulation pathways. Cooperative and antagonizing allosteric effects are integrated at the active site and result in distinct cellular output.

PRC2 displays a high degree of regulatory plasticity through numerous auxiliary factors. Many of these factors act on Ezh2 directly to modulate PRC2 enzyme activity. The SRM is well positioned on the surface of PRC2 to allow access by other nuclear factors. In addition, at least one of the SRM-mediated allosteric pathways involving a conserved salt bridge of the SET-I region may tip the balance of the three methylation states of H3K27 toward H3K27me₃, the functional histone mark for gene repression, in a

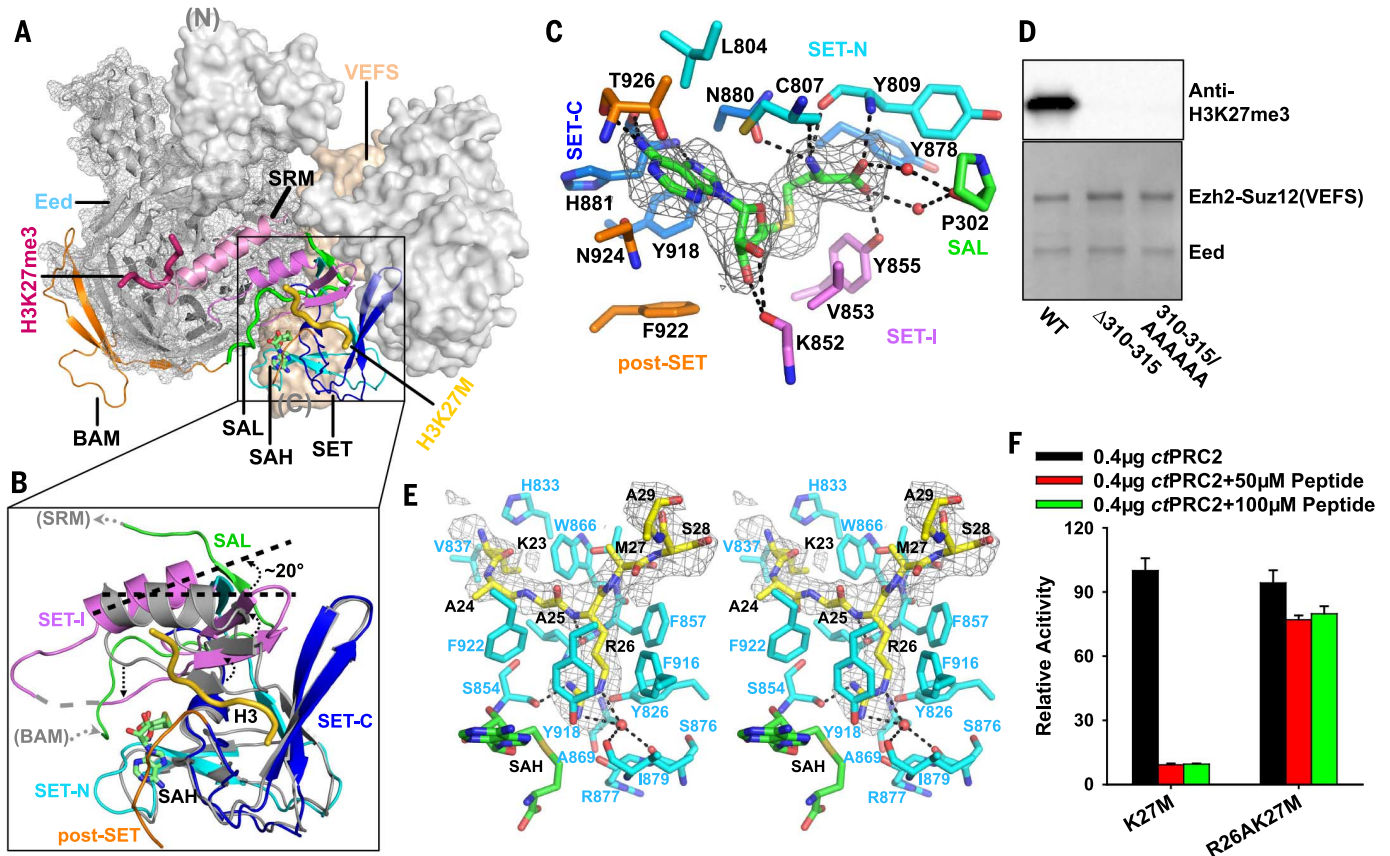


Fig. 3. Conformation of the active catalytic SET domain of Ezh2. (A) The trajectory of the SAL of Ezh2 is highlighted as a green ribbon in the context of the overall structure. The catalytic SET domain of Ezh2 is zoomed in and shown in Fig. 3B. (B) The catalytic SET domain from the current structure is superimposed with the isolated inactive SET domain of human Ezh2 (PDB:4MI0, shown in gray). SET-I swings about 20° counterclockwise relative to the inactive conformation. The SAL region of Ezh2 required to maintain the active conformation is also shown as a green ribbon. (C) Close-up view of Ezh2 residues involved in SAH interaction. The Fo – Fc omit electron density map for SAH contoured to 2.2 σ is also shown as a gray mesh. (D) Deletion or mu-

tation of residues 310 to 315 in the SAL of Ezh2 abolishes enzyme activity. Purified wild-type and mutant ternary complexes are shown below the result of the Western blot-based activity assay. (E) The lysine access channel of the active SET domain is shown as a stereo pair. The Fo – Fc omit electron density map contoured at 2.5 σ that corresponds to the inhibiting H3K27M peptide is indicated by a gray mesh. Residue H3R26 occupying the lysine channel is unambiguously defined by the electron density map. (F) Inhibition of PRC2 enzyme activity by the H3K27M and H3R26AK27M mutant histone peptides. Relative enzyme activities from the ELISA-based assays are shown. Data are mean \pm SD based on three trials.

manner similar to that of the A677G cancer mutation of human Ezh2. Lastly, the SRM and Eed together dictate the specificity and possibly the strength of stimulation, which adds a second layer of control for H3K27me3 deposition besides that offered by the catalytic SET domain. Since allosteric stimulation of PRC2 is probably necessary for formation of the repressive H3K27me3 domains (12), H3K27 trimethylation initiated at the SET domain of Ezh2 may be promoted or suppressed by distinct cellular mechanisms through the SRM surface of Ezh2 during the stimulation step to generate desired biological outcomes.

Dinucleosomes with four copies of histone H3 are known to be much better substrates for PRC2 than mononucleosomes (7, 35, 36). Coincidentally, this and previous studies have suggested that at least four distinct PRC2 surfaces are available to interact with histone H3, including the SET domain of Ezh2 for an H3K27 substrate, the SRM of Ezh2 and Eed for a stimulating H3K27me3 histone tail (10), Suz12(VEFS) for residues 31 to 42 of a neighboring histone H3 in a dense chromatin environment (7), and Rbbp4 for an unmodified N terminus of histone H3 (17). Therefore, a dinucleosome may represent a minimal unit for optimal chromatin context-dependent PRC2 binding and catalysis (13).

The current structure reveals the spatial arrangement of the first three H3-binding surfaces of PRC2 mentioned above, which may correlate with a defined conformation of a dinucleosome substrate with a preferred linker DNA length for PRC2 catalysis (7). Mechanistic analysis of PRC2-mediated methylation of chromatin templates will entail high-resolution structural information of PRC2 fully engaged on a dinucleosome substrate.

Materials and methods

Cloning

DNA encoding Ezh2, Eed, and Suz12 was amplified from the extracted genomic DNA of *Chaetomium thermophilum* var. *thermophilum* DSM 1495 or synthesized by Integrated DNA Technologies (IDT). A DNA fragment corresponding to the sequence, 2×Protein A-SSGENLYFQSNHHHHHHA, was added N-terminal to the fused Ezh2 (residues 191 to 950)-LVPRGS-Suz12 (residues 530 to 691) (hereafter referred to as Ezh2-VEFS) fragment, and the Ezh2-VEFS construct was subcloned into the p416GAL1 vector. Full-length Eed (residues 1 to 565) was tagged with an N-terminal twin-strep tag (IBA Lifesciences) and was cloned into a modified p416GAL1 plasmid with the selection marker replaced by TRP1. All the constructs harboring mutations were

generated with the site-directed mutagenesis strategy.

Protein expression and purification

Constructs of Ezh2-VEFS and EED were cotransformed into *S. cerevisiae* CB010 strain (*MATa pep4::HIS3 prb1::LEU2 prc::HISG can1 ade2 trp1 ura3 his3 leu2-3,112*). Cell starters were grown in synthetic complete drop out medium without uracil and tryptophan (Sc-Ura-Trp) supplemented with 2% raffinose at 30°C for 24 hours. Protein expression was induced by inoculating the cell starters into the Sc-Ura-Trp medium supplemented with 2% galactose at 30°C for an additional 24 hours. Cells were harvested by centrifugation and resuspended in lysis buffer containing 100 mM Tris-HCl (pH 8.5), 300 mM NaCl, 2.5 mM dithiothreitol (DTT), 10% glycerol, 0.5 mM phenylmethylsulfonyl fluoride, and protease inhibitors. After lysis by bead beating and clarification by centrifugation, the supernatant was mixed with equilibrated immunoglobulin G (IgG) resin and allowed to bind for 2 hours at 4°C. The IgG resin was made by coupling purified rabbit IgG to the CNBr-activated Sepharose 4 Fast Flow resin according to the manufacturer's protocol (GE Healthcare). The binding mixture was then applied to an empty column to capture the IgG resin with the bound ternary complex. The resin was washed stepwise by buffer

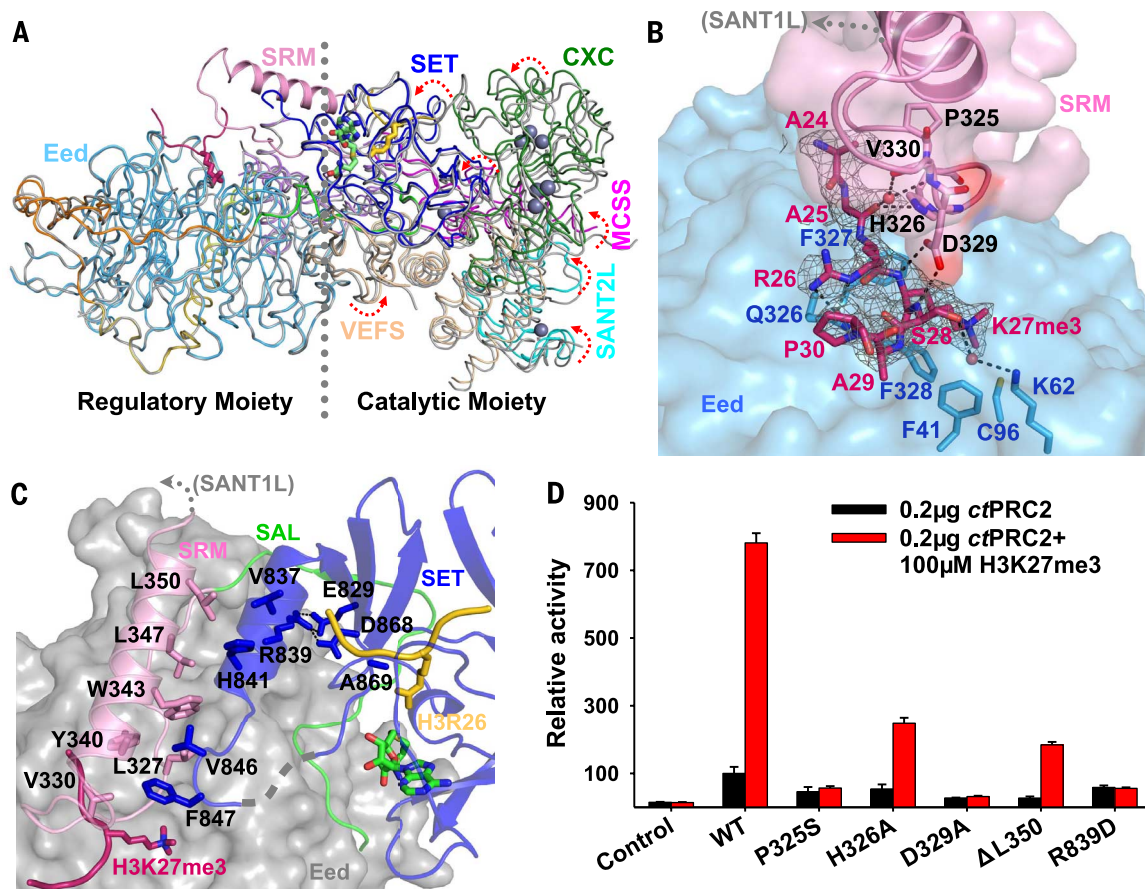
Fig. 4. Allosteric regulation of the PRC2 enzyme activity. (A)

The crystal structures of the ternary complexes in the basal (gray ribbons) and stimulated (colored ribbons) states are aligned on the basis of Eed. The catalytic moiety is rotated counter-clockwise toward the SRM from the basal to the stimulated state.

The SRM of Ezh2, which experiences disorder-to-order conformational transition, is highlighted in cartoon representation. (B) Close-up view of interactions between the H3K27me3 peptide (red), the SRM (pink), and Eed (light blue). Interacting residues are shown as sticks.

The $F_o - F_c$ omit electron density map corresponding to the H3K27me3 peptide is contoured at 2.5σ and is shown as a gray mesh. (C) Close-up view of interactions between the SRM (pink) and the SET domain (deep blue) of Ezh2.

(D) Enzyme stimulation assay of the wild-type and mutant ternary complexes. Relative enzyme activities from the triplicated ELISA-based assays are shown. Data are mean \pm SD based on three trials.



A [50 mM Tris-HCl (pH 8.0), 500 mM NaCl, 2.5 mM DTT, 10% glycerol, and 0.1% NP40], buffer B [50 mM Tris-HCl (pH 8.0), 1 M NaCl, 2.5 mM DTT, and 10% glycerol], and buffer C [50 mM Tris-HCl (pH 8.0), 100 mM NaCl, 2.5 mM DTT, and 10% glycerol]. Tobacco etch virus (TEV) protease was added to the column and mixed thoroughly with the resin. After cleavage at 4°C for 12 hours, the flow-through was collected and the protein was eluted with an additional five bed volumes of buffer C. The eluted protein was then applied to a gravity column with Strep-Tactin resin equilibrated with buffer C. A quick buffer C wash was performed, and the ternary complex was eluted with buffer C supplemented with 5 mM d-desthiobiotin. Protein-containing fractions were pooled, concentrated, and loaded onto a Superdex S200 preparative size exclusion chromatography column (GE Healthcare) equilibrated with 20 mM Tris-HCl (pH 8.0), 100 mM NaCl, and 2 mM DTT. The peak fractions were concentrated to about 20 mg/ml and stored at -80°C. Thirty liters of yeast cells will typically yield 10 mg of purified ternary complex.

Crystallization and structure determination

Prior to crystallization, two peptides, H3K27M (KQLATKAARM**S**APATGGVKK) and H3K27me3 (TKAARK**M**e3SAPAT) (the mutated or modified residue is highlighted in bold), and SAH were added to the protein in a molar ratio of 1:5:5:10 (protein: H3K27M:H3K27me3:SAH). Initial crystallization conditions were screened by sitting drop vapor diffusion method at 22°C. Crystals were refined by mixing equal volumes of the protein solution at 10 to 25 mg/ml with the reservoir solution in 2- μ l drops over 500 μ l of the latter, containing 15% polyethylene glycol (PEG) 4000 and 175 mM ammonium citrate (pH 7.0). Crystals were harvested after 2 to 3 weeks, cryoprotected by mother liquor with 35% xylitol, and flash frozen in liquid nitrogen.

Diffraction data were collected at Advanced Light Source (ALS) beamline BL5.0.2 and Advanced Photo Source (APS) beamline 19ID. Data sets were indexed, integrated, and scaled with HKL2000 (37) and further processed with the CCP4 suite of programs (38). The structure was determined in $P2_1$ space group with one complex in an asymmetric unit by the single-wavelength anomalous dispersion method with data collected from platinum derivatized crystals. Briefly, Pt sites were identified with Phenix_autosol (39) and a partial model was generated by Phenix_autobuild (39). Further model building and iterative refinement were carried out with Coot (40), Phenix_refine (39), Refmac (41) and autoBUSTER (42). Phases were extended to native data sets by molecular replacement with Phaser (43). The final models were obtained by using TLS (translation, libration and screw-motion) refinement with autoBUSTER (42). Molecular graphics were generated with Pymol (44). Statistics for data collection, phase calculation, and refinement are summarized in table S1.

Histone methyltransferase assay

Mutant and wild-type ternary complexes for the methyltransferase assay were purified from 100-ml

cell culture with a protocol similar to that described above. Concentration of the purified proteins was normalized visually by SDS-polyacrylamide gel electrophoresis (SDS-PAGE). Proteins were aliquoted, flash frozen, and stored at -80°C. For assays with Western blotting, about 0.4 μ g of purified ternary complex was incubated with 600 nM histone H3 and 32 μ M SAM in 20 μ l of histone methyltransferase assay buffer [50 mM Tris-HCl (pH 8.0), 100 mM NaCl, 2.5 mM MgCl₂, 1 mM EDTA, and 2.5 mM DTT] at 30°C for 2 hours. The reaction was stopped by adding 6 μ l of 4 \times sample loading dye and boiling at 95°C for 5 min. Trimethylated H3 product was separated by SDS-PAGE, transferred to polyvinylidene difluoride membrane, and detected by Western blotting with anti-H3K27me3 primary antibody (Cell Signaling, catalog no. 9733S). For assays with the enzyme-linked immunosorbent assay (ELISA) method, 0.2 or 0.4 μ g of enzyme was incubated with 1 μ M biotinylated histone H3 (residues 21 to 44) peptide (AnaSpec, catalog no. AS-64641) and 32 μ M SAM in 20 μ l of the histone methyltransferase assay buffer with or without 50 or 100 μ M synthesized stimulating or inhibiting histone peptides at 30°C for 2 hours. The reaction was stopped by adding 80 μ l of 100 mM sodium acetate (pH 4.5). Methylated product was captured by a streptavidin-coated plate (Pierce, catalog no. 15502) and detected by standard ELISA procedure with the same anti-H3K27me3 primary antibody as used for the Western blot method.

REFERENCES AND NOTES

- R. Cao, Y. Zhang, The functions of E(Z)/EZH2-mediated methylation of lysine 27 in histone H3. *Curr. Opin. Genet. Dev.* **14**, 155–164 (2004). doi: [10.1016/j.gde.2004.02.001](https://doi.org/10.1016/j.gde.2004.02.001); pmid: [15196462](https://pubmed.ncbi.nlm.nih.gov/15196462/)
- J. A. Simon, R. E. Kingston, Mechanisms of polycomb gene silencing: Knowns and unknowns. *Nat. Rev. Mol. Cell Biol.* **10**, 697–708 (2009). pmid: [19738629](https://pubmed.ncbi.nlm.nih.gov/19738629/)
- R. Margueron, D. Reinberg, The Polycomb complex PRC2 and its mark in life. *Nature* **469**, 343–349 (2011). doi: [10.1038/nature09784](https://doi.org/10.1038/nature09784); pmid: [21248841](https://pubmed.ncbi.nlm.nih.gov/21248841/)
- A. Delest, T. Sexton, G. Cavalli, Polycomb: A paradigm for genome organization from one to three dimensions. *Curr. Opin. Cell Biol.* **24**, 405–414 (2012). doi: [10.1016/j.cob.2012.01.008](https://doi.org/10.1016/j.cob.2012.01.008); pmid: [22336329](https://pubmed.ncbi.nlm.nih.gov/22336329/)
- L. Di Croce, K. Helin, Transcriptional regulation by Polycomb group proteins. *Nat. Struct. Mol. Biol.* **20**, 1147–1155 (2013). doi: [10.1038/nsmb.2669](https://doi.org/10.1038/nsmb.2669); pmid: [24096405](https://pubmed.ncbi.nlm.nih.gov/24096405/)
- Y. B. Schwartz, V. Pirrotta, A new world of Polycombs: Unexpected partnerships and emerging functions. *Nat. Rev. Genet.* **14**, 853–864 (2013). doi: [10.1038/nrg3603](https://doi.org/10.1038/nrg3603); pmid: [24217316](https://pubmed.ncbi.nlm.nih.gov/24217316/)
- W. Yuan et al., Dense chromatin activates Polycomb repressive complex 2 to regulate H3 lysine 27 methylation. *Science* **337**, 971–975 (2012). doi: [10.1126/science.1225237](https://doi.org/10.1126/science.1225237); pmid: [22923582](https://pubmed.ncbi.nlm.nih.gov/22923582/)
- K. J. Ferrari et al., Polycomb-dependent H3K27me1 and H3K27me2 regulate active transcription and enhancer fidelity. *Mol. Cell* **53**, 49–62 (2014). doi: [10.1016/j.molcel.2013.10.030](https://doi.org/10.1016/j.molcel.2013.10.030); pmid: [24289921](https://pubmed.ncbi.nlm.nih.gov/24289921/)
- K. H. Hansen et al., A model for transmission of the H3K27me3 epigenetic mark. *Nat. Cell Biol.* **10**, 1291–1300 (2008). doi: [10.1038/ncb1787](https://doi.org/10.1038/ncb1787); pmid: [18931660](https://pubmed.ncbi.nlm.nih.gov/18931660/)
- R. Margueron et al., Role of the polycomb protein EED in the propagation of repressive histone marks. *Nature* **461**, 762–767 (2009). doi: [10.1038/nature08398](https://doi.org/10.1038/nature08398); pmid: [19767730](https://pubmed.ncbi.nlm.nih.gov/19767730/)
- C. Xu et al., Binding of different histone marks differentially regulates the activity and specificity of polycomb repressive complex 2 (PRC2). *Proc. Natl. Acad. Sci. U.S.A.* **107**, 19266–19271 (2010). doi: [10.1073/pnas.1008937107](https://doi.org/10.1073/pnas.1008937107); pmid: [20974918](https://pubmed.ncbi.nlm.nih.gov/20974918/)
- S. Sanulli et al., Jarid2 methylation via the PRC2 complex regulates H3K27me3 deposition during cell differentiation. *Mol. Cell* **57**, 769–783 (2015). doi: [10.1016/j.molcel.2014.12.020](https://doi.org/10.1016/j.molcel.2014.12.020); pmid: [25620564](https://pubmed.ncbi.nlm.nih.gov/25620564/)
- C. Ciferri et al., Molecular architecture of human polycomb repressive complex 2. *eLife* **1**, e00005 (2012). doi: [10.7554/eLife.00005](https://doi.org/10.7554/eLife.00005); pmid: [23110252](https://pubmed.ncbi.nlm.nih.gov/23110252/)
- Z. Han et al., Structural basis of EZH2 recognition by EED. *Structure* **15**, 1306–1315 (2007). doi: [10.1016/j.str.2007.08.007](https://doi.org/10.1016/j.str.2007.08.007); pmid: [17937919](https://pubmed.ncbi.nlm.nih.gov/17937919/)
- H. Wu et al., Structure of the catalytic domain of EZH2 reveals conformational plasticity in cofactor and substrate binding sites and explains oncogenic mutations. *PLOS ONE* **8**, e83737 (2013). doi: [10.1371/journal.pone.0083737](https://doi.org/10.1371/journal.pone.0083737); pmid: [24367611](https://pubmed.ncbi.nlm.nih.gov/24367611/)
- S. Antonyam et al., Structural context of disease-associated mutations and putative mechanism of autoinhibition revealed by X-ray crystallographic analysis of the EZH2-SET domain. *PLOS ONE* **8**, e84147 (2013). pmid: [24367637](https://pubmed.ncbi.nlm.nih.gov/24367637/)
- F. W. Schmitges et al., Histone methylation by PRC2 is inhibited by active chromatin marks. *Mol. Cell* **42**, 330–341 (2011). doi: [10.1016/j.molcel.2011.03.025](https://doi.org/10.1016/j.molcel.2011.03.025); pmid: [21549310](https://pubmed.ncbi.nlm.nih.gov/21549310/)
- J. A. Simon, C. A. Lange, Roles of the EZH2 histone methyltransferase in cancer epigenetics. *Mutat. Res.* **647**, 21–29 (2008). doi: [10.1016/j.mrfmmm.2008.07.010](https://doi.org/10.1016/j.mrfmmm.2008.07.010); pmid: [18723033](https://pubmed.ncbi.nlm.nih.gov/18723033/)
- T. Ernst et al., Inactivating mutations of the histone methyltransferase gene EZH2 in myeloid disorders. *Nat. Genet.* **42**, 722–726 (2010). doi: [10.1038/ng.621](https://doi.org/10.1038/ng.621); pmid: [20601953](https://pubmed.ncbi.nlm.nih.gov/20601953/)
- G. Nikoloski et al., Somatic mutations of the histone methyltransferase gene EZH2 in myelodysplastic syndromes. *Nat. Genet.* **42**, 665–667 (2010). doi: [10.1038/ng.620](https://doi.org/10.1038/ng.620); pmid: [20601954](https://pubmed.ncbi.nlm.nih.gov/20601954/)
- W. T. Gibson et al., FORGE Canada Consortium, Mutations in EZH2 cause Weaver syndrome. *Am. J. Hum. Genet.* **90**, 110–118 (2012). doi: [10.1016/j.ajhg.2011.11.018](https://doi.org/10.1016/j.ajhg.2011.11.018); pmid: [22177091](https://pubmed.ncbi.nlm.nih.gov/22177091/)
- P. W. Lewis et al., Inhibition of PRC2 activity by a gain-of-function H3 mutation found in pediatric glioblastoma. *Science* **340**, 857–861 (2013). doi: [10.1126/science.1232245](https://doi.org/10.1126/science.1232245); pmid: [23539183](https://pubmed.ncbi.nlm.nih.gov/23539183/)
- S. Amlacher et al., Insight into structure and assembly of the nuclear pore complex by utilizing the genome of a eukaryotic thermophile. *Cell* **146**, 277–289 (2011). doi: [10.1016/j.cell.2011.06.039](https://doi.org/10.1016/j.cell.2011.06.039); pmid: [21784248](https://pubmed.ncbi.nlm.nih.gov/21784248/)
- C. U. Stirnimann, E. Petsalaki, R. B. Russell, C. W. Müller, WD40 proteins propel cellular networks. *Trends Biochem. Sci.* **35**, 565–574 (2010). doi: [10.1016/j.tibs.2010.04.003](https://doi.org/10.1016/j.tibs.2010.04.003); pmid: [20451393](https://pubmed.ncbi.nlm.nih.gov/20451393/)
- L. A. Boyer, R. R. Latak, C. L. Peterson, The SANT domain: A unique histone-tail-binding module? *Nat. Rev. Mol. Cell Biol.* **5**, 158–163 (2004). doi: [10.1038/nrm1314](https://doi.org/10.1038/nrm1314); pmid: [15040448](https://pubmed.ncbi.nlm.nih.gov/15040448/)
- T. L. Cha et al., Akt-mediated phosphorylation of EZH2 suppresses methylation of lysine 27 in histone H3. *Science* **310**, 306–310 (2005). doi: [10.1126/science.1118947](https://doi.org/10.1126/science.1118947); pmid: [16224021](https://pubmed.ncbi.nlm.nih.gov/16224021/)
- P. Ntziachristos et al., Genetic inactivation of the polycomb repressive complex 2 in T cell acute lymphoblastic leukemia. *Nat. Med.* **18**, 298–301 (2012). pmid: [22237151](https://pubmed.ncbi.nlm.nih.gov/22237151/)
- J. Score et al., Inactivation of polycomb repressive complex 2 components in myeloproliferative and myelodysplastic/myeloproliferative neoplasms. *Blood* **119**, 1208–1213 (2012). doi: [10.1182/blood-2011-07-367243](https://doi.org/10.1182/blood-2011-07-367243); pmid: [22053108](https://pubmed.ncbi.nlm.nih.gov/22053108/)
- A. N. Rai et al., Elements of the polycomb repressor SU(Z)2 needed for histone H3-K27 methylation, the interface with E(Z), and in vivo function. *Mol. Cell Biol.* **33**, 4844–4856 (2013). doi: [10.1128/MCB.00307-13](https://doi.org/10.1128/MCB.00307-13); pmid: [24100017](https://pubmed.ncbi.nlm.nih.gov/24100017/)
- S. Kaneko et al., Phosphorylation of the PRC2 component Ezh2 is cell cycle-regulated and up-regulates its binding to ncRNA. *Genes Dev.* **24**, 2615–2620 (2010). doi: [10.1101/gad.1983810](https://doi.org/10.1101/gad.1983810); pmid: [21123648](https://pubmed.ncbi.nlm.nih.gov/21123648/)
- B. Xiao, J. R. Wilson, S. J. Gamblin, SET domains and histone methylation. *Curr. Opin. Struct. Biol.* **13**, 699–705 (2003). doi: [10.1016/j.sbi.2003.10.003](https://doi.org/10.1016/j.sbi.2003.10.003); pmid: [14675547](https://pubmed.ncbi.nlm.nih.gov/14675547/)
- W. Zheng et al., Sinefungin derivatives as inhibitors and structure probes of protein lysine methyltransferase SETD2. *J. Am. Chem. Soc.* **134**, 18004–18014 (2012). doi: [10.1021/ja307060p](https://doi.org/10.1021/ja307060p); pmid: [23043551](https://pubmed.ncbi.nlm.nih.gov/23043551/)
- R. Bejar et al., Clinical effect of point mutations in myelodysplastic syndromes. *N. Engl. J. Med.* **364**, 2496–2506 (2011). doi: [10.1056/NEJMoal013343](https://doi.org/10.1056/NEJMoal013343); pmid: [21714648](https://pubmed.ncbi.nlm.nih.gov/21714648/)
- M. T. McCabe et al., Mutation of A677 in histone methyltransferase EZH2 in human B-cell lymphoma promotes hypertrimethylation of histone H3 on lysine 27 (H3K27). *Proc.*

- Natl. Acad. Sci. U.S.A.* **109**, 2989–2994 (2012). doi: [10.1073/pnas.1116418109](https://doi.org/10.1073/pnas.1116418109); pmid: [22323599](https://pubmed.ncbi.nlm.nih.gov/22323599/)
35. A. Kuzmichev, T. Jenuwein, P. Tempst, D. Reinberg, Different EZH2-containing complexes target methylation of histone H1 or nucleosomal histone H3. *Mol. Cell* **14**, 183–193 (2004). doi: [10.1016/S1097-2765\(04\)00185-6](https://doi.org/10.1016/S1097-2765(04)00185-6); pmid: [15099518](https://pubmed.ncbi.nlm.nih.gov/15099518/)
 36. C. Martin, R. Cao, Y. Zhang, Substrate preferences of the EZH2 histone methyltransferase complex. *J. Biol. Chem.* **281**, 8365–8370 (2006). doi: [10.1074/jbc.M513425200](https://doi.org/10.1074/jbc.M513425200); pmid: [16431907](https://pubmed.ncbi.nlm.nih.gov/16431907/)
 37. Z. Otwinowski, W. Minor, Processing of X-ray diffraction data collected in oscillation mode. *Methods Enzymol.* **276**, 307–326 (1997). doi: [10.1016/S0076-6879\(97\)76066-X](https://doi.org/10.1016/S0076-6879(97)76066-X)
 38. M. D. Winn *et al.*, Overview of the CCP4 suite and current developments. *Acta Crystallogr. D Biol. Crystallogr.* **67**, 235–242 (2011). doi: [10.1107/S0907444910045749](https://doi.org/10.1107/S0907444910045749); pmid: [21460441](https://pubmed.ncbi.nlm.nih.gov/21460441/)
 39. P. D. Adams *et al.*, PHENIX: A comprehensive Python-based system for macromolecular structure solution. *Acta Crystallogr. D Biol. Crystallogr.* **66**, 213–221 (2010). doi: [10.1107/S0907444909052925](https://doi.org/10.1107/S0907444909052925); pmid: [20124702](https://pubmed.ncbi.nlm.nih.gov/20124702/)
 40. P. Emsley, K. Cowtan, Coot: Model-building tools for molecular graphics. *Acta Crystallogr. D Biol. Crystallogr.* **60**, 2126–2132 (2004). doi: [10.1107/S0907444904019158](https://doi.org/10.1107/S0907444904019158); pmid: [15572765](https://pubmed.ncbi.nlm.nih.gov/15572765/)
 41. G. N. Murshudov, A. A. Vagin, E. J. Dodson, Refinement of macromolecular structures by the maximum-likelihood method. *Acta Crystallogr. D Biol. Crystallogr.* **53**, 240–255 (1997). doi: [10.1107/S0907444996012255](https://doi.org/10.1107/S0907444996012255); pmid: [15299926](https://pubmed.ncbi.nlm.nih.gov/15299926/)
 42. G. Bricogne *et al.*, BUSTER version 2.10.1 Ed., Global Phasing, Cambridge, UK (2011).
 43. A. J. McCoy *et al.*, Phaser crystallographic software. *J. Appl. Crystallogr.* **40**, 658–674 (2007). doi: [10.1107/S0021889807021206](https://doi.org/10.1107/S0021889807021206); pmid: [19461840](https://pubmed.ncbi.nlm.nih.gov/19461840/)
 44. The PyMOL Molecular Graphics System, version no. 1.7.4.3, Schrodinger, LLC (2010).
 45. J. D. Thompson, D. G. Higgins, T. J. Gibson, CLUSTAL W: Improving the sensitivity of progressive multiple sequence alignment through sequence weighting, position-specific gap penalties and weight matrix choice. *Nucleic Acids Res.* **22**, 4673–4680 (1994). doi: [10.1093/nar/22.22.4673](https://doi.org/10.1093/nar/22.22.4673); pmid: [7984417](https://pubmed.ncbi.nlm.nih.gov/7984417/)
 46. E. F. Pettersen *et al.*, UCSF Chimera—a visualization system for exploratory research and analysis. *J. Comput. Chem.* **25**, 1605–1612 (2004). doi: [10.1002/jcc.20084](https://doi.org/10.1002/jcc.20084); pmid: [15264254](https://pubmed.ncbi.nlm.nih.gov/15264254/)

ACKNOWLEDGMENTS

This research was supported by Welch Foundation research grant I-1790, CPRIT research grant R1119, Rita Allen Foundation research grant, University of Texas Southwestern Medical Center

Endowed Scholar fund, and NIH grant GM114576 to X.L. X.L. is a W. W. Caruth, Jr. Scholar in Biomedical Research. This research also received support from the Cecil H. and Ida Green Center Training Program in Reproductive Biology Sciences Research. This research used resources of the Advanced Photon Source, a U.S. Department of Energy (DOE) Office of Science User Facility operated for the DOE Office of Science by Argonne National Laboratory under contract no. DE-AC02-06CH11357. The Advanced Light Source is supported by the Director, Office of Science, Office of Basic Energy Sciences, of the U.S. DOE under contract no. DE-AC02-05CH11231. We thank R. Kornberg, R. Marmorstein, and L. Kraus for critical reading of the manuscript. The crystal structures described in this study have been deposited in the Protein Data Bank under accession number 5CH1 (PRC2 in the stimulated state) and 5CH2 (PRC2 in the basal state).

SUPPLEMENTARY MATERIALS

www.sciencemag.org/content/350/6258/aac4383/suppl/DC1

Figs. S1 to S16

Table S1

References (45, 46)

28 April 2015; accepted 28 August 2015

10.1126/science.aac4383

RESEARCH ARTICLE SUMMARY

PLANETARY SCIENCE

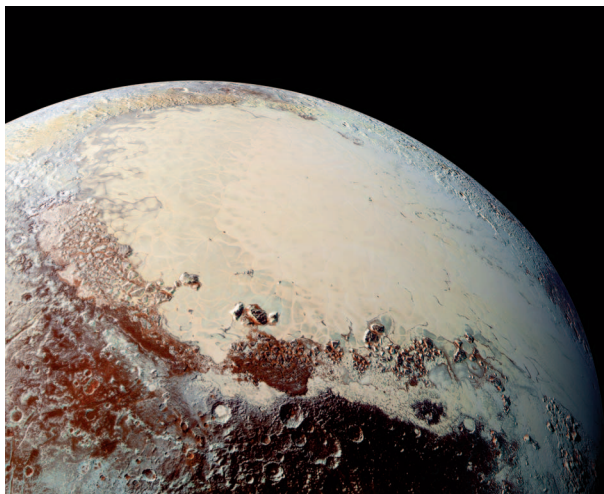
The Pluto system: Initial results from its exploration by New Horizons

S. A. Stern,* F. Bagenal, K. Ennico, G. R. Gladstone, W. M. Grundy, W. B. McKinnon, J. M. Moore, C. B. Olkin, J. R. Spencer, H. A. Weaver, L. A. Young, T. Andert, J. Andrews, M. Banks, B. Bauer, J. Bauman, O. S. Barnouin, P. Bedini, K. Beisser, R. A. Beyer, S. Bhaskaran, R. P. Binzel, E. Birath, M. Bird, D. J. Bogan, A. Bowman, V. J. Bray, M. Brozovic, C. Bryan, M. R. Buckley, M. W. Buie, B. J. Buratti, S. S. Bushman, A. Calloway, B. Carcich, A. F. Cheng, S. Conard, C. A. Conrad, J. C. Cook, D. P. Cruikshank, O. S. Custodio, C. M. Dalle Ore, C. Deboy, Z. J. B. Dischner, P. Dumont, A. M. Earle, H. A. Elliott, J. Ercol, C. M. Ernst, T. Finley, S. H. Flanigan, G. Fountain, M. J. Freeze, T. Greathouse, J. L. Green, Y. Guo, M. Hahn, D. P. Hamilton, S. A. Hamilton, J. Hanley, A. Harch, H. M. Hart, C. B. Hersman, A. Hill, M. E. Hill, D. P. Hinson, M. E. Holdridge, M. Horanyi, A. D. Howard, C. J. A. Howett, C. Jackman, R. A. Jacobson, D. E. Jennings, J. A. Kammer, H. K. Kang, D. E. Kaufmann, P. Kollmann, S. M. Krimigis, D. Kusnierkiewicz, T. R. Lauer, J. E. Lee, K. L. Lindstrom, I. R. Linscott, C. M. Lisse, A. W. Lunsford, V. A. Mallder, N. Martin, D. J. McComas, R. L. McNutt Jr., D. Mehoke, T. Mehoke, E. D. Melin, M. Mutchler, D. Nelson, F. Nimmo, J. I. Nunez, A. Ocampo, W. M. Owen, M. Paetzold, B. Page, A. H. Parker, J. W. Parker, F. Pelletier, J. Peterson, N. Pinkine, M. Piquette, S. B. Porter, S. Protopapa, J. Redfern, H. J. Reitsema, D. C. Reuter, J. H. Roberts, S. J. Robbins, G. Rogers, D. Rose, K. Runyon, K. D. Retherford, M. G. Ryschkewitsch, P. Schenk, E. Schindhelm, B. Sepan, M. R. Showalter, K. N. Singer, M. Soluri, D. Stanbridge, A. J. Steffl, D. F. Strobel, T. Stryk, M. E. Summers, J. R. Szalay, M. Tapley, A. Taylor, H. Taylor, H. B. Throop, C. C. C. Tsang, G. L. Tyler, O. M. Umurhan, A. J. Verbiscer, M. H. Versteeg, M. Vincent, R. Webbert, S. Weidner, G. E. Weigle II, O. L. White, K. Whittenburg, B. G. Williams, K. Williams, S. Williams, W. W. Woods, A. M. Zangari, E. Zirnstein

INTRODUCTION: Pluto was discovered in 1930 and was long thought to be a misfit or anomaly in the solar system. However, the 1992 discovery of the Kuiper Belt—a torus-shaped region beyond Neptune's orbit, and the largest structure in our three-zoned planetary system—provided new context, showing Pluto to be the largest of a new class of small planets formed in the outer solar system during the ancient era of planetary accretion ~4.5 billion years ago. NASA's New Horizons spacecraft made the first exploration of Pluto, culminating on 14 July 2015; it collected numerous remote sensing and in situ measurements of Pluto and its system of five moons. We report the first scientific results and interpretations of that flyby.

RATIONALE: The New Horizons spacecraft completed a close approach to the Pluto system at a distance of 13,691 km from Pluto's center. The spacecraft carries a sophisticated suite of scientific instruments, including the Ralph multicolor/panchromatic mapper and mapping infrared composition spectrometer; the LORRI long-focal-

length panchromatic visible imager; the Alice extreme/far ultraviolet mapping spectrograph; twin REX radio science experiments; the



Pluto mosaic made from New Horizons LORRI images taken 14 July 2015 from a distance of 80,000 km. This view is projected from a point 1800 km above Pluto's equator, looking northeast over the dark, cratered, informally named Cthulhu Regio toward the bright, smooth expanse of icy plains informally called Sputnik Planum. Pluto's north pole is off the image to the left. This image mosaic was produced with panchromatic images from the New Horizons LORRI camera, with color overlaid from the Ralph color mapper onboard New Horizons.

SWAP solar wind detector; the PEPSSI high-energy charged particle spectrometer; and VBSDC, a dust impact detector. Together these instruments collected more than 50 gigabits of data on the Pluto system near the time of the spacecraft's closest approach.

RESULTS: We found that Pluto's surface displays a wide variety of landforms and terrain ages, as well as substantial albedo, color, and compositional variation. Evidence was also found for a water ice-rich crust, geologically young surface units, tectonic extension, surface volatile ice convection, possible wind streaks, volatile transport, and glacial flow. Pluto's atmosphere is highly extended, with trace hydrocarbons, a global haze layer, and a surface pressure near 10 microbars. The bulk densities of Pluto and Charon were found to differ by less than 10%, which is consistent with bulk rock contents for the two bodies that are likewise similar. This could imply that both precursor bodies were undifferentiated (or only modestly differentiated) prior to their collision—which would have profound implications for the timing, the duration, and even the mechanism of accretion in the ancestral Kuiper Belt.

Pluto's large moon Charon displays extensional tectonics and extensive resurfacing, as well as possible evidence for a heterogeneous crustal composition; its north pole displays puzzling dark terrain. The sizes of Pluto's small satellites Nix and Hydra were measured for the first time, as were their surface reflectivities, which are puzzlingly higher than Charon's. No new satellites were detected.

CONCLUSION: The New Horizons encounter revealed that Pluto displays a surprisingly wide variety of geological landforms, including those resulting from glaciological and surface-atmosphere interactions as well as impact, tectonic, possible cryovolcanic, and mass-wasting processes. This suggests that other small planets of the Kuiper Belt, such as Eris, Makemake, and Haumea, could express similarly complex histories that rival those of terrestrial planets. Pluto's diverse surface geology and long-term activity also raise fundamental questions about how it has remained active many billions of years after its formation. ■

The list of affiliations is available in the full article online.
*Corresponding author. E-mail: astern@boulder.swri.edu
Cite this article as S. A. Stern *et al.*, *Science* 350, aad1815 (2015). DOI: 10.1126/science.aad1815

RESEARCH ARTICLE

PLANETARY SCIENCE

The Pluto system: Initial results from its exploration by New Horizons

S. A. Stern,^{1*} F. Bagenal,² K. Ennico,³ G. R. Gladstone,⁴ W. M. Grundy,⁵ W. B. McKinnon,⁶ J. M. Moore,³ C. B. Olkin,¹ J. R. Spencer,¹ H. A. Weaver,⁷ L. A. Young,¹ T. Andert,⁸ J. Andrews,¹ M. Banks,⁹ B. Bauer,⁷ J. Bauman,¹⁰ O. S. Barnouin,⁷ P. Bedini,⁷ K. Beisser,⁷ R. A. Beyer,³ S. Bhaskaran,¹¹ R. P. Binzel,¹² E. Birath,¹ M. Bird,¹³ D. J. Bogan,¹⁴ A. Bowman,⁷ V. J. Bray,¹⁵ M. Brozovic,¹¹ C. Bryan,¹⁰ M. R. Buckley,⁷ M. W. Buie,¹ B. J. Buratti,¹¹ S. S. Bushman,⁷ A. Calloway,⁷ B. Carcich,¹⁶ A. F. Cheng,⁷ S. Conard,⁷ C. A. Conrad,¹ J. C. Cook,¹ D. P. Cruikshank,³ O. S. Custodio,⁷ C. M. Dalle Ore,³ C. Deboy,⁷ Z. J. B. Dischner,¹ P. Dumont,¹⁰ A. M. Earle,¹² H. A. Elliott,⁴ J. Ercol,⁷ C. M. Ernst,⁷ T. Finley,¹⁷ S. H. Flanigan,⁷ G. Fountain,⁷ M. J. Freeze,⁷ T. Greathouse,⁴ J. L. Green,¹⁷ Y. Guo,⁷ M. Hahn,¹⁸ D. P. Hamilton,¹⁹ S. A. Hamilton,⁷ J. Hanley,⁴ A. Harch,²⁰ H. M. Hart,⁷ C. B. Hersman,⁷ A. Hill,⁷ M. E. Hill,⁷ D. P. Hinson,²¹ M. E. Holdridge,⁷ M. Horanyi,² A. D. Howard,²² C. J. A. Howett,¹ C. Jackman,¹⁰ R. A. Jacobson,¹¹ D. E. Jennings,²³ J. A. Kammer,¹ H. K. Kang,⁷ D. E. Kaufmann,¹ P. Kollmann,⁷ S. M. Krimigis,⁷ D. Kusnierkiewicz,⁷ T. R. Lauer,²⁴ J. E. Lee,²⁵ K. L. Lindstrom,⁷ I. R. Linscott,²⁶ C. M. Lisse,⁷ A. W. Lunsford,²³ V. A. Mallder,⁷ N. Martin,²⁰ D. J. McComas,⁴ R. L. McNutt Jr.,⁷ D. Mehoke,⁷ T. Mehoke,⁷ E. D. Melin,⁷ M. Mutchler,²⁷ D. Nelson,¹⁰ F. Nimmo,²⁸ J. I. Nunez,⁷ A. Ocampo,⁷ W. M. Owen,¹¹ M. Paetzold,¹⁸ B. Page,¹⁰ A. H. Parker,¹ J. W. Parker,¹ F. Pelletier,¹⁰ J. Peterson,¹ N. Pinkine,⁷ M. Piquette,² S. B. Porter,¹ S. Protopapa,¹⁹ J. Redfern,¹ H. J. Reitsema,²⁰ D. C. Reuter,²³ J. H. Roberts,⁷ S. J. Robbins,¹ G. Rogers,⁷ D. Rose,¹ K. Runyon,⁷ K. D. Retherford,⁴ M. G. Ryschkewitsch,⁷ P. Schenk,²⁹ E. Schindhelm,¹ B. Sepan,⁷ M. R. Showalter,²¹ K. N. Singer,¹ M. Soluri,³⁰ D. Stanbridge,¹⁰ A. J. Steffl,¹ D. F. Strobel,³¹ T. Stryk,³² M. E. Summers,³³ J. R. Szalay,² M. Tapley,⁴ A. Taylor,¹⁰ H. Taylor,⁷ H. B. Throop,⁹ C. C. C. Tsang,¹ G. L. Tyler,²⁶ O. M. Umurhan,³ A. J. Verbiscer,³⁴ M. H. Versteeg,⁴ M. Vincent,¹ R. Webber,⁷ S. Weidner,⁴ G. E. Weigle II,⁴ O. L. White,³ K. Whittenburg,⁷ B. G. Williams,¹⁰ K. Williams,¹⁰ S. Williams,⁷ W. W. Woods,²⁶ A. M. Zangari,¹ E. Zirnstein⁴

The Pluto system was recently explored by NASA's New Horizons spacecraft, making closest approach on 14 July 2015. Pluto's surface displays diverse landforms, terrain ages, albedos, colors, and composition gradients. Evidence is found for a water-ice crust, geologically young surface units, surface ice convection, wind streaks, volatile transport, and glacial flow. Pluto's atmosphere is highly extended, with trace hydrocarbons, a global haze layer, and a surface pressure near 10 microbars. Pluto's diverse surface geology and long-term activity raise fundamental questions about how small planets remain active many billions of years after formation. Pluto's large moon Charon displays tectonics and evidence for a heterogeneous crustal composition; its north pole displays puzzling dark terrain. Small satellites Hydra and Nix have higher albedos than expected.

Pluto was discovered in 1930 (1); it forms a binary system with its moon Charon, and the system's basic properties have been measured remotely from Earth (1). Pluto was long thought to be a misfit or anomaly in the solar system. However, the 1992 discovery of the Kuiper Belt—the largest structure in our planetary system (2)—provided important context demonstrating that Pluto is the largest of a class of small planets formed in the outer solar system during the ancient era of planetary accretion ~4.5 billion years ago.

New Horizons (3) launched on 19 January 2006 and successfully completed a close approach to

the Pluto system on 14 July 2015 at a distance of 13,691 km from Pluto's center. It carries a sophisticated suite of instruments summarized in (4), including the Ralph multicolor/panchromatic mapper and mapping infrared (IR) composition spectrometer; the Long Range Reconnaissance Imager (LORRI), a long-focal length panchromatic visible imager; the Alice extreme/far ultraviolet (UV) mapping spectrograph; REX (Radio Experiment); the Solar Wind Around Pluto (SWAP) instrument; PEPSSI (Pluto Energetic Particle Spectrometer Science Instrument); and the VBSDC (Venetia Burney Student Dust Counter), a dust impact detector.

This article contains the first scientific results and post-flyby interpretations from the New Horizons Pluto flyby, organized according to the objects in the system.

Pluto Geology and imaging

New Horizons has so far provided coverage (Fig. 1A) of the near-encounter, anti-Charon-facing hemisphere north of 30° south latitude at 2.2 km/pixel, with limited areas on that hemisphere covered at a higher resolution of 400 m/pixel. On the Charon-facing opposite hemisphere of Pluto, imaging resolution varies from 13 to 27 km/pixel. Dynamical and physical properties of Pluto and its satellites are given in Table 1. Limb fits using full-disk images, combined in a joint solution, give a mean radius for Pluto of 1187 ± 4 km (5), at the larger end of a previously uncertain range of 1150 to 1200 km (6). No oblateness has been detected (5), yielding a conservative upper limit on Pluto's polar flattening (a difference of <12 km between equatorial and polar axes) of 1%. We conclude from this that Pluto does not record significant shape evidence of an early, high-spin period after Pluto-Charon binary formation (7), presumably because it was warm and deformable during or after tidal spindown.

Pluto displays a diverse range of landforms, as well as evidence for geological and other processes that have substantially modified its surface up to geologically recent times. Pluto's

¹Southwest Research Institute, Boulder, CO 80302, USA.

²Laboratory for Atmospheric and Space Physics, University of Colorado, Boulder, CO 80303, USA. ³National Aeronautics and Space Administration (NASA) Ames Research Center, Space Science Division, Moffett Field, CA 94035, USA.

⁴Southwest Research Institute, San Antonio, TX 78210, USA.

⁵Lowell Observatory, Flagstaff, AZ 86001, USA. ⁶Department of Earth and Planetary Sciences, Washington University, St. Louis, MO 63130, USA. ⁷Johns Hopkins University Applied Physics Laboratory, Laurel, MD 20723, USA. ⁸Universität der Bundeswehr München, Neubiberg 85577, Germany.

⁹Planetary Science Institute, Tucson, AZ 85719, USA.

¹⁰KinetX Aerospace, Tempe, AZ 85284, USA. ¹¹NASA Jet Propulsion Laboratory, La Cañada Flintridge, CA 91011, USA.

¹²Massachusetts Institute of Technology, Cambridge, MA 02139, USA. ¹³University of Bonn, Bonn D-53113, Germany.

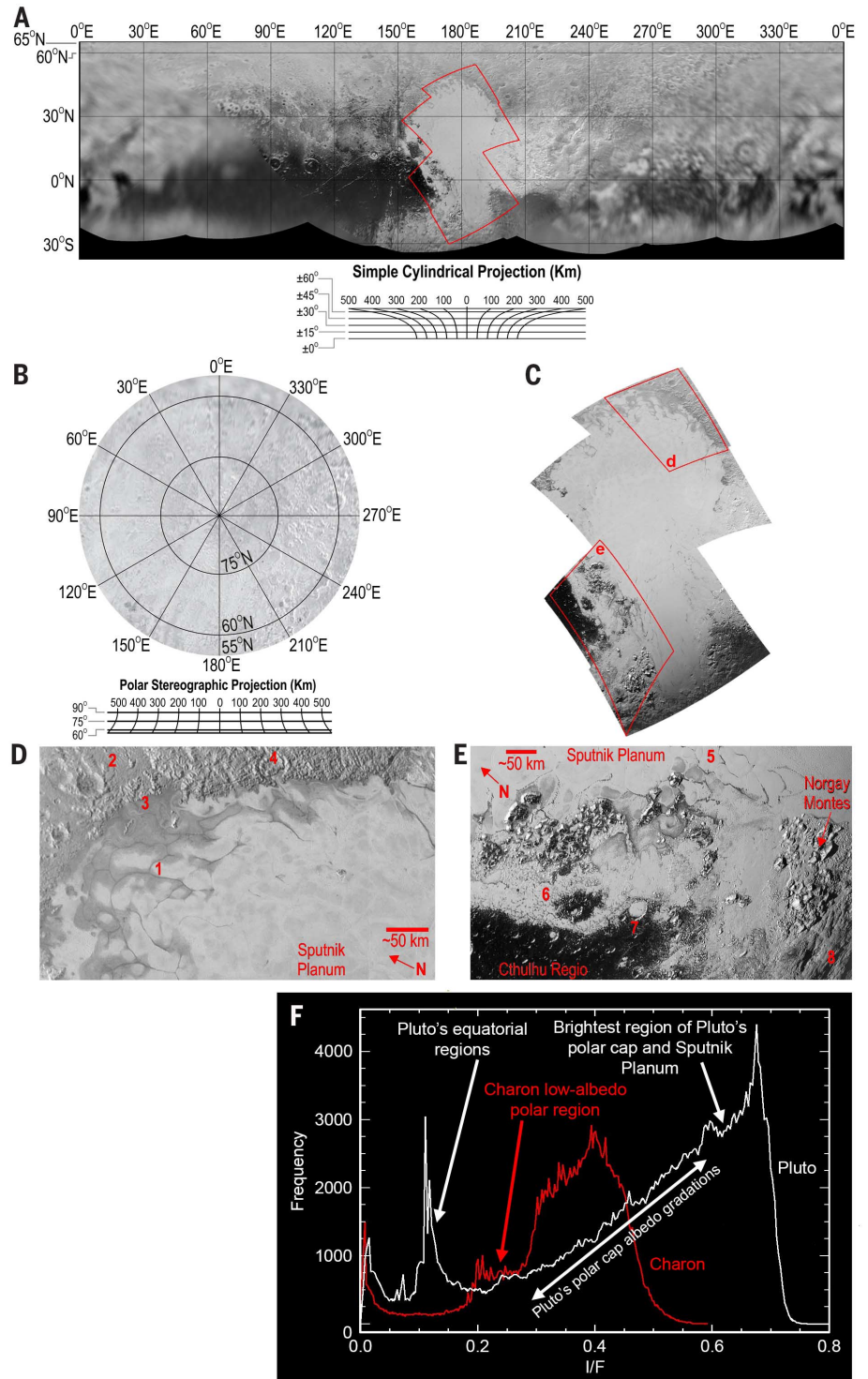
¹⁴NASA Headquarters (retired), Washington, DC 20546, USA.

¹⁵University of Arizona, Tucson, AZ 85721, USA. ¹⁶Cornell University, Ithaca, NY 14853, USA. ¹⁷NASA Headquarters, Washington, DC 20546, USA. ¹⁸Rheinisches Institut für Umweltforschung an der Universität zu Köln, Cologne 50931, Germany. ¹⁹Department of Astronomy, University of Maryland, College Park, MD 20742, USA. ²⁰Southwest Research Institute, Boulder, CO 80302, USA. ²¹Search for Extraterrestrial Intelligence Institute, Mountain View, CA 94043, USA. ²²Department of Environmental Sciences, University of Virginia, Charlottesville, VA 22904, USA.

²³NASA Goddard Space Flight Center, Greenbelt, MD 20771, USA. ²⁴National Optical Astronomy Observatory, Tucson, AZ 26732, USA. ²⁵NASA Marshall Space Flight Center, Huntsville, AL 35812, USA. ²⁶Stanford University, Stanford, CA 94305, USA. ²⁷Space Telescope Science Institute, Baltimore, MD 21218, USA. ²⁸University of California, Santa Cruz, CA 95064, USA. ²⁹Lunar and Planetary Institute, Houston, TX 77058, USA. ³⁰Michael Soluri Photography, New York, NY 10014, USA. ³¹Johns Hopkins University, Baltimore, MD 21218, USA. ³²Roane State Community College, Jamestown, TN 38556, USA. ³³George Mason University, Fairfax, VA 22030, USA. ³⁴Department of Astronomy, University of Virginia, Charlottesville, VA 22904, USA.

*Corresponding author. E-mail: astern@boulder.swri.edu

Fig. 1. Pluto surface imaging results. (A) Simple cylindrical mosaic of Pluto; the area covered by the seven highest-resolution (400 m/pixel) frames is highlighted by a red boundary and is shown in (C). (B) Polar stereographic mosaic of Pluto's north pole. (C) Seven-image, 400 m/pixel mosaic covering the majority of Sputnik Planum (SP), with Norgay Montes and Hillary Montes bordering to the south. Areas shown in (D) and (E) are labeled d and e. (D) Detail of the northern margin of SP: (1) Polygonal terrain at the northern margin of SP. (2) Rugged, cratered terrain north of SP. (3) Patterns indicative of viscous flow in the ice (see text). (4) A crater (diameter ~40 km) that has been breached by ice from SP. (E) Detail of SP's southwest margin. (5) Polygonal terrain in SP. (6) Ice plains separating Hillary Montes from the dark terrain of Cthulhu Regio (CR). The ice appears to cover and embay portions of CR. (7) Ice infilling a crater at SP's margin. (8) Rough, undulating terrain south of Norgay Montes displaying very few impact craters at 400 m/pixel. (F) Histograms of the I/F distributions of Pluto and Charon. Note the wider range of I/F values for Pluto than for Charon.



latitudinal band from about 25°S to 10°N features large, discrete expanses of low-albedo terrain interspersed with brighter regions. Terrain that is more reflective generally occurs in mid- and high latitudes. The large, prominent high-albedo region of the New Horizons encounter hemisphere that we call Tombaugh Regio (TR; all surface feature names currently used are informal) straddles the equator on the anti-Charon hemisphere (Fig. 2A).

TR measures about 1800 km east to west and 1500 km north to south.

At 2.2 km/pixel, widely distributed impact craters up to 260 km in diameter are seen in the near-encounter hemisphere. Many appear to be substantially degraded or infilled, and some are highlighted by bright ice-rich deposits on their rims and/or floors. This includes the dark equatorial terrain immediately west of TR, called

Cthulhu Regio (CR), which appears densely cratered. Tectonic features, including scarps and troughs up to 600 km in length, occur within and to the north of CR.

A large, apparently level plains unit we call Sputnik Planum (SP) constitutes the west half of TR. Several physiographic provinces have been identified in this region (Figs. 1 and 2). Mountains locally rise 2 to 3 km above their surrounding

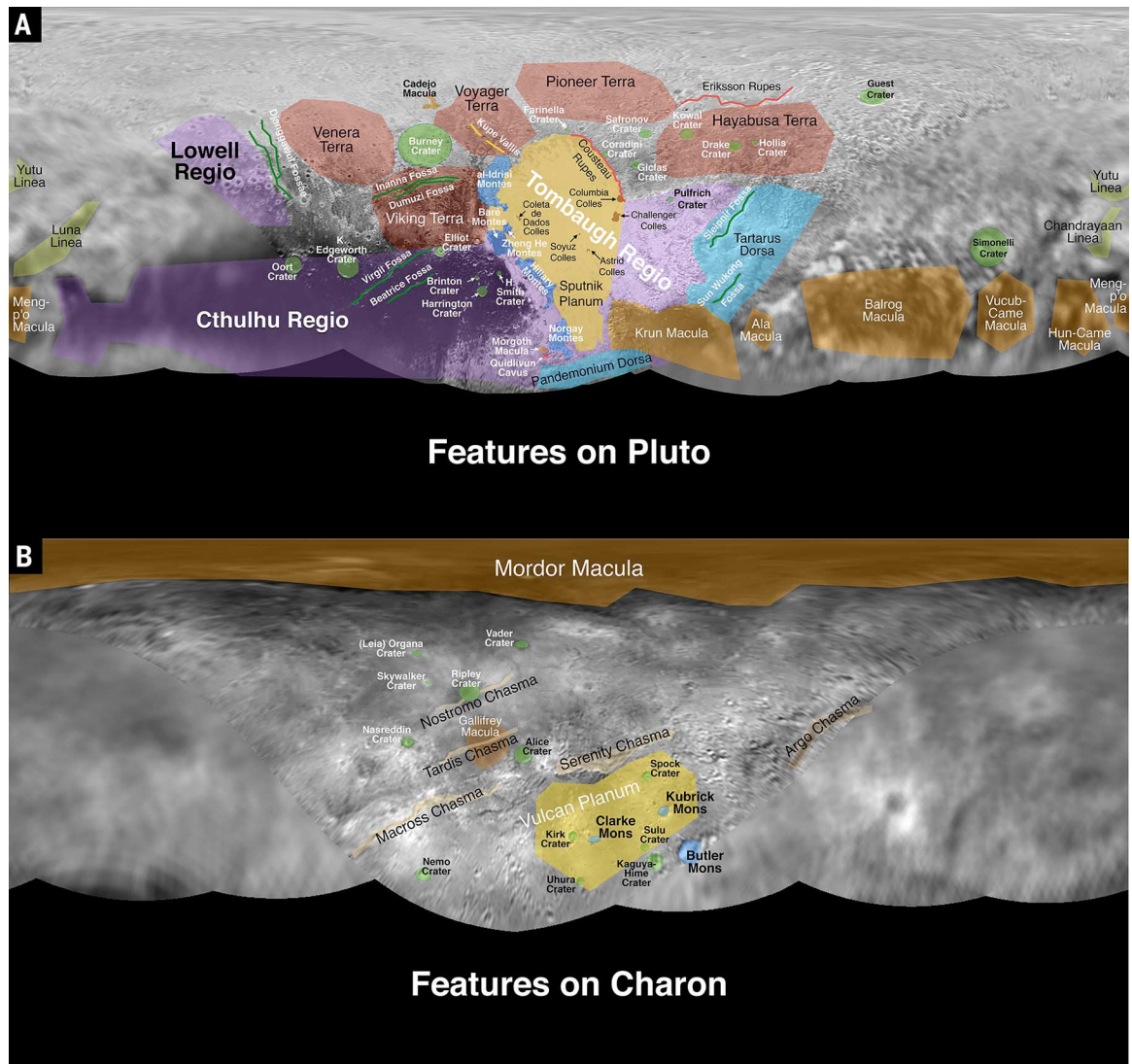
Table 1. Properties of the Pluto-Charon system. Boldface entries are values from New Horizons. Mean orbital elements (semimajor axis, orbital period, eccentricity, and inclination) for Charon are Plutocentric, whereas those for the small satellites are barycentric and are based on numerical integrations (35); GM (standard gravitational parameter) values are also from (35).

Body	Semimajor axis (km)	Period (days)	Eccentricity	Inclination (degrees)	Radius (km)	GM (km ³ s ⁻²)	Density (kg m ⁻³)
Pluto		6.3872			1187 ± 4*	869.6 ± 1.8	1860 ± 13
Charon	19,596	6.3872	0.00005	0.0	606 ± 3*	105.88 ± 1.0	1702 ± 21
Styx	42,413	20.1617	0.00001	0.0	1.8 to 9.8†	0.0000 ± 0.0001	
Nix	48,690	24.8548	0.00000	0.0	54 × 41 × 36‡	0.0030 ± 0.0027	
Kerberos	57,750	32.1679	0.00000	0.4	2.6 to 14†	0.0011 ± 0.0006	
Hydra	64,721	38.2021	0.00554	0.3	43 × 33‡	0.0032 ± 0.0028	

*From limb fits to LORRI images; radius error is pixel scale of best resolved image for each. Pluto's radius is consistent with radio occultation results as well; see (36) for technique. †From (32). ‡Axial dimensions derived from LORRI and MVIC images (see text).

Fig. 2. Maps with informal feature names used on Pluto (A) and Charon (B).

Geomorphological regions that we consider to be distinct are colored as follows: red, terrae; green, craters; light yellow, chasmata; orange, maculae; blue, montes; purple, regio; yellow, plana; cyan, dorsae; pink, cavi; light green, lineae; golden yellow, colles; red lines, rupes; green lines, fossae; yellow lines, valles.



terrain, as calculated from shadow length measurements. These and other high, steep-sided topographic features seen across Pluto require materials that will not relax under their own weight on geologic time scales. The nitrogen (N₂), carbon monoxide (CO), and methane (CH₄) ices

that were known from ground-based spectroscopy (1) to dominate Pluto's visible surface would collapse exceptionally rapidly (8, 9) because they are weak, van der Waals-bonded solids. The mountains detected by New Horizons imagery therefore imply the presence of a widespread,

stronger, presumably water ice-based, solid "bedrock." We further conclude that the observed N₂, CO, and CH₄ ices must only be a surface veneer above this bedrock.

Portions of the mountainous terrain are broken into hummocky regions of varying scale. An

undulating, lightly cratered terrain occurs at the south end of Fig. 1C and in a large region at the eastern edge of TR; its broadly rounded undulations are separated by linear depressions and troughs. The hummocks range from 20 to 150 km across and a few hundred meters in relief (as derived principally from shadow measurements) and feature smaller superimposed, rounded ridges. This terrain may be tectonic in origin.

SP (Fig. 1, C and D) has no confirmed craters. Much of its surface is divided into polygonal and ovoid-shaped cells tens of kilometers wide, themselves bordered by shallow troughs of characteristic width 2 to 3 km. Some troughs have darker material within them and some are traced by clumps of hills that rise up to a few hundred meters above the surrounding terrain; others contain narrow medial ridges tens of meters high. Around the margins of SP, portions of the surface appear to be etched by fields of small pits that may have formed by sublimation. Aligned dark streaks in SP are tentatively interpreted as wind streaks (fig. S1). The central, brightest region of SP contains N₂ and CH₄ ices and also coincides with a surface enhancement in CO ice (see below). SP is mostly bordered by locally higher terrain, which suggests that it fills a topographic basin.

Some features of SP suggest bulk flow similar to terrestrial glaciers. Two lobes with sharp margins extend south; topographic shading suggests a convex upward profile (Fig. 1C, bottom). Along the northern margin of SP, hills of apparent basement materials protrude above the smooth terrain (possibly water-ice nunataqs). Albedo features on SP's smooth terrain appear to be diverted around these hills (Fig. 1D), suggesting flow around obstacles. Elsewhere, SP material embays the interior of a degraded crater through a rim breach (Fig. 1D). Such bulk flow driven by modest topographic gradients is consistent with the rheological characteristics of N₂, CO, or CH₄ ices at Pluto surface conditions (i.e., near Pluto's ~38 K surface temperature) (9).

The origin of the polygonal and ovoid features on SP is uncertain. They could be the surface manifestation of contraction (analogous to mud or cooling cracks), or insolation-related processes, or the result of fracture of the surface due to extension and/or uplift of the subsurface, but they are perhaps most consistent morphologically with solid-state convection [see, e.g., (10)]. Internal convection is also consistent with evidence cited above for the flow of the material that fills SP, in that the surface ice apparently possesses a low enough viscosity that it can creep or flow under low driving stresses.

Varying crater abundances indicate wide-ranging surface ages on Pluto, in the sense that numerous large craters are seen on certain regions (such as CR), whereas no craters with diameters of >10 km can be identified on SP. Model ages for SP derived from estimates of Kuiper Belt bombardment (see the discussion of Charon crater counts below) imply active geomorphic processes within the last few hundred million years (11, 12) and possibly continuing to the present. Such re-

surfacing can occur via surficial erosion/deposition (as at Titan), crater relaxation (as at Enceladus), crustal recycling or tectonism (as at Europa), or some combination of these processes (13). For icy satellites, resurfacing is generally associated with eccentricity tides (14), but these are not a viable heat source today for Pluto or Charon, whose orbital eccentricities are fully damped (Table 1); as such, the young surface units on Pluto present a puzzle regarding the energy source(s) that power such resurfacing over time scales of billions of years.

Surface color and composition

The radiance factor I/F (the ratio of reflected to incident flux) of Pluto's surface at our approach solar phase angle of 15° ranges from 0.1 in the dark equatorial regions to a peak of 0.7 in TR and the north polar cap. This is a wider range than any other solar system body except Iapetus (15).

Color imaging of the encounter hemisphere through three broadband filters (400 to 550 nm, 540 to 700 nm, and 780 to 975 nm) at 5 and 28 km/pixel spatial resolution reveals spectacular diversity across Pluto (Fig. 3). The bright, heart-shaped TR region divides into two distinct color units: The eastern half is more rugged, apparently physically thinner, and less red across the three broadband filters; this material may originate via some transport mechanism from SP. Dark equatorial regions (e.g., CR and Krun Macula) are particularly red at visible wavelengths and border a brighter region (exemplified by Viking Terra) to the north. At higher latitudes, this terrain grades into a unit that is bluer across the same three filters. We find that this unit brightens noticeably for high Sun elevations, a photometric behavior that contrasts with the flatter center-to-limb profiles of other Pluto regions and is potentially related to sea-

sonal volatile ice sublimation. Interspersed with this bluer unit, especially above 60°N latitude, a redder unit appears. Contacts between these two high-latitude color units do not appear to consistently correlate with the underlying geomorphology and may be related to volatile transport processes.

Colors on Pluto are characteristic of refractory organic residues called tholins, which are readily formed by UV or charged-particle irradiation of mixtures of nitrogen and methane in both the gaseous and frozen states (16). Energetic radiation falling on Pluto's atmosphere and surface, each rich in nitrogen and methane, likely creates tholins that even in small concentrations yield colors ranging from yellow to dark red.

Ralph instrument images at a few IR wavelengths (e.g., fig. S2) have been downlinked to date. In Fig. 4, we show such images with 9 km/pixel spatial resolution, representing vibrational absorptions of CH₄ ice at 1.66 and 1.79 μm and CO ice at 1.58 μm. CO absorption, previously reported in ground-based Pluto spectra (17–19), is found to be strongest in SP's center (Fig. 4C). CH₄ ice is distributed widely, but the absorption depths vary from strong in the northern polar cap and SP to weak or nonexistent in the dark terrains (Fig. 4B). Sharp contrasts in CH₄ absorption correlate with geological units along the western edge of SP, with much weaker absorption associated with the bounding mountainous terrain.

The composition, extent, and uniqueness of SP's ices suggest that this region may be a major reservoir of volatile ices. It could also conceivably be a source region connected to the deep interior, or it could be a major sink for volatiles released planetwide, or both. Whether deep or surficial processes dominate is currently unclear, but the actual processes involved must be

Fig. 3. Pluto color/panchromatic composite image. This is a composite of high-resolution panchromatic images and lower-resolution color images enhanced to show the diversity of surface units on Pluto; it was constructed from blue (400 to 550 nm), red (540 to 700 nm), and near-IR filter (780 to 975 nm) images from the Ralph instrument. The panchromatic observations were taken by the LORRI instrument from a distance of ~450,000 km from Pluto at a pixel scale of 2.2 km/pixel; the color observations were taken from a distance of ~250,000 km from Pluto at a pixel scale of 5.0 km/pixel.

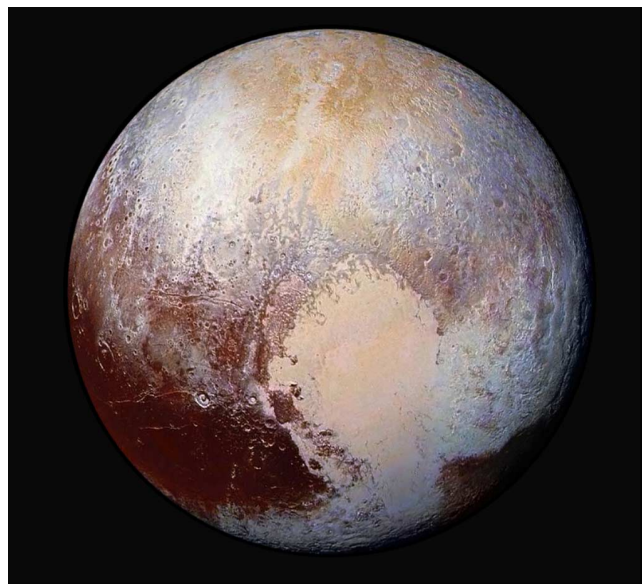
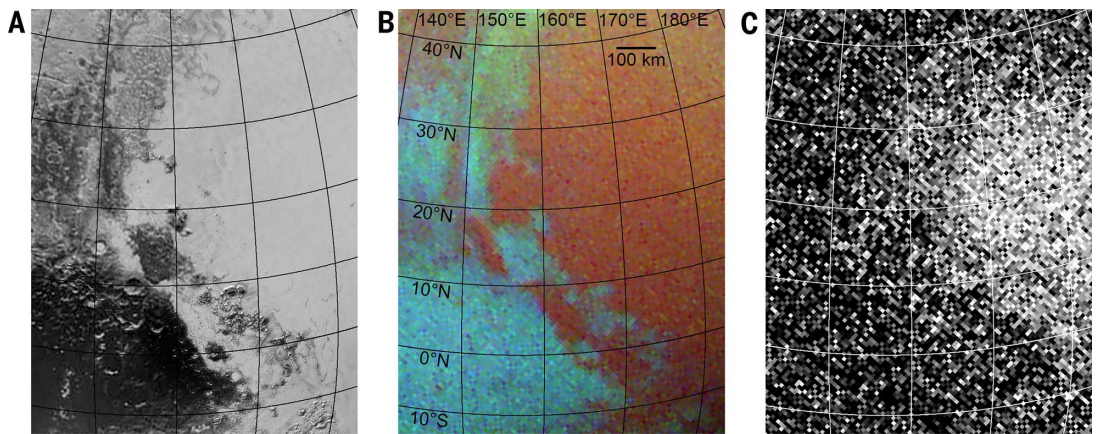


Fig. 4. Pluto Ralph surface imaging over the western side of Sputnik Planum.

(A) Orthographic projection of the LORRI mosaic. (B) False-color Ralph image from three near-IR wavelengths (blue, 1.66 μm ; green, 1.79 μm ; red, 1.89 μm) selected to highlight methane ice absorption. Each color is mapped linearly from zero to the maximum reflectance at each wavelength. Regions with greater CH_4 absorption appear red; regions with weaker CH_4



absorption appear blue-green. Regions with greater contrast between the 1.66- μm and 1.79- μm CH_4 absorptions tend toward yellow shades. Comparison with the associated LORRI mosaic shows a sharp transition from the strong CH_4 absorption on SP to much lower levels of CH_4 absorption on the montes along the west flank of SP as well as the portion of dark CR in the southwest corner. (C) LEISA (Linear Etalon Imaging Spectral Array) map of CO ice absorption in SP produced by subtracting the 1.58- μm image from the mean of the 1.57- and 1.59- μm images. Note the elevated CO abundance in the central region of SP indicated by the brighter pixels.

consistent with resupply of atmospheric N_2 and other volatiles against Pluto's rather prodigious atmospheric escape (20).

Atmosphere

REX radio occultation measurements by New Horizons unequivocally reached Pluto's surface, providing the first direct measure of the temperature and pressure structure of the lower atmosphere (5). Preliminary results indicate that the surface pressure is $\sim 10 \mu\text{bar}$ (5); this is lower than expected from the downward extrapolation of Earth-based stellar occultation measurements (21–24). At present it is unclear whether this reflects a recent decrease in the mass of the atmosphere—a reversal of the trend inferred from stellar occultations—or uncertainty in the relative calibration of the two techniques. These radio occultation measurements by New Horizons also suggest the presence of a shallow tropospheric boundary layer, consistent with recent predictions (25). High-altitude radio occultation data have not yet been sent to Earth but should provide ionospheric detections or constraints in the future.

High-phase angle images of Pluto made during flyby departure reveal a global atmospheric haze extending to ~ 150 km above the surface (Fig. 5A), with a derived normal optical depth of ~ 0.004 . The high extent of the haze layer suggests a formation mechanism involving ion-molecule reactions or meteoritic dust. The atmospheric haze also shows structure, including possible waves and/or layering near 50 and 80 km altitude, which could be connected to buoyancy waves, as previously inferred from ground-based stellar occultation data (26).

UV solar occultation count rates have been sent to Earth; UV spectra themselves have not yet been. The occultation count rate data (Fig. 5B) show structure indicating absorption by N_2 starting at ~ 1670 km altitude, by CH_4 below ~ 960 km, by C_2H_x hydrocarbons below 420 km, and haze below ~ 150 km. Ingress and egress ob-

servations made at opposite longitudes show nearly symmetric line-of-sight vertical absorption profiles (Fig. 5B), indicating a globally uniform upper atmospheric structure. These data are best fit with a CH_4 fractional number density abundance of $\sim 0.25\%$ (27), somewhat less than previous best estimates of 0.44% (28), indicating a slightly cooler atmosphere than expected. UV observations also indicate the discovery of two new atmospheric species from their far-UV absorption signatures: C_2H_2 and C_2H_4 at lower atmospheric mixing ratios of $\sim 3 \times 10^{-6}$ and $\sim 1 \times 10^{-6}$, respectively. Their opacities (and the solar occultation count rates) are consistent with a relatively stagnant atmosphere at 50 to 300 km altitude.

Charon

Geology and imaging

Our derived radius of Charon is 606 ± 3 km, similar to ground-based measurements (29); we also determined that Charon is not detectably oblate, with an upper bound on polar flattening of 1% (5). Substantial vertical relief of greater than 3 km is seen on the limb of Charon (fig. S3), which suggests that the widespread water ice seen spectroscopically across Charon is not a surface veneer and runs deep.

Charon mapping data that have arrived on Earth (Fig. 6) primarily cover the northern hemisphere and ranges from 32 km/pixel on the anti-Pluto (far approach) hemisphere to 4 km/pixel on the sub-Pluto (close approach) hemisphere (Fig. 6A; see also Fig. 2B). The only two images at ~ 400 m/pixel received to date reveal a complex geology characterized by numerous bright and dark spots, abundant fault scarps and darker curvilinear markings, both cratered and smooth plains, an extensive system of faults and graben, and a broad and prominent dark area centered on the north pole.

The dark polar spot, called Mordor Macula (Fig. 6B), is the most prominent albedo marking

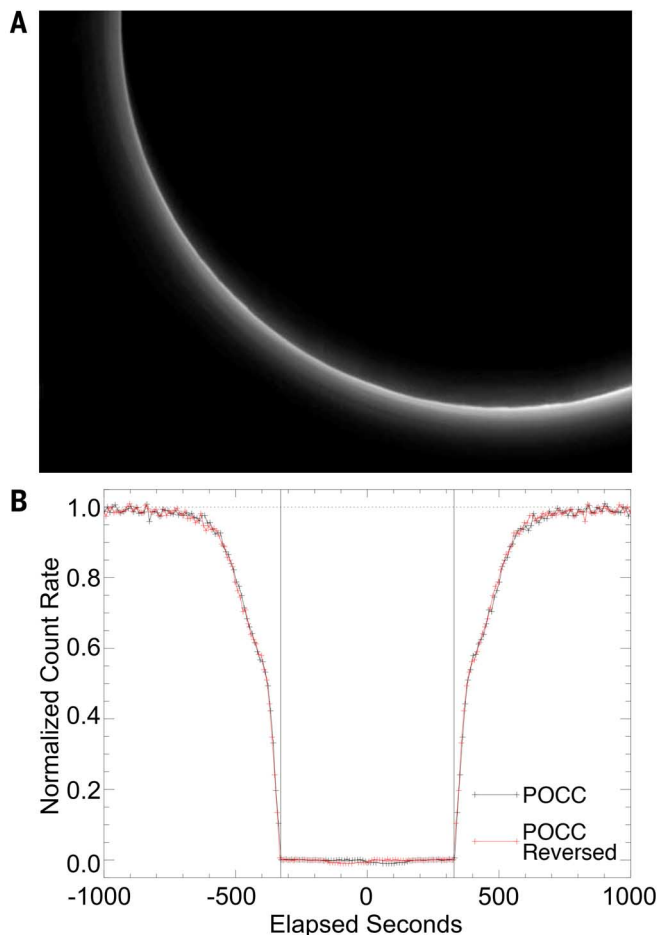
seen on Charon. This quasi-circular feature has a dark inner zone ~ 275 km across and roughly half as bright as the average surface of Charon (Fig. 1F). Its less dark outer zone is ~ 450 km across and fades gradually onto higher-albedo cratered plains. The inner zone of the dark spot is partly defined by a curvilinear marking that may be either a ridge or an exposed fault, indicating that this feature may be due to a large impact or complex tectonic structure, and suggests the possibility of a compositionally heterogeneous substrate.

Charon appears variably cratered across its surface, indicating variations in crater retention age. Both bright-rayed and dark-ejecta craters are also apparent at higher resolution (figs. S3 and S4). Such albedo variations may imply a compositionally variable surface, age effects, and/or impactor contamination.

A network of northeast-southwest-trending fractures cuts across most of the sub-Pluto hemisphere. The largest of these, called Macroch and Serenity Chasmata (fig. S3), form a belt that extends at least 1050 km across the surface. Serenity Chasma is resolved as a double-walled graben-like structure, 60 km across at its widest and a few kilometers deep (Fig. 6D, 1). A deep trough observed on the limb at 30°N , 80°E has a depth of ~ 5 km. We interpret several dark curvilinear markings, observed on the less well-resolved anti-Pluto hemisphere, as global extensions of this fracture network.

An extensive area of rolling plains occurs south of the equator on Charon's sub-Pluto hemisphere (Fig. 6D, 2). The known extent of the plains, which stretch southward into the unimaged portions of Charon, is at least $400 \text{ km} \times 1000 \text{ km}$. These plains are moderately cratered and show several narrow rille-like features several kilometers wide when observed at 400 m/pixel (Fig. 6D, 3). Several large peaks of unknown origin extend 2 to 4 km above the rolling plains and are surrounded by moat-like depressions 1 to 3 km deep. The

Fig. 5. Pluto LORRI and Alice atmospheric data. (A) LORRI image of haze particle scattering in Pluto's atmosphere with solar phase angle of 167°. The haze exhibits a maximum I/F of ~ 0.22 and extends to ~ 150 km altitude with a vertical scale height of 45 to 55 km. Its strong forward scattering suggests particles of $\sim 0.5 \mu\text{m}$ effective diameter. (B) Total UV solar occultation count rates versus time. Horizontal scale is the time from center point of occultation. Black line shows ingress count rate; red (egress) count rate is overplotted in the reverse time direction to demonstrate their symmetry. The Sun's tangent altitude changes at 3.57 km/s during ingress and egress; the change in observed count rate is consistent with absorption by N_2 detected at ± 800 s (~ 1670 km), CH_4 at ± 600 s (~ 960 km), higher hydrocarbons at ± 450 s (~ 420 km), and possibly haze at ± 375 s (~ 150 km).



most prominent of these, Kubrick Mons, is 20×25 km across and 3 to 4 km high (Fig. 6D, 4). Photoclinometry algorithms were used to estimate the relative elevations of these features, and they are consistent with shadow height measurements.

Craters were identified with some confidence on Vulcan Planum (Fig. 6 and fig. S5) because of the low Sun angles near the terminator and because of the generally level elevation of the terrain. For crater diameters of ≥ 10 km, we judge the cumulative areal crater density, 3×10^{-4} to $4 \times 10^{-4} \text{ km}^{-2}$, to be reliable (fig. S5). Model ages can be assigned according to estimates of the impacting Kuiper Belt object (KBO) population (11, 12). The KBO population is estimated at large (diameter ≥ 100 km) sizes from astronomical observations and can be extrapolated to smaller impactor sizes (the sizes that make the observable craters) under a variety of plausible assumptions; numerical integrations also provide estimates of the time rate of decay of the various Kuiper Belt subpopulations (11). These then provide a range of model ages for a given terrain with crater counts. For Vulcan Planum, most model ages from Greenstreet *et al.* (11) are ~ 4 billion years or older (i.e., equivalent to the presumed high-impact

time period of the Late Heavy Bombardment or Nice model rearrangement of the outer solar system). Only the model age based on an estimate of the small KBO population from putative stellar occultations (30) (which has the largest number of small KBOs and thus the highest cratering rate) indicates that this region could be younger, perhaps 100 to 300 million years old.

Surface brightness, color, and composition

Charon's panchromatic surface I/F at our approach solar phase angle of 15° and available resolution ranges between 0.2 and 0.5, much more limited than Pluto's. Charon's north polar region is distinctly red at Ralph/MVIC (Multispectral Visible Imaging Camera) wavelengths, as shown in Fig. 6E. The reddish area encompasses the darkest region of the polar dark feature Mordor Macula but also extends well beyond. The boundary is indistinct and shows little correlation with geologic features.

One hypothesis for the reddish coloration is seasonal cold trapping of volatiles at Charon's poles followed by energetic radiation processing into more chemically complex, less volatile tholins that can remain after the pole emerges back into

sunlight. Another possibility is a different composition at depth, as noted above.

Atmosphere

As for Pluto, only solar occultation count rate data have arrived on Earth; no actual spectra have been downlinked as yet. The solar occultation total count rate showed sharp cutoffs at Charon ingress and egress, consistent with no atmosphere or an atmosphere far lower in column abundances than Pluto's. Upper limits were obtained for the vertical column densities of N_2 ($\sim 9 \times 10^{16} \text{ cm}^{-2}$), CH_4 ($\sim 5.6 \times 10^{15} \text{ cm}^{-2}$), and higher hydrocarbons ($\sim 2.6 \times 10^{15} \text{ cm}^{-2}$); much better constraints (or detections) will be possible when the solar occultation spectra are downlinked. No evidence of haze above Charon's limb is seen in high-phase angle (166°) imaging.

Small satellites

Observations by New Horizons have provided the first spatially resolved measurements of Pluto's small moons Nix and Hydra; measurements of Styx and Kerberos have not yet been downlinked. We summarize these and other available results for Nix and Hydra next, and then report on our satellite and ring searches.

Nix

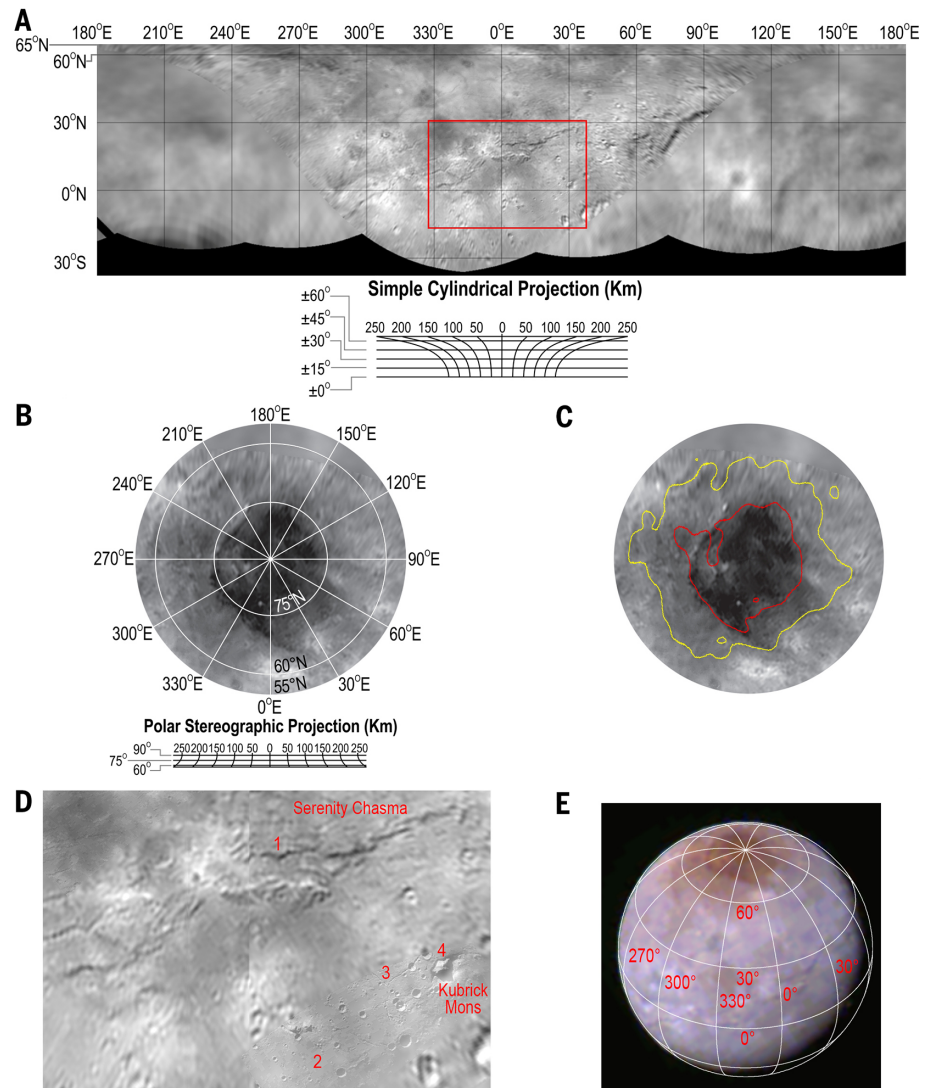
A color composite image (Fig. 7A) shows a highly elongated body with dimensions of 49×32 km and an effective projected two-dimensional (2D) diameter of $\sim 40 \pm 2$ km; a LORRI panchromatic image taken 128 s earlier gives essentially the same result. Another LORRI Nix image taken 8.73 hours earlier shows a nearly circular cross section with a projected 2D diameter of 34.8 ± 1 km. A triaxial ellipsoid shape with dimensions $54 \times 41 \times 36$ km is consistent with both the resolved images and an extensive series of unresolved light curve measurements taken during the approach to Pluto, but Nix's mass is not yet well enough constrained to derive a reliable density. Nix shows evidence of compositional diversity in the color image, including a nonuniform distribution of red material possibly associated with a crater. Adopting reasonable phase laws of 0.02 to 0.03 mag/degree, we estimate that in visible light, the mean observed geometric albedo is 0.43 to 0.50. These high albedos indicate that Nix is likely covered with cleaner water ice than that on Charon.

Hydra

Resolved panchromatic (but not color) measurements of Hydra are available (Fig. 7B); these show a highly nonspherical body with dimensions of roughly $43 \text{ km} \times 33 \text{ km}$ (i.e., axial ratio of ~ 1.3) and an effective projected 2D diameter of $\sim 41.1 \pm 1$ km. Surface albedo variations are seen, as are several crater-like features. Neither Hydra's mass nor its volume are well enough measured as yet to derive a reliable density. Hydra's average geometric albedo is 0.51 for a linear phase law coefficient of 0.02 mag/degree, derived from the observed brightness differences at the two epochs. Like Nix, Hydra

Fig. 6. Charon surface imaging results.

(A) Simple cylindrical mosaic of Charon. The area shown in detail in (D) is highlighted by a red boundary. (B) Polar stereographic mosaic of Charon's north pole. (C) Polar stereographic projection of Charon imagery as in (B). Contour lines are based on a color ratio between red and near-IR filters (0.54 to 0.70 μm and 0.78 to 0.98 μm , respectively) and highlight the two reddish color units discussed in the text (red, inner zone; yellow, outer zone). The red coloration is most pronounced in Mordor Macula but extends well beyond that central dark region. (D) Detail of Charon's sub-Pluto equatorial region [refer to red-outlined box in (A) for scale]; 400 m/pixel coverage can be seen at top left and bottom right. (1) Serenity Chasma, a graben ~ 60 km wide. (2) Sparsely cratered plains. (3) Surface fractures. (4) Kubrick Mons and its surrounding moat. (E) Enhanced color composite of Charon at 5 km/pixel resolution produced by placing blue, red, and near-IR Ralph instrument images (see Fig. 3) into the blue, green, and red color channels, and linearly stretching each color from zero.



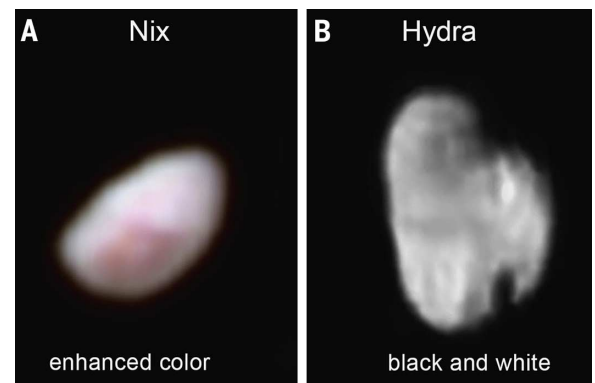
has a highly reflective surface, which suggests relatively clean water ice. How such bright surfaces can be maintained on Nix and Hydra over billions of years is puzzling, given that a variety of external processes (e.g., radiation darkening, transfer of darker material from Charon via impacts, impacts with dark Kuiper Belt meteorites, etc.) would each tend to darken and redden the surfaces of these satellites over time.

Searches for small satellites and rings

New Horizons conducted seven deep searches for satellites and rings between 64 and 13 days before closest approach. No detections were made. For a Charon-like albedo of 0.38, diameter upper limits for undetected moons, determined by recovering model test objects implanted in the images, were 4.5 km at 110,000 to 180,000 km from Pluto, 2.4 km at 50,000 to 110,000 km from Pluto, 1.5 km at 19,000 to 50,000 km from Pluto (Charon is 19,600 km from Pluto), and 2.0 km at 5000 to 19,000 km from Pluto. No rings were found at an I/F upper limit of 1.0×10^{-7} . These

Fig. 7. LORRI and Ralph surface imaging of Nix and Hydra.

(A) Nix Ralph color composite image at 3.14 km/pixel with a solar phase angle of 15°, created by combining images taken through three filters (near-IR, 780 to 975 nm; red, 540 to 700 nm; blue, 400 to 550 nm) that were respectively loaded in the red, green, and blue planes of the color composite. (B) LORRI panchromatic (350 to 850 nm) image of Hydra at 1.13 km/pixel, solar phase angle 34°.



satellite and ring upper limits constitute substantial improvements over previous limits (5, 31, 32) (fig. S6).

Implications for origin and evolution

The New Horizons encounter with the Pluto system revealed a wide variety of geological activity—broadly taken to include glaciological

and surface-atmosphere interactions as well as impact, tectonic, cryovolcanic, and mass-wasting processes (13)—on both the planet and its large satellite Charon. This suggests that other small planets of the Kuiper Belt, such as Eris, Make-make, and Haumea, could also express similarly complex histories that rival those of terrestrial planets such as Mars, as Pluto does.

It is notable that Triton—likely a Kuiper Belt planet captured by Neptune—was considered the best analog for Pluto before the encounter (13). However, our assessment is that the geologies of both worlds are more different than similar, although more quantitative consideration of this must await further data downlinks.

For Pluto, the rugged mountains and undulating terrain in and around TR require geological processes to have deformed and disrupted Pluto's water ice-rich bedrock. Some of the processes operating on Pluto appear to have operated geologically recently, including those that involve the water ice-rich bedrock as well as the more volatile, and presumably more easily mobilized, ices of SP and elsewhere. This raises questions of how such processes were powered so long after the formation of the Pluto system.

The bulk densities of Pluto and Charon differ by less than 10%, which is consistent with bulk rock contents for the two bodies that are likely similar. Comparing models for the formation of the system by giant impact (7, 13) indicates that this similarity could imply that both precursor bodies were undifferentiated or only modestly differentiated before the collision, which would have profound implications for the timing, duration (33), and even the mechanism (34) of accretion in the ancestral Kuiper Belt.

REFERENCES AND NOTES

- S. A. Stern, The Pluto-Charon system. *Annu. Rev. Astron. Astrophys.* **30**, 185–233 (1992). doi: [10.1146/annurev.aa.30.090192.001153](https://doi.org/10.1146/annurev.aa.30.090192.001153)
- J. K. Davies, J. McFarland, M. E. Bailey, B. G. Marsden, W.-H. Ip, in *The Solar System Beyond Neptune*, M. A. Barucci, H. Boehnhardt, D. P. Cruikshank, A. Morbidelli, Eds. (Univ. of Arizona Press, Tucson, AZ, 2008), pp. 11–23.
- S. A. Stern, The New Horizons Pluto Kuiper Belt mission: Overview with historical context. *Space Sci. Rev.* **140**, 3–22 (2008). doi: [10.1007/s11214-007-9295-y](https://doi.org/10.1007/s11214-007-9295-y)
- H. A. Weaver, W. C. Gibson, M. B. Tapley, L. A. Young, S. A. Stern, Overview of the New Horizons science payload. *Space Sci. Rev.* **140**, 75–92 (2008). doi: [10.1007/s11214-008-9376-6](https://doi.org/10.1007/s11214-008-9376-6)
- See supplementary materials on Science Online.
- M. Person *et al.*, The June 23 stellar occultation by Pluto: Airborne and ground observation. *Astron. J.* **146**, 83–98 (2013). doi: [10.1088/0004-6256/146/4/83](https://doi.org/10.1088/0004-6256/146/4/83)
- W. B. McKinnon, On the origin of the Pluto-Charon binary. *Astrophys. J.* **344**, L41–L44 (1989). doi: [10.1086/185526](https://doi.org/10.1086/185526)
- J. Eluszkiewicz, D. J. Stevenson, Rheology of solid methane and nitrogen: Application to Triton. *Geophys. Res. Lett.* **17**, 1753–1756 (1990). doi: [10.1029/GL017i010p01753](https://doi.org/10.1029/GL017i010p01753)
- Y. Yamashita, M. Kato, M. Arakawa, Experimental study on the rheological properties of polycrystalline solid nitrogen and methane: Implications for tectonic processes on Triton. *Icarus* **207**, 972–977 (2010). doi: [10.1016/j.icarus.2009.11.032](https://doi.org/10.1016/j.icarus.2009.11.032)
- P. J. Tackley, Self-consistent generation of tectonic plates in time-dependent three-dimensional mantle convection simulations I. Pseudoplastic yielding. *Geochem. Geophys. Geosyst.* **1**, 1021 (2000). doi: [10.1029/2000GC000036](https://doi.org/10.1029/2000GC000036)
- S. Greenstreet, B. Gladman, W. B. McKinnon, Impact and cratering rates onto Pluto. *Icarus* **258**, 267–288 (2015). doi: [10.1016/j.icarus.2015.05.026](https://doi.org/10.1016/j.icarus.2015.05.026)
- E. B. Bierhaus, L. Dones, Craters and ejecta on Pluto and Charon: Anticipated results from the New Horizons flyby. *Icarus* **246**, 165–182 (2014). doi: [10.1016/j.icarus.2014.05.044](https://doi.org/10.1016/j.icarus.2014.05.044)
- J. M. Moore *et al.*, Geology before Pluto: Pre-encounter considerations. *Icarus* **246**, 65–81 (2015). doi: [10.1016/j.icarus.2014.04.028](https://doi.org/10.1016/j.icarus.2014.04.028)
- S. J. Peale, Tidally induced volcanism. *Celestial Mech. Dyn. Astron.* **87**, 129–155 (2003). doi: [10.1023/A:1026187917994](https://doi.org/10.1023/A:1026187917994)
- B. J. Buratti, J. A. Mosher, The dark side of Iapetus: Additional evidence for an exogenous origin. *Icarus* **115**, 219–227 (1995). doi: [10.1006/icar.1995.1093](https://doi.org/10.1006/icar.1995.1093)
- D. P. Cruikshank, H. Imanaka, C. M. Dalle Ore, Tholins as coloring agents on outer solar system bodies. *Adv. Space Res.* **36**, 178–183 (2005). doi: [10.1016/j.asr.2005.07.026](https://doi.org/10.1016/j.asr.2005.07.026)
- T. C. Owen *et al.*, Surface ices and the atmospheric composition of Pluto. *Science* **261**, 745–748 (1993). doi: [10.1126/science.261.5122.745](https://doi.org/10.1126/science.261.5122.745); pmid: [17757212](https://pubmed.ncbi.nlm.nih.gov/17757212/)
- W. M. Grundy, C. B. Olkin, L. A. Young, M. W. Buie, E. F. Young, Near infrared spectral monitoring of Pluto's ices: Spatial distribution and secular evolution. *Icarus* **223**, 710–721 (2013). doi: [10.1016/j.icarus.2013.01.019](https://doi.org/10.1016/j.icarus.2013.01.019)
- W. M. Grundy, C. B. Olkin, L. A. Young, B. J. Holler, Near infrared spectral monitoring of Pluto's ices II: Recent decline of CO and N₂ absorptions. *Icarus* **235**, 220–224 (2014). doi: [10.1016/j.icarus.2014.02.025](https://doi.org/10.1016/j.icarus.2014.02.025)
- K. N. Singer, S. A. Stern, On the provenance of Pluto's nitrogen (N₂). *Astrophys. J.* **808**, L50–L55 (2015). doi: [10.1088/2041-8205/808/2/L50](https://doi.org/10.1088/2041-8205/808/2/L50)
- E. Lellouch *et al.*, Pluto's lower atmosphere structure and methane abundance from high-resolution spectroscopy and stellar occultations. *Astron. Astrophys.* **495**, L17–L21 (2009). doi: [10.1051/0004-6361/200911633](https://doi.org/10.1051/0004-6361/200911633)
- B. Sicardy *et al.*, Large changes in Pluto's atmosphere as revealed by recent stellar occultations. *Nature* **424**, 168–170 (2003). doi: [10.1038/nature01766](https://doi.org/10.1038/nature01766); pmid: [12853950](https://pubmed.ncbi.nlm.nih.gov/12853950/)
- J. L. Elliot *et al.*, Changes in Pluto's atmosphere: 1988–2006. *Astron. J.* **134**, 1–13 (2007). doi: [10.1086/517998](https://doi.org/10.1086/517998)
- C. B. Olkin *et al.*, Evidence that Pluto's atmosphere does not collapse from occultations including the 2013 May 4 event. *Icarus* **246**, 220–225 (2015). doi: [10.1016/j.icarus.2014.03.026](https://doi.org/10.1016/j.icarus.2014.03.026)
- A. M. Zalucha, X. Zhu, A. A. S. Gulbis, D. F. Strobel, J. L. Elliot, An analysis of Pluto's troposphere using stellar occultation light curves and an atmospheric radiative conductive convective model. *Icarus* **214**, 685–700 (2011). doi: [10.1016/j.icarus.2011.05.015](https://doi.org/10.1016/j.icarus.2011.05.015)
- M. J. Person *et al.*, Waves in Pluto's atmosphere. *Astron. J.* **136**, 1510–1518 (2008). doi: [10.1088/0004-6256/136/4/1510](https://doi.org/10.1088/0004-6256/136/4/1510)
- G. R. Gladstone, Y. L. Yung, M. L. Wong, Pluto atmosphere photochemical models. *Lunar Planet. Sci.* **XLVI**, abstract 3008 (2015).
- E. Lellouch *et al.*, Exploring the spatial, temporal, and vertical distribution of methane in Pluto's atmosphere. *Icarus* **246**, 268–278 (2015). doi: [10.1016/j.icarus.2014.03.027](https://doi.org/10.1016/j.icarus.2014.03.027)
- M. J. Person *et al.*, Charon's radius and density from the combined data sets of the 2005 July 11 occultation. *Astron. J.* **132**, 1575–1580 (2006). doi: [10.1086/507330](https://doi.org/10.1086/507330)
- H. E. Schlichting, C. I. Fuentes, D. E. Trilling, Initial planetesimal sizes and the size distribution of small Kuiper belt objects. *Astron. J.* **146**, 36–42 (2013). doi: [10.1088/0004-6256/146/2/36](https://doi.org/10.1088/0004-6256/146/2/36)
- A. J. Steffl *et al.*, New constraints on additional satellites in the Pluto system. *Astron. J.* **132**, 614–619 (2006). doi: [10.1086/505424](https://doi.org/10.1086/505424)
- M. R. Showalter, D. P. Hamilton, Resonant interactions and chaotic rotation of Pluto's small moons. *Nature* **522**, 45–49 (2015). doi: [10.1038/nature14469](https://doi.org/10.1038/nature14469); pmid: [26040889](https://pubmed.ncbi.nlm.nih.gov/26040889/)
- W. B. McKinnon, D. Prialnik, S. A. Stern, A. Coradini, in *The Solar System Beyond Neptune*, M. A. Barucci, H. Boehnhardt, D. P. Cruikshank, A. Morbidelli, Eds. (Univ. of Arizona Press, Tucson, AZ, 2008), pp. 213–241.
- D. Nesvorný, A. N. Youdin, D. C. Richardson, Formation of Kuiper Belt binaries by gravitational collapse. *Astron. J.* **140**, 785–793 (2010). doi: [10.1088/0004-6256/140/3/785](https://doi.org/10.1088/0004-6256/140/3/785)
- M. Brozović, M. R. Showalter, R. A. Jacobson, M. W. Buie, The orbits and masses of satellites of Pluto. *Icarus* **246**, 317–329 (2015). doi: [10.1016/j.icarus.2014.03.015](https://doi.org/10.1016/j.icarus.2014.03.015)
- G. L. Tyler *et al.*, The New Horizons Radio Science Experiment (REX). *Space Sci. Rev.* **140**, 217–259 (2008). doi: [10.1007/s11214-007-9302-3](https://doi.org/10.1007/s11214-007-9302-3)

ACKNOWLEDGMENTS

We thank M. Sykes and three anonymous referees for their careful work to improve this paper, and R. Tedford and C. Chavez for logistical support. We also thank the many engineers who have contributed to the success of the New Horizons mission and NASA's Deep Space Network (DSN) for a decade of excellent support to New Horizons. We acknowledge the contributions to New Horizons of our late colleagues David C. Slater and Thomas C. Coughlin. Supporting imagery is available in the supplementary material. As contractually agreed to with NASA, fully calibrated New Horizons Pluto system data will be released via the NASA Planetary Data System at <https://pds.nasa.gov/> in a series of stages in 2016 and 2017 as the data set is fully downlinked and calibrated. This work was supported by NASA's New Horizons project.

SUPPLEMENTARY MATERIALS

www.sciencemag.org/content/350/6258/aad1815/suppl/DC1
Materials and Methods
Supplementary Text
Figs. S1 to S6

5 August 2015; accepted 25 September 2015
[10.1126/science.aad1815](https://doi.org/10.1126/science.aad1815)

RESEARCH ARTICLE SUMMARY

SYNTHETIC BIOLOGY

Remote control of therapeutic T cells through a small molecule-gated chimeric receptor

Chia-Yung Wu, Kole T. Roybal, Elias M. Puchner, James Onuffer,*
Wendell A. Lim*

INTRODUCTION: Cell-based therapies have emerged as a promising treatment modality for diseases such as cancer and autoimmunity. T cells engineered with synthetic receptors known as chimeric antigen receptors (CARs) have proven effective in eliminating chemotherapy-resistant forms of B cell cancers. Such CAR T cells recognize antigens on the surface of tumor cells and eliminate them. However, CAR T cells also have adverse effects, including life-threatening inflammatory side effects associated with their potent immune activity. Risks for severe toxicity present a key challenge to the effective administration of such cell-based therapies on a routine basis.

RATIONALE: Concerns about the potential for severe toxicity of cellular therapeutics primarily stem from a lack of precise control over the

activity of the therapeutic cells once they are infused into patients. Exogenously imposed specific regulation over the location, duration, and intensity of the therapeutic activities of engineered cells would therefore be desirable. One way to achieve the intended control is to use small molecules to gate cellular functions. Small molecules with desired pharmacologic properties could be systemically or locally administered at varying dosages to achieve refined temporal and spatial control over engineered therapeutic cells.

RESULTS: We developed an ON-switch CAR that enables small molecule-dependent, titratable, and reversible control over CAR T cell activity. ON-switch CAR T cells required not only a cognate antigen but also a priming small molecule to activate their therapeutic functions.

Depending on the amount of small molecule present, ON-switch CAR T cells exhibited titratable therapeutic activity, from undetectable to as strong as that of conventional CAR T cells. The ON-switch CAR was constructed by splitting key signaling and recognition modules into distinct polypeptides appended to small molecule-dependent heterodimerizing domains. The ON-switch CAR design is modular; different antigen recognition domains and small-molecule dimerizing modules can be swapped in.

CONCLUSION: The ON-switch CAR exemplifies a simple and effective strategy to integrate cell-autonomous decision-making (e.g., detection of disease signals)

ON OUR WEB SITE

Read the full article at <http://dx.doi.org/10.1126/science.aab4077>

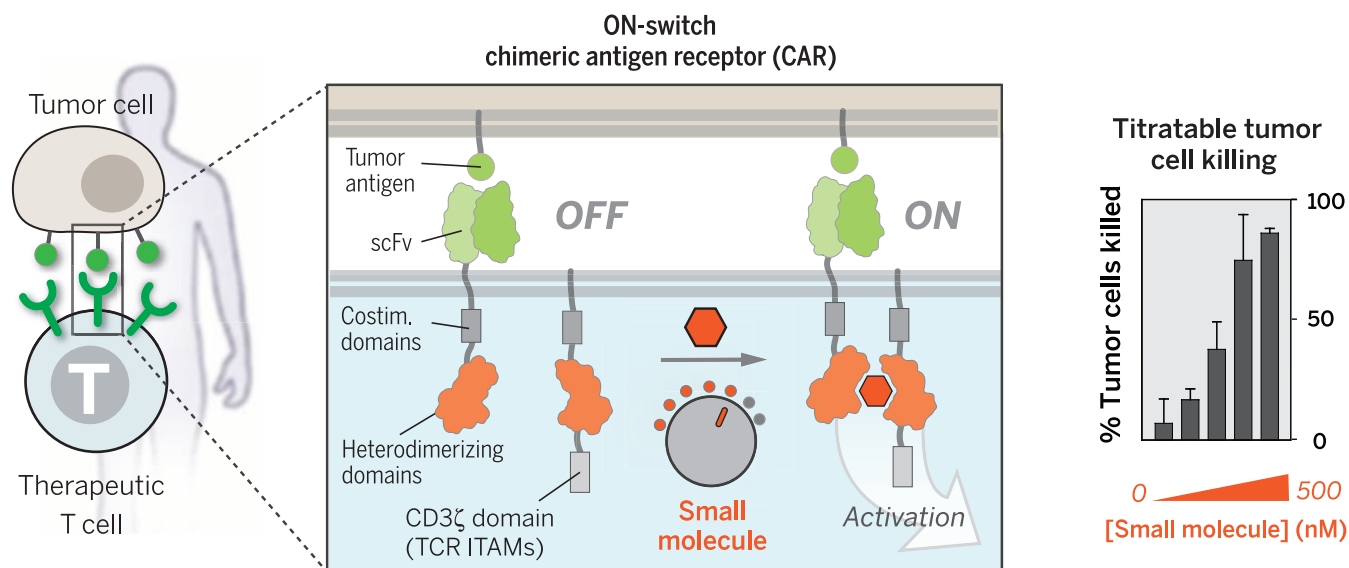
with exogenous, reversible user control. The rearrangement and splitting of key modular components provides a simple strategy for achieving integrated multi-input regulation. This work also highlights the importance of developing optimized bio-inert, orthogonal control agents such as small molecules and light, together with their cellular cognate response components, in order to advance precision-controlled cellular therapeutics. ■

The list of author affiliations is available in the full article online.

*Corresponding author. E-mail: jamesonuffer@gmail.com (J.O.); wendell.lim@ucsf.edu (W.A.L.)

Cite this article as C.-Y. Wu et al., *Science* 350, aab4077 (2015). DOI: 10.1126/science.aab4077

Titration control of engineered therapeutic T cells through an ON-switch chimeric antigen receptor. A conventional CAR design activates T cells upon target cell engagement but can yield severe toxicity due to excessive immune response. The ON-switch CAR design, which has a split architecture, requires a priming small molecule, in addition to the cognate antigen, to trigger therapeutic functions. The magnitude of responses such as target cell killing can be titrated by varying the dosage of small molecule to mitigate toxicity. scFv, single-chain variable fragment; ITAM, immunoreceptor tyrosine-based activation motif.



RESEARCH ARTICLE

SYNTHETIC BIOLOGY

Remote control of therapeutic T cells through a small molecule-gated chimeric receptor

Chia-Yung Wu,^{1,2} Kole T. Roybal,^{1,2} Elias M. Puchner,^{1*}
James Onuffer,^{1,2†} Wendell A. Lim^{1,2,3†}

There is growing interest in using engineered cells as therapeutic agents. For example, synthetic chimeric antigen receptors (CARs) can redirect T cells to recognize and eliminate tumor cells expressing specific antigens. Despite promising clinical results, these engineered T cells can exhibit excessive activity that is difficult to control and can cause severe toxicity. We designed “ON-switch” CARs that enable small-molecule control over T cell therapeutic functions while still retaining antigen specificity. In these split receptors, antigen-binding and intracellular signaling components assemble only in the presence of a heterodimerizing small molecule. This titratable pharmacologic regulation could allow physicians to precisely control the timing, location, and dosage of T cell activity, thereby mitigating toxicity. This work illustrates the potential of combining cellular engineering with orthogonal chemical tools to yield safer therapeutic cells that tightly integrate cell-autonomous recognition and user control.

Cell-based therapies have emerged as promising treatments for a range of disorders, including cancer, autoimmunity, and injury or degeneration (1–6). In contrast to small molecules and macromolecules, cellular therapeutic agents have the potential to sense inputs, make decisions, and execute highly complex tasks (7–9). A recent example is the use of engineered T cells for adoptive immunotherapy of cancer. Primary T cells can be isolated and engineered to express synthetic chimeric antigen receptors (CARs)—receptors that combine an extracellular, single-chain antibody domain, which recognizes a specific tumor-associated antigen, with intracellular signaling domains from the T cell receptor (TCR) and costimulatory receptors (2–4, 10). In clinical trials, CAR T cells directed against the B cell antigen CD19 have proven effective against chemotherapy-resistant forms of B cell cancers (11–15). Upon antigen ligand engagement, CAR T cells execute multiple key therapeutic functions, including production of antitumor cytokines and killing of target tumor cells (Fig. 1A). Antigen binding also stimulates exponential proliferation of the therapeutic T cells in vivo. Infused CAR T cells can expand by a factor of >1000, resulting in a highly amplified response and consequent eradication of a large number of tumor cells within weeks (17).

Such cell-based therapies, however, can also be associated with severe toxicities (Fig. 1A). Off-tumor cross-reaction of engineered T cells can lead to killing of nontumor cells. If such cross-reaction occurs to cells in the heart, lung, or liver, then the high doses of CAR T cells that these tissues are exposed to upon initial cell injection can lead to rapid death (16). Even with successful tumor targeting, the rapid rise in the overall T cell activity fueled by CAR signaling during treatment can also lead to systemic life-threatening side effects, such as those caused by release of excessive cytokines. Rapid elimination of large numbers of tumor cells in a short time frame also can result in tumor lysis syndrome. Both conditions can trigger multi-organ failure and require urgent medical intervention. Patient-to-patient variations in T cell responses and in risks for toxicity make it challenging to predict the optimal number of T cells to infuse (2). Thus, the engineering of regulatory systems that allow for control over the dose and timing of T cell function is an important priority.

One approach is to engineer suicide switches to eliminate the infused T cells if their toxic effects begin to get out of control (17, 18). Examples include a small molecule-regulated caspase that triggers apoptosis of the T cells (Fig. 1B). Another approach is to engineer negative regulatory co-receptors that can override killing responses when a specific “do not kill” ligand is recognized (19). Although these strategies are important elements in the toolbox for engineering therapeutic T cells, they have several drawbacks. The suicide switches irreversibly abort the complex and expensive treatment, and they may not act fast enough to prevent cross-reaction during initial cell transfer. Overriding

inhibitory co-receptors can prevent killing of particular cells that express a specific ligand, but they cannot control the timing and intensity of T cell activity more generally.

We therefore aimed to develop a complementary strategy for controlling CAR T cells that focused instead on positive regulation, in which an exogenous, user-provided signal such as a small molecule is required for activation (Fig. 1B). This kind of “ON-switch” would complement the other classes of control systems and provide important advantages. Positive regulation could allow for gradual titration of activity to appropriate therapeutic levels, as well as control of the timing of activation, thus preventing first-pass toxicities that could occur immediately upon cell transplantation. Coupled to technologies for localized and sustained delivery of small molecules (20), an ON-switch could impart spatial control over the therapeutic effects to mitigate off-tumor toxicities. Several features would be important for an ON-switch CAR design: (i) The receptor would still need to be dependent on specific tumor antigen recognition for T cell activation; small molecule alone or antigen alone should not activate. (ii) The therapeutic activity of the T cell population should be titratable by varying the concentration of the small molecule, and at high enough levels this activity should be comparable to that of conventional CAR T cells. (iii) The timing of the CAR T cell response should be reversibly controllable by addition or removal of the small molecule.

The engineering goal for an ON-switch CAR embodies a general problem that evolution has repeatedly faced: how to convert a signaling molecule that is gated by a single input into a molecule that is combinatorially gated by two inputs (in this case, a receptor that requires both an antigen and a small molecule for T cell activation). Natural signaling systems often achieve tight control over critical processes through this type of combinatorial regulation. The general ability to engineer synthetic receptors that function as Boolean AND-gates responding to two inputs—one an autonomously recognized disease signal (i.e., tumor antigen), and the other a user-controlled signal (i.e., small molecule)—would be broadly useful for engineering safe cellular therapeutic agents of any kind.

One can imagine highly complex regulatory mechanisms involving precise conformational allostery that could yield a signaling receptor that functions as a Boolean AND gate. However, very often, controls that have evolved in living systems use simpler strategies such as controlled assembly: An active molecular system can be split into multiple parts, such that it is dependent on multiple inputs that promote assembly of the intact molecular system (21). Thus, we focused on constructing split synthetic receptor systems in which the assembly of an activated complex was dependent on both binding of a small molecule and antigen engagement (Fig. 1C). The concept of splitting key components from the CAR is itself inspired by the natural process of T cell activation, which normally requires the coengagement of the T cell receptor (by peptide-major histocompatibility complex)

¹Department of Cellular and Molecular Pharmacology, University of California, San Francisco, CA 94158, USA. ²The Cell Propulsion Lab, an NIH Nanomedicine Development Center, University of California, San Francisco, CA 94158, USA. ³Howard Hughes Medical Institute, University of California, San Francisco, CA 94158, USA.

*Present address: School of Physics and Astronomy, University of Minnesota, Minneapolis, MN 55455, USA. †Corresponding author. E-mail: jamesonuffer@gmail.com (J.O.); wendell.lim@ucsf.edu (W.A.L.)

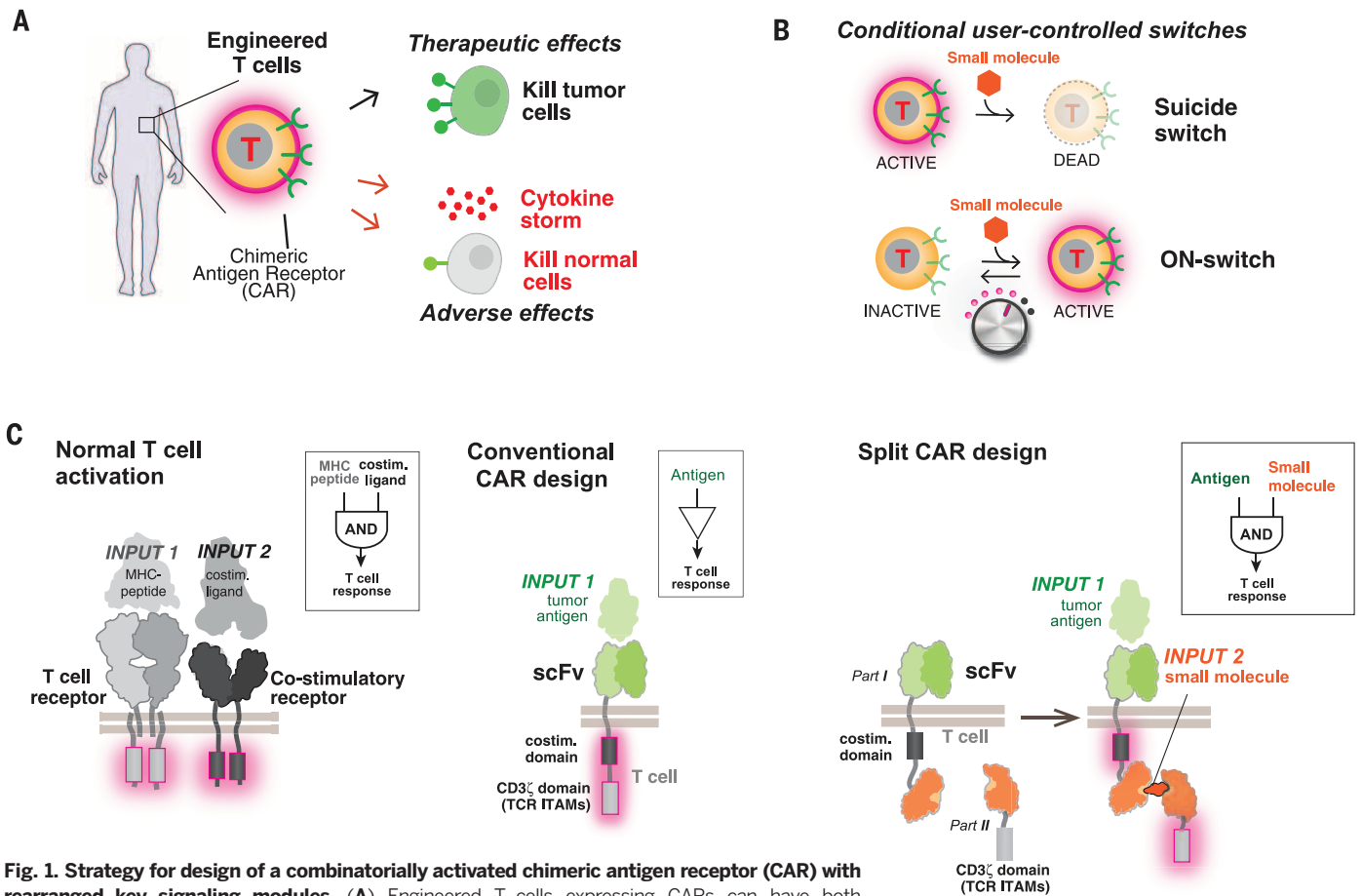


Fig. 1. Strategy for design of a combinatorially activated chimeric antigen receptor (CAR) with rearranged key signaling modules. (A) Engineered T cells expressing CARs can have both therapeutic and adverse effects. (B) User-controlled switches. A suicide switch triggers apoptosis of the engineered cells. An alternative, complementary approach is keeping the cells inactive until addition of an activating small-molecule drug signal. Such an ON-switch could allow for titratable control (dialing up or down) of T cell activity. (C) Molecular strategies to control T cell activation. The normal T cell activation pathway (left) entails dual activation of the TCR and a costimulatory receptor to trigger key cellular responses such as cytokine production and proliferation. The conventional CAR (center) combines an antigen recognition domain (scFv) with main signaling motifs (such as ITAMs from TCR subunit CD3 ζ) and costimulatory motifs constitutively linked in a single molecule. A strategy for constructing a split CAR design (right) distributes key components from the conventional CAR into two physically separate polypeptides that can be conditionally reassembled when a heterodimerizing small-molecule agent is present. The design resembles an AND logic gate that requires “antigen + small molecule” combinatorial inputs for T cell activation.

and costimulatory receptors (e.g., 4-1BB or CD28) (Fig. 1C). The conventional CAR represents a construct in which components from the TCR and costimulatory receptors are artificially colocalized. Thus, our strategy represents resplitting key signaling modules in a different, small molecule-controlled configuration.

We used this strategy to engineer a robust ON-switch CAR design that fulfills the criteria of yielding titratable, reversible, and temporarily controllable activity in CAR T cell populations. This work provides a general strategy for how to engineer dual-input synthetic receptors that require a small molecule as a coactivation signal. The ON-switch CAR framework also provides an important tool for developing the next generation of precision-controlled therapeutic T cells.

Design of ON-switch CARs

To construct a CAR that required both an antigen AND a small molecule for activation, we used

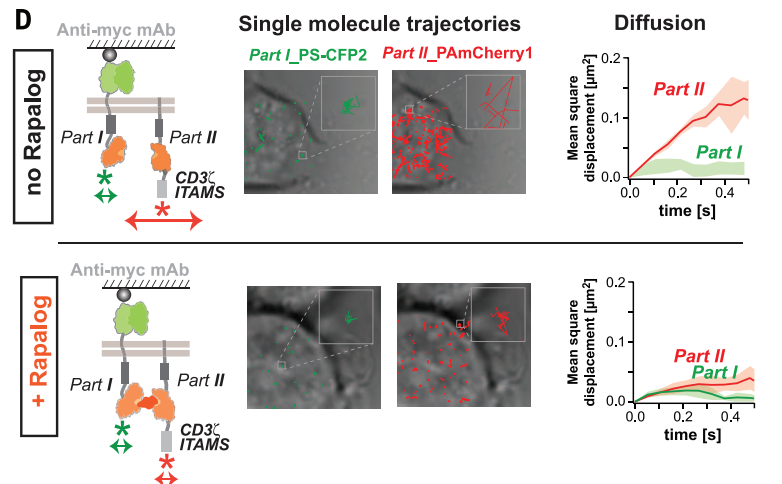
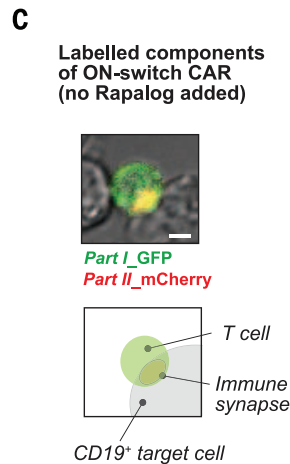
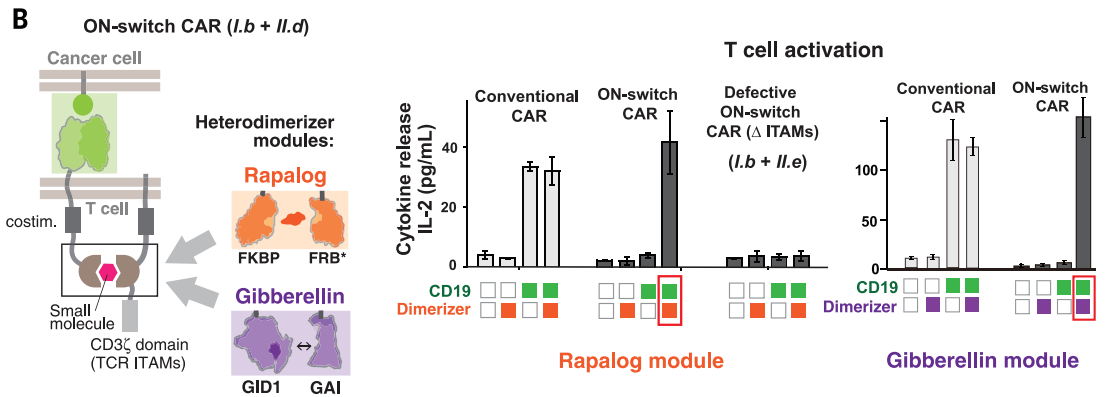
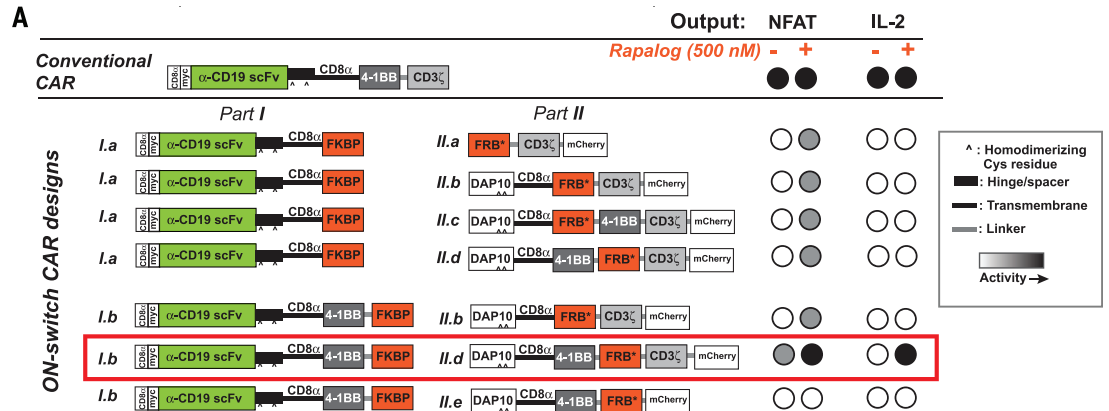
a split-receptor design that structurally resembles natural immune receptors such as the B and T cell receptors (BCRs and TCRs), whose antigen-binding and intracellular signaling domains are found on separately expressed polypeptides. In these natural cases, heterodimerization of these distinct polypeptides is required to assemble a functioning receptor complex (22). This type of multipolypeptide assembly presents the opportunity to engineer receptor control by enforcing small-molecule dependence on this assembly. The envisioned ON-switch CAR (Fig. 1C) consists of two parts that assemble in a small molecule-dependent manner. Part I of the receptor features an extracellular antigen-binding domain [a single-chain variable fragment (scFv)]. Part II has a key downstream signaling element: the immunoreceptor tyrosine-based activation motifs (ITAMs) from the T cell receptor CD3 ζ subunit (22). The ITAM motifs are phosphorylated upon T cell receptor activation, resulting in the recruitment of

Src homology 2 (SH2) domain effectors (such as the kinase ZAP70) and triggering the cascade of T cell activation. The two parts of the split receptor contain heterodimerization domains that conditionally interact upon binding of a heterodimerizing small molecule. Particular cellular responses, including T cell activation, have been engineered to be triggered solely by small molecule-induced dimerization (23, 24). Our goal, in contrast, was to design a new class of CAR whose small molecule-induced assembly is necessary but not sufficient for cellular activation. The small molecule thus acts as a priming or licensing factor that is a precondition for antigen-triggered activation.

We explored multiple ways of splitting components of the conventional CAR molecule to find a configuration that would strongly impair its activity but still allow for strong antigen-induced signaling when the receptor components were assembled in the presence of the small molecule (Fig. 2A). To facilitate the design of a prototype,

Fig. 2. Construction and screening of an ON-switch CAR that is dependent on the presence of a small-molecule dimerizer.

(A) ON-switch CAR candidate constructs and their functional behavior. Candidate construct pairs were expressed in Jurkat T cells. Cells were incubated with K562 target cells expressing the cognate antigen CD19⁺ in the presence or absence of 500 nM rapalogs. Activation was quantified via expression of a NFAT-dependent GFP reporter gene and production of the cytokine IL-2. The part I constructs of the ON-switch CAR share many features with the conventional CAR: the CD8 α signal sequence, a Myc epitope, the anti-CD19 scFv, and the CD8 α hinge and transmembrane domain, in addition to the FKBP domain for heterodimerization. The part II constructs consisted of the T cell receptor CD3 ζ signaling chain that is critical for T cell activation, the FRB* domain for heterodimerization, and the mCherry tag. More advanced part II variants contained the additional DAP10 ectodomain for homodimerization and the CD8 α transmembrane domain for membrane anchoring. The 4-1BB costimulatory motif was inserted in various locations, depending on the construct. The best ON-switch construct (I.b + II.d) is outlined in red.



(B) Response of ON-switch CAR (I.b + II.d) to rapalog and antigen stimulation. Jurkat cells expressing the specified CARs were incubated with K562 target cells expressing either the cognate antigen (CD19; green squares) or a noncognate antigen (mesothelin; white squares). Presence of 500 nM rapalog in the sample is indicated by orange squares. Production of IL-2 after an overnight incubation was quantified by enzyme-linked immunosorbent assay (ELISA); $n = 3$, error bars denote SD. Similar results were observed for ON-switch CARs in which the rapalog heterodimerization module was replaced by an alternative module, the gibberellic acid (GA) heterodimerization module (using *Arabidopsis* GID1 and GAI domains). The ON-switch CAR with GA dimerizing domains requires both cognate antigen and GA (purple squares) to trigger cytokine production. **(C)** The ON-switch CAR components colocalize in the absence of dimerizing rapalog. Parts I and II of the receptor are labeled with GFP and mCherry, respectively. The confocal microscopy images are pseudo-colored to indicate localization of both parts. Image shows a primary human CD8⁺ T cell expressing the anti-CD19 ON-switch CAR engaged

with a CD19⁺ K562 target cell in the absence of rapalog. Scale bar, 5 μm . **(D)** Two-color single-molecule tracking shows independent movement of ON-switch CAR components in the absence of rapalog. Left panels: Jurkat T cells were adhered to a cover slip coated with an antibody to the Myc epitope in order to immobilize the receptors (extracellular region of part I CAR is tagged with Myc). Individual parts of the ON-switch CAR were each tagged with photoactivatable fluorescent proteins PS-CFP2 and PAmCherry1. Center panels: The single-molecule trajectories of part I (green) and part II (red) are superimposed on transmitted light images of the cells (gray). Right panels: The average mean-square displacement of trajectories quantifies the diffusive behavior (solid lines, average from multiple cells; colored band, SD to represent cell-cell variability). Part I molecules are immobile because of antibody tethering, whereas in the absence of rapalog (top), part II molecules exhibited fast diffusion. In the presence of 500 nM rapalog (bottom), however, the part II molecules became immobile, confirming rapalog-induced assembly of the two-component receptor.

we used a set of structurally well-defined heterodimerizing components: the FK506 binding protein (FKBP) domain and the T2089L mutant of FKBP-rapamycin binding domain (FRB*) that heterodimerize in the presence of the rapamycin analog AP21967, which has less immunosuppressive activity than does rapamycin (25–27). We refer to this modified rapamycin as the rapalog. We screened candidate receptors for rapalog-dependent activation in the human CD4⁺ Jurkat T cell line with two assays. We assayed the activity of a synthetic promoter composed of multiple copies of NFAT (nuclear factor of activated T cells) response elements (28), a highly sensitive readout for T cell receptor activation. We also measured interleukin-2 (IL-2) cytokine secretion, which represents a more stringent, integrated cellular response. The simplest split ON-switch design examined, comprising constructs Ia + II.a (Fig. 2A), consisted of a cytoplasmic ITAM fragment that could be recruited to an antigen-binding membrane receptor component upon addition of rapalog. This initial receptor design failed to signal strongly in either assay, despite abundant expression of both receptor parts in Jurkat cells (figs. S1 to S3).

We suspected that the entropic cost for driving a cytoplasmic fragment to bind its membrane-associated partner might be too high for this small molecule-induced interaction. Thus, we explored localization of both receptor parts at the plasma membrane. We designed constructs that targeted both fragments to the plasma membrane but varied the domain composition and order within both parts of the CAR (Fig. 2A). We targeted part II to the plasma membrane by appending the same CD8 α transmembrane domain used in part I. We also appended the ectodomain of DNAX-activating protein 10 (DAP10) to part II. The DAP10 ectodomain mediates homodimerization (29), effectively doubling the copy number of ITAMs per part II molecule. This modification was expected to increase receptor output activity, as the copy number of ITAMs correlates positively with receptor signaling strength (30, 31). We also varied the positioning of the 4-1BB costimulatory domain, which promotes T cell proliferation and survival, in both parts I and II. Previous work suggests that the 4-1BB costimulatory domain functions best when placed adjacent to the plasma membrane (32). We also varied the position of the FKBP and FRB* heterodimerizing domains. These changes led to the design of constructs Ib, II.b, II.c, and II.d (Fig. 2A). Molecule II.e, which lacks the CD3 ζ sequence, was constructed as a corresponding negative control (defective ON-switch CAR).

Identification of a dual input-gated ON-switch CAR construct

The most promising design from this set of components comprised the components Ib and II.d (Fig. 2A). When stimulated by target cells expressing the cognate antigen (CD19) in the presence of 500 nM rapalog, this combination led to strong cytokine production comparable to that stimulated by the conventional single-component CAR. The response was highly small molecule-dependent. This was the only split-

receptor design within this subset that signaled as strongly as did the conventional CAR (fig. S3). Further evaluation confirmed that neither the CD19 cognate antigen nor the small molecule alone was sufficient to trigger IL-2 production (Fig. 2B). These results in the Jurkat T cell line indicate the successful construction of an AND-gate receptor requiring dual inputs.

ON-switch CAR architecture is compatible with alternative heterodimerization modules and alternative antigen-binding domains

We tested whether this ON-switch CAR architecture would show similar dual-input regulation with different small-molecule heterodimerization domains or with different antigen recognition domains. We used the gibberellin-induced dimerization system GID1-GAI (Fig. 2B) (33). Derived from plants and structurally unrelated to FKBP-FRB* (27, 34), this alternative small-molecule input system yielded an ON-switch CAR population that was inactive in the absence of gibberellin but became activated when stimulated by both antigen (CD19) and gibberellin. This alternative system worked equally well to gate T cell activation (Fig. 2B). Thus, the ON-switch CAR design appears to work with alternative heterodimerization systems.

To test whether the design would function with alternative antigen-binding domains, we reconstructed the system with a single-chain antibody that recognizes the antigen mesothelin instead of the antigen CD19. Jurkat T cells expressing this version of the receptor maintained dual input control, requiring both stimulation with mesothelin-expressing target cells and addition of rapalog (fig. S4).

Single-molecule imaging shows that two components of the ON-switch CAR assemble only in the presence of small-molecule dimerizer

The ON-switch CAR was designed to conditionally assemble only in the presence of rapalog. To determine the localization of the two parts and how this changed with the addition of rapalog, we labeled part I with green fluorescent protein (GFP) and part II with mCherry. When we mixed the ON-switch CAR T cells with cognate antigen-expressing cells in the absence of rapalog, the T cells formed stable cell-cell junctions (immune synapses) with the target cells. Both part I and part II of the ON-switch CAR localized at the synapse, even in the absence of rapalog. Fluorescence microscopy of these components revealed overlapping localization (Fig. 2C).

To better understand how the interaction of the two molecular parts changes with addition of rapalog, we used photoactivated localization microscopy (PALM) (35–37). This type of imaging can yield critical information about the location and dynamics of the individual molecules. We expressed the ON-switch CAR in Jurkat cells, with each component labeled with a distinct photoactivatable fluorescent protein [part I was labeled with photoswitchable cyan fluorescent

protein 2 (PS-CFP2) and part II with photoactivatable mCherry1 (PAmCherry1)]. Cells were placed on glass slides coated with an antibody that binds to a Myc epitope tag placed at the N terminus (extracellular region) of part I of the receptor (Fig. 2D, left). Interaction with the antibody effectively immobilized the cells and anchored the part I molecules to the slide surface (fig. S5). The distribution of individual part I and part II molecules at the slide interface was then traced over time by tracking the photoactivatable fluorescent protein tags.

We observed small, constrained dynamic trajectories for part I molecules, confirming the immobility of this component upon antibody tethering. In contrast, the large, unconstrained dynamic trajectories of the part II molecules indicated fast diffusion of this component in the absence of rapalog (Fig. 2D, top, and movie S1). The measured average diffusion coefficient of $\sim 0.1 \mu\text{m}^2/\text{s}$ observed for the part II molecules is well within the range expected for unconstrained transmembrane proteins (38). The major change that we observed upon addition of rapalog was that the part II molecules also became immobile; their trajectories decreased to match those of the antibody-tethered part I molecules (Fig. 2D, bottom, and movie S2).

Thus, although both components of the ON-switch CAR appeared to be colocalized at a macroscopic level in the absence of the dimerizing small molecule, at the single-molecule level the two components were not appreciably physically associated. Without the dimerizing small molecule, the part II molecules diffused within the membrane in an unconstrained manner, even though the part I molecules were firmly anchored to an extracellular antibody. However, upon addition of the small molecule, the diffusion of part II became equally constrained, consistent with a model in which the two parts tightly associate only in the presence of the dimerizing small molecule. These findings are consistent with a model in which a critical part of the switch design is the localization of both parts of the receptor to the plasma membrane. The interaction mediated by small-molecule addition is sufficient to drive a large change in the molecular association of the two parts.

ON-switch CAR requires small molecule and antigen to activate primary human CD4⁺ T cells

We tested the effectiveness of this ON-switch CAR (I.b + II.d; the rapalog-controlled version) in therapeutically relevant T cells. We expressed the components in primary human CD4⁺ helper T cells and examined multiple T cell responses (Fig. 3A). Expression of the ON-switch CAR was similar to that of the conventional CAR in primary T cells (fig. S6). CAR T cells were incubated with antigen-expressing target cells in varying concentrations of rapalog. All of the tested CD4⁺ T cell responses showed the dual requirement for stimulation with cognate antigen (CD19⁺ target cells) and small-molecule dimerizer. These responses included IL-2 production (a general readout for effector T cell activation) and interferon- γ

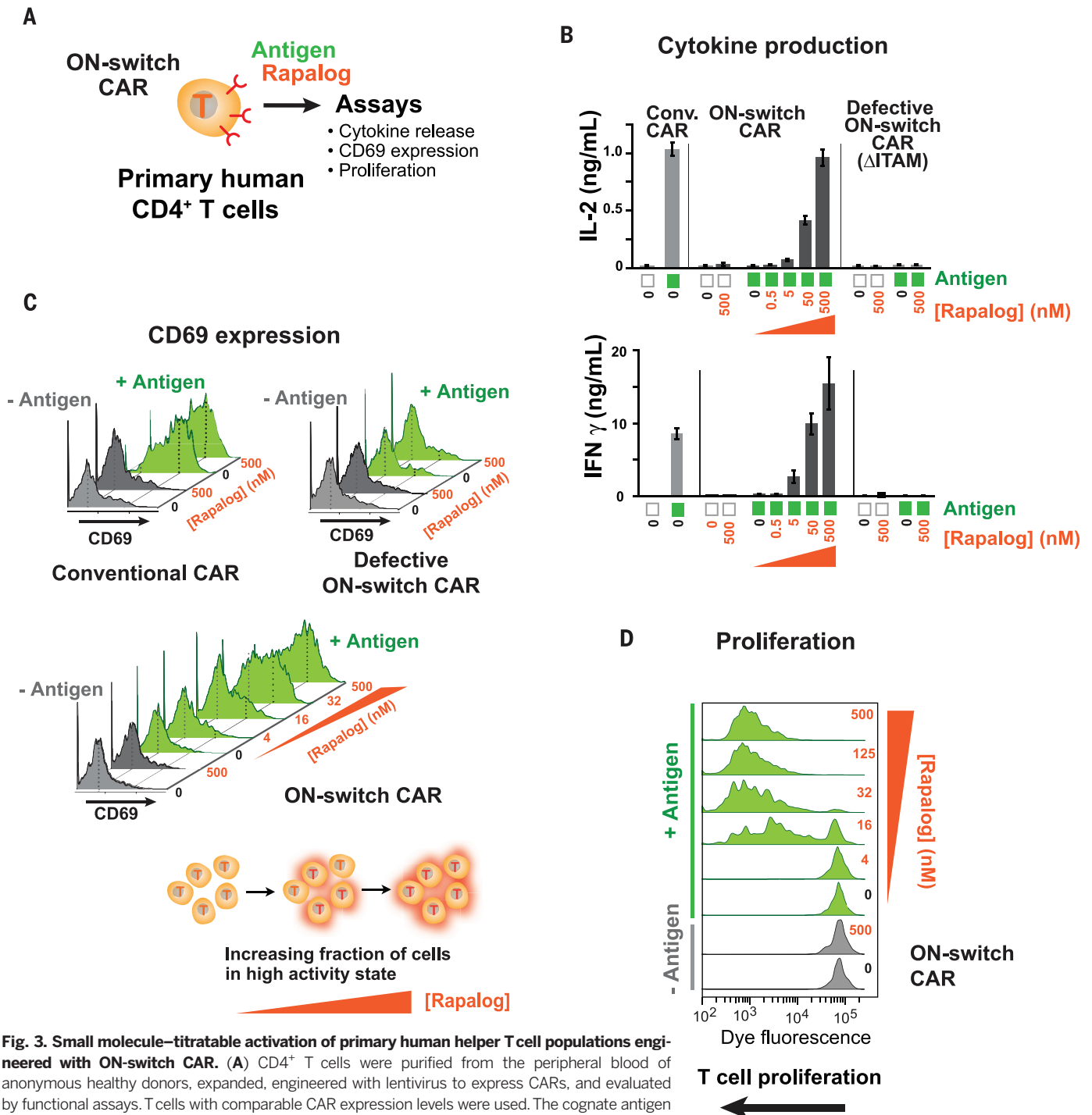


Fig. 3. Small molecule–titratable activation of primary human helper T cell populations engineered with ON-switch CAR. (A) CD4⁺ T cells were purified from the peripheral blood of anonymous healthy donors, expanded, engineered with lentivirus to express CARs, and evaluated by functional assays. T cells with comparable CAR expression levels were used. The cognate antigen CD19 was presented to T cells as a cell surface protein on K562 target cells. Various concentrations of the dimerizer rapalog were added to reaction mixtures to examine effects of rapalog titration. (B) Production of the cytokines IL-2 and IFN- γ quantified by ELISA after an overnight incubation, as described in supplementary material; $n = 3$, error bars denote SD. (C) Monitoring T cell activation in single cells by quantifying expression of the cell surface protein CD69, whose up-regulation occurs early during T cell activation. T cells in overnight assay mixtures were stained with a fluorophore-conjugated antibody to CD69 and analyzed by flow cytometry. Green histograms denote T cells stimulated with CD19⁺ target cells (+ antigen). Gray peaks denote T cells treated with target cells lacking the CD19 antigen (– antigen). T cell population shows bimodal response, and addition of rapalog increases the fraction of cells in the high-response population. (D) Dimerizer small molecule– and antigen-dependent T cell proliferation. T cells expressing the ON-switch CAR were prelabeled with the intracellular dye CellTrace Violet, whose fluorescence intensity per cell progressively decreases with increasing rounds of cell division. Cells were processed in a flow cytometer after 5 days of incubation. Leftward shift of peaks in the histogram indicates T cell proliferation.

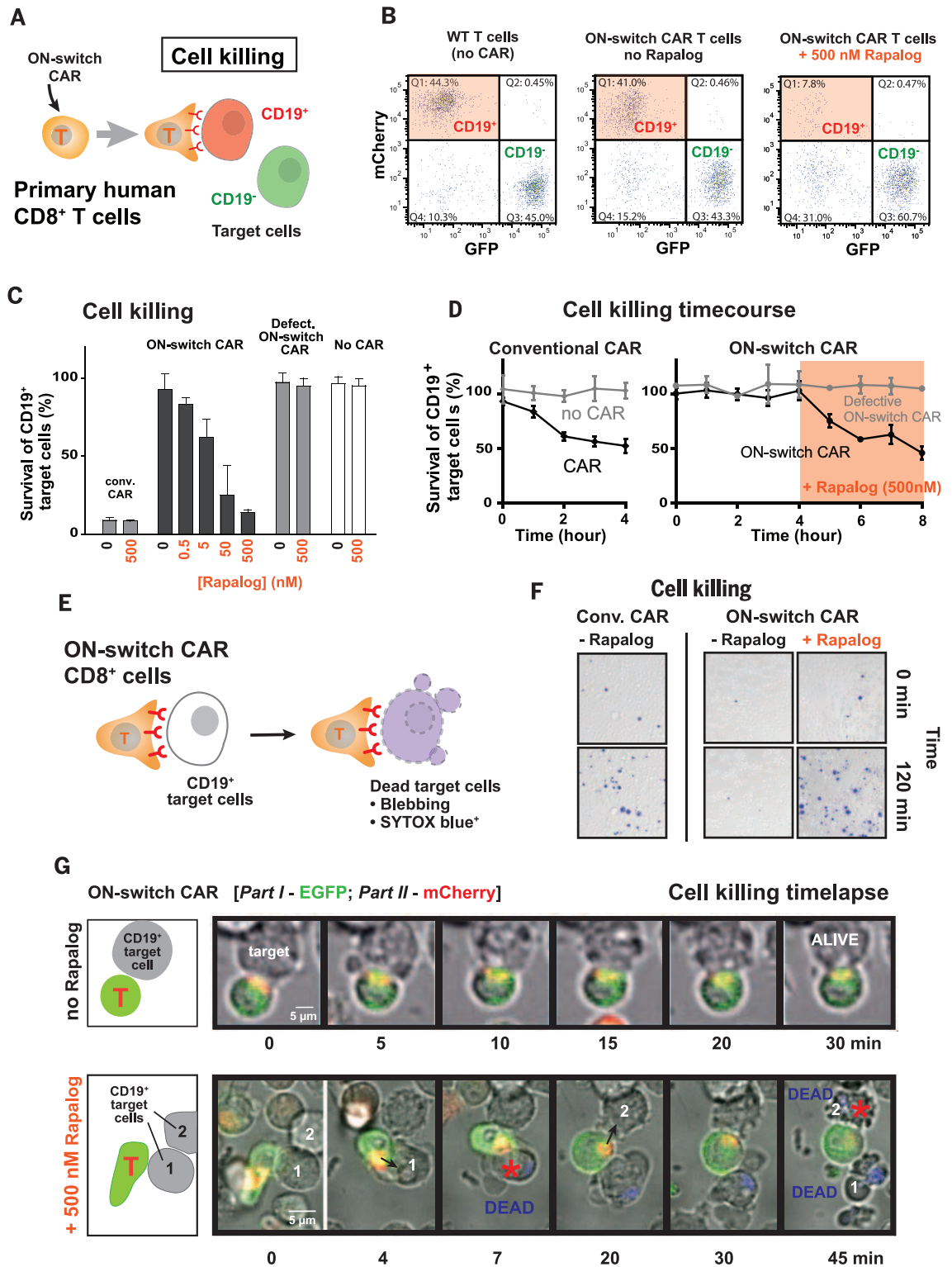
(IFN- γ) production [an indicator for T helper cell 1 (T_H1) antitumor response]. Production of IL-2 and IFN- γ was minimal when cells were

stimulated by either the small-molecule dimerizer or the cognate antigen individually. Dual stimulation with the cognate antigen and increasing

amounts of small molecule led to a dose-dependent increase in cytokine secretion by the ON-switch CAR T cells. Notably, at high concentrations of

Fig. 4. ON-switch CAR yields antigen-specific and titratable killing of target cell population by engineered primary cytotoxic (CD8⁺) T cells. (A) Schematic of a flow cytometry–based cell-killing assay. Primary human CD8⁺ T cells were isolated, expanded, and engineered to express CARs by transduction with lentivirus. T cells with comparable CAR expression levels were used.

T cells were incubated with a mixture of cognate target cells (CD19⁺, mCherry⁺) and non-cognate target cells (CD19⁻, GFP⁺). Rapalogs were added to specified concentrations. After incubation for a designated period of time, the abundance of both types of K562 target cells within the overall surviving target cell population was quantified by flow cytometry. (B) Representative flow cytometry data. Surviving target cells in sample mixtures at the end of an overnight assay were segregated into cognate (mCherry⁺) and noncognate (GFP⁺) subpopulations. The percentage of CD19⁺ cells (quadrant 1) was divided by that of CD19⁻ cells (quadrant 3) to calculate the normalized percentage of survival of cognate target cells in each sample. (C) Cytotoxicity mediated by CARs in an overnight (22 hours) end-point experiment. A low percentage for survival of cognate target cells indicates a high degree of specific target cell killing by CAR T cells. (D) Cytotoxicity mediated by CARs in a kinetic experiment. Target cell killing by conventional CAR was quantified hourly during a 4-hour incubation period. Cytotoxic activities of the ON-switch CAR were first monitored in the absence of dimerizing small molecule hourly for 4 hours, followed by four more hourly time points in the presence of small molecule (500 nM rapalogs). (E) Schematic of the experimental setup of the time-lapse imaging experiments. (F) Representative differential interference contrast (DIC) images of primary human CD8⁺ T cells expressing the conventional CAR or the ON-switch CAR (± rapalogs) incubated with CD19⁺ K562 target cells, overlaid with SYTOX blue



dead stain fluorescent images, to assay target cell death after 0 and 2 hours of interaction ($n = 3$). (G) A time-lapse montage of DIC and fluorescence image overlays of primary human CD8⁺ T cells expressing ON-switch CAR (part I tagged with EGFP; part II tagged with mCherry) and their interaction with CD19⁺ K562 targets. The top montage is in the absence of rapalogs and shows T cell binding, but no killing of target cells, over the course of the 30-min experiment (movie S3). The bottom montage is in the presence of 500 nM rapalogs and shows killing of tumor cells, indicated by blebbing and SYTOX blue dye uptake, within 45 min (movie S4).

dimerizing molecule, cytokine production rivaled that obtained with T cells expressing the conventional CAR (Fig. 3B).

Similarly, dual-gated and titratable responses were seen for expression of the induced cell surface marker CD69. Increased cell surface expression of the CD69 protein occurs within hours after T cell activation and provides a standard method to monitor the activation status of T cells at the single-cell level by flow cytometry (39). As was observed with the conventional CAR T cells, cells expressing the ON-switch CAR displayed a bimodal CD69 expression pattern upon activation. However, unlike the conventional CAR that only required the cognate CD19 antigen to activate T cells, the ON-switch CAR also required the dimerizer molecule to be present (Fig. 3C). Increasing dimerizer concentrations did not appear to titrate the activity level of individual cells, but rather increased the fraction of cells in the CD69^{high} activated state.

ON-switch CAR T cells require both antigen and small-molecule dimerizer to drive cell proliferation

Antigen-induced proliferation of CAR T cells is a critical facet of therapeutic responses (31, 39–41). Proliferation allows for amplification of T cell action, but excessive proliferation allows for systemic and severe toxicities. We thus tested whether the ON-switch CAR T cells displayed combinatorially gated cell proliferation (Fig. 3D). In a flow cytometry experiment, we labeled human primary CD4⁺ T cells with an intracellular fluorescent dye that is progressively diluted with increasing rounds of cell division, allowing us to monitor cell proliferation. Proliferation of these cells indeed required both the cognate antigen and rapalog. The observed small molecule-gated control over T cell proliferation is important; controlling the degree of cell expansion *in vivo* may be a highly effective way to tune and optimize the strength of the therapeutic response.

Our results with primary human CD4⁺ helper T cells confirm that the ON-switch CAR enables the key therapeutic behaviors of CAR T cells to be gated and regulated by a small-molecule drug. At the single-cell level, our flow cytometry data (for CD69 surface expression and proliferation) indicate that a small molecule-dependent bistable switch alters the number of cells in the ON versus OFF state in the presence of cognate antigen. On the population level, the ON-switch design additionally functions as a dial that yields a titratable dosage of key antitumor responses. The ON-switch CAR T cell populations displayed a high dynamic range of signaling, with a maximum response (at saturating concentrations of small-molecule dimerizer) comparable to that of the conventional CAR T cells.

Small molecule-controlled cancer cell killing by ON-switch CAR CD8⁺ T cells

We tested the ON-switch CAR's ability to control tumor cell killing by primary human CD8⁺ cytotoxic T cells. Targeted apoptosis of tumor cells is one of the hallmarks of antitumor immunity and

CAR T cell action. A major purpose of CARs is to redirect CD8⁺ T cell cytotoxicity selectively toward cancer cells expressing antigens of interest. Relative to cytokine production and proliferation, T cell-mediated cell killing occurs on a faster time scale (minutes) and with different thresholds (42, 43). Thus, we examined whether primary human CD8⁺ T cells expressing the ON-switch CAR could mount a cytotoxic response that was still antigen-specific but gated by the dimerizing small molecule. Control over cytotoxic activity is one of the most important needs for CAR T cell regulation.

To test cell killing, we labeled target cells expressing either the cognate antigen (CD19⁺) or a noncognate antigen (mesothelin⁺) by the selective expression of distinct fluorescent proteins, such that in a mixed population the two target cell types could be independently identified and tracked by flow cytometry (Fig. 4A and fig. S7A). The cytotoxic activity of CD8⁺ T cells expressing the CD19-directed ON-switch CAR was then quantified according to reduction in the fraction of cognate target cells among all viable target cells (Fig. 4B). After an overnight incubation (22 hours), no cell-mediated cytotoxicity was observed in the absence of rapalog. When 500 nM rapalog was added, efficient killing of the cognate target cells was observed. Killing of noncognate target cells was not observed, and the degree of cognate target cell killing could be titrated by changing the concentration of rapalog (Fig. 4C and fig. S7A). The degree of targeted cell killing with saturating rapalog matched the level observed with the conventional CAR.

In an 8-hour time course experiment, T cells expressing the conventional CAR immediately induced specific cytotoxicity in cognate target cells. T cells expressing the ON-switch CAR did not commence killing until addition of rapalog (Fig. 4D). These results confirmed that the ON-switch CAR T cells allow for titratable control over the magnitude and timing of apoptosis in the target cell population. We next tested whether the ON-switch CAR T cells would stop cell killing after rapalog removal and then resume killing upon reintroduction of rapalog. This coculturing experiment consisted of three stages to implement the “on-off-on” sequence of exposure to rapalog, and each stage lasted 36 hours (fig. S8A). Target cell survival was quantified at the beginning and the end of each stage. Target cell killing was only detectable in the first and last 36-hour periods when the rapalog was present (fig. S8, B and C). Our proof-of-principle experiments with CD8⁺ T cells illustrate that the ON-switch design provides a flexible platform for temporal control over CAR T cell action. In therapeutic settings, the kinetics of on-off and off-on transitions could in principle be tuned with small molecules with different pharmacodynamics, or with competitive (nondimerizing) antagonist molecules.

To confirm the relevance of our observations made with engineered K562 (human chronic myelogenous leukemia) target cell lines, we investigated rapalog-gated killing of natural CD19⁺ cancer cells by ON-switch CAR T cells. The Raji and Daudi human B cell lines both naturally ex-

press CD19 in amounts greater than that in the CD19⁺ K562 cell line we had used (fig. S7B). Cytotoxicity experiments showed that both B cell lines were subject to killing by CD8⁺ ON-switch CAR T cells in a manner dependent on the dose of the rapalog (fig. S7C). In summary, we observed titratable killing of multiple types of CD19⁺ target cell populations.

Imaging of ON-switch CAR T cell killing

To better characterize the spatiotemporal aspects of ON-switch CAR-mediated killing, we performed microscopy-based assays. We quantitatively monitored cell killing by CD8⁺ T cells by means of SYTOX nucleic acid binding dye, which only permeates dead cells (Fig. 4E). Images taken after 2 hours confirmed killing of CD19⁺ target cells by the ON-switch CAR T cells, but only in the presence of the small molecule (Fig. 4F).

We directly followed the dynamics of cell death with live-cell time-lapse confocal microscopy. In primary human CD8⁺ T cells, we expressed the ON-switch CAR components labeled with distinct fluorescent proteins (part I comprising the extracellular scFv domain was labeled with enhanced GFP at the C terminus; part II comprising the CD3 ζ domain was labeled with mCherry at the C terminus). We tracked the physical interaction between T cells and cognate target cells as well as the killing of cognate target cells. In the absence of rapalog, T cells and target cells associated and formed an immune synapse-like structure, but target cells remained alive for the duration of the 30-min experiment (movie S3; Fig. 4G, top). Quantitative analysis of time-lapse images revealed that even in the absence of rapalog, ON-switch CAR T cells formed conjugates with cognate target cells as frequently as did conventional CAR T cells (fig. S9). However, the physical association alone did not induce target cell death. In contrast, in the presence of rapalog, multiple target cells were rapidly killed within the 45-min time window (movie S4; Fig. 4G, bottom).

In vivo small-molecule regulation of cognate tumor cell killing

We tested whether the tumor cell killing by primary ON-switch CAR T cells could be regulated *in vivo* in a mouse xenograft model. In preliminary pharmacokinetic studies, rapalog had a plasma half-life in mice of approximately 4 hours. This property necessitated multiple injections of rapalog per day (three injections at 3 mg/kg to maintain 50 ng/ml in plasma), which, combined with the high cost of the compound, precluded the performance of extended multiweek studies with statistically sufficient numbers of mice. Thus, we used a shorter protocol of *in vivo* tumor killing (Fig. 5A). We implanted a mixture of cognate (CD19⁺ mCherry⁺) and noncognate (CD19⁺ GFP^{high}) K562 cells into the peritoneal cavity. Fourteen hours later, CAR-expressing CD8⁺ T cells and the first dose of rapalog (or vehicle control) were injected intraperitoneally (i.p.). Three additional doses of the rapalog or vehicle were injected at 6-hour intervals. Mice were euthanized at the experimental end point (after

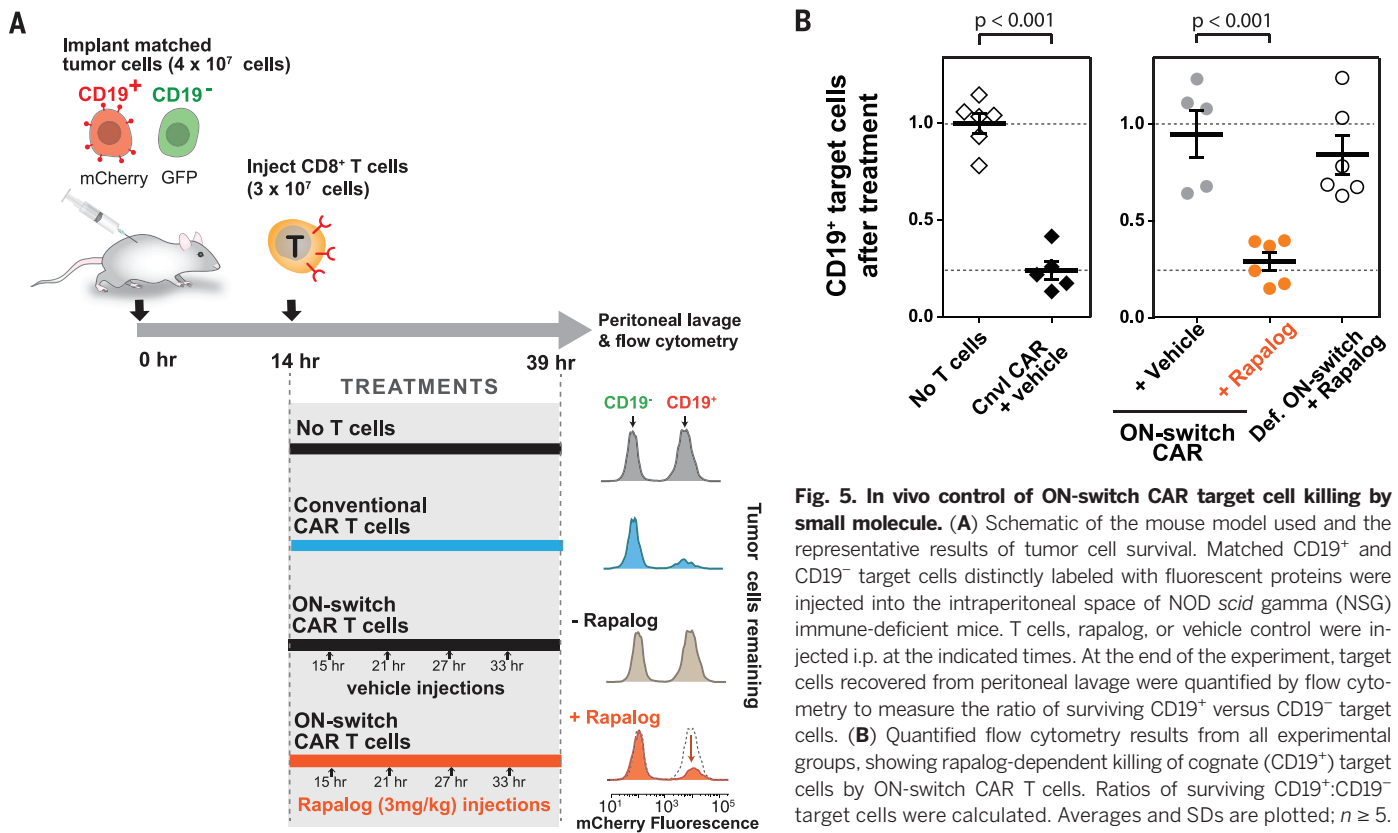


Fig. 5. In vivo control of ON-switch CAR target cell killing by small molecule. (A) Schematic of the mouse model used and the representative results of tumor cell survival. Matched CD19⁺ and CD19⁻ target cells distinctly labeled with fluorescent proteins were injected into the intraperitoneal space of NOD scid gamma (NSG) immune-deficient mice. T cells, rapalog, or vehicle control were injected i.p. at the indicated times. At the end of the experiment, target cells recovered from peritoneal lavage were quantified by flow cytometry to measure the ratio of surviving CD19⁺ versus CD19⁻ target cells. (B) Quantified flow cytometry results from all experimental groups, showing rapalog-dependent killing of cognate (CD19⁺) target cells by ON-switch CAR T cells. Ratios of surviving CD19⁺:CD19⁻ target cells were calculated. Averages and SDs are plotted; $n \geq 5$. P values to compare pairs of experimental groups were calculated with Student's t test.

39 hours) for collection of peritoneal lavage (44), from which recovered cells were analyzed by flow cytometry.

Relative to mice that did not receive any T cells, mice injected with conventional CAR T cells showed selective depletion of the CD19⁺ K562 cell population (Fig. 5A). ON-switch CAR T cells produced a similar result, but only in mice treated with rapalog. Normalized numbers of remaining CD19⁺ target cells (relative to numbers of remaining CD19⁻ target cells) are plotted in Fig. 5B. These data show that the ON-switch CAR T cells, in the absence of rapalog, led to the same outcome as in conditions where no T cells were given or defective ON-switch T cells and rapalog were given. However, when the mice injected with ON-switch CAR T cells were also treated with rapalog, the decrease in CD19⁺ cells matched that observed with the conventional CAR T cells.

These studies confirmed that the ON-switch CAR T cells can be effectively controlled with a small molecule in vivo. Both in vitro and in vivo, the engineered cells demonstrate no constitutive killing of target cells, but show selective killing of cognate target cells when exposed to the dimerization-inducing molecule. The rapalog we used in vivo is not ideal given its short half-life in plasma. However, we demonstrated that unrelated dimerization systems can be used to control the ON-switch CAR architecture (Fig. 2B). Thus, it is likely that heterodimerization systems optimized for in vivo pharmacokinetic properties and safety could

be used to tightly control ON-switch CAR T cell activity in patients.

Safer therapeutic immune cells by integrating autonomous and user control

We engineered a class of synthetic T cell receptors that allow for effective exogenous control over T cell antitumor activity, including cytokine production, proliferation, and cytotoxicity. This receptor design is modular, in that customizable small-molecule dimerization systems can be used to gate signaling. As with conventional CARs, various extracellular domains for recognition of distinct ligand antigens can be used. Further analysis shows that the ON-switch design is also compatible with further customization through a mutated 4-1BB signaling domain in part I or a monomeric form of part II, if it is preferred that these individual components not associate with the endogenous TRAF or DAP10 molecules (figs. S10 and S11) (29, 45, 46).

The ON-switch receptor system depends on two combined inputs to trigger T cell activation: a disease-specific ligand and a small-molecule drug. This type of antigen ligand + small-molecule combinatorial control made possible by the ON-switch design might make adoptive T cell therapy safer, as the activities of an infused T cell population could be selectively regulated in a temporal and titratable manner to minimize both off-target and on-target toxicities (7).

T cells engineered with an anti-HER2 CAR to treat metastatic colon cancer have caused severe and rapid cross-reaction with normal cells expressing low amounts of HER2 in the lung; CAR T cells first concentrate and transit through the lung immediately after infusion (16). This “first pass” toxicity involving lung, heart, and liver, which occurs immediately after T cell infusion, could potentially be limited by delaying activation of the T cells until after they have distributed throughout the body. Using locally administered small molecules, ON-switch CAR T cells could allow for titratable control over T cell activity, as well as the location of therapeutic action when combined with technologies that can locally deliver small molecules into targeted tissues (20).

Need to develop modules for orthogonal chemical control of engineered cells

More generally, this and related work highlights the value of orthogonal chemical control as an interface for any kind of cellular therapeutic agent. Toxicity concerns of cell-based therapies primarily stem from a lack of efficient methods to specifically communicate with and regulate the cells once they are in the patient (aside from systemic treatments such as immunosuppression). A small-molecule drug-inducible “suicide” switch that induces apoptosis in engineered T cells can be used to abort cellular therapeutics (18, 24). A modular, RNA-based system has also been

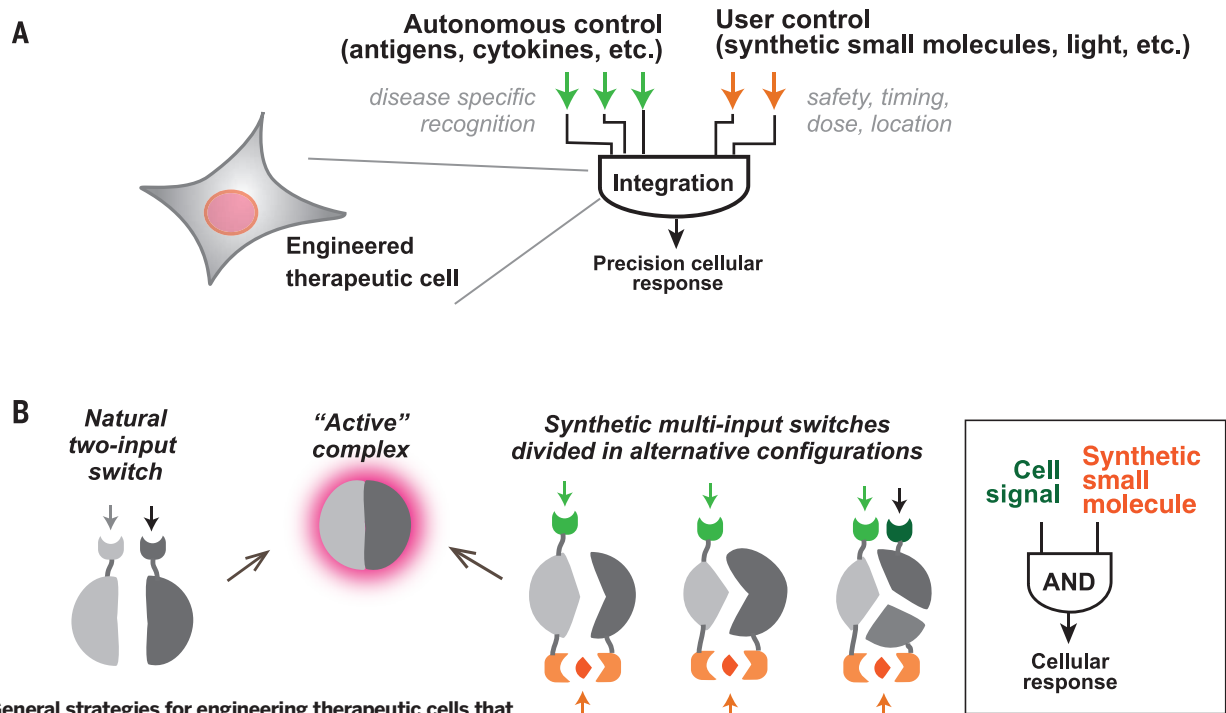


Fig. 6. General strategies for engineering therapeutic cells that integrate autonomous and user control. (A) Ideal therapeutic

cells are expected to (i) produce potent therapeutic effects upon recognizing disease-specific signals and (ii) act in a temporally and spatially regulated manner. As illustrated in this work, cell-autonomous signaling in response to disease-specific inputs can be integrated with exogenous, user-supplied inputs to produce more precisely regulated therapeutic responses. **(B)** Regulated assembly into conditionally active complexes is commonly observed in natural regulatory systems. This strategy can be exploited to generate synthetic multi-input control by generating alternative split configurations of the active state that are conditionally assembled only with the proper combination of input molecules.

developed for small molecule-dependent cytokine production and proliferation of engineered T cells *in vivo* (47). Orthogonal ligands of G protein-coupled receptors can be used to guide T cell migration *in vivo* (48). The ON-switch CAR described in this study can be implemented along with these other synthetic control devices to produce “smart T cells” whose key therapeutic behaviors are individually under exogenous control.

This work also emphasizes the need for the development of additional orthogonal channels for molecular control. Reagents such as the rapalog molecule used here were primarily developed as tools for chemical biology studies, and they do not have ideal pharmacokinetic properties for clinical use. Advancement in cellular therapeutics may thus require the development of new classes of controller drugs that are optimized for clinical use in combination with engineered therapeutic cells. Such drugs should be safe and bio-inert, have good pharmacokinetic properties, and have cognate response modules that can be flexibly incorporated into the molecular machinery of the engineered cells (48–50). Other modalities of control—such as light, which can be detected by optogenetic modules (51–55) or other physical signals—could in principle also be useful as additional channels to control therapeutic cells. Combining the tools and strategies of chemical biology with genetic engineering may produce more control-

lable cellular therapeutic agents with improved therapeutic profiles.

Strategies for engineering new layers of combinatorial control in synthetic receptors

The type of cellular control engineered here represents the general principle of integrating autonomous control (e.g., targeting of disease ligands) with user control (e.g., small molecules) (Fig. 6A). As we begin to engineer more cellular therapies, integration of these two modes of cellular regulation is likely to become increasingly important. Regulation by user inputs allows the physician more precise control over the timing, dose, and location of a cellular action and thus more flexible safety control.

This work also demonstrates that it is possible to engineer additional layers of positive control into an already complex synthetic receptor. The engineering of the CAR performed here is analogous to changes in regulatory function that occur in signaling proteins over the course of evolution, when new regulatory inputs are layered and integrated with one another. We used the simple strategy of harnessing controlled molecular complex assembly as a way to achieve combinatorial multi-input regulation (Fig. 6B). The active signaling complex at the T cell plasma membrane is normally conditionally assembled when the TCR and co-receptors are stimulated, whereas the CAR preassembles this complex.

Thus, to achieve multi-input control, we have resplit this assembly in a different configuration and in a manner such that its reassembly is dependent on small-molecule binding. This technique of synthetic division and reassembly constitutes a robust strategy for integrating and layering different control modules over cellular responses in order to develop synthetic combinatorial control systems that mimic the precision of natural cellular signaling responses (56, 57).

REFERENCES AND NOTES

1. J. A. Bluestone, H. Bour-Jordan, Current and future immunomodulation strategies to restore tolerance in autoimmune diseases. *Cold Spring Harb. Perspect. Biol.* **4**, a007542 (2012). doi: [10.1101/cshperspect.a007542](https://doi.org/10.1101/cshperspect.a007542)
2. M. Sadelain, R. Brentjens, I. Riviere, The basic principles of chimeric antigen receptor design. *Cancer Discov.* **3**, 388–398 (2013). doi: [10.1158/2159-8290.CD-12-0548](https://doi.org/10.1158/2159-8290.CD-12-0548); pmid: [23550147](https://pubmed.ncbi.nlm.nih.gov/23550147/)
3. M. Kalos, C. H. June, Adoptive T cell transfer for cancer immunotherapy in the era of synthetic biology. *Immunity* **39**, 49–60 (2013). doi: [10.1016/j.immuni.2013.07.002](https://doi.org/10.1016/j.immuni.2013.07.002); pmid: [23890063](https://pubmed.ncbi.nlm.nih.gov/23890063/)
4. J. N. Kochenderfer, S. A. Rosenberg, Treating B-cell cancer with T cells expressing anti-CD19 chimeric antigen receptors. *Nat. Rev. Clin. Oncol.* **10**, 267–276 (2013). doi: [10.1038/nrclinonc.2013.46](https://doi.org/10.1038/nrclinonc.2013.46)
5. N. Gupta *et al.*, Neural stem cell engraftment and myelination in the human brain. *Sci. Transl. Med.* **4**, 155ra137 (2012). pmid: [23052294](https://pubmed.ncbi.nlm.nih.gov/23052294/)
6. P. Lu *et al.*, Long-distance growth and connectivity of neural stem cells after severe spinal cord injury. *Cell* **150**, 1264–1273 (2012). doi: [10.1016/j.cell.2012.08.020](https://doi.org/10.1016/j.cell.2012.08.020); pmid: [22980985](https://pubmed.ncbi.nlm.nih.gov/22980985/)
7. M. A. Fischbach, J. A. Bluestone, W. A. Lim, Cell-based therapeutics: The next pillar of medicine. *Sci. Transl. Med.* **5**,

- 179ps7 (2013). doi: [10.1126/scitranslmed.3005568](https://doi.org/10.1126/scitranslmed.3005568); pmid: 23552369
8. C. Mason, D. A. Brindley, E. J. Culme-Seymour, N. L. Davie, Cell therapy industry: Billion dollar global business with unlimited potential. *Regen. Med.* **6**, 265–272 (2011). doi: [10.2217/rme.11.28](https://doi.org/10.2217/rme.11.28); pmid: 21548728
 9. H. Ye, D. Aubel, M. Fussenegger, Synthetic mammalian gene circuits for biomedical applications. *Curr. Opin. Chem. Biol.* **17**, 910–917 (2013). doi: [10.1016/j.cbpa.2013.10.006](https://doi.org/10.1016/j.cbpa.2013.10.006); pmid: 24466575
 10. M. R. Roberts *et al.*, Targeting of human immunodeficiency virus-infected cells by CD8⁺ T lymphocytes armed with universal T-cell receptors. *Blood* **84**, 2878–2889 (1994). pmid: 7949163
 11. M. Kalos *et al.*, T cells with chimeric antigen receptors have potent antitumor effects and can establish memory in patients with advanced leukemia. *Sci. Transl. Med.* **3**, 95ra73 (2011). pmid: 21832238
 12. J. N. Kochenderfer *et al.*, B-cell depletion and remissions of malignancy along with cytokine-associated toxicity in a clinical trial of anti-CD19 chimeric-antigen-receptor-transduced T cells. *Blood* **119**, 2709–2720 (2012). pmid: 22160384
 13. S. A. Grupp *et al.*, Chimeric antigen receptor-modified T cells for acute lymphoid leukemia. *N. Engl. J. Med.* **368**, 1509–1518 (2013). doi: [10.1056/NEJMoa1215134](https://doi.org/10.1056/NEJMoa1215134); pmid: 23527958
 14. M. L. Davila *et al.*, Efficacy and toxicity management of 19-28z CAR T cell therapy in B cell acute lymphoblastic leukemia. *Sci. Transl. Med.* **6**, 224ra25 (2014). doi: [10.1126/scitranslmed.3008226](https://doi.org/10.1126/scitranslmed.3008226); pmid: 24553386
 15. M. V. Maus, S. A. Grupp, D. L. Porter, C. H. June, Antibody-modified T cells: CARs take the front seat for hematologic malignancies. *Blood* **123**, 2625–2635 (2014). doi: [10.1182/blood-2013-11-492231](https://doi.org/10.1182/blood-2013-11-492231)
 16. R. A. Morgan *et al.*, Case report of a serious adverse event following the administration of T cells transduced with a chimeric antigen receptor recognizing ERBB2. *Mol. Ther.* **18**, 843–851 (2010). doi: [10.1038/mt.2010.24](https://doi.org/10.1038/mt.2010.24); pmid: 20179677
 17. F. Ciceri *et al.*, Infusion of suicide-gene-engineered donor lymphocytes after family haploidentical haemopoietic stem-cell transplantation for leukaemia (the TK007 trial): A non-randomised phase III study. *Lancet Oncol.* **10**, 489–500 (2009). doi: [10.1016/S1470-2045\(09\)70074-9](https://doi.org/10.1016/S1470-2045(09)70074-9); pmid: 19345145
 18. T. Sato *et al.*, Engineered human tmprk/AZT as a novel enzyme/prodrug axis for suicide gene therapy. *Mol. Ther.* **15**, 962–970 (2007). doi: [10.1038/mt.sj.6300122](https://doi.org/10.1038/mt.sj.6300122); pmid: 17375075
 19. V. D. Fedorov, M. Themeli, M. Sadelain, PD-1- and CTLA-4-based inhibitory chimeric antigen receptors (iCARs) divert off-target immunotherapy responses. *Sci. Transl. Med.* **5**, 215ra172 (2013). doi: [10.1126/scitranslmed.3006597](https://doi.org/10.1126/scitranslmed.3006597); pmid: 24337479
 20. J. D. Byrne *et al.*, Local iontophoretic administration of cytotoxic therapies to solid tumors. *Sci. Transl. Med.* **7**, 273ra14 (2015). doi: [10.1126/scitranslmed.3009951](https://doi.org/10.1126/scitranslmed.3009951); pmid: 25653220
 21. W. Lim, B. Mayer, T. Pawson, *Cell Signaling* (Garland Science, New York, 2014).
 22. A. Weiss, D. R. Littman, Signal transduction by lymphocyte antigen receptors. *Cell* **76**, 263–274 (1994). doi: [10.1016/0092-8674\(94\)90334-4](https://doi.org/10.1016/0092-8674(94)90334-4); pmid: 8293463
 23. I. A. Graef, L. J. Holsinger, S. Diver, S. L. Schreiber, G. R. Crabtree, Proximity and orientation underlie signaling by the non-receptor tyrosine kinase ZAP70. *EMBO J.* **16**, 5618–5628 (1997). doi: [10.1093/emboj/16.18.5618](https://doi.org/10.1093/emboj/16.18.5618); pmid: 9312021
 24. A. Di Stasi *et al.*, Inducible apoptosis as a safety switch for adoptive cell therapy. *N. Engl. J. Med.* **365**, 1673–1683 (2011). doi: [10.1056/NEJMoa1106152](https://doi.org/10.1056/NEJMoa1106152); pmid: 22047558
 25. J. H. Bayle *et al.*, Rapamycin analogs with differential binding specificity permit orthogonal control of protein activity. *Chem. Biol.* **13**, 99–107 (2006). doi: [10.1016/j.chembiol.2005.10.017](https://doi.org/10.1016/j.chembiol.2005.10.017); pmid: 16426916
 26. S. D. Liberles, S. T. Diver, D. J. Austin, S. L. Schreiber, Inducible gene expression and protein translocation using nontoxic ligands identified by a mammalian three-hybrid screen. *Proc. Natl. Acad. Sci. U.S.A.* **94**, 7825–7830 (1997). doi: [10.1073/pnas.94.15.7825](https://doi.org/10.1073/pnas.94.15.7825); pmid: 9223271
 27. J. Choi, J. Chen, S. L. Schreiber, J. Clardy, Structure of the FKBP12-rapamycin complex interacting with the binding domain of human FRAP. *Science* **273**, 239–242 (1996). doi: [10.1126/science.273.5272.239](https://doi.org/10.1126/science.273.5272.239); pmid: 8662507
 28. J. Lin, A. Weiss, The tyrosine phosphatase CD148 is excluded from the immunologic synapse and down-regulates prolonged T cell signaling. *J. Cell Biol.* **162**, 673–682 (2003). doi: [10.1083/jcb.200303040](https://doi.org/10.1083/jcb.200303040); pmid: 12913111
 29. J. Wu *et al.*, An activating immunoreceptor complex formed by NKG2D and DAP10. *Science* **285**, 730–732 (1999). doi: [10.1126/science.285.5428.730](https://doi.org/10.1126/science.285.5428.730); pmid: 10426994
 30. B. A. Irving, A. C. Chan, A. Weiss, Functional characterization of a signal transducing motif present in the T cell antigen receptor zeta chain. *J. Exp. Med.* **177**, 1093–1103 (1993). doi: [10.1084/jem.177.4.1093](https://doi.org/10.1084/jem.177.4.1093); pmid: 8459204
 31. C. S. Guy *et al.*, Distinct TCR signaling pathways drive proliferation and cytokine production in T cells. *Nat. Immunol.* **14**, 262–270 (2013). pmid: 23377202
 32. M. C. Milone *et al.*, Chimeric receptors containing CD137 signal transduction domains mediate enhanced survival of T cells and increased antileukemic efficacy in vivo. *Mol. Ther.* **17**, 1453–1464 (2009). doi: [10.1038/mt.2009.83](https://doi.org/10.1038/mt.2009.83); pmid: 19384291
 33. T. Miyamoto *et al.*, Rapid and orthogonal logic gating with a gibberellin-induced dimerization system. *Nat. Chem. Biol.* **8**, 465–470 (2012). doi: [10.1038/nchembio.922](https://doi.org/10.1038/nchembio.922); pmid: 22446836
 34. K. Murase, Y. Hirano, T. P. Sun, T. Hakoshima, Gibberellin-induced DELLA recognition by the gibberellin receptor GID1. *Nature* **456**, 459–463 (2008). doi: [10.1038/nature07519](https://doi.org/10.1038/nature07519); pmid: 19037309
 35. S. Manley *et al.*, High-density mapping of single-molecule trajectories with photoactivated localization microscopy. *Nat. Methods* **5**, 155–157 (2008). doi: [10.1038/nmeth.1176](https://doi.org/10.1038/nmeth.1176); pmid: 18193054
 36. E. M. Puchner, J. M. Walter, R. Kasper, B. Huang, W. A. Lim, Counting molecules in single organelles with superresolution microscopy allows tracking of the endosome maturation trajectory. *Proc. Natl. Acad. Sci. U.S.A.* **110**, 16015–16020 (2013). doi: [10.1073/pnas.1309676110](https://doi.org/10.1073/pnas.1309676110); pmid: 24043832
 37. E. Betzig *et al.*, Imaging intracellular fluorescent proteins at nanometer resolution. *Science* **313**, 1642–1645 (2006). doi: [10.1126/science.1127344](https://doi.org/10.1126/science.1127344); pmid: 16902090
 38. A. D. Douglass, R. D. Vale, Single-molecule microscopy reveals plasma membrane microdomains created by protein-protein networks that exclude or trap signaling molecules in T cells. *Cell* **121**, 937–950 (2005). doi: [10.1016/j.cell.2005.04.009](https://doi.org/10.1016/j.cell.2005.04.009); pmid: 15960980
 39. P. E. Simms, T. M. Ellis, Utility of flow cytometric detection of CD69 expression as a rapid method for determining poly- and oligoclonal lymphocyte activation. *Clin. Diagn. Lab. Immunol.* **3**, 301–304 (1996). pmid: 8705673
 40. O. Boyman, J. Sprent, The role of interleukin-2 during homeostasis and activation of the immune system. *Nat. Rev. Immunol.* **12**, 180–190 (2012). pmid: 22343569
 41. H. Ikeda, L. J. Old, R. D. Schreiber, The roles of IFN γ in protection against tumor development and cancer immunotherapy. *Cytokine Growth Factor Rev.* **13**, 95–109 (2002). doi: [10.1016/S1359-6101\(01\)00038-7](https://doi.org/10.1016/S1359-6101(01)00038-7); pmid: 11900986
 42. J. B. Huppa, M. Gleimer, C. Sumen, M. M. Davis, Continuous T cell receptor signaling required for synapse maintenance and full effector potential. *Nat. Immunol.* **4**, 749–755 (2003). doi: [10.1038/nri951](https://doi.org/10.1038/nri951); pmid: 12858171
 43. M. A. Purbhoo, D. J. Irvine, J. B. Huppa, M. M. Davis, T cell killing does not require the formation of a stable mature immunological synapse. *Nat. Immunol.* **5**, 524–530 (2004). doi: [10.1038/ni1058](https://doi.org/10.1038/ni1058); pmid: 15048111
 44. A. Ray, B. Dittel, *J. Visual. Exp.* www.jove.com/video/1488/isolation-of-mouse-peritoneal-cavity-cells (2010). doi: [10.3791/1488](https://doi.org/10.3791/1488)
 45. H. Ye, Y. C. Park, M. Kreishman, E. Kieff, H. Wu, The structural basis for the recognition of diverse receptor sequences by TRAF2. *Mol. Cell* **4**, 321–330 (1999). doi: [10.1016/S1097-2765\(00\)80334-2](https://doi.org/10.1016/S1097-2765(00)80334-2); pmid: 10518213
 46. I. K. Jang, Z. H. Lee, Y. J. Kim, S. H. Kim, B. S. Kwon, Human 4-1BB (CD137) signals are mediated by TRAF2 and activate nuclear factor- κ B. *Biochem. Biophys. Res. Commun.* **242**, 613–620 (1998). doi: [10.1006/bbrc.1997.8016](https://doi.org/10.1006/bbrc.1997.8016); pmid: 9464265
 47. Y. Y. Chen, M. C. Jensen, C. D. Smolke, Genetic control of mammalian T-cell proliferation with synthetic RNA regulatory systems. *Proc. Natl. Acad. Sci. U.S.A.* **107**, 8531–8536 (2010). doi: [10.1073/pnas.1001721107](https://doi.org/10.1073/pnas.1001721107); pmid: 20421500
 48. J. S. Park *et al.*, Synthetic control of mammalian-cell motility by engineering chemotaxis to an orthogonal bioinert chemical signal. *Proc. Natl. Acad. Sci. U.S.A.* **111**, 5896–5901 (2014). doi: [10.1073/pnas.1402087111](https://doi.org/10.1073/pnas.1402087111); pmid: 24711398
 49. A. Bishop *et al.*, Unnatural ligands for engineered proteins: New tools for chemical genetics. *Annu. Rev. Biophys. Biomol. Struct.* **29**, 577–606 (2000). doi: [10.1146/annurev.biophys.29.1.577](https://doi.org/10.1146/annurev.biophys.29.1.577); pmid: 10940260
 50. L. A. Banaszynski, T. J. Wandless, Conditional control of protein function. *Chem. Biol.* **13**, 11–21 (2006). doi: [10.1016/j.chembiol.2005.10.010](https://doi.org/10.1016/j.chembiol.2005.10.010); pmid: 16426967
 51. W. Bacchus, M. Fussenegger, The use of light for engineered control and reprogramming of cellular functions. *Curr. Opin. Biotechnol.* **23**, 695–702 (2012). doi: [10.1016/j.copbio.2011.12.004](https://doi.org/10.1016/j.copbio.2011.12.004); pmid: 22204821
 52. J. E. Toettcher, D. Gong, W. A. Lim, O. D. Weiner, Light-based feedback for controlling intracellular signaling dynamics. *Nat. Methods* **8**, 837–839 (2011). doi: [10.1038/nmeth.1700](https://doi.org/10.1038/nmeth.1700); pmid: 21909100
 53. A. Levskaya, O. D. Weiner, W. A. Lim, C. A. Voigt, Spatiotemporal control of cell signalling using a light-switchable protein interaction. *Nature* **461**, 997–1001 (2009). doi: [10.1038/nature08446](https://doi.org/10.1038/nature08446); pmid: 19749742
 54. M. J. Kennedy *et al.*, Rapid blue-light-mediated induction of protein interactions in living cells. *Nat. Methods* **7**, 973–975 (2010). doi: [10.1038/nmeth.1524](https://doi.org/10.1038/nmeth.1524); pmid: 21037589
 55. Y. I. Wu *et al.*, A genetically encoded photoactivatable Rac controls the motility of living cells. *Nature* **461**, 104–108 (2009). doi: [10.1038/nature08241](https://doi.org/10.1038/nature08241); pmid: 19693014
 56. K. E. Prehoda, J. A. Scott, R. D. Mullins, W. A. Lim, Integration of multiple signals through cooperative regulation of the N-WASP-Arp2/3 complex. *Science* **290**, 801–806 (2000). doi: [10.1126/science.290.5492.801](https://doi.org/10.1126/science.290.5492.801); pmid: 11052943
 57. J. E. Dueber, B. J. Yeh, R. P. Bhattacharyya, W. A. Lim, Rewiring cell signaling: The logic and plasticity of eukaryotic protein circuitry. *Curr. Opin. Struct. Biol.* **14**, 690–699 (2004). doi: [10.1016/j.sbi.2004.10.004](https://doi.org/10.1016/j.sbi.2004.10.004); pmid: 15582393

ACKNOWLEDGMENTS

C.-Y.W., J.O., W.A.L., and the Regents of the University of California have filed a patent application (WO2014127261) that relates to the ON-SWITCH CAR. We thank the Preclinical Therapeutics Core at UCSF for helping with in vivo studies; K. McNally, S. Johnston, D. Ng, D. Nunez, H. Yan, and S. Zorn for technical assistance; B. Huang for providing a custom-built microscope for PALM imaging; Y. Huang for mass spectroscopy-based pharmacokinetic analysis; M. Milone, C. June, D. Campana, I. Pastan, T. Meyer, and T. Inoue for providing materials; and A. Weiss, J. Bluestone, Q. Tang, A. Marson, L. Lanier, and members of the Lim Lab, Cell Propulsion Lab, and Weiss Lab for advice and feedback. Supported by NIH grant F32 GM01782 (C.-Y.W.), Jane Coffin Childs Memorial Fund grant A121505 (K.T.R.), and NIH grants PN2 EY016546, P50 GM081879, R01 GM055040, and R01 CA196277 and HHMI (W.A.L.).

SUPPLEMENTARY MATERIALS

www.sciencemag.org/content/350/6258/aab4077/suppl/DC1
Materials and Methods
Figs. S1 to S11
Movies S1 to S4

22 April 2015; accepted 9 September 2015
Published online 24 September 2015
[10.1126/science.aab4077](https://doi.org/10.1126/science.aab4077)

REPORTS

ORGANIC SYNTHESIS

Concise total synthesis of glucosepane

Cristian Draghici,^{1*} Tina Wang,^{1†} David A. Spiegel^{1,2‡}

Glucosepane is a structurally complex protein posttranslational modification that is believed to exist in all living organisms. Research in humans suggests that glucosepane plays a critical role in the pathophysiology of both diabetes and human aging, yet comprehensive biological investigations of this metabolite have been hindered by a scarcity of chemically homogeneous material available for study. Here we report the total synthesis of glucosepane, enabled by the development of a one-pot method for preparation of the nonaromatic 4*H*-imidazole tautomer in the core. Our synthesis is concise (eight steps starting from commercial materials), convergent, high-yielding (12% overall), and enantioselective. We expect that these results will prove useful in the art and practice of heterocyclic chemistry and beneficial for the study of glucosepane and its role in human health and disease.

Posttranslational modifications (PTMs) of proteins are responsible for a number of critical functions, ranging from acceleration of protein folding to mediation of protein-protein interactions (1). Protein glycation is a nonenzymatic process for PTM formation wherein protein side chains react spontaneously with open-chain tautomers of carbohydrates. Mounting evidence suggests that protein glycation adducts [also called advanced glycation end products (AGEs)] are critically involved in both healthy and disease processes, including inflammation, diabetes, cancer, and normal human aging (2, 3). AGEs often possess highly complex chemical structures, impeding their detailed chemical and biological characterization (4).

Glucosepane (1) is an AGE formed as a cross-link from reaction sequences between arginine and lysine side chains and one equivalent of hexose carbohydrate, most commonly glucose (Fig. 1). Glucosepane is present on long-lived proteins in the human body, such as collagen and lens crystallin (3, 5), and is also found in high levels in various dietary sources, especially alkali-treated baked goods (6). Researchers have speculated that glucosepane is directly involved in the pathophysiology of various conditions (e.g., diabetes, diabetes-related complications, and aging), owing to the patterns of glucosepane formation on disease-associated proteins. For example, via analysis of skin biopsies obtained through the Diabetes Control and Complications Trial, Monnier *et al.* have determined that increases in skin glucosepane levels represent an independent risk factor for the onset of diabetic

nephropathy, retinopathy, and neuropathy (3, 7). Additional studies have demonstrated that non-enzymatic glucosepane cross-links outnumber enzyme-catalyzed cross-links in the collagen of people over 65 years of age (8). By age 100, glucosepane levels reach 2 nmol/mg of collagen, almost 10 times the normal level, and levels in diabetic patients can reach up to 20 times those in healthy controls (9, 10).

Despite glucosepane's health implications, biological investigations have been hampered by a scarcity of chemically homogeneous material available for study. Its complex nonenzymatic biosynthesis involves serial tautomerizations of Amadori adduct 3 to provide glucosone 4 (a process known as carbonyl mobility) (Fig. 1B). During this process, each stereocenter undergoes epimerization, and therefore the glucosepane core exists naturally as a mixture of all eight possible diastereomers (3, 11). These stereoisomers can only be chromatographically resolved into four binary mixtures, each putatively containing two spectroscopically indistinguishable diastereomers with the same relative configuration at the 6, 7, and 8a positions but opposite absolute configurations with respect to the enantiomerically pure backbone amino acids (11). Despite substantial effort, purification of stereochemically homogeneous glucosepane from biological samples has proven elusive. It is therefore unknown which of the eight stereoisomers is the most prevalent *in vivo*. Furthermore, these binary diastereomeric mixtures can only be isolated in low yields (0.2 to 1.4%) following model reactions between lysine, arginine, and glucose, and via extensive chromatographic purification (5, 11). Because of these difficulties in purification, antibody reagents that would enable biological detection of glucosepane in unprocessed tissue preparations are unavailable. Published investigations into glucosepane biology have thus had to rely on time-consuming extraction protocols involving exhaustive enzymatic hydrolysis followed by high-performance

liquid chromatography (HPLC) separation. The development of synthetic routes toward chemically defined glucosepane constructs represents an essential next step toward our understanding of the roles that this compound plays in human health and disease and also toward the identification of associated therapeutic and/or diagnostic agents.

Glucosepane incorporates a stereogenic polyol motif within a fused hetero-bicyclic constitution, an epimerizable stereocenter at C-8a, and an arginine-derived 4*H*-imidazole at its core. At first glance, one would expect glucosepane to tautomerize spontaneously to the corresponding aromatic 1*H*-imidazole (Fig. 1A); however, reported structural assignments of the 4*H*-imidazole in glucosepane are consistent with one- and two-dimensional nuclear magnetic resonance (NMR) data reported by Biemel *et al.* (11). Furthermore, because glucosepane forms naturally as a protein adduct (not as the free bis-amino acid cross-link), any useful synthesis needs to be compatible with glucosepane incorporation into peptides. Also, because glucosepane is formed naturally as a mixture of all eight possible diastereomers, synthetic efforts targeting both enantio- and diastereomerically pure material are essential for detailed biochemical study.

In analyzing the glucosepane core, we were first intrigued by its reported tendency to adopt a 4*H*-imidazole constitution rather than that of the corresponding aromatic 1*H*-imidazole. We therefore set out to investigate this tautomeric preference through theoretical calculations performed on model compounds designed to mimic the glucosepane core and protonation state (Table 1). Although unsubstituted imidazolium (entry 1) greatly prefers the aromatic arrangement, addition of methylamino substituents to the 2 or 5 positions (entries 2 and 3) decreases this preference substantially. The 2,5-diamino-substituted derivative (entry 4), which contains the same substitution pattern as glucosepane, exhibits a strong preference for the nonaromatic tautomer. This trend may be partly explained by the decreasing aromatic stabilization of imidazole upon addition of electron-donating substituents to the 2 and 5 positions, as indicated in prior work and additional calculations provided in the supplementary materials (fig. S5) (12). This model is further supported by geometry minimization experiments (tables S10 and S11), which demonstrate for the 2,5-diamino imidazole system that the substituent at the 5 position is rotated such that *N* lone pairs only partially overlap with the heterocycle's π system. The inability of electron-donating substituents at this position to delocalize into the imidazole ring may drive a decrease in stabilization energy, as well as a tendency to tautomerize into the 4*H*-imidazole, which permits such delocalization. We hypothesize that in the setting of 5- and 2,5-diamino imidazoles, the decrease in aromaticity does not afford a sufficiently high degree of energetic stabilization. In the 4*H*-imidazole tautomer, on the other hand, electron-donating amines can contribute extensively to resonance stabilization.

¹Department of Chemistry, Yale University, 225 Prospect Street, New Haven, CT 06520, USA. ²Department of Pharmacology, Yale University, 333 Cedar Street, New Haven, CT 06520, USA.

*Present address: Broad Institute of MIT and Harvard, 415 Main Street, Cambridge, MA 02142, USA. †Present address: Department of Chemistry and Chemical Biology, Harvard University, 12 Oxford Street, Cambridge, MA 02138, USA. ‡Corresponding author. E-mail: david.spiegel@yale.edu

With this information in mind, we constructed our retrosynthesis (Fig. 1C). We reasoned that, given the strong thermodynamics driving the core heterocycle's tautomerization state, formation of C–N bonds between the arginine guanidine and the lysine-derived azepane (**6** + Arg → **5**) would be accompanied by spontaneous isomerization to the correct structure. Therefore, we first chose to disconnect at the two C–N bonds endocyclic to the imidazole motif. This is the same disconnection suggested by Biemel *et al.* for the final step in the biosynthesis of glucosepane (**11**), wherein arginine is proposed to condense directly with an α -keto iminium intermediate (**6**) formed from an adduct derived from lysine and glucose (Fig. 1B). We then reasoned that **6** could be generated through N-fluorination and regioselective elimination of fluorine from azepane **7**. In turn, azepane **7** could be deconstructed via an Amadori rearrangement sequence to a suitably protected lysine derivative and known epoxide **8** (**13**). In this sense, **8** would serve as the source of the

chiral diol encountered in glucosepane diastereomer **5**. As it is unknown which stereoisomer(s) of glucosepane are most prevalent in vivo, **8** was chosen because it reflects the stereochemistry of glucose, which is the most common precursor in vivo. In future studies, simply inverting the C-6 and C-7 stereocenters of the starting epoxide **8** would then permit access to other reported diastereomers.

Our synthesis began with epoxide **8**, which was prepared from diacetone-D-glucose as previously described (Fig. 2) (**13**, **14**). Nucleophilic addition of Dod-protected lysine derivative **9** to the less-substituted side of the epoxide in **8**, followed by acidic deprotection of the resulting tertiary amine, provided amino alcohol **10** in 80% yield over two steps. Acetonide removal in the presence of aqueous acetic acid then afforded azepane acetal **13**. The conversion of **10** to **13** proceeded by way of intramolecular attack of the lysine amino group onto the anomeric carbon of the carbohydrate with accompanying acetonide loss to give bicyclic intermediate **11** (**15**). This material

spontaneously underwent Amadori rearrangement (**16**, **17**) to give an intermediate ketone **12**, which was then trapped intramolecularly by the C-6 hydroxyl to produce bridged bicyclic acetal **13** in 60% yield. Reinstallation of the acetonide group proceeded with reformation of the ketone functionality to afford the desired protected ketone (**14**).

Access to **14** set the stage for oxidation-trapping attempts, outlined in our retrosynthesis. Although we were able to achieve the desired α -keto iminium intermediate (**16**) by way of oxidation with 1-(chloromethyl)-4-fluoro-1,4-diazoniabicyclo[2.2.2]octane ditetrafluoroborate (Selectfluor), this material rapidly underwent ring contraction to produce aldehyde **17** (Fig. 3A). All attempts to condense **17** with guanidine derivatives, including various protected forms of arginine, were met only by complete decomposition of **17** and recovery of the guanidine nucleophile. Furthermore, attempts to perform oxidation and guanidine trapping in one pot were also unsuccessful, providing similar results to the two-step process.

In light of these observations, we decided to reengineer our synthetic strategy. Though we were encouraged by our ability to access α -keto iminium **16**, the inability of this species to undergo intermolecular trapping suggested that perhaps condensation with the arginine guanidine functionality succeeds in vivo because of proximity effects. In other words, cross-linking is only likely to occur for proteins in which an appropriately modified lysine residue is directly adjacent to the attacking arginine, rendering the process functionally intramolecular (even for proteins such as collagen, in which intermolecular cross-linking is accelerated due to the high local concentration of reactive side chains) (**3**, **18**). Hence, for the reaction to be successful, the nucleophilic (guanidine) and electrophilic (iminium) components must be tethered together at the time of oxidation.

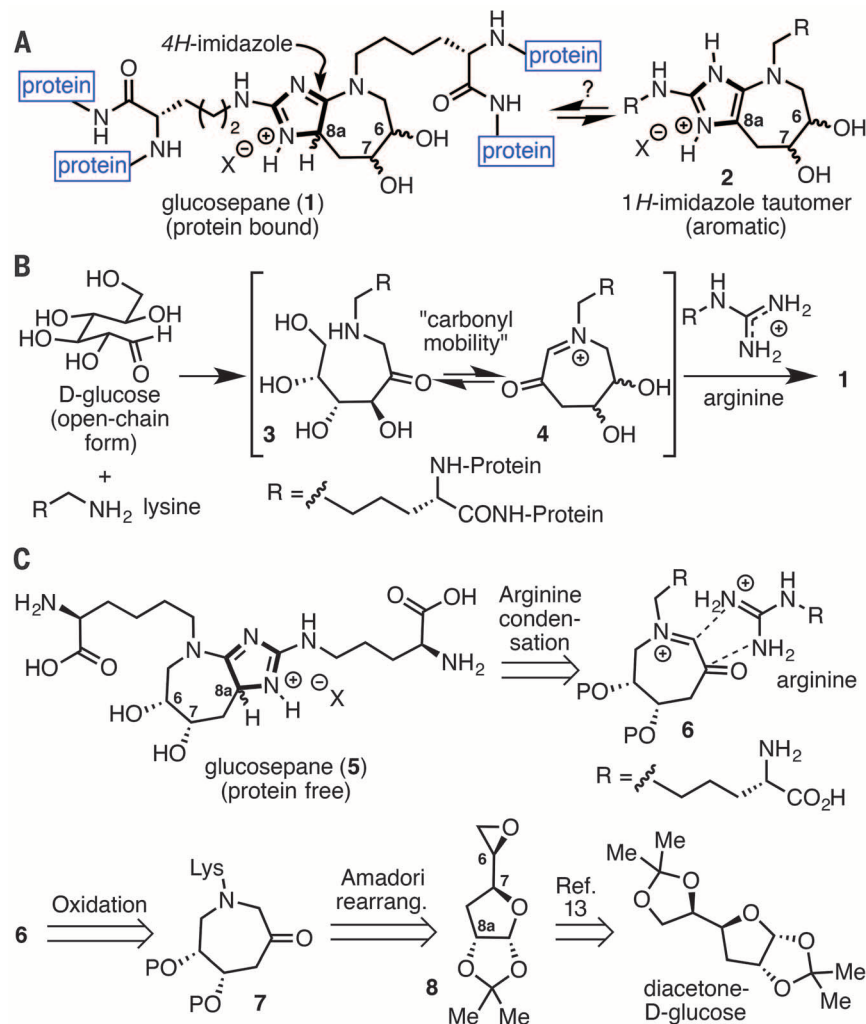


Fig. 1. Glucosepane and the 4H-imidazole. (A) Chemical structure of the protein-bound glucosepane cross-link, depicting both nonaromatic 4H-imidazole (**1**) and aromatic 1H-imidazole (**2**) tautomers. (B) Proposed biosynthetic pathway for glucosepane cross-links. (C) Retrosynthetic analysis employed in this work for glucosepane total synthesis.

Table 1. Results from DFT calculations comparing energies of various tautomerization states of protonated imidazoles. ΔG , Gibbs free energy; Me, methyl.

Entry	X	Y	ΔG (kcal/mol) ^a
1	H	H	26.7
2	H	NHMe	10.5
3	NMe ₂	H	-1.5
4	NMe ₂	NHMe	-14.8

^aAll calculations were performed using the Gaussian 09 program suite using the CBS-QB3 method. All calculations implemented a continuum model to account for the effects of water solvent.

We recognized that an intramolecular oxidation transfer process, by way of a [3,3]-sigmatropic rearrangement from semicarbazone tautomer **19**, would afford an intermediate (**20**) with the same core oxidation state as α -keto iminium **16** (Fig. 3B). Furthermore, **20** also contains a tethered guanidine function that is perfectly poised for subsequent intramolecular cyclization and tautomerization to afford the glucosepane core. We reasoned that simple condensation of lysine-derived ketone **14** with semicarbazide derivatives (Fig. 3C) would permit rapid access to semicarbazone **19**, which is capable of tautomerizing to the desired [3,3] rearrangement substrate (**20**). In this sense, **20** would function as a masked version of α -keto iminium **16**, possessing the correct oxidation state and functional group disposition to afford the desired 4*H*-imidazole **18**. We were encouraged by previous reports of analogous hetero-Claisen rearrangements (*19–23*). On the whole, we envisioned that this sequence would accomplish the goal of directly coupling the oxidation and condensation steps, thus solving the problems associated with our intermolecular-trapping sequence.

With this analysis in mind, we began with the condensation of thiomethyl semicarbazone **22** with ketone **14**, which proceeded smoothly to afford semicarbazone **24** (as a mixture of *E/Z* isomers) in 78% yield (Fig. 4A). After several failed attempts, we discovered that treating semicarbazone **24** with excess chlorotrimethylsilane (TMSCl) in anhydrous, refluxing chloroform induced the formation of 4*H*-thioimidazole **26**. We believe that this material forms via the pathway predicted in Fig. 3C—by way of tautomerization, [3,3]-sigmatropic rearrangement, and

cyclodeamination—and is accompanied by acetone removal, which likely results from HCl generated by aqueous quenching of excess TMSCl. Compound **26** was isolated as an epimeric mixture at C-8a, as confirmed by NMR analysis (*24*). Our attempts to purify 4*H*-thioimidazole **26** under open atmosphere led only to the isolation of C-8a-

oxidized product **27**. By displacing the thiomethyl group with an ornithine derivative followed by C-8a reduction using Na(OAc)₃BH (OAc, acetate), we were able to access protected glucosepane **28** as a 4:1 mixture of epimers.

Despite this result, we sought a more concise route to intermediate **28**. Replacement of **22** in

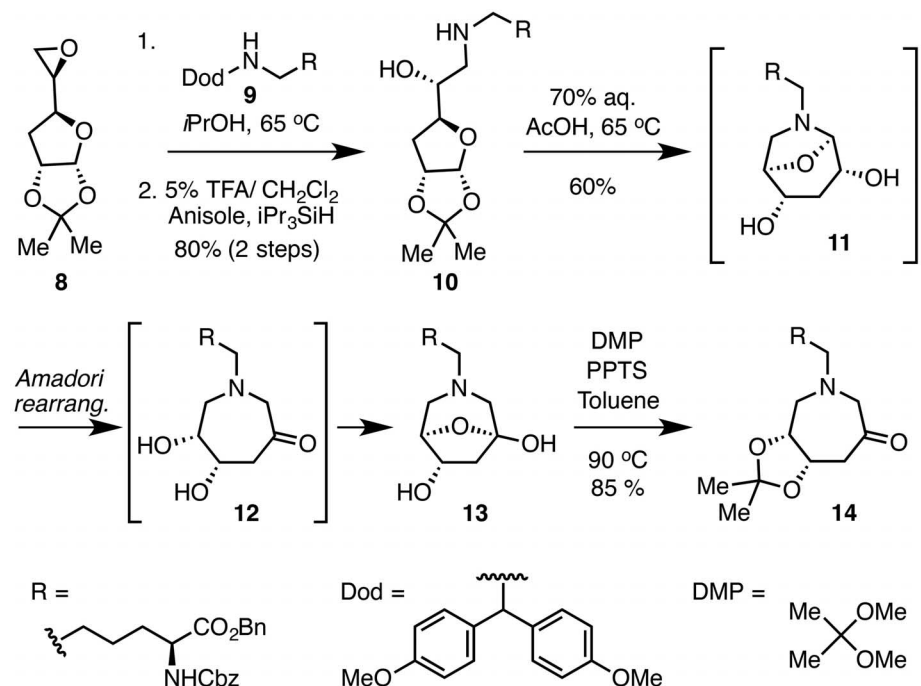


Fig. 2. Preparation of the lysine-derived azepane intermediate (**14**). iPr, isopropyl; PPTS, pyridinium *p*-toluenesulfonate; Cbz, carboxybenzy.

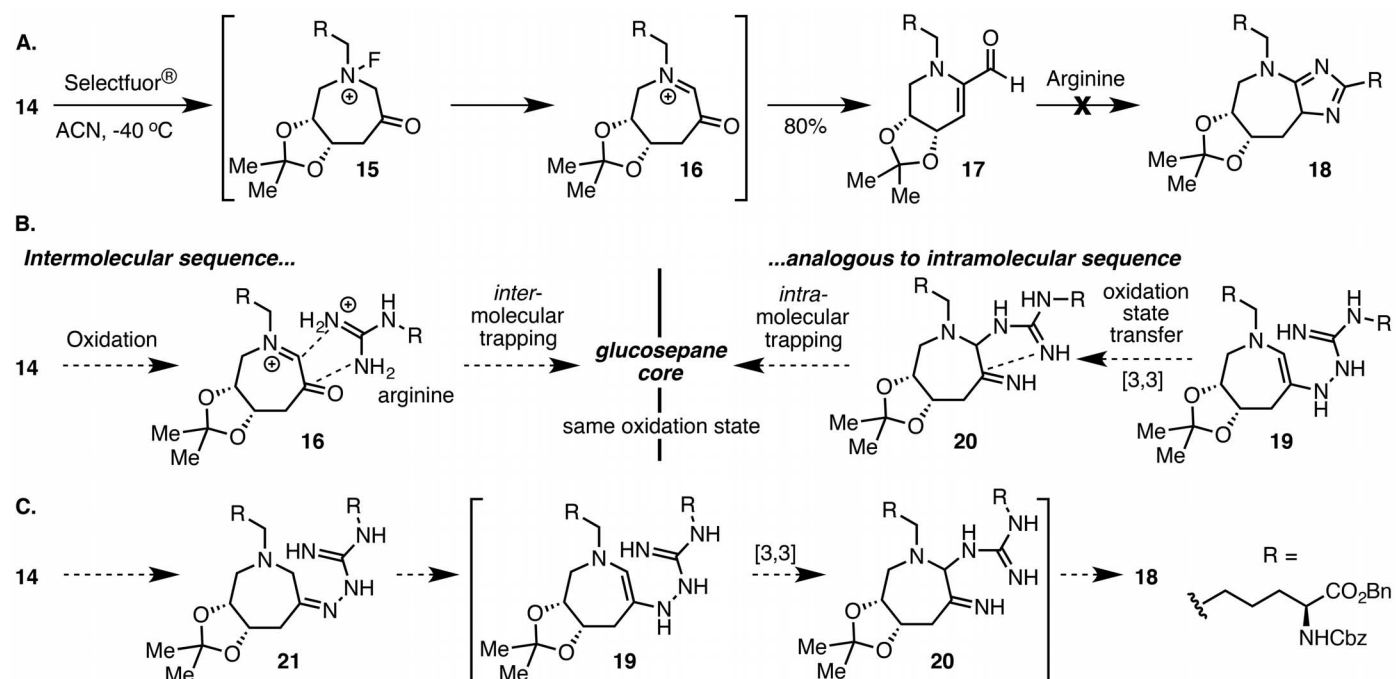


Fig. 3. Synthesis of glucosepane's 4*H*-imidazole core. (A) Attempted oxidation-trapping sequence. (B) Reformulation of the synthetic sequence in terms of sequential sigmatropic rearrangement and cyclization reactions. (C) Mechanistic details of the proposed sigmatropic rearrangement-cyclization sequence.

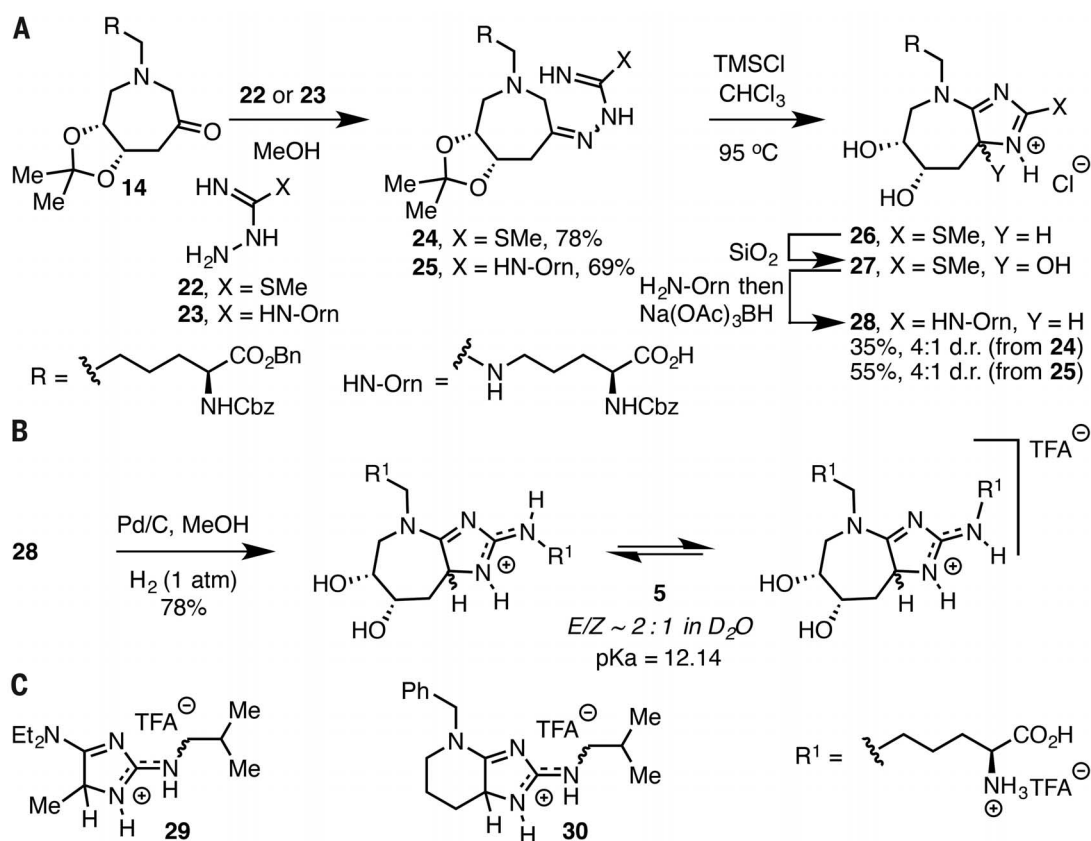


Fig. 4. Completion of the synthesis. (A) Formation of glucosepane's 4*H*-imidazole core using a cascade [3,3]-sigmatropic rearrangement-and-cyclization sequence. (B) Completion of the total synthesis and characterization of synthetic glucosepane. (C) 4*H*-imidazoles prepared using our sequence. d.r., diastereomeric ratio; Et, ethyl.

this sequence with a fully elaborated arginine derivative (**23**) readily afforded **25** in good yield (69%), and this intermediate also underwent the desired rearrangement, cyclization, and acetonide removal sequence. Therefore, this sequence furnished fully protected glucosepane derivative **28** in a 4:1 diastereomeric ratio in a single synthetic step.

With backbone-protected glucosepane in hand, completion of the synthetic sequence proved straightforward (Fig. 4B). Global hydrogenolytic deprotection of carboxybenzyl and benzyl ester protecting groups was achieved using palladium on carbon under an atmosphere of hydrogen gas and either trifluoroacetic acid (TFA) or formic acid, enabling rapid access to **5** as either the formate or TFA salt. Although two C-8a epimers are produced in a 4:1 ratio via this route, these can be separated by preparative HPLC. Spectral data obtained from ^1H and ^{13}C NMR experiments using synthetic **5** proved identical to that reported by Lederer and colleagues for material isolated from model reactions (II). Overall, the full synthetic route proceeded in a total of eight steps and 12% overall yield.

To provide further experimental evidence that 2,5-diaminoimidazoles adopt the 4*H*-imidazole tautomer, we applied our newly developed rearrangement to the synthesis of two additional 2,5-diaminoimidazoles (**29** and **30**) (Fig. 4C) (**25**). These compounds were prepared in two steps from commercially available starting materials and, as expected, adopted the 4*H*-imidazole tautomer exclusively, based on NMR analysis. These

results support our computational data and confirm that imidazoles with electron-rich amino substituents at the 2 and 5 positions are more stable as the 4*H*-imidazole tautomer.

With synthetic glucosepane (**5**) in hand, we used multidimensional NMR techniques to investigate its structural features. Two-dimensional ^1H NMR nuclear Overhauser effect spectroscopy (NOESY) experiments with compound **5** revealed the presence of conformational exchange peaks (26), which we attribute to E/Z isomerization about the exocyclic C2-N bond in glucosepane. Although the original glucosepane isolation report noted the possibility of E/Z isomerism in acyclic 2-amino imidazoles, the presence of these exchange peaks in the case of glucosepane had previously been incorrectly attributed to stereoisomerism at the C-8a stereocenter (27). Using an exchange spectroscopy NOESY sequence (fig. S1) (26), we were able to calculate an approximate rate for this conformational exchange process on the order of 3 s^{-1} in D_2O (24).

We next took advantage of glucosepane's intrinsic spectral properties to measure the pK_a (K_a , acid dissociation constant) of the 4*H*-imidazole core (fig. S2). These experiments revealed compound **5** to possess only one basic site under aqueous conditions with a pK_a of ~ 12 , which we believe to reflect protonation at the 4*H*-imidazole N1 atom, consistent with both NMR data and density functional theory (DFT) calculations (24). Exposure of either epimer of **5** to D_2O leads to quantitative hydrogen-deuterium exchange at the C-8a H atom, which occurs rapidly (< 60 min)

under basic conditions (aqueous NaOD). Taken together, these studies suggest that glucosepane contains both acidic and basic sites, the latter of which possesses a pK_a quite close to that of native arginine ($\text{pK}_a = 12.5$).

We believe that the brevity and modularity of our synthesis will render it compatible with the site-specific incorporation of glucosepane into synthetic oligopeptides, preparation of affinity reagents to identify molecular targets of glucosepane, development of immunogens for raising antibodies against glucosepane, and perhaps also the identification of novel therapeutic strategies for breaking glucosepane cross-links.

REFERENCES AND NOTES

- C. T. Walsh, S. Garneau-Tsodikova, G. J. Gatto Jr., *Angew. Chem. Int. Ed. Engl.* **44**, 7342–7372 (2005).
- R. Singh, A. Barden, T. Mori, L. Beilin, *Diabetologia* **44**, 129–146 (2001).
- V. M. Monnier et al., *Clin. Chem. Lab. Med.* **52**, 21–32 (2014).
- M. Hellwig, T. Henle, *Angew. Chem. Int. Ed.* **53**, 10316–10329 (2014).
- K. M. Biemel, D. A. Friedl, M. O. Lederer, *J. Biol. Chem.* **277**, 24907–24915 (2002).
- K. M. Biemel, H. P. Bühler, O. Reihl, M. O. Lederer, *Nahrung* **45**, 210–214 (2001).
- V. M. Monnier et al., *J. Diabetes Complications* **27**, 141–149 (2013).
- J. S. Sjöberg, S. Bulterijs, *Rejuvenation Res.* **12**, 137–148 (2009).
- X. Fan et al., *Free Radic. Biol. Med.* **49**, 847–856 (2010).
- D. R. Sell et al., *J. Biol. Chem.* **280**, 12310–12315 (2005).
- K. M. Biemel, J. Conrad, M. O. Lederer, *Angew. Chem. Int. Ed. Engl.* **41**, 801–804 (2002).

12. A. N. Chermahini, B. Hosseinzadeh, A. S. Beni, A. Teimouri, *Comput. Theor. Chem.* **994**, 97–104 (2012).
13. A. P. Rauter et al., *Tetrahedron Asymmetry* **12**, 1131–1146 (2001).
14. The full synthetic sequence from diacetone- β -glucose to epoxide **8** is presented in detail in the supplementary materials.
15. Analysis of the crude reactions always showed 15 to 20% of hemiaminal present, even after prolonged exposure to reaction conditions.
16. J. E. Hodge, C. E. Rist, *J. Am. Chem. Soc.* **75**, 316–322 (1953).
17. E. M. Sánchez-Fernández, E. Álvarez, C. Ortiz Mellet, J. M. García Fernández, *J. Org. Chem.* **79**, 11722–11728 (2014).
18. Z. Dai et al., *J. Proteome Res.* **7**, 2756–2768 (2008).
19. M. J. Martin, L. J. Dorn, J. M. Cook, *Heterocycles* **36**, 157–189 (1993).
20. Z. Rappaport, J. F. Liebman, Eds., *The Chemistry of Hydroxylamines, Oximes and Hydroxamic Acids* (Wiley, Chichester, UK, 2008), vol. 175.
21. A. J. Lawson, *J. Chem. Soc. Chem. Commun.* **1979**, 456 (1979).
22. L. E. Overman, *Angew. Chem. Int. Ed. Engl.* **23**, 579–586 (1984).
23. R. M. Aranha, A. M. Bowser, J. S. Madalengoitia, *Org. Lett.* **11**, 575–578 (2009).
24. See the supplementary materials for more information.
25. The full synthetic sequence to 4*H*-imidazoles **29** and **30** is presented in detail in the supplementary materials.
26. C. L. Perrin, T. J. Dwyer, *Chem. Rev.* **90**, 935–967 (1990).
27. M. O. Lederer, F. Gerum, T. Severin, *Bioorg. Med. Chem.* **6**, 993–1002 (1998).

ACKNOWLEDGMENTS

We thank the SENS Foundation for financial support and G. Micalizio, A. de Grey, and W. Bains for helpful discussions.

SUPPLEMENTARY MATERIALS

www.sciencemag.org/content/350/6258/294/suppl/DC1
Materials and Methods
Supplementary Text
Figs. S1 to S5
Tables S1 to S11
References (28–32)
Spectral Data

6 July 2015; accepted 8 September 2015
10.1126/science.aac9655

CATALYSIS

Hydrogenation of carboxylic acids with a homogeneous cobalt catalyst

Ties J. Korstanje, Jarl Ivar van der Vlugt, Cornelis J. Elsevier,* Bas de Bruin*

The reduction of esters and carboxylic acids to alcohols is a highly relevant conversion for the pharmaceutical and fine-chemical industries and for biomass conversion. It is commonly performed using stoichiometric reagents, and the catalytic hydrogenation of the acids previously required precious metals. Here we report the homogeneously catalyzed hydrogenation of carboxylic acids to alcohols using earth-abundant cobalt. This system, which pairs $\text{Co}(\text{BF}_4)_2 \cdot 6\text{H}_2\text{O}$ with a tridentate phosphine ligand, can reduce a wide range of esters and carboxylic acids under relatively mild conditions (100°C, 80 bar H_2) and reaches turnover numbers of up to 8000.

There is great interest among the pharmaceutical and fine-chemical industries in finding more sustainable methods to reduce moieties such as esters and carboxylic acids to alcohols. In the emerging field of biomass feedstock conversion to produce high-value chemicals, the reduction of these abundantly available oxygen-containing functional groups is also of crucial importance. Traditionally, esters and carboxylic acids are reduced using stoichiometric reagents, such as aluminum- or borohydrides, but these pose an inherent safety risk and produce large amounts of waste material (1). Selective catalytic hydrogenation of esters and carboxylic acids to the corresponding alcohols could facilitate the synthesis of many products in various sectors of the chemical industry; for instance, it could facilitate the conversion of (biomass-derived) succinic acid into the bulk chemicals 1,4-butanediol, tetrahydrofuran (THF), or γ -butyrolactone, which can be used as solvents and as intermediates for the production of plastics and fibers (2). Also, numerous pharmaceuticals require a selective hydrogenation step of either an ester or a carboxylic acid moiety in their synthetic route (3).

The catalytic hydrogenation of esters and carboxylic acids is performed industrially by using heterogeneous catalysts that typically operate at

high temperatures and pressures (4). A milder enzymatic hydrogenation route using *Pyrococcus furiosus* cells has been reported recently (5). In recent years, however, much progress has also been made with using homogeneous catalysts for the hydrogenation of esters and acids under mild reaction conditions (6–8). Thus far, primarily ruthenium-based catalysts, in combination with multidentate ligands such as triphos [tridentate phosphine, $\text{CH}_3\text{C}(\text{CH}_2\text{PPh}_2)_3$] (9–12) or PNN pinners (PNN, 2-di-*tert*-butylphosphinomethyl-6-diethylaminomethylpyridine) (13–15), have been used for the hydrogenation of esters. Carboxylic acids, however, are difficult to hydrogenate in comparison with ketones and esters. Ligand protonation and resultant ligand dissociation, combined with overcoordination of the generated vacant sites at the metal center by the (bidentate) carboxylate conjugated base, result in detrimental catalyst deactivation. These pathways are especially problematic with first-row transition metals, which typically have weaker metal-ligand bonds than their second- and third-row congeners. To date, homogeneously catalyzed hydrogenation of carboxylic acids has only been achieved with two systems: a ruthenium/triphos system (16–19) and an iridium/bipyridine system (20, 21). Although these systems provide good activity and selectivity, the replacement of the scarce and expensive noble metals by cheaper, more abundant, and less toxic first-row transition metals, such as iron or cobalt, would enhance the sustainability of these hydrogenation reactions (Fig. 1). Recently,

iron-based catalysts for the hydrogenation of esters have been reported (22–24). Here we present a cobalt-based catalytic system capable of hydrogenating both esters and carboxylic acids to the corresponding alcohols, using H_2 as the reductant. The catalyst is generated in situ from a $\text{Co}(\text{BF}_4)_2 \cdot 6\text{H}_2\text{O}$ precursor and the triphos ligand, which are both commercially available, making this method highly suitable for use in practical organic synthesis and biomass conversion.

Initially, various cobalt precursors were tested, in combination with the triphos ligand, in the hydrogenation of methyl benzoate to yield benzyl alcohol and methanol. Combining methyl benzoate with 10 mole percent (mol %) of the metal precursor and the triphos ligand in distilled methanol, under 80 bar of initial H_2 pressure and at a 100°C reaction temperature, produced only minor amounts of alcohol with cobalt(III) acetylacetonate, cobalt(II) acetylacetonate, and cobalt(II) acetate (table S1). Using $\text{Co}(\text{BF}_4)_2 \cdot 6\text{H}_2\text{O}$ as the metal precursor resulted in almost full substrate conversion within 5 hours, providing the desired benzyl alcohol in excellent yield. Decreasing the catalyst loading to 5 mol % resulted in full conversion within 22 hours, with a good yield of benzyl alcohol. Lower catalyst loadings required very long reaction times (2 mol %, 94 hours) or led to lower overall activity (1 mol %). Based on this initial catalyst optimization, the substrate scope of the $\text{Co}(\text{BF}_4)_2 \cdot 6\text{H}_2\text{O}$ and triphos (Co/triphos) hydrogenation system was investigated (Table 1 and table S2). Using *tert*-butylbenzoate, an ester substrate that has low activity with many catalysts due to the steric hindrance of the *tert*-butyl group, full conversion was obtained within 5 hours. Also, with aliphatic esters such as methyl butyrate and methyl 3-*trans*-hexenoate, good yields of the fully reduced corresponding alcohol were obtained within 22 hours. Hydrogenation of γ -valerolactone, a substrate that can easily be obtained from biomass and, as such, is of interest for biomass valorization, produced 2-methyltetrahydrofuran and 1,4-pentanediol in good yields. These products have attracted attention for their respective applications as a fuel additive and as a monomer for polyester production (2). A long-chain fatty acid methyl ester and even a triglyceride could also be smoothly hydrogenated to obtain the corresponding reduced fatty alcohol in good yields, using the Co/triphos system.

Van 't Hoff Institute for Molecular Sciences, University of Amsterdam, Science Park 904, 1098 XH Amsterdam, Netherlands.
*Corresponding author. E-mail: c.j.elsevier@uva.nl (C.J.E.); b.debruin@uva.nl (B.d.B.)

The successful application of the Co/triphos system for ester hydrogenation led us to investigate its efficacy in the more challenging conversion of carboxylic acids (Table 2). Using benzoic acid as the substrate, with 2.5 mol % catalyst loading and THF as the solvent (to prevent in situ esterification and

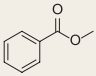
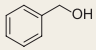
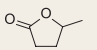
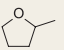
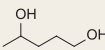
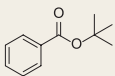
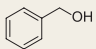
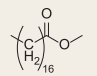
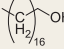
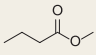
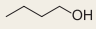
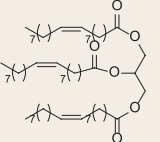
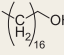
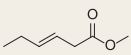
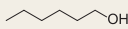
thus to ensure that the system is truly hydrogenating acids), benzyl alcohol was obtained in good yield within 22 hours. Removal of any remaining acid starting material and the majority of the catalyst can be easily accomplished by washing with a saturated aqueous sodium carbonate solution.

Further purification using column chromatography yielded the isolated alcohol product. Increasing the catalyst loading to 5 mol % led to full conversion after 4 hours, compared with 22 hours for methyl benzoate. This indicates that hydrogenation of carboxylic acids with the Co/triphos system outcompetes the conversion of the corresponding carboxylic esters, which is surprising, considering the difficulties associated with hydrogenating carboxylic acids in most systems. The system tolerates several functional groups, such as chlorides, fluorides, trifluoromethyls, and hydroxides, which can be used for further synthetic processing, such as C-C cross-coupling. More labile groups such as bromide, iodide, boronate, and methoxy functionalities undergo (partial) defunctionalization, but they do not hamper the reactivity (table S3).

Furthermore, the catalytic system is capable of hydrogenating a wide scope of carboxylic acid substrates, including aromatic and long- and short-chain aliphatic acids, all of which are smoothly hydrogenated to the corresponding alcohols. From a biomass viewpoint, the direct hydrogenation of levulinic acid to 2-methyltetrahydrofuran and 1,4-pentanediol is relevant, because it eliminates the need to isolate γ -valerolactone as the cyclic ester intermediate. The hydrogenation of succinic acid is also of interest, because it produces 1,4-butanediol, which is a comonomer in the production of polyesters such as polybutylene terephthalate. Furthermore, polymerization of 1,4-butanediol with (potentially biomass-derived) succinic acid constitutes a completely biomass-derived route to polybutylene succinate. In our system, short-chain acids are hydrogenated more easily than long-chain acids, which is in agreement with previous research on acid hydrogenation (20). Moreover, it is possible to reduce the liquid acids under solventless conditions, allowing low catalyst loadings (down to 0.1 mol %) for butyric acid and acetic acid, while still giving good yields of 1-butanol and ethanol, respectively. Under these conditions, esterification of the carboxylic acid starting material by the alcohol product also takes place, as demonstrated by the observation of butyl butyrate and ethyl acetate, respectively. When using formic acid or trifluoroacetic acid, neat conditions did not produce any alcohol, probably because of the high polarity of these acids. With THF as the solvent, however, a very low catalyst amount of 125 parts per million can be used for trifluoroacetic acid, while still reaching full conversion in 22 hours and giving a good yield of 50% of trifluoroethanol (the remaining mass balance consists of trifluoroethyl trifluoroacetate and an unidentified side product). Hydrogenation of formic acid in THF also proceeds smoothly, but it requires a somewhat higher catalyst loading of 0.25 to 0.5 mol %.

In comparison with the reported *P. furiosus* biocatalytic system (5), which uses a reaction temperature of 40°C and 5 bar H₂ pressure, our system generally has a lower activity and requires harsher reaction conditions; however, it is able to convert a much wider substrate scope and can obtain higher conversions of the carboxylic acid within the same period of time. Relative to our

Table 1. Hydrogenation of esters using Co(BF₄)₂·6H₂O and triphos. General conditions used, unless otherwise noted, were 0.15 M substrate, 1:1 ratio of Co(BF₄)₂·6H₂O and triphos (mol % loading shown), distilled MeOH, 80 bar initial H₂ pressure, 100°C, 22 hours. In the substrate columns, catalyst amounts are given per ester group, and in the product columns, conversions are given with gas chromatography (GC) yields in parentheses.

Substrate	Product	Substrate	Product(s)
			 
10% (5h)	98 (95)	10%	98 (ether: 25, diol: 63)
5%	99 (79)		
			
10%	>99 (98)	10%	86 (75)
			
5%	50 (47)	10%	>75 (72)
			
10%	>99 (90)		

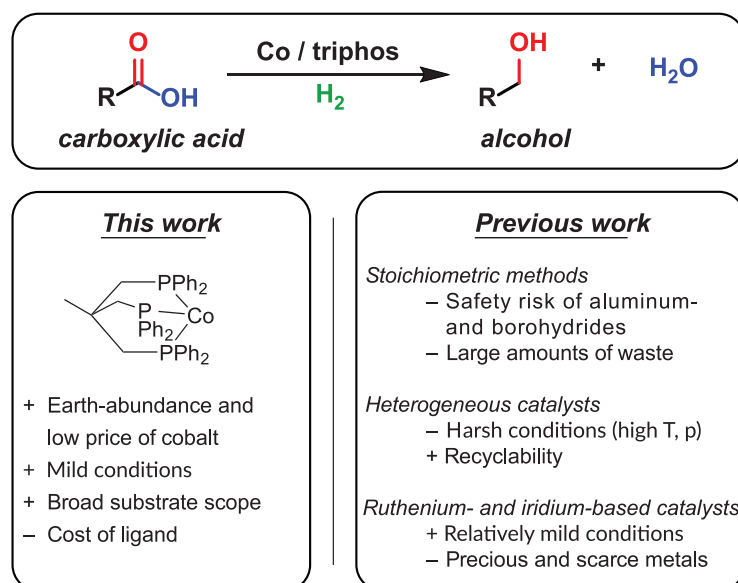


Fig. 1. Hydrogenation of carboxylic acid to alcohol. Advantages and drawbacks of previous approaches are compared with those of our catalytic system.

system, noble metal-based heterogeneous catalysts such as Ru-Sn/Al₂O₃ (25) and Pt-Re/TiO₂ (26), operating at temperatures of 240° and 130°C and pressures of 80 and 20 bar, respectively, give slightly lower conversions (82%), higher turnover numbers of stearic acid (512 and 97, respectively), and a lower selectivity due to the formation of decarboxylation and dehydration products. Furthermore, leaching of tin occurs when using the former catalyst, which is highly undesirable for a pharmaceutical application, and the Pt-Re/TiO₂ catalyst suffers from aromatic ring hydrogenation when using aromatic substrates. In comparison with previously reported homogeneous catalysts, our cobalt-based system outperforms both the ruthenium- and iridium-based systems for acid hydrogenation (19, 20): The ruthenium-based system operates at much higher temperatures (140° to 220°C) and with higher catalyst loadings (>2 mol %) than our system, and the iridium-based system requires a higher reaction temperature (120° versus 100°C) and much longer reaction times (65 versus 22 hours) to produce similar turnover numbers with acetic acid (777 for iridium versus 780 for cobalt).

To investigate the specificity of the triphos ligand, different ligand systems were tested. The tetradentate analog tetraphos [P(CH₂CH₂PPh₂)₃], known to be active in CO₂ hydrogenation in combination with cobalt (27), did not show any activity in ester hydrogenation. In addition, the combination of various bidentate phosphines with monodentate phosphines did not show any reactivity for either esters or acids. The influence of additives was investigated, but neither acid nor base had a positive effect on the reactivity in the ester hydrogenation reaction, nor did an additional reducing agent, such as zinc dust (10). The analogous cobalt precursor [Co(NCCH₃)₆](BF₄)₂, in combination with triphos, also did not show any activity in ester or acid hydrogenation under dry conditions. However, when methyl benzoate was used as the substrate, the activity was restored by adding six equivalents of water (relative to the catalyst), and [Co(THF)₆](BF₄)₂ showed carboxylic acid conversion under dry conditions. The inactivity of the [Co(NCCH₃)₆](BF₄)₂ precursor in the absence of water was probably caused by the stronger coordination of the acetonitrile ligands, which hamper reactivity under dry conditions.

The known dinuclear cobalt trihydride complex [Co₂(triphos)₂(μ-H)₃](BF₄)₂ was found to be inactive in this reaction. The inactive cobalt precursor Co(OAc)₂·4H₂O (OAc, acetate) could be activated by the addition of two equivalents of BF₃·OEt₂ (OEt₂, diethylether) or by the addition of various noncoordinating salts, such as HBF₄, NaSBF₆, or LiB(C₆F₅)₄. In contrast, the addition of NaBF₄, NaPF₆, or NaBPh₄ did not provide this activating effect. The addition of BF₃·OEt₂ or HBF₄ however, does not improve the activity in the case of the Co(BF₄)₂·6H₂O precursor. Furthermore, the addition of other Lewis acids, such as scandium (III) triflate or iron(III) chloride, had a detrimental effect on the reactivity of the Co/triphos system. This indicates that a noncoordinating anion is required to provide catalytic activity, although

further research is required to completely explain the observed counterion effect.

To further investigate the reaction mechanism, we performed partial poisoning studies using TEMPO (2,2,6,6-tetramethylpiperidine-1-oxyl) as a radical inhibitor and TMTU (tetramethylthiourea) as a strongly binding poison (28). With both reagents, the reaction was completely inhibited by one equivalent per catalyst, and for TMTU, only half an equivalent was sufficient (fig. S1). This suggests that TMTU deactivates two cobalt centers, either by acting as a bridging poison ligand or by acting on a dinuclear cobalt species, whereas TEMPO poisons a monomeric cobalt species. Furthermore, this result excludes the formation of nanoparticles

as the active catalyst, because this would require a much lower amount of poison for full inhibition of the catalysis (29). This result is consistent with a mercury poison test, which did not show any considerable inhibition of the catalysis.

We studied the reaction further by means of high-resolution electron spray ionization mass spectrometry (ESI-MS). Using benzoic acid as the substrate, a catalytic sample was analyzed after 1 hour of reaction time; the major signal detected (mass/charge ratio = 804.1875) has a mass consistent with that of a [Co(triphos)(benzoate)]⁺ species (fig. S2). The same species was detected upon separately mixing the cobalt precursor, triphos, and benzoic acid in a 1:1:1 ratio and heating

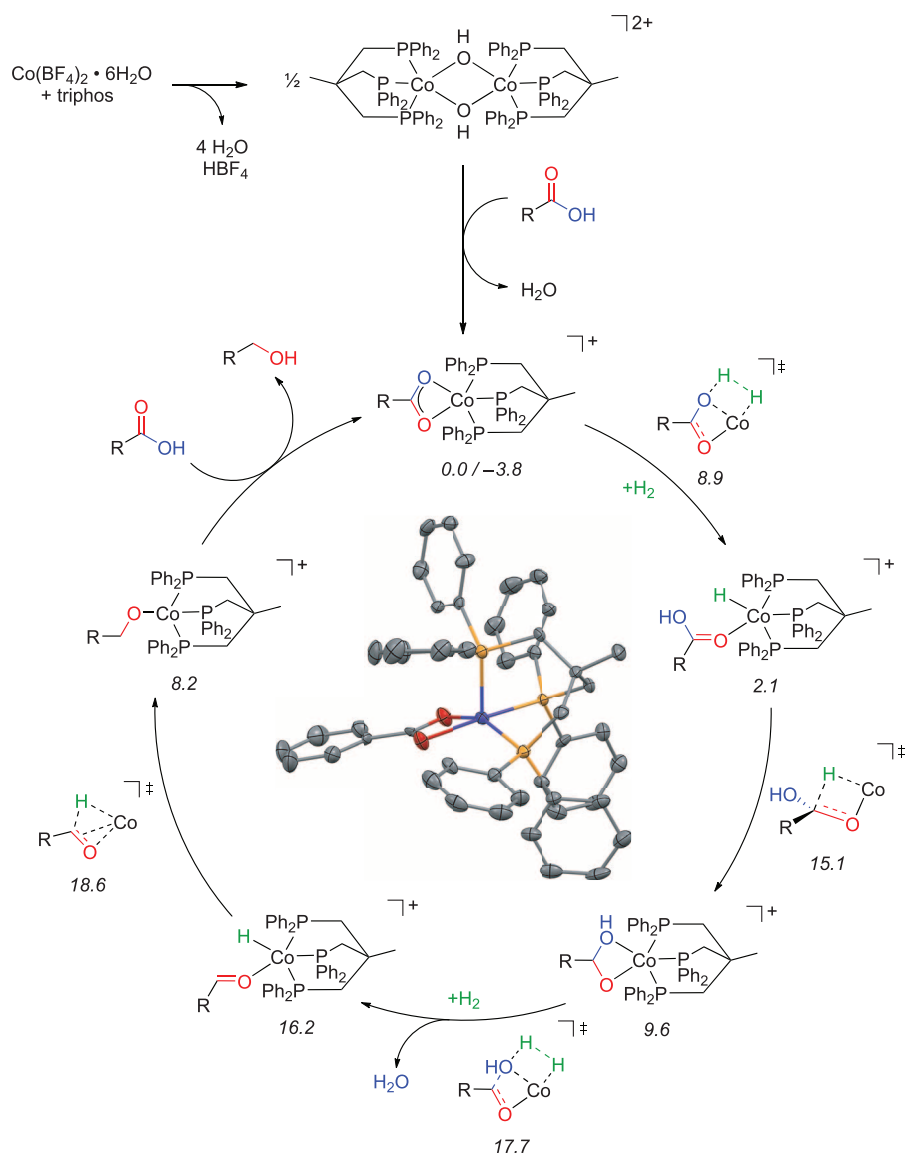


Fig. 2. Proposed mechanism for the Co/triphos-catalyzed hydrogenation of carboxylic acids to alcohols. BF₄ anions are omitted for clarity. The central area shows the crystal structure of the proposed resting state, [Co(triphos)(κ²-OOCPh)]⁺. The numbers below the structures indicate the relative enthalpies (kcal mol⁻¹) at 373 K, obtained from dispersion-corrected density functional theory (DFT-D3), using the BP86 functional, def2-TZVP basis set, and Grimme's version 3 dispersion corrections (disp3). Colors in the central structure correspond to cobalt (blue), oxygen (red), phosphorus (yellow), and carbon (gray).

this mixture briefly under an inert atmosphere. Because ESI-MS does not provide information on the oxidation state, we also performed in situ electron paramagnetic resonance (EPR) spectroscopy. The catalytic reaction was carried out in a high-pressure EPR tube, using 2-methyltetrahydrofuran as the solvent (to obtain a good glass) and 15 bar of H₂ pressure, followed by rapid cooling of the reaction mixture from 100° to -198°C (76 K) after 2 hours of reaction time. The EPR tube was subsequently cooled to 20 K in the EPR cavity to record the EPR spectrum. Two signals were observed: a broad signal, arising from a high-spin species (electron spin, $S = 3/2$) and a well-defined signal from a low-spin species ($S = 1/2$) with a complex hyperfine coupling pattern due to coupling with cobalt (nuclear spin, $I = 7/2$) and three phosphorus atoms ($I = 1/2$) (fig. S3). The high-spin species originated from a small excess amount of Co(BF₄)₂·6H₂O, whereas the low-spin species

produced an identical signal to that of an independently prepared 1:1:1 mixture of Co(BF₄)₂·6H₂O, triphos, and benzoic acid (fig. S2). This confirms the results obtained by ESI-MS and also shows that the cobalt center in this species remains in the +2 oxidation state. Based on these results, we propose the mechanism depicted in Fig. 2.

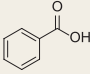
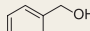
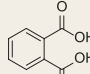
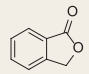
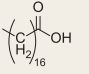
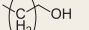
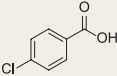
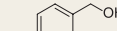
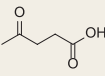


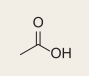
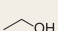
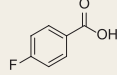
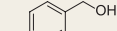
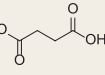
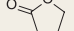
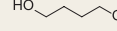
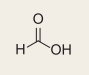
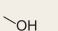
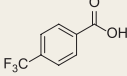
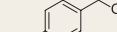
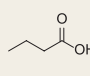
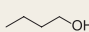
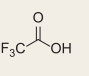
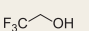
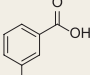
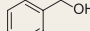
The proposed mechanism starts with the formation of a precatalytic species, [Co₂(triphos)₂(μ-OH)₂](BF₄)₂, which is known to form spontaneously when Co(BF₄)₂·6H₂O and triphos are mixed (30). This dimer is split by the substitution of the hydroxyl ligand for an alkanooate, producing the catalytically active species [Co(triphos)(alkanoate)] BF₄, which is observed in EPR and ESI-MS and is known to be a stable species (30). By means of slow vapor diffusion of diethyl ether into a CH₂Cl₂ solution of the complex, we were also able to obtain single crystals that enabled x-ray crystal structure determination of this species as the

BPh₄ salt. The complex was prepared by mixing Co(BF₄)₂·6H₂O, triphos, and benzoic acid in a 1:1:1 ratio in THF, followed by the addition of NaBPh₄ in a 10-fold excess amount. The x-ray crystal structure (Fig. 2 and table S5) shows the expected bidentate (κ^2) binding mode of the benzoate and a slightly distorted square pyramidal structure around the cobalt center [$\tau = 0.11$ (37)], as expected for a low-spin cobalt(II) species. This species produces the same EPR spectrum as the catalytic mixture, confirming the Co(triphos)(κ^2 -alkanoate) species as the resting state, but it was found to be inactive in catalysis because of the presence of the BPh₄ anion [which has a deactivating effect on catalysis, as we also observed when NaBPh₄ was added to the catalytically active 1:1 mixture of triphos and Co(BF₄)₂·6H₂O].

From this Co(triphos)(κ^2 -alkanoate) species, we propose that initial heterolytic hydrogen splitting occurs over the Co-O bond, followed by the migratory insertion of the hydride into the carbonyl carbon and a second heterolytic hydrogen splitting step over the cobalt(II) hydroxyalkanoate intermediate, thereby expelling one equivalent of water and producing the [Co(triphos)(H(aldehyde))] species (32). A final hydride migration step, followed by proton transfer and ligand exchange with another carboxylic acid substrate, gives the desired alcohol and regenerates the active catalyst. This mechanism fits the ESI-MS and EPR results that show [Co(triphos)(OOCR)]⁺ as the resting state under catalytic conditions, and it also correlates well with the quantitative poisoning studies. The proposed mechanism is also supported by density functional theory (DFT) calculations (performed on the complete system, using acetic acid as the substrate; Fig. 2 and figs. S4 and S5), showing that the (lowest-energy) resting state is the Co(triphos)(κ^2 -alkanoate) species. The overall calculated reaction barrier is 18.6 kcal mol⁻¹, which is a reasonable energy barrier for a reaction proceeding smoothly at 100°C. The rate-determining transition state involves hydride migration to the coordinated aldehyde, whereafter energetically favorable steps occur involving proton transfer and exchange of the product for a carboxylic acid substrate, thus resulting in an overall mildly exothermic reaction (-3.8 kcal mol⁻¹).

The results presented here describe the first catalytic system based on a cheap and abundant first-row transition metal that is capable of hydrogenating carboxylic acids to the corresponding alcohols, using molecular hydrogen as the reductant. Insight into the mechanism of this system was obtained by means of ESI-MS, in situ EPR, x-ray crystallography, and DFT calculations, all of which support a Co(triphos)(κ^2 -alkanoate) resting state. The DFT calculations suggest a mechanism that involves heterolytic H₂ splitting over cobalt(II) alkanooate and cobalt(II) hydroxyalkanoate intermediates as key steps in the catalytic cycle.

Table 2. Hydrogenation of carboxylic acids using Co(BF₄)₂·6H₂O and triphos. General conditions used, unless otherwise noted, were 0.15 M substrate, 1:1 ratio of Co(BF₄)₂·6H₂O and triphos (mol % loading shown), distilled THF, 80 bar initial H₂ pressure, 100°C, 22 hours. In the substrate columns, catalyst amounts are given per acid group, and in the product columns, conversions are shown with GC yield/isolated yield in parentheses.

Substrate	Product	Substrate	Product(s)	Substrate	Product
					
5% (4h)	>85 (65)	2.5%	>99 (71)	5%	95 (92)
2.5%	>85 (62 / 39)				
			 		
5%	>99 (82 / 70)	10%	>99 (ether: 14, diol: 47)	0.25%*	94 (81)
				0.1%*	78 (48 [‡])
			 		
5%	>99 (96 / 84)	2.5%	>85 (lactone: 23, diol: 61)	0.5%	>99 (76)
				0.25%	56 (22 [‡])
					
5%	98 (98 / 82)	5%	>99 (95)	125 ppm	97 (50 ^{ll})
		0.1%*	53 (17 / 5 [†])		
					
5%	>90 (89 / 66)				

*Neat conditions. †36% GC yield and 24% isolated yield of butyl butyrate obtained. Isolated yields shown here are the amounts present in the isolated mixture of 1-butanol and butyl butyrate, because it proved difficult to separate these compounds by distillation (probably because of azeotrope formation). ‡31% ethyl acetate obtained. §29% methyl formate formed. ||Based on fluorine-19 nuclear magnetic resonance. Mass balance is completed by an unknown side product.

REFERENCES AND NOTES

- J. Seyden-Penne, *Reductions by the Almino- and Borohydrides in Organic Synthesis* (Wiley-VCH, New York, ed. 2, 1997).
- T. Werpy, G. Petersen, Eds., *Top Value Added Chemicals From Biomass, Volume 1—Results of Screening for Potential*

Candidates from Sugars and Synthesis Gas (U.S. Department of Energy, Oak Ridge, TN, 2004); available at www.nrel.gov/docs/fy04osti/35523.pdf.

- J. Magano, J. R. Dunez, *Org. Process Res. Dev.* **16**, 1156–1184 (2012).
- T. Turek, D. L. Trimm, N. W. Cant, *Catal. Rev.* **36**, 645–683 (1994).
- Y. Ni, P.-L. Hagedoorn, J.-H. Xu, I. W. C. E. Arends, F. Hollmann, *Chem. Commun. (Camb.)* **48**, 12056–12058 (2012).
- P. A. Dub, T. Ikariya, *ACS Catal.* **2**, 1718–1741 (2012).
- S. Werkmeister, K. Junge, M. Beller, *Org. Process Res. Dev.* **18**, 289–302 (2014).
- J. Pritchard, G. A. Filonenko, R. van Putten, E. J. M. Hensen, E. A. Pidko, *Chem. Soc. Rev.* **44**, 3808–3833 (2015).
- H. T. Teunissen, C. J. Elsevier, *Chem. Commun. (Camb.)* **1997**, 667–668 (1997).
- H. T. Teunissen, C. J. Elsevier, *Chem. Commun. (Camb.)* **1998**, 1367–1368 (1998).
- M. C. van Engelen, H. T. Teunissen, J. G. de Vries, C. J. Elsevier, *J. Mol. Catal. Chem.* **206**, 185–192 (2003).
- Y. Li, C. Topf, X. Cui, K. Junge, M. Beller, *Angew. Chem. Int. Ed.* **54**, 5198–5200 (2015).
- J. Zhang, G. Leitius, Y. Ben-David, D. Milstein, *Angew. Chem. Int. Ed.* **45**, 1113–1115 (2006).
- J. Zhang, E. Balaraman, G. Leitius, D. Milstein, *Organometallics* **30**, 5716–5724 (2011).
- E. Balaraman, E. Fogler, D. Milstein, *Chem. Commun. (Camb.)* **48**, 1111–1113 (2012).
- M. Kilner, D. V. Tyers, S. P. Crabtree, M. A. Wood, World Intellectual Property Organization (WO) Patent 03/093208 (2003).
- M. A. Wood, S. P. Crabtree, D. V. Tyers, WO Patent 2005/051875 (2005).
- F. M. A. Geilen, B. Engendahl, M. Hölscher, J. Klankermayer, W. Leitner, *J. Am. Chem. Soc.* **133**, 14349–14358 (2011).
- T. vom Stein *et al.*, *J. Am. Chem. Soc.* **136**, 13217–13225 (2014).
- T. P. Brewster, A. J. M. Miller, D. M. Heinekey, K. I. Goldberg, *J. Am. Chem. Soc.* **135**, 16022–16025 (2013).
- K. Goldberg, D. M. Heinekey, J. M. Mayer, A. J. M. Miller, T. P. Brewster, WO Patent 2014/130714 (2014).
- T. Zell, Y. Ben-David, D. Milstein, *Angew. Chem. Int. Ed.* **53**, 4685–4689 (2014).
- S. Werkmeister *et al.*, *Angew. Chem. Int. Ed.* **53**, 8722–8726 (2014).
- S. Chakraborty *et al.*, *J. Am. Chem. Soc.* **136**, 7869–7872 (2014).
- M. Toba *et al.*, *Appl. Catal. A Gen.* **189**, 243–250 (1999).
- H. G. Manyar *et al.*, *Chem. Commun. (Camb.)* **46**, 6279–6281 (2010).
- C. Federsel, C. Ziebart, R. Jackstell, W. Baumann, M. Beller, *Chemistry* **18**, 72–75 (2012).
- R. M. Drost *et al.*, *ChemCatChem* **7**, 2095–2107 (2015).
- R. H. Crabtree, *Chem. Rev.* **112**, 1536–1554 (2012).
- C. Mealli, S. Midollini, L. Sacconi, *Inorg. Chem.* **14**, 2513–2521 (1975).
- A. W. Addison, T. N. Rao, J. Reedijk, J. van Rijn, G. C. Verschoor, *J. Chem. Soc., Dalton Trans.* **1984**, 1349–1356 (1984).
- A similar structure with a PEt_3 group instead of the acetaldehyde, $[\text{Co}(\text{triphos})(\text{H})(\text{PEt}_3)]\text{BPh}_4$ is described in (33).
- C. Bianchini, D. Masi, C. Mealli, A. Mei, M. Sabat, *Gazz. Chim. Ital.* **116**, 201–204 (1986).

ACKNOWLEDGMENTS

This research was performed within the framework of the CatchBio program. The authors gratefully acknowledge the support of the Smart Mix Program of the Netherlands Ministry of Economic Affairs and the Netherlands Ministry of Education, Culture and Science. We thank E. Zuidinga for ESI-MS analysis and L. Lefort and P. Alsters for useful discussions. The supplementary crystallographic data for this structure can be obtained free of charge from The Cambridge Crystallographic Data Centre (CCDC) at www.ccdc.cam.ac.uk/getstructures (CCDC number 1420869).

SUPPLEMENTARY MATERIALS

www.sciencemag.org/content/350/6258/298/suppl/DC1

Materials and Methods

Figs. S1 to S39

Tables S1 to S5

References (34–46)

Cartesian Coordinates (XYZ Format) for All Calculated Structures

3 April 2015; accepted 8 September 2015

10.1126/science.aaa8938

SEPARATION MEMBRANES

CO₂ capture from humid flue gases and humid atmosphere using a microporous coppersilicate

Shuvo Jit Datta,¹ Chutharat Khumnoon,¹ Zhen Hao Lee,¹ Won Kyung Moon,¹ Son Doaco,¹ Thanh Huu Nguyen,¹ In Chul Hwang,¹ Dohyun Moon,² Peter Oleynikov,³ Osamu Terasaki,^{3,4,5} Kyung Byung Yoon^{1*}

Capturing CO₂ from humid flue gases and atmosphere with porous materials remains costly because prior dehydration of the gases is required. A large number of microporous materials with physical adsorption capacity have been developed as CO₂-capturing materials. However, most of them suffer from CO₂ sorption capacity reduction or structure decomposition that is caused by co-adsorbed H₂O when exposed to humid flue gases and atmosphere. We report a highly stable microporous coppersilicate. It has H₂O-specific and CO₂-specific adsorption sites but does not have H₂O/CO₂-sharing sites. Therefore, it readily adsorbs both H₂O and CO₂ from the humid flue gases and atmosphere, but the adsorbing H₂O does not interfere with the adsorption of CO₂. It is also highly stable after adsorption of H₂O and CO₂ because it was synthesized hydrothermally.

Efforts to curtail the increase in atmospheric CO₂ concentrations rely on the development of economical methods of capturing CO₂ from flue gas and the atmosphere (1–5). One possible approach involves capture of CO₂ by physical adsorption on microporous materials that have high surface areas. To date, various materials that have high CO₂ sorption capabilities at 298 K have been developed. They include zeolites (6–10), metal-organic frameworks (MOFs) (11–16), and zeolitic imidazolate frameworks (17, 18). However, these materials require the incoming gas stream to be completely dehydrated, as water causes a drastic reduction in the CO₂ sorption capabilities (19, 20) or may even promote their decomposition (13, 14). Although such moisture-sensitive CO₂ sorbents can still be used to capture CO₂ directly from nonpretreated humid flue gases by charging the column with a water-sorbing layer before the CO₂-sorbing layer, the use of a single moisture-insensitive layer would be preferable (4, 5, 21).

Only a limited number of materials meeting this requirement have been discovered, and these substances can only adsorb small to moderate amounts of CO₂ from humid flue gas (13, 14, 18–20). Furthermore, most flue gases are hot, with temperatures ranging between 373 and 403 K at the point they are released into the atmosphere. Therefore, thermal stability under humid conditions is another key property.

Using a gel consisting of sodium silicate and copper sulfate, we synthesized microporous coppersilicate crystals of uniform size and shape (see supplementary materials). The crystals, which we call SGU-29, have a square bipyramid crystal morphology, which suggests that each crystal has pseudo-four-fold symmetry along the axis (assigned later as the *c* axis) from the center of the square to the top of the pyramid. Two typical scanning electron microscopy (SEM) images with different crystal sizes are shown in Fig. 1A and the inset. The determined chemical formula was Na₂CuSi₅O₁₂. Almost all reflections observed in the x-ray powder diffraction pattern matched well with those of ETS-10 (22, 23) and AM-6 (fig. S1) (24, 25). The crystals are stable in air up to 550°C (fig. S2). The effective magnetic moment of Cu (fig. S3A) confirmed that the oxidation state of Cu is 2+. The electron spin resonance spectrum of SGU-29 showed that the electron spins on Cu²⁺ ions are strongly coupled (fig. S3B). Characteristic features observed by transmission electron microscopy (TEM) can be summarized as follows: (i) In the high-resolution TEM (HRTEM) image taken along the 110 direction (parallel to the channel direction; Fig. 1B), large bright ellipses are arranged horizontally with a period of 14.7 Å with a dark contrast observed between any two neighboring ellipses. Simultaneously, a horizontal row of small white dots arranged in a zigzag manner can also be noticed between the successive arrays of ellipses. The bright contrast of ellipses and small dots corresponds to large and small pores, respectively. The large pores resemble channels formed by 12-membered rings judging from their sizes. These pores belong to single layers that are marked as A, B, C, and D. (ii) There is a horizontal shift by one-quarter of the ellipses between successive layers either to the right in the upper part of the image forming ABCD stacking sequence or

¹Korea Center for Artificial Photosynthesis, Department of Chemistry, Sogang University, Seoul 121-742, Korea. ²Pohang Accelerator Laboratory, Pohang University of Science and Technology, Pohang 790-784, Korea. ³Department of Materials and Environmental Chemistry, Stockholm University, SE-106 91 Stockholm, Sweden. ⁴Graduate School of EEWs, KAIST, Daejeon 305-701, Korea. ⁵School of Physical Science and Technology, ShanghaiTech University, Shanghai 201210, China. *Corresponding author. E-mail: yoomb@sogang.ac.kr

to the left in the lower part with that of DCBA. (iii) A stacking sequence of BABAB can be observed at the boundary between the two parts.

The monoclinic stacking sequences ABCD and DCBA form crystalline regions on either side, which are mirror images of each other due to the horizontal mirror plane. The boundary BABAB stacking represents the tetragonal structure. The corresponding configurations were confirmed by single-crystal x-ray diffraction analysis. Electron diffraction pattern taken along the channels direction can be interpreted using the above description (Fig. 1C). Diffuse streaks induced by the layer-stacking disorder can be observed. The diffraction pattern taken along the [001]T zone axis (Fig. 1D) confirms the similarity of SGU-29 and the monoclinic polymorph type B reported for the ETS-10 structure by Anderson *et al.* (22). From these observations we conclude that SGU-29 has the same basic framework structure with stacking defects as they were observed in ETS-10 and AM-6 systems (22–25).

Using a synchrotron radiation source ($\lambda = 0.700 \text{ \AA}$), the crystal structure solution of SGU-29 was retrieved from a single crystal. The most probable solution was obtained in the centrosymmetric monoclinic lattice system (space group $C2/c$) with unit cell parameters of $a = 20.820 \text{ \AA}$, $b = 20.819 \text{ \AA}$, $c = 14.697 \text{ \AA}$, and $\beta = 110.73^\circ$ with $R_{\text{sym}} = 0.080$ (see table S1 for detailed crystal structure information). The bulk density (final column density) of the SGU-29 powder shown in Fig. 1A is 0.84 g/cm^3 .

The projections of the monoclinic structure along the [001] and $[\bar{1} \ 10]$ directions are shown

in Fig. 1, E and F, respectively, and the perspective view along the $[\bar{1} \ 10]$ direction is shown in Fig. 1G. Relative to the crystal structures of ETS-10 (22, 23) and AM-6 (24, 25), the most critical difference in the crystal structure of SGU-29 is that copper(II) ions adopt a square planar geometry (Fig. 1, H and I), whereas titanium(IV) in ETS-10 and vanadium(IV) in AM-6 have octahedral geometries. Unlike ETS-10 and AM-6, which respectively have one-dimensional -O-Ti(O)₄-O- and -O-V(O)₄-O- wires, there is no bridging oxygen atom between the neighboring Cu(II) centers. Each CuO₄ square plane is supported by four surrounding SiO₄ tetrahedra (Fig. 1H) and is arranged almost parallel to each other with the distances of 3.629 and 3.732 Å (Fig. 1I). The positions of five crystallographically distinct Na⁺ ion positions are shown in Fig. 1, J and K. Na2 exists at the cross section of two channels, and Na3 binds to four oxygen atoms bound to Cu(II) ions from the channel side. Accordingly, Na2 and Na3 can interact with molecules incorporated into the silica channels. The effective window size of the silica channel in SGU-29 is $4.5 \times 7.3 \text{ \AA}$ (fig. S11), which is slightly smaller than the reported values of ETS-10 ($4.7 \times 7.7 \text{ \AA}$, $4.5 \times 7.6 \text{ \AA}$) (22, 23).

For the purpose of obtaining CO₂ adsorption isotherms and dynamic CO₂ breakthrough profiles at various temperatures for SGU-29 and the related materials, we used pure CO₂ gas and four simulated flue gases denoted F0, F29, F92, and F201, and three simulated air samples denoted A70, A80, and A90 (Table 1). They differ in their compositions of H₂O, CO₂, O₂, and N₂

which are represented by their partial pressures (mbar) of the component gases ($^pP_{\text{gas}}$). F0 is a dry flue gas and F29, F92, and F201 are humid flue gases with $^pP_{\text{H}_2\text{O}}$ of 29, 92, and 201 mbar, respectively. A70, A80, and A90 are humid air samples with different relative humidities of 70, 80, and 90%, respectively. The $^pP_{\text{CO}_2}$ values of F0, F29, F92, and F201 are ~100 mbar, which corresponds to the average $^pP_{\text{CO}_2}$ in flue gas, and that of A70, A80, and A90 is 0.4 mbar or 400 ppm, which corresponds to the average $^pP_{\text{CO}_2}$ in the atmosphere. The temperatures of the simulated gases are 298 K, except for F92 (318 K) and F201 (338 K).

The CO₂ adsorption isotherms of SGU-29 in the $0 \leq P_{\text{CO}_2} \leq 1000$ mbar and $0 \leq P_{\text{CO}_2} \leq 100$ mbar regions at temperatures between 273 and 373 K are shown in Fig. 2, A and B, respectively. The CO₂ adsorption isotherms for SGU-29 in the $0 \leq P_{\text{CO}_2} \leq 100$ and $0 \leq P_{\text{CO}_2} \leq 0.4$ mbar regions at 298 K are compared with the corresponding isotherms (Fig. 2, C and D) of AM-6, Mg-DOBDC, ETS-4, ETS-10, and SIFSIX-3-Cu. NaX is also included in the comparisons because it has been considered as a material for industrial applications (4, 9, 21). The U_{CO_2} values of SGU-29 at $P_{\text{CO}_2} = 1000$, 100, and 0.4 mbar and 298 K are 156, 126, and $26 \text{ cm}^3/\text{cm}^3$, respectively. Although U_{CO_2} of SGU-29 at $P_{\text{CO}_2} = 1000$ mbar ranks third among the top seven materials (Fig. 2E, fig. S12A, and table S4), it ranks first at $P_{\text{CO}_2} = 100$ mbar (Fig. 2F, fig. S12B, and table S4). We further found that the U_{CO_2} values of AM-6, ETS-4, and ETS-10 at $P_{\text{CO}_2} = 100$ mbar rank second, fourth, and fifth, respectively, indicating that the four materials with the

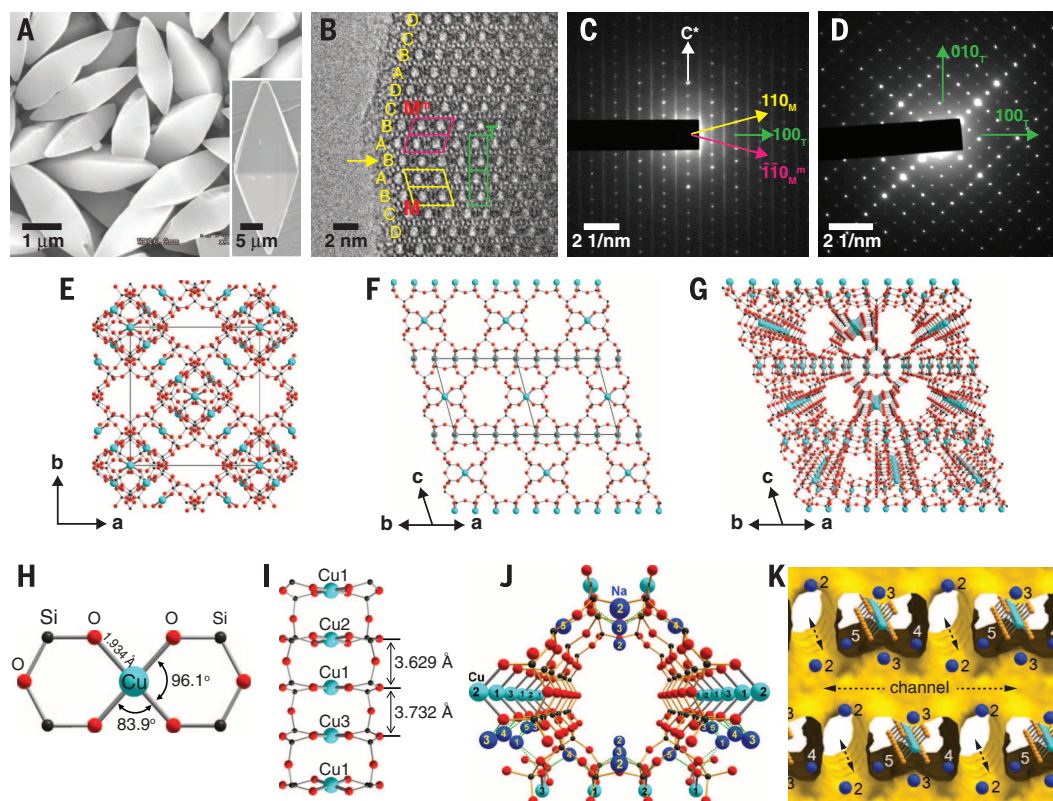


Fig. 1. Crystal structure of SGU-29.

(A) SEM image of crystals with uniform size and regular square bipyramidal morphology. Inset: An individual single crystal. (B) HRTEM image with marked unit cells corresponding to monoclinic (M, yellow), monoclinic mirrored (M^m, pink), and tetragonal (T, green) structures. (C) Electron diffraction pattern taken along the $[\bar{1}10]_M$ zone axis (alternatively $[010]_T$). The arrows mark the principal directions for corresponding unit cells drawn in (B). (D) Electron diffraction pattern along the $[001]_T$ zone axis. (E) Structure view along the c axis. (F) Structure view along the channel direction. (G) Perspective projection of several unit cells along the channel direction. (H) $[\text{CuO}_4]$ square planar geometry, with the average bond length and two Cu–O bond angles that form the fundamental secondary building unit shown in (I). (I) $[\text{CuO}_4]$ column side view. (J) Five different Na⁺ positions shown in the channel. (K) Positions of Na⁺ ions in the channel system.

same structural origin (SGU-29, AM-6, ETS-10, and ETS-4) are among the top five materials. This indicates that the very high CO₂-capturing ability of SGU-29 at $P_{\text{CO}_2} = 100$ mbar arises primarily from its structure. The increase in U_{CO_2} ongoing from ETS-10 to AM-6 and to SGU-29 seems to arise from the fine structural variation of the TiO₆²⁻, VO₆²⁻, and CuO₄²⁻ centers within the structures and the corresponding change of the electronic properties of the framework oxygen

and the charge-balancing cations along the silica channels.

At $P_{\text{CO}_2} = 0.4$ mbar, U_{CO_2} of SGU-29 ranks second after that of SIFSIX-3-Cu (43 cm³/cm³) (Fig. 2G and fig. S13); the U_{CO_2} values of AM-6 and ETS-10 rank third and fourth, confirming the intrinsically high affinity of the ETS-10-type framework structure for CO₂.

The isosteric heats of adsorption of CO₂, H₂O, N₂, and O₂ [($Q_{\text{st}}^{\text{gas}}$) onto SGU-29 and NaX are

compared in Fig. 2H. For both sorbents, the order of ($Q_{\text{st}}^{\text{gas}}$) values is ($Q_{\text{st}}^{\text{H}_2\text{O}}$) > ($Q_{\text{st}}^{\text{CO}_2}$) >> ($Q_{\text{st}}^{\text{N}_2}$) > ($Q_{\text{st}}^{\text{O}_2}$) in the region of U between 0 and 200 cm³/cm³. The initial ($Q_{\text{st}}^{\text{CO}_2}$) of SGU-29 is higher than those of most of the materials listed in table S5, including NaX (48.2 kJ/mol). Note that ($Q_{\text{st}}^{\text{CO}_2}$) of SGU-29 remains nearly constant regardless of U_{CO_2} , whereas that of NaX sharply decreases when U_{CO_2} reaches about two-thirds of its maximum (Fig. 2H). This shows that ($Q_{\text{st}}^{\text{CO}_2}$) of SGU-29 is not only higher but also more constant with respect to U_{CO_2} than that of NaX.

These observations suggest that the attractive interaction between CO₂ and the adsorption site in SGU-29 is not only stronger but also more homogeneous than that of NaX, regardless of U_{CO_2} . They also suggest that the adsorption sites for CO₂ in this substance do not cooperate in a negative manner to prevent adsorption of this gas. More important, ($Q_{\text{st}}^{\text{H}_2\text{O}}$) of SGU-29 is lower than that of NaX by 8 to 14 kJ/mol, regardless of $U_{\text{H}_2\text{O}}$, which indicates that SGU-29 has much lower affinity to H₂O than does NaX. Furthermore, the amount of H₂O adsorbed onto SGU-29 is much smaller than the amount adsorbed onto NaX and most of the materials shown in figs. S14 and S15. In general, SGU-29 and the materials that belong to the same structural family have

Table 1. Compositions of the simulated flue gases used in this study.

Gas stream	Temperature (K)	Partial pressure (mbar)*			
		$P_{\text{H}_2\text{O}}$	P_{CO_2}	P_{O_2}	P_{N_2}
F0	298	0	100	190	723
F29	298	29	97	185	702
F92	318	92	100	173	648
F201	338	201	100	148	564
A70	298	22	0.4	209	782
A80	298	25	0.4	209	779
A90	298	29	0.4	208	776

*Total pressure = 1013 mbar.

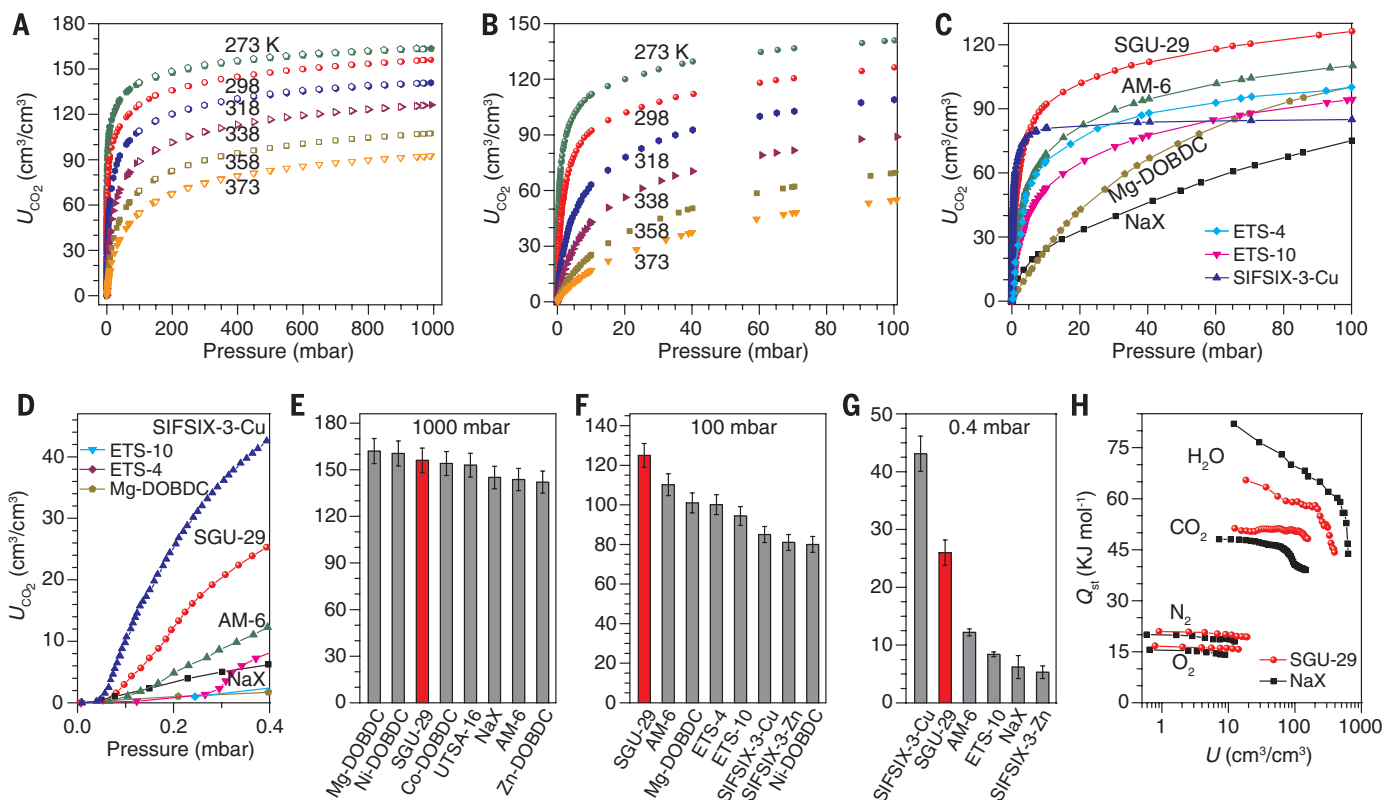


Fig. 2. CO₂ adsorption isotherms and isosteric heats of adsorption. (A and B) CO₂ adsorption isotherms of SGU-29 in two different P_{CO_2} regions. (C and D) Comparison of the CO₂ adsorption isotherms of SGU-29, AM-6, ETS-4, ETS-10, SIFSIX-3-Cu, Mg-DOBDC, and NaX in the P_{CO_2} region between 0 and 100 mbar (C) and between 0 and 0.4 mbar (D) at 298 K. (E to G) Comparison of CO₂ uptakes of SGU-29 at $P_{\text{CO}_2} = 1000$ mbar (E), 100 mbar (F), and 0.4 mbar (G) relative to previously reported CO₂ sorbent. (H) Plots of isosteric heat versus uptake of SGU-29 and NaX for H₂O, CO₂, N₂, and O₂.

much lower $U_{\text{H}_2\text{O}}$ values than that of NaX. Even among the group of low- $U_{\text{H}_2\text{O}}$ materials, SGU-29 shows the lowest $U_{\text{H}_2\text{O}}$ (fig. S14). Such a high affinity and capacity for CO_2 , together with a very low affinity and capacity for H_2O , make SGU-29 a much more suitable CO_2 remover from the humid flue gas than NaX and the other materials tested.

The dynamic breakthrough (dynamic column CO_2 separation) profiles of seven CO_2 adsorbents were obtained at 298 K using a column CO_2 separation setup (fig. S10), with F0 (Fig. 3A and table S5) and F29 (Fig. 3B and table S5) as flue gases. The U_{CO_2} values of SGU-29 from F0 (dry) and F29 (humid) are $117 \text{ cm}^3/\text{cm}^3$ and $115 \text{ cm}^3/\text{cm}^3$, respectively. The small decrease in U_{CO_2} arises from the decrease of $^pP_{\text{CO}_2}$ by 3 mbar upon changing F0 to F29. Thus, moisture does not affect the CO_2 capture ability of SGU-29, which is a very important feature of SGU-29. The ratio of the U_{CO_2} obtained from the humid flue gas (F29) to the U_{CO_2} obtained from dry flue gas (F0) [$U_{\text{CO}_2}(\text{humid})/U_{\text{CO}_2}(\text{dry})$] is plotted for various materials in Fig. 3C. The ratios of SGU-29 (1.0), AM-6 (1.0), ETS-10 (0.96), SIFSIX-3-Zn (0.96), ETS-4 (0.95), SIFSIX-3-Cu (0.93), and UTSA-16 (0.90) fall between 1.0 and 0.9. They are categorized as moisture-insensitive CO_2 sorbents. The ratios of NaX (0.81), Ni-DOBDC (0.78), and Mg-DOBDC (0.35) fall between 0.8 and 0.35; they are categorized as moisture-sensitive CO_2 sorbents. Interestingly, SGU-29, AM-6, and ETS-10 are the top three materials in the group of moisture-insensitive sorbents, indicating that the very high $U_{\text{CO}_2}(\text{humid})/U_{\text{CO}_2}(\text{dry})$ ratio of SGU-29 arises from its structure.

We measured Fourier transform infrared (FTIR) spectra of SGU-29 and NaX while passing F0 or F29 (flow rate 5 ml/min) onto each dried sor-

bent placed in an environmental chamber. With F0 as the flue gas and dry SGU-29 as the sorbent, the absorption peaks due to the adsorbed CO_2 gradually increased in the 2250 to 2450 cm^{-1} region and the absorbance reached 2.75 during the period of 40 min (Fig. 4A). When the flow rate of F0 was increased to 50 ml/min, it took only 2 min for the absorbance to reach the maximum (2.75), indicating that the CO_2 uptake is a very rapid process (fig. S16). Even with F29 as the flue gas, the growth rate, peak shapes, and intensities of the adsorbed CO_2 peaks were identical to those with F0 as the flue gas, as if F29 were a dry flue gas. However, the broad peaks due to adsorbed H_2O simultaneously appeared in the 3700 to 2800 cm^{-1} region, and their intensities gradually grew with time, with the absorbance reaching a maximum at 0.75. These results show that both CO_2 and H_2O simultaneously adsorb on SGU-29 but the H_2O adsorption does not interfere with the CO_2 adsorption, indicating that there are different H_2O -specific and CO_2 -specific sites in SGU-29 and they do not interfere with each other (fig. S17A). A similar phenomenon was observed for AM-6 (fig. S18). Recently, various amine-functionalized porous materials have been introduced (26–30) and it has been shown that H_2O does not interfere with the chemical adsorption of CO_2 by amine groups (29), indicating that the chemical reaction between amine groups and CO_2 is highly specific, such that water cannot interfere with the reaction. In that respect, SGU-29 can be regarded to have chemical reaction-like, highly specific CO_2 sorption selectivity.

With F0 as the flue gas and dry NaX as the sorbent, the IR absorption peaks due to the adsorbed CO_2 gradually increased and the absorbance reached 2.75 during the period of 40 min

(Fig. 4C). However, with F29 as the flue gas and dry NaX as the sorbent, a very broad (3750 to 2000 cm^{-1}) absorption peak due to the adsorbed H_2O appeared, with a maximum absorbance of 1.25 at 3400 cm^{-1} (Fig. 4D). The integrated area of H_2O peak is much larger than that of SGU-29, consistent with the fact that a much larger amount of water is adsorbed into NaX than into SGU-29 (figs. S14 and S15). In NaX, the intensity of the H_2O peak rapidly increased to 1.1 during the first 20 min and then slowly increased to 1.25 during the next 20 min. Simultaneously, the intensity of the CO_2 peak reached 2.25 during the initial 20 min and subsequently decreased to 2.0 during the next 20 min. This shows that a portion of the adsorbed CO_2 is replaced by H_2O molecules. We therefore conclude that, in NaX, there are $\text{H}_2\text{O}/\text{CO}_2$ -sharing sites as well as H_2O -specific and CO_2 -specific sites (fig. S17B). From the observation that $U_{\text{CO}_2}(\text{humid})/U_{\text{CO}_2}(\text{dry}) = 0.82$ (Fig. 3C), the percentage of the $\text{H}_2\text{O}/\text{CO}_2$ -sharing sites in the total CO_2 -sorbing sites is 18% in NaX. By the same analysis, the percentage of the $\text{H}_2\text{O}/\text{CO}_2$ -sharing sites in Ni-DOBDC and Mg-DOBDC are 22 and 65%, respectively.

Both SGU-29 and NaX display negative linear relationships between U_{CO_2} and temperature (T_{ad}), as is demonstrated by $U_{\text{CO}_2} = -aT_{\text{ad}} + b$ plots, where a is the slope and b is the intercept at $T = 298 \text{ K}$ (Fig. 3D). Plot I in Fig. 3D corresponds to a CO_2 isotherm for SGU-29 determined by using pure CO_2 gas at temperatures between 298 and 373 K. Plots II, III, and IV were obtained by CO_2 breakthrough experiments at different T_{ad} using F0, F92, and F201 as flue gases, respectively. The respective slopes of the lines in plots I to IV are -0.97 , -0.92 , -0.89 , and -0.83 . The downward shift of the plot ongoing from plot I obtained by

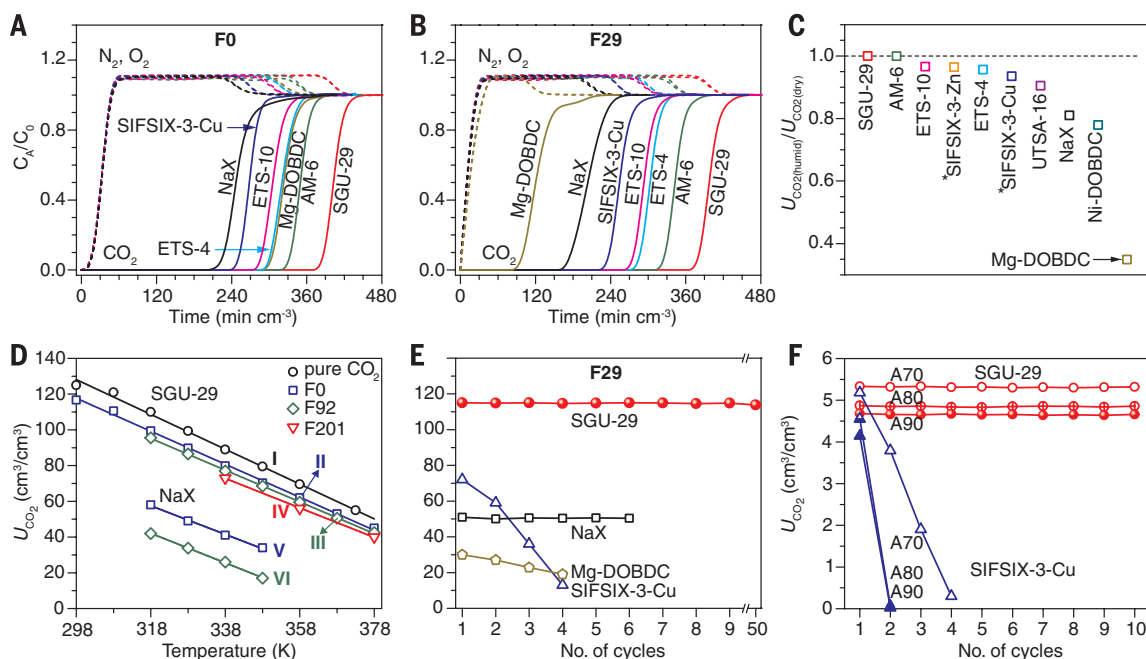
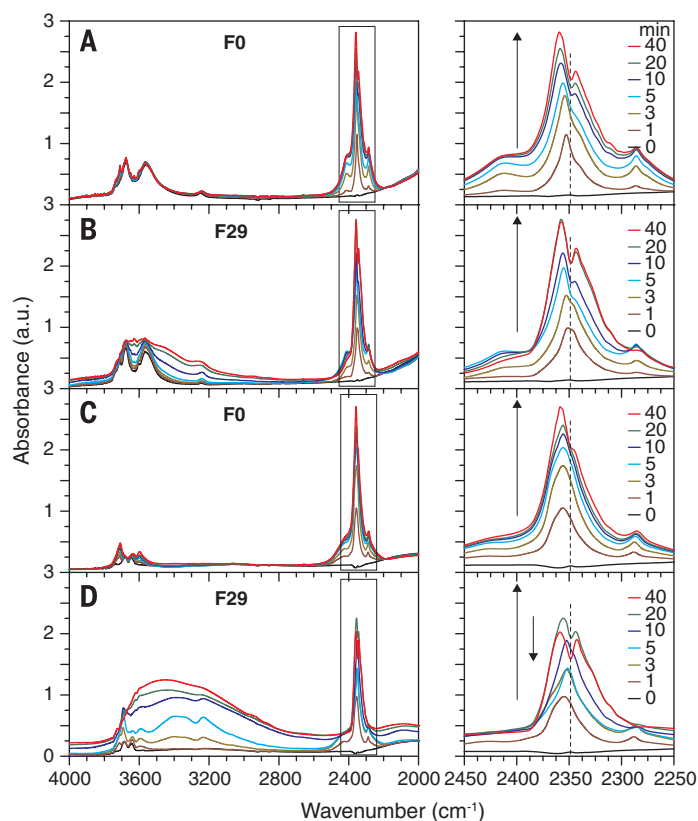


Fig. 3. Dynamic CO_2 breakthrough profiles, linear U_{CO_2} - T_{ad} relationship, and recyclability. (A and B) Dynamic CO_2 breakthrough profiles of SGU-29, AM-6, and the other reported best-performing materials with F0 (A) and F29 (B). (C) Plot of $U_{\text{CO}_2}(\text{humid})/U_{\text{CO}_2}(\text{dry})$ with respect to various materials as indicated. (D) Linear relationships between U_{CO_2} and T_{ad} for SGU-29 and NaX. (E and F) Comparisons of U_{CO_2} and the recyclability of SGU-29 with those of the other indicated materials, with humid F29 flue gas (E) and humid A70, A80, and A90 air (F), at 298 K.

Fig. 4. Effect of adsorbed water on adsorbed CO₂. Progressive change of the Fourier transform infrared spectra of (A and B) dried SGU-29 and (C and D) dried NaX, with time (as indicated) under the flow of dry flue gas F0 [(A) and (C)] and humid flue gas F29 [(B) and (D)] at 298 K. Flow rate = 5 ml/min.



pure CO₂ gas to plot II obtained by F0 is ascribed to interference of U_{CO_2} by coexisting N₂ and O₂, which are the major components of the flue gas. Despite the fact that the increase in $P_{\text{H}_2\text{O}}$ on going from F0 to F92 to F201 is drastic, plots II, III, and IV essentially overlap on each other. Accordingly, the U_{CO_2} values at 378 K are similar (40 to 45 cm³/cm³) for F0, F92, and F201, respectively. The above results again show that $P_{\text{H}_2\text{O}}$ does not affect the $U_{\text{CO}_2} = -aT_{\text{ad}} + b$ plots.

Plot V, generated from NaX using F0, has a slope of -0.82 and an intercept of 73 cm³/cm³; plot VI, generated from NaX using F92, has a slope of -0.80 and an intercept of 58 cm³/cm³. The slopes are similar to those of plots I to IV, but the intercepts are much lower than the corresponding values of SGU-29, consistent with the fact the intrinsic affinity of NaX for CO₂ is lower than that of SGU-29. The downward shift from plot V to plot VI is much larger than that from plot II to plot III, which again demonstrates that whereas U_{CO_2} of NaX is sensitively affected by $P_{\text{H}_2\text{O}}$, that of SGU-29 is not. At 368 K, the U_{CO_2} values of plot III (by SGU-29 with F92) and plot VI (by NaX with F92) are 51 cm³/cm³ and 0 cm³/cm³, respectively; hence, SGU-29 can remove a substantial amount of CO₂ directly from a hot and humid flue gas, whereas NaX cannot.

SGU-29 is also repeatedly reusable (Fig. 3E) after desorption of the adsorbed CO₂ by evacuation at room temperature or at elevated temperatures such as 523 K. This indicates that its structure and CO₂ sorption sites remain intact during repeated exposure to hot and hu-

mid flue gases. Specifically, the U_{CO_2} of SGU-29 obtained from F29 (relative humidity 90%) at 298 K does not change over the course of 50 CO₂ breakthrough experiments. Also, the U_{CO_2} (40 cm³/cm³) of SGU-29 for flue gas F201 at 378 K remains constant during 10 CO₂ breakthrough experiments, confirming the recyclability of this material for CO₂ capture from the hot and humid flue gases. Although NaX and some MOFs such as Ni-DOBDC and UTSA-16 (fig. S19) were also found to be recyclable, their U_{CO_2} values (53, 50, and 37 cm³/cm³) are half that of SGU-29. In contrast, the U_{CO_2} values of SIFSIX-3-Cu, Mg-DOBDC, and SIFSIX-3-Zn (fig. S19) were found to decrease progressively during repeated use. The estimated power consumption by vacuum swing adsorption at room temperature was 2.04 MJ per kg of CO₂ (4, 5).

The initial U_{CO_2} values for air samples A70, A80, and A90 were 5.3, 4.9, and 4.7 cm³/cm³, respectively; again, these values did not change over repeated experiments. Although the U_{CO_2} value of SIFSIX-3-Cu was higher than that of SGU-29 at $P_{\text{CO}_2} = 0.4$ mbar under the dry condition (Fig. 2, D and G), its initial U_{CO_2} values for CO₂ capture from the simulated humid air samples A70, A80, and A90 were lower than those of SGU-29. Furthermore, as the data in Fig. 3F show, SIFSIX-3-Cu is not recyclable under humid conditions.

SGU-29 is a microporous coppersilicate that can be immediately applied in the field as a material for capturing CO₂ from humid flue gases without involving the costly prior dehydration step. SGU-29, AM-6, and ETS-10 form an

important class of materials having an isostructural platform that gives rise to very high U_{CO_2} (humid)/ U_{CO_2} (dry) ratios (>0.96).

REFERENCES AND NOTES

1. K. Sumida et al., *Chem. Rev.* **112**, 724–781 (2012).
2. Z. Zhang, Z.-Z. Yao, S. Xiang, B. Chen, *Energy Environ. Sci.* **7**, 2868–2899 (2014).
3. Y.-S. Bae, R. Q. Snurr, *Angew. Chem. Int. Ed.* **50**, 11586–11596 (2011).
4. L. Wang et al., *Ind. Eng. Chem. Res.* **52**, 7947–7955 (2013).
5. Z. Liu et al., *Ind. Eng. Chem. Res.* **51**, 7355–7363 (2012).
6. T.-H. Bae et al., *Energy Environ. Sci.* **6**, 128–138 (2013).
7. M. M. Lozinska et al., *J. Am. Chem. Soc.* **134**, 17628–17642 (2012).
8. A. Anson, C. C. H. Lin, S. M. Kuznicki, J. A. Sawada, *Chem. Eng. Sci.* **64**, 3683–3687 (2009).
9. F. Su, C. Lu, *Energy Environ. Sci.* **5**, 9021–9027 (2012).
10. J. Shang et al., *J. Am. Chem. Soc.* **134**, 19246–19253 (2012).
11. S. R. Caskey, A. G. Wong-Foy, A. J. Matzger, *J. Am. Chem. Soc.* **130**, 10870–10871 (2008).
12. D. Britt, H. Furukawa, B. Wang, T. G. Glover, O. M. Yaghi, *Proc. Natl. Acad. Sci. U.S.A.* **106**, 20637–20640 (2009).
13. P. Nugent et al., *Nature* **495**, 80–84 (2013).
14. O. Shekhat et al., *Nat. Commun.* **5**, 4228 (2014).
15. S. Xiang et al., *Nat. Commun.* **3**, 954 (2012).
16. Q. Yang et al., *Angew. Chem. Int. Ed.* **125**, 10506–10510 (2013).
17. R. Banerjee et al., *Science* **319**, 939–943 (2008).
18. N. T. T. Nguyen et al., *Angew. Chem. Int. Ed.* **53**, 10645–10648 (2014).
19. A. C. Kizzie, A. G. Wong-Foy, A. J. Matzger, *Langmuir* **27**, 6368–6373 (2011).
20. J. Liu, J. Tian, P. K. Thallapally, B. P. McGrail, *J. Phys. Chem. C* **116**, 9575–9581 (2012).
21. L. Wang et al., *Chem. Eng. Sci.* **101**, 615–619 (2013).
22. M. W. Anderson et al., *Nature* **367**, 347–351 (1994).
23. X. Wang, A. J. Jacobson, *Chem. Commun.* **11**, 973–974 (1999).
24. J. Rocha et al., *Angew. Chem. Int. Ed. Engl.* **36**, 100–102 (1997).
25. S. J. Datta, K. B. Yoon, *Angew. Chem. Int. Ed.* **49**, 4971–4975 (2010).
26. J. C. Hicks et al., *J. Am. Chem. Soc.* **130**, 2902–2903 (2008).
27. R. Vaidhyanathan et al., *Science* **330**, 650–653 (2010).
28. T. M. McDonald et al., *Nature* **519**, 303–308 (2015).
29. J. A. Mason et al., *J. Am. Chem. Soc.* **137**, 4787–4803 (2015).
30. J. P. Sculley, H.-C. Zhou, *Angew. Chem. Int. Ed.* **51**, 12660–12661 (2012).

ACKNOWLEDGMENTS

Supported by the Korea Center for Artificial Photosynthesis, located at Sogang University and funded by the Ministry of Science, ICT and Future Planning through the National Research Foundation of Korea, grant 2009-0093886. We thank C.-H. Shin at Chungbuk National University for helpful discussions regarding the isosteric heats of adsorption, and J. Y. Lee for help in drawing the figures.

SUPPLEMENTARY MATERIALS

www.sciencemag.org/content/350/6258/302/suppl/DC1
Materials and Methods
Figs. S1 to S19
Tables S1 to S5
References (31–48)

20 March 2015; accepted 28 August 2015
10.1126/science.aab1680

QUANTUM INFORMATION

A near-quantum-limited Josephson traveling-wave parametric amplifier

C. Macklin,^{1,2*} K. O'Brien,³ D. Hover,⁴ M. E. Schwartz,¹ V. Bolkhovskiy,⁴ X. Zhang,^{3,5,6} W. D. Oliver,^{4,7} I. Siddiqi¹

Detecting single-photon level signals—carriers of both classical and quantum information—is particularly challenging for low-energy microwave frequency excitations. Here we introduce a superconducting amplifier based on a Josephson junction transmission line. Unlike current standing-wave parametric amplifiers, this traveling wave architecture robustly achieves high gain over a bandwidth of several gigahertz with sufficient dynamic range to read out 20 superconducting qubits. To achieve this performance, we introduce a subwavelength resonant phase-matching technique that enables the creation of nonlinear microwave devices with unique dispersion relations. We benchmark the amplifier with weak measurements, obtaining a high quantum efficiency of 75% (70% including noise added by amplifiers following the Josephson amplifier). With a flexible design based on compact lumped elements, this Josephson amplifier has broad applicability to microwave metrology and quantum optics.

Coherent superconducting circuits play a key role in exploring the interaction between light and matter at microwave frequencies, particularly at the level of single photons and artificial atoms where quantum effects dominate. Recent advances span quantum measurement (1–4), control (5–7), optics (8, 9), and information processing (10–12). Many of these developments have relied on ultralow-noise Josephson parametric amplifiers (JPAs) (13–15) to detect microwave frequency signals with a sensitivity approaching the minimum allowed by quantum mechanics (16). Although several refinements have been incorporated into JPAs (17–20), the basic architecture remains that of a cavity where anharmonicity is introduced via the nonlinear inductance of a Josephson junction. This architecture is well suited for detecting a few photons over a bandwidth of tens of megahertz; however, applications such as quantum computation and simulation with many bits motivate the development of a versatile, general-purpose, quantum-limited microwave frequency amplifier with gigahertz-scale bandwidth and larger power-handling capability. Semiconductor amplifiers based on high-electron mobility transistors (HEMTs) fulfill some of these requirements, but generally achieve noise temperatures 10 to 20 times greater than the quantum limit.

We introduce a style of Josephson amplifier that sidesteps the primary limiting factor in JPAs—the use of a resonator to enhance the interaction between incident waves and the Josephson nonlinearity. Instead, we use a long chain of Josephson junctions, forming a metamaterial transmission line (21). We call this device a Josephson traveling-wave parametric amplifier (JTWPA). The JTJWPA does not have the fixed gain-bandwidth product intrinsic to resonant JPAs and can achieve power gain larger than 20 dB over a 3-GHz bandwidth. This performance is the result of a nonlinear phase-matching technique specific to the microwave domain that we call resonant phase match-

ing (RPM), in which we manipulate the dispersion using an array of deep subwavelength resonators. The RPM technique could prove a fruitful tool in developing novel quantum optical devices at microwave frequencies.

Several features of the JTJWPA make it attractive for a general-purpose ultralow-noise cryogenic measurement system. The JTJWPA does not inherently require a bulky, lossy microwave circulator at the input to separate incoming and outgoing modes. Furthermore, higher pump powers can be used in the JTJWPA than in JPAs, enabling an order-of-magnitude increase in the input signal power that can be faithfully amplified. We measure noise performance of the JTJWPA with a noise power technique and a fiducial quantum measurement, demonstrating a whole-system quantum efficiency of 49%—comparable to that of the most faithful JPAs. We use the JTJWPA to make a projective qubit measurement to a fidelity of 96.7% in 100 ns at a measurement power 14 dB below the 1-dB compression power, implying the possibility of simultaneous readout of more than 20 qubits. These factors make the JTJWPA a more versatile measurement tool than the traditional JPA, providing the benefits of nearly quantum-limited performance with an ease of use comparable to that of a semiconductor amplifier. Traveling-wave kinetic inductance amplifiers have recently been demonstrated (22, 23), though an intense microwave drive of -10 dBm and a very long propagation length of 4.4 m are required for gain of 20 dB, rendering integration with quantum information systems challenging.

The architecture of the JTJWPA (Fig. 1) is a lumped-element transmission line with a Josephson junction as the inductive element, shunted to ground through a capacitor. The length of each unit cell is $a = 16$ μm ; the device presented here

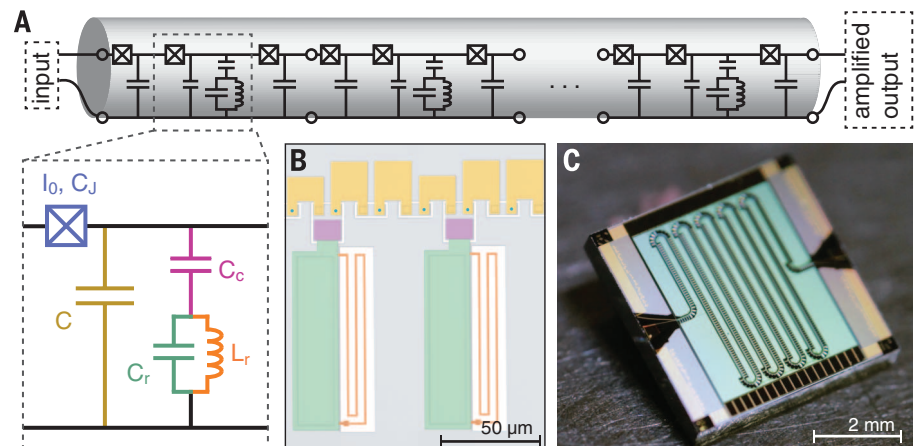


Fig. 1. Josephson traveling-wave parametric amplifier. (A) Circuit diagram. The JTJWPA is implemented as a nonlinear lumped-element transmission line; one unit cell consists of a Josephson junction with critical current $I_0 = 4.6$ μA and intrinsic capacitance $C_j = 55$ fF with a capacitive shunt to ground $C = 45$ fF. Every third unit cell includes a lumped-element resonator designed with capacitance $C_r = 6$ pF and inductance $L_r = 120$ pH, with coupling strength set by a capacitor $C_c = 20$ fF. The value of C in the resonator-loaded cell is reduced to compensate for the addition of C_c . (B) False-color optical micrograph. The coloring corresponds to the inset in (A), with the lower metal layer shown in gray. (C) Photograph of a 2037 junction JTJWPA. The line is meandered several times on the 5 mm by 5 mm chip to achieve the desired amplifier gain.

¹Quantum Nanoelectronics Laboratory, University of California, Berkeley, Berkeley, CA 94720, USA.

²Computational Research Division, Lawrence Berkeley National Laboratory, Berkeley, CA 94720, USA. ³Nanoscale Science and Engineering Center, University of California, Berkeley, Berkeley, CA 94720, USA. ⁴Massachusetts Institute of Technology (MIT) Lincoln Laboratory, 244 Wood Street, Lexington, MA 02420, USA. ⁵Materials Sciences Division, Lawrence Berkeley National Laboratory, Berkeley, CA 94720, USA. ⁶Department of Physics, King Abdulaziz University, Jeddah 21589, Saudi Arabia. ⁷Research Laboratory of Electronics, Massachusetts Institute of Technology, 77 Massachusetts Avenue, Cambridge, MA 02139, USA.

*Corresponding author. E-mail: chris.macklin@berkeley.edu

comprises 2037 unit cells for a propagation length of 3.3 cm. The devices are fabricated in a niobium trilayer process on silicon (24, 25). We have presented a theoretical treatment of the JTWPA in (21). When a strong microwave pump wave propagates down the line, the nonlinear inductance of the junctions permits four-wave mixing. Efficient parametric amplification requires the waves at the pump (ω_p), signal (ω_s), and idler (ω_i) frequencies to satisfy energy conservation, $2\omega_p = \omega_s + \omega_i$, and momentum conservation (or, equivalently, phase matching), $\Delta k = 2k_p - k_s - k_i = 0$, where k is the wave vector. The former is satisfied by the creation of the idler at ω_i , but the latter is only satisfied for certain dispersion relations $k(\omega)$.

For small signals, $k(\omega)$ is approximately a linear function of frequency and $\Delta k \approx 0$. However, when the line is strongly driven, the pump wave induces additional power-dependent phase shifts (26). In the case of the JTWPA, this shift is well approximated by

$$\Delta k = 2k_p - k_s - k_i - 2k_p \kappa_{nl} \quad (1)$$

where the fractional nonlinear wave vector shift $\kappa_{nl} = (a^2 k_p^2 |Z|^2 / 16L^2 \omega_p^2) (I_p / I_0)^2$, Z is the characteristic impedance, L is the Josephson inductance, and I_p / I_0 is the ratio of the pump current to the junction critical current (21). To satisfy this relation, we introduce the RPM technique: We add a series of linear lumped-element resonators (Fig. 1A), creating a stop band near 7.25 GHz. Nearby but outside the stop band, wave propagation is unchanged aside from a small increase in $k(\omega)$. Choosing a pump frequency in this region provides the necessary increase in k_p to partially compensate the power-dependent term in Eq. 1.

The setup for measuring amplifier gain is depicted in Fig. 2A. All measurements take place in a dilution refrigerator with a base temperature of 30 mK. We measure a 1-dB insertion loss for the JTWPA in the small-signal regime at 4 GHz, smoothly increasing to 4 dB at 10 GHz, in good agreement with capacitive dielectric loss (fig. S3). The RPM stop band is visible as a dip in transmission at 7.25 GHz (Fig. 2B).

The effect of RPM on the phase mismatch Δk is shown in Fig. 2C. For a pump far from the dispersion feature, $\Delta k \sim 0$ in the weak-pump regime and becomes poorly phase-matched as the pump power is increased. For a pump near the dispersion feature, the phase matching is sufficiently improved to realize an appreciable enhancement in gain. We focus here on one operating condition, with a pump at 7.157 GHz and $I_p / I_0 = 0.91$; the resulting gain profile is shown in Fig. 2D. This represents the most general-purpose operating configuration, with 20 dB of gain over a 3-GHz bandwidth.

We use a circuit quantum electrodynamics (QED) system (27) in the weak measurement limit to assess the noise performance of the JTWPA. By measuring the system parameters and using the AC Stark shift of the qubit to calibrate the dispersive shift χ and the mean photon number occupation of the cavity \bar{n} , we extract a precisely calibrated power at the output of the cavity as

$P = \kappa \hbar \omega_r \bar{n}$, where κ and ω_r are the cavity's linewidth and frequency. This technique yields the system noise temperature at the reference plane relevant to quantum measurement with no additional uncertainty. This is a notable improvement over cryogenic power references that require additional components between the calibration device and the measurement reference plane (28, 29), resulting in uncertainties in extracted system noise temperatures of 1 to 2 dB (20, 30).

A simplified schematic for this measurement is shown in Fig. 3A. The qubit and cavity are of the "3D transmon" variety (31); the single-junction transmon qubit has a fixed frequency $\omega_{qb} / 2\pi = 3.58$ GHz and is antenna-coupled to an aluminum waveguide cavity with a resonant frequency $\omega_r / 2\pi = 5.984$ GHz and output coupling rate $\kappa / 2\pi = 18.5$ MHz. We measure the dispersive coupling rate to be $\chi / 2\pi = 584 \pm 5$ kHz. For additional details, see (25). Noise power spectra

taken of the output microwave field in the vicinity of the cavity frequency are shown in Fig. 3B. A coherent tone corresponding to a mean cavity occupation $\bar{n} = 3.62 \pm 0.04$ allows us to directly refer the measured spectra to the output plane of the cavity. With the JTWPA pump off, we extract a system noise of 9.01 ± 0.23 K. We turn the pump on and measure a signal gain of 21.6 dB; we refer the resulting noise level to the cavity output by subtracting this gain from the measured trace, permitting a direct comparison of noise temperature. We measure a system noise of 602 ± 15 mK, equivalent to a quantum measurement efficiency $\eta = \frac{\hbar \omega_r}{k_B T_{\text{sys}}} = 0.48 \pm 0.016$.

Several factors contribute to the measured reduction in η from 1, including insertion loss in the microwave network between the cavity and JTWPA ($\eta_L = 0.69$), distributed loss in the JTWPA itself ($\eta_D = 0.9$), and the finite gain of the JTWPA compared to the HEMT noise ($\eta_H = 0.93$) (25). If we calculate $\eta = \eta_L \cdot \eta_H \cdot \eta_D \cdot \eta_J$,

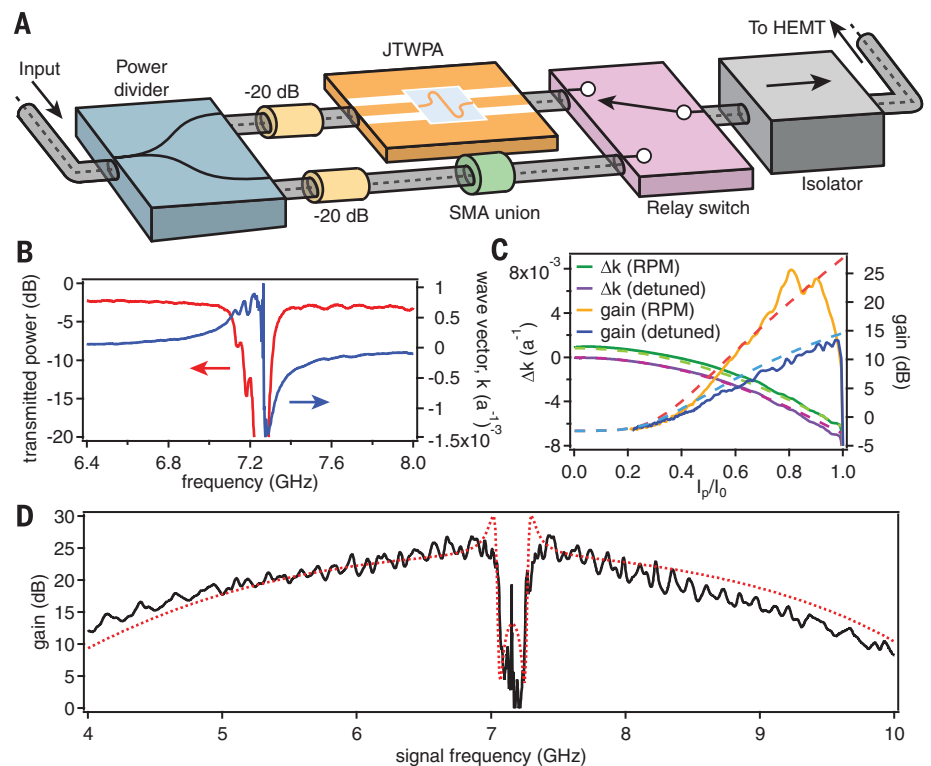


Fig. 2. Resonant phase matching. (A) Cryogenic transmission calibration setup. Input signals are split by means of a power divider followed by a 20-dB attenuator. We connect a JTWPA to one arm and a microwave union to the other arm using identical microwave cables. A switch selects which measurement chain is connected to the HEMT amplifier. (B) Small-signal transmission of the JTWPA, showing the transmission dip (red) and wave vector shift (blue) due to the dispersion feature near 7.25 GHz. The small ripples are due to inhomogeneity in the frequency of the RPM resonators. (C) Phase mismatch and gain. The phase mismatch Δk is shown for a pump at 7.157 GHz (solid green, "RPM") and at 6.5 GHz (solid purple, "detuned") versus pump power, with a signal at 6.584 GHz. The decrease in $|\Delta k|$ at large pump power for the RPM case corresponds to an enhancement in the gain (solid gold) compared to a detuned pump (solid blue). Theory overlays are shown as dashed lines in complementary colors. The measured gain curve slumps because of a drop in pump transmission for pump currents near the junction critical current. Improvements to the RPM resonators could enable further enhancement of gain. (D) Gain profile of the JTWPA with a strong pump applied at 7.157 GHz and $I_p / I_0 = 0.91$. The ripples are due to imperfect impedance matching between the JTWPA and the embedding environment. A predicted gain profile (dotted red) is overlaid, in good agreement with the measured performance.

where η_j is an extra factor that we attribute to unaccounted inefficiency in amplifier operation, we extract the intrinsic quantum efficiency of the JTWPA to be $\eta_D \cdot \eta_j = 0.75$. The signal power calibration also allows us to directly assess the dynamic range of the TWPA. We measure 1-dB gain compression at an input power of -99 dBm (fig. S9), about 7 to 10 dB higher than demonstrated in any resonator-based JPAs with comparable gain (8, 20).

We make an independent assessment of the quantum efficiency using the results for dephasing in a circuit QED measurement (32). In the limit relevant to weak measurement, the dephasing rate is given by $\Gamma_m = 8\chi^2\bar{n}/\kappa$. The rate of qubit state information collection is related to the signal-to-noise ratio (SNR) of integrated readout histograms as $\Gamma'_m = (\text{SNR})^2/8\tau$, where τ is the measurement integration time. The quantum efficiency is the ratio of these two quantities,

$\eta = \Gamma'_m/\Gamma_m$, which saturates to 1 when the dephasing rate and the rate of information collection are equal (33).

The control sequence for this measurement is shown in Fig. 3C. We use heralding to postselect a pure ground state ensemble (34). We prepare half of the ensemble in $|1\rangle$ by applying a π -pulse and leave the other half in $|0\rangle$, followed by a weak measurement of variable amplitude. A final strong measurement allows the use of postselection to eliminate records that underwent an undesired state transition. We integrate the weak measurement for a variable time and display the results as histograms, fit the histograms for the $|0\rangle$ and $|1\rangle$ subensembles to Gaussian functions, and extract the SNR. Example histograms are shown in Fig. 3D for $\bar{n} = 3.62$ and $\tau = 1 \mu\text{s}$. We repeat this experiment for a range \bar{n} from 0.3 to 3.6 and τ from 1 to 4.6 μs , extracting a mean quantum efficiency $\eta = 0.49 \pm 0.01$, in excellent agreement with the result obtained from the noise power method.

To test the performance of the JTWPA in a high-fidelity projective measurement, we exchange the weak-measurement optimized qubit and cavity for another pair more optimized for strong measurement, with $\chi/2\pi = 2.2$ MHz and $\kappa/2\pi = 8.7$ MHz. The control sequence for projective readout is the same as in Fig. 3C except for the absence of the weak measurement. Using $\bar{n} = 23.3$ and a 100-ns integration window, we measure well-separated readout histograms shown in Fig. 4A. We extract a raw measurement fidelity $F = 1 - P_{1|0} - P_{0|1} = 0.967$, where $P_{a|b}$ is the probability of identifying the qubit state as $|a\rangle$ when it was prepared as $|b\rangle$.

The error is dominated by relaxation of the qubit and spurious excitation between the heralding readout and the final readout, contributing about 0.026 and 0.007, respectively. On the basis of Gaussian fits to the state histograms, the intrinsic overlap of the histograms contributes about 10^{-5} of the total measurement error. The readout error due to histogram overlap associated with the quantum efficiency is plotted versus readout power and \bar{n} in Fig. 4B. The readout power needed to achieve a 10^{-5} error level is 14 dB below the 1-dB compression power of the JTWPA, implying that more than 20 qubits could be simultaneously read out without a degradation in performance. The prospect of multiplexing so many qubits onto a single readout line marks important progress toward a scalable readout architecture for a quantum computer based on superconducting qubits. Further improvements in the dynamic range of the JTWPA leveraging Josephson junction arrays could enable even greater multiplexing ability.

The large bandwidth and power-handling ability of the JTWPA are well suited for a variety of detector applications. Additionally, such an amplifier provides a resource for microwave quantum optics, with the possibility of generating broadband or multimode squeezed radiation. The inherent transmission geometry may reduce or eliminate the need for intermediate isolators if the passive microwave embedding environment is carefully

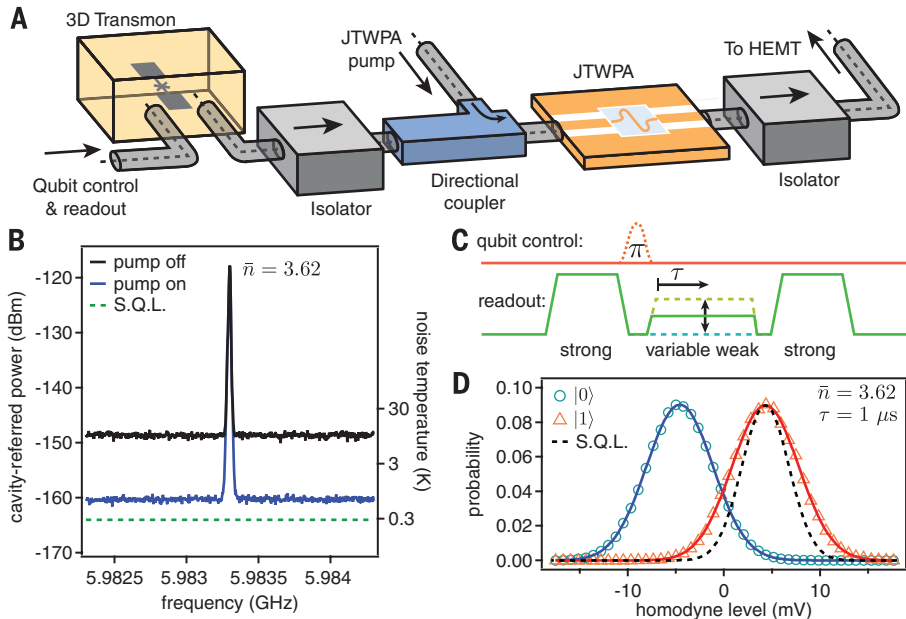


Fig. 3. Noise performance of JTWPA. (A) Cryogenic circuit schematic. Readout and control pulses enter the 3D transmon system at left. The transmitted readout signal leaves through the strongly coupled port at right. The pump tone for the JTWPA enters via a directional coupler. (B) Calibrated noise spectra. The known signal power calibrates the spectra to the cavity output plane. Using a measurement bandwidth of 10 kHz, we extract the system noise on the right axis. With the pump on (blue trace), we find a system noise of 2.10 ± 0.05 times the standard quantum limit (S.Q.L., green dashes). (C) Pulse sequence for weak measurement. An initial strong measurement heralds the ground state. The qubit is then prepared in the excited state or left in the ground state. A variable-strength weak measurement is applied, followed by a final strong measurement. (D) Example weak measurement histograms with $\bar{n} = 3.62$ and $\tau = 1 \mu\text{s}$ with Gaussian fits. The black dashed line illustrates the histogram width expected for a fully quantum-limited measurement.

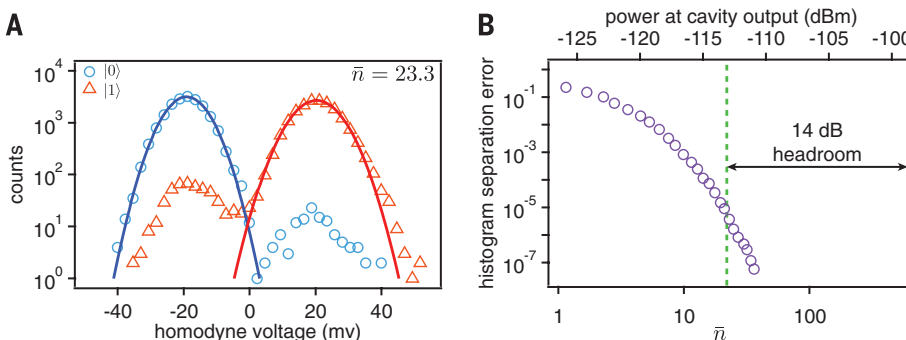


Fig. 4. High-fidelity projective measurement. (A) Optimized projective readout histograms. The intrinsic overlap of the histograms contributes less than 10^{-5} of the total error. (B) Histogram separation error for 100-ns integration window. The measurement power required to achieve a histogram separation error below 10^{-5} (dashed green line) is 14 dB below the measured 1-dB compression power of the JTWPA (dashed red line).

engineered. The low-loss deep-subwavelength loading structures used in RPM would be challenging or impossible to implement in optical-frequency systems, enabling a rich landscape of phase-matched nonlinear microwave circuits.

REFERENCES AND NOTES

1. S. J. Weber *et al.*, *Nature* **511**, 570–573 (2014).
2. N. Roch *et al.*, *Phys. Rev. Lett.* **112**, 170501 (2014).
3. P. Campagne-Ibarcq *et al.*, *Phys. Rev. Lett.* **112**, 180402 (2014).
4. M. Hatridge *et al.*, *Science* **339**, 178–181 (2013).
5. R. Vijay *et al.*, *Nature* **490**, 77–80 (2012).
6. G. de Lange *et al.*, *Phys. Rev. Lett.* **112**, 080501 (2014).
7. S. Shankar *et al.*, *Nature* **504**, 419–422 (2013).
8. C. Eichler, Y. Salathe, J. Mlynek, S. Schmidt, A. Wallraff, *Phys. Rev. Lett.* **113**, 110502 (2014).
9. E. Flurin, N. Roch, F. Mallet, M. H. Devoret, B. Huard, *Phys. Rev. Lett.* **109**, 183901 (2012).
10. R. Barends *et al.*, *Nature* **508**, 500–503 (2014).
11. D. Ristè *et al.*, *Nat. Commun.* **6**, 6983 (2015).
12. J. M. Chow *et al.*, *Nat. Commun.* **5**, 4015 (2014).
13. M. A. Castellanos-Beltran, K. W. Lehnert, *Appl. Phys. Lett.* **91**, 083509 (2007).
14. N. Bergeal *et al.*, *Nature* **465**, 64–68 (2010).
15. M. Hatridge, R. Vijay, D. H. Slichter, J. Clarke, I. Siddiqi, *Phys. Rev. B* **83**, 134501 (2011).
16. C. Caves, *Phys. Rev. D Part. Fields* **26**, 1817–1839 (1982).
17. T. Yamamoto *et al.*, *Appl. Phys. Lett.* **93**, 042510 (2008).
18. N. Roch *et al.*, *Phys. Rev. Lett.* **108**, 147701 (2012).
19. C. Eichler, A. Wallraff, *EPJ Quantum Technology* **1**, 2 (2014).
20. J. Y. Mutus *et al.*, *Appl. Phys. Lett.* **104**, 263513 (2014).
21. K. O'Brien, C. Macklin, I. Siddiqi, X. Zhang, *Phys. Rev. Lett.* **113**, 157001 (2014).
22. B. Ho Eom, P. K. Day, H. G. LeDuc, J. Zmuidzinas, *Nat. Phys.* **8**, 623–627 (2012).
23. C. Bockstiegel *et al.*, *J. Low Temp. Phys.* **176**, 476–482 (2014).
24. S. K. Tolpygo *et al.*, *IEEE Trans. Appl. Supercond.* **25**, 1101312 (2015).
25. Materials and methods are available as supplementary materials on Science Online.
26. G. P. Agrawal, *Nonlinear Fiber Optics* (Academic Press, Oxford, ed. 5, 2013).
27. A. Blais, R.-S. Huang, A. Wallraff, S. M. Girvin, R. J. Schoelkopf, *Phys. Rev. A* **69**, 062320 (2004).
28. J. E. Fernandez, "A Noise Measurement System Using a Cryogenic Attenuator," *TMO Prog. Rep.* **42-135** (1998).
29. L. Spietz, K. W. Lehnert, I. Siddiqi, R. J. Schoelkopf, *Science* **300**, 1929–1932 (2003).
30. M. A. Castellanos-Beltran, K. D. Irwin, G. C. Hilton, L. R. Vale, K. W. Lehnert, *Nat. Phys.* **4**, 929–931 (2008).
31. H. Paik *et al.*, *Phys. Rev. Lett.* **107**, 240501 (2011).
32. M. Boissonneault, J. M. Gambetta, A. Blais, *Phys. Rev. A* **79**, 013819 (2009).
33. A. Korotkov, *Phys. Rev. B* **63**, 115403 (2001).
34. J. E. Johnson *et al.*, *Phys. Rev. Lett.* **109**, 050506 (2012).

ACKNOWLEDGMENTS

We acknowledge A. Kamal, S. Tolpygo, and G. Fitch for useful discussions and technical assistance. C.M. acknowledges E. Hassell and J. Luke for useful discussions. This research is based on work supported in part by the Army Research Office (under grant no. W911NF-14-1-0078); the Office of the Director of National Intelligence (ODNI), Intelligence Advanced Research Projects Activity (IARPA), via MIT Lincoln Laboratory under Air Force Contract FA8721-05-C-0002; and a Multidisciplinary University Research Initiative from the Air Force Office of Scientific Research MURI grant no. FA9550-12-1-0488. The views and conclusions contained herein are those of the authors and should not be interpreted as necessarily representing the official policies or endorsements, either expressed or implied, of ODNI, IARPA, or the U.S. government. The U.S. government is authorized to reproduce and distribute reprints for governmental purpose notwithstanding any copyright annotation thereon. M.E.S. acknowledges support from a Hertz Foundation Fellowship.

SUPPLEMENTARY MATERIALS

www.sciencemag.org/content/350/6258/307/suppl/DC1
Materials and Methods
Figs. S1 to S12

5 February 2015; accepted 19 August 2015
Published online 3 September 2015
10.1126/science.aaa8525

OCEANOGRAPHY

Sensitivity of seafloor bathymetry to climate-driven fluctuations in mid-ocean ridge magma supply

J.-A. Olive,^{1*} M. D. Behn,² G. Ito,³ W. R. Buck,¹ J. Escartin,⁴ S. Howell³

Recent studies have proposed that the bathymetric fabric of the seafloor formed at mid-ocean ridges records rapid (23,000 to 100,000 years) fluctuations in ridge magma supply caused by sea level changes that modulate melt production in the underlying mantle. Using quantitative models of faulting and magma emplacement, we demonstrate that, in fact, seafloor-shaping processes act as a low-pass filter on variations in magma supply, strongly damping fluctuations shorter than about 100,000 years. We show that the systematic decrease in dominant seafloor wavelengths with increasing spreading rate is best explained by a model of fault growth and abandonment under a steady magma input. This provides a robust framework for deciphering the footprint of mantle melting in the fabric of abyssal hills, the most common topographic feature on Earth.

Seafloor abyssal hills are the most common topographic feature on the surface of the solid Earth. They consist of a juxtaposition of bathymetric highs and lows with a characteristic spacing of 1 to 10 km and amplitude of up to a few hundred meters, elongated parallel to crustal isochrons (*1–3*). These features form at mid-ocean ridges (MORs) through the interaction of

volcanism and faulting coincident with the creation of new oceanic lithosphere (*2, 4, 5*) (Fig. 1).

The fabric of abyssal hills has recently been proposed to record fluctuations in MOR magma supply driven by climatically controlled sea level variations with a periodicity of up to 100 thousand years (ky) (*6*). It was shown that sea level changes of ~100 m associated with glacial (Milankovitch) cycles could induce pressure changes on the subridge mantle undergoing decompression melting, thereby modulating the flux of melt supplied to the ridge axis (*6, 7*). This mechanism was proposed to drive oceanic crustal thickness

¹Lamont-Doherty Earth Observatory, Columbia University, Palisades NY, USA. ²Woods Hole Oceanographic Institution, Woods Hole MA, USA. ³University of Hawaii, Honolulu HI, USA. ⁴CNRS, Institut de Physique du Globe de Paris, Paris, France.
*Corresponding author. E-mail: jaolive@ldeo.columbia.edu

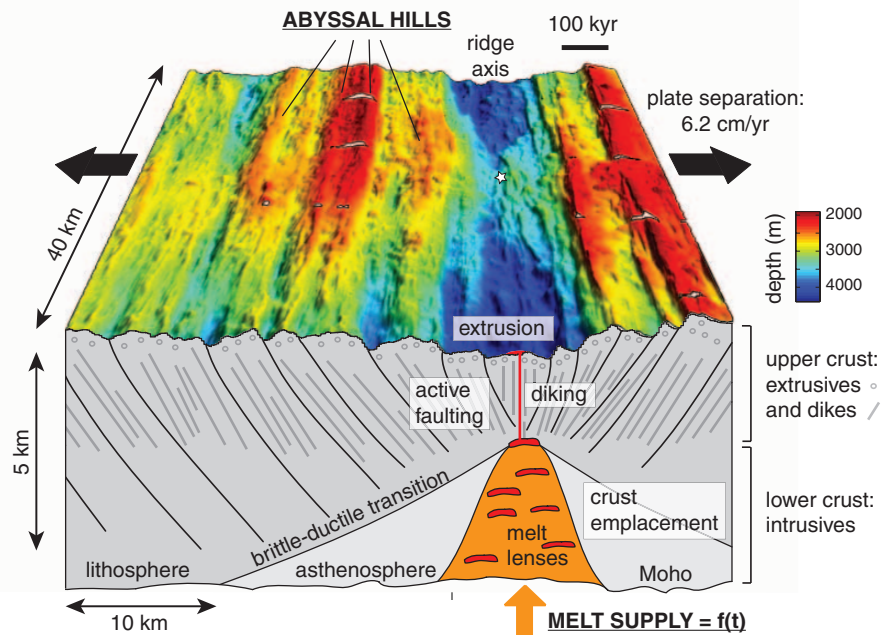


Fig. 1. Abyssal hill fabric formed at the intermediate-spreading Chile Ridge. Bathymetry of a segment of the intermediate-spreading Chile Ridge (*29*) located at 39°12'S, 91°30'W (white star), looking south. Beneath is a schematic cross section showing the major tectono-magmatic processes that shape the seafloor as melt supplied from below is emplaced as new oceanic crust.

fluctuations of ~600 m and give rise to isostatically compensated seafloor topography with wavelengths reflecting Milankovitch periodicities (23, 41, and 100 ky). Spectral power at these wavelengths in the bathymetry of the intermediate-spreading Australian-Antarctic Ridge (AAR) was presented as evidence for this process (6). Moreover, an independent study revealed a strong spectral peak near the 100-ky period for seafloor created at the fast-spreading East Pacific Rise, although peaks at the 23- and 41-ky periods were not observed (8). If confirmed, a major implication of this model is that abyssal hill fabric represents a proxy for paleo sea-level change.

Climate-driven changes in magma supply in several terrestrial settings have been attributed to the loss of glaciers, some up to 2 km thick (9, 10). However, whether ~100-m change in sea level can be effectively recorded in seafloor bathymetry is unclear (6, 7, 11). We combine classic seafloor observations with recently developed and improved models of MOR dynamics to determine whether oscillations in melt supply of a given period (τ) can imprint seafloor bathymetry through three mechanisms: (i) static topographic compensation, (ii) volcanic extrusion on the seafloor, and (iii) tectonomagmatic interactions during normal fault growth.

The first mechanism linking MOR magma supply and seafloor bathymetry is (i) temporal (and hence cross-axis) oscillations in crustal thickness, applying a vertical load on the oceanic lithosphere that can deflect the seafloor (6). The

wavelength of the load ($U \times \tau$, where U is the spreading half-rate) strongly controls the response of the lithosphere, which is commonly described as the flexing of a thin elastic plate of effective thickness T_e (12, 13) (Fig. 2A). Because ~70% of the entire crust at intermediate- and fast-spreading ridges accretes as intrusive lower crust (14), fluctuations in melt supply will be expressed primarily as vertical undulations of the crust-mantle interface loading the lithosphere from below. In (6), however, flexure was ignored in favor of an Airy isostasy approximation. This yielded variations in seafloor topography of ~150 m in response to 600-m variations in crustal thickness driven by sea level changes over a range of spreading rates. This approximation is valid when $U \times \tau$ is greater than ~100 T_e , but this is not likely to be the case in general.

At slow-spreading ridges, Milankovitch cycles would create crustal loads of wavelength <3 km, which is considerably less than 10 T_e , as T_e has been shown to be greater than ~1 km (13, 15). Such loads should result in essentially no seafloor topography (Fig. 2A). By contrast, T_e is likely to be minimal at fast-spreading ridges, such as the East Pacific Rise, where the observed rise crest topography is best explained by a T_e of 100 m at the axis, although it thickens rapidly with lithosphere age to reach ~800 m in 100-ky-old lithosphere (16). A value of $T_e = 100$ m could explain topographic variations of ~70 to 110 m at the wavelength corresponding to the longest Milankovitch period (i.e., 8 km for $U = 8$ cm/year, assuming average

crustal densities between 2850 and 3000 kg m^{-3}). However, this estimate drops to ~5 m when using a value of T_e averaged over the wavelength of the load ($T_e = 500$ m) (Fig. 2A). Finally, at the AAR ($U = 3$ cm/year), creating seafloor topography greater than 10 m would require a $T_e \leq 100$ m, unrealistically low for an intermediate-spreading ridge. In short, the lithosphere most often constitutes a strong topographic filter to such short wavelength oscillations in crustal thickness.

Yet, another consideration suggests that a ~600-m variation in crustal thickness is an overestimate. Namely, magma arising out of the mantle is delivered to a magma storage (accretion) region of finite width within the crust, before solidifying in a neovolcanic zone of comparable width (17, 18) (Fig. 1). If the melt input (volume per unit time per unit length of ridge) fluctuates by an amount $\Delta\Phi_0$ on a period shorter than its characteristic residence time in the accretion zone, these oscillations will generate crustal thickness variations that are reduced compared to estimates that assume an infinitesimally narrow accretion zone [$\Delta h_0 = \Delta\Phi_0 / 2U \sim 600$ m, as in (6)]. For example, simple mass balance arguments (12) predict that an intermediate-spreading ridge such as the AAR with a characteristic accretion zone width of 1 km would more realistically produce crustal thickness oscillations of ~410, 220, and 120 m on Milankovitch periods of 100, 41, and 23 ky, respectively (Fig. 2B). However, again at slow-to-intermediate spreading

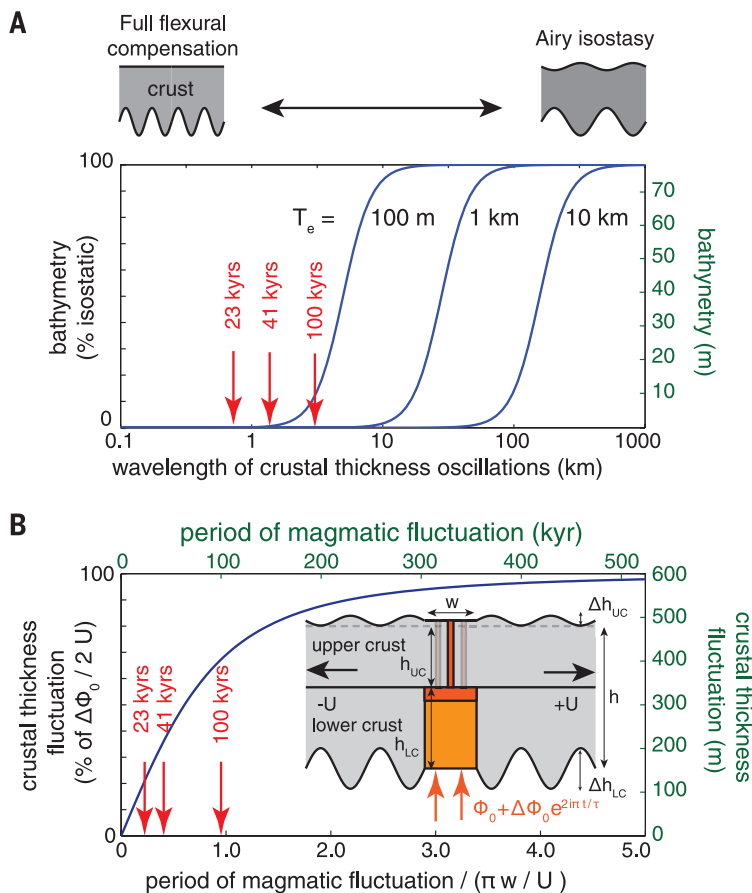


Fig. 2. Seafloor topography from static compensation mechanisms. (A) Bathymetric relief created in response to oscillations in crustal thickness on a given wavelength, assuming three different effective elastic thicknesses (T_e) for the lithosphere. Relief amplitude is given in percentage of the isostatic end-member (black axis) and in meters, assuming a crustal thickness fluctuation of 600 m and a density of 3000 kg m^{-3} for the oceanic crust (green axis). Red arrows indicate the seafloor wavelengths corresponding to Milankovitch periods for a spreading half-rate $U = 3$ cm/year. (B) Crustal thickness fluctuation ($\Delta h = \Delta h_{UC} + \Delta h_{LC}$) resulting from emplacement of a melt flux oscillating by $\Delta\Phi_0$, within a zone of width w , on a period τ . Green axes (dimensional) illustrate the case where $U = 3$ cm/year and $w = 1$ km. Black axes are normalized.

Fig. 3. A tectono-magmatic interaction model for the spacing of abyssal hills.

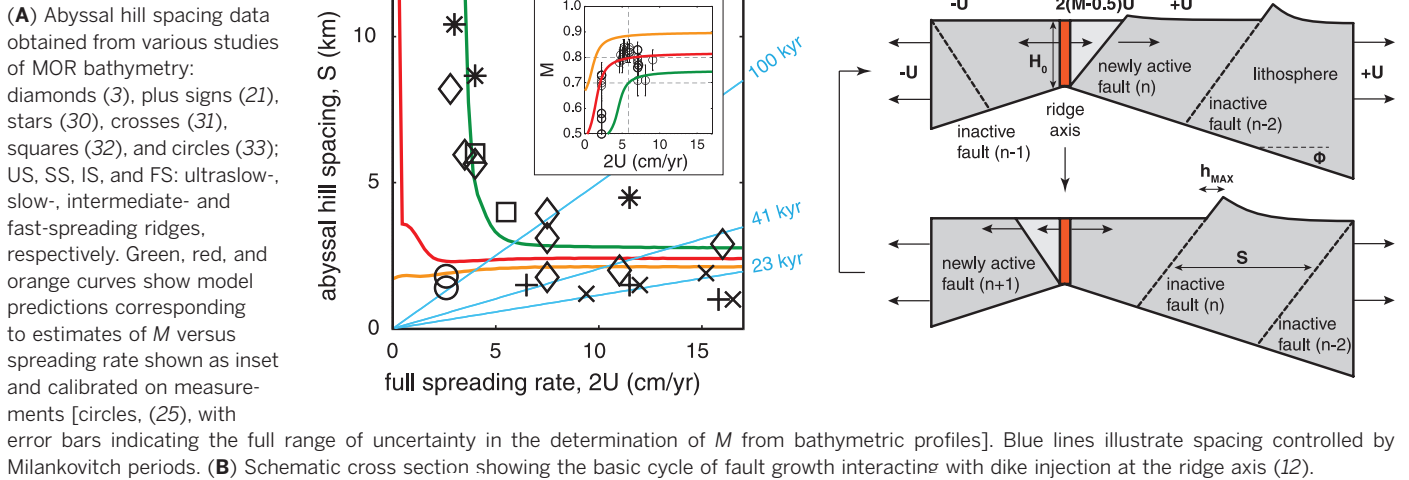
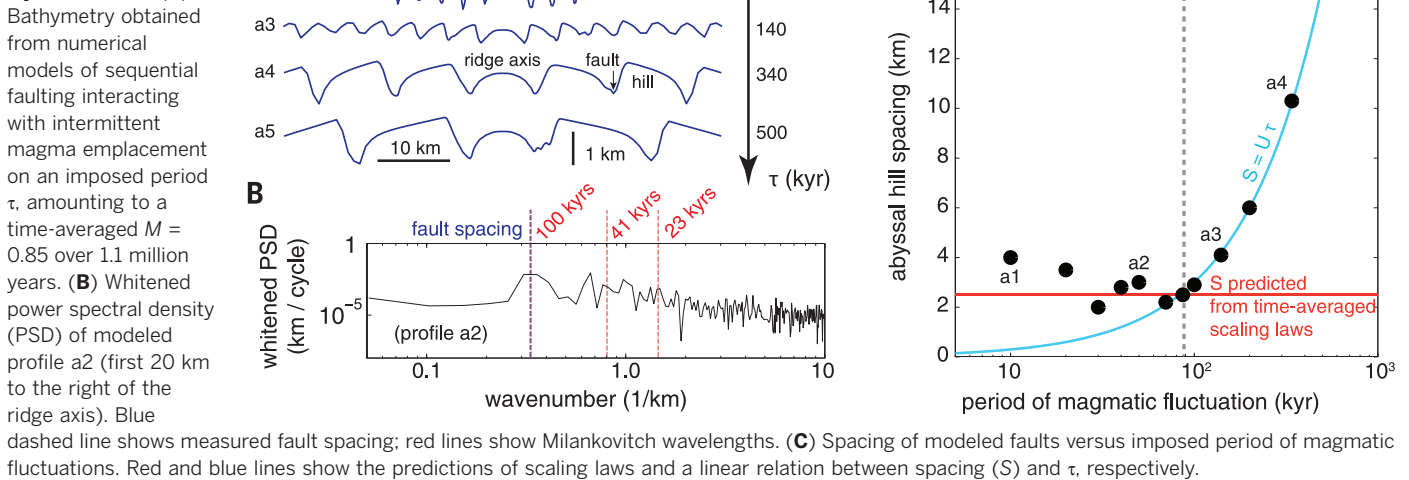


Fig. 4. Sensitivity of MOR bathymetry to fluctuating dike injection rates.



rates, lithospheric flexure should drastically impede any topographic expression of these reduced thickness oscillations. At the fast-spreading East Pacific Rise ($U = 8$ cm/year), seismic evidence points to a characteristic accretion width of ~ 5 km (19). This would reduce both the estimated 100-ky crustal thickness variation and its topographic expression by a factor of 0.45, enabling at most 30 to 50 m of topography for the lowest estimate of lithospheric strength ($T_e = 100$ m).

The second mechanism for generating topography in response to oscillations in magma supply considers (ii) the portion added to the extrusive upper crust. The time-averaged volume of extruded material is thought to reflect the overpressure in an axial melt lens pushing magma upward to the seafloor (20). When transitioning from a period of thin to thick axial crust due to a change in melt supply, the overpressure must increase to compensate the replacement of dense mantle by lighter lower crust. This assumption (12) is different from

that of isostatic or flexural equilibrium explored earlier, because a column of magma rising to the surface is mechanically decoupled from the rest of the lithosphere. We can use it to estimate the thickness variation of the extrusive portion of the crust Δh_{UC} that results from the crustal thickness variations $\Delta h = 410, 220,$ and 120 m expected at the AAR (Fig. 2B). This yields $\Delta h_{UC} = 60$ to $85, 33$ to $46,$ and 18 to 25 m, respectively, depending on the density assumed for the oceanic crust. A similar reasoning predicts topographic fluctuations of 40 to 55 m on a 100-ky period at the East Pacific Rise. They are, however, unlikely to strongly overprint the tectonic fabric of the seafloor, which typically consists of fault scarps greater than 200 m at slow and intermediate-spreading ridges (3) and about 50 to 100 m at fast-spreading ridges (21). Moreover, these amplitudes are probably upper bounds, because seafloor eruptions involve lava flows spreading up to a few km in the cross-axis direction (22), providing another topographic damping process.

An important corollary to both of the above mechanisms (i and ii) is that the wavelength of the sea level–modulated topography should increase in proportion to spreading rate. However, the spacing of abyssal hills, which constitutes the dominant wavelength in the spectrum of the seafloor (23), is observed to decrease with increasing spreading rate from ~ 10 km at slow-spreading ridges down to ~ 2 km at fast-spreading ridges (Fig. 3A). Thus, any viable model for abyssal hill formation must explain this global trend.

Given that abyssal hills are typically bounded by major normal faults (2), we favor an alternative model in which the decrease in abyssal hill spacing reflects the increasing importance of magmatically versus tectonically accommodated extension at faster-spreading ridges (24). With this framework, we explore the possibility that (iii) a fluctuating magma supply influences the pattern of faulting, which shapes the seafloor fabric.

In a time-averaged sense, dike intrusion in the axial lithosphere accommodates a fraction

M of the total plate separation (Fig. 3B). The remaining fraction $(1 - M)$ is accommodated by slip on normal faults that initiate near the axis and are subsequently pushed off-axis by magmatic intrusion at a rate that increases with M (24, 25). As a fault encounters progressively thicker off-axis lithosphere, the work required to keep it active increases until it becomes mechanically favorable to abandon it in favor of a new fault forming closer to the axis (Fig. 3B). Mechanical scaling laws (12) predict that thick or rapidly thickening lithosphere with a robust magma supply (high M) produces relatively short-lived, and therefore closely spaced, faults (24, 25). Upon parameterizing axial lithospheric thickness, thickening rate, and M , versus spreading rate through empirical fits to observations (Fig. 3A, inset, and fig. S2), we use these mechanical scaling laws to predict a decrease in abyssal hill spacing from ~ 10 to ~ 2.5 km with increasing spreading rate, following the trend of the observations (Fig. 3A). Thus, the systematic variations in abyssal hill fabric with spreading rate are best explained by a model of tectono-magmatic extension under a steady magma input.

Steady magma input is an oversimplification of the ridge magmatic system, even without climatic variations in magma flux (26, 27). Thus, we consider the possibility that an oscillating magma input could alter the above behavior by directly affecting the duration that individual faults remain active (28), and therefore imprint the seafloor fabric. We performed two-dimensional numerical simulations of normal fault growth coupled with magmatic injection in the lithosphere that fluctuates on a period τ (12). During 85% of the cycle, magma injection accommodates 100% of plate separation ($U = 3$ cm/year), whereas during the remaining 15%, extension is fully accommodated on faults that form spontaneously in the lithosphere. This scenario maximizes the effects of magmatic modulation but has a time-averaged M equal to 0.85 (28).

We ran 12 simulations with τ ranging from 10 to 500 ky. The modeled seafloor shows abyssal hill-like topography, from which we measure the mean fault spacing (Fig. 4A). The spectrum of topography clearly shows that fault spacing expresses a dominant wavelength (Fig. 4B). It also reveals a number of peaks at higher wave numbers (within the Milankovitch range) that cannot be directly interpreted in terms of seafloor length scales. Simulations with short τ consistently produce abyssal hills with a characteristic spacing of ~ 2 to 4 km, as predicted by the mechanical scaling laws that assume a steady magma input (horizontal red line in Fig. 4C). Simulations with a longer τ , however, reveal a direct control of the forcing period on fault spacing (blue curve). The transition between the two regimes occurs at a period set by the mechanically controlled fault spacing divided by the spreading half-rate, which at intermediate-spreading ridges is ~ 100 ky. We therefore expect the tectonic fabric of the AAR to be insensitive to even extreme fluctuations in melt supply on Milankovitch frequencies. The spectral peaks observed there (6) likely reflect only the

mechanically controlled spacing of fault-bounded abyssal hills as shaped by the time-averaged melt supply ($M \sim 0.85$) (Figs. 3A and 4B).

Each of the three mechanisms of topography development acts as a low-pass filter of melt supply with strong damping of periods shorter than ~ 100 ky. Therefore, the fingerprints of a climate modulation in MOR melt supply may be found more easily through multichannel seismic imaging of the crust-mantle boundary than through bathymetric analysis. If short-wavelength topography on the base of the crust is observed, comparing its spectral characteristics in crust younger and older than the onset of pronounced glacial cycles would provide a valuable test of the predictions made here and by earlier studies (6–8).

REFERENCES AND NOTES

1. H. Menard, J. Mammerrickx, *Earth Planet. Sci. Lett.* **2**, 465–472 (1967).
2. K. C. Macdonald, P. J. Fox, R. T. Alexander, R. Pockalny, P. Gente, *Nature* **380**, 125–129 (1996).
3. J. A. Goff, Y. Ma, A. Shah, J. R. Cochran, J.-C. Sempéré, *J. Geophys. Res.* **102**, 15521–15534 (1997).
4. D. K. Rea, *Geology* **3**, 77–80 (1975).
5. E. S. Kappel, W. B. F. Ryan, *J. Geophys. Res.* **91**, 13925–13940 (1986).
6. J. W. Crowley, R. F. Katz, P. Huybers, C. H. Langmuir, S. H. Park, *Science* **347**, 1237–1240 (2015).
7. D. C. Lund, P. D. Asimow, *Geochem. Geophys. Geosyst.* **12**, 12009 (2011).
8. M. Tolstoy, *Geophys. Res. Lett.* **42**, 1346–1351 (2015).
9. M. Nakada, H. Yokose, *Tectonophysics* **212**, 321–329 (1992).
10. M. Jull, D. McKenzie, *J. Geophys. Res.* **101**, 21815–21828 (1996).
11. P. J. Huybers, C. H. Langmuir, *Earth Planet. Sci. Lett.* **286**, 479–491 (2009).
12. Materials and methods are available as supplementary materials on Science Online.
13. A. B. Watts, *Isostasy and Flexure of the Lithosphere* (Cambridge Univ. Press, Cambridge, 2001).
14. J. P. Morgan, Y. J. Chen, *J. Geophys. Res.* **98**, 6283–6297 (1993).
15. J. R. Cochran, *J. Geophys. Res.* **84**, 4713 (1979).
16. B.-Y. Kuo, D. W. Forsyth, E. M. Parmentier, *Geophys. Res. Lett.* **13**, 681–684 (1986).
17. J. M. Sinton, R. S. Detrick, *J. Geophys. Res.* **97**, 197–216 (1992).
18. M. R. Perfit, W. W. J. Chadwick, in *Faulting and Magmatism at Mid-Ocean Ridges*, W. R. Buck et al., Eds. (AGU, Washington DC, 1998), pp. 59–115.
19. R. A. Dunn, D. R. Toomey, *Nature* **388**, 259–262 (1997).
20. W. R. Buck, S. M. Carbotte, C. Z. Mutter, *Geology* **25**, 935–938 (1997).
21. S. M. Carbotte, K. C. Macdonald, *J. Geophys. Res.* **99**, 13609–13633 (1994).
22. J. Escartin et al., *Geochem. Geophys. Geosyst.* **8**, Q06005 (2007).
23. J. A. Goff, T. H. Jordan, *J. Geophys. Res.* **93**, 13589–13608 (1988).
24. W. R. Buck, L. L. Lavier, A. N. B. Poliakov, *Nature* **434**, 719–723 (2005).
25. M. D. Behn, G. Ito, *Geochem. Geophys. Geosyst.* **9**, Q08010 (2008).
26. J. P. Canales, J. A. Collins, J. Escartin, R. S. Detrick, *J. Geophys. Res.* **105**, 28411–28425 (2000).
27. E. Bonatti et al., *Nature* **423**, 499–505 (2003).
28. G. Ito, M. D. Behn, *Geochem. Geophys. Geosyst.* **9**, Q09012 (2008).
29. J. Karsten et al., *Intern. Ridge-Crest Res.* **8**, 15–21 (1999).
30. A. Malinverno, R. A. Pockalny, *Earth Planet. Sci. Lett.* **99**, 154–169 (1990).
31. P. A. Cowie, A. Malinverno, W. B. F. Ryan, M. H. Edwards, *J. Geophys. Res.* **99**, 15205–15218 (1994).
32. A. Macario et al., *J. Geophys. Res.* **99**, 17921–17934 (1994).
33. J. Escartin et al., *J. Geophys. Res.* **104**, 10421–10437 (1999).

ACKNOWLEDGMENTS

This work greatly benefited from discussions with P. Canales, A. Soule, S. Carbotte, R. Katz, P. Huybers, and B. Ryan, as well as the constructive feedback from three anonymous reviewers. Funding was provided by NSF grants OCE-1154238 (J.-A.O. and M.D.B.), OCE-1155098 (G.I. and S.H.), EAR-1009839 (W.R.B.), CNRS support to J.E., a Woods Hole Oceanographic Institution IR&D award to M.D.B. and a Lamont-Doherty Earth Observatory Postdoctoral Fellowship for J.-A.O. The data and model results presented here are included or fully referenced in the supplementary materials.

SUPPLEMENTARY MATERIALS

www.sciencemag.org/content/350/6258/310/suppl/DC1
Materials and Methods
Figs. S1 and S2
References (34–44)

22 July 2015; accepted 3 September 2015
10.1126/science.aad0715

BIOMATERIALS

A skin-inspired organic digital mechanoreceptor

Benjamin C.-K. Tee,^{1*} Alex Chortos,^{2*} Andre Berndt,^{3*} Amanda Kim Nguyen,¹ Ariane Tom,³ Allister McGuire,⁴ Ziliang Carter Lin,⁴ Kevin Tien,¹ Won-Gyu Bae,⁵ Huiliang Wang,² Ping Mei,⁶ Ho-Hsiu Chou,⁵ Bianxiao Cui,⁴ Karl Deisseroth,³ Tse Nga Ng,^{6†} Zhenan Bao^{5†}

Human skin relies on cutaneous receptors that output digital signals for tactile sensing in which the intensity of stimulation is converted to a series of voltage pulses. We present a power-efficient skin-inspired mechanoreceptor with a flexible organic transistor circuit that transduces pressure into digital frequency signals directly. The output frequency ranges between 0 and 200 hertz, with a sublinear response to increasing force stimuli that mimics slow-adapting skin mechanoreceptors. The output of the sensors was further used to stimulate optogenetically engineered mouse somatosensory neurons of mouse cortex in vitro, achieving stimulated pulses in accordance with pressure levels. This work represents a step toward the design and use of large-area organic electronic skins with neural-integrated touch feedback for replacement limbs.

Neurally controlled prosthetic devices improve mobility and independence for disabled people (1). The addition of tactile sensing can benefit the utility of these neuroprosthetics by enhancing motor control

(2–4) and relieving phantom limb pain associated with limb loss (5, 6). Thus, the implementation of human mechanoreceptor-like sensing systems would be an important step toward highly functional prosthetics.

Flexible and stretchable tactile sensors have achieved a high level of sophistication using both organic (7–10) and inorganic electronic materials (11–13). For example, Kim and co-workers recently demonstrated silicon nanoribbon strain and pressure sensor arrays that output voltage signals and stretchable multielectrode arrays for nerve stimulation (12). Although these technologies have focused on pushing the performance boundaries of mechanical sensitivities and large-area integration, the sensors rely on direct-current (dc) amplitude-modulated signals that may suffer from drift and noise over a long transmission distance. Furthermore, powering and obtaining readings of an enormously large density of sensors as found in human skin may not be energy-efficient using dc signal approaches. In contrast, each tactile mechanoreceptor in the human skin is a highly sophisticated, low-power biological circuit capable of transducing mechanical strain to oscillating electrical action potentials (14). This transduction mechanism is inherently power-efficient and robust to noise, allowing for mechanical sensations to be transmitted over long distances, such as from extremities. Previous reports on prosthetic skin systems have used a computer or microcontroller to convert the sensors' analog signals into signals that are appropriate for stimulating neurons (4, 12). To enable large-scale integration, it is advantageous for the sensors to directly produce digital signals with relevant frequencies.

We present a skin-inspired artificial mechanoreceptor system (the Digital Tactile System, or

DiTact) composed of flexible organic electronic materials. The organic circuits emulate the response of slow-adapting tactile receptors by encoding static pressure stimuli into digital signals whose frequency varies with stimulation intensity (Fig. 1A). Our digitizing system has three key components (Fig. 1B): (i) voltage-controlled oscillators constructed with printed organic circuits, (ii) flexible microstructured resistive pressure sensors with sensitivity in the range of human pressure-sensing capability, and (iii) a channelrhodopsin engineered specifically to enable optical neuron stimulation above 100 Hz (a range similar to that of slow-adapting mechanoreceptors).

Printed organic circuits are a promising scalable technology to use for electronic skins because of their potential for low-cost, large-area processing and compatibility with flexible substrates (10). Printed organic ring oscillator circuits, consisting of odd numbers of repeating inverter stages based on complementary field-effect transistors, were used (figs. S1 and S2) to generate the series of voltage spikes. Complementary ring oscillators are desirable because of their simplicity relative to other electrical oscillators, their low static power dissipation, and the dependence of the oscillation frequency on the supply voltage. By using a piezoresistive element as a component in a voltage divider, we modulated the time delay of the oscillations. As the applied force increased, the supply voltage increased and the propagation delay of the transistors was reduced, thereby increasing the frequency of the oscillations in a way that mimics the slow-adapting mechanoreceptors.

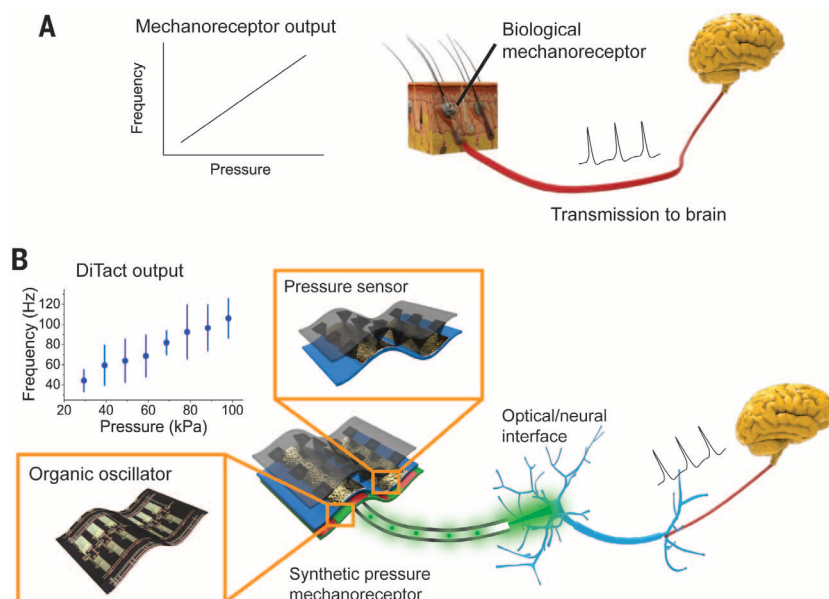
Our DiTact prototype uses a three-inverter (three-stage) ring oscillator, which is the minimum number of inverters required to maintain stable oscillations. Using fewer stages has the advantages of higher-frequency operation, lower power consumption, and smaller footprint of the devices. The complementary oscillators (fig. S1) were printed on a flexible plastic sheet (15) with a

modified dielectric with a high dielectric constant (16) (see supplementary materials). The DiTact prototype relies on a change in the voltage supply to modulate the frequency output of the sensors. The oscillation frequency depends quadratically on the supply voltage (Fig. 2A) for the voltage range used in this work. A supply voltage of 11 V was chosen to set the maximum frequency to 200 Hz, so as to match the typical frequency range of biological mechanoreceptors. The supply voltage can be further reduced via reduction of the dielectric thickness, and organic oscillators operating at 3 V have been demonstrated (17). Because the oscillator is used in a voltage divider configuration, the impedance through the oscillator under different biasing conditions (Fig. 2B) is important for the design of the sensor circuit. To emulate human tactile perception, the DiTact system must have slow or no oscillation in the absence of pressure stimulation, and the frequency should increase with pressure (18). In the voltage divider configuration, the impedance of the pressure sensor must be larger than the impedance of the oscillator in the “off” state (several hundred megohms), therefore requiring gigaohm range. This is also useful for conserving power by minimizing off-state leakage. However, in the “on” state, the impedance of the sensor must be smaller than the impedance of the oscillator (10 megohms). Furthermore, the sensors should operate within the range of pressures used for typical grip control, from several to several hundred kilopascals (19).

To create such a wide-impedance piezoresistor, we constructed sensors composed of a carbon nanotube (CNT) composite dispersed in a polyurethane elastomer that was molded into pyramidal microstructures (Fig. 2D) (see supplementary materials). The choice of microstructures is essential to achieve the desired working range and sensing characteristics. Incorporation of pyramidal structures reduces the effective modulus (20) and concentrates the electric field, resulting in

¹Department of Electrical Engineering, Stanford University, Stanford, CA, USA. ²Department of Materials Science and Engineering, Stanford University, Stanford, CA, USA. ³Department of Bioengineering, Stanford University, Stanford, CA, USA. ⁴Department of Chemistry, Stanford University, Stanford, CA, USA. ⁵Department of Chemical Engineering, Stanford University, Stanford, CA, USA. ⁶Xerox Palo Alto Research Center, Palo Alto, CA, USA. *These authors contributed equally to this work. †Present address: Department of Electrical Engineering, University of California, San Diego, CA, USA. ‡Corresponding author. E-mail: zbao@stanford.edu

Fig. 1. DiTact concept design. (A) Schematic of the function of a biological somatosensory system. Voltage pulses are generated in the skin and transported to the brain. (B) DiTact is composed of a pressure-sensitive tactile element and an organic ring oscillator. Optogenetic pulses were used to stimulate live neurons.



improved piezoresistive properties relative to an unstructured film. Moreover, the size and spacing of the pyramidal microstructures have important effects on the sensitivity and working range (figs. S3 and S4). Because their function is based on tunneling between CNTs and an electrode, the devices show substantial voltage dependence in the sensing characteristics (Fig. 2F and fig. S5). The pressure- and voltage-dependent impedance was fitted to a mathematical model (fig. S6) for use in circuit characterization (fig. S7). When the sensor and oscillator were in series in a voltage divider, the frequency of the oscillator increased with pressure (Fig. 2G). In the on state (at 100 kPa, with all voltage dropping across the oscillator), the power dissipation of the DiTact prototype was 18.4 μ W at 11 V and 2.0 μ W at 6 V, which compares favorably to analog approaches. A model hand depicts how sensors could be incorporated into a prosthetic device (Fig. 2H). The electrical components were connected with stretchable silver nanowire conductors. In addition, the DiTact sensors were incorporated with a wearable glove to show the frequency variation of the voltage signal with the application of pressure in a wearable system (movie S1).

We used the pressure-induced, frequency-encoded digital signal output from the DiTact system to directly stimulate mouse cortical neurons both electrically (fig. S13) and optically (Fig. 3 and fig. S12). Although electrical stimulation is

more applicable to conventional prosthetics (4, 12, 21, 22), optogenetic stimulation is a promising new approach that we used as a reliable noncontact method to demonstrate the feasibility of interfacing with biological neural circuits. Optogenetics induces action potentials with excellent fidelity, allowing the DiTact signal to be very effectively transmitted to the target neurons. Using this approach, the output signal of the DiTact sensor was set to directly modulate the frequency of an LED light source. Light application evokes neuronal firing in neurons that express light-activated ion channels such as channelrhodopsin-2 (ChR2) or its mutations such as H134R [ChR2(HR)], which are among the standard tools for optogenetic applications.

The DiTact sensor was engineered to have a maximum frequency of 200 Hz, which is comparable to the upper limit for the generation of action potentials during tactile stimulation in humans. Consequently, the optogenetic neural interface must be capable of stimulating neurons with a frequency up to 200 Hz for several seconds. However, sustained high-frequency stimulation is difficult to achieve using conventional optogenetic channel proteins. Mutations of channelrhodopsin such as ChR2-E123A [ChETA(EA)] accelerate channel opening and closure. They are commonly used for modification of neurons for optogenetic applications and could potentially meet our requirement (23, 24). However, we found that

ChETA activity was not well suited in cultured pyramidal neurons to mediate spikes for extended periods of time (Fig. 3A, fig. S10, and table S1). Therefore, we engineered the channelrhodopsin hybrid C1C2 (25) because of its larger activity relative to ChR2 (fig. S10). The resulting construct, termed bC1C2(s/v), had larger photocurrents than ChR2(HR) and ChETA(EA), as well as fast off-kinetics (fig. S11). We expressed ChETA(EA) and bC1C2(s/v) separately in cortical fast-spiking parvalbumin-positive (PV⁺) neurons and compared both constructs using whole-cell patch-amp recordings of acute slices; the results confirmed the larger photocurrents and fast kinetics of bC1C2(s/v) (Fig. 3A, fig. S11, and table S2). bC1C2(s/v) was able to reliably evoke action potentials at frequencies up to 200 Hz for more prolonged intervals (Fig. 3, A and B), which mimics the frequency range of slow-adapting and fast-spiking tactile receptors such as Merkel cells (26).

To interface the digital signal from the DiTact system with live neurons, we connected the sensor output to the setup shown in Fig. 3C. The DiTact signal was conditioned via an edge detector to a 2-ms pulse that triggered the LED once per oscillation. The light pulse from the LED was used to optogenetically stimulate PV⁺ neurons in an acute slice of primary somatosensory cortex from mice. For the sensor composition used in the neuron stimulation study, the frequency exhibited a sublinear dependence on the pressure

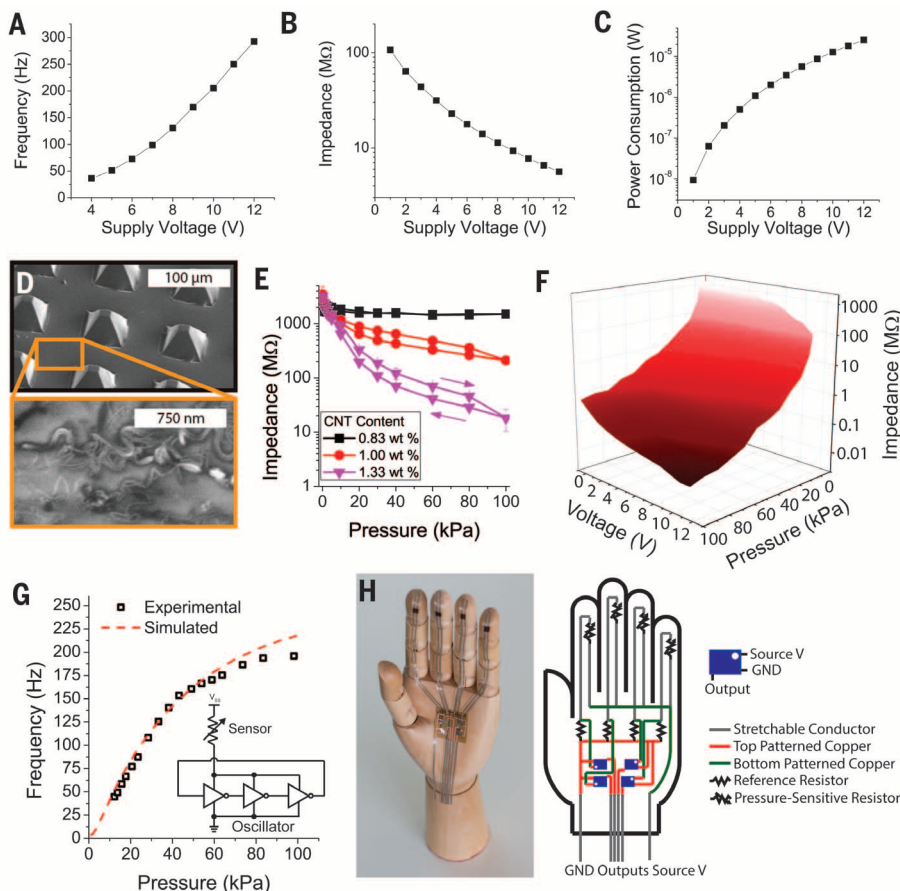
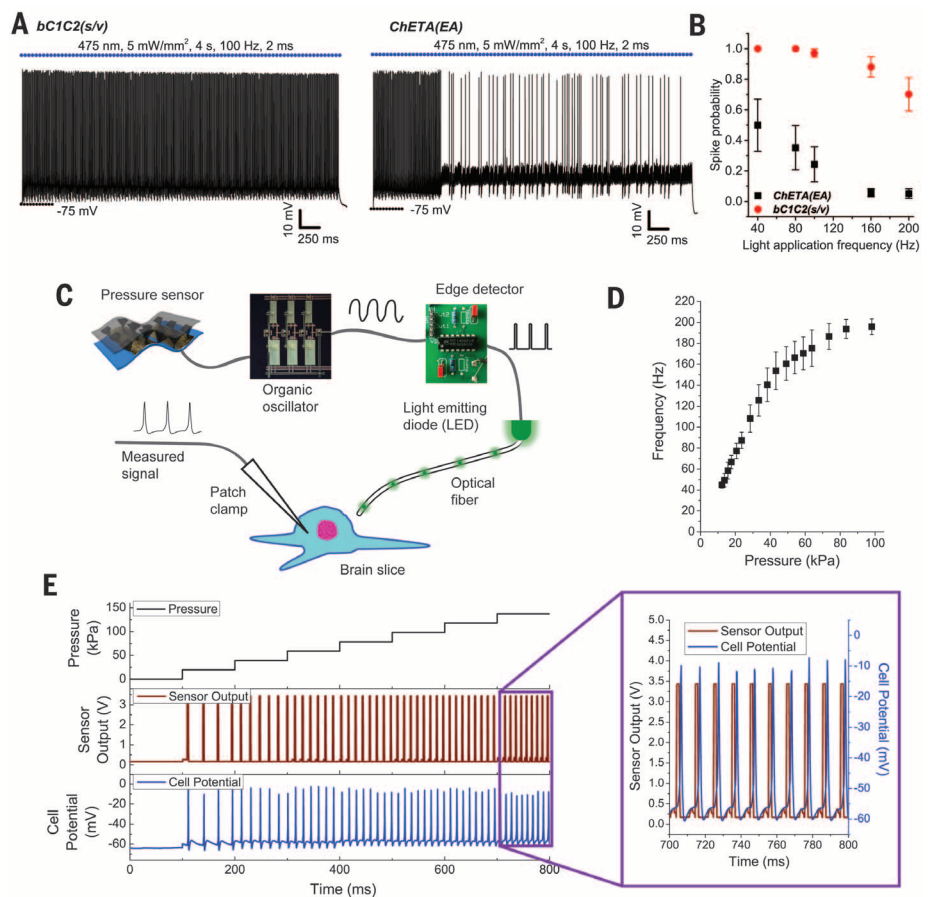


Fig. 2. Oscillator and pressure sensor characteristics and integration. (A to C) Frequency, impedance, and power dissipation as a function of supply voltage for the oscillators. (D) Scanning electron micrographs of the pyramids and the elastomer-CNT composite used to fabricate the piezoresistive sensors. (E) Pressure response of sensors as a function of CNT concentration. (F) Three-dimensional contour plot of impedance as a function of pressure and voltage. (G) Plot of frequency output as a function of pressure for an example DiTact sensor (see supplementary materials for description of circuit simulation). (H) Image and circuit schematic of a model hand with DiTact sensors on the fingertips connected with stretchable interconnects.

Fig. 3. Optogenetic stimulation of somatosensory cortex neurons using DiTact. (A)

Time-resolved voltage traces of cortical fast-spiking PV⁺ interneurons expressing bC1C2(s/v) (left) and ChETA (EA) (right). Cells were recorded using whole-cell patch clamping in acute slice of mice medial prefrontal cortex. Neurons were stimulated for 4 s with pulsed 475-nm light (5 mW/mm², pulse width 2 ms) at 100 Hz with to evoke action potentials. Spike probability is at 100% in bC1C2(s/v)-expressing neuron during prolonged stimulation. (B) Summary of spike probability in response to light stimulation applied at frequencies from 40 to 200 Hz. ChETA(EA), *n* = 16; bC1C2(s/v), *n* = 10. All error bars denote SEM; *n* indicates number of cells. (C) Setup of the optoelectronic stimulation system for pressure-dependent neuron stimulation. (D) Frequency output recorded from in vitro somatosensory cortical mouse neurons as a function of the pressure applied to the DiTact sensor. The error bars represent one standard deviation from 10 samples. Individual trials are shown in fig. S13D. (E) Correlation among pressure, sensor output, and cell potential. The expanded section shows that the neurons' action potentials closely follow the pulses from the LED.



(Fig. 3D). The neurons fired in accordance with the stimulation pulse, which was generated at frequencies determined by the pressure applied to the DiTact system (Fig. 3E). The output of the DiTact system had pressure-dependent frequency characteristics with a threshold and range similar to those of biological mechanoreceptors (fig. S12).

Our system currently encodes static pressure stimuli. To fully mimic the properties of biological mechanoreceptors, it will be important to implement temporal adaptation to both static and nonstatic stimuli (18)—for example, an increased firing rate due to moving stimuli (e.g., nonstatic brushing action) and decreased firing rates due to constant stimuli (static contact force). To demonstrate the compatibility of the DiTact approach with electrical stimulation methods, we coupled an inorganic oscillator to the pressure sensor, and the resulting frequency signal was successfully used to stimulate hippocampal neurons in a multielectrode array (fig. S13). The compatibility of the DiTact sensor with optogenetic stimulation of somatosensory cortex interneurons (Fig. 3) and parvalbumin neurons (fig. S12B), as well as electrical stimulation of hippocampal neurons (fig. S13), suggests that the system would be compatible with other fast-spiking neurons, including peripheral nerves.

Our DiTact sensors encode pressure stimulation magnitude with sublinear digital responses similar to human mechanoreceptors. The output of the sensors can stimulate in vitro neurons

both electrically and optically with engineered optogenetic neurons that respond to the range of human action potential frequencies. This system can be potentially integrated over large areas as electronic skins for conventional neural prosthetics or optogenetic-based prosthetic interfaces. Furthermore, the digital nature of the output could be advantageous in high-density prosthetic sensor systems, using strategies similar to code division multiple access (CDMA) that allow for greater bandwidths with fewer interconnections.

REFERENCES AND NOTES

1. L. R. Hochberg *et al.*, *Nature* **485**, 372–375 (2012).
2. J. E. O'Doherty *et al.*, *Nature* **479**, 228–231 (2011).
3. A. Abbott, *Nature* **442**, 125–127 (2006).
4. S. Raspopovic *et al.*, *Sci. Transl. Med.* **6**, 222ra19 (2014).
5. M. Lotze *et al.*, *Nat. Neurosci.* **2**, 501–502 (1999).
6. D. W. Tan *et al.*, *Sci. Transl. Med.* **6**, 257ra138 (2014).
7. S. C. B. Mannsfeld *et al.*, *Nat. Mater.* **9**, 859–864 (2010).
8. G. Schwartz *et al.*, *Nat. Commun.* **4**, 1859 (2013).
9. M. Kaltenbrunner *et al.*, *Nature* **499**, 458–463 (2013).
10. T. Sekitani *et al.*, *Science* **326**, 1516–1519 (2009).
11. D.-H. Kim *et al.*, *Science* **333**, 838–843 (2011).
12. J. Kim *et al.*, *Nat. Commun.* **5**, 5747 (2014).
13. K. Takei *et al.*, *Nat. Mater.* **9**, 821–826 (2010).
14. E. P. Gardner, *Touch* (eLS/Wiley Online Library, 2001).
15. T. N. Ng *et al.*, *Sci. Rep.* **2**, 585 (2012).
16. P. Mei *et al.*, *Appl. Phys. Lett.* **105**, 123301 (2014).
17. T. Sekitani, U. Zschieschang, H. Klauk, T. Someya, *Nat. Mater.* **9**, 1015–1022 (2010).
18. M. Knibestöl, *J. Physiol.* **245**, 63–80 (1975).
19. D. A. Nowak, J. Hermsdörfer, *Mov. Disord.* **20**, 11–25 (2005).

20. B. C. K. Tee *et al.*, *Adv. Funct. Mater.* **24**, 5427–5434 (2014).
21. A. Canales *et al.*, *Nat. Biotechnol.* **33**, 277–284 (2015).
22. I. R. Mineev *et al.*, *Science* **347**, 159–163 (2015).
23. L. A. Gunaydin *et al.*, *Nat. Neurosci.* **13**, 387–392 (2010).
24. J. Mattis *et al.*, *Nat. Methods* **9**, 159–172 (2012).
25. H. E. Kato *et al.*, *Nature* **482**, 369–374 (2012).
26. H. Haerberle, E. A. Lumpkin, *Chemosens. Percept.* **1**, 110–118 (2008).

ACKNOWLEDGMENTS

B.C.-K.T., A.C., A.B., and Z.B. conceived the experiments; T.N.N., P.M., B.C.-K.T., K.T., and H.W. worked on equipment and fabricated oscillators; A.C. and B.C.-K.T. designed pressure sensors and A.C. and H.-H.C. characterized them; B.C.-K.T., A.K.N., and A.C. implemented measurement electronics; A.B. and K.D. engineered the channelrhodopsin protein; A.B., A.C., A.K.N., and A.T. performed optogenetic measurements; B.C.-K.T., A.M., and Z.C.L. did measurements using electrical stimulation of neurons; W.-G.B. improved data visualization; B.C.-K.T., A.C., A.B., and Z.B. wrote the manuscript; and all authors reviewed and critiqued the results and made key revisions to the manuscript. We thank N. Liu for taking SEM images and Lubrizol Co. for supplying SG80A elastomer for the pressure sensors. Supported by the Xerox Foundation; the MSIP (Ministry of Science, ICT and Future Planning), Korea, under the IT Consilience Creative Program (grant NIPA-2014-H0201-14-1001) supervised by the National IT Industry Promotion Agency; Agency for Science Technology and Research Singapore (A*STAR); and Samsung Electronics.

SUPPLEMENTARY MATERIALS

www.sciencemag.org/content/350/6258/313/suppl/DC1
Materials and Methods
Figs. S1 to S14
Tables S1 and S2
Movie S1
References (27–33)

16 February 2015; accepted 7 August 2015
10.1126/science.aaa9306

NEURAL PROGENITORS

Opposing intrinsic temporal gradients guide neural stem cell production of varied neuronal fates

Zhiyong Liu,^{1*} Ching-Po Yang,^{1*} Ken Sugino,^{1*} Chi-Cheng Fu,^{1,2*†} Ling-Yu Liu,¹ Xiaohao Yao,¹ Luke P. Lee,² Tzumin Lee^{1‡}

Neural stem cells show age-dependent developmental potentials, as evidenced by their production of distinct neuron types at different developmental times. *Drosophila* neuroblasts produce long, stereotyped lineages of neurons. We searched for factors that could regulate neural temporal fate by RNA-sequencing lineage-specific neuroblasts at various developmental times. We found that two RNA-binding proteins, IGF-II mRNA-binding protein (*Imp*) and Syncrip (*Syp*), display opposing high-to-low and low-to-high temporal gradients with lineage-specific temporal dynamics. *Imp* and *Syp* promote early and late fates, respectively, in both a slowly progressing and a rapidly changing lineage. *Imp* and *Syp* control neuronal fates in the mushroom body lineages by regulating the temporal transcription factor Chinmo translation. Together, the opposing *Imp*/*Syp* gradients encode stem cell age, specifying multiple cell fates within a lineage.

Diverse neural stem cells produce distinct sets of specialized neurons. The suite of daughter neurons generated by common neural stem cells can further change as development progresses, which suggests that the neural stem cells themselves change over time (1–4). In *Drosophila*, the neuroblast, a type of neural stem cell, can bud off about 100 ganglion mother cells that each divide once to produce two, often different, daughter neurons (5, 6). Mapping the serially derived neurons based on birth order/time has revealed that each individual neuroblast makes an invariant series of morphologically distinct neuronal types (7–9).

Drosophila central brain neuroblasts differ greatly in the number of neuronal types produced and the tempo at which changes occur. The four mushroom body neuroblasts divide continuously throughout larval and pupal development, but each produces only three classes of neurons (7). By contrast, the antennal lobe anterodorsal 1 (*ALad1*) neuroblast generates 22 neuronal types during larval development (9). Although sequential neuroblast expression of temporal transcription factors specifies neuronal cell fates in lineages of the *Drosophila* ventral nerve cord and optic lobes (10, 11), this mechanism is not easily applied to central brain. Here, we analyze fate determinants that direct neuronal diversification based on the age of the neuroblast.

Genes with age-dependent changes in expression levels throughout the life of a neuroblast could confer different temporal fates upon the neuronal daughter cells born at different times. Thus, we aimed to find genes dynamically expressed in mushroom body and antennal lobe neuroblasts by sequencing transcriptomes over the course of larval and pupal neurogenesis. We marked mushroom body or antennal lobe neuroblasts persistently and exclusively with green fluorescent protein (GFP) by genetic intersection and immortalization tactics (12, 13) (fig. S1, A to F). We isolated approximately 100 GFP+ neuroblasts for each RNA/cDNA preparation. Quantitative polymerase chain reaction (qPCR) showed that known neuroblast genes, including *deadpan* (*dpn*) and *asense*, are enriched in mushroom body and antennal lobe neuroblasts compared with total larval brains (fig. S1, G and H). Samples passing this qPCR quality check were sequenced. We obtained the transcriptomes of mushroom body neuroblasts at 24, 50, and 84 hours after larval hatching (ALH), as well as 36 hours after puparium formation (APF), and the transcriptomes of antennal lobe neuroblasts at 24, 36, 50, and 84 hours ALH (table S1). We did not sequence the antennal lobe neuroblasts at 36 hours APF because they stop producing neurons around puparium formation. Also, we did not analyze mushroom body neuroblasts at 36 hours ALH because the mushroom body lineages do not undergo detectable fate or molecular changes between 24 and 50 hours ALH.

We defined strongly dynamic genes as those with a greater than fivefold change in expression level across different time points and a maximum average abundance higher than 50 transcripts per million (see the supplementary materials). We found 83 strongly dynamic genes in the mushroom body and 63 in the antennal lobe (fig. S2).

The two sets shared 16 genes in common (Fig. 1A). Among these 16 common genes, *pncr002:3R*, a putative noncoding RNA, ranks highest in absolute abundance, the importance of which remains unclear.

IGF-II mRNA-binding protein (*Imp*) and *Syncrip* (*Syp*), which code for two evolutionarily conserved RNA-binding proteins (14, 15), rank second and third in absolute abundance (Fig. 1A). *Imp* is expressed abundantly at 24 hours ALH and declines to a minimum at 84 hours ALH in antennal lobe and 36 hours APF in mushroom body neuroblasts, whereas *Syp* increases from minimal expression at 24 hours ALH to become one of the most abundant genes at late larval stages (Fig. 1B). *Imp*/*Syp* gradients with larger amplitudes and steeper slopes characterize antennal lobe neuroblasts (Fig. 1B), which yield more diverse neuron types at faster tempos than the mushroom body neuroblasts. Antibodies to *Imp* and *Syp* (14, 16) showed similar patterns in shifts of protein abundance in both mushroom body neuroblasts and neuronal daughter cells (Fig. 1C). We therefore investigated the roles of *Imp* and *Syp* in neuronal temporal fate specification in both mushroom body and antennal lobe lineages.

The post-embryonic mushroom body neuroblasts sequentially produce γ , α'/β' , and α/β neurons, which can be distinguished by a variety of markers (7, 17, 18). Fasciclin II (*FasII*) is expressed in the perimeter of the α/β lobes, is weakly expressed in the γ lobe, and is not expressed in the α'/β' lobes. Trio, a Dbl family protein, is expressed in the γ and α'/β' lobes. The γ neurons can also be identified in wandering larvae by expression of ecdysone receptor B1 isoform (*EcR-B1*) (19). Moreover, one can predict the fate of newborn mushroom body neurons based on the protein levels of Chinmo, a known temporal transcription factor, as abundant Chinmo specifies the γ fate, weak Chinmo expression confers the α'/β' fate, and absence of Chinmo permits the α/β fates (20).

RNA interference (RNAi) aimed to reduce *Imp* expression resulted in up-regulated *Syp*, whereas knocking down *Syp* expression caused increased *Imp* expression (Fig. 2, A to D). This reciprocal derepression was evident in protein and transcript content (Fig. 2, A to E) as well as phenotype. Silencing *Imp* triggered precocious production of α/β neurons throughout larval development; these neurons lacked *EcR-B1* at the wandering larval stage (Fig. 2, F and G) and showed no Chinmo at 24 hours ALH (Fig. 2, H and I). *Imp*-depleted neuroblasts ended neurogenesis prematurely: By 28 hours APF, no neuroblasts remained in the mushroom body ($n = 10$ brain tissue samples). This resulted in small adult mushroom bodies with only α/β lobes (Fig. 3, A and B, and fig. S4, A and B) (21). By contrast, silencing *Syp* extended the production of Chinmo-positive γ neurons through pupal development (Fig. 2, J and K, and fig. S3). The *Syp*-depleted adult mushroom bodies consisted of a single prominent γ lobe (Fig. 3C and fig. S4C). The reciprocal temporal fate transformations

¹Howard Hughes Medical Institute, Janelia Research Campus, 19700 Helix Drive, Ashburn, VA, USA. ²Departments of Bioengineering, Electrical Engineering, and Computer Science, and Biophysics Graduate Program, University of California Berkeley, 408C Stanley Hall, Berkeley, CA, USA. *These authors contributed equally to this work. †Present address: Suzhou Iwelfie Co., Ltd, Biobay A5-105, 218 Xinghu St, Suzhou Industrial Park, China. ‡Corresponding author. E-mail: leet@janelia.hhmi.org

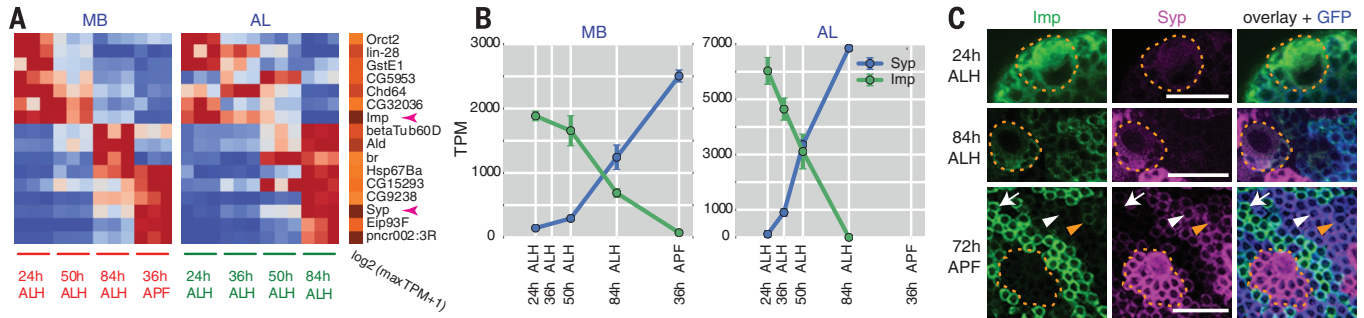


Fig. 1. RNA sequencing identified temporally dynamic genes in neuroblasts. (A) Sixteen common dynamic genes in mushroom body (MB) or antennal lobe (AL) neuroblasts were shown. The entire lists of 83 dynamic genes in mushroom body and 63 in antennal lobe neuroblasts are in fig. S2. On the left, normalized expression levels (maximum set to 1) are shown in blue (low) to red (high). On the right, logarithmic scales of the maximum expression level [transcripts per million (TPM)] are shown in white (low) to

orange (high). *Imp* and *Syp* are indicated with arrowheads. (B) Dynamic changes of *Imp* and *Syp* expression (mean \pm SD, $n = 3$ replicates. Each replicate contains 100 GFP+ neuroblasts.) (C) Immunostaining shows that *Imp* protein decreases and *Syp* protein increases over time in mushroom body neuroblasts and newly born neurons (circled regions). Reciprocal protein levels of *Imp* and *Syp* are also present in older neurons (arrows and arrow heads). Representative images of $n = 15$ brain tissue samples. Scale bars, 20 μ m.

were also seen in the mushroom body neuroblast clones homozygous for various *Imp* or *Syp* loss-of-function mutations (fig. S4, D to F). Thus, *Imp* specifies early γ neurons and *Syp* specifies late α/β neurons.

We next asked whether prolonged coexpression of *Imp* and *Syp* can increase the number of α/β' neurons, which are typically born at a time when *Imp* and *Syp* expression levels are similar. Ectopic induction of *Imp* or *Syp* transgenes enhanced *Imp* or *Syp* protein levels in mushroom body newborn neuronal daughter cells but not in the neuroblasts (fig. S5). In the case of *Syp* overexpression, the early larval neuroblasts still contained abundant *Imp*, as did their newborn neurons expressing ectopic *Syp* (fig. S5C). Analogously, overexpressing *Imp* rendered the pupal-born neurons strongly positive for *Syp* as well as ectopic *Imp* (fig. S5E). Therefore, after *Imp* or *Syp* overexpression, many more newborn neurons simultaneously expressed *Imp* and *Syp*, and the normally modest α'/β' neuronal lobes were enlarged in adult brains (Fig. 3, D and E, and fig. S4, G and H). Cell death was unlikely to distort the developmental outcomes, as rare sporadic cell death was only detected in mushroom body neurons expressing ectopic *Syp* at 50 hours ALH (fig. S6). Taken together, our data demonstrate that relative levels of *Imp* and *Syp* dictate mushroom body neuronal temporal fates.

The altered *Chinmo* protein levels upon *Imp* or *Syp* depletion (Fig. 2, H to K, and fig. S3) prompted us to ask whether *Imp* and *Syp* regulate *chinmo* expression. The abundance of *chinmo* transcripts normally decreases as neuroblasts age (fig. S7, A and B). This pattern was unperturbed in *Imp* or *Syp*-depleted neuroblasts (fig. S7, C and D). Together, these data suggest that *Imp* and *Syp* regulate *chinmo* expression at a post-transcriptional level.

We further explored by epistasis whether *Imp* and *Syp* act to regulate mushroom body neuronal temporal fates through *Chinmo*. Overexpressing a *chinmo* transgene partially restored

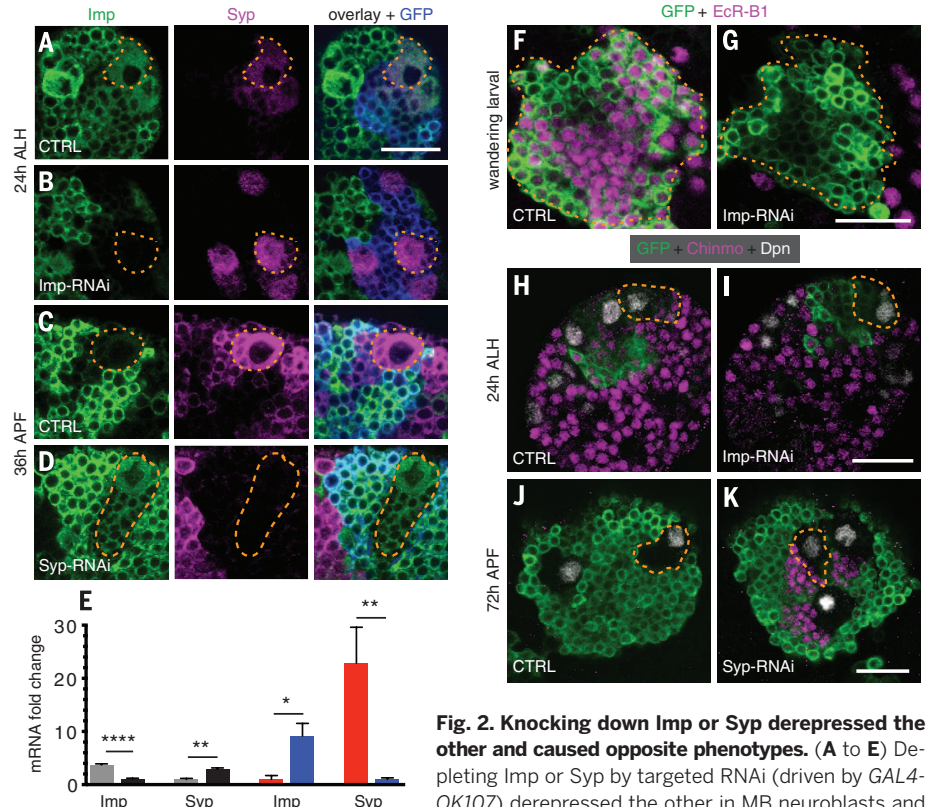


Fig. 2. Knocking down *Imp* or *Syp* derepressed the other and caused opposite phenotypes. (A to E) Depleting *Imp* or *Syp* by targeted RNAi (driven by *GAL4-OK107*) derepressed the other in MB neuroblasts and newborn born neurons (circled regions), as evidenced by immunostaining [(A) to (D)] and qPCR (mean \pm SD, $n = 3$ replicates. Each replicate contains 100 GFP+ neuroblasts.) (E). Student's *t* test was performed. * $P < 0.05$, ** $P < 0.01$, **** $P < 0.0001$. Gray, control (CTRL) group at 24 hours ALH; black, *Imp*-RNAi at 24 hours ALH; red, CTRL at 36 hours APF; blue, *Syp*-RNAi at 36 hours APF. (F and G) *Ecr-B1* was absent in *Imp*-depleted wandering-larval MB neurons (circled regions). (H to K) *Chinmo* protein precociously became undetectable in *Imp*-depleted MB early larval-born neurons [(H) and (I)] but ectopically existed in *Syp*-depleted MB pupal-born neurons [(J) and (K)]. Circled regions contain one MB neuroblast (Dpn+) and its newborn daughter cells. All images are representative of $n = 15$ brain tissue samples. Scale bars, 20 μ m.

the production of γ neurons by the short-lived, *Imp*-depleted neuroblasts (Fig. 3F). Moreover, silencing *chinmo* transformed the supernumerary γ neurons made by the *Syp*-depleted neuroblasts into α/β neurons (Fig. 3G). Together, these

observations place *Chinmo* downstream of *Imp* and/or *Syp* in the temporal fate specification of mushroom body neurons.

To ascertain whether *Imp/Syp* gradients serve as a general temporal-fating mechanism, we

examined the roles of *Imp* and *Syp* in the rapidly changing antennal lobe anterodorsal 1 (ALad1) lineage that yields ~60 larval-born neurons of

22 types. Although all 22 types express *acj6-GAL4*, only the first 12 types generated express *GAL4-GHI46* (9). *Imp* depletion reduced the

ALad1 daughter cell number (*acj6+*) from 64.0 ± 2.0 to 50.7 ± 4.9 ($P < 0.05$) but increased the ratio of late-type to early-type neurons (early-type GHI46+ neurons decreased from 40.3 ± 2.1 to 13.3 ± 2.6 , $P < 0.0001$) (Fig. 4 and fig. S8). By contrast, *Syp* depletion increased total ALad1 daughter cells from 64.0 ± 2.0 to 100.0 ± 4.1 ($P < 0.0001$) and increased the percentage of the early-type (GHI46+) neurons from $63.0 \pm 3.2\%$ to $93.5 \pm 5.1\%$ ($P < 0.001$) (Fig. 4 and fig. S8). Despite precocious production of late-type neurons or prolonged generation of early-type neurons, 21 of the 22 neuron types were preserved (fig. S8). In summary, the opposing *Imp/Syp* gradients govern temporal fates in at least two different neuroblast lineages that produce mushroom body and antennal lobe neurons functioning in memory and olfaction, respectively.

The opposite temporal gradients of *Imp* and *Syp* in neuroblasts confer the serially derived daughter cells with graded levels of *Imp/Syp*. The acquisition of distinct daughter cell fates based on the *Imp/Syp* morphogens is reminiscent of early embryonic patterning by the opposite spatial gradients of maternally inherited Bicoid and Nanos. Different levels of Bicoid and Nanos are incorporated into cells along the anterior-posterior axis after cellularization of the blastoderm. Bicoid and Nanos function as RNA-binding proteins to initiate anterior-posterior spatial patterning via translational control of maternal transcripts that encode transcription factors (22). Analogously, temporal fate patterning of newborn neurons is orchestrated by post-transcriptional control of *chinmo* and potentially other genes by *Imp* and *Syp*. Because *Imp* and *Syp* may share common targets (14, 15) but show affinity for different RNA motifs (15, 23), it is possible that *Imp* and *Syp* can both bind *chinmo* transcripts, but they may differentially target *chinmo* transcripts for translation versus sequestration. Descending *Imp* temporal gradients governs aging of *Drosophila* testis stem cell niche (24). *Imp-1*, the mammalian ortholog of *Imp*, is also needed to maintain mouse neural stem cells (25). We propose that graded *Imp/Syp*

Fig. 3. *Imp* and *Syp* govern MB neuronal temporal fates via *Chinmo* regulation. (A to G)

Representative confocal projections of adult MBs immunostained by GFP and FasII antibodies. Cartoons on the right illustrate the lobe phenotypes and were constructed by examining individual Z planes. Consistent phenotypes were seen in all examined samples ($n = 20$ brain tissue samples per genotype). Notably, transgenic *Chinmo* partially rescued early γ neurons in the *Imp*-depleted MB [compare (B) with (F)], and depleting *Chinmo* converted the supernumerary early γ neurons present in the *Syp*-depleted MB into late-born α/β neurons [compare (C) and (G)]. Scale bars, 20 μm .

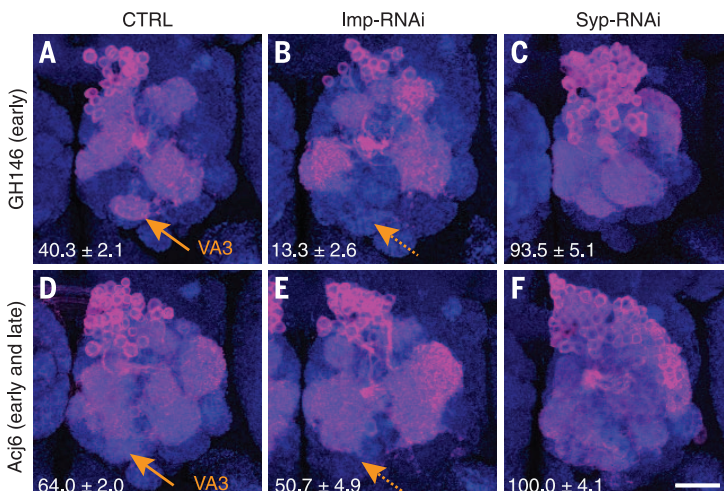
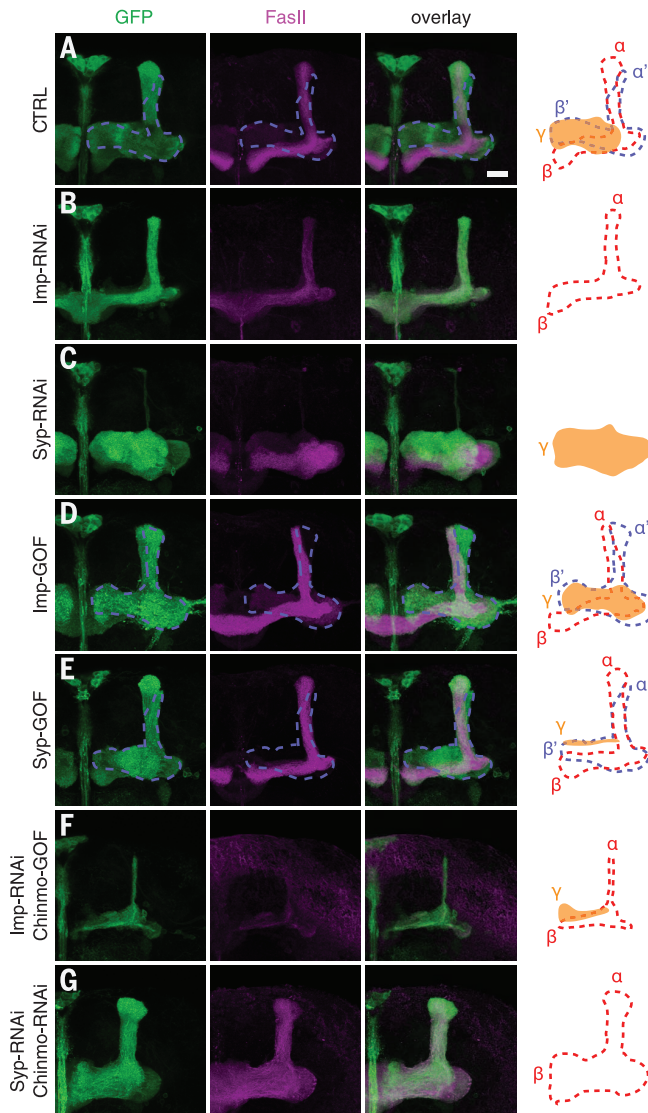


Fig. 4. Depleting *Imp* or *Syp* elicited temporal fate transformation of antennal lobe neurons.

Composite confocal images of adult fly brain antennal lobe regions counterstained with nc82 monoclonal antibody (blue). ALad1 neuroblast clones of various genotypes were labeled with GFP (magenta) driven by *GAL4-GHI46* (A to C) or *acj6-GAL4* (D to F), respectively; cell counts (mean \pm SD) are indicated at the bottom left of each panel. Compared to control (CTRL) (D), total cell (*acj6+*) numbers of the ALad1 lineage were significantly decreased ($P < 0.05$) in *Imp*-RNAi (E) but increased ($P < 0.0001$) in *Syp*-RNAi clones (F). All 22 neuronal types were maintained, with the exception of VA3 (arrows) in *Imp*-RNAi clones. However, the cell number ratio between early- and late-born neuronal types were significantly decreased ($P < 0.001$) in *Imp*-RNAi but increased ($P < 0.001$) in *Syp*-RNAi clones. Consistent phenotypes were seen in all examined neuroblast clones ($n = 6$ brain tissue samples per genotype). Scale bars, 20 μm . Detailed analysis is presented in fig. S8.

expression constitutes an evolutionally conserved mechanism for governing time-dependent stem cell fates, including temporal fate progression in neural stem cells and their derived neuronal lineages.

REFERENCES AND NOTES

- P. Mattar, J. Ericson, S. Blackshaw, M. Cayouette, *Neuron* **85**, 497–504 (2015).
- P. Gao *et al.*, *Cell* **159**, 775–788 (2014).
- X. Li, Z. Chen, C. Desplan, *Curr. Top. Dev. Biol.* **105**, 69–96 (2013).
- M. Kohwi, C. Q. Doe, *Nat. Rev. Neurosci.* **14**, 823–838 (2013).
- J. W. Truman, W. Moats, J. Altman, E. C. Marin, D. W. Williams, *Development* **137**, 53–61 (2010).
- S. Lin *et al.*, *Development* **137**, 43–51 (2010).
- T. Lee, A. Lee, L. Luo, *Development* **126**, 4065–4076 (1999).
- S. Lin, C. F. Kao, H. H. Yu, Y. Huang, T. Lee, *PLOS Biol.* **10**, e1001425 (2012).
- H. H. Yu *et al.*, *PLOS Biol.* **8**, e1000461 (2010).
- X. Li *et al.*, *Nature* **498**, 456–462 (2013).
- T. Isshiki, B. Pearson, S. Holbrook, C. Q. Doe, *Cell* **106**, 511–521 (2001).
- T. Awasaki *et al.*, *Nat. Neurosci.* **17**, 631–637 (2014).
- K. J. Venken, J. H. Simpson, H. J. Bellen, *Neuron* **72**, 202–230 (2011).
- S. M. McDermott, C. Meignin, J. Rappalber, I. Davis, *Biol. Open* **1**, 488–497 (2012).
- T. P. Munro, S. Kwon, B. J. Schnapp, D. St Johnston, *J. Cell Biol.* **172**, 577–588 (2006).
- C. Geng, P. M. Macdonald, *Mol. Cell Biol.* **26**, 9508–9516 (2006).
- J. R. Crittenden, E. M. Skoulakis, K. A. Han, D. Kalderon, R. L. Davis, *Learn. Mem.* **5**, 38–51 (1998).
- T. Awasaki *et al.*, *Neuron* **26**, 119–131 (2000).
- X. Zheng *et al.*, *Cell* **112**, 303–315 (2003).
- S. Zhu *et al.*, *Cell* **127**, 409–422 (2006).
- C. Medioni, M. Ramialison, A. Ephrussi, F. Besse, *Curr. Biol.* **24**, 793–800 (2014).
- P. Lasko, *RNA* **2**, 408–416 (2011).
- Y. V. Svitkin *et al.*, *PLOS Biol.* **11**, e1001564 (2013).
- H. Toledano, C. D'Alterio, B. Czeck, E. Levine, D. L. Jones, *Nature* **485**, 605–610 (2012).
- J. Nishino, S. Kim, Y. Zhu, H. Zhu, S. J. Morrison, *eLife* **2**, e00924 (2013).

ACKNOWLEDGMENTS

We thank L. Jones, T. S. Hays, P. Macdonald, and I. Davis for sharing reagents. We thank the Transgenic RNAi Project at Harvard Medical School (NIH/NIGMS R01-GM084947) and the Vienna Drosophila Resource Center for providing transgenic RNAi fly stocks used in this study. We thank R. Miyares, G. Rubin, J. Truman, C. Wu, and I. Davis and his group for comments. This work was supported by Howard Hughes Medical Institute. RNA-sequencing data are available in the National Center for Biotechnology Information Gene Expression Omnibus, accession no. GSE71103. The supplementary materials contain additional data.

SUPPLEMENTARY MATERIALS

www.sciencemag.org/content/350/6258/317/suppl/DC1
Materials and Methods
Figs. S1 to S8
Table S1
References (26–29)

5 August 2015; accepted 16 September 2015
10.1126/science.aad1886

OCEAN VARIABILITY

The Atlantic Multidecadal Oscillation without a role for ocean circulation

Amy Clement,^{1*} Katinka Bellomo,¹ Lisa N. Murphy,¹ Mark A. Cane,² Thorsten Mauritsen,³ Gaby Rädcl,³ Bjorn Stevens³

The Atlantic Multidecadal Oscillation (AMO) is a major mode of climate variability with important societal impacts. Most previous explanations identify the driver of the AMO as the ocean circulation, specifically the Atlantic Meridional Overturning Circulation (AMOC). Here we show that the main features of the observed AMO are reproduced in models where the ocean heat transport is prescribed and thus cannot be the driver. Allowing the ocean circulation to interact with the atmosphere does not significantly alter the characteristics of the AMO in the current generation of climate models. These results suggest that the AMO is the response to stochastic forcing from the mid-latitude atmospheric circulation, with thermal coupling playing a role in the tropics. In this view, the AMOC and other ocean circulation changes would be largely a response to, not a cause of, the AMO.

The observed variability of North Atlantic sea surface temperatures (SSTs) is characterized by a horseshoe pattern (Fig. 1A) and a predominately multidecadal time scale (Fig. 1C). This pattern is commonly referred to as the Atlantic Multidecadal Oscillation (AMO). The AMO index is defined as the average SST from 0° to 60°N, 80°W to 0°, detrended to isolate the natural variability (*I*). Temperature changes associated with the AMO have been shown to affect weather and climate around the North Atlantic basin and possibly throughout the global tropics (*I*–*6*). However, the physical mechanism of the AMO is not well understood.

Previous explanations for the AMO have focused almost exclusively on the role of naturally occurring changes in ocean circulation, primarily the Atlantic Meridional Overturning Circulation (AMOC) (*7*–*12*). Based on model experiments and paleoclimate proxy data, it has been suggested that at times when the AMOC is weak, or at the extreme, completely shut down, the North Atlantic ocean cools because of reduced northward ocean heat transport (*9*, *13*). Direct observational evidence that this mechanism explains 20th-century AMO variability is not available, because continuous measurements of the AMOC have only been available since 2004. In climate models, the AMOC and North Atlantic SST are correlated (weak AMOC when the North Atlantic is warm), but there is no robust lead-lag relationship between the two (*11*, *14*), which makes it difficult to argue that AMOC changes drive SST changes in

models. In addition to the AMOC, some studies have made a case for a strong aerosol forcing of this variability (*15*, *16*), but this has been disputed in recent studies (*17*, *18*).

Although the causes of the AMO are unclear, climate models are nonetheless capable of reproducing the spatial pattern of observed SST variability and the associated changes in atmospheric circulation. Figure 1B shows the pattern of SST, sea-level pressure (SLP), and surface winds regressed on the AMO index derived from a subset of fully coupled climate models that participated in the Coupled Model Intercomparison Projects 3 and 5 (CMIP3/5) (Table 1 and methods). In these simulations, the climate forcings (greenhouse gases, anthropogenic aerosols, orbital parameters, and solar irradiance) are prescribed at preindustrial values, so simulated variability arises from “natural” processes internal to the climate system. Earlier studies have attempted to show that these simulated natural variations in North Atlantic SST are the surface expression of the internal variability in the ocean circulation, the AMOC in particular (*11*, *14*, *19*, *20*).

Here we show, however, that this pattern of variability can be produced without ocean circulation changes. To do so, we used results from the same atmospheric general circulation models used in Fig. 1B, coupled to a 50-m-deep slab-ocean mixed-layer model (hereafter referred to as slab-ocean models), rather than being coupled to an ocean general circulation model (hereafter referred to as fully coupled models). Slab-ocean simulations are run with constant preindustrial forcing and a prescribed annual cycle of ocean heat transport (methods). In these models, the atmosphere and ocean exchange heat and moisture (hence are thermally coupled), but because the ocean heat transport is unchanging, it cannot drive SST variability. Despite the absence of interactive ocean circulation, the slab-ocean models are capable of widespread warming of the North Atlantic. The spatial pattern and magnitude (Fig. 1D) of the slab-ocean simulations are indistinguishable from those of their coupled model versions

¹Rosenstiel School of Marine and Atmospheric Science, University of Miami, Miami, FL, USA. ²Lamont-Doherty Earth Observatory of Columbia University, New York, NY, USA. ³Max Planck Institute for Meteorology, Hamburg, Germany.
*Corresponding author. E-mail: aclement@rsmas.miami.edu

(Fig. 1B), with a pattern correlation of 0.87 (Table 2). Furthermore, the magnitude of the AMO index variance is similar in the multimodel mean of fully coupled (0.053) and slab-ocean (0.058) models (Table 1), which compares with the 0.051 mean of the three observational data sets. (methods). These results are unchanged if we isolate only low-frequency variability in the AMO index (fig. S1).

Whereas conventional wisdom is that interactive ocean circulation is important in generating decadal to multidecadal time scale climate variability, the spectral characteristics of the slab-ocean and fully coupled models are nearly in-

distinguishable. Figure 2A shows that the spectra of the multimodel mean preindustrial slab-ocean simulations are essentially the same as those of the fully coupled models. For periods longer than 10 years (beyond the El Niño/Southern Oscillation band of 2 to 7 years), both resemble a red noise process, suggesting that there is nothing distinctive about decadal and multidecadal variability in these models. The same is true of the later-generation CMIP5 models (Fig. 2B). It may be objected that individual fully coupled models have low frequency spectral peaks that are averaged out in the ensemble mean. However, Fig. 3, which shows the spectra of the North Atlantic

SST index for individual models, makes it clear that this is not the case (Fig. 3 includes all the fully coupled models that have a respective slab-ocean simulation of at least 70 years in length; Table 1). The only fully coupled model that produces variability at decadal or longer time scales that is significantly greater than in the slab-ocean version is the GFDL_CM2_1 model. The enhanced quasidecadal variability in the fully coupled version of this model is mainly in the sub-polar gyre (fig. S2), which suggests that it is tied to the ocean circulation, but it is not clear whether it is enhanced by the AMOC or by the upper ocean sub-polar gyre circulation. Three of the fully coupled

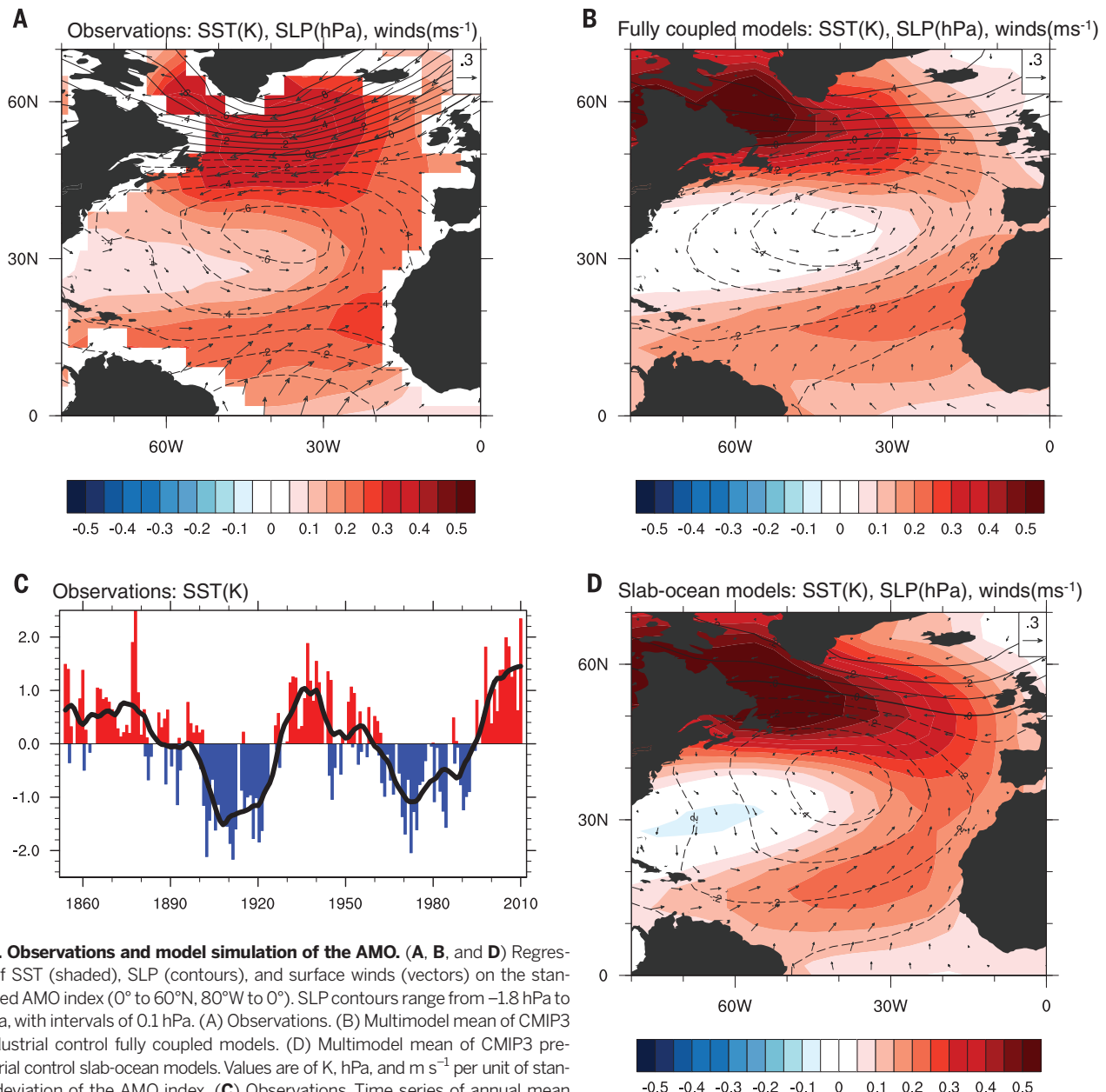


Fig. 1. Observations and model simulation of the AMO. (A, B, and D) Regression of SST (shaded), SLP (contours), and surface winds (vectors) on the standardized AMO index (0° to 60°N, 80°W to 0°). SLP contours range from -1.8 hPa to 1.8 hPa, with intervals of 0.1 hPa. (A) Observations. (B) Multimodel mean of CMIP3 preindustrial control fully coupled models. (D) Multimodel mean of CMIP3 preindustrial control slab-ocean models. Values are of K, hPa, and m s⁻¹ per unit of standard deviation of the AMO index. (C) Observations. Time series of annual mean anomalies of the standardized AMO index (colored bars) with a 10-year running average superimposed (black line). The observed SST is from ERSSTv3b, whereas surface winds and SLP are from the NCEP/NCAR (National Centers for Environmental Prediction/National Center for Atmospheric Research) reanalysis. All fields are detrended.

models produce peaks at shorter interannual time scales that are not present in the slab-ocean model (Fig. 3), but this is due to the tropical Atlantic response to El Niño/Southern Oscillation, which is known to influence the tropical Atlantic (21).

Our interpretation of these results is that the AMO is the response of the upper ocean mixed layer to forcing by the atmosphere, projecting mostly on the North Atlantic Oscillation (NAO), with thermal coupling playing a fundamental role in generating the tropical component of the AMO signal. The NAO is a mode of atmospheric variability, which represents a shift in the westerly jet in the Atlantic basin, along with a change in strength of the subtropical high. The wind and SLP patterns associated with the AMO (Fig. 1A) clearly show the NAO signature: Periods when the North Atlantic is warm occur when the subtropical high is weak and the westerly jet shifts poleward, resulting in weaker westerly winds in the mid-latitudes. The NAO itself is internal to the atmosphere and does not require coupling with the ocean (22, 23). This is demonstrated in Fig. 4A, which shows the NAO in the Community Atmosphere Model version 4 (CAM4) forced with climatological SST (CAM4-sstClim). This pattern has no dependence on time scale, and the power spectra of the mid-latitude surface winds are consistent with white noise (fig. S3) as in previous studies (24).

However, observations, slab-ocean models, and fully coupled models simulate surface wind changes in the tropics associated with the AMO, which can explain the tropical part of the horseshoe warming pattern (25) (Fig. 1, A, B, and D). These wind changes are absent in the uncoupled CAM4-sstClim model (Fig. 4A), and only when the atmosphere is coupled to the slab-ocean model do the tropical winds show a response to the NAO (Fig. 4B). The spectra of the tropical meridional winds in the slab-ocean model are slightly red, with considerably enhanced variability (fig. S3), which we interpret as arising from thermal coupling between the atmospheric circulation and the mixed-layer ocean, and adding year-to-year persistence to otherwise uncorrelated variability.

Coherent changes in SST and trade winds in the northern tropical Atlantic due to thermal coupling have been extensively documented and arise from a wind-evaporation-SST feedback (26, 27). Weaker winds in the northern tropics induce weaker evaporation, resulting in warmer SST. The SST change then drives a low-level wind response, which allows the signals to expand equatorward. It has also been suggested that a local positive feedback between atmospheric circulation, SST, and low-level clouds can contribute to the persistence of these climate anomalies (28). Thus, thermal coupling between the mixed-layer ocean and the atmosphere in the northern tropics results in a warming of the North Atlantic Ocean that extends into the tropics as the low-frequency response to the NAO.

The pattern of the AMO in these unforced simulations is not perfectly correlated with the

observed pattern (Table 2). The most likely cause of the difference is model biases in their simulation of the mean climate. Because their resolution is coarse (~1° to 2°), all of these models underestimate the strong SST fronts in the Gulf Stream region, which leads to differences in the patterns and magnitude of variability in that re-

gion. It is possible that high-resolution global climate models, which are starting to become available, may simulate more of a role for the ocean circulation than do current-generation models. There are also persistent biases in the simulation of the tropical Atlantic climate in coupled models, which can imprint on the

Table 1. Variance of the AMO index (0° to 60°N, 80°W to 0°) in observations, preindustrial slab-ocean model simulations, and their respective fully coupled model versions. All time series are detrended. Observational values cover the years 1920–2014.

Data set	Length of slab-ocean models (years)	Length of fully coupled models (years)	Resolution (latitude × longitude)	AMO variance	AMO variance in slab-ocean models	AMO variance in fully coupled models
Kaplan			5.0° × 5.0°	0.046		
ERSSTv3b			2.0° × 2.0°	0.056		
HADISST			1.0° × 1.0°	0.052		
Multi-Model Mean				0.058		0.053
CCCMA_CGCM3_1	30	500	3.75° × 3.75°	0.052		0.068
CCCMA_CGCM3_1_T63	30	350	2.8° × 2.8°	0.069		0.054
GFDL_CM2_0	50	500	2.0° × 2.5°	0.053		0.064
GFDL_CM2_1	100	500	2.0° × 2.5°	0.054		0.063
INMCM3	60	330	4.0° × 5.0°	0.084		0.049
MIROC3_2_HIRES	20	500	1.125° × 1.125°	0.052		0.041
MIROC3_2_MEDRES	60	100	2.8° × 2.8°	0.055		0.044
MPI_ESM_LR	180	1000	3.75° × 3.75°	0.047		0.056
MRI_CGCM2_3_2A	100	350	2.8° × 2.8°	0.038		0.043
NCAR_CCSM4	450	500	0.90° × 1.25°	0.049		0.042
UKMO_HADGEM1	70	240	1.25° × 1.75°	0.115		0.078
GISS_MODEL_E_R	120	500	3.9° × 5.0°	0.031		0.037

Table 2. Spatial correlations between regressions of SST on the standardized AMO index in various observational and multimodel mean data sets. All data are detrended.

	Kaplan	ERSSTv3b	HADISST	Slab-ocean models	Fully coupled models	PiCntrl (CMIP5)	Historical (CMIP5 1865 to 2005)
Kaplan	1						
ERSSTv3b	0.84	1					
HADISST	0.90	0.88	1				
Slab-ocean models	0.79	0.83	0.77	1			
Fully coupled models	0.76	0.70	0.68	0.87	1		
PiCntrl (CMIP5)	0.80	0.70	0.68	0.85	0.96	1	
Historical (CMIP5 1865–2005)	0.76	0.62	0.60	0.74	0.90	0.97	1

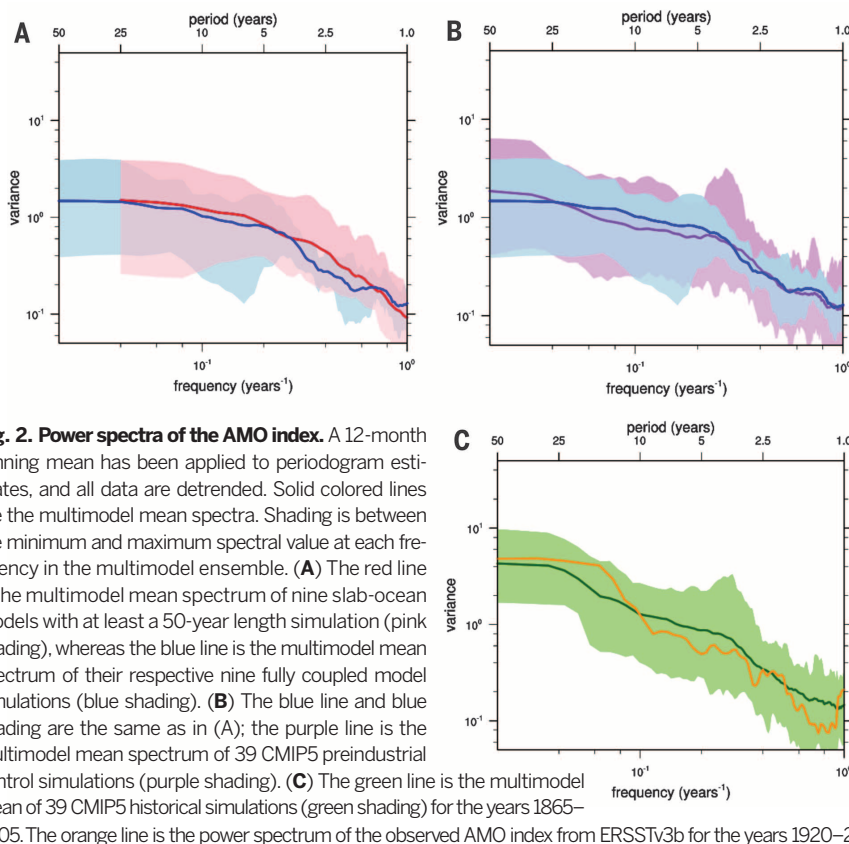


Fig. 2. Power spectra of the AMO index. A 12-month running mean has been applied to periodogram estimates, and all data are detrended. Solid colored lines are the multimodel mean spectra. Shading is between the minimum and maximum spectral value at each frequency in the multimodel ensemble. **(A)** The red line is the multimodel mean spectrum of nine slab-ocean models with at least a 50-year length simulation (pink shading), whereas the blue line is the multimodel mean spectrum of their respective nine fully coupled model simulations (blue shading). **(B)** The blue line and blue shading are the same as in (A); the purple line is the multimodel mean spectrum of 39 CMIP5 preindustrial control simulations (purple shading). **(C)** The green line is the multimodel mean of 39 CMIP5 historical simulations (green shading) for the years 1865–2005. The orange line is the power spectrum of the observed AMO index from ERSSTv3b for the years 1920–2014.

pattern of variability. The fact that the slab-ocean models have a higher correlation with the observed pattern is likely due to the fact that those models have a SST climatology prescribed from observations, whereas coupled-model climatologies exhibits significant SST biases, a problem that perhaps worsens in CMIP5 as compared to CMIP3, as evident in the correlations in Table 2. The inclusion of historical climate forcings in model simulations does not improve the pattern correlation with observations (Table 2).

It could be argued that the preindustrial simulations underestimate the magnitude of observed multidecadal variability (Fig. 2C). The inclusion of historical climate forcings does enhance multidecadal variability, bringing it into better agreement with observations (Fig. 2C), although it has been shown that several models overestimate the impact of atmospheric aerosols (18). On the other hand, a possible source of persistence that is missing in climate models is cloud feedbacks, particularly in the tropical Atlantic (28). Climate models show a strong sensitivity of low-level marine cloudiness to thermodynamic variations of the mean state (29), whereas observations show that cloudiness covaries much more strongly with low-level winds, and in ways that would amplify the interactions, discussed here (30). Proper simulation of these feedbacks may lead to models with enhanced low-frequency variability in the Atlantic basin (31).

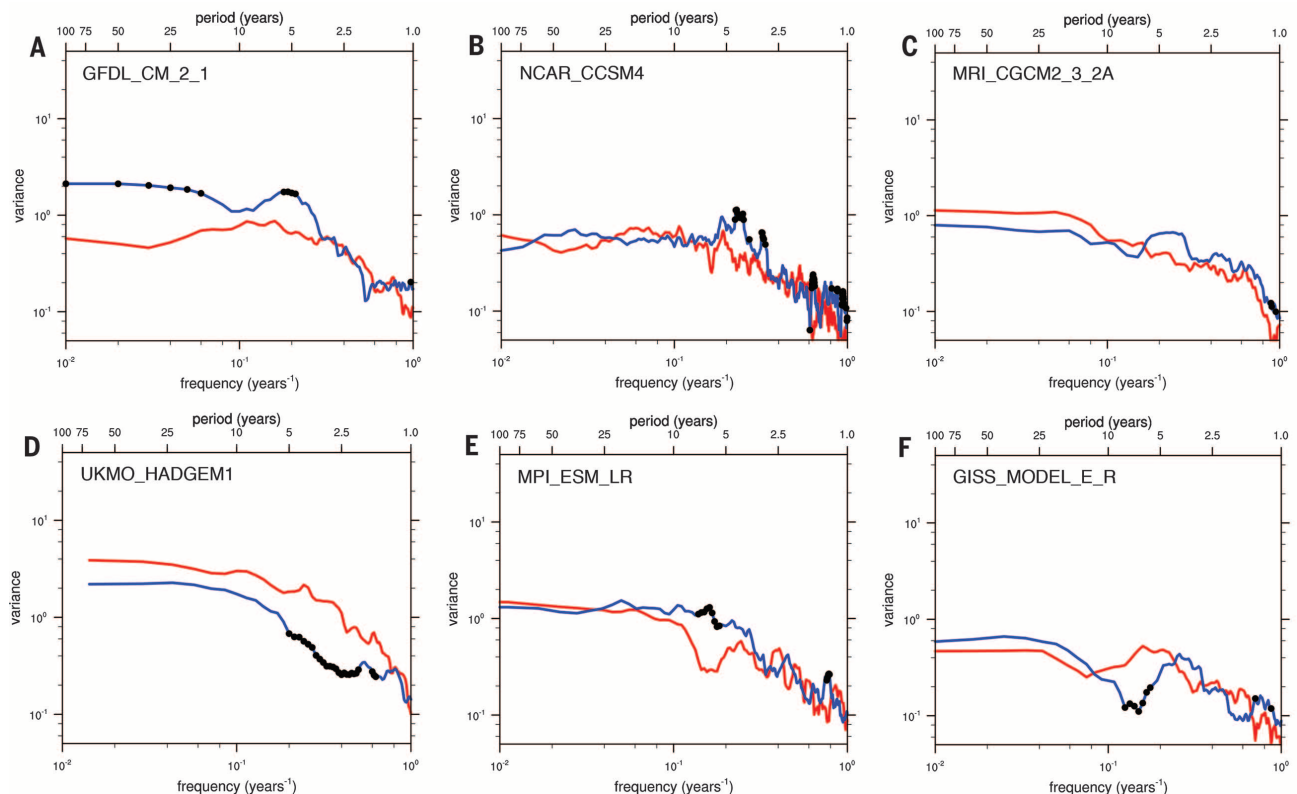


Fig. 3. Paired power spectra of the AMO index in models with at least 70 years of simulation (Table 1). (A to F) Red curves are for the slab-ocean simulations; blue curves are for their respective coupled simulations. A 12-month smoothing has been applied to the periodogram estimates, and all data are detrended. Black markings indicate where the variance of the blue curve is significantly different than the variance of the red curve at the 95% confidence level according to Fisher's *F* test.

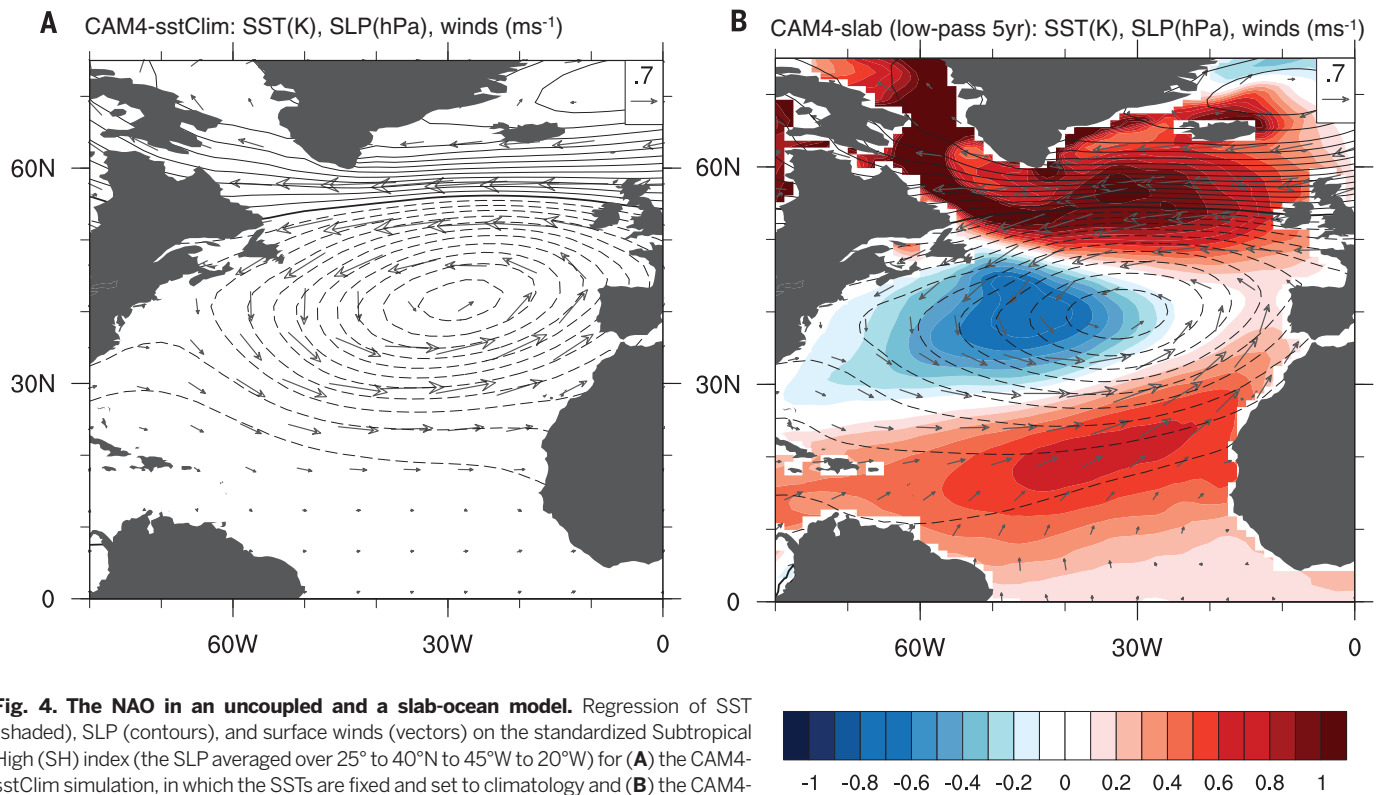


Fig. 4. The NAO in an uncoupled and a slab-ocean model. Regression of SST (shaded), SLP (contours), and surface winds (vectors) on the standardized Subtropical High (SH) index (the SLP averaged over 25° to 40°N to 45°W to 20°W) for (A) the CAM4-sstClim simulation, in which the SSTs are fixed and set to climatology and (B) the CAM4-slab simulation that includes thermal coupling. In (B), the SH index is filtered using a low-pass Lanczos filter to remove variability in the sub-5-year time scale. Units are of °C, hPa, and m s^{-1} per standard deviation of the SH index. SLP contours range from -4 hPa to 4 hPa, with intervals of 0.25 hPa.

We have shown that simulations of the AMO using fully coupled atmosphere-ocean models, which produce spatial and temporal characteristics consistent with observations, are essentially indistinguishable from those produced by the equivalent slab-ocean model versions, which lack interactive ocean dynamics. Instead, the simplest explanation for the AMO is that it is the low-frequency response to the high-frequency atmospheric “noise” embodied, for example, in the NAO, with thermal coupling extending the signal into the tropics to produce the characteristic horseshoe pattern of warming. The ocean circulation, including surface layer Ekman currents and possibly the AMOC (32, 33), would respond to these changes in atmospheric circulation as demonstrated by McCarthy *et al.* (34), but a feedback from the ocean circulation on the AMO is not supported by our analysis. Our analysis does not rule out that the ocean circulation may contribute to low-frequency variability in parts of the ocean, such as the subpolar gyre, as suggested in (34). Nor does it rule out the possibility that massive changes in the AMOC suggested in the paleoclimate record had profound consequences for global climate (13). However, the current-generation models analyzed here do not support the idea that ocean circulation drives the AMO.

REFERENCES AND NOTES

- D. B. Enfield, A. M. Mestas-Nunez, P. J. Trimble, *Geophys. Res. Lett.* **28**, 2077–2080 (2001).
- R. T. Sutton, D. L. R. Hodson, *Science* **309**, 115–118 (2005).
- J. R. Knight, C. K. Folland, A. A. Scaife, *Geophys. Res. Lett.* **33**, L17706 (2006).
- V. A. Semenov *et al.*, *J. Clim.* **23**, 5668–5677 (2010).
- R. Zhang, T. L. Delworth, *Geophys. Res. Lett.* **33**, L17712 (2006).
- R. A. Kerr, *Science* **309**, 41–43 (2005).
- T. Delworth, S. Manabe, R. J. Stouffer, *J. Clim.* **6**, 1993–2011 (1993).
- M. Latif *et al.*, *J. Clim.* **17**, 1605–1614 (2004).
- T. L. Delworth, M. E. Mann, *Clim. Dyn.* **16**, 661–676 (2000).
- J. R. Knight, R. J. Allan, C. K. Folland, M. Vellinga, M. E. Mann, *Geophys. Res. Lett.* **32**, L20708 (2005).
- C. Z. Wang, L. P. Zhang, *J. Clim.* **26**, 6137–6162 (2013).
- J. Ba *et al.*, *Clim. Dyn.* **43**, 2333–2348 (2014).
- R. Zhang, T. L. Delworth, *J. Clim.* **18**, 1853–1860 (2005).
- N. F. Tandon, P. J. Kushner, *J. Clim.* **28**, 6309–6323 (2015).
- M. E. Mann, K. A. Emanuel, *Eos* **87**, 233, 238, 241 (2006).
- B. Booth, N. J. Dunstone, P. R. Halloran, T. Andrews, N. Bellouin, *Nature* **484**, 228–232 (2012).
- R. Zhang *et al.*, *J. Atmos. Sci.* **70**, 1135–1144 (2013).
- B. Stevens, Rethinking the lower bound on aerosol radiative forcing. *J. Clim.* (2015). <http://journals.ametsoc.org/doi/abs/10.1175/JCLI-D-14-00656.1>
- M. Klöwer, M. Latif, H. Ding, R. J. Greatbatch, W. Park, *Earth Planet. Sci. Lett.* **406**, 1–6 (2014).
- C. Marini, C. Frankignoul, *Clim. Dyn.* **43**, 607–625 (2014).
- D. B. Enfield, D. A. Mayer, *J. Geophys. Res.* **102**, 929–945 (1997).
- I. M. Held, in *Large-Scale Dynamical Processes in the Atmosphere*, B. J. Hoskins, R. F. Pearce, Eds. (Academic Press, New York, 1983), pp. 127–169.
- R. Saravanan, *J. Clim.* **11**, 1386–1404 (1998).
- C. Wunsch, *Bull. Am. Meteorol. Soc.* **80**, 245–255 (1999).
- R. Seager *et al.*, *J. Clim.* **13**, 2845–2862 (2000).
- S. P. Xie, *J. Clim.* **12**, 64–70 (1999).
- J. C. H. Chiang, D. J. Vimont, *J. Clim.* **17**, 4143–4158 (2004).
- A. T. Evan, R. J. Allen, R. Bennartz, D. J. Vimont, *J. Clim.* **26**, 3619–3630 (2013).
- X. Qu, A. Hall, S. A. Klein, P. M. Caldwell, *Clim. Dyn.* **42**, 2603–2626 (2014).
- M. Brueck, L. Nuijens, B. Stevens, *J. Atmos. Sci.* **72**, 1428–1446 (2015).
- K. Bellomo, A. Clement, T. Mauritsen, G. Radel, B. Stevens, *J. Clim.* **28**, 2725–2744 (2015).
- T. L. Delworth, R. J. Greatbatch, *J. Clim.* **13**, 1481–1495 (2000).
- M. Visbeck, H. Cullen, G. Krahnmann, N. H. Naik, *Geophys. Res. Lett.* **25**, 4521–4524 (1998).
- G. D. McCarthy, I. D. Haigh, J. J. Hirschi, J. P. Grist, D. A. Smeed, *Nature* **521**, 508–510 (2015).

ACKNOWLEDGMENTS

This work was supported by grants from the U.S. Department of Energy and the National Oceanographic and Atmospheric Administration. M.A.C. was supported by Office of Naval Research grant N00014-12-1-0911. The authors are grateful to Y. Kushnir, G. Schmidt, B. Kirtman, C. Frankignoul, and C. Deser for lively discussions. All CMIP data are available at <http://cmip-pcmdi.llnl.gov/>. Data from simulations with the CAM4 model can be obtained by e-mailing the corresponding author.

SUPPLEMENTARY MATERIALS

www.sciencemag.org/content/350/6258/320/suppl/DC1
Materials and Methods
Figs. S1 to S3
References (35–41)

21 April 2015; accepted 18 September 2015
10.1126/science.aab3980

GENE EXPRESSION

Suboptimization of developmental enhancers

Emma K. Farley,^{1,2*} Katrina M. Olson,^{1,2} Wei Zhang,³ Alexander J. Brandt,⁴ Daniel S. Rokhsar,¹ Michael S. Levine^{1,2*}

Transcriptional enhancers direct precise on-off patterns of gene expression during development. To explore the basis for this precision, we conducted a high-throughput analysis of the *Otx-a* enhancer, which mediates expression in the neural plate of *Ciona* embryos in response to fibroblast growth factor (FGF) signaling and a localized GATA determinant. We provide evidence that enhancer specificity depends on submaximal recognition motifs having reduced binding affinities (“suboptimization”). Native GATA and ETS (FGF) binding sites contain imperfect matches to consensus motifs. Perfect matches mediate robust but ectopic patterns of gene expression. The native sites are not arranged at optimal intervals, and subtle changes in their spacing alter enhancer activity. Multiple tiers of enhancer suboptimization produce specific, but weak, patterns of expression, and we suggest that clusters of weak enhancers, including certain “superenhancers,” circumvent this trade-off in specificity and activity.

The *Orthodenticle homeobox (Otx)* gene is crucial for patterning the anterior neural plate of vertebrate embryos (1, 2). In the invertebrate chordate *Ciona intestinalis*, *Ci-Otx* is activated in the anterior neural plate and dorsal nerve chord by a maternal GATA transcription factor and localized fibroblast growth factor (FGF) signaling (Fig. 1A) (3–6). A minimal 69-base pair (bp) enhancer (*Otx-a*) was previously identified in *Ciona*. It contains three GATA binding sites and two ETS sites, which mediate induction by FGF signaling (Fig. 1B) (3–5). This *Otx-a* enhancer recapitulates the native expression pattern in the neural plate when attached

to a minimal promoter and reporter gene and electroporated into *Ciona* embryos (Fig. 1C). The enhancer has a regulatory logic that is pervasively used in development; namely, a broadly distributed tissue (ectoderm) determinant (GATA) works in concert with a localized signaling event to mediate restricted expression within a subset of the total sites of FGF signaling (7–9).

To identify all of the sequences important for enhancer activity, we created a library of random synthetic (RS) *Otx-a* enhancer variants that retain each of the five core recognition sequences, GATA and GGAA, in their native positions (Fig. 1B). Each of these variants was attached to a green

fluorescent protein (GFP) coding sequence and unique 30-bp barcode tag, which uniquely identifies each of the different enhancer variants. The *fog* promoter was used for these assays because it produces the lowest background expression among the different *Ciona* promoters tested in previous transgene assays (3). The resulting library has a complexity of 2.5×10^6 unique RS enhancer–barcode tag combinations, and we determined each enhancer–barcode association by deep sequencing. The library was electroporated into thousands of fertilized eggs. Once embryos developed to the late gastrula stage, RNA was extracted, reverse-transcribed, amplified by polymerase chain reaction (PCR), and sequenced to identify transcribed barcodes (fig. S1).

Among the RNA barcodes, 163,708 unique barcodes exhibited expression, and 21,799 of these produced the same or higher levels of activity than the wild-type (WT) enhancer, ≥ 4 normalized reads per million (RPM) (table S1). The vast majority (hundreds of thousands) of enhancer variants failed to produce significant expression, less than one RPM. We randomly selected and individually tested 34 of the RS *Otx-a* enhancer variants with ≥ 4 RPM by electroporation. Of the 34 enhancer variants, 24 mediated restricted expression of the GFP reporter gene (table S2). As negative controls, we tested

¹Department of Molecular and Cell Biology, Division of Genetics, Genomics and Development, Center for Integrative Genomics, University of California, Berkeley, CA 94720-3200, USA. ²Lewis-Sigler Institute for Integrative Genomics, Princeton University, Princeton, NJ 08544, USA. ³Department of Medicine, University of California, San Diego, CA 92093-0688, USA. ⁴Department of Chemistry, University of California, Berkeley, CA 94720-3200, USA. *Corresponding author. E-mail: msl2@princeton.edu (M.S.L.); ekfarley@princeton.edu (E.K.F.)

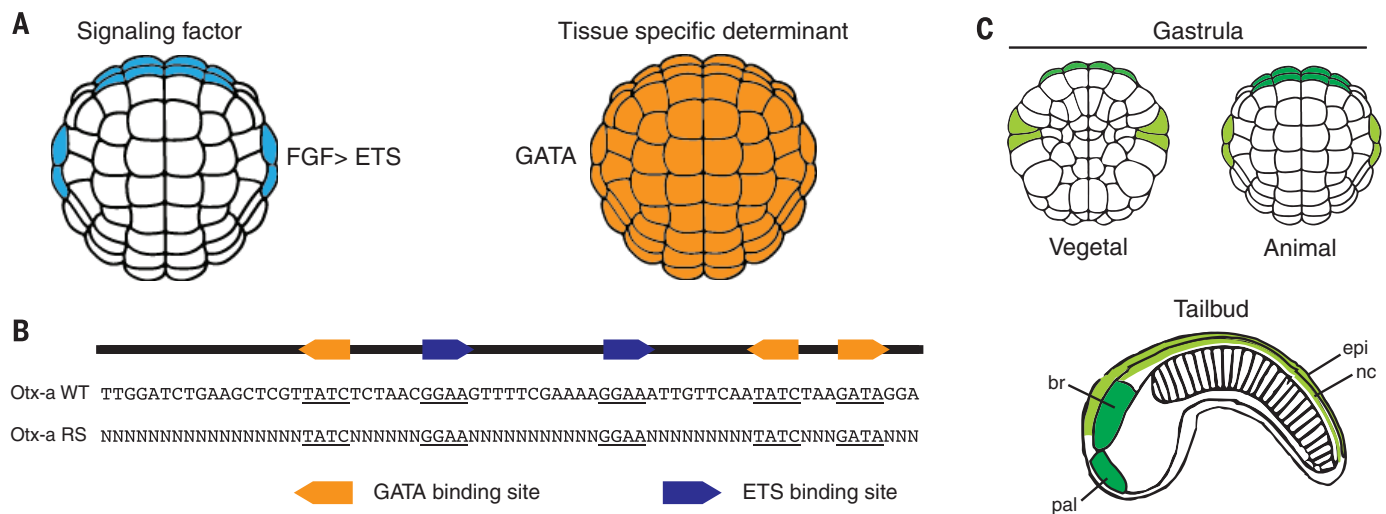
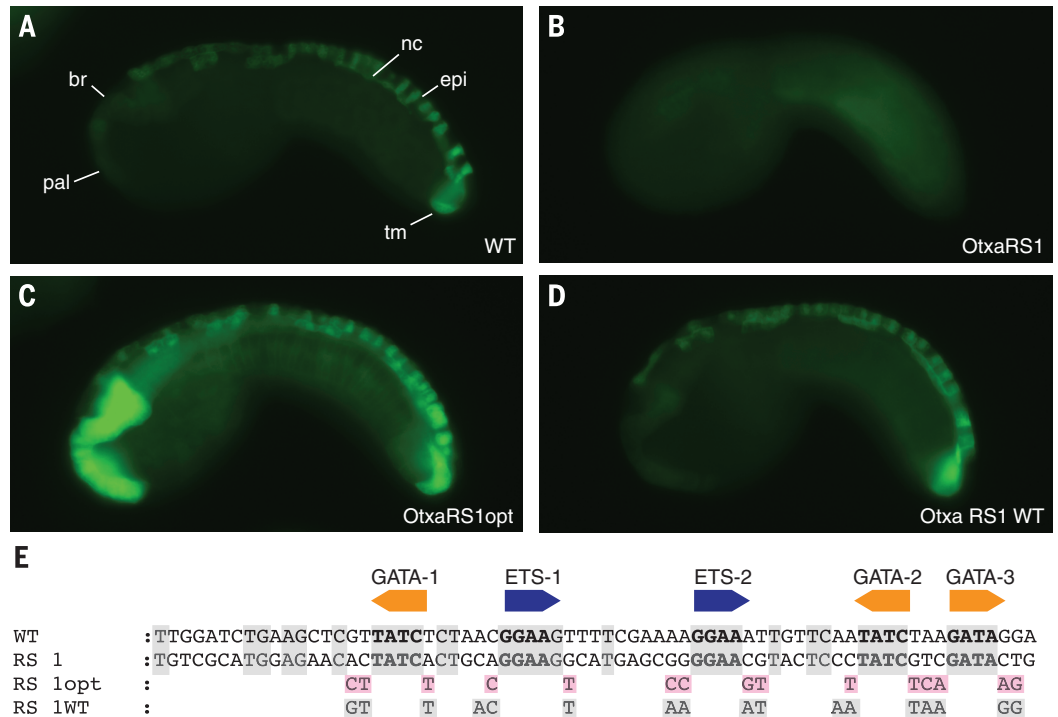


Fig. 1. *Otx-a* enhancer is activated by FGF and maternal determinant GATA. (A) Expression of direct activators of *Otx-a* enhancer, FGF and GATA. (B) The sequence of the 69-bp *Otx-a* enhancer, showing the five core binding sites: three for GATA (GATA) and two for ETS (GGAA). The core binding site is defined as the 4 bp recognized by all GATA and ETS transcription factors, and they are the major sites of protein–DNA interactions (32, 33). RS *Otx-a* en-

hancer variants retain all five core binding sites with the remaining sequence (49 bp) randomized. (C) *Otx-a* enhancer drives expression in the a6.5 (dark green) and b6.5 (light green) lineages, beginning at gastrulation. In the tailbud stage, a6.5 cells give rise to the anterior brain (br) and palps (pal), and b6.5 cells give rise to the dorsal nerve cord (nc), dorsal epidermis (epi), and two tail muscle cells (not shown).

Fig. 2. Suboptimal binding sites are sufficient for tissue-specific expression.

(A) Embryo electroporated with WT Otx-a enhancer; GFP can be seen in the anterior brain (br), palps (pal), dorsal nerve cord (nc), dorsal midline epidermis (epi), and two tail muscle cells (tm). **(B)** Embryo electroporated with Otx-a RS1, a synthetic enhancer variant identified in our screen that shows no GFP expression. **(C)** Embryo electroporated with Otx-a RS1opt, with all five core sites changed to have optimized flanking sequence; expression can be seen in endogenous location and in notochord, mesenchyme, endoderm, and posterior brain. **(D)** Embryo electroporated with Otx-a RS1 WT with all five core sites mutated to have WT flanking sequences; expression can be seen in endogenous Otx-a location only. **(E)** Sequence of WT, Otx-a RS1, Otx-a RS1 opt, and Otx-a RS1 WT enhancer variants. Gray boxes



highlight bases conserved in WT *Ciona intestinalis* Otx-a sequence; pink boxes highlight bases that were changed to match identified "optimal" flanking motifs. All images were taken at the same exposure time, 500 ms.

four enhancers that displayed little or no expression of the barcode tag RNAs (≤ 0.01 RPM), and none produced detectable GFP signals when individually tested by electroporation into embryos (table S2).

Computational analysis of the ~20,000 active enhancers identified short sequence motifs flanking the core GATA and ETS binding sites as the key determinants of enhancer function (fig. S2). Additional sequences residing outside these regions—including those conserved in the Otx-a enhancer of the distantly related *Ciona savignyi*—were not recovered among the active enhancers in our high-throughput screen. The consensus flanking sequences that were identified, CCGGARY and SMGATAAS, have 0.98 and 0.96 Pearson coefficient correlations, with the highest-affinity-position weight matrices identified by high-throughput binding assays for orthologous ETS and GATA transcription factors in flies, mice, and humans (10–13) (figs. S3 and S4).

To determine the sufficiency of the flanking motifs, we created "up" mutations, by restoring the activities of inactive derivatives of Otx-a enhancer variants, including RS1 (Fig. 2B). This enhancer contains all five core GATA and ETS binding sites but completely lacks consensus or WT flanking motifs and shares just 13 of 49 matches outside the core sites. Nonetheless, modifying the flanking regions of RS1 to mimic the extended binding motifs of the WT enhancer (RS1wt) is sufficient to restore full activity (Fig. 2D, compare with 2A).

The WT Otx-a enhancer contains imperfect matches to the "optimal" GATA and ETS ex-

tended motifs identified in this study and previous binding assays (figs. S2 to S4) (10, 11, 13). It is possible to determine relative binding affinities of the native sites by analyzing the frequency of selected sequences using high-throughput binding data sets (13–15). The GATA-1, -2, and -3 binding sites contain 0.8, 0.3, and 0.4 relative binding frequencies, respectively, whereas the ETS-1 and -2 sites contain 0.6 and 0.4 relative binding frequencies, respectively (fig. S5). In other words, each of the GATA and ETS motifs has, on average, half the binding affinity of the optimal motifs. We therefore consider the native binding sites as suboptimal because they have submaximal binding affinities.

To determine whether the native, suboptimal binding motifs are an important feature of normal Otx-a enhancer activity, we created perfect matches for all five GATA and ETS binding motifs (Fig. 2C). The resulting enhancer, RS1opt, mediates intense expression in the neural plate, as well as weaker expression in a variety of ectopic tissues, including the notochord. Similar results were obtained by creating optimal flanking sequences in the WT enhancer (fig. S6).

These results suggest that too many optimal motifs cause the Otx-a enhancer to capture additional sites of FGF signaling, such as the notochord. Thus, "suboptimization" of the enhancer for transcription factor binding appears to be essential for restricted activity in the neural plate. Recent studies also provide evidence that suboptimal binding sites are important for the specificity of Hox transcription factors in *Drosophila* development (16). Such sites are also

an important feature of the classical eve stripe 2 enhancer (17) and other developmental enhancers (18, 19). In all of these examples, an excess of optimal binding sites leads to a loss of specificity and ectopic sites of gene expression.

Having observed the importance of suboptimal GATA and ETS motifs, we asked whether the spacing between motifs might also be suboptimized. The importance of spacing in developmental gene expression is controversial (18, 20–22), although induction of the interferon- β enhanceosome by viral infections relies on stringently spaced binding sites (23, 24). Our high-throughput analysis of the Otx-a enhancer identified the sufficiency of ETS and GATA motifs for correct expression and thus provided an opportunity to determine whether spacing of these motifs influences enhancer function. For example, the 5' GATA-1 and 3' GATA-2 motifs are located 10 bp and 13 bp, respectively, from central ETS-1 and ETS-2 sites within the Otx-a enhancer. It is conceivable that only one, or neither, of these intervals represents an optimal spacing. To explore this possibility, we created 21 Otx-a enhancer derivatives (tables S3 and S4) with altered spacing between GATA-1 and ETS-1, ETS-1 and ETS-2, and ETS-2 and GATA-2 (Fig. 3). For simplicity, many of these experiments were done in the context of a minimal 46-bp enhancer that contained a single 3' GATA site.

The most striking finding of these studies is that enhancer activity is augmented by inserting 3 bp between the GATA-1 and ETS-1 sites (Fig. 3B, compare with 3A; this was also done on two other synthetic variants—see figs. S7 to S9). Quantitative

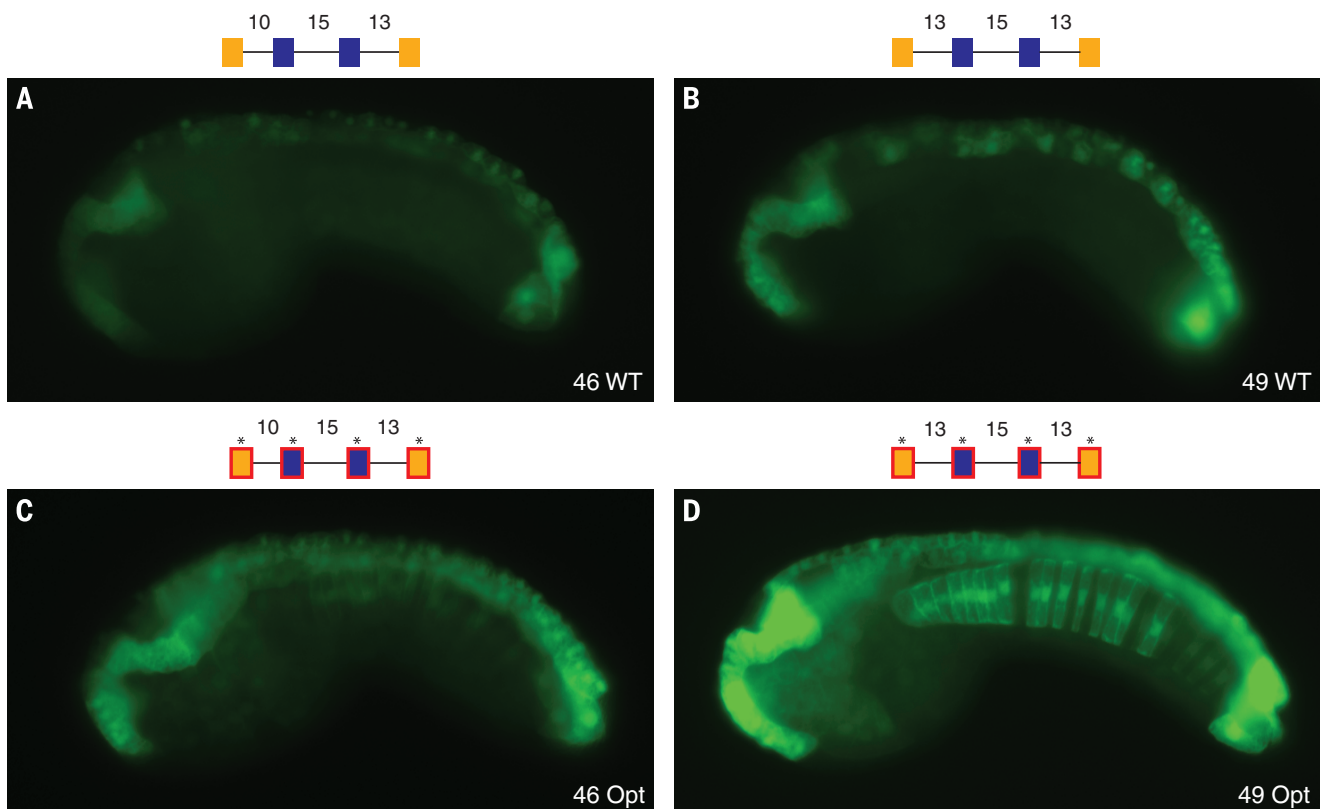


Fig. 3. Suboptimization of spacing and flanking motifs is required for tissue specificity. Spacing between adjacent binding sites is important for tissue specificity. **(A)** Embryo electroporated with Otx-a 46 (10-15-13 spacing); GFP expression can be seen in WT location. **(B)** Embryo electroporated with Otx-a 49 (13-15-13 spacing); addition of 3 bp between GATA1 and ETS1 leads to a significant increase in neural expression; and no ectopic expression is seen. **(C)** Embryo electroporated with Otx-a 46opt (10-15-13 spacing and all

five core sites with optimized flanking); expression can be seen at higher levels in WT location and ectopic expression in notochord, mesenchyme, and posterior brain. **(D)** Embryo electroporated with Otx-a 49opt (13-15-13 spacing and all five core sites with optimized flanking); this enhancer shows strong expression in the endogenous neural location and ectopic expression in the notochord, posterior neural tube, and endoderm (see also fig. S12). All images were taken at the same exposure time, 250 ms.

PCR assays indicate a consistent threefold increase in the levels of expression after insertion of 3 bp (fig. S7). In contrast, reducing the distance of the 3' ETS-2–GATA-2 linkage from 13 to 10 bp causes a marked reduction in the levels of expression (fig. S8). All of the tested changes in the spacing of the two ETS sites result in reduced expression (figs. S10 and S11).

Of all the manipulations tested, increasing the distance of GATA-1 and ETS-1 from 10 bp to 13 bp is the only one that causes a significant increase in enhancer activity. We observed increases for both the WT 69-bp enhancer and smaller derivatives (Fig. 3 and figs. S7 to S9). It is unlikely that these increases are due to the fortuitous introduction of an unknown activator element, because different trinucleotide motifs were inserted between the GATA-1 and ETS-1 sites. We therefore conclude that the native Otx-a enhancer contains a mixture of good and poor arrangements of linked binding sites. This suboptimization might be the basis for the general view that most developmental enhancers lack “grammar” and are composed of random arrangements of clustered binding sites.

We next asked whether the improved arrangement of binding sites augments activity only

within the native site of expression, the neural plate, or also increases expression in other tissues. As shown previously (Fig. 2C), optimized GATA and ETS sites result in ectopic sites of expression (Fig. 3C). Combining these motifs with optimal spacing (13-15-13 rather than 10-13-15) creates a “supercharged” enhancer that drives robust expression in a variety of tissues, including the neural plate, anterior endoderm, and notochord, which are known sites of FGF signaling (5, 6, 25–28) (Fig. 3D; see also fig. S12). These results emphasize the importance of both the quality and spacing of binding sites in enhancer activity.

In summary, we have presented evidence that regulatory specificity is achieved through multiple tiers of enhancer suboptimization. This suboptimization is balanced across the Otx-a enhancer. For example, the highest-affinity binding sites, GATA-1 and ETS-1, exhibit suboptimal spacing (10 bp rather than 13 bp), whereas the weakest sites, ETS-2 and GATA-2, display optimal spacing (13 bp). Suboptimal binding motifs and spacing attenuate enhancer activity, ensuring restricted expression within specific tissues. Optimal sites and spacing cause ectopic activation in other tissues (fig. S13). In the case of the

Otx-a enhancer, this ectopic induction is due to the pleiotropic activities of the FGF signaling pathway. Our study suggests that enhancer evolution is not driven by strongest binding, but is constrained by the need for specificity. This constraint obscures critical properties of enhancer design, such as the spacing of linked binding sites. Suboptimization results in specific, but weak, enhancer activities. Multimerization of suboptimal enhancers leads to augmented levels of expression within specific tissues (fig. S14). We therefore propose that clusters of weak enhancers, such as certain superenhancers (29–31), circumvent this trade-off in specificity and activity and generate robust but localized patterns of expression.

REFERENCES AND NOTES

1. D. Acampora *et al.*, *Brain Res. Bull.* **66**, 410–420 (2005).
2. F. Beby, T. Lamonerie, *Exp. Eye Res.* **111**, 9–16 (2013).
3. U. Rothbächer, V. Bertrand, C. Lamy, P. Lemaire, *Development* **134**, 4023–4032 (2007).
4. P. Khoueiry *et al.*, *Curr. Biol.* **20**, 792–802 (2010).
5. V. Bertrand, C. Hudson, D. Caillol, C. Popovici, P. Lemaire, *Cell* **115**, 615–627 (2003).
6. C. Hudson, P. Lemaire, *Mech. Dev.* **100**, 189–203 (2001).
7. S. Barolo, J. W. Posakony, *Genes Dev.* **16**, 1167–1181 (2002).
8. T. Oosterveen *et al.*, *Proc. Natl. Acad. Sci. U.S.A.* **110**, 7330–7335 (2013).

9. K. A. Guss, C. E. Nelson, A. Hudson, M. E. Kraus, S. B. Carroll, *Science* **292**, 1164–1167 (2001).
10. G. H. Wei et al., *EMBO J.* **29**, 2147–2160 (2010).
11. G. Badis et al., *Science* **324**, 1720–1723 (2009).
12. A. Jolma et al., *Cell* **152**, 327–339 (2013).
13. K. R. Nitta et al., *eLife* **4**, e04837 (2015).
14. M. A. Hume, L. A. Barrera, S. S. Gisselbrecht, M. L. Bulyk, *Nucleic Acids Res.* **43**, D117–D122 (2015).
15. H. Zhang, M. Levine, H. L. Ashe, *Genes Dev.* **15**, 261–266 (2001).
16. J. Crocker et al., *Cell* **160**, 191–203 (2015).
17. S. Small, R. Kraut, T. Hoey, R. Warrior, M. Levine, *Genes Dev.* **5**, 827–839 (1991).
18. C. I. Swanson, D. B. Schwimmer, S. Barolo, *Curr. Biol.* **21**, 1186–1196 (2011).
19. J. Jiang, M. Levine, *Cell* **72**, 741–752 (1993).
20. R. W. Lusk, M. B. Eisen, *PLoS Genet.* **6**, e1000829 (2010).
21. M. M. Kulkarni, D. N. Arnosti, *Mol. Cell Biol.* **25**, 3411–3420 (2005).
22. C. I. Swanson, N. C. Evans, S. Barolo, *Dev. Cell* **18**, 359–370 (2010).
23. A. Muhlethaler-Mottet et al., *J. Biol. Chem.* **279**, 40529–40535 (2004).
24. D. Panne, T. Maniatis, S. C. Harrison, *Cell* **129**, 1111–1123 (2007).
25. W. Shi, M. Levine, *Development* **135**, 931–940 (2008).
26. H. Yasuo, C. Hudson, *Dev. Biol.* **302**, 92–103 (2007).
27. A. Stolfi, E. Wagner, J. M. Taliaferro, S. Chou, M. Levine, *Development* **138**, 5429–5439 (2011).
28. E. Wagner, M. Levine, *Development* **139**, 2351–2359 (2012).
29. W. A. Whyte et al., *Cell* **153**, 307–319 (2013).
30. D. Hnisz et al., *Cell* **155**, 934–947 (2013).
31. Q. Li, K. R. Peterson, X. Fang, G. Stamatoyannopoulos, *Blood* **100**, 3077–3086 (2002).
32. G. M. Clore, A. Bax, J. G. Omichinski, A. M. Gronenborn, *Structure* **2**, 89–94 (1994).
33. R. Kodandapani et al., *Nature* **380**, 456–460 (1996).

ACKNOWLEDGMENTS

Sequencing data for this project have been deposited in the National Center for Biotechnology Information, NIH, Sequencing Read Archive (www.ncbi.nlm.nih.gov/sra), PRJNA294804. We thank M. Chung, C. Anderson, E. Wagner, J. Lyons, and members of the Levine and Rokhsar labs for helpful discussions. This work

was supported by grants from the NIH (GM46638 and NS076542). There are no conflicts of interest to declare. Author contributions are as follows: E.K.F., D.S.R., and M.S.L. devised experiments; E.K.F. and K.M.O. performed experiments; W.Z. designed and executed bioinformatics analysis; A.J.B. conducted bioinformatics analyses; and E.K.F., D.S.R., and M.S.L. wrote the paper. All authors discussed the results and commented on the manuscript. M.S.L., D.S.R., and E.K.F. have filed a patent application (no. 62/169,458) that relates to the production of enhancer variants using the SEL-Seq method.

SUPPLEMENTARY MATERIALS

www.sciencemag.org/content/350/6258/325/suppl/DC1
Materials and Methods
Figs. S1 to S14
Tables S1 to S4
References (34–41)

29 May 2015; accepted 10 September 2015
10.1126/science.aac6948

T CELL IMMUNITY

RIPK1 and NF- κ B signaling in dying cells determines cross-priming of CD8⁺ T cells

Nader Yatim,^{1,2,3} Hélène Jusforgues-Saklani,^{1,2} Susana Orozco,⁴ Oliver Schulz,⁵ Rosa Barreira da Silva,^{1,2} Caetano Reis e Sousa,⁵ Douglas R. Green,⁶ Andrew Oberst,⁴ Matthew L. Albert^{1,2*}

Dying cells initiate adaptive immunity by providing both antigens and inflammatory stimuli for dendritic cells, which in turn activate CD8⁺ T cells through a process called antigen cross-priming. To define how different forms of programmed cell death influence immunity, we established models of necroptosis and apoptosis, in which dying cells are generated by receptor-interacting protein kinase-3 and caspase-8 dimerization, respectively. We found that the release of inflammatory mediators, such as damage-associated molecular patterns, by dying cells was not sufficient for CD8⁺ T cell cross-priming. Instead, robust cross-priming required receptor-interacting protein kinase-1 (RIPK1) signaling and nuclear factor κ B (NF- κ B)-induced transcription within dying cells. Decoupling NF- κ B signaling from necroptosis or inflammatory apoptosis reduced priming efficiency and tumor immunity. Our results reveal that coordinated inflammatory and cell death signaling pathways within dying cells orchestrate adaptive immunity.

Phagocytosis of dying cells by dendritic cells (DCs) results in cross-presentation of cell-associated antigen and the priming of CD8⁺ T cells (1). This pathway mediates the processing and presentation of tumor antigens (2), as well as viral and self proteins in instances where expression is restricted to nonhematopoietic

cells (3, 4). However, the manner by which different forms of programmed cell death (PCD) influence the ability of DCs to cross-present and initiate CD8⁺ T cell responses is still poorly understood.

Until recently, apoptosis was thought to be immunologically quiescent, in contrast to necrosis, which is characterized by rapid membrane permeabilization and the release of inflammatory mediators called damage-associated molecular patterns (DAMPs). Paradoxically, the inflammatory nature of necrotic cells (defined by their ability to activate innate immune cells) (5–8) does not correlate with their ability to serve as a source of antigen for the initiation of CD8⁺ T cell immunity (defined as immunogenicity) (1, 9–12). Moreover, immunogenic cell death has often been associated with apoptotic pathways (1, 10, 13–15). Several recent studies highlighted the interconnections between cell death and inflammatory

signal transduction. For example, proteins such as receptor-interacting protein kinase-3 (RIPK3) and caspase-8, which respectively initiate necroptosis and apoptosis, are incorporated into dynamic innate immune signaling modules (e.g., ripoptosome) (16–19). These cytosolic scaffolds establish the cross-talk between innate immune and cell death programs, and, in some instances, both pathways may be simultaneously engaged (fig. S1A). This integration of pathways, combined with the recent discovery of necroptosis (a regulated form of necrosis), prompted us to reevaluate how different PCD pathways affect cross-priming of CD8⁺ T cells.

To selectively induce apoptosis or necroptosis, we constructed “pure” cell death systems, in which the death effector proteins caspase-8 or RIPK3 were fused to a modified FK506 binding protein (FKBP) domain (Fv- Δ N-caspase-8 and RIPK3-2xFv, respectively) (20–22) (fig. S1B). RIPK3 oligomerization results in the recruitment of RIPK1 via interactions with the RIPK3-RIP homotypic interaction motif (RHIM^{RIPK3}) domain, leading to the formation of a cytosolic ripoptosome-like complex (21, 23). Therefore, we also generated a C-terminally truncated construct (RIPK3 Δ C-2xFv) (fig. S1B), which lacks the RHIM^{RIPK3} domain and does not recruit RIPK1 (21). NIH 3T3 cells were stably transduced with these activatable constructs (referred to herein as acC8, acR3, and acR3 Δ C). Dimerization of caspase-8 resulted in the induction of apoptosis, whereas oligomerization of full-length RIPK3 and RHIM-less RIPK3 induced rapid cell swelling and membrane rupture (<3 hours) in the absence of caspase activation (Fig. 1, A and B; fig. S2, A to C; and movies S1 to S3). The ability to induce necroptosis in the absence of the RHIM^{RIPK3} domain enabled us to decouple the formation of RIPK1-dependent ripoptosome complex from cell death (21), hence eliminating the activation of other pathways emanating from the ripoptosome.

Cell death-associated molecules such as calreticulin (CRT), adenosine triphosphate (ATP), and high-mobility group box-1 (HMGB1) have been shown to trigger inflammation and to regulate immunogenic cell death (8, 15, 24–26). We therefore quantified CRT surface exposure and the

¹Laboratory of Dendritic Cell Biology, Department of Immunology, Institut Pasteur, 25 Rue du Docteur Roux, 75015 Paris, France. ²Institut National de la Santé et de la Recherche Médicale, U818, 25 Rue du Docteur Roux, 75015 Paris, France. ³Frontières du Vivant Doctoral School, École Doctorale 474, Université Paris Diderot-Paris 7, Sorbonne Paris Cité, 8-10 Rue Charles V, 75004 Paris, France. ⁴Department of Immunology, University of Washington, Campus Box 358059, 750 Republican Street, Seattle, WA 98109, USA. ⁵Immunobiology Laboratory, The Francis Crick Institute, Lincoln's Inn Fields Laboratory, 44 Lincoln's Inn Fields, London WC2A 3LY, UK. ⁶Department of Immunology, St. Jude Children's Research Hospital, 262 Danny Thomas Place, Memphis, TN 38105, USA.

*Corresponding author. E-mail: albertm@pasteur.fr

release of both ATP and HMGB1 by apoptotic or necroptotic cells. Low levels of CRT exposure were observed during the three forms of cell death, and only the acR3- and acR3 Δ C-expressing NIH 3T3 cells rapidly released high concentrations of

ATP and HMGB1 upon treatment (Fig. 1, C to E). In all cases, no detectable levels of interleukin-1 α (IL-1 α), IL-1 β , or uric acid were released. We next evaluated phagocytosis by DCs (i.e., acquisition of antigen) and subsequent DC maturation,

which are two steps required for achieving CD8⁺ T cell cross-priming (27, 28). We found that bone marrow-derived dendritic cells (BMDCs) and a CD8 α ⁺ DC-derived cell line (MuTuDC) acquired similar amounts of dimerizer-treated acC8-, acR3-,

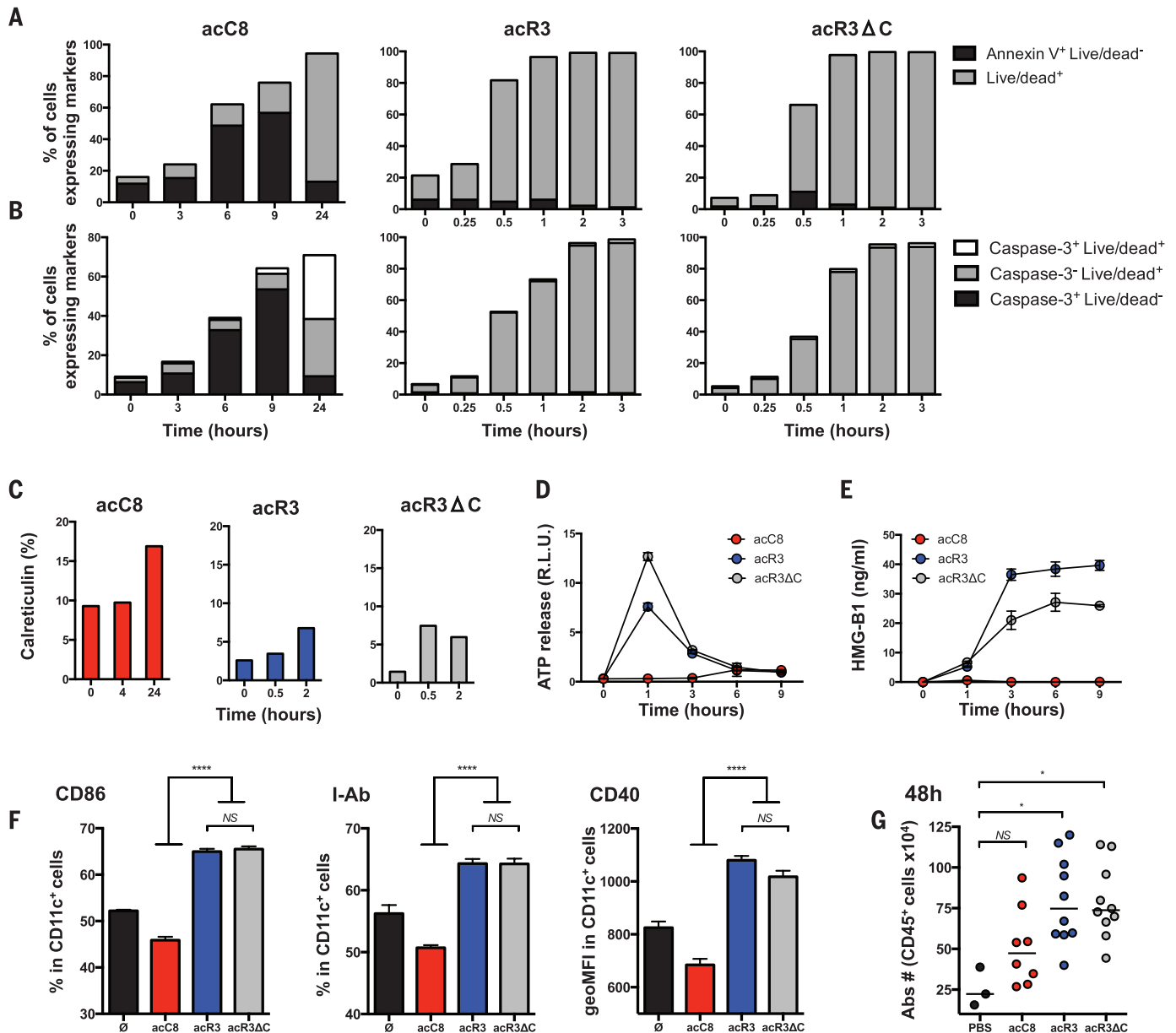


Fig. 1. Necroptotic cells release DAMPs and induce dendritic cell maturation.

(A to C) NIH 3T3 cells expressing the death constructs were stimulated with dimerizer. Cells were harvested at the indicated times and stained with Annexin-V and Live/Dead reagent (A); cleaved caspase-3 antibody and Live/Dead reagent (B); or CRT antibody (C). Cells that are Annexin V⁺ Live/Dead⁻ (indicating phosphatidylserine exposure before membrane permeabilization) or cleaved caspase-3⁺ (indicating the activation of executioner caspases) are undergoing apoptosis. At later times (24 hours), staining with Live/Dead reagent indicates a loss of plasma membrane integrity and characterizes secondary necrotic cells. Rapid membrane permeabilization without activation of executioner caspases (caspase-3⁻ Live/Dead⁺) is a feature of necroptosis. Results are from one representative experiment ($n = 2$ independent experiments). (D and E) ATP and HMGB1 were quantified from dying cell culture supernatants. Results are reported as means (\pm SEM) of triplicates of one rep-

resentative experiment ($n = 3$ independent experiments). (F) BMDCs were cocultured with dimerizer-treated acC8-, acR3-, and acR3 Δ C-expressing cells for 24 hours. DC maturation phenotypes were assessed by flow cytometry. Results are reported as in (D) and (E) ($n = 4$ independent experiments). (G) 2×10^5 dimerizer-treated cells were injected into the peritoneal cavity of WT C57BL/6 mice. Forty-eight hours later, peritoneal cells were collected, and immune cells were enumerated by cytometry. Bars indicate means of two pooled independent experiments with four to five mice per group [except in the phosphate-buffered saline (PBS) group]. Each circle represents one mouse. P values for (F) were determined by the one-way ANOVA test; P values for (G) were determined by the Kruskal-Wallis test (multigroup comparison), followed by Dunn's post-test, comparing each group to the PBS group. * $P < 0.05$; **** $P < 0.0001$; NS, not significant. acC8, caspase-8 apoptosis; acR3, RIPK3 necroptosis; acR3 Δ C, RHIM-less RIPK3 necroptosis.

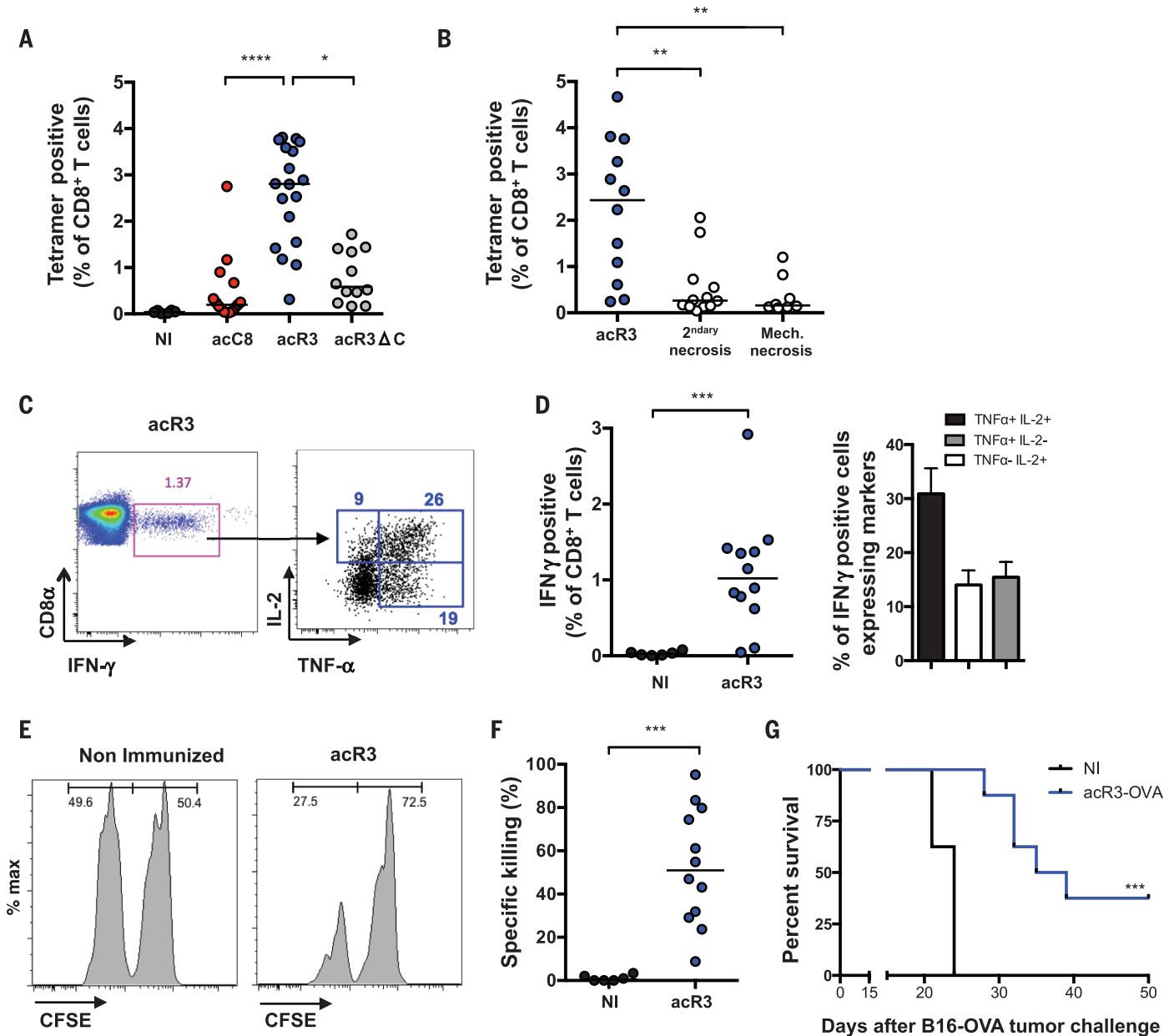


Fig. 2. Necroptotic cells are immunogenic and require RHIM-dependent ripoptosome formation for efficient cross-priming of CD8⁺ T cells.

To elicit cross-priming, we intradermally injected OVA-expressing dying cells (H-2^a) into mice (H-2^b), and we analyzed them on day 9 postimmunization (p.i.). (A and B) Using K^b-SIINFEKL tetramers, OVA-specific CD8⁺ T cells were quantified and plotted as a percentage of total CD8⁺ T cells. Bars indicate medians, and results are pooled from three independent experiments with three to six mice per group (each circle represents one mouse). NI, nonimmunized. (C and D) We quantified the production of IFN-γ, tumor necrosis factor-α (TNF-α), and IL-2 in response to ex vivo SIINFEKL peptide restimulation. In (C), representative fluorescence-activated cell sorting (FACS) plots are shown, with a pseudo-colored density plot in the left panel. Numbers indicate the percentage of gated cells. In (D), the frequency of IFN-γ-expressing and polyfunctional cells is plotted. Results are pooled from three independent experiments with three to six mice per group and reported as individual mice (each circle represents one mouse). The left panel shows medians as horizontal bars (IFN-γ); the right panel shows means with SEM (error bars)

(TNF-α and IL-2). (E and F) In vivo cytotoxicity assays were performed in acR3-OVA-immunized mice. At day 8 p.i., mice were adoptively transferred with carboxyfluorescein diacetate succinimidyl ester (CFSE)-labeled splenocytes. The frequency of CFSE^{hi} (irrelevant peptide control) and CFSE^{low} (SIINFEKL-loaded) splenocytes (injected at a 1:1 ratio) was determined at day 9. Representative FACS plots are shown in (E), and the percent of specific killing is plotted in (F). In (F), bars indicate medians, and results are pooled from three independent experiments with four mice per group (each circle represents one mouse). (G) Tumor challenge experiments were performed, involving the injection of 5×10^5 B16F10-OVA cells on day 12 p.i. Results are reported as a survival curve from one representative experiment with 8 to 11 mice per group ($n = 2$ independent experiments). For (A) and (B), *P* values were determined by the Kruskal-Wallis test, followed by Dunn's post-test; for (D) and (F), *P* values were determined by the Mann-Whitney test; and in (G), mice survival percentages were compared using the log-rank test. **P* < 0.05; ***P* < 0.01; ****P* < 0.001; *****P* < 0.0001.

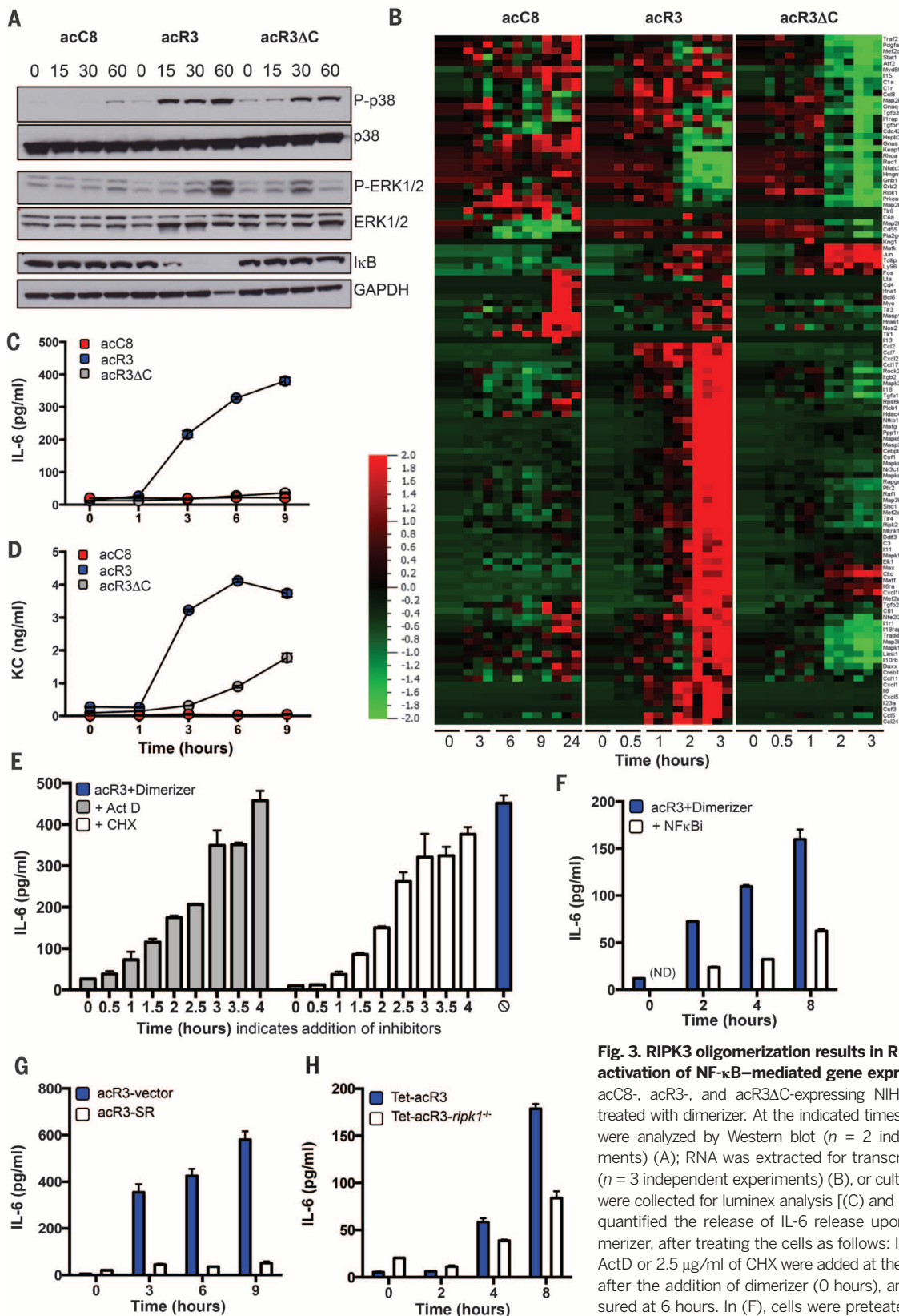


Fig. 3. RIPK3 oligomerization results in RIPK1-dependent activation of NF- κ B-mediated gene expression. (A to D) acC8-, acR3-, and acR3 Δ C-expressing NIH 3T3 cells were treated with dimerizer. At the indicated times, protein extracts were analyzed by Western blot ($n = 2$ independent experiments) (A); RNA was extracted for transcriptional profiling ($n = 3$ independent experiments) (B), or culture supernatants were collected for luminex analysis [(C) and (D)]. (E to H) We quantified the release of IL-6 release upon addition of dimerizer, after treating the cells as follows: In (E), 2 μ g/ml of ActD or 2.5 μ g/ml of CHX were added at the indicated times, after the addition of dimerizer (0 hours), and IL-6 was measured at 6 hours. In (F), cells were pretreated with 10 μ M of Wedelolactone (NF κ Bi), and IL-6 was measured at the indicated times. In (G), acR3 cells that were stably expressing the control vector (acR3-vector) or the mutant SR κ B (acR3-SR) were used. In (H), control NIH 3T3 cells (Tet-acR3), and cells lacking RIPK1 and expressing RIPK3 2xVv under a tetracycline promoter (Tet-acR3-*ripk1*^{-/-}), were treated overnight with 500 ng/ml of doxycycline before the addition of dimerizer. In (C) to (H), the data are presented as means (\pm SEM) of triplicates from one representative experiment ($n \geq 2$ independent experiments). The heat map indicates the relative expression of the indicated transcript (red indicates high levels and green indicates low levels of expression).

indicated times. In (G), acR3 cells that were stably expressing the control vector (acR3-vector) or the mutant SR κ B (acR3-SR) were used. In (H), control NIH 3T3 cells (Tet-acR3), and cells lacking RIPK1 and expressing RIPK3 2xVv under a tetracycline promoter (Tet-acR3-*ripk1*^{-/-}), were treated overnight with 500 ng/ml of doxycycline before the addition of dimerizer. In (C) to (H), the data are presented as means (\pm SEM) of triplicates from one representative experiment ($n \geq 2$ independent experiments). The heat map indicates the relative expression of the indicated transcript (red indicates high levels and green indicates low levels of expression).

and acR3ΔC-expressing NIH 3T3 cells, but they did not efficiently phagocytose live cells (fig. S4, A and B). Moreover, both acR3 and acR3ΔC induced the up-regulation of DC activation markers, whereas acC8-expressing NIH 3T3 cells did not (Fig. 1F and fig. S4C). Similarly, intraperitoneal injection of dimerizer-treated acR3- or acR3ΔC-expressing cells induced higher recruitment of immune cells, as compared with injection of acC8-expressing cells (Fig. 1G). Together, these data suggest that necroptotic cells released DAMPs, induced maturation of DCs in vitro, and induced inflammation in vivo.

To assess the respective immunogenicity of apoptotic and necroptotic cells, we immunized C57BL/6 mice by intradermally injecting 10^6 dimerizer-treated NIH 3T3 cells that stably expressed a nonsecretable form of ovalbumin (OVA)

(fig. S5A) (29). Cells were exposed to dimerizer immediately before injection, thereby enabling them to undergo cell death in situ. We observed significantly higher CD8⁺ T cell cross-priming when mice were immunized with cells undergoing RIPK3-mediated necroptosis than with cells undergoing caspase-8-mediated apoptosis (Fig. 2A and fig. S5B; $P < 0.0001$). Immunization with acR3ΔC-OVA NIH 3T3 cells did not result in robust CD8⁺ T cell cross-priming (Fig. 2A and fig. S5B; $P < 0.01$ in a comparison with acR3-OVA NIH 3T3 cells), indicating that RHIM-dependent interactions are required for the immunogenicity of necroptotic cells.

We next compared the cross-priming efficiency of cells undergoing necroptosis with that of cells undergoing unregulated necrosis, such as “mechanical” necrosis (also called primary ne-

rosis, and achieved by repeated freezing and thawing) or “secondary” necrosis (achieved by incubating apoptotic cells for 24 hours before immunization). We found that mechanical and secondary necrotic cells induced only weak CD8⁺ T cell responses (Fig. 2B; $P < 0.01$). Although the latter results could be partially explained by the loss of antigen after necrotic membrane permeabilization (fig. S6), the findings suggest that in vivo necroptosis is a more efficient inducer of cross-priming, as compared with apoptotic or necrotic cells.

The efficiency and outcome of antigen cross-presentation have been shown to depend on a subset of CD8α⁺-CD103⁺ DCs, whose differentiation is driven by the transcription factor for the *Batf3* gene (30). We found that immunization of *Batf3*^{-/-} mice with acR3-OVA cells failed to elicit

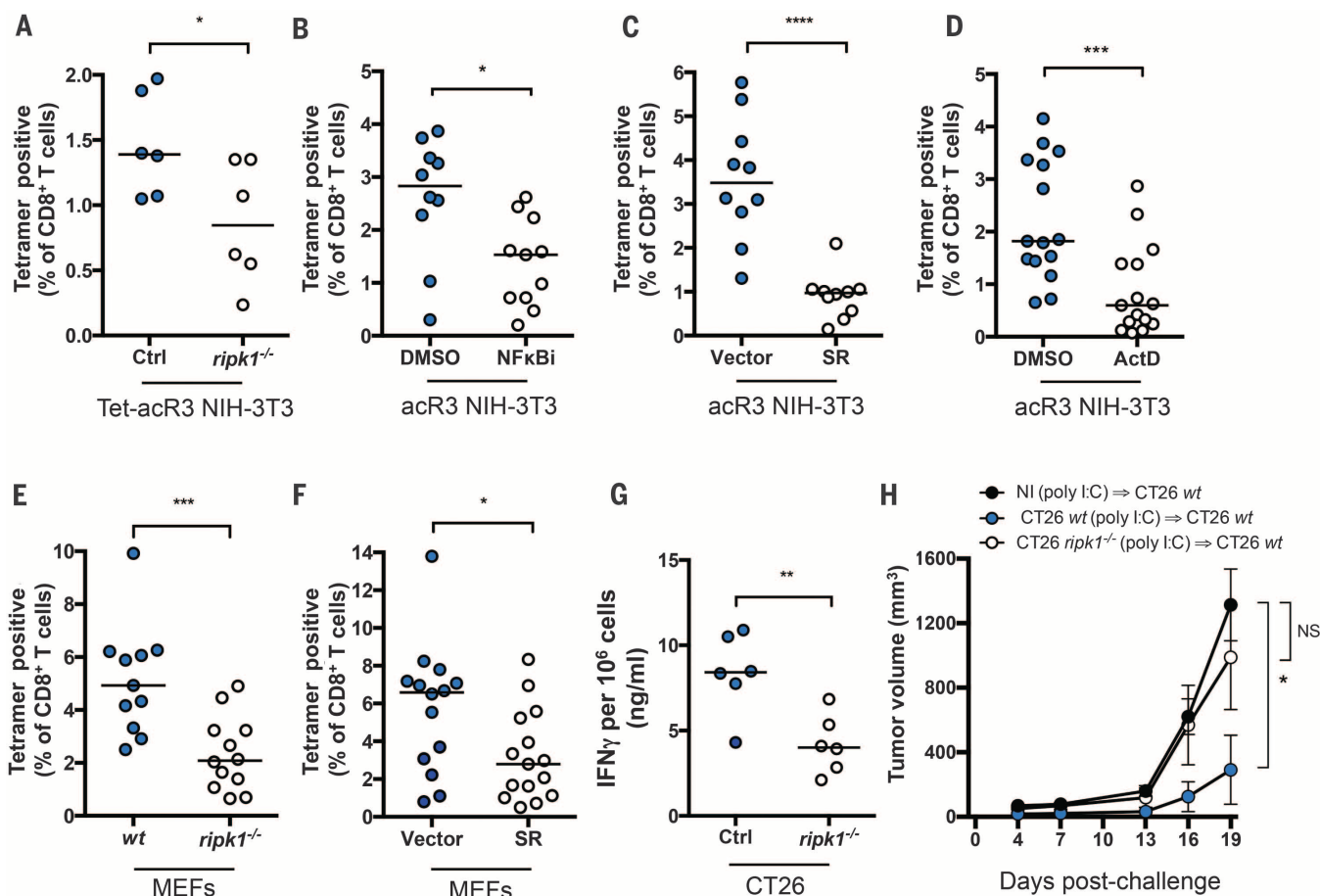


Fig. 4. RIPK1 expression and NF-κB activation during cell death are required for efficient cross-priming and anti-tumor immunity. (A) Mice were immunized with Tet-acR3-OVA and Tet-acR3-OVA-*ripk1*^{-/-} NIH 3T3 cells. Data represent one experiment with six mice per group; bars indicate medians. (B) acR3-OVA NIH 3T3 cells were pretreated with dimethyl sulfoxide (DMSO) or BAY 11-7085 (NFκBi, 10 μM) for 10 min before the addition of dimerizer and immunization. (C) Mice were immunized with acR3-OVA cells expressing NF-κB SR or the control vector. In (D), acR3-OVA were pretreated with DMSO or ActD for 45 min before immunization. (E and F) OVA-expressing MEFs were transfected with 10 μg/ml of poly I:C and, after 6 hours, used for immunization. WT or *ripk1*^{-/-} cells were used in (E); cells expressing the control vector or NF-κB SR were used in (F). Cross-priming was assessed on day 9 p.i. In (B) to (F), results

shown are pooled from three independent experiments with three to six mice per group. (G and H) CT26 control (Ctrl) cells or cells from a CRISPR/cas9 (clustered regularly interspaced short palindromic repeat/CRISPR-associated nuclease 9)-modified line that lacks RIPK1 expression (CT26 *ripk1*^{-/-}) were poly I:C-transfected and injected into *Balb/cByJ* mice. Seven days later, spleens and lymph nodes were harvested, and IFN-γ production was quantified (G). In (H), mice were challenged with 5×10^5 WT CT26 cells injected in the opposite flank, and tumor growth was monitored every 3 days. Results are from one representative experiment with six mice per group ($n = 3$ independent experiments). P values were determined by the Mann-Whitney test [(A) to (G)] or the two-way ANOVA test (multiple group comparison, comparing each group to the NI group) (H). * $P < 0.05$; ** $P < 0.01$; *** $P < 0.001$; **** $P < 0.0001$.

a CD8⁺ T cell response (fig. S7, A and B), confirming that cross-presentation of antigen associated with necroptotic cells is mediated by this DC lineage. We next characterized the CD8⁺ T cells induced by acR3-OVA immunization. CD8⁺ T cells primed by immunization with necroptotic cells produced multiple effector cytokines (Fig. 2, C and D), exhibited *in vivo* cytolytic activity (Fig. 2, E and F), and protected mice from tumor challenge (Fig. 2G). Together, these data indicate that necroptotic cells are able to provide both antigen and immune stimulation, in turn supporting DC-mediated cross-priming of CD8⁺ T cells. The requirement of RHIM^{RIPK3} for the immunogenicity of necroptotic cells suggests that classical DAMPs (e.g., HMGB1) are insufficient to achieve robust cross-priming and supports a critical role for RIPK1, independent of cell death.

To understand the requirement of RHIM for immunogenic necroptosis, we studied the signaling pathways that were engaged during the different forms of cell death and assessed mitogen-activated protein kinase (MAPK) and NF- κ B activation after dimerizer treatment. Oligomerization of RIPK3 in acR3-expressing NIH 3T3 cells resulted in the rapid phosphorylation of p38 and extracellular signal-regulated kinase-1 and -2 and the degradation of I κ B (Fig. 3A). Activation of these inflammatory pathways was not observed after dimerization of caspase-8 and was attenuated in acR3 Δ C-expressing NIH 3T3 cells, with the greatest difference corresponding to the NF- κ B pathway (Fig. 3A). To determine the impact on the transcriptional profile, we quantified the mRNA expression of 179 immune-related genes at different stages of cell death (Fig. 3B). Despite the rapid cell death kinetics, full-length RIPK3 activation triggered a significant up-regulation of 72 inflammatory genes, many of which are regulated by NF- κ B and MAPK activation (fig. S8A and table S1; rank regression on time with adjustment for false discovery rate, $q < 0.05$). In contrast, we observed only modest changes in dimerizer-treated acC8-expressing cells (three genes differentially expressed) and acR3 Δ C-expressing cells (17 genes differentially expressed) (fig. S8A and table S1). We next measured inflammatory cytokines in the supernatant from dimerizer-treated cell cultures and found that acR3 cells released high amounts of IL-6 (Fig. 3C) and CXCL1 (Fig. 3D), validating our transcriptional analysis. IL-6 production was inhibited in a time-dependent manner by treating the cells with actinomycin-D (ActD) or cycloheximide (CHX) (Fig. 3E). These data suggest that necroptotic cells actively transcribe and translate inflammatory cytokines during cell death (fig. S8B). Moreover, chemical inhibition of IKK kinase activity diminished the release of IL-6 (Fig. 3F), and stable expression of an I κ B dominant negative protein [NF- κ B (S32A, S36A) super repressor, SR] also inhibited cytokine secretion (Fig. 3G).

To formally test the contribution of RIPK1, we deleted RIPK1 from NIH 3T3 cells and stably expressed the RIPK3-2xFv construct under a tetracycline-inducible promoter (Tet-acR3) (fig. S9, A and B). The addition of dimerizer trig-

gered necroptosis in both cell lines (fig. S9C); however, NF- κ B activation (fig. S9D) and IL-6 production (Fig. 3H) were reduced in the cells lacking RIPK1. These results revealed an NF- κ B transcriptional and translational activity that is engaged during RIPK3 necroptosis.

We next tested the hypothesis that RIPK1 signaling and NF- κ B-dependent gene expression within the dying cell are critical for cross-priming. We immunized mice using necroptotic cells that lacked RIPK1 (Tet-acR3-*Ripk1*^{-/-}) (Fig. 4A), cells that lacked NF- κ B signaling [pretreated with NF- κ B inhibitor (NF κ Bi) (Fig. 4B) or overexpressing the NF- κ B SR (Fig. 4C)], or cells in which transcription was inhibited (pretreated with ActD) (Fig. 4D). Cross-priming was significantly reduced in all instances, thus establishing that active RIPK1-NF- κ B signaling is essential for the immunogenicity of necroptotic cells.

To extend our findings to a second model that leads to simultaneous RIPK1-dependent NF- κ B activation and cell death, we used the transfection of polyinosinic-polycytidylic acid (poly I:C) (fig. S10A), which engages the cytosolic RNA sensors RIG-I and MDA5, in turn recruiting the adaptor proteins IPS-1, RIPK1, TRADD, and FADD (37). We confirmed that in this model, RIPK1 was essential for NF- κ B activation (fig. S10, B and C) and cytokine secretion (fig. S10D) (37). Moreover, poly I:C transfection results in intrinsic apoptosis, rather than necroptosis (32). We found that in both wild-type (WT) and *Ripk1*^{-/-} cells, poly I:C is capable of inducing similar levels of caspase-3 activation and cell death (fig. S10, E and F). Thus, we were able to decouple NF- κ B activation from apoptosis induction downstream of double-stranded RNA sensors.

We next tested the hypothesis that immunogenic apoptosis induced by poly I:C (33) was regulated by the RIPK1-NF- κ B axis. We immunized mice with poly I:C-transfected OVA-expressing mouse embryonic fibroblasts (MEFs) (Fig. 4, E and F). Compared with immunization with WT cells, immunization with *Ripk1*^{-/-} (Fig. 4E) or NF- κ B SR-expressing cells (Fig. 4F) resulted in a significant reduction in CD8⁺ T cell priming. These data reinforce the crucial role of RIPK1-mediated NF- κ B activation within dying cells during the initiation of CD8⁺ T cell immune responses, despite the presence of a strong inflammatory pathogen-associated molecular pattern such as poly I:C.

Finally, we tested the relevance of our findings in the context of tumor immunity. Deletion of RIPK1 from poly I:C-transfected CT26 colon carcinoma cells (fig. S10G) rendered them poorly immunogenic in comparison with WT cells, as measured by interferon- γ (IFN- γ) production (Fig. 4G) and protection from tumor challenge (Fig. 4H). Overall, our results reveal RIPK1-induced NF- κ B activation as the critical determinant of CD8⁺ T cell immunity to cell-associated antigens.

The danger model predicts that cell death resulting from tissue damage and stress induces the passive release of preformed danger molecules that mediate subsequent immune responses (34). Breaking from this model, the present study

reveals an unexpected role for RIPK1- and NF- κ B-driven gene expression during cell death as a key determinant for cross-priming of CD8⁺ T cells. Thus, although the release of DAMPs can trigger inflammatory responses, we show that RIPK1-mediated induction of NF- κ B and its downstream target genes is necessary for initiating CD8⁺ T cell adaptive immunity. To date, PCD pathways have been defined by morphological and biochemical methods; our results highlight the need for a transcriptional definition of cell death, as a means of understanding the relationship between dying cells and immunity. Whether these findings apply to other aspects of adaptive immunity (e.g., B cell or CD4 T cell priming) remains to be determined (7, 35).

NF- κ B is a critical regulator of innate immune responses, and its pathway is a prime target of interference by pathogens; our results suggest an additional benefit for microbes that interfere with both NF- κ B signaling (36) and cell death pathways (37, 38). For example, viral inhibitors of RHIM-dependent interactions (e.g., mouse cytomegalovirus M45) may have evolved to subvert CD8⁺ T cell cross-priming. In turn, scaffold proteins such as RIPK1, which are an assemblage of multiple domains (RHIM domain, death domain, and kinase domain), may have evolved to coordinate cell death and innate signaling modules (39), together orchestrating adaptive immunity. Thus, investigation and targeting of scaffold proteins at the intersection of cell death pathways and host-defense pathways may provide new therapeutic opportunities in the field of immunotherapy.

REFERENCES AND NOTES

- M. L. Albert, B. Sauter, N. Bhardwaj, *Nature* **392**, 86–89 (1998).
- M. L. Albert et al., *Nat. Med.* **4**, 1321–1324 (1998).
- M. J. Bevan, *J. Exp. Med.* **143**, 1283–1288 (1976).
- S. Turley, L. Poirot, M. Hattori, C. Benoist, D. Mathis, *J. Exp. Med.* **198**, 1527–1537 (2003).
- S. S. Iyer et al., *Proc. Natl. Acad. Sci. U.S.A.* **106**, 20388–20393 (2009).
- Y. Shi, J. E. Evans, K. L. Rock, *Nature* **425**, 516–521 (2003).
- H. Kazama et al., *Immunity* **29**, 21–32 (2008).
- P. Scaffidi, T. Misteli, M. E. Bianchi, *Nature* **418**, 191–195 (2002).
- B. Sauter et al., *J. Exp. Med.* **191**, 423–434 (2000).
- S. R. Scheffer et al., *Int. J. Cancer* **103**, 205–211 (2003).
- A. F. Ochsenbein et al., *Proc. Natl. Acad. Sci. U.S.A.* **96**, 2233–2238 (1999).
- J. Gamrekashvili et al., *J. Clin. Invest.* **123**, 4755–4768 (2013).
- M. L. Albert, *Nat. Rev. Immunol.* **4**, 223–231 (2004).
- N. Casares et al., *J. Exp. Med.* **202**, 1691–1701 (2005).
- M. Obeid et al., *Nat. Med.* **13**, 54–61 (2007).
- M. Feoktistova et al., *Mol. Cell* **43**, 449–463 (2011).
- T. Tenev et al., *Mol. Cell* **43**, 432–448 (2011).
- J. M. Blander, *Nat. Rev. Immunol.* **14**, 601–618 (2014).
- S. J. Martin, C. M. Henry, S. P. Cullen, *Mol. Cell* **46**, 387–397 (2012).
- A. Oberst et al., *J. Biol. Chem.* **285**, 16632–16642 (2010).
- S. Orozco et al., *Cell Death Differ.* **21**, 1511–1521 (2014).
- S. W. G. Tait et al., *Cell Reports* **5**, 878–885 (2013).
- C. P. Dillon et al., *Cell* **157**, 1189–1202 (2014).
- F. Ghiringhelli et al., *Nat. Med.* **15**, 1170–1178 (2009).
- A. Tesniere et al., *Oncogene* **29**, 482–491 (2010).
- M. Michaud et al., *Science* **334**, 1573–1577 (2011).
- O. Schulz, C. Reis e Sousa, *Immunology* **107**, 183–189 (2002).
- C. Kurts, B. W. S. Robinson, P. A. Knolle, *Nat. Rev. Immunol.* **10**, 403–414 (2010).

29. D. Sancho *et al.*, *Nature* **458**, 899–903 (2009).
 30. K. Hildner *et al.*, *Science* **322**, 1097–1100 (2008).
 31. M.-C. Michallet *et al.*, *Immunity* **28**, 651–661 (2008).
 32. R. Besch *et al.*, *J. Clin. Invest.* **119**, 2399–2411 (2009).
 33. O. Schulz *et al.*, *Nature* **433**, 887–892 (2005).
 34. P. Matzinger, *Annu. Rev. Immunol.* **12**, 991–1045 (1994).
 35. S. Gallucci, M. Lolkema, P. Matzinger, *Nat. Med.* **5**, 1249–1255 (1999).
 36. M. M. Rahman, G. McFadden, *Nat. Rev. Microbiol.* **9**, 291–306 (2011).
 37. M. Lamkanfi, V. M. Dixit, *Cell Host Microbe* **8**, 44–54 (2010).
 38. N. Yatim, M. L. Albert, *Immunity* **35**, 478–490 (2011).
 39. R. Weinlich, D. R. Green, *Mol. Cell* **56**, 469–480 (2014).

ACKNOWLEDGMENTS

The authors thank S. Zelenay for the LA- Δ OVA-mCherry and Δ OVA-mCherry constructs; R. Weil for the dominant negative NF- κ B plasmid; P. O. Vidalain for the NF- κ B-Luciferase reporter

plasmid; P. Fitzgerald for cell lines; and M.A. Ingersoll, D. Duffy, O. Schwartz, J. Boussier, and A. Yatim for their critical reading of the manuscript and advice. We also thank M. A. Ingersoll for mouse protocols, M. Fontes for assistance with Qluore Omics software, and the Centre for Human Immunology for providing technical support and project management. The data from this study are tabulated here and in the supplementary materials. Dimerizable RIPK3 and caspase-8 constructs are available from D.O. under a materials transfer agreement with the University of Washington. U.S. Patent PCT/US2014/036196 has been filed by St. Jude Children's Research Hospital, covering the induction of necroptosis using RIPK3 oligomerization. Funding for the work was provided by the Agence Nationale de Recherches sur le Sida et les Hépatites; Projet ANUBIS of the Agence Nationale de la Recherche (ANR-12-BSV3-0011-01) and a Laboratories of Excellence Immuno-Onco grant (ANR-11-IDEX-0005-02) (M.L.A., N.Y., H.J.-S., and R.B.d.S.); the French National Cancer Institute (INCa) (Plan Cancer 2014–2019) and the Ecole de l'Inserm Liliane Bettencourt (N.Y.); NIH grants R21CA185681 and R01AI108685 (A.O.); NIH grant

AI44848 (D.R.G.); and NIH award 5R01AI108685-02 (S.O.). C.R.S. and O.S. were supported by grants from Cancer Research UK, The Francis Crick Institute, and the European Research Council. The authors thank the Genomics Platform of the Department of Translational Research at Institut Curie for experiments conducted using Nanostring tools (grants INCa-DGOS-4654, SIRIC11-002, ANR-10-IDEX-0001-02 PSL, and ANR-11-LBX-0044).

SUPPLEMENTARY MATERIALS

www.sciencemag.org/content/350/6258/328/suppl/DC1

Materials and Methods

Figs. S1 to S11

Table S1

References (40–48)

Movies S1 to S3

16 July 2015; accepted 11 September 2015

Published online 24 September 2015

10.1126/science.aad0395

T CELL IMMUNITY

Stable inhibitory activity of regulatory T cells requires the transcription factor Helios

Hye-Jung Kim,^{1,2} R. Anthony Barnitz,^{3,4} Taras Kreslavsky,^{1,2} Flavian D. Brown,³ Howell Moffett,¹ Madeleine E. Lemieux,⁵ Yasemin Kaygusuz,¹ Torsten Meissner,^{1,2} Tobias A. W. Holderried,^{1,2} Susan Chan,^{6,7} Philippe Kastner,^{6,7} W. Nicholas Haining,^{3,4,8} Harvey Cantor^{1,2,*}

The maintenance of immune homeostasis requires regulatory T cells (T_{regs}). Given their intrinsic self-reactivity, T_{regs} must stably maintain a suppressive phenotype to avoid autoimmunity. We report that impaired expression of the transcription factor (TF) Helios by FoxP3⁺ CD4 and Qa-1–restricted CD8 T_{regs} results in defective regulatory activity and autoimmunity in mice. Helios-deficient T_{regs} develop an unstable phenotype during inflammatory responses characterized by reduced FoxP3 expression and increased effector cytokine expression secondary to diminished activation of the STAT5 pathway. CD8 T_{regs} also require Helios-dependent STAT5 activation for survival and to prevent terminal T cell differentiation. The definition of Helios as a key transcription factor that stabilizes T_{regs} in the face of inflammatory responses provides a genetic explanation for a core property of T_{regs} .

Regulatory T cells (CD4 and CD8 T_{regs}) dampen excessive immune responses and prevent or ameliorate autoimmune tissue damage, whereas immune suppression exerted by T_{regs} can impede anti-tumor immune responses. In contrast to effector T cells (T_{eff}), which rely on robust activation and differentiative plasticity, T_{regs} depend on the preservation of a stable,

anergic, and suppressive phenotype to maintain immune homeostasis (1, 2). Although FoxP3⁺ CD4 T_{regs} are remarkably stable (1, 2), the genetic mechanisms that ensure phenotypic stability after expansion during inflammation, infection, or autoimmunity (i.e., conditions that most require maintenance of an anergic and inhibitory T_{regs} phenotype) are poorly understood.

The Helios (Ikzf2) transcription factor (TF) is expressed by two T_{reg} lineages: FoxP3⁺ CD4⁺ and Ly49⁺ CD8⁺ T_{regs} (fig. S1) (3–6). To determine the contribution of Helios to the regulatory phenotype, we analyzed mice deficient in *Ikzf2* (*Helios*^{−/−}), the gene that encodes Helios (5). *Helios*^{−/−} mice (6 to 8 weeks old) displayed reduced numbers of CD8 but not CD4 T_{regs} (fig. S2) and no obvious signs of autoimmune disorder. However, 5-month-old *Helios*-deficient mice exhibited increased numbers of activated CD4 and CD8 T cells, T follicular helper (T_{FH}) cells, and germinal center (GC) B cells as compared to wild-type (WT) mice (Fig. 1A and

fig. S3A). Autoimmune disease was apparent by 6 to 8 months of age, accompanied by the infiltration of immune cells into nonlymphoid tissues (Fig. 1B), the production of autoantibodies (Fig. 1C), and glomerular nephritis (fig. S3B). *Rag2*^{−/−} mice reconstituted with bone marrow (BM) from *Helios*^{−/−} donors also developed autoimmunity (fig. S4), indicating a lymphocyte-intrinsic effect.

Although *Helios*^{−/−} mice did not develop overt signs of autoimmunity until 5 to 6 months of age, upon challenge with viral infection by LCMV-Armstrong (LCMV, lymphocytic choriomeningitis virus), both young (2 months) and older (6 months) *Helios*^{−/−} mice but not *Helios*^{+/+} mice developed inflammatory and autoimmune changes characterized by increased levels of T_{FH} and GC B cells (Fig. 1D) and immunoglobulin G (IgG) deposition in the kidney (Fig. 1E), although *Helios*^{+/+} and *Helios*^{−/−} mice cleared virus with equal efficiency (fig. S5).

Because autoimmunity in *Helios*^{−/−} mice did not result from defective negative selection (figs. S6 to S8), we asked whether it instead reflected defective T_{reg} activity. Analyses of BM chimeras that express a selective Helios deficiency in either CD4 or CD8 T cells revealed that mice with either Helios-deficient CD4 or CD8 T cells develop autoimmune disease with similar features (fig. S9). Moreover, tolerance was dominant, because *Rag2*^{−/−} mice given *Helios*^{−/−} BM + *Helios*^{+/+} BM did not develop autoimmunity (fig. S10).

Direct evidence for the contribution of Helios to CD4 T_{reg} activity and the prevention of autoimmune disease came from analysis of *Helios*^{fl/fl}. FoxP3^{YFP}-Cre mice, which develop autoimmune disease at >5 months of age, characterized by increased numbers of activated CD4 and CD8 T cells, T_{FH} and GC B cells (Fig. 2, A and B), autoantibody production (Fig. 2C), and immune cell infiltration (fig. S11). Moreover, BM chimeras from *Helios*^{fl/fl}. FoxP3-Cre donors developed this disorder within 6 weeks (fig. S12).

Helios-sufficient but not *Helios*-deficient FoxP3⁺ CD4 T_{regs} exerted dominant, lymphocyte-intrinsic inhibition that prevented autoimmune disease in the presence of highly activated self-reactive T cells from scurfy mice, which have no FoxP3 forkhead domain. BM chimeras reconstituted with *Helios*^{−/−}/Scurfy BM but not *Helios*^{+/+}/Scurfy BM

¹Department of Cancer Immunology and Virology, Dana-Farber Cancer Institute, 450 Brookline Avenue, Boston, MA 02215, USA. ²Department of Microbiology and Immunobiology, Division of Immunology, Harvard Medical School, Boston MA. ³Department of Pediatric Oncology, Dana-Farber Cancer Institute, 450 Brookline Avenue, Boston, MA 02215, USA. ⁴Department of Pediatrics, Boston Children's Hospital, Boston, MA, USA. ⁵Bioinfo, Plantagenet, Canada. ⁶Institut de Génétique et de Biologie Moléculaire et Cellulaire (IGBMC), INSERM U964, CNRS UMR 7104, Université de Strasbourg, 67404 Illkirch, France. ⁷Faculté de Médecine, Université de Strasbourg, Strasbourg, France. ⁸Broad Institute of MIT and Harvard, Cambridge, MA, USA. *Corresponding author. E-mail: harvey_cantor@dfci.harvard.edu

cells rapidly developed autoimmunity (Fig. 2D and fig. S13, A and B).

Impaired suppressive activity of Helios-deficient FoxP3⁺ CD4 T_{regs} was observed when FoxP3⁺ CD4 cells (YFP⁺) from Helios^{fl/fl}.FoxP3^{YFP}.Cre were cotransferred into *Rag2*^{-/-} hosts with naïve CD4⁺ T cells, resulting in wasting disease (Fig. 2E and fig. S14A). Analysis of CD4 T_{regs} from *Helios*^{-/-} mice with a global Helios deletion (5) showed that mice given naïve CD4 cells developed colitis that could be prevented by Helios^{+/+} but not Helios^{-/-} FoxP3⁺ CD4 T_{regs} (Fig. 2F and fig. S14B).

Helios deficiency also resulted in defective CD8 T_{reg} function. CD8 T_{regs} (CD44⁺CD122⁺Ly49⁺) recognize target T_H cells through a Qa-1/peptide-T cell receptor (TCR) interaction that prevents autoantibody-mediated autoimmune disease (3). Helios-deficient CD8 T_{regs} failed to inhibit the adoptive helper response of T_{FH} cells (Fig. 2G). Defective suppressive activity of Helios^{-/-} CD8 T_{regs} was lymphocyte-intrinsic, because Ly49⁺ CD8 cells

isolated from *Rag2*^{-/-} recipients reconstituted with Helios^{+/+} but not Helios^{-/-} BM cells mediated inhibitory activity (fig. S14C), which is consistent with impaired suppressive activity by CD8 T_{regs} from Helios^{fl/fl}.CD4-Cre mice (fig. S14D). These data indicate that Helios-dependent suppressive activity exerted by both CD4 and CD8 T_{regs} is required to maintain self-tolerance.

These findings suggested that Helios may control common genetic pathway(s) in CD4 and CD8 T_{regs}. To address this issue, we defined the genome-wide distribution of Helios binding sites in these cells by chromatin immunoprecipitation followed by DNA sequencing (ChIP-Seq) (7). The chromatin state of Helios-bound regions was determined according to acetylation of histone H3 at Lys²⁷ (H3K27ac) for active regulatory regions and trimethylation of histone H3 at Lys²⁷ for polycomb-repressed regions (H3K27me3) (8).

This analysis revealed that Helios bound mainly to promoter regions of (~85%) target genes

in both CD4 and CD8 T_{regs} (Fig. 3A); 1602 and 828 genes, respectively, with 649 shared target genes (Fig. 3B). Analysis of DNA regions bound by Helios showed significant enrichment of NRFL, Sp1/Sp4, and IKAROS binding motifs (Fig. 3C), as well as genes that regulate cell cycle progression and apoptosis/cell survival (table S1A), including *STAT5b*, *Jak2*, *NFAT5*, and *Birc2*, and autophagy genes, whose loci showed activated chromatin marks, as evidenced by expression of H3K27ac (Fig. 3D and table S1B). Pathway analysis of Helios target genes in CD4 and CD8 T_{regs} revealed STAT5b/interleukin-2 receptor α (IL-2R α) as a central node within a Helios target gene network, suggesting that Helios might regulate genes involved in IL-2 signaling and sustained survival (Fig. 3E).

The IL-2R α -STAT5 pathway is essential for CD4 T_{reg} survival, whereas the maintenance of FoxP3 expression reflects binding of activated STAT5 to the *Foxp3* promoter and CNS2 regions (9). Identification of the IL-2R α -STAT5 pathway as a

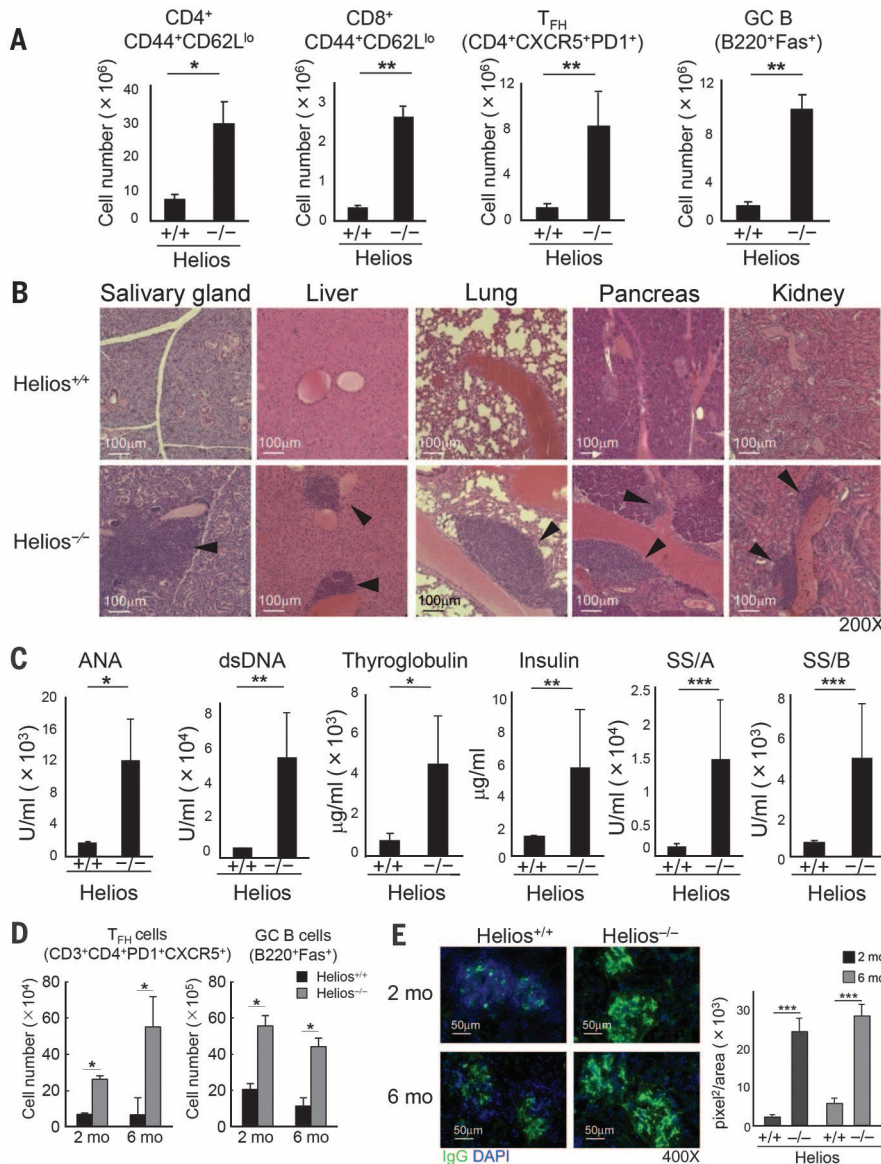


Fig. 1. Helios^{-/-} mice develop an autoimmune phenotype. (A) Activated CD4 and CD8 T cells (CD44⁺CD62L^{lo}), T_{FH} (CD4⁺PD1⁺CXCR5⁺), and GC B (B220⁺Fas⁺) cells in spleens from (5-month-old) *Helios*^{+/+} and *Helios*^{-/-} mice were compared ($n = 3$ to 6 mice). Representative data from three independent experiments are shown. The mean \pm SEM is indicated. * $P < 0.05$ and ** $P < 0.01$ (Mann-Whitney test). (B) Microscopy ($\times 200$) of representative hematoxylin and eosin staining of salivary gland, liver, lung, pancreas, and kidney sections from (7-month-old) *Helios*^{+/+} and *Helios*^{-/-} mice ($n = 4$ mice per group). Representative data from two independent experiments are shown. (C) The generation of autoantibodies was compared in sera from 7-month-old *Helios*^{+/+} and *Helios*^{-/-} mice ($n = 7$ to 10 mice per group). Representative data from three independent experiments are shown. ANA, anti-nuclear Ab; SS/A, Sjögren's syndrome-related antigen/A; SS/B, Sjögren's syndrome-related antigen/B. The mean \pm SEM is indicated. * $P < 0.05$, ** $P < 0.01$, and *** $P < 0.001$ (Mann-Whitney test). (D) Viral infection of Helios-deficient mice. Two-month-old and 6-month-old *Helios*^{+/+} and *Helios*^{-/-} mice were infected intraperitoneally (i.p.) with 2×10^5 plaque-forming units of LCMV-Armstrong. 30 days later, spleen cells were analyzed for T_{FH} and GC B cells ($n = 4$ mice per group). Representative data from two independent experiments are shown. The mean \pm SEM is indicated. * $P < 0.05$ (Mann-Whitney test). (E) Kidney sections from virus-infected mice were analyzed for IgG deposition and IgG⁺ areas in glomeruli ($n = 4$ mice per group). Representative data from two independent experiments are shown. The mean \pm SEM is indicated. *** $P < 0.001$ (Mann-Whitney test).

major Helios gene network opened the possibility that Helios contributed to T_{reg} survival and/or FoxP3 stability through increased STAT5 activation and enhanced IL-2 responsiveness (10, 11). We noted reduced survival of Helios^{-/-} CD4 T_{regs} after transfer into lymphopenic hosts (Fig. 4A, left and middle), which is consistent with an essential contribution of the IL-2R α -STAT5 signaling pathway to T_{reg} viability. Moreover, Helios-deficient CD4 T_{regs} displayed reduced coexpression of FR4 and CD73 (Fig. 4A, right), markers that indicate anergy by self-reactive CD4 cells (12). Indeed, a significant portion of Helios-deficient CD4 T_{regs} developed into non-anergic cells under inflammatory conditions, including autoimmunity and infection (figs. S12C and S15). Because cytokine signaling can induce binding of activated STAT6 to the *Foxp3* locus and competition with p-STAT5 (10), diminished STAT5 activation in Helios-deficient CD4 T_{regs} may allow increased STAT6 binding to the *Foxp3* locus and diminished FoxP3 expression. Reduced STAT5 activation by Helios-deficient T_{regs} was accompanied by reduced expression of FoxP3 under conditions

including progressive autoimmune disease (6-month-old Helios^{fl/fl}.FoxP3-Cre mice) and colitis (Fig. 4B), consistent with the contribution of STAT5 to stable FoxP3 expression (10).

Examination of STAT5-dependent IL-2 responsiveness revealed decreased STAT5 activation in FoxP3⁺ CD4⁺ cells from Helios^{-/-} and Helios^{fl/fl}.FoxP3-Cre mice as compared to Helios^{+/+} mice (Fig. 4C). Enforced expression of constitutively active STAT5 (STAT5-CA) (13) in Helios-deficient CD4 T_{regs} restored FoxP3 expression to levels similar to WT CD4 T_{regs} and prevented the expression of interferon- γ , an effector cytokine (Fig. 4D and fig. S16).

Decreased FoxP3 expression may result in phenotypic instability, including derepression of T_{eff} programs (10, 11). Analysis of the CD4 T_{reg} phenotype after immunization of mice with sheep red blood cells revealed that Helios-deficient (Helios^{fl/fl}.FoxP3-Cre) but not Helios-sufficient (Helios^{fl/fl}) CD4 T_{regs} express effector cytokines, including interferon- γ (IFN- γ) and IL-17 (Fig. 4E). Acquisition of a T_{eff} phenotype under inflammatory conditions by Helios-deficient

CD4 T_{regs} was a cell-intrinsic phenotype. *Rag2*^{-/-} hosts were injected with CD4 T cells that transgenically express the OT-II T cell receptor (Helios WT), Helios^{+/+} (CD45.1⁺), and Helios^{-/-} (CD45.2⁺) T_{regs} and were immunized with OT-II peptide. Helios-deficient but not Helios-sufficient CD4 T_{regs} displayed reduced FoxP3 expression and produced effector cytokines, including IFN- γ , IL-17, and tumor necrosis factor- α (Fig. 4F). Decreased FoxP3 expression by Helios-deficient CD4 T_{regs} during colitis progression was also accompanied by the expression of effector cytokines, including IFN- γ and IL-17 and the FR4^{lo}CD73^{lo} phenotype (fig. S17).

Defective suppressive activity by Helios-deficient CD8 T_{regs} was associated with a similar phenotypic defect under inflammatory conditions. In adoptive *Rag2*^{-/-}.*Prf1*^{-/-} hosts, Helios-deficient CD8 T_{regs} exhibited increased apoptosis and reduced cell recovery as compared to Helios WT CD8 T_{regs} , as observed for Helios-deficient FoxP3⁺ CD4 T_{regs} (fig. S18A).

In CD8 T cells, cytokines IL-2 and IL-15 induce STAT5 activation, whereas sustained activation

Fig. 2. Helios-deficient CD4 and CD8 T_{regs} contribute to autoimmune disease.

(A) Phenotype of Helios^{fl/fl}.FoxP3-Cre mice at 6 months of age. The percentage and numbers of activated CD4 T cells (CD44⁺ CD62L^{lo}) in the spleen are shown ($n = 4$ or 5 mice per group). Data representative of two independent experiments are shown. The mean \pm SEM is indicated. *** $P < 0.001$ (Mann-Whitney test).

(B) Fluorescence-activated cell sorting profiles for T_{FH} and GC B cells from spleens of FoxP3-Cre and Helios^{fl/fl}.FoxP3-Cre mice ($n = 4$ or 5 mice per group). Data are representative of two independent experiments.

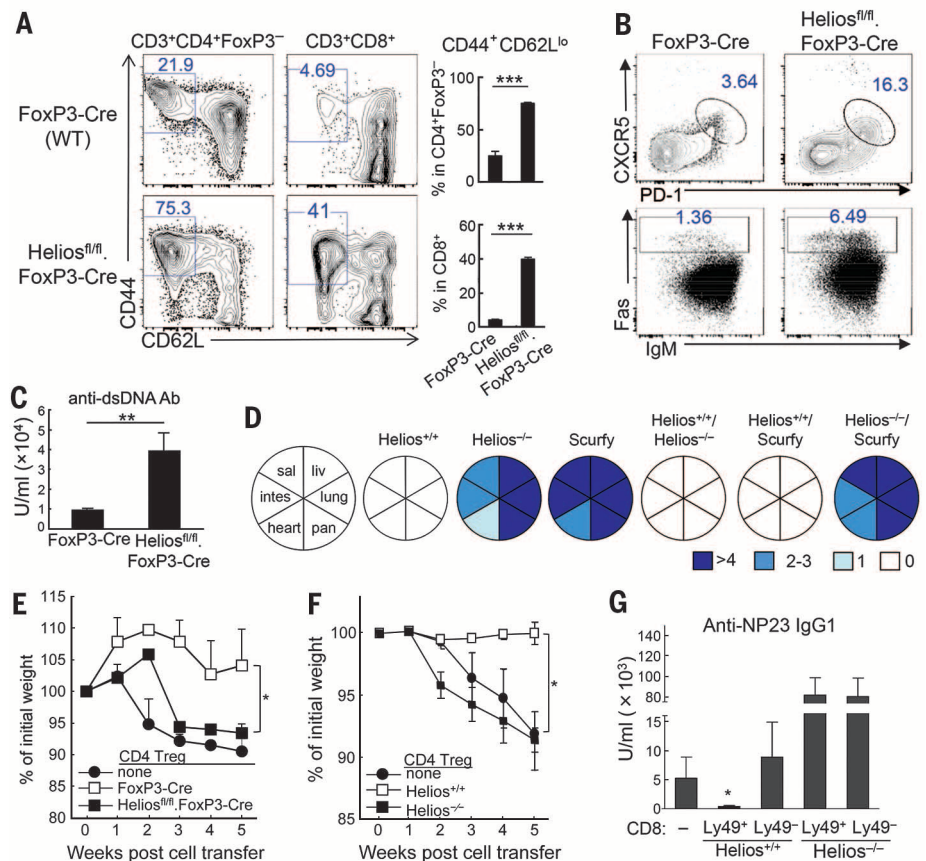
(C) Levels of antibody to double-stranded DNA in sera of FoxP3-Cre and Helios^{fl/fl}.FoxP3-Cre mice at 6 months of age ($n = 4$ or 5 mice per group). Data are representative of two independent experiments. The mean \pm SEM is indicated. ** $P < 0.01$ (Mann-Whitney test).

(D) Lethally irradiated *Rag2*^{-/-} mice were reconstituted with hematopoietic progenitors from Helios^{+/+}, Helios^{-/-}, Scurfy, Helios^{+/+}/Helios^{-/-} (1:1), Helios^{+/+}/Scurfy (1:1), and Helios^{-/-}/Scurfy (1:1) mice ($n = 4$ to 6 mice per group). The intensity of immune cell infiltration was quantified by scoring immune cell infiltration 7 weeks after reconstitution: >4 (most severe), 2 to 3 (severe), 1 (mild), and 0 (none). Data are representative of two independent experiments.

(E) Defective inhibitory activity of Helios-deficient CD4 and CD8 T_{regs} . *Rag2*^{-/-} hosts received sort-purified T_{eff} cells (CD25⁺CD44^{lo}CD62L^{hi}, CD45.1) and CD4 T_{regs} (CD3⁺CD4⁺YFP⁺) from spleens of FoxP3-Cre or Helios^{fl/fl}.FoxP3-Cre mice. Recipients were examined for changes in weight ($n = 4$ mice per group). Representative data from two independent experiments are shown. The mean \pm SEM is indicated. * $P < 0.05$ (Kruskal-Wallis test).

(F) *Rag2*^{-/-} hosts received CD4 T cells (T_{eff} : CD25⁺CD44^{lo}CD62L^{hi}, CD4 T_{reg} : CD3⁺CD4⁺CD25⁺) from spleens of defined donor mouse strains. Recipients were examined for changes in weight ($n = 4$ mice per group). Representative data from three independent experiments are shown. The mean \pm SEM is indicated. * $P < 0.05$ (Kruskal-Wallis test).

(G) WT B and CD25-depleted CD4 T cells were transferred into *Rag2*^{-/-} hosts along



with Ly49⁺ or Ly49⁻ CD8 T cells from spleens of Helios^{+/+} or Helios^{-/-} mice. *Rag2*^{-/-} adoptive hosts were immunized with NP₁₉-KLH [(4-hydroxy-3-nitrophenyl acetyl)₁₉-keyhole limpet hemocyanin] in Freund's complete adjuvant (FCA) at day 0 and reimmunized with NP₁₉-KLH in Freund's incomplete adjuvant at day 10. NP-specific IgG1 responses were measured at day 15 ($n = 3$ mice per group). Data are representative of three independent experiments. The mean \pm SEM is indicated. * $P < 0.05$ (Kruskal-Wallis test).

depends on IL-2 (14, 15). Helios-deficient CD8 T_{regs} displayed reduced IL-2 responsiveness and diminished STAT5 activation (figs. S18B), suggesting that Helios may serve an overlapping function in both regulatory cell types through promotion of STAT5-dependent IL-2 responsiveness and increased survival under inflammatory conditions. Indeed, *in vitro* stimulation of Ly49⁺ CD8 T_{regs} versus Ly49⁻ CD8 Tcon in the presence of STAT5 inhibitor (AG490) revealed impaired survival of CD8 T_{regs} but not of conventional memory CD8 cells (fig. S18C).

Analysis of CD8 T_{reg} responses under inflammatory conditions revealed that Helios^{-/-} CD8 T_{regs} expressed high levels of PD-1, TIM-3, and Lag3 and low levels of CD127 (figs. S18D and S19A). Transfer of Helios^{+/+} and Helios^{-/-} CD8 T_{regs} (>99% Ly49⁺ from 2-month-old mice) into *Rag2*^{-/-} hosts along with OT-II cells and antigen also revealed that Helios^{-/-} Ly49⁺ CD8 cells expressed high levels of PD-1 and TIM3 (fig. S19B) and reduced survival (fig. S19C). These findings suggest that a Helios-dependent genetic program that enhances the STAT5-dependent IL-2 responsiveness of T_{regs} may promote survival

and maintenance of an inhibitory CD8 T_{reg} phenotype.

Earlier studies of Helios and FoxP3⁺ CD4 T_{regs} suggesting no impact on T_{regs} (4, 5) relied mainly on analysis in the steady state of non-immune mice. Although young *Helios*^{-/-} mice do not develop signs of disease, they develop a dysregulated immune response at ~5 months of age that is markedly accelerated by immune stimulation, including viral infection. Although Helios belongs to a set of TFs that regulate FoxP3⁺ T_{regs} (16–18), Helios does not form protein complexes with FoxP3 (19) nor bind to the *Foxp3* locus (fig. S20). Down-regulation of FoxP3 expression and expression of effector cytokines by Helios-deficient T_{regs} may reflect reduced activation of the IL-2R α -STAT5 pathway and diminished binding of STAT5b to CNS-2, resulting in T_{reg} conversion into T_{eff} cells (fig. S21) (10). The ability of T_{regs} to sense IL-2 may also be particularly critical under inflammatory conditions, where small changes in proliferation rate or apoptosis can exert major changes in the niche-filling response by T_{regs} and T_{reg} insufficiency (20). Current views that thymic-derived T_{regs} are phenotypically and functionally more sta-

ble than induced T_{regs} may reflect, in part, Helios-dependent activation of the T_{reg} IL-2R α -STAT5 pathway described here. Recently developed surrogate surface markers may allow the isolation of stable Helios⁺ CD4 T_{regs} for the treatment of autoimmune disease or after organ transplantation (21, 22).

Helios-dependent maintenance of CD8 T_{reg} integrity also includes the inhibition of terminal differentiation and maintenance of suppressive/cytolytic activity by activating the STAT5 signaling pathway (fig. S21). Although Helios-dependent regulation of overlapping genetic pathways, including cell survival, may stabilize the suppressive phenotype of both FoxP3⁺ CD4 T_{regs} and CD8⁺ T_{regs}, much of the Helios⁺ phenotype may reflect subset-specific disparities in lineage commitment and development and distinct mechanisms of suppression.

Identification of bona fide signaling pathways that induce and maintain Helios expression in FoxP3⁺ CD4 T_{regs} may allow Helios inhibition and conversion of memory T_{regs} into T_{eff} cells that express self-reactive TCR with specificity for tumor antigens (23). Because

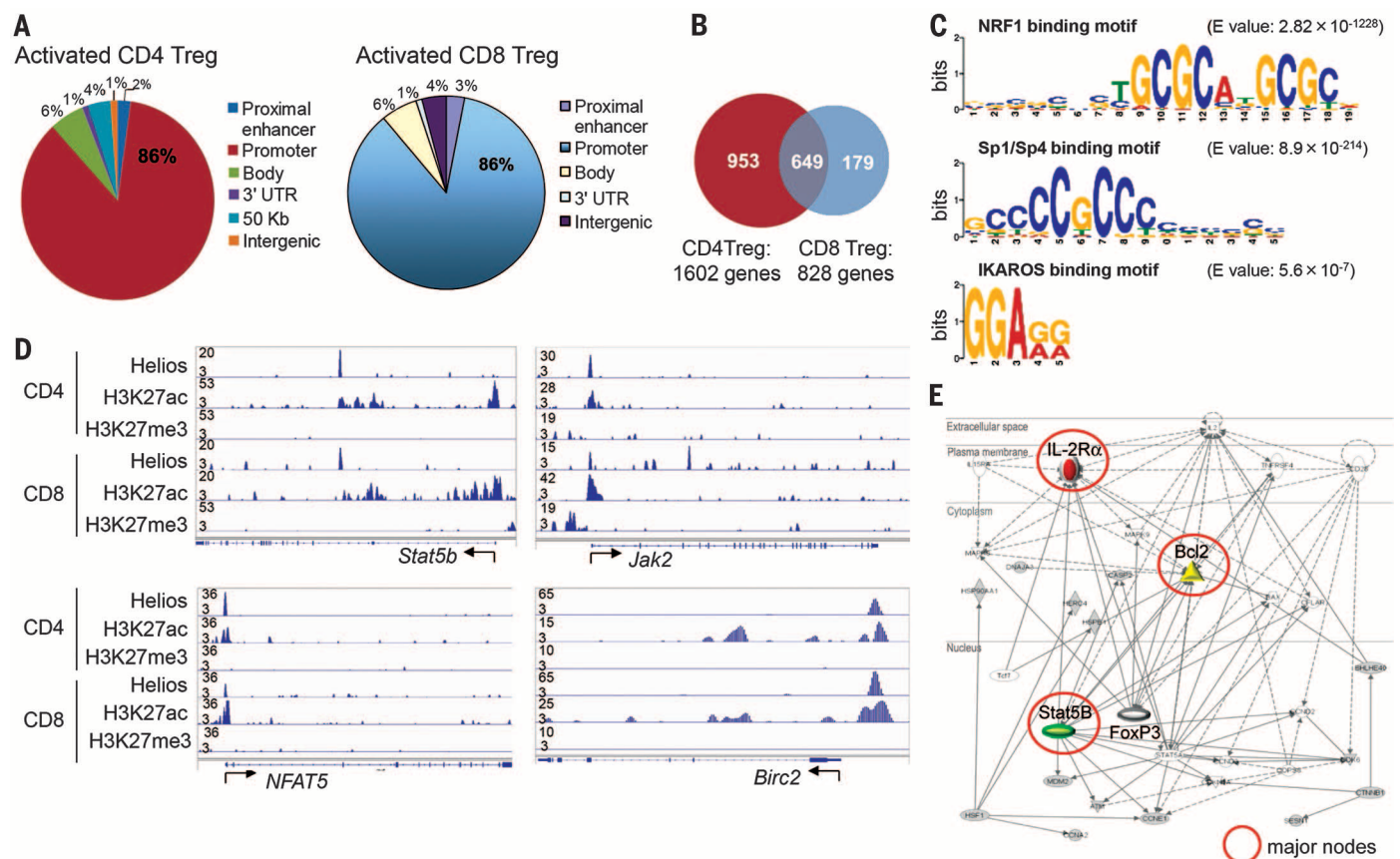


Fig. 3. Helios-dependent STAT5 activation and stabilization of CD4 T_{regs}. (A) Distribution of genome-wide Helios binding sites in activated FoxP3⁺ CD4 and Ly49⁺ CD8 T_{regs}. (B) Number of Helios target genes and overlapping Helios binding sites in CD4 and CD8 T_{regs}. (C) DNA motif analysis of Helios-bound regions. (D) ChIP-Seq analysis of Helios binding and modified histones at *STAT5b*, *Jak2*, *NFAT5*, and *Birc2* in CD4 and CD8 T_{regs}. Start sites of each gene locus are indicated. Vertical lines in gene

diagrams (bottom) indicate exons. (E) Pathway analysis of genes targeted by Helios in CD4 and CD8 T_{regs}. Solid lines represent genes known to have a direct connection. Dotted lines represent a presumptive interaction based on reported studies. Major nodes of genes are marked by red circles. Solid symbols indicate Helios target genes, and white symbols indicate neighboring genes that are functionally associated but not included in the Helios target genes.

Fig. 4. Helios-dependent STAT5 activation and stabilization of CD4 T_{regs}

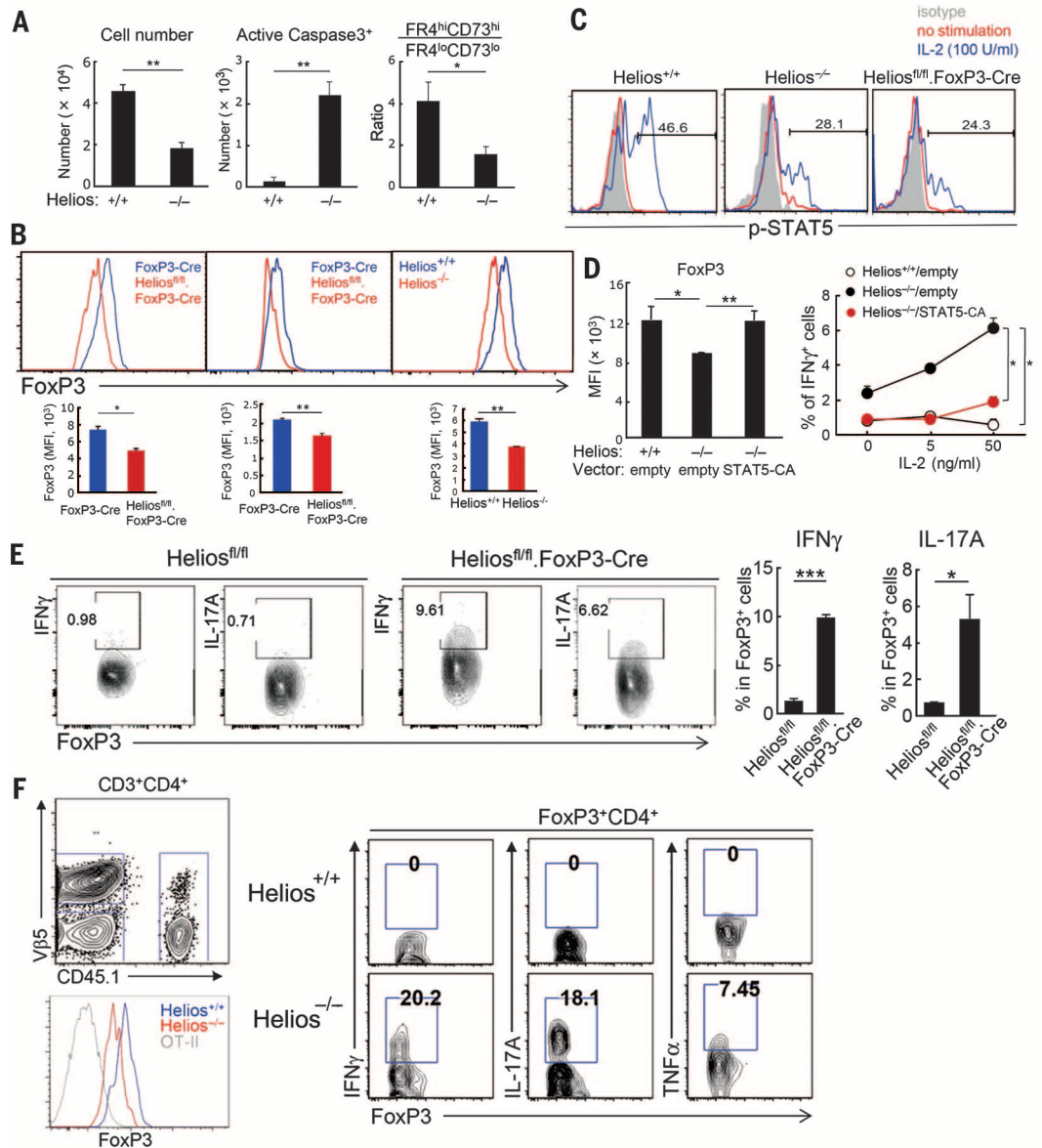
(A) CD4 T_{regs} from spleens of Helios^{+/+} and Helios^{-/-} mice were transferred into Rag2^{-/-}γC^{-/-} mice and numbers, apoptosis, and the anergic phenotype of recovered CD4 T_{regs} from spleens were analyzed 5 days after transfer (*n* = 4 mice per group). Representative data from three independent experiments are shown. The mean ± SEM is indicated. **P* < 0.05 and ***P* < 0.01 (Mann-Whitney test).

(B) Levels of FoxP3 expression were compared between splenic CD4 T_{regs} from 6-month-old FoxP3-Cre and Helios^{fl/fl}.FoxP3-Cre mice (left panel) and from indicated hosts in which colitis had been induced (*n* = 4 mice per group) (middle, right panels). Representative plots of more than three different experiments are shown. The mean ± SEM is indicated. **P* < 0.05 and ***P* < 0.01 (Mann-Whitney test).

(C) BM chimeras were generated by reconstituting Rag2^{-/-} mice with hematopoietic progenitors from Helios^{+/+}, Helios^{-/-}, or Helios^{fl/fl}.FoxP3-Cre mice. After 6 to 8 weeks, the IL-2 responsiveness of FoxP3⁺ CD4 cells from spleens was tested as described in the methods. Representative histograms for the expression of p-STAT5 from two independent experiments are shown. **(D)** CD4 T_{regs} from Helios^{+/+} and Helios^{-/-} mice were transduced with retrovirus expressing green fluorescent protein (GFP) or STAT5-CA/GFP, before stimulation with antibodies to CD3/CD28 in the presence of IL-2 (0 to 50 ng/ml) and IL-4 (20 ng/ml). Levels of FoxP3 expression after 5 days at 5 ng/ml IL-2 are shown (left panel). IFN-γ production by FoxP3⁺ cells is shown (right panel). Representative data from two independent experiments are shown. The mean ± SEM is indicated. **P* < 0.05 and ***P* < 0.01 (Mann-Whitney test).

(E) Two-month-old Helios^{fl/fl} and Helios^{fl/fl}.FoxP3-Cre mice were immunized i.p. with 8 × 10⁸ sheep red blood cells. After 7 days, FoxP3⁺ cells from spleens were analyzed for IFN-γ and IL-17A expression (*n* = 4 or 5 mice per group). Representative data from two independent ex-

periments are shown. The mean ± SEM is indicated. **P* < 0.05 and ****P* < 0.001 (Mann-Whitney test). **(F)** OT-II cells (1 × 10⁶) were transferred into Rag2^{-/-} hosts along with CD25⁺CD4⁺ T cells (2 × 10⁵) from spleens of CD45.1⁺ Helios^{+/+} or CD45.2⁺ Helios^{-/-} mice followed by immunization with OT-II peptide (10 μg) in FCA. After 5 days, spleen cells from Rag2^{-/-} hosts were analyzed for FoxP3 expression and effector cytokine expression by CD4 T_{regs} (*n* = 4 mice per group). Representative data from three independent experiments are shown.



T_{reg} → T_{eff} conversion may be confined to inflammatory intratumoral microenvironments, antibody- or small-molecule-based approaches that target Helios may lead to improved T_{reg}-dependent cancer immunotherapy.

REFERENCES AND NOTES

- Y. P. Rubtsov et al., *Science* **329**, 1667–1671 (2010).
- T. Miyao et al., *Immunity* **36**, 262–275 (2012).
- H. J. Kim, B. Verbrinnen, X. Tang, L. Lu, H. Cantor, *Nature* **467**, 328–332 (2010).
- A. M. Thornton et al., *J. Immunol.* **184**, 3433–3441 (2010).
- Q. Cai, A. Dierich, M. Oulad-Abdelghani, S. Chan, P. Kastner, *J. Immunol.* **183**, 2303–2311 (2009).
- H. J. Kim, H. Cantor, *Semin. Immunol.* **23**, 446–452 (2011).
- M. Kurachi et al., *Nat. Immunol.* **15**, 373–383 (2014).
- J. Ernst et al., *Nature* **473**, 43–49 (2011).
- S. Z. Josefowicz, L. F. Lu, A. Y. Rudensky, *Annu. Rev. Immunol.* **30**, 531–564 (2012).
- Y. Feng et al., *Cell* **158**, 749–763 (2014).
- X. Li, Y. Liang, M. LeBlanc, C. Benner, Y. Zheng, *Cell* **158**, 734–748 (2014).
- R. J. Martinez et al., *J. Immunol.* **188**, 170–181 (2012).
- R. J. Johnston, Y. S. Choi, J. A. Diamond, J. A. Yang, S. Crotty, *J. Exp. Med.* **209**, 243–250 (2012).
- P. Tripathi et al., *J. Immunol.* **185**, 2116–2124 (2010).
- I. Castro, A. Yu, M. J. Dee, T. R. Malek, *J. Immunol.* **187**, 5170–5182 (2011).
- M. Feuerer, J. A. Hill, D. Mathis, C. Benoist, *Nat. Immunol.* **10**, 689–695 (2009).
- N. Ohkura et al., *Immunity* **37**, 785–799 (2012).
- J. A. Hill et al., *Immunity* **27**, 786–800 (2007).
- D. Rudra et al., *Nat. Immunol.* **13**, 1010–1019 (2012).
- W. Pierson et al., *Nat. Immunol.* **14**, 959–965 (2013).
- A. Golding, S. Hasni, G. Illei, E. M. Shevach, *Arthritis Rheum.* **65**, 2898–2906 (2013).

22. K. Bin Dhuban *et al.*, *J. Immunol.* **194**, 3687–3696 (2015).
 23. S. Malchow *et al.*, *Science* **339**, 1219–1224 (2013).

ACKNOWLEDGMENTS

We thank A. Thornton and E. Shevach (NIH) for provision of Helios^{fl/fl}.CD4-Cre mice, S. Crotty (La Jolla Institute for Allergy and Immunology) for provision of retroviral vector STAT5-CA, R. Bronson (DF/HCC Rodent Histopathology Core) for histology analysis, and A. Angel for manuscript and figure preparation.

The data reported in this manuscript are tabulated in the main paper and in the supplementary materials. Raw data are archived in the Gene Expression Omnibus under accession numbers GSE72997 (ChIP-Seq) and GSE73015 (microarray). These studies were supported in part by research grants NIH R01AI37562 and the LeRoy Schechter Research Foundation to H.C. and the Arthritis National Research Foundation to H.-J.K. A provisional patent (U.S. patent application 62/170,379) has been filed pertaining to biological applications relating to the conversion of regulatory T cells into effector T cells for immunotherapy.

SUPPLEMENTARY MATERIALS

www.sciencemag.org/content/350/6258/334/suppl/DC1
 Materials and Methods
 Figs. S1 to S22
 Table S1
 References (24, 25)

20 July 2015; accepted 17 September 2015
 10.1126/science.aad0616

SMALL NONCODING RNA

Panoramix enforces piRNA-dependent cotranscriptional silencing

Yang Yu,^{1,2} Jiaqi Gu,^{1,2,3} Ying Jin,¹ Yicheng Luo,^{1,2} Jonathan B. Preall,^{1,2} Jinbiao Ma,³ Benjamin Czech,^{1,2,4} Gregory J. Hannon^{1,2,4,5*}

The Piwi-interacting RNA (piRNA) pathway is a small RNA-based innate immune system that defends germ cell genomes against transposons. In *Drosophila* ovaries, the nuclear Piwi protein is required for transcriptional silencing of transposons, though the precise mechanisms by which this occurs are unknown. Here we show that the CG9754 protein is a component of Piwi complexes that functions downstream of Piwi and its binding partner, Asterix, in transcriptional silencing. Enforced tethering of CG9754 to nascent messenger RNA transcripts causes cotranscriptional silencing of the source locus and the deposition of repressive chromatin marks. We have named CG9754 “Panoramix,” and we propose that this protein could act as an adaptor, scaffolding interactions between the piRNA pathway and the general silencing machinery that it recruits to enforce transcriptional repression.

The Piwi-interacting RNA (piRNA) pathway controls transposons through a number of distinct, but likely interlinked, mechanisms. Whereas cytoplasmic Piwi proteins silence their targets posttranscriptionally through piRNA-directed cleavage and the ping-pong cycle, nuclear Piwi-piRNA complexes function at the transcriptional level (1). Piwi-directed repression of transcription is thought to be dependent on piRNA-guided recognition of nascent transposon transcripts (1, 2). Transcriptional gene silencing (TGS) correlates with the presence of histone H3 lysine 9 trimethylation (H3K9me3) marks (3–7), yet the mechanism through which Piwi binding promotes the deposition of these marks remains enigmatic. With the exception of the zinc finger protein Asterix (also known as DmGTSF1), the components of Piwi effector complexes at target loci are largely unexplored (7–9).

We systematically mined candidate genes from RNA interference (RNAi) screens for potential TGS effector proteins and identified CG9754 in three independently published screens as being

critical in both the germ cells and follicle cells for transposon silencing (8, 10, 11). Loss of CG9754 had essentially no effect on the abundance or content of piRNA populations or on the nuclear localization of Piwi protein (fig. S1), suggesting that it is probably an effector component (11). CG9754 encodes a ~60-kD nuclear protein with no identifiable domains (11). The expression of CG9754 is restricted to the female gonads, as is seen for other core piRNA pathway components such as Asterix (fig. S2).

To examine global effects on transposon expression, we used RNA sequencing (RNA-seq) to measure steady-state RNA levels from ovaries with germline-specific knockdowns of either CG9754 or Piwi (Fig. 1A) (also see supplementary materials and methods). Piwi knockdown caused a sharp rise in transposon transcripts, with minimal effects on protein-coding gene expression (Fig. 1A and fig. S3A). Knockdown of CG9754 caused effects very similar to those of Piwi (Fig. 1A and fig. S3), with most transposon targets being shared (Fig. 1B). Changes in steady-state RNA levels could have resulted from alterations in either element transcription or the stability of transposon mRNAs. We used global run-on sequencing (GRO-seq) to measure nascent RNA synthesis following gene knockdown (Fig. 1C and fig. S4). Loss of either CG9754 or Piwi produced very similar profiles (Fig. 1D), suggesting that CG9754 is specifically required for transcriptional silencing of transposons targeted by Piwi.

Piwi-mediated TGS correlates with the presence of H3K9me3 marks at silenced transposons (1–6). Depletion of either CG9754 or Piwi resulted in nearly identical losses of H3K9me3 over transposons (Fig. 2, A and B, and fig. S6A). Four independent frameshift mutations of CG9754 generated via the CRISPR/Cas9 (clustered regularly interspaced short palindromic repeats/CRISPR-associated protein 9) system were isolated (fig. S5A) (12). We observed a consistent global up-regulation of transposable elements (fig. S5, B to E) and the corresponding loss of H3K9me3 marks in CG9754 mutant ovaries without changes in piRNA levels (figs. S1 and S6B). Similarly to other core piRNA pathway mutants, female flies lacking CG9754 were sterile. Moreover, flies double-mutant for CG9754 and Asterix showed transposon derepression comparable to that of flies with either single mutation, suggesting that both genes act in the same pathway (fig. S7). Thus, CG9754 functions along with Piwi and Asterix in the repression of transposon transcription.

Next, we asked whether the presence of CG9754 at a target locus might be sufficient to induce its silencing. Because piRNAs likely direct binding to nascent RNAs rather than to the DNA of their targets (13), we delivered CG9754 via protein-RNA interactions. We constructed a series of luciferase reporters with BoxB sites in their 3' untranslated regions (UTRs) and used them to create transgenic reporter flies (fig. S8A). BoxB sites are bound by the λN protein, which can also bring other components to the RNA as part of a fusion (14). We also generated flies expressing λN proteins fused to CG9754, Asterix, nuclear Piwi, and, as a negative control, a cytoplasmic Piwi missing its nuclear localization signal (dN-Piwi). When coexpressed with the reporter, the dN-Piwi fusion failed to induce any change in luciferase expression (Fig. 2C and fig. S12). Of the remainder, only the CG9754 fusion considerably reduced luciferase activity (Fig. 2, C and D). Silencing appeared to be dosage-dependent, as the degree of repression correlated with the number of BoxB binding sites inserted into the reporter mRNA (fig. S9). Consistent with a role for CG9754 in transcriptional silencing, the abundance of the reporter mRNAs was significantly reduced upon tethering (Fig. 2D).

Although CG9754-triggered repression appeared to be independent of chromatin context (Fig. 2, C and D), integration of the reporter into genomic DNA appeared to be critical for repression. Transient cotransfection of reporter constructs into the OSS cell line, which contains an active piRNA

¹Watson School of Biological Sciences, Cold Spring Harbor Laboratory, Cold Spring Harbor, NY 11724, USA. ²Howard Hughes Medical Institute, Chevy Chase, MD 20815, USA.

³State Key Laboratory of Genetic Engineering, Collaborative Innovation Center of Genetics and Development, Department of Biochemistry, School of Life Sciences, Fudan University, Shanghai, China. ⁴Cancer Research UK Cambridge Institute, Li Ka Shing Centre, University of Cambridge, Cambridge, UK.

⁵The New York Genome Center, 101 Avenue of the Americas, New York, NY 10013, USA.

*Corresponding author. E-mail: greg.hannon@cruk.cam.ac.uk

pathway, resulted in little to no detectable silencing (Fig. 2E). In contrast, tethering *Drosophila* Ago1 (λ N-dAgo1) to the luciferase reporter mRNA in OSS cells caused substantial repression of the same reporter (Fig. 2E) (15). These results indicate that CG9754 can function properly only in the context of chromatin, likely acting at the transcriptional level, by interacting with nascent transcripts.

To test the hypothesis that λ N-CG9754 acts on nascent transcripts, we generated a reporter for which the BoxB binding sites were located within the intron of the primary transcript (fig. S8B). λ N-CG9754 maintained the ability to repress this reporter but not a similar transcript carrying BoxB sites in the antisense orientation integrated into the same genomic locus (Fig. 2F). Because the spliced, mature reporter transcripts lack the BoxB sites (fig. S10), we reason that λ N-CG9754 must be able to exert its effects by binding to unspliced precursor mRNAs. Given that splicing occurs cotranscriptionally (16), this implies that CG9754 confers its effects by interaction with the nascent transcript.

If CG9754 mediates Piwi-dependent transcriptional silencing, delivery of CG9754 alone might recapitulate hallmarks of piRNA-directed repression. Tethering of CG9754 had a highly specific effect, changing levels of only the reporter mRNA

(Fig. 3A). Repression occurred at the transcriptional level, as GRO-seq indicated a loss of nascent RNA from the integrated reporter (Fig. 3B and fig. S11B). Repression by CG9754 also correlated with specific deposition of H3K9me3 marks over the reporter locus (Fig. 3, C and E, and fig. S11C). Tethering of CG9754 failed to trigger piRNA production from the reporter, as has been seen previously for some loci that become targets of the piRNA pathway (Fig. 3D) (17, 18). Of note, we observed spreading of H3K9me3 marks to other regions of the reporter gene (Fig. 3E), as described previously for regions flanking piRNA-targeted transposon insertions (4). Thus, delivering CG9754 to the nascent RNA causes repression of a locus in a manner that mimics targeting by the piRNA pathway.

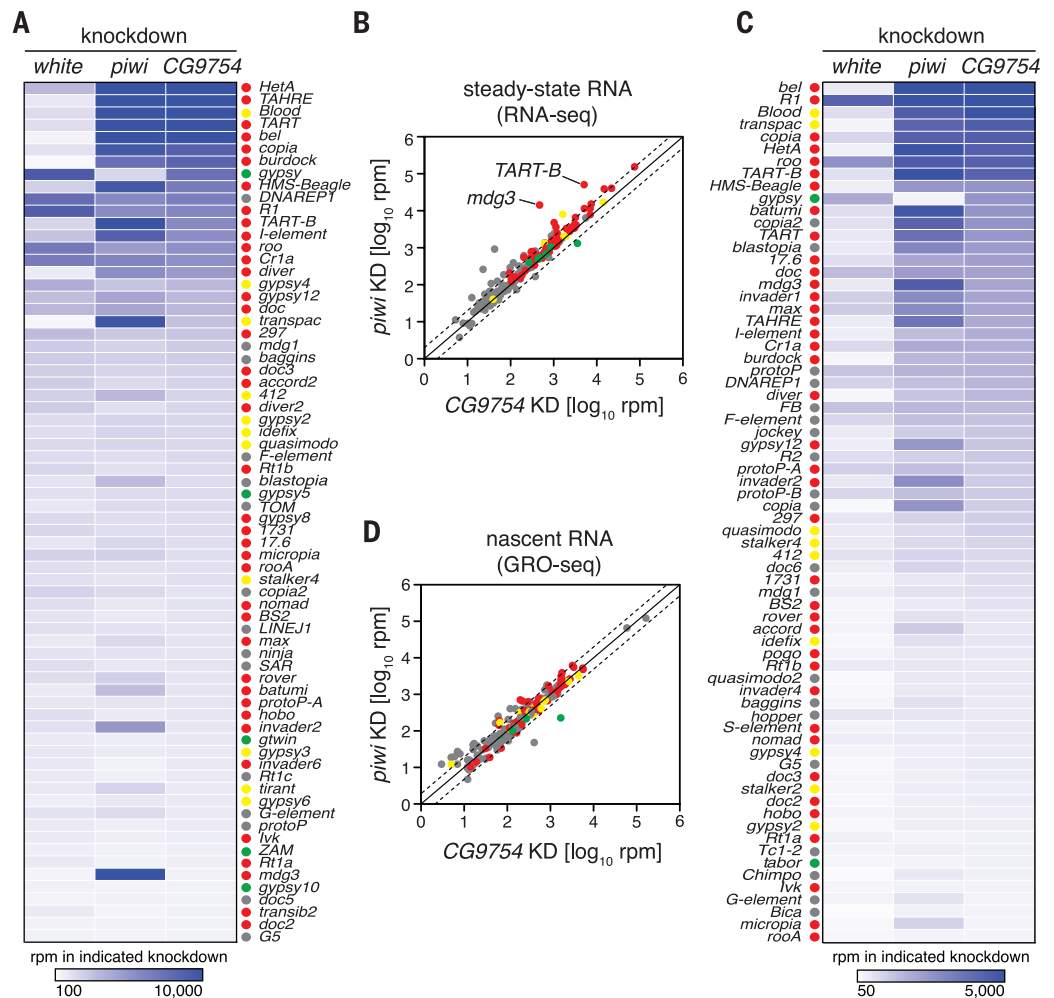
We next tested whether CG9754 might be a component of Piwi complexes, as predicted by our epistasis experiments. Functional GFP-Piwi fusion proteins copurified with hemagglutinin (HA)-tagged CG9754 from OSS cells, but not with a negative-control fusion (HA-mKate2) (Fig. 4A). Conversely, Flag-tagged CG9754 was able to specifically precipitate endogenous Piwi proteins from OSS cell lysates (Fig. 4B), confirming the interaction between these two proteins. Given its properties, we named CG9754 “Panoramix,”

after the mentor who empowers the French comic book character Asterix to perform his feats of strength.

The identification of Panoramix as a key mediator of piRNA-directed TGS presented an opportunity to use the tethering assay to dissect the mechanism of transcriptional silencing. We used RNAi to deplete selected piRNA pathway genes in flies in which λ N-Panoramix was tethered to the luciferase-BoxB reporter (Fig. 4C). Knockdown of Panoramix itself weakened the repression significantly, as compared with a control knockdown (mCherry). Silencing of factors required for piRNA biogenesis (Zuc and Armi) or those that are expected to act upstream of Panoramix (Piwi and Asterix) did not significantly affect repression. Depletion of dLSD1/Su(var)3-3 and its cofactor, CoREST, which normally form a complex that removes H3K4me2 marks from promoters (19, 20), had significant effects on the ability of Panoramix to repress the reporter. Because H3K4me2 marks actively transcribed genes, it is possible that dLSD1-mediated removal of these marks is a key step in Panoramix-mediated transcriptional silencing. This raises a potential parallel with piRNA-directed silencing in mice, wherein engagement by DNMT3L, which is necessary for piRNA-induced DNA

Fig. 1. Knockdown of CG9754 increases transposon expression.

(A) Heat map displaying steady-state RNA levels (measured with RNA-seq) as reads per million (rpm) for the top 70 detected transposons from *nanos*-GAL4-driven knockdowns of the indicated genes. The average of two replicates is shown. (B) Comparison of steady-state RNA levels is shown as rpm mapping to the sense strands of each transposon consensus from the *nanos*-GAL4-driven knockdowns (KD) of the indicated genes. Dashed lines indicate twofold changes. (C) Heat map displaying nascent RNA levels (GRO-seq) as rpm for the top 70 detected transposons [organized exactly as described for (A)]. (D) Data are presented for nascent RNA levels measured by GRO-seq [organized as described for (B)]. In (A) to (D), red dots indicate germline-biased elements, green dots represent soma-biased elements, yellow dots denote intermediate elements targeted in both compartments, and gray dots indicate elements with no apparent designation.



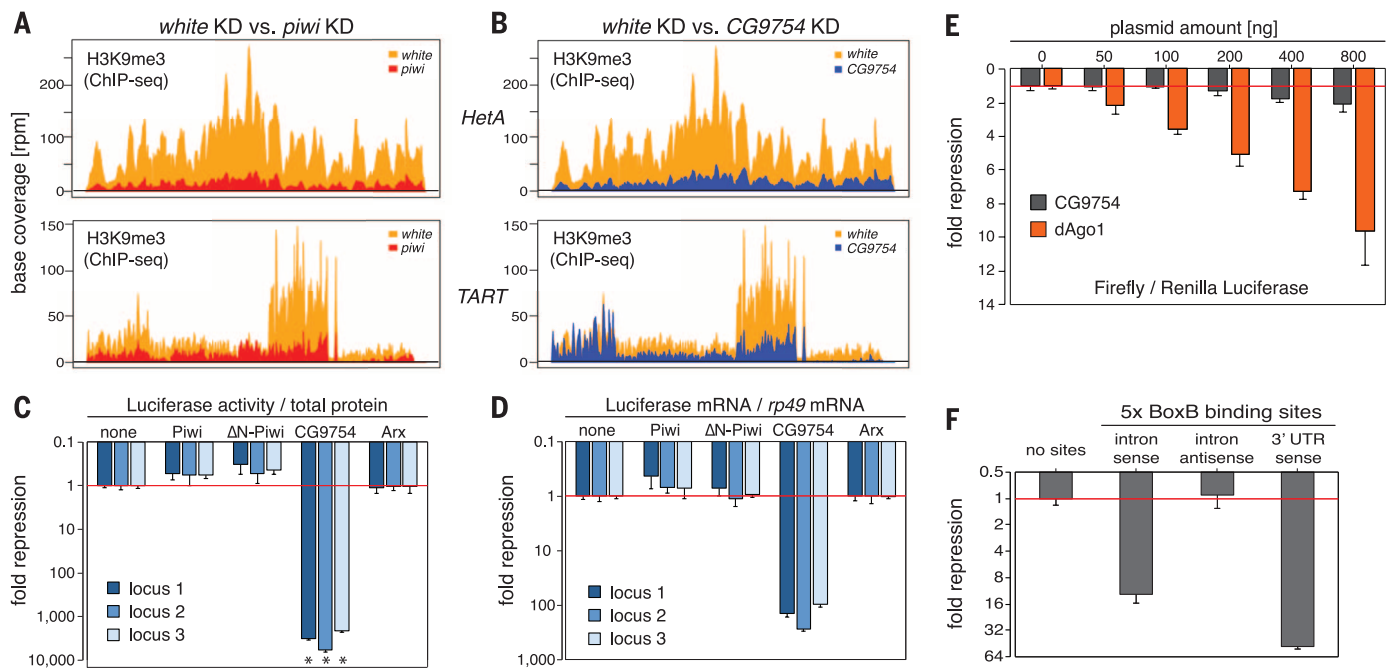


Fig. 2. Tethering of CG9754 to RNA leads to cotranscriptional silencing.

(A and B) Comparisons of normalized H3K9me3 densities mapping to the indicated transposons in the control knockdown versus the indicated knockdown. (Top) *HetA*; (bottom) *TART*. Yellow, red, and blue denote H3K9me3 enrichments over input in control *white* knockdown, *piwi* knockdown, and *CG9754* knockdown samples, respectively. (C) Effects of the indicated λ N fusion proteins on luciferase activity of reporters integrated into different genomic loci. Data show mean \pm SD (error bars); $n = 15$ replicates; $*P = 1.41387 \times 10^{-7}$. (D) Results of reverse transcriptase quantitative polymerase chain

reaction experiments, showing *rp49*-normalized RNA levels of the luciferase reporters [as described in (C); mean values \pm SD from three independent experiments]. (E) Effects of the indicated λ N fusion proteins on luciferase activity of a reporter containing 10 copies of BoxB sites transiently transfected into OSS cells. Mean values \pm SD from three independent experiments are shown. (F) Effects of λ N-CG9754 tethering on luciferase activity of the indicated reporters with varying positions (intron versus 3' UTR) or orientations (sense versus antisense) of the BoxB sites. Error bars indicate SD.

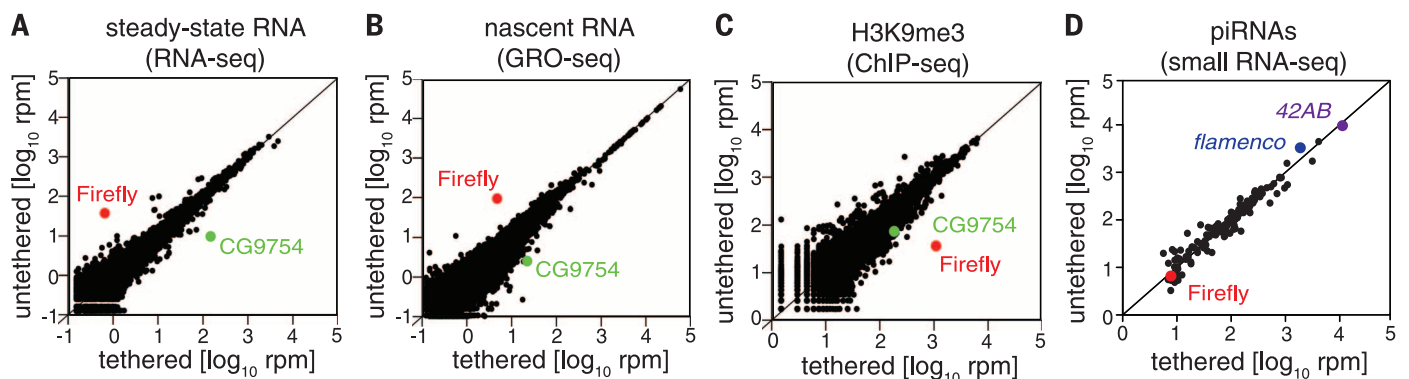


Fig. 3. Tethering of CG9754 to RNA recapitulates targeting by the piRNA pathway.

(A) Comparison of steady-state RNA levels (measured with RNA-seq) for the absence (untethered) or presence (tethered) of λ N-CG9754. Red dot, Firefly luciferase; green dot, CG9754. (B) Data for nascent RNA levels (GRO-seq) [organized as in (A)]. (C) Same as in (A) but showing H3K9me3 reads [chromatin immunoprecipitation sequencing (ChIP-seq)]. (D) Comparison of small RNA reads (24 to 29 nucleotides) mapping uniquely to piRNA clusters and Firefly luciferase in the absence (untethered) or presence (tethered) of λ N-CG9754. Red dot, Firefly luciferase; blue dot, *flamenco*; purple dot, *42AB*. (E) Normalized H3K9me3 densities mapping to the luciferase transgene in the absence (gray, untethered) or presence (red, tethered) of λ N-CG9754. A schematic of the integrated transgene is shown below. For all analyses, only reads uniquely mapping to the reporter gene were considered.

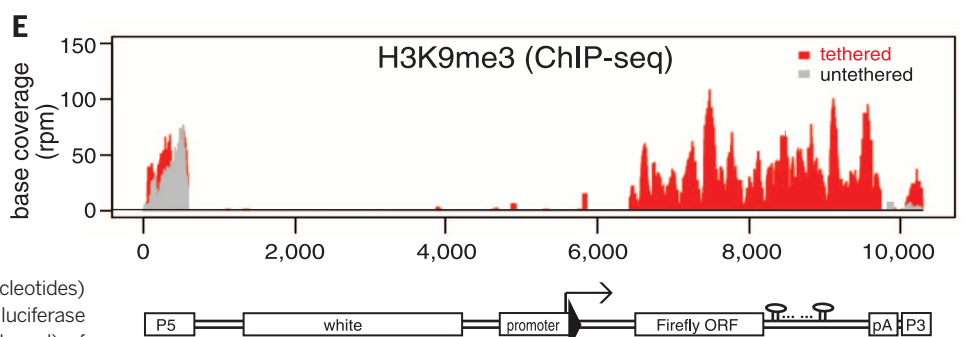
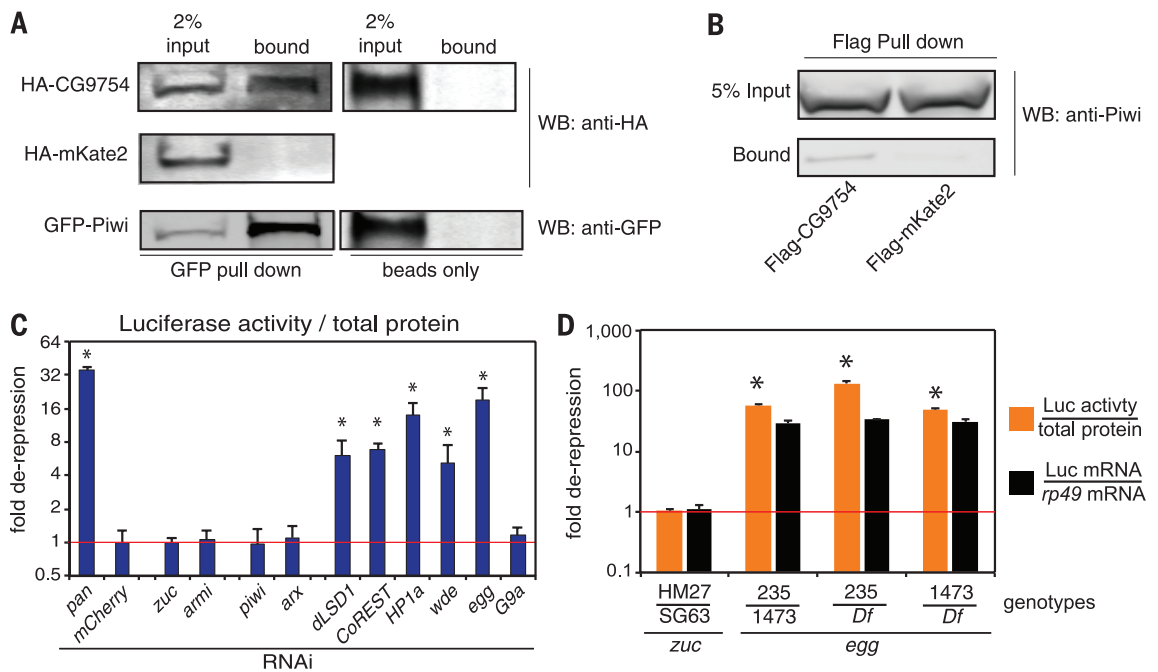


Fig. 4. Panoramix (CG9754) links the piRNA pathway to the general transcriptional silencing machinery.

(A) Western blots (WB) showing coimmunoprecipitation of HA-tagged CG9754 with GFP-Piwi from OSS cells. GFP, green fluorescent protein. (B) Western blots showing coimmunoprecipitation of Flag-tagged CG9754 with endogenous Piwi from OSS cells. (C) Effects of somatic (*tj*-GAL4) knockdown of the indicated genes on luciferase activity of the reporter while tethering λ N-Panoramix. (D) Expression of the reporter under the indicated transheterozygous mutant backgrounds while tethering λ N-Panoramix. Orange bars, total protein-normalized luciferase fold changes; black bars, *rp49*-normalized RNA fold changes. (C and D) Mean values \pm SD from three independent experiments are shown (for luciferase data, $n = 15$; $*P = 1.41387 \times 10^{-7}$).



methylation, requires removal of such marks (fig. S13) (21, 22). Similarly, knockdown of HP1a caused derepression, in agreement with its role as a constitutive heterochromatin component required for transposon silencing (23) and with the observation that the presence of Panoramix is correlated with the deposition of H3K9me3 marks at target loci (Figs. 2, A and B, and 3E). The H3K9 methyltransferase Eggless/dSETDB1 and its cofactor Windei appeared to be required specifically for Panoramix-mediated silencing, as knockdown of G9a, another H3K9 methyltransferase, showed no effect on the reporter (Fig. 4C). In *eggless* mutants, we observed essentially complete derepression of the reporter, despite Panoramix tethering (Fig. 4D). In contrast, the piRNA biogenesis mutant *zuc* showed little to no effect on the repression of the reporter, as also observed in *zuc* RNAi experiments (Fig. 4C). Our data raise the possibility that Eggless could be one of the enzymes responsible for the deposition of H3K9me3 marks over silenced transposons in a Piwi-targeted fashion.

Panoramix functions downstream of Piwi and Asterix and is both necessary and sufficient to elicit transcriptional repression when bound to nascent transcripts. Panoramix represents an example in metazoans of a protein inducing cotranscriptional silencing when recruited to the nascent transcript from a locus (24). In fact, only cotranscriptional silencing can resolve the conundrum of a target being transcriptionally repressed while transcripts from that target locus are responsible for recruiting their own repres-

sors. Orthologs of some of the general silencing factors that act with Panoramix to deposit and interpret repressive chromatin marks have also been implicated in mammalian transposon silencing, in which the pathway functions by causing heritable DNA methylation (fig. S13) (21, 24–27). Though one cannot identify a mammalian ortholog of Panoramix based on primary sequence alone, the overall conservation of the piRNA-mediated transcriptional machinery suggests that a protein with an equivalent function likely exists in mammals (fig. S13).

REFERENCES AND NOTES

- M. C. Siomi, K. Sato, D. Pezic, A. A. Aravin, *Nat. Rev. Mol. Cell Biol.* **12**, 246–258 (2011).
- D. T. Ge, P. D. Zamore, *Curr. Biol.* **23**, R318–R320 (2013).
- M. S. Klenov *et al.*, *Proc. Natl. Acad. Sci. U.S.A.* **108**, 18760–18765 (2011).
- G. Sienski, D. Donertas, J. Brennecke, *Cell* **151**, 964–980 (2012).
- N. V. Rozhkov, M. Hammell, G. J. Hannon, *Genes Dev.* **27**, 400–412 (2013).
- A. Le Thomas *et al.*, *Genes Dev.* **27**, 390–399 (2013).
- D. Donertas, G. Sienski, J. Brennecke, *Genes Dev.* **27**, 1693–1705 (2013).
- F. Muerdter *et al.*, *Mol. Cell* **50**, 736–748 (2013).
- H. Ohtani *et al.*, *Genes Dev.* **27**, 1656–1661 (2013).
- B. Czech, J. B. Preall, J. McGinn, G. J. Hannon, *Mol. Cell* **50**, 749–761 (2013).
- D. Handler *et al.*, *Mol. Cell* **50**, 762–777 (2013).
- F. Port, H. M. Chen, T. Lee, S. L. Bullock, *Proc. Natl. Acad. Sci. U.S.A.* **111**, E2967–E2976 (2014).
- C. Post, J. P. Clark, Y. A. Sytnikova, G. W. Chirn, N. C. Lau, *RNA* **20**, 1977–1986 (2014).
- J. Baron-Benhamou, N. H. Gehring, A. E. Kulozik, M. W. Hentze, *Methods Mol. Biol.* **257**, 135–154 (2004).

- J. Rehwinkel, I. Behm-Ansmant, D. Gattfield, E. Izaurralde, *RNA* **11**, 1640–1647 (2005).
- T. Maniatis, R. Reed, *Nature* **416**, 499–506 (2002).
- A. Le Thomas *et al.*, *Genes Dev.* **28**, 1667–1680 (2014).
- F. Mohn, G. Sienski, D. Handler, J. Brennecke, *Cell* **157**, 1364–1379 (2014).
- Y. Shi *et al.*, *Cell* **119**, 941–953 (2004).
- L. Di Stefano, J. Y. Ji, N. S. Moon, A. Herr, N. Dyson, *Curr. Biol.* **17**, 808–812 (2007).
- A. A. Aravin *et al.*, *Mol. Cell* **31**, 785–799 (2008).
- S. K. Ooi *et al.*, *Nature* **448**, 714–717 (2007).
- M. S. Klenov *et al.*, *Nucleic Acids Res.* **35**, 5430–5438 (2007).
- D. Holloch, D. Moazed, *Nat. Rev. Genet.* **16**, 71–84 (2015).
- S. Kuramochi-Miyagawa *et al.*, *Genes Dev.* **22**, 908–917 (2008).
- A. Molaro *et al.*, *Genes Dev.* **28**, 1544–1549 (2014).
- D. Pezic, S. A. Manakov, R. Sachidanandam, A. A. Aravin, *Genes Dev.* **28**, 1410–1428 (2014).

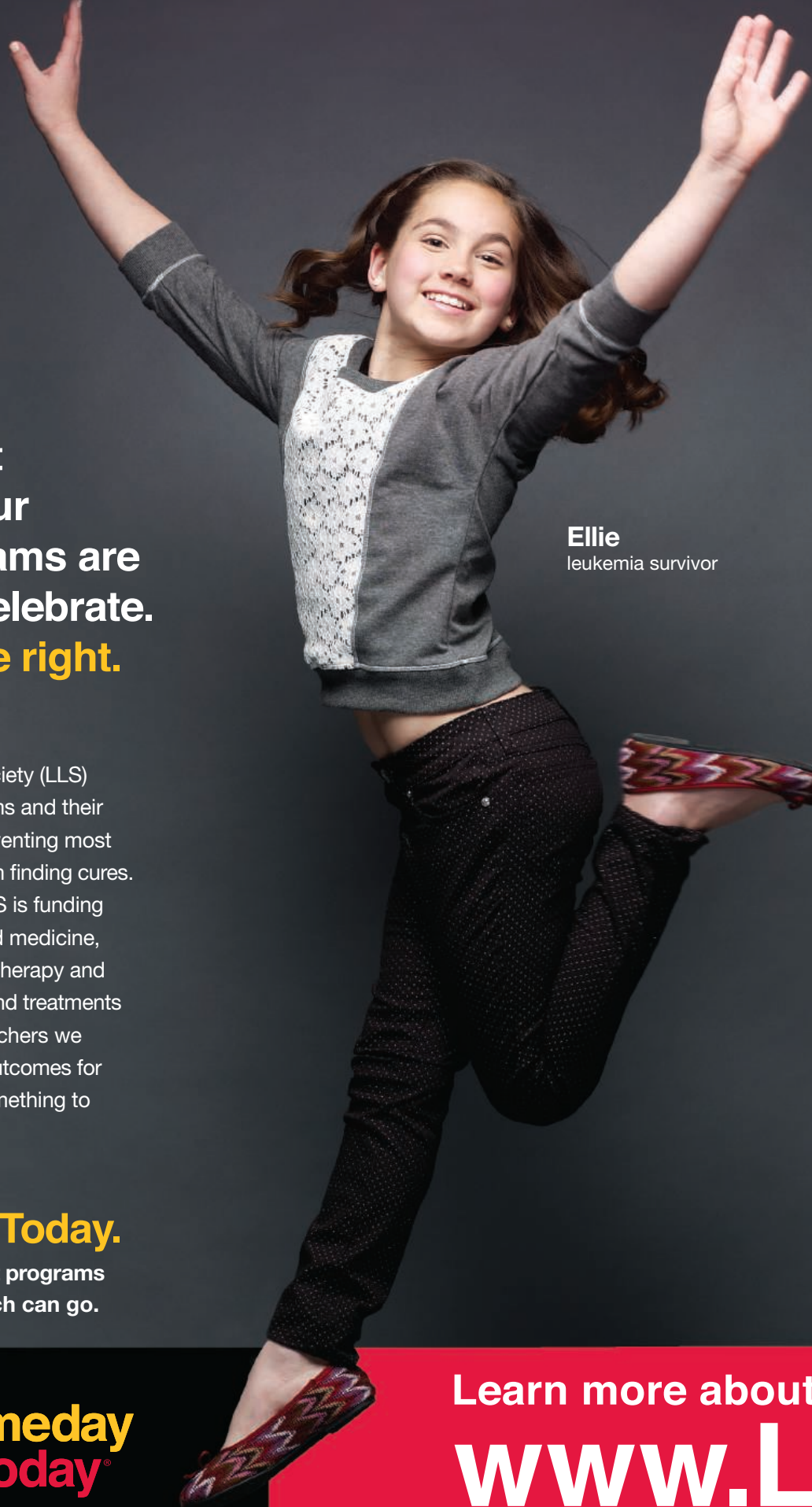
ACKNOWLEDGMENTS

We thank T. Nilsen and members of the Hannon lab for helpful discussions and comments on the manuscript and E. Izaurralde, S. Bullock, T. Schupbach, J. Brennecke, and T. Hazelrigg for sharing reagents. All constructs and strains generated for this study are available under a material transfer agreement with Cold Spring Harbor Laboratories. This work was supported in part by grants from the NIH (5R37GM062534-15 to G.J.H.) and the Ministry of Science and Technology (2011CB966304 to J.M.). Y.Y. was supported by a postdoctoral fellowship from the American Heart Association (2009–2011).

SUPPLEMENTARY MATERIALS

www.sciencemag.org/content/350/6258/339/suppl/DC1
Materials and Methods
Supplementary Text
Figs. S1 to S13
Table S1
References (28–40)

9 March 2015; accepted 27 August 2015
10.1126/science.aab0700



**Some think that
the results of our
research programs are
something to celebrate.
We think they're right.**

Ellie
leukemia survivor

The Leukemia & Lymphoma Society (LLS) is proud of our research programs and their grantees. With no means of preventing most blood cancers, LLS is focused on finding cures. Through its academic grants LLS is funding science to advance personalized medicine, multiple approaches to immunotherapy and other leading edge research to find treatments and cures. Thanks to our researchers we are saving lives and improving outcomes for patients. And that's certainly something to jump up about!

Make Someday Today.

Learn more about LLS's grant programs and see how far your research can go.



**someday
is today®**

Learn more about
www.L

LLS honors this year's research grantees

Career Development Program (CDP)

- **Uttiya Basu**
Columbia University Medical Center
- **Nicholas Brown**
St. Jude Children's Research Hospital
- **Fernando Camargo**
Children's Hospital Boston
- **Ahmet Coskun**
California Institute of Technology
- **Dan Dominissini**
University of Chicago
- **Craig Forester**
University of California, San Francisco
- **Benjamin Garcia**
University of Pennsylvania School of Medicine
- **Ramiro Garzon**
Ohio State University
- **David Guertin**
University of Massachusetts Medical School
- **Andrew Intlekofer**
Memorial Sloan-Kettering Cancer Center
- **Neeraj Joshi**
University of California, San Francisco
- **I-Ju Lee**
Dana-Farber Cancer Institute
- **Qiming Liang**
University of Southern California
- **Ravindra Majeti**
Stanford University
- **Vera Mugoni**
Beth Israel Deaconess Medical Center
- **Jagan Muppidi**
University of California, San Francisco
- **Lars Plate**
Scripps Research Institute
- **Prabha Sarangi**
Dana-Farber Cancer Institute
- **Daniel Starczynowski**
Cincinnati Children's Hospital Medical Center
- **Zuzana Tothova**
Dana-Farber Cancer Institute
- **Christopher Vakoc**
Cold Spring Harbor Laboratory
- **Bas Wouters**
Erasmus University Rotterdam
- **Heping Xu**
Children's Hospital Medical Center Research Foundation

- **Chao Yang**
Johns Hopkins University School of Medicine
- **Hufeng Zhou**
Brigham & Women's Hospital

Myeloproliferative Neoplasms (MPN)

- **Nadia Carlesso**
Indiana University School of Medicine
- **Robert Kralovics**
Center for Molecular Medicine of the Austrian Academy of Sciences
- **Zhijian Qian and Wen-Shu Wu**
University of Illinois College of Medicine
- **Katya Ravid**
Boston University School of Medicine
- **Brady Stein**
Northwestern University
- **Zhaohui Ye**
Johns Hopkins University School of Medicine
- **Leonard Zon**
Boston Children's Hospital

Specialized Center of Research (SCOR)

- **David Weinstock**
Dana-Farber Cancer Institute

Transforming CURES Initiative (TCI)

- **John Crispino**
Northwestern University
- **Phillip Koeffler**
Cedars-Sinai Medical Center
- **Raghuveer Mali**
Indiana University (Indianapolis)
- **Akiko Shimamura**
Fred Hutchinson Cancer Research Center

Translational Research Program (TRP)

- **Iannis Aifantis**
New York University School of Medicine
- **Stephen Ansell**
Mayo Clinic Rochester
- **Caroline Arber**
Baylor College of Medicine

- **Smita Bhatia**
University of Alabama at Birmingham
- **Giulia Casorati**
Fondazione Centro San Raffaele
- **Leandro Cerchietti**
Joan & Sanford I. Weill Medical College of Cornell University
- **Li Chai**
Brigham & Women's Hospital
- **Sandeep Dave**
Duke University Medical Center
- **Stephen Gottschalk**
Baylor College of Medicine
- **Douglas Graham**
University of Colorado at Denver
- **Jolanta Grembecka**
University of Michigan
- **Marina Konopleva**
University of Texas MD Anderson Cancer Center
- **William Matsui**
Johns Hopkins University School of Medicine
- **Nikhil Munshi**
Dana-Farber Cancer Institute
- **Antonio Palumbo**
University of Torino Medical School
- **Feyruz Rassool**
University of Maryland
- **Alain Rook**
University of Pennsylvania
- **Stefanie Sarantopoulos**
Duke University Medical Center
- **Kris Thielemans**
Vrije Universiteit Brussel
- **Andrei Thomas-Tikhonenko**
Children's Hospital of Philadelphia
- **Amit Verma**
Albert Einstein College of Medicine
- **David Wald**
Case Western Reserve University School of Medicine
- **Roland Walter**
Fred Hutchinson Cancer Research Center
- **Ryan Wilcox**
University of Michigan

our research program

LS.org/research

THE TOUGHEST CHALLENGES. THE WORLD'S SMARTEST SCIENTISTS. £20 MILLION AWARDS.

Grand Challenge is an ambitious international research funding scheme offering a series of £20 million awards to solve cancer's toughest questions. We're looking for big, innovative ideas from interdisciplinary teams across the world. If you think you have what it takes, we want to hear from you.

Rise to the challenge
CRUK.ORG/GRANDCHALLENGE

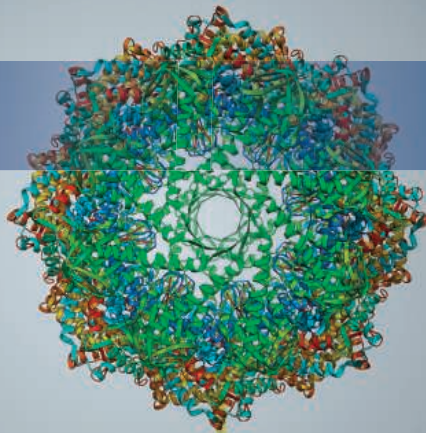
Call closes 12th February 2016.

GRAND
CHALLENGE



CANCER
RESEARCH
UK

gibco



WELCOME TO THE FUTURE OF TRANSIENT EXPRESSION

Achieve 3 g/L protein yields in transient CHO with the ExpiCHO™ Expression System

Switching from 293 to CHO cells during drug development may cost you precious time and create uncertainty. Now there's a better way. The new Gibco™ ExpiCHO™ Expression System provides the highest protein yields possible in a transient system. That means you can always work in CHO cells, starting from discovery.

See the future of transient expression at
thermofisher.com/expicho

ThermoFisher
SCIENTIFIC

For Research Use Only. Not for use in diagnostic procedures. © 2015 Thermo Fisher Scientific Inc. All rights reserved.
All trademarks are the property of Thermo Fisher Scientific and its subsidiaries unless otherwise specified. CO018951 0915

Fusion Transcripts Detection

Cancer researchers now have a set of TaqMan gene expression assays designed to detect fusion transcripts using real-time polymerase chain reaction (PCR). Certain fusion transcripts are considered rare and are not well characterized; therefore, detecting these rare events using a single technology can deliver ambiguous results. As such, researchers often employ an orthogonal method of validation to confirm results. As a complementary solution to next generation sequencing (NGS) panels, including the OncoPrint Focus Assay, the TaqMan gene expression assays are designed to serve as an orthogonal validation method for confirming NGS results. Assay benefits include proven TaqMan assay chemistry, guaranteed performance for all pre-designed assays, single-tube construction (containing a probe, forward primer, and reverse primer for each target used in the simple, fast PCR workflow), and the use of universal cycling conditions—making it possible to run any combination of assays in parallel on a single real-time PCR instrument.

Life Technologies

For info: 800-955-6288

www.lifetechnologies.com/allgenes

Prevalidated Fluorinated Fragment Library

A new library of fluorinated compounds with superior drug-like characteristics has been designed to maximize the efficiency of fluorine nuclear magnetic resonance (NMR) and X-ray crystallography screening, saving both time and cost in the process. The new Maybridge fluorine labeled fragment library is a diverse fragment library of 480 fluorinated compounds. Approximately 20% of known drug compounds contain a fluorine atom. As such, fluorine NMR is a fast-growing technique used in fragment screening, an important method for rapid identification of new lead molecules in drug discovery due to higher hit probability and fewer fragments needing to be screened. This Maybridge library was derived from more than 5,000 fluorinated candidates and was optimized through a stringent biophysical selection process to increase the probability of hit generation. Each compound has been validated using fluorine and standard NMR, solubility testing, X-ray crystallography, and surface plasmon resonance techniques to provide the highest quality.

Thermo Fisher Scientific

For info: 800-678-5599

www.thermofisher.com



Surface Plasmon Resonance System

The Reichert 4SPR is a new, four-channel surface plasmon resonance (SPR) system for label-free, real-time investigation of biomolecular interactions. By combining four channels with improved industry-leading sensitivity and baseline stability, Reichert 4SPR enables drug discovery researchers to maximize their efficiency, flexibility, and throughput. A researcher can run three experimental channels with one reference, two experimental channels with two separate references, or test different immobilization chemistries or regeneration schemes on each channel. The Reichert 4SPR's high sensitivity (± 0.05 μ RIU rms noise) reduces the amount of sample required for each experiment and produces results even if a large portion of the protein sample is inactive or denatured. This makes the instrument perfect for analyzing small molecules or very low concentrations of larger biomolecules. The Reichert 4SPR is also able to determine picomolar concentrations and equilibrium dissociation constants and has a low baseline drift (0.01 μ RIU min⁻¹), which improves data fitting.

Reichert Life Sciences

For info: 716-686-4522

www.reichertspr.com

chemical and biological systems under investigation. With REIMS, direct, rapid heating of samples leads to the formation of vapor that is rich in sample-specific chemical information. The vapor is taken directly into the mass spectrometer (Xevo G2-XS QToF or SYN-APT G2-Si HDMS), where the molecules are analyzed by TOF mass spectrometry.

Waters

For info: 800-252-4752

www.waters.com

Dual-Luciferase Reporter Assay

The new Nano-Glo Dual-Luciferase Reporter (NanoDLR) Assay is a two-reporter system that incorporates NanoLuc luciferase technology, providing increased data quality and greater sensitivity for biologically complex applications. The new NanoDLR assay allows researchers to measure NanoLuc and firefly luciferases together in a convenient, easy-to-use format. The NanoDLR Assay's improved firefly chemistry and small, ultrasensitive NanoLuc luciferase provide researchers with more sensitivity to detect small changes in expression, more flexibility in assay design, and more robust control reporter options. In the NanoDLR Assay, both firefly luciferase and NanoLuc luciferase can be used as dynamic reporters, greatly increasing versatility by allowing researchers to choose the primary reporter that best meets their experimental needs. The NanoDLR's new assay chemistry also provides improved reagent stability over time.

Promega

For info: 608-274-4330

www.promega.com

Mass Spectrometry System

Combining direct-from-sample ionization with high-performance, time-of-flight (TOF) mass spectrometry and powerful, intuitive analytics, the rapid evaporative ionization mass spectrometry (REIMS) research system with the iKnife sampling system eliminates the need for sample preparation and chromatographic separation, providing food, microbiology, and tissue researchers with near-instantaneous data acquisition. Using REIMS, researchers can quickly and easily differentiate samples from one another and confidently identify the differentiating features, allowing greater insight into the

Electronically submit your new product description or product literature information! Go to www.sciencemag.org/products/newproducts.dtl for more information.

Newly offered instrumentation, apparatus, and laboratory materials of interest to researchers in all disciplines in academic, industrial, and governmental organizations are featured in this space. Emphasis is given to purpose, chief characteristics, and availability of products and materials. Endorsement by *Science* or AAAS of any products or materials mentioned is not implied. Additional information may be obtained from the manufacturer or supplier.

want new technologies?

antibodies

apoptosis

biomarkers

cancer

cytometry

data

diseases

DNA

epigenetics

genomics

immunotherapies

medicine

microbiomics

microfluidics

microscopy

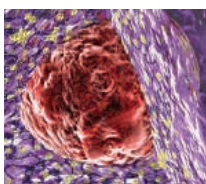
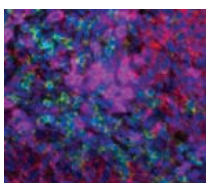
neuroscience

proteomics

sequencing

toxicology

transcriptomics



watch our **webinars**

Learn about the latest breakthroughs, new technologies, and ground-breaking research in a variety of fields. Our expert speakers explain their quality research to you and answer questions submitted by live viewers.

VIEW NOW!

webinar.sciencemag.org

Science



Brought to you by the Science/AAAS
Custom Publishing Office



@SciMagWebinars

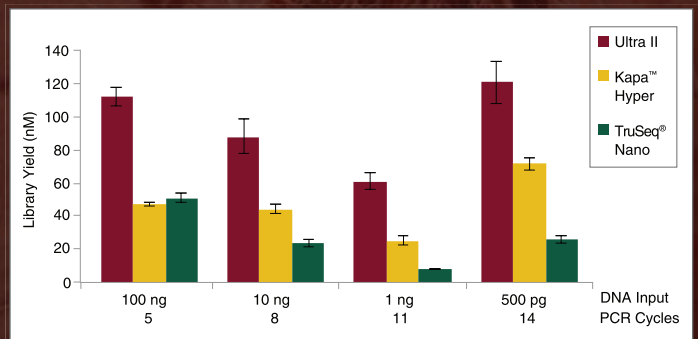
Even more
from less.

NEBNext[®] Ultra[™] II DNA Library Prep Kit for NGS

Are you challenged with trying to get higher library yields using ever-decreasing input amounts? Each component in the NEBNext Ultra II DNA Library Prep Kit from NEB[®] has been reformulated, resulting in a several-fold increase in library yield with as little as 500 picograms of input DNA. These advances deliver unprecedented performance, while enabling lower inputs and fewer PCR cycles. Get even more from less with NEBNext Ultra II.

Visit NEBNextUltraII.com to learn more and request a sample.

The NEBNext Ultra II DNA Library Prep Kit for Illumina[®] produces the highest yield libraries from a broad range of input amounts.



Libraries were prepared from Human NA19240 genomic DNA using the input amounts and numbers of PCR cycles shown. Manufacturers' recommended protocols were followed, with the exception that size selection was omitted.



There's only one **Science**

Science Careers Advertising

For full advertising details, go to ScienceCareers.org and click For Employers, or call one of our representatives.

Tracy Holmes

Worldwide Associate Director
Science Careers
Phone: +44 (0) 1223 326525

THE AMERICAS

E-mail: advertise@sciencecareers.org

Fax: +1 (202) 289 6742

Tina Burks

Phone: +1 (202) 326 6577

Nancy Toema

Phone: +1 (202) 326 6578

Online Job Posting Questions

Phone: +1 (202) 312 6375

EUROPE / INDIA / AUSTRALIA / NEW ZEALAND / REST OF WORLD

E-mail: ads@science-int.co.uk

Fax: +44 (0) 1223 326532

Sarah Lelarge

Phone: +44 (0) 1223 326527

Kelly Grace

Phone: +44 (0) 1223 326528

Online Job Posting Questions

Phone: +44 (0) 1223 326528

JAPAN

Katsuyoshi Fukamizu (Tokyo)

E-mail: kfukamizu@aaas.org

Phone: +81 3 3219 5777

Hiroyuki Mashiki (Kyoto)

E-mail: hmashiki@aaas.org

Phone: +81 75 823 1109

CHINA / KOREA / SINGAPORE / TAIWAN / THAILAND

Ruolei Wu

Phone: +86 186 0082 9345

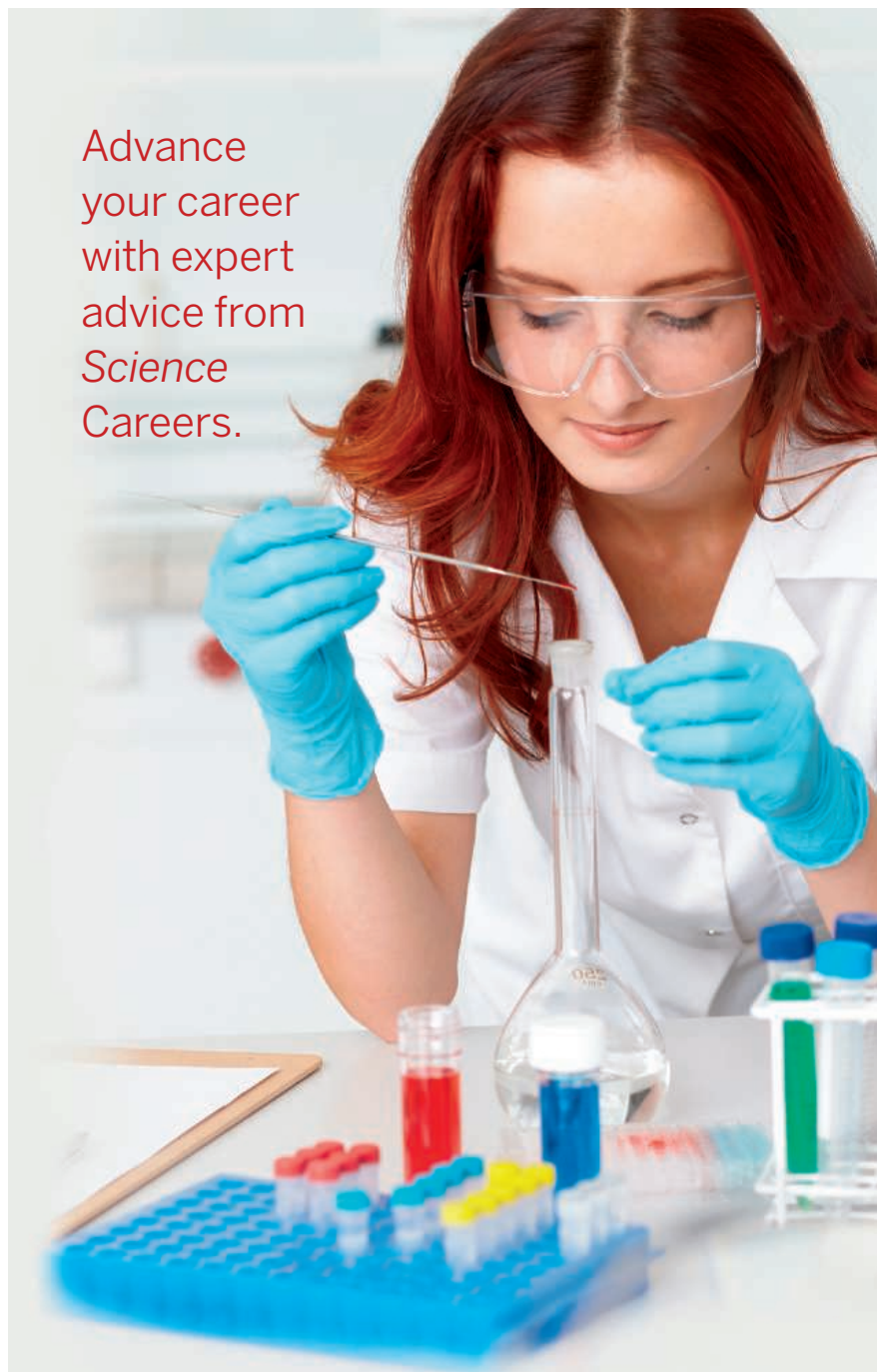
E-mail: rwu@aaas.org

All ads submitted for publication must comply with applicable U.S. and non-U.S. laws. *Science* reserves the right to refuse any advertisement at its sole discretion for any reason, including without limitation for offensive language or inappropriate content, and all advertising is subject to publisher approval. *Science* encourages our readers to alert us to any ads that they feel may be discriminatory or offensive.

ScienceCareers

FROM THE JOURNAL SCIENCE AAAS

ScienceCareers.org



Advance
your career
with expert
advice from
Science
Careers.



Download Free Career Advice Booklets!

ScienceCareers.org/booklets

Featured Topics:

- Networking
- Industry or Academia
- Job Searching
- Non-Bench Careers
- And More



ScienceCareers

FROM THE JOURNAL SCIENCE AAAS

PROGRAM TEAM

Tufts Institute for Innovation (TII), a major new university initiative, is seeking to hire a program team of up to four senior-level faculty as the initial members of its core faculty. Institute Faculty will hold senior-level academic appointments in one or more schools/departments at any of the three campuses of Tufts University.

TII's mission is "Improving the Human Condition" and its theme is Global Health. Specific topical areas of interest include microbes and diagnostics/advanced analytics, however other compelling programs in other areas of Global Health are encouraged. Led by Founding Institute Director David Walt, TII is focused squarely on blending the best of both academia and industry, to identify and address unsolved problems and to deliver implementable solutions. Impact and outcome will be the measures of our success. TII will accomplish its mission by assembling multidisciplinary teams of researchers to address these problems comprehensively and actively to generate solutions.

TII Core Faculty will be housed in a state of the art facility on Tufts Boston campus, co-located with Tufts School of Medicine, the Friedman School of Nutrition Science and Policy, Tufts Human Nutrition Research Center on Aging, Tufts School of Dental Medicine, as well as Tufts Medical Center. Cummings School of Veterinary Medicine on the Tufts Grafton Campus, together with the School of Engineering, the School of Arts & Sciences, the Fletcher School of Law and Diplomacy, and Tisch College of Citizenship and Public Service all on the Tufts Medford Campus also provide rich opportunities for collaboration. TII's lab and office complex will be designed to maximize teamwork and interaction between faculty, students and staff. TII will house several major core facilities to be designed and built by TII faculty and staffed by experienced professionals. Substantial funding and other support (e.g. clinical access, core facilities) will be provided to enable teams to build first in class research programs.

Applicants should be senior investigators who have identified a problem for which solutions can be designed and implemented to effect change in a target community or a target population. Team members should include an individual who understands the specific needs of the target community for effective implementation, either as part of the initial program team or at an appropriate time once the program begins. Demonstrated success in translational activities/enacting change, including interactions with the commercial sector and/or NGOs, policy groups, etc. is desirable. Investigators with industrial experience are encouraged as members of a program team.

Teams should send curriculum vitae including records of funding, a vision statement describing a proposed program, and funding requirements for the five-year program. Teams may propose staged projects in which part of the team is brought on board in Year 1 while subsequent team members are brought on, or networked in, at a later date. Program teams are encouraged to leverage existing strengths and expertise at Tufts. All application materials should be submitted via <https://apply.interfolio.com/32239>. Members of a program team should apply individually via Interfolio, and indicate in their cover letters the names of the other members of their program team. Review of applications will begin November 30, 2015, and continue until the positions are filled.

This is an extraordinary opportunity for entrepreneurial teams of investigators to partner in building a transformative initiative with the potential to have tremendous global impact and serve as a model for academic research in the 21st century.

Change the world with us: <https://tii.tufts.edu/>

Tufts University is an Affirmative Action/Equal Opportunity Employer. We are committed to increasing the diversity of our faculty. Members of underrepresented groups and women are strongly encouraged to apply.

Distinguished Professor and Endowed Chair Diabetes and Obesity Research Center, Winthrop-University Hospital

Mineola, LI, NY. Winthrop-University Hospital Research Institute is searching for an exceptional senior scientist to fill the newly established Distinguished Professorship in Diabetes and serve as the Director of its Diabetes and Obesity Research Center. The successful candidate will be an experienced clinical or basic scientist with a strong track record of obtaining extramural funding, leadership skills to build a nationally recognized program of research, as well as academic achievement supporting appointment at the Professor level.

The Director will play a pivotal role in advancing Winthrop's diabetes-focused mission and enhancing research collaboration with Stony Brook University School of Medicine. The development of Winthrop research is strongly supported by the Board of Trustees and a highly competitive recruitment package includes resources to recruit additional tenure-track investigators in diabetes and related fields in order to expand the program.

Winthrop-University Hospital is a 591-bed hospital, which serves as clinical campus of Stony Brook University School of Medicine. Winthrop's recently constructed 95,000 square foot Research and Academic Center houses basic science laboratories and a clinical research center, as well as adult/pediatric endocrine and diabetes services. The facility is designed to support translational studies and provides ample space for expansion of the research program. Currently, diabetes related research is being carried out by basic and clinical investigators in beta cell biology, vascular biology, renal, cardiovascular and central nervous system complications, effects of diabetes on wound healing, and obesity interventions. Winthrop has a strong set of clinical and educational programs in diabetes and there are a growing number for collaborations between researchers and clinical faculty. Our investigators also actively collaborate with scientists at other major academic centers.

DRIVEN TO BE
the best.

Winthrop-University Hospital is conveniently located on Long Island in Western Nassau County just 25 miles from Manhattan and one block from the Mineola LIRR station.

Please send C.V. and cover letter to:
amjacobson@winthrop.org

Alan M. Jacobson, M.D.
Chief Research Officer
Winthrop-University Hospital
222 Station Plaza North, Suite 510
Mineola, NY 11501



Your Health Means Everything.™





Bioinformatics Faculty Positions: Caltech Pasadena, CA, United States

The California Institute of Technology is seeking outstanding candidates for tenure-track or tenured professorial faculty positions in the Division of Biology and Biological Engineering. Applications are invited in any area of bioinformatics research, broadly defined. We are interested in candidates who develop and employ informatics and computational approaches to understand complex biological systems, ranging widely from microbial systems to humans and from molecular level systems to whole organism physiology. Applicants at all professorial levels are encouraged to apply. For untenured positions, initial appointments are for four years and are contingent upon completion of the Ph.D. degree. For tenured Professor positions, we seek candidates who have developed cutting edge research programs that are having exceptional impact. Candidates with strong commitments to research and teaching excellence are encouraged to apply.

Please submit online application at <http://bbe.caltech.edu/Positions> and include a brief cover letter, curriculum vitae, relevant publications, a description of proposed research, and a statement of teaching interests. Instructions will be given for submission of letters of reference when you apply on-line.

Positions will remain open until filled; however, applicants for the assistant professor level should plan on **completing an application by December 1, 2015** in order to **attend a recruiting symposium at Caltech on January 14-15, 2016**, where they will present their research and future directions.

EOE of Minorities/Females/Protected Vets/Disability.



Biology Faculty Positions: Caltech Pasadena, CA, United States

The California Institute of Technology is seeking outstanding candidates for tenure-track professorial positions in the Division of Biology and Biological Engineering. Applicants should have a highly successful record of using molecular, cellular, and/or systems approaches in any area of biology, including neuroscience.

Successful applicants are expected to develop innovative research programs and to be committed to high quality teaching. Preference will be given to candidates at the Assistant Professor level; however, well-qualified applicants at the associate or full professor level may also be considered. The term of an initial untenured appointment is for four years and is contingent upon completion of the Ph.D. degree.

Please submit on-line application at <http://bbe.caltech.edu/Positions> and include a brief cover letter, curriculum vitae, relevant publications, a description of proposed research, and a statement of teaching interests. Instructions will be given for submission of letters of reference when you apply on-line.

Positions will remain open until filled; however, applicants for the assistant professor level should plan on **completing an application by January 15, 2016**, in order to **attend a recruiting symposium at Caltech on March 17-18, 2016**, where they will present their research and future directions.

EOE of Minorities/Females/Protected Vets/Disability.



CASE WESTERN RESERVE UNIVERSITY
SCHOOL OF MEDICINE

Open Rank Protein Biophysics/Structural Biology Faculty Position Department of Physiology and Biophysics

We invite outstanding individuals to apply for a faculty position at any rank in the area of Protein Biophysics and/or Structural Biology. Mid-career scientists with outstanding accomplishments at the level of Associate Professor or full Professor are especially encouraged to apply. We are particularly interested in applicants who are using interdisciplinary approaches to work on basic or translational aspects of human diseases. Visit our website at <http://Biophysics.case.edu>. The Department and School have excellent infrastructure, particularly in x-ray crystallography and solution NMR spectroscopy (see <http://Ccmsb.case.edu>).

Applicants for a position as Assistant Professor should have a Ph.D. and/or M.D. degree, 3-5 years postdoctoral experience, and a strong record of scholarly activity. Competitive candidates for Associate Professor should have a strong publication record and an international reputation. Competitive candidates for Professor should have achieved records of leadership in the profession and have a substantial record of scholarly publications.

Applicants should submit a cover letter, a full *Curriculum Vitae*, including a record of prior/current funding, a brief description of their research, as well as the contact information for three professional references. Candidates at the Assistant Professor level should also submit a research plan. Please submit application materials with separate file attachments by email to: **Dr. Walter F. Boron, Chair, Department of Physiology and Biophysics, Case Western Reserve University; BiophysicsSearch@case.edu**.

"In employment, as in education, Case Western Reserve University is committed to Equal Opportunity and Diversity. Women, veterans, members of underrepresented minority groups, and individuals with disabilities are encouraged to apply."

"Case Western Reserve University provides reasonable accommodations to applicants with disabilities. Applicants requiring a reasonable accommodation for any part of the application and hiring process should contact the Office of Inclusion, Diversity and Equal Opportunity at 216-368-8877 to request a reasonable accommodation. Determinations as to granting reasonable accommodations for any applicant will be made on a case-by-case basis."

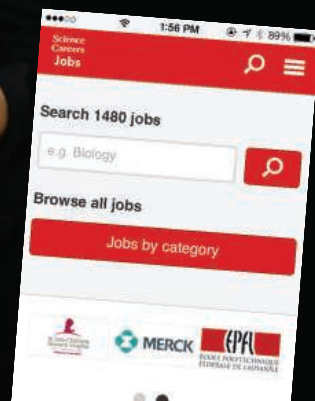
Download the Science Careers jobs app from Science



Jobs are updated 24/7

**Search thousands of jobs
on your schedule**

**Receive push notifications
per your job search criteria**



Get a job on the go.

Search worldwide for thousands of scientific jobs in academia, industry, and government. The application process is seamless, linking you directly to job postings from your customized push notifications.



Scan this code to download app or visit apps.sciencemag.org for information.

ScienceCareers | AAAS
FROM THE JOURNAL SCIENCE

ScienceCareers.org

7389 - Director, Oncology Cambridge

Medimmune seeks an exceptionally strong individual to join their Oncology Research team in Cambridge, UK. This is a strategic position with responsibilities that are of major significance to the success of the Oncology portfolio. Medimmune's oncology research team consists of approximately 85 people roughly divided equally between Cambridge, UK and Gaithersburg, MD, USA. The Oncology Research Group in Cambridge consists of 2 teams each led by a Director. A vacancy has arisen to replace one of those Directors.

Reporting to the VP Oncology Research who is based in the US, the incumbent will lead a team of approximately 20 people consisting of scientists, technicians and post-docs. Importantly the successful candidate will bring substantial research experience in tumour-immunology and be a well-respected and recognised scientist in academia and/or bio-pharmaceutical industry. The primary responsibility of the Oncology Research Group is to bring new and innovative science that can lead to the development of new immune-therapies. The group addresses basic science including investigating new mechanisms/pathways, validation of targets and further in-vivo and in-vitro validation of models and determining mode of action.

Major Duties and Responsibilities:

- Providing scientific, operational and strategic leadership for Oncology Research activities at Medimmune, Cambridge.
- Bringing cell and molecular immunology expertise to the development of novel cancer therapeutics as well as providing scientific and managerial leadership for cross-functional teams. Direct responsibility for managing and mentoring scientists and teams, ensuring appropriate resourcing for work plans and projects.
- Using scientific knowledge and expertise to review and support key investment decisions and provide guidance to the Oncology governance committees for project progression.
- Implementation of strategies to ensure a sustainable Oncology Research pipeline.
- Establishing and maintaining innovation and capability in complex models of disease, with a particular focus on tumour immunology.
- Promoting awareness of the competitive environment and helping to build Medimmune's external presence in key areas of research.
- Providing clear communication of results with conclusions and recommendations to key stake holders and preparing documents and reports for internal governance committees and regulatory agencies, including INDs.
- Establishing and managing external collaborations; and contributing to assessment of external business alliance and in-licensing opportunities.

This senior and highly visible position within the Medimmune organisation requires an experienced oncology research professional whose qualities and experience include the following parameters.

Education:

Your career will be built on a strong academic background. With a PhD or MD/PhD qualification and with excellent interpersonal and communication skills the incumbent will have a proven track record in tumour-immunology, preferably in aspects of innate immunology and/or immune suppressive components in the tumour microenvironment.

Experience & Skillset

A thought leader in Immuno-Oncology;

- Strong understanding of developing drugs within the field of Immuno-Oncology is a plus.
- Strong understanding of the cellular processes underlying cancer.
- Strong background in understanding, elucidating and manipulating the immune system in various solid and hematologic oncology settings.
- Experience and familiarity of cell-based assays and models with industry-standard techniques.
- Target Identification and Target Validation experience would be advantageous.
- Experience of developing data packages suitable for supporting IND filings would be beneficial.
- Able to demonstrate strong mentoring skills to scientists as well as postdocs.
- Proven ability to lead innovative research and the validation of novel targets.
- A strong background of in vitro and in vivo experimentation and functional assay development is essential.
- Experience of championing and guiding projects from inception to candidate drug.
- Ability to prioritise and clearly define those priorities to others and monitor progress.
- Motivated to work in a fast paced and highly collaborative environment.
- Leadership and Line management expertise are essential to the post with evidence of developing a strong team ethic.

Visit the MedImmune career portal (<https://www.medimmune.com/careers>) using reference 7389

Competitive remuneration and company benefits apply.

Closing date for submissions – 30th Nov 2015

ASSISTANT PROFESSOR POSITIONS

Plant Systematics, Disease Ecology and Cellular & Molecular Immunology

The Department of Biological Sciences at The University of Alabama invites applications for three full-time (9-month) tenure-track faculty positions at the rank of **Assistant Professor in Plant Systematics, Disease Ecology and Cellular & Molecular Immunology** to begin August 2016.

For the **Plant Systematics** position, all taxonomic groups of vascular plants will be considered. Applicants whose research integrates field and museum-based studies with modern genomic approaches to address fundamental questions in taxonomy, systematics, biogeography, and evolution of vascular plants are encouraged to apply. The successful applicant is expected to curate The University of Alabama Herbarium (UNA) maintained by the Department of Biological Sciences and must provide evidence of curatorial experience and/or other relevant abilities. The Herbarium at the University of Alabama contains significant holdings of vascular plants from the USA and the neotropics, and particularly from SE USA freshwater habitats. Individuals interested in diversifying this actively growing collection are encouraged to apply. The successful candidate also would serve as the Department's liaison with the University of Alabama Arboretum. Teaching responsibilities will include undergraduate courses in plant systematics, dendrology or field botany, and one or more graduate courses in the successful candidate's area of expertise.

For the **Disease Ecology** position, successful candidates should have a strong background in research examining host-parasite or host-pathogen interactions at the population and/or community level. Applicants should employ integrative approaches to characterize the dynamics of disease transmission, parasite/pathogen manipulation of host behavior and physiology, links between social context and disease susceptibility, phenotypic evolution driven by host-parasite/pathogen interactions, or related areas. Candidates that utilize either field-based approaches or laboratory-based investigations are encouraged to apply. Teaching responsibilities will include introductory biology, undergraduate courses in disease ecology or parasitology, and graduate courses in the successful candidate's area of expertise.

For the **Cellular & Molecular Immunology** position we seek applicants with research interests in all areas of innate and/or adaptive immunology, including but not limited to comparative immunology, inflammation biology, and computational immunology. Candidates using model or non-model organisms, including invertebrates and plants, are encouraged to apply. Teaching responsibilities will include an undergraduate course in immunology and one or more graduate courses in the successful candidate's area of expertise.

Candidates for all positions must have a Ph.D. in the Biological Sciences or a related field and postdoctoral (or equivalent job) experience. Evidence of significant intellectual contributions to their respective fields and a demonstrated commitment to teaching at both the undergraduate and graduate levels are also required. The successful applicants will also be expected to establish extramurally funded and relevant research programs.

A complete application includes (1) an application letter; (2) CV; (3) statement of research interests and goals; (4) statement of teaching interests and philosophy; and (5) a list of at least four references (including contact information). Letters of reference will be requested by the search committee as appropriate.

To apply, go to <https://facultyjobs.ua.edu/postings/37672> for the Plant Systematics position; <https://facultyjobs.ua.edu/postings/37673> for the Disease Ecology position; or <http://facultyjobs.ua.edu/postings/37667> for the Cellular & Molecular Immunology position; complete the online application and upload all requested documents.

Questions about the Plant Systematics position may be addressed to Dr. Juan Lopez-Bautista (jlopez@ua.edu; 205-348-1791). Questions about the Disease Ecology position may be addressed to Dr. Ryan Earley (rearley@ua.edu; 205-348-1827). Questions about the Cellular & Molecular Immunology position may be addressed to Dr. Matthew Jenny (mijenny@ua.edu; 205-348-8225). Consideration of applications will begin October 28, 2015 and will continue until the positions are filled. Prior to hiring, the final candidates will be required to pass a pre-employment background investigation. The anticipated start date is August 16, 2016. Additional information about the Department of Biological Sciences and this available position can be found on our website at <http://bsc.ua.edu>. Applications from minority and members of traditionally under-represented groups in Biology are especially encouraged. The University of Alabama is an Equal Opportunity/Equal Access Employer and actively seeks diversity among its employees.





Come work with us!

Faculty Position

Department of Materials Science and Engineering

The Department of Materials Science and Engineering (DMSE) seeks candidates for open tenure-track faculty positions to begin July 2016 or thereafter. Appointments would be at the assistant or untenured associate professor level and will be located in Cambridge, Massachusetts. In special cases, a senior faculty appointment may be possible. Faculty duties include teaching at the graduate and undergraduate levels, research, and supervision of student research.

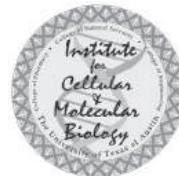
Candidates should hold a Ph.D. in Materials Science and Engineering or a related field by the start of employment. DMSE intends to broaden its research portfolio in computational materials science and in particular seeks candidates who conduct research in theory, modeling and simulation of materials. All areas of computational materials science and materials classes will be considered, including application and development of first-principles methods; materials theory; data-driven design and discovery of materials; and development and application of meso-scale, multi-scale, and multi-physics methods.

DMSE has strengths and interests across the full spectrum of materials science and engineering, and excellent candidates with expertise in any and all areas of the field are welcomed. This includes candidates who can engage with Institute initiatives in Manufacturing, Energy, Environment, Health, and Data.

Interested candidates should submit application materials electronically at <http://dmsefacsrch.mit.edu>. Each application should include: a curriculum vitae; a statement of research interests; and a statement of teaching interests. We request that each candidate arrange for 3 letters of reference to be uploaded at <http://dmsefacsrch.mit.edu/letters/>. Questions should be addressed to DMSE-Search-Master@dmsefacsrch.mit.edu. Responses received by December 31, 2015, will be given priority. No application received after March 1, 2016, will be considered in this year's search.

MIT is an Equal Opportunity/Affirmative Action employer. MIT is committed to diversity in engineering education, research and practice, and we especially encourage minorities and women to apply.

<http://web.mit.edu>



The Institute for Cellular and Molecular Biology (ICMB), at the University of Texas at Austin, is seeking a level III Director for the Genomic Sequencing and Analysis Facility (GSAF). Established in 2008 and housed in 2,000+ square feet of controlled-access laboratory space, the GSAF provides next-generation DNA sequencing (NGS) services, including sample preparation and sequencing, for a wide variety of applications.

This position requires a PhD in the life sciences or engineering, at least 5 years experience with next-generation sequencing and related technologies, and working knowledge of bioinformatics and laboratory information management systems. An equivalent combination of relevant education and experience may be substituted as appropriate. Preferred qualifications include experience in data analysis and the use of NGS tools including command-line utilities, R, bash and python.

Additional information about the GSAF and the Institute may be found at <https://www.icmb.utexas.edu/research/core-facilities/gsaf> or <https://www.icmb.utexas.edu>

Interested individuals are encouraged to apply at <http://www.utexas.edu/hr/prospective/apply/process.html> for job posting **15-09-09-01-0421**

Applications and inquiries should be addressed to the Search Committee chair, Dr. Rick Russell (rick_russell@cm.utexas.edu).

Austin is located in the Texas Hill Country and is widely recognized as one of America's most beautiful and livable cities.

The University of Texas at Austin is an Equal Opportunity Employer. Qualified women and minorities are encouraged to apply; a background check will be conducted on the applicant selected.

Cell Biology Feature

Issue date: December 4, 2015
Reserve ads by November 17

Ads accepted until November 30 on a first-come, first-served basis

For recruitment in science, there's only one **Science**

Looking to hire cell biologists?

Why choose this cell biology feature for your advertisement?

- Relevant ads lead off the career section with special cell biology banner
- Bonus distribution to the American Society for Cell Biology meeting, December 12–16 in San Diego, CA.



SCIENCECAREERS.ORG

To book your ad: advertise@sciencecareers.org

The Americas: 202-326-6582

Europe/RoW: +44-0-1223-326500

Japan: +81-3-3219-5777

China/Korea/Singapore/Taiwan: +86-186-0082-9345

ScienceCareers
FROM THE JOURNAL SCIENCE AAAS

POSITION OPEN

PROFESSOR OF PRACTICE Ecology and Evolutionary Biology

The Department of Ecology and Evolutionary Biology, Tulane University, invites applications for one full-time, non-tenure-track Professor of Practice beginning fall 2016. Candidates must hold a Ph.D. in biological sciences and have teaching experience at college level, preferably with experience in active learning. We seek an individual with expertise in ecology, evolution and organismal biology as well as commitment to excellence in undergraduate education and scholarship of teaching and learning. For more details about the position, department, search and applications, see website: <http://tulane.edu/sse/ecbio/about/positions>. Apply to website: <http://apply.interfolio.com/32032>. Review of applications will begin November 15 2015, and the search will remain open until the position is filled. *Tulane is an Equal Opportunity Employer/ Male/Female/Veteran/Disabled Employer.*



Join the Conversation!

Twitter is a great way to connect with AAAS members and staff about the issues that matter to you most. Be a part of the discussion while staying up-to-date on the latest news and information about your personal member benefits.

Follow us @AAASmember
and join the conversation
with #AAAS



Post Your Jobs

1 million candidates*
151,000 job applications*



Reach Scientists.
Fill Positions.

*Jan-Dec 2014

ScienceCareers
employers.sciencecareers.org



Institute for Systems Genetics New York, NY

The newly formed Institute for Systems Genetics at NYU Langone Medical Center invites applications for tenure-track faculty positions at the assistant professor level. The Institute, headed by Jef Boeke, Ph.D., will combine the latest technologies in systems, sequence and synthetic biology to tackle fundamental and translational questions in genetics and epigenetics. The Institute occupies new space which is designed to foster highly collaborative and innovative research, and operate side-by-side with new initiatives in metabolism, microbiology, cancer biology, and immunology to complement the vibrant overall biomedical research environment at NYU Langone Medical Center, as well as the growing 'omics community in New York City. State-of-the-art genomics, proteomics, and robotics facilities will be integral components of the Institute, and will leverage outstanding existing core facilities at NYU School of Medicine. Collaborations with the New York Genome Center and related entities will be encouraged. We seek junior colleagues with hypothesis-driven research programs that exploit:

- Human genetics and genomics
- Proteomics
- Functional genomics
- Synthetic biology/genome engineering
- High throughput imaging or phenotyping

Candidates from nontraditional backgrounds such as computer science, engineering, physics, chemistry and mathematics are encouraged to apply. The successful candidate will hold a primary appointment in one of the many relevant NYU School of Medicine Departments, and will have opportunities to participate in one or more graduate programs.

For consideration, candidates should send a CV, research plan, and the name, telephone number and email address of four references (consolidated into a single pdf document) by **12/31/15**, to: ISGNYUjobs2015@gmail.com. Candidates are responsible for having their referees send their recommendations. Incomplete applications will not be considered.

NYU Langone Medical Center is an Equal Opportunity Employer.



CHAIR, DIVISION OF MICROBIOLOGY TULANE NATIONAL PRIMATE RESEARCH CENTER TULANE UNIVERSITY

The Tulane National Primate Research Center (TNPRC) is seeking an accomplished dynamic leader to chair its Division of Microbiology. The Division currently consists of 8 faculty members with research programs involving AIDS, tuberculosis, emerging infectious diseases and biodefense. Work in these areas includes a focus on disease pathogenesis and applying this information to development of vaccines, diagnostics and therapeutics. Funding for the Division is approximately \$5.6M for the current year, predominantly from NIH.

The Chair of the Division will be appointed at the rank of Associate, or Full Professor. The academic appointment will be in an appropriate Department of either the Tulane University School of Medicine (SOM) or the Department of Tropical Medicine of the Tulane School of Public Health and Tropical Medicine (SPHTM). Significant collaborations exist among the TNPRC, SOM and SPHTM which offer unique and highly synergistic resources and opportunities.

The research portfolio and infrastructure of the TNPRC are focused primarily on nonhuman primate models of disease but other animal models are also available. The successful candidate will be expected to contribute to existing research programs and to build or bring their own independent research agenda. All necessary resources to assure that the candidate is successful will be provided including ample laboratory and office space and administrative assistance.

The TNPRC has excellent infrastructure to support collaborative and independent research using nonhuman primates. In addition to holding one of the largest colonies of nonhuman primates in the country, the TNPRC is the only National Primate Research Center that houses a Regional Biosafety Laboratory, to support research under the NIH/NIAID National Biodefense Program. Research resources include extensive BSL2/ABSL2 and BSL3/ABSL3 facilities and highly integrated clinical and laboratory support for studies using nonhuman primates. This includes a full time staff of clinical veterinarians and technicians and core services including: (1) Anatomic Pathology, (2) Biotelemetry, (3) Cellular Immunology, (4) Clinical Pathology, (5) Confocal Microscopy and Image Analysis, (6) Diagnostic Parasitology, (7) DNA Microarray and Gene Expression, (8) Flow Cytometry, (9) Infectious Disease Aerobiology, (10) Pathogen Detection and Quantification, (11) Vector-Borne Diseases (maintains arthropod vectors such as anopheline mosquitoes for malaria research, and tick-borne disease vectors), (12) Virus Characterization, Isolation and Production. More information is available at the following link <http://tulane.edu/tmprc/research/resources>.

To apply, send a letter indicating your research interests and experience, a statement of your "administrative philosophy", a curriculum vitae, and the names of three individuals who may be contacted for references to: **Ms. Debbie Dawsey, Coordinator, TNPRC Search Committee, Tulane National Primate Research Center, 18703 Three Rivers Road, Covington, LA 70433.** E-mail: ddawsey@tulane.edu.

Tulane University is an Affirmative Action and Equal Opportunity Educator and Employer. Women and minorities are strongly encouraged to apply.

By Xin Lu

The rewards of roughing it

Modern life, concentrated in cities and lived online, is corroding many young people's innate love for nature. Much of science, too, is moving away from fieldwork. Biology is increasingly lab-based, and much important earth science research is now done in front of a computer screen rather than out in the physical world. As an ornithologist working on the Tibetan Plateau, I've found fieldwork both scientifically and spiritually rewarding. My experience has convinced me that any young scientist involved in revealing natural processes at a macro scale should seize opportunities for fieldwork, which enriches not only one's science but one's life.

I first visited Tibet in 1995, as a Ph.D. student enrolled at Beijing Normal University. To reach the study site in southeastern Tibet, I traveled for 3 days in a jeep from Lhasa to a small town, and for another 3 days riding a horse through virgin forests. I stayed there for 6 months to study the ecology and social behavior of Tibetan eared pheasants. In 1997, after I joined Wuhan University as a faculty member, I continued my work from a Buddhist nunnery in the mountains around the middle of the Yarlung Tsangpo River in southern Tibet. The nunnery served as my field station for studying alpine birds until 2004. Since then, I have focused my research on grassland birds in northern Tibet.

Doing fieldwork on the cold, windy, and oxygen-poor Tibetan Plateau is a challenge for anybody. I have struggled through deep valleys, climbed steep cliffs, cooked my meals using firewood for fuel, and lain in an unheated hut without electricity, missing my family. Nevertheless, the thrill of discovering the unknown world has eased the physical and emotional hardships. It's fun to probe the enigmas of the highland birds' natural history, which ornithologists have never before unraveled.

Besides academic payoffs, fieldwork offers emotional and spiritual rewards. The molecules and cells that other biologists study in their labs are full of wonder, but they can't be directly seen or heard. In contrast, mountains and glaciers, rivers and lakes, and plants and animals excite the senses, inspiring anyone with poetry in their souls. I'm a conservationist and amateur writer of fairy tales. Getting into the fantastic wild of Tibet through fieldwork feeds my imagination and inspires me to view the world in ways that go beyond science.

Gaining an in-depth understanding of local culture is another unique charm of fieldwork. I have watched Buddhist banners flying in the blue sky, and I have heard Buddhist



"I've found fieldwork both scientifically and spiritually rewarding."

nuns chanting to morning bells and evening drums. I have experienced the generosity of Tibetan villagers who, despite the hardships they have suffered, always gave me as much help as they could when I needed shelter, food, horses, and dogs.

Fieldwork teaches me that struggle can lead to joy. After an exhausting search through thorny undergrowth, I have the pleasure of discovering a bird's nest. After hours of hunger, I can enjoy a Tibetan-style lunch near a stream. After a day of climbing, sleeping in a rough bed under the stars is a delight. And all that physical hardship makes my body stronger. While sitting at high elevations, a person burns far more calories than she or he would at rest in the lowlands, according to physiologists. Add to that the trekking and climbing, and I return from fieldwork with a bonus in fitness.

I cherish my memories of field time: singing loudly on horseback, petting the villager's dog that had safeguarded me against bears, getting lost in forests filled with misty rain. All those memories are a kind of wealth—a reward that goes beyond the scientific papers I have published about my findings. My attitude toward fieldwork is influencing my students. Following in my footsteps, they go to the Tibetan Plateau every year, dedicating their youth, talent, and love to alpine ornithology. I like to think they feel as fortunate and happy as I do. ■

Xin Lu is a professor of zoology at Wuhan University in China and the co-director of the Wuhan University-Tibet University Field Research Station for Tibetan Wildlife. He is vice president of the China Ornithological Society. He would like to thank Ronna Edelstein, Lugene Calderone, and Marinne Renton for comments. For more on life and careers, visit sciencecareers.org. Send your story to SciCareerEditor@aaas.org.